Many-body quantum phases of dipolar gases

– DISSERTATION –

by

Claudia Politi, MSc.

submitted to the Faculty of Mathematics, Computer Science, and Physics of the University of Innsbruck

in partial fulfillment of the requirements
for the degree of Doctor of Philosophy (PhD)

advisors:
Univ. - Prof. Dr. Francesca Ferlaino,
Institute for Experimental Physics, University of Innsbruck
Institute for Quantum Optics and Quantum Information of the Austrian Academy of Sciences

Univ. - Prof. Dr. Helmut Ritsch,
Institute for Theoretical Physics, University of Innsbruck

Innsbruck, December 2022

To my family and to the game of basketball,
for teaching me the values of perseverance,
respect, teamwork, and the importance of
"rest at the end and not in the middle".

Declaration

I hereby declare that I have written this dissertation independently and have not used any sources other than those specified. All passages that were taken from the specified sources, either verbatim or in terms of content, are marked as such. This dissertation has not yet been submitted as a scientific work in the same or a similar form in this, or any other university.

Claudia Politi, MSc.

Innsbruck, December 2022

Synopsis

Since the realization of the first Bose-Einstein condensate in 1995, the number of quantum-gas experiments grew enormously, involving different atomic species ranging from alkali metals, such as rubidium, to triel elements, with the new-come indium. This huge interest is motivated by the high control that quantum gases offer in terms of interatomic interactions, dimensionality of the system, and the possibility of adding complexity in a controlled manner. For this reason, in the past decades, ultracold atoms revealed to be ideal platforms for simulating many-body phenomena, linked to various fields as condensed-matter physics, high-energy physics, and quantum optics.

Ultracold gases interact usually with a short-range and isotropic contact-type interaction. The achievement of degenerate gases with highly-magnetic atoms, such as chromium, erbium, dysprosium, and just recently thulium and europium, which possess a permanent magnetic moment in the ground state, led to richer interactions, showing a long-range and anisotropic nature. The addition of this new ingredient to the quantum-gas tool box brought to the discovery of interesting many-body phases, as quantum droplets, and supersolid states, showing both superfluid and crystalline order.

The work presented in this thesis focuses on two main topics. The first part reports on the investigation of the interspecies interactions between the two highly magnetic lanthanides, erbium and dysprosium, with a focus on the role played by the dipole-dipole interaction. It presents an alternative method to estimate the interspecies scattering length from the in-trap clouds displacement, and it shows how tuning the interspecies repulsion can lead to binary supersolid states.

The second part focuses on the creation of a dipolar supersolid state with dysprosium atoms. It first gives insights on the role played by finite temperatures in the superfluid-to-supersolid phase transition. It then presents the first realization of two-dimensional supersolid states, first in a zig-zag pattern, and then in a hexagon pattern. The realization of two-dimensional supersolidity opens the door to many research directions,

such as the investigation of the excitation modes, quantized vortices, and persistent currents.

Zusammenfassung

Seit der Realisierung des ersten Bose-Einstein-Kondensats im Jahr 1995 hat die Zahl der Quantengasexperimente enorm zugenommen, wobei verschiedene Atomarten von Alkalimetallen wie Rubidium bis zu Trielelementen mit dem neu hinzugekommenen Indium einbezogen wurden. Dieses enorme Interesse wird durch die hohe Kontrolle motiviert, die Quantengase in Bezug auf interatomare Wechselwirkungen, die Dimensionalität des Systems und die Möglichkeit, Komplexität auf kontrollierte Weise hinzuzufügen, bieten. Aus diesem Grund haben sich ultrakalte Atome in den vergangenen Jahrzehnten als ideale Plattformen für die Simulation von Vielteilchenphänomenen erwiesen, die mit verschiedenen Bereichen wie der Physik der kondensierten Materie, der Hochenergiephysik und der Quantenoptik verknüpft sind.

Ultrakalte Gase interagieren normalerweise mit einer kurzreichweitigen und isotropen Wechselwirkung, einer sogenannten Kontaktwechselwirkung. Das Erreichen entarteter Gase mit hochmagnetischen Atomen wie Chrom, Erbium, Dysprosium und erst kürzlich Thulium und Europium, die im Grundzustand ein permanentes magnetisches Moment besitzen, ermöglichte die Nutzung von Wechselwirkungen, die eine langreichweitige und anisotrope Natur zeigen. Die Aufnahme dieses neuen Inhaltsstoffs in die Quantengas-Werkzeugkiste führte zur Entdeckung exotischer Vielteilchenphasen wie Quantentröpfchen und suprasolide Zustände, die sowohl eine supraflüssige als auch eine kristalline Ordnung zeigen.

Diese Dissertation konzentriert sich auf zwei Hauptthemen. Der erste Teil berichtet über die Untersuchung der Interspezies-Wechselwirkungen zwischen den beiden hochmagnetischen Lanthanoiden Erbium und Dysprosium, wobei der Schwerpunkt auf der Rolle der Dipol-Dipol-Wechselwirkung liegt. Wir beschreiben eine alternative Methode zur Abschätzung der Interspezies-Streulänge aus der Verschiebung der Wolken innerhalb der Falle und zeigen, wie die Abstimmung der Interspezies-Abstoßung zu binären suprasoliden Zuständen führen kann.

Der zweite Teil konzentriert sich auf die Erzeugung eines dipolaren Suprasolids mit Dysprosiumatomen. Zunächst wird diskutiert, welche Rolle endliche Temperaturen

beim Phasenübergang von suprafluid zu suprasolid spielen. Danach präsentieren wir die erste Realisierung von zweidimensionalen Suprasoliden, zuerst in einem Zick-Zack-Muster und dann in einem Hexagon-Muster. Die Realisierung der zweidimensionalen Supersolidität öffnet die Tür zu vielen Forschungsrichtungen, wie der Untersuchung von Anregungsmoden, quantisierten Wirbeln und Dauerströmen.

Contents

Introduction

Since the first experimental realization of a Bose-Einstein condensate (BEC) [5, 35, 48] and a degenerate Fermi gas (dFg) [53], ultracold gases have demonstrated to be ideal platforms to study many-body quantum phenomena. Prominent examples are the observation of long-range phase coherence [28] and quantized vortices [1, 121, 124], common to superconductivity and superfluidity. Furthermore, ultracold gases feature several attractive properties, as the tunability of the atomic interactions via Feshbach resonances [39], and the possibility of changing the dimensionality of the system and realizing ideal strong periodic potentials, through the use of far off-resonant laser light. These features led to the investigation of strongly correlated regimes, as the superfluid-to-Mott insulator transition [70] and Bardeen–Cooper–Schrieffer (BCS) pairing [13, 33, 164]. It is clear now that quantum gases represent a powerful tool for simulating and understanding complex condensed-matter problems, as well as engineering novel quantum phases that have not been observed yet.

In ultracold gases, the form of the atomic interactions strongly affects the quantum phases and the system's dynamics. For this reason, in the last 20 years, a lot of experimental effort was spent in creating ultracold gases with richer interactions, e.g. long-range and anisotropic dipole-dipole interactions. The addition of this ingredient to ultracold systems led to interesting predictions of many-body phases in optical lattices, such as charged-density wave and supersolid phases, where superfluidity and crystalline order coexist [11]. Another way of enriching the atomic interactions is through atomic mixtures. In fact, by tuning the interspecies interactions, miscible and immiscible quantum phases have been experimentally observed in alkali mixtures made of two spin states [178], two different isotopes of the same species [142], or two species [126]. Theoretical works predict that dipole-dipole interactions add interesting features to miscible and immiscible phases [69, 101, 195]. Moreover, exotic supersolid phases are predicted to appear due to the competition between intra- and interspecies interactions both in optical lattices [36, 186] and in the bulk [26, 169].

Long-range interaction can be achieved in different ways. In ultracold-gas experiments, it can arise from strong magnetic or electric dipole moments, as in magnetic lanthanides, and hetero-nuclear molecules and Rydberg atoms [106], respectively. Moreover, by placing the atomic cloud in an optical resonator, long-range interactions can be achieved by coupling the atoms to a single or multiple modes of the cavity [14, 123, 131]. Finally, long-range interactions can be engineered via atom-light interactions, see e.g. Refs. [68, 140]. Each of these platforms is characterized by a different strength of the long-range interactions, which makes them unique for investigating various phenomena. For instance, in magnetic lanthanides, such as erbium and dysprosium, short-range and long-range interactions have similar strength and can compete with each other giving rise to exotic quantum phases, as discussed in this thesis.

In 2003, theoretical works [139, 168] predicted that this competition leads to the appearance of a roton-maxon excitation spectrum, a precursor of crystallization, which is a fundamental ingredient for supersolidity. Experimentally, the investigation of quantum gases possessing a large permanent magnetic moment started in 2005 with the realization of a Bose-Einstein condensate of chromium atoms [71]. Chromium was followed, in 2011 and 2012, by dysprosium [119] and erbium [3], respectively. The list of Bose-condensed magnetic lanthanides continues to grow, and more recently includes thulium [49] as well as europium [129]. Breakthrough experiments, as the observation of the roton mode in erbium [44] and the realization of a density-modulated state with dysprosium [91], in a regime in which the mean-field physics predicts a collapse, led to the discovery of the supersolid state in 2019 [32, 42, 182].

The Er-Dy experiment in Innsbruck, which is the focus of this work, links together the world of hetero-nuclear mixtures with the one of magnetic lanthanides with long-range interactions. This enables to perform experiments with erbium, or dysprosium, but also combining the two. Since the first realization of double BECs of erbium and dysprosium, and the creation of a single-component long-lived supersolid state with dysprosium, the experiment has improved the knowledge of dipolar gases, including the recent works presented in this thesis, such as the first experimental realization of two-dimensional supersolidity.

During my PhD in the Er-Dy experiment, I contributed to two main research topics: the investigation of erbium-dysprosium quantum mixtures, and the study of supersolidity in dipolar quantum gases of dysprosium atoms. This resulted in a total of 12 publications, among which 7 constitute the core of this thesis.

Erbium-dysprosium quantum mixtures. When I started my PhD in January 2018, the team was working on the realization of the first dipolar quantum mixtures of erbium and dysprosium. This study revealed a first hint of repulsive interaction between the species, from a shift and a deformation of the atomic clouds. This brought to one of the main results of this thesis. In fact, in collaboration with M. Modugno from the University of the Basque Country in Bilbao (Spain), we investigated the interspecies interactions in an erbium-dysprosium quantum mixture, with a focus on the role played by the dipole-dipole interactions. Furthermore, by probing the in-trap clouds displacement as a function of the magnetic-field orientation, and by comparing our experimental results to ground-state calculations, we were able to estimate the interspecies scattering length. This study is reported in the publication below:

- *Interspecies interactions in an ultracold dipolar mixture.*
  C. Politi, A. Trautmann, P. Ilzhöfer, G. Durastante, M. J. Mark, M. Modugno, and F. Ferlaino,
  Phys. Rev. A, 105, 023304 (2022)

Supersolidity with dysprosium atoms. Another topic on which I contributed during my PhD is the realization and the investigation of supersolidity in dipolar quantum gases of dysprosium atoms. This subject can be divided in two more branches: one-dimensional supersolid states, where the system consists of a linear chain of quantum droplets linked to each other via a superfluid background, and two-dimensional supersolid states, where the supersolid properties are extended along two directions.

Regarding the first research branch, we investigated the formation of a supersolid state via evaporative cooling from a thermal cloud, from the birth until its disappearance. Moreover, in collaboration with the group of T. Pohl at Aarhus University (Denmark), we proved the important role played by thermal fluctuations in the formation of supersolid states. These works are presented in the following publications:

- *Birth, life, and death of a dipolar supersolid.*
  M. Sohmen, C. Politi, L. Klaus, L. Chomaz, M. J. Mark, M. A. Norcia, and F. Ferlaino,
  Phys. Rev. Lett.,126, 233401 (2021)

- *Heating a quantum dipolar fluid into a solid.*
  J. Sanchez-Baena, C. Politi, F. Maucher, F. Ferlaino, and T. Pohl,
  arXiv:2209.00335 (2022)

In the second research branch, we were able to extend, for the first time, the supersolid properties from one to two dimensions. In particular, we performed a structural phase transition from a linear supersolid state to, first, a supersolid made of quantum droplets arranged in a zig-zag pattern, and then in an isotropic hexagon configuration. The realization of such supersolid states opened many research directions. For instance, we investigated the excitations of two-dimensional supersolids, including angular oscillations and their role as a potential probe of the superfluid fraction in dipolar supersolids. The publications related to this research topic are listed below:

- *Two-dimensional supersolidity in a dipolar quantum gas.*
  M. A. Norcia*, C. Politi*, L. Klaus, E. Poli, M. Sohmen, M. J. Mark, R. Bisset, L. Santos, and F. Ferlaino,
  Nature 596, 357 (2021)
  *These authors contributed equally.

- *Maintaining supersolidity in one and two dimensions.*
  E. Poli, T. Bland, C. Politi, L. Klaus, M. A. Norcia, F. Ferlaino, R. N. Bisset, and L. Santos.,
  Phys. Rev. A, 104, 063307 (2021)

- *Two-dimensional supersolid formation in dipolar condensates.*
  T. Bland, E. Poli, C. Politi, L. Klaus, M. A. Norcia, F. Ferlaino, L. Santos, and R. N. Bisset,
  Phys. Rev. Lett., 128, 195302 (2022)

- *Can angular oscillations probe superfluidity in dipolar supersolids?*
  M. A. Norcia, E. Poli, C. Politi, L. Klaus, T. Bland, M. J. Mark, L. Santos, R. N. Bisset, and F. Ferlaino,
  Phys. Rev. Lett., 129, 040403 (2022)

Thesis overview

This thesis work consists of four chapters, which are briefly introduced below.

Chapter 1 gives an overview on supersolidity, mentioning the experimental efforts in solid helium and the results achieved with ultracold gases. It then introduces the main ingredients necessary to realize supersolidity in ultracold dipolar gases. Finally, it describes the extended Gross-Pitaevskii equation with the beyond mean-field term,

which constitutes the main theoretical tool to represent various quantum phases of a dipolar gas.

Chapter 2 describes the basic properties of erbium and dysprosium atoms, as the electronic configuration and the optical transitions used to cool, manipulate and image the atoms. It then gives a brief overview of the experimental apparatus with a focus on the optical-dipole-trap setup used to confine the atomic cloud and produce supersolid states.

Chapter 3 focuses on the first main result of this thesis: the study of the interspecies interactions in an erbium-dysprosium mixture. First, it gives an overview on heteronuclear mixture experiments and describes the experimental tools commonly used to determine the interspecies scattering lengths. It then introduces the method developed in our experiment to estimate the interspecies scattering length from the in-trap displacement between the clouds. Finally, it gives an outlook on the interesting quantum phases achievable by tuning the erbium-dysprosium interactions.

Chapter 4 is dedicated to the investigation of supersolidity in a cloud of dysprosium atoms. This chapter first presents the technique developed in our experiment to create supersolid states by directly evaporating from a thermal cloud and describes the tools we use to probe such a state. It then focuses on the role played by finite temperatures. Finally, it describes how to create two-dimensional supersolid states and it gives an overview of the many research directions that this state offers, with the investigation of excitation modes and quantized vortices.

Additional publications

Beside the above listed publications, in the past five years, I also contributed to other publications which are not discussed in this thesis work. These publications are presented in the Appendix A and listed below:

- *Dipolar Quantum Mixtures of Erbium and Dysprosium Atoms.*
  A. Trautmann*, P. Ilzhöfer*, G. Durastante, C. Politi, M. Sohmen, M. J. Mark, and F. Ferlaino,
  Phys. Rev. Lett., 121, 213601 (2018)
  *These authors contributed equally.

- *Long-lived and transient supersolid behaviors in dipolar quantum gases.*
  L. Chomaz, D. Petter, P. Ilzhöfer, G. Natale, A. Trautmann, C. Politi, G. Durastante, R. M. W. van Bijnen, A. Patscheider, M. Sohmen, M. J. Mark, and F. Ferlaino,
  Phys. Rev. X, 9, 021012 (2019)

- *Feshbach resonances in an erbium-dysprosium dipolar mixture.*
  G. Durastante, C. Politi, M. Sohmen, P. Ilzhöfer, M. J. Mark, M. A. Norcia, and F. Ferlaino,
  Phys. Rev. A, 102, 033330 (2020)

- *Phase coherence in out-of-equilibrium supersolid states of ultracold dipolar atoms.*
  P. Ilzhöfer*, M. Sohmen*, G. Durastante, C. Politi, A. Trautmann, G. Natale, G. Morpurgo, T. Giamarchi, L. Chomaz, M. J. Mark, and F. Ferlaino,
  Nature Physics 17, 356-361 (2021)
  *These authors contributed equally.

- *Observation of vortices and vortex stripes in a dipolar Bose-Einstein condensate.*
  L. Klaus*, T. Bland*, E. Poli, C. Politi, G. Lamporesi, E. Casotti, R. N. Bisset, M. J. Mark, and F. Ferlaino,
  Nature Physics (2022)
  *These authors contributed equally.

Chapter 1

Supersolidity in dipolar quantum gases

Supersolidity is a counterintuitive state of matter, combining both density modulation and superfluid properties. Initially predicted in the late '50s by E. P. Gross for a system of interacting bosons [73], it was intensively searched in consensed-matter systems, with solid helium as the prime candidate. However, the limited control of interactions and imperfections in solid-state systems have pushed the theoretical investigations towards ultracold atoms. It was then about a decade ago that the supersolid physics became a topic of growing interest for the ultracold-gas community, triggered by the high degree of control over many-body systems, e.g. over the interatomic interactions, geometry, and dimensionality. In 2010, and later in 2017, two experimental groups reported the observation of supersolid properties using two different settings: BECs of rubidium atoms with cavity-mediated interactions [14, 112], and spin mixtures of sodium atoms coupled via a two-photon Raman transition [114]. More recently, experiments with dipolar gases of erbium and dysprosium, including the ones in our group, demonstrated the existence of a supersolid state intrinsically arising from the competition between the contact interactions and the long-range anisotropic dipole-dipole interactions (DDI) [32, 42, 182]. This chapter gives a brief historical overview of supersolidity and introduces the key ingredients to achieve simultaneous density modulation and global phase coherence in dipolar gases. Finally, the last section recalls the Gross-Pitaevskii equation and the relevant energy terms necessary to describe an ultracold gas of dipolar atoms.

1.1 Brief historical overview

Supersolidity was for the first time predicted in 1957 by Gross [72, 73]. In his works, Gross considered a system of bosonic particles in a box, interacting via a two-body potential, and demonstrated that, together with the standard uniform solution, for strong enough attractive interactions, a ground state showing periodic density modulation exists. In these seminal papers, Gross investigated the excitations of such a system and showed that at long wavelengths they have a phonon character, while at short wavelengths they have a band character. These works unify for the first time the theory of superfluidity and solids. Such a prediction have been object of theoretical controversies with notable works by Penrose and Onsager [146], who pointed out that localization and superfluidity are competing orders. However, over the years, the existence of supersolidity as a possible quantum state gathered momentum, with several theoretical works on this topic [6, 38, 111, 199]. Among them, Leggett suggested an experimental measurement to determine the presence of superfluidity in solid He, through the detection of a reduction of the moment of inertia with respect to the classical value, below the critical temperature for superfluidity [111].

Experimental efforts in helium. Helium has always been considered a prime candidate for observing supersolidity. This arises from its special quantum properties with respect to other solids. In fact, its light mass and weak interatomic potential leads to an exceptional high zero-point energy with respect to the depth of the molecular potential wells for helium atoms, leading to an exchange of atoms via tunneling, which makes the Bose (^{4}He) or Fermi (^{3}He) statistics relevant even in the solid phase [16]. As known, helium has two liquid phases, with a superfluid phase at temperatures below the λ transition at about 2K. A fundamental property arising from the large zero-point energy and that distinguishes liquid helium from other liquids, is the possibility of reaching the solid phase only by applying a pressure greater than about 2MPa.

Following Leggett's suggestion to determine the superfluid fraction, several experiments used a torsional oscillator to investigate the properties of solid helium. The torsional oscillator consists of a cell filled with He connected to a base via a torsional rod. The resonant frequency of this oscillator can be directly connected to the moment of inertia I through the relation $f_{\text{res}} = (1/2\pi)\sqrt{K/I}$, where K is the torsional stiffness. At constant K, a reduction of the moment of inertia can be directly connected to an increase of f_{res}, suggesting a transition to a supersolid phase, with the superfluid part decoupling from the rest of the oscillator [15].

In 2004, Kim and Chan performed a measurement of the resonant frequency and observed an increase when lowering the temperature below 200mK [95, 96]. They attributed this behaviour to a possible transition to a supersolid state. Several experimental works tried to replicate Kim and Chan's observation, with most of them showing qualitative agreement. However, in 2007, Day and Beamish reported on the experimental determination of the shear modulus of solid helium as a function of the temperature [50]. The authors measured an increase of stiffness when lowering the temperature below a critical value, which was consistent with the critical temperature to observe the increase of the resonant frequency in the torsional-oscillator experiment. This behaviour was confirmed by a later work [82] and it is attributed to the motion of crystal defects, which changes with temperature.

The temperature dependence of the shear modulus started to pose doubts on the observation of supersolidity claimed by Kim and Chan, and in 2012 this claim was disproved, see Ref. [94]. It is now clear that the increase in the resonant frequency is related to a change in the shear modulus μ_{shear}, and therefore a change in the stiffness K, rather than to a variation in the superfluid fraction. This was confirmed in 2016, when a simultaneous measurement of the torsional oscillation frequency and the shear modulus showed that the two quantities exhibited identical dependences on temperature, driving frequency, and ^{3}He impurities. A different behaviour with the driving amplitude was observed, but this was confirmed to be induced by a change in the elastic properties of solid ^{4}He [172].

Ultracold quantum gases. The fast development of new techniques for controlling and detecting ultracold atoms, makes these systems an ideal platform for investigating many-body phenomena and overcome the issues related to imperfections and complexity of condensed matter systems. For these reasons, in the quest for supersolidity, a lot of theoretical effort moved in the direction of ultracold atoms. In 2010 and in 2017, states with supersolid properties were observed in experiments with Bose-Einstein condensates (BECs) coupled to light [14, 112, 114]. In particular, two different methods were used. In one experiment, in 2010, rubidium atoms were coupled to the light field of an optical cavity and a phase transition to a modulated state was observed [14]. Some years later, the supersolid properties were confirmed in similar settings [112]. In a second experiment, in 2017, the supersolid properties were achieved by inducing spin-orbit coupling in an ultracold spin mixture of sodium atoms [114].

In the meantime, ultracold systems with dipolar interaction started to draw great attention in the community, because of the momentum dependence of the interactions.

Theoretical works predicted a supersolid phase for ultracold systems with a soft-core potential, achievable in the experiment via Rydberg excitation [46, 83, 203]. This idea followed the prediction by Andreev and Lifshitz [6], and Chester [38] of a solid phase where particles can flow without friction due to the presence of zero-point defects. A system interacts via a soft-core potential if the interatomic potential assumes a constant value $V_{\text{soft}} > 0$ for distances r smaller than the particle diameter and zero otherwise. This means that, as the density increases, it is more energetically favourable for the system to cluster some particles together, leaving empty cells. In a lattice, this translates in the possibility of tunnelling between different lattice sites and defects delocalization, favouring superfluid motion inside the crystal [47].

Other promising candidates for supersolidity were polar molecules and ultracold gases with magnetic dipole-dipole interactions [120]. An important turning point in the quest of supersolidity in the ultracold realm was the observation of the roton mode and its softening with erbium atoms in experiments in Innsbruck [45]. Later on, the same experiment demonstrated the existence of a roton-maxon excitation spectrum [150]. More breakthrough experiments with dysprosium experimentally proved the transition to a density modulated state in a parameter regime where the mean-field theory predicts a collapse [91]. However, the proof of global phase coherence had to wait until 2019, when supersolidity in dipolar gases was simultaneously proved in three experiments, including ours, by tuning the interactions [32, 42, 182]. Moreover, in our experiment, we were able to prove direct evaporative cooling into a supersolid state and achieve lifetime on the order of seconds [42, 177].

1.2 Supersolidity in dipolar gases: main ingredients

Supersolidity is a phase of matter whose properties challenge our imagination due to the antithetical behaviours of solids and superfluids. There are different ways to address this challenge. One can consider a solid and ask the question "Can a solid be superfluid?", such as for example the quest of supersolidity in solid He. For ultracold dipolar gases, which are superfluids, the question is reversed and becomes "Can a superfluid be solid?". The following section answers this question and focuses on the main ingredients necessary to achieve a supersolid state with ultracold dipolar gases, namely a source for the development of density modulation and a stabilization mechanism.

1.2.1 Crystallization mechanism

The knowledge of the excitation spectrum is crucial to understand whether an external perturbation with energy ϵ and momentum p can create an excitation in the system. One of the most important theoretical predictions in the quest for supersolidity, is the emergence of a minimum in the excitation spectrum at large momenta, which is considered a precursor for crystallization [97, 157]. In superfluid He, the existence of this minimum was originally predicted by Landau [108], it relates to its nature of strongly correlated liquid, and it was thought to be linked to a local vorticity. In Ref [138], Nozières addresses the roton in a different way, as a soft mode, and states: "a superfluid close to a charged density-wave instability has a dip in its excitation spectrum near the incipient Bragg spot.".

This minimum is usually not present in ultracold bosonic gases, whose isotropic and short-range interactions[1] are generally weak. In these systems, by following the Bogoliubov approach, the excited states can be described in terms of non-interacting quasi-particles of energy $\epsilon(p)$, which follows the Bogoliubov dispersion relation. For small momenta p, the dispersion has a linear phonon-like behaviour ($\propto p$), while, for larger momenta, it follows a free-particle behaviour ($\propto p^2$). The transition point between the two regimes is given by the healing length $\xi = \sqrt{\hbar^2/2mgn}$ [153].

In 2003, two important theoretical proposals appeared in the ultracold-gas community. In Ref. [139], O'Dell *et al.* predicted the formation of a roton minimum at finite momenta in the excitation spectrum, for a BEC with long-range interactions induced by illuminating the atomic cloud with far off-resonant laser light. The position of the roton minimum and the roton energy gap are tunable by changing the radial width of the BEC, and the intensity and the wavelength of the laser light. In Ref. [168], Santos *et al.* predicted that for an ultracold dipolar gas, when the contribution of the long-range and anisotropic dipolar interaction is dominant over the contact interaction, the spectrum of excitations develops a roton minimum at finite momenta k_{rot} with an energy gap Δ_{rot}. In this work, the authors considered an infinite pancake trap with the dipoles aligned along the tight confinement.

This behaviour relates to the momentum dependence of the DDI, which in real space has the following form:

$$U_{\mathrm{dd}}(\mathbf{r}) = \frac{4\pi\ \hbar^2\ a_{\mathrm{dd}}}{m}\left[1 - 3(\hat{\mathbf{r}}\cdot\hat{\mu}_{\mathrm{m}})^2\right], \tag{1.1}$$

[1] We refere to those interactions as contact interactions.

where m is the atomic mass, $a_{\rm dd} = \mu_0 \mu_{\rm m}^2 m/12\pi\hbar^2$ is the dipolar length[2], and $\mu_{\rm m}$ is the magnetic dipole moment (see Fig. 1.1a). For atoms confined in traps, if the dipoles are aligned along the tight direction of the trap, the total mean-field interaction has a negative contribution at large momenta, causing the dispersion relation to soften. Figure 1.1b displays the effective 1D mean-field interaction $\tilde{U}$, from Ref. [141], which includes contact interactions and DDI and it is obtained from a variational theory; see Refs [23, 24]. The effective interaction $\tilde{U}$ is shown as a function of the momentum k, for ^{164}Dy atoms and for two values of the scattering length, $a_{\rm s} = (115, 140)\ a_0$. For $a_{\rm s} > a_{\rm dd}$, $\tilde{U}$ becomes negative for $k \gtrsim 1/l_z$. The appearance of a roton minimum at large momenta can be also understood by looking at the excitations. Figure 1.1c shows the case of an infinite cigar-shaped harmonic trap with the dipoles oriented along the direction othogonal to the tight confinement, of size l_z. For small momenta $k << 1/l_z$, and therefore long wavelengths, the excitations have a two-dimensional character and the dipoles, which sit side-by-side, mainly repel each other. Whereas, for large momenta $k >> 1/l_z$, and therefore short wavelengths, the excitations have a three-dimensional character and the dipoles mainly sit head-to-tail attracting each other and reducing the interparticle interaction.

The energy gap $\Delta_{\rm rot}$ depends on the density and on the interactions. For example, by reducing the scattering length $a_{\rm s}$ via Feshbach resonaces, it is possible to decrease $\Delta_{\rm rot}$ until, when $\Delta_{\rm rot}$ becomes imaginary, in the mean-field picture, all the population is transferred in $\pm k_{\rm rot}$. At this point, it is energetically free for the system to develop a density modulation with periodicity $\sim 2\pi/k_{\rm rot}$. Experimentally, the roton mode was first observed in erbium via a softening of the excitation spectrum [45] and few years later the same experiment measured the full spectrum of excitations via Bragg spectroscopy and observed the appearance of a roton minimum when increasing the dipolar strength [150]. More recent experiments with Dy have inferred the spectrum of excitations by looking at the static structure factor determined from insitu density fluctuations in a 1D cigar-shaped trap [85] and later in a oblate trap [170]. The existence of a roton minimum at large momenta lays the basis for the first ingredient necessary for a supersolid state: a crystallization mechanism.

1.2.2 Stabilization mechanism

In a dipolar gas, when reducing the strength of the repulsive contact interaction $a_{\rm s}$ via Feshbach resonances, below a certain threshold, the mean-field theory predicts a

[2] $a_{\rm dd} = 130\ a_0$ for ^{164}Dy.

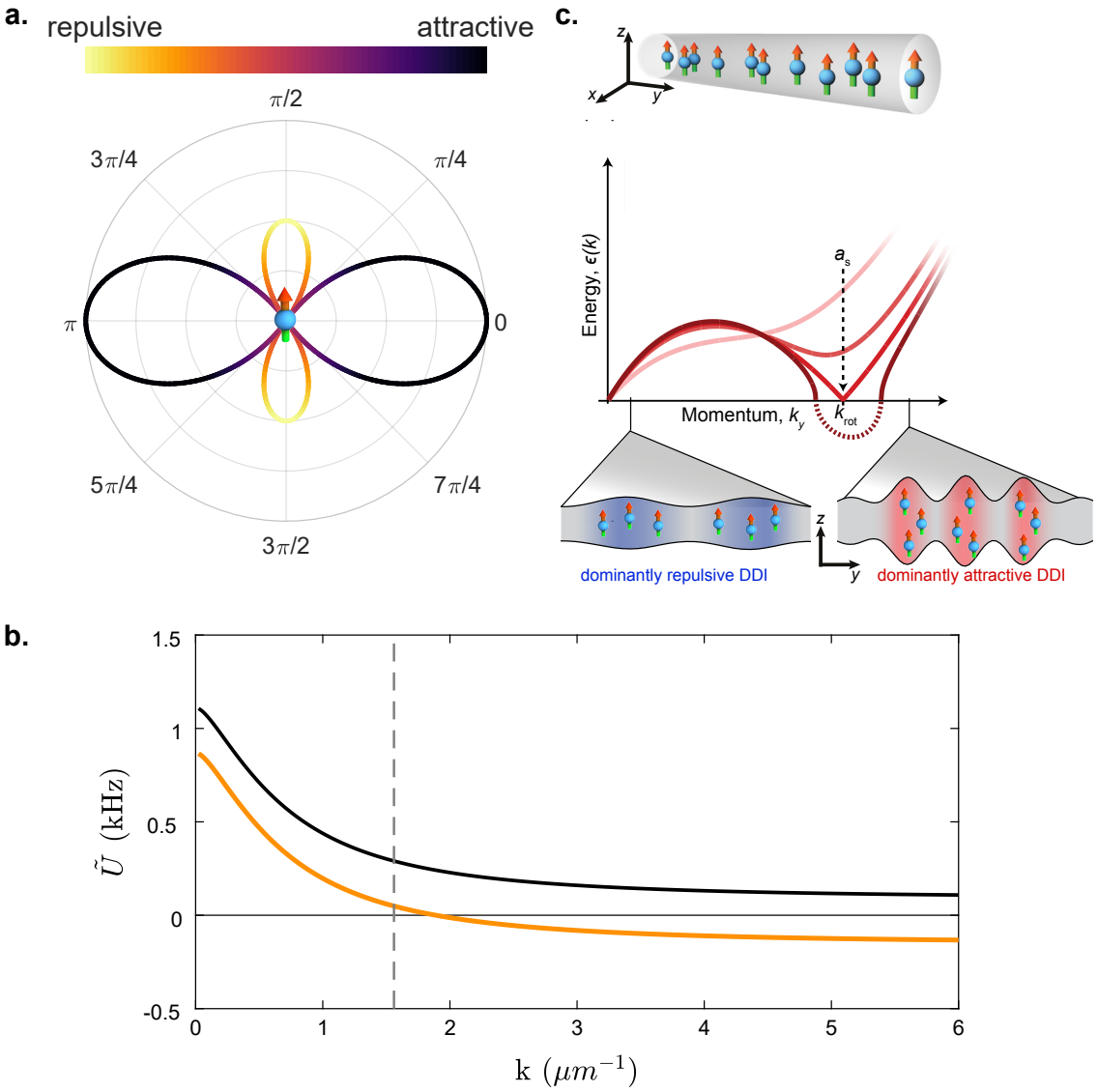

Figure 1.1 (a) DDI at fixed distance r as a function of the angle θ. (b) Effective mean-field interactions as a function of the momentum k, for ^{164}Dy atoms, where $a_{\rm dd} = 130\ a_0$, and for two values of the scattering length: $a_{\rm s} = 140\ a_0$ (black), and $a_{\rm s} = 115\ a_0$ (orange). For $a_{\rm s} = 115\ a_0$, $a_{\rm s} < a_{\rm dd}$ and the effective interaction becomes negative at momenta approximately larger than $1/l_z$ (grey dashed line). Parameters and analytic formula taken from Ref. [141]. (c) Excitation spectrum for a dipolar BEC in an infinite cigar-shaped trap. By decreasing the scattering length the spectrum develops a roton minimum at a finite momentum $k_{\rm rot}$. This can be understood by looking at the excitations, where a change of the DDI from mainly repulsive at small momenta to mainly attractive at large momenta happens. Figure adapted from [45].

collapse. This is due to the attractive contribution of the DDI. First studies of the

dipolar collapse were performed with chromium [107, 127]. Here, the collapse showed a pattern given by the d-wave anisotropy of the DDI. However, precursor experiments with Dy showed that the system, instead of collapsing, splits into multiple peaks, which are known as quantum droplets [91], leading to a density modulated state. The behaviour of these quantum droplets is reminiscent of ordinary liquid droplets. For high enough atom numbers, they show a self-bound nature and the system stays bound even without any trapping confinement [40, 171].

This observation triggered a lot of theoretical effort in understanding the origin of the stabilization mechanism, with a three-body conservative repulsion[3] [21, 198] and quantum fluctuations as possible candidates. The first experimental work aimed at elucidating the stabilization mechanism was performed with Dy and pointed at the quantum fluctuations [61]. Few months later, experiments with Er confirmed that the transition to a droplet state was driven by the quantum fluctuations. Furthermore, thanks to the unique control and knowledge of the scattering length, the erbium experiments revealed the role of quantum fluctuations on the system's properties, such as e.g. atom losses, expansion dynamics, and collective modes [41]. These experimental observations were promptly confirmed by theoretical works [22, 189, 190]. The beyond mean-field effects have not been seen in chromium due to the weak dipolar length ($15\ a_0$). In fact, in chromium, the losses due to three-body recombinations, overcome the beyond mean-field effects, which can be neglected [43].

The effect of quantum fluctuations can be well described by the first-order correction to the mean-field energy, namely the LHY term. A more detailed description of this term will be given in the next section (Sec. 1.3). When the repulsive contact interactions and the attractive dipole-dipole interactions almost balance each other, the beyond mean-field term, which is positive and scales with a higher power of the density with respect to the mean-field energy, becomes relevant preventing the system from collapsing. The quantum fluctuations constitute the second ingredient necessary for a supersolid state: a stabilization mechanism.

1.3 Many-body interactions

In standard conditions in which the overall interactions are repulsive, ultracold dipolar gases are generally well pictured by mean-field theory, where the field operator $\hat{\Psi} =$

[3] Earlier on, Ref. [120] proposed three-body interactions as stabilization mechanism for a supersolid states in two-dimensional dipolar bosons.

$\psi(r,t)+\delta\psi$ can be safely replaced with its mean value $\psi(r,t)$. This section briefly recalls the basic steps necessary to derive the Gross-Pitaevskii equation (GPE) [153].

The time evolution of the field operator $\hat{\Psi}$ follows the Heisenberg equation:

$$i\,\hbar\frac{\partial\hat{\Psi}(\mathbf{r},t)}{\partial t}=\left[\hat{\Psi}(\mathbf{r},t),\hat{H}\right]=\left[-\frac{\hbar^2\nabla^2}{2\,m}+V(\mathbf{r})+\int \mathrm{d}\mathbf{r}\;\hat{\Psi}^{\dagger}(\mathbf{r},t)U(\mathbf{r}-\mathbf{r}')\hat{\Psi}(\mathbf{r},t)\right]\hat{\Psi}(\mathbf{r},t), \tag{1.2}$$

where the Hamiltonian operator $\hat{H}$ includes the one-particle operators describing kinetic and trapping potential, and the two-particle operator describing the two-body interaction.

Under the assumption of zero temperature and that most of the atoms occupy the ground state of the system, the effect of quantum fluctuations, as the quantum depletion or a shift of the ground state energy, can be usually neglected. This means ignoring the term $\delta\psi$. Furthermore, the real interatomic potential can be replaced by a soft pseudopotential, which gives the same scattering length a_{s} as the exact one. The system's behaviour can be then described through the GPE:

$$i\,\hbar\frac{\partial\psi(\mathbf{r},t)}{\partial t}=\left[-\frac{\hbar^2\nabla^2}{2\,m}+V(\mathbf{r})+\int \mathrm{d}\mathbf{r}'U(\mathbf{r}-\mathbf{r}')n(\mathbf{r}')\right]\psi(\mathbf{r},t), \tag{1.3}$$

with $n(\mathbf{r}')=|\psi(\mathbf{r}',t)|^2$. Equation 1.3 includes the kinetic term, the trapping potential V and the mean-field interaction U. For what concern the phenomena investigated in this thesis, the trapping term V is described by a harmonic potential with trapping frequencies $(\omega_x,\omega_y,\omega_z)$:

$$V=\frac{1}{2}m\sum_{x_i=x,y,z}\omega_{x_i}^2x_i^2. \tag{1.4}$$

The mean-field interaction term U includes the contact interaction, characterized by the s-wave scattering length a_{s}, and the long-range dipole-dipole interaction, as follows:

$$U(\mathbf{r})=g\left(\delta(\mathbf{r})+\frac{3\epsilon_{\mathrm{dd}}}{4\pi}\frac{1-3\cos^2\theta}{|\mathbf{r}|^3}\right), \tag{1.5}$$

where $g=4\pi\;\hbar^2a_{\mathrm{s}}/m$ is the coupling constant and $\epsilon_{\mathrm{dd}}=a_{\mathrm{dd}}/a_{\mathrm{s}}$ is the relative dipolar strength. The angle θ is the angle between the dipoles orientation and the interparticle separation vector $\mathbf{r}$.

The beyond-mean field term $\delta\psi$ can become relevant when energy terms with opposite sign compete, enahancing the effect of quantum fluctuations in the system. The important role of quantum fluctuations in stabilizing the system against the collapse was originally proposed by Petrov for Bose-Bose mixtures [149], where beyond mean-field effects can be enhanced by tuning the competition between intra- and inter-species interactions close to the mean-field instability condition[4]. For dipolar gases, when a_s is below a critical value, the repulsive contact interaction can not overcome the attractive dipole-dipole interaction, inducing the collapse at the mean-field level. Note that the exact critical scattering length depends on the trap geometry.

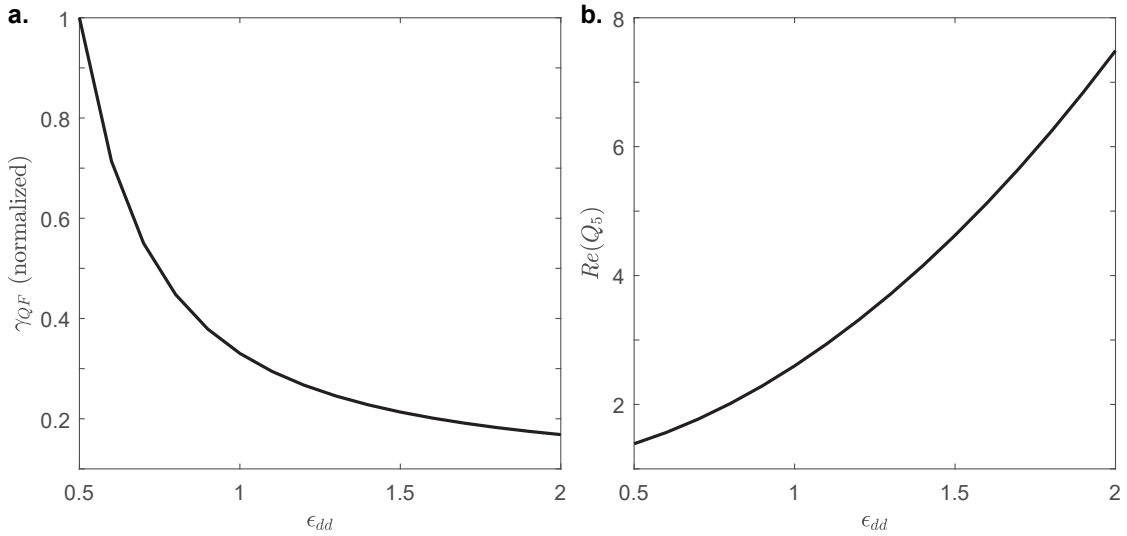

Figure 1.2 (a) Beyond mean-field quantum fluctuation term γ_{QF} of Eq. 1.6 as a function of the dipolar strength with fixed a_{dd}, and (b) $Re(Q_5)$ of Eq. 1.7 as a function of the dipolar strength ϵ_{dd}.

The effect of quantum fluctuations can be described by the first-order correction to the mean-field energy, known as Lee-Huang-Yang (LHY) correction. This term, originally formulated for weakly interacting ultracold Bose gases [110], was then extended to ultracold dipolar gases [115, 116] and has the expression:

$$\gamma_{\mathrm{QF}} = \frac{128\ \hbar^2}{3m}\sqrt{\pi a_{\mathrm{s}}^5}\,Re\{Q_5(\epsilon_{\mathrm{dd}})\}, \tag{1.6}$$

where Q_5 is a monotonic function of ϵ_{dd} and reads as below:

$$Q_5(\epsilon_{\mathrm{dd}}) = \int_0^1 (1-\epsilon_{\mathrm{dd}}+3\epsilon_{\mathrm{dd}}u^2)^{5/2}\mathrm{d}u. \tag{1.7}$$

[4]In Bose-Bose mixtures, the instability happens when the interspecies attraction overcomes the geometrical average of the intraspecies repulsion.

Figure 1.2 displays γ_{QF} and $Re(Q_5)$ as a function of ϵ_{dd}. By including the first-order correction, the GPE takes the form:

$$i\,\hbar\frac{\partial\psi(\mathbf{r},t)}{\partial t} = \Big[-\frac{\hbar^2\nabla^2}{2\,m} + V(\mathbf{r}) + \int \mathrm{d}\mathbf{r}' U(\mathbf{r}-\mathbf{r}')n(\mathbf{r}') + \gamma_{\mathrm{QF}}|\psi(\mathbf{r},t)|^3\Big]\psi(\mathbf{r},t). \tag{1.8}$$

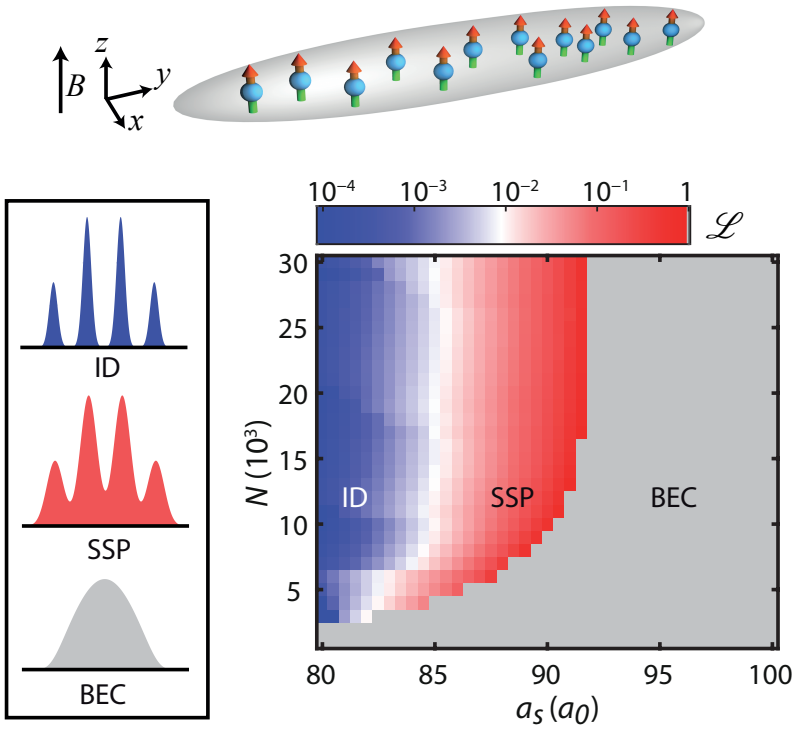

Figure 1.3 Ground-state phase diagram for a ^{164}Dy gas confined in a cigar-shaped trap with trapping frequencies $\omega_{x,y,z} = 2\pi \times (229, 37, 135)s^{-1}$. At high a_{s}, the system is in the standard dBEC phase (grey region). At low a_{s}, the ground state consists of a chain of quantum droplets with independent phases (blue region). In a narrow range of a_{s}, where the link $\mathcal{L}$ is significant, the ground state is a supersolid (red region) showing density modulation and global phase coherence. Figure adapted from [89].

So far only two-body collisions are taken into account but, for high densities, the approximation of considering only two-body interactions breaks down and inelastic three-body collisions can have a big impact on the system. Three-body losses can be included in Eq. 1.8, by adding the following term:

$$-\frac{i\,\hbar}{2}L_3 n^2(\mathbf{r})\psi(\mathbf{r},t), \tag{1.9}$$

where L_3 is the three-body collision coefficient.

By minimizing the energy functional of Eq. 1.8, one can find the ground-state of the system and develop a phase diagram as a function of atom number and scattering length. Figure 1.3 shows the phase diagram for ^{164}Dy in a cigar-shaped trap with the magnetic field aligned along the tight axis. From the phase diagram the following phases can be identified. At high scattering lengths, the ground-state of the system is a standard dipolar BEC. By reducing the scattering length, the system enters the supersolid regime (SSP), in which a density modulation develops in form of quantum droplets linked to each other by a superfluid background, allowing global phase coherence. When lowering the scattering length further, the link between the droplets decreases until it becomes neglegible and the system enters the so-called isolated-droplet regime (ID) and the global phase coherence is lost. The link strength is encoded in the color map and it is defined as $\mathcal{L} = 1-(n_{\max}-n_{\min})/(n_{\max}+n_{\min})$, where $n_{\max}$ and $n_{\min}$ are the density maximum and minimum in the center region of the density distribution, respectively. The experimental tools to realize a long-lived linear and two-dimensional supersolid are described in more details in Chapter 4.

1.3.1 Thermal fluctuations

So far, this section underlined the important role of quantum fluctuations in stabilizing a dipolar gas and avoiding the collapse when the dipolar strength $\epsilon_{\rm dd} \gtrsim 1$. The GPE in Eq. 1.8, which includes the beyond mean-field term describing the quantum fluctuations, assumes a dipolar quantum gas at zero temperature. However, in experiments, the temperature of the system is finite and the condensed cloud usually coexists with a thermal component, which can be a non-negligible fraction of the total atoms, leading to a considerable interaction between condensed atoms and thermal excitations. In this case, the fluctuation term $\delta\psi$ includes quantum as well as thermal fluctuations. In this regard, later on in this thesis, we demonstrate how not only quantum fluctuations, but also thermal fluctuations have a determinant role in the supersolid formation; see Chapter 4.

In fact, in dipolar gases, finite temperatures can have an important effect on the properties of the system. For instance, theoretical works reported on the role of thermal fluctuations in stabilizing quantum droplets and changing their density profiles [7], even at temperatures as low as 100 nK. Moreover, our works reported in Sec. 4.4 and

Sec. 4.9 show how thermal fluctuations shift the transition to a supersolid state towards lower dipolar strengths, favouring the appearance of density modulation [180]. In the latter, a temperature-dependent GPE, obtained by minimizing the grand-canonical potential with respect to the wave function $\psi(r)$ [67], well captures the phase diagram of our dysprosium cloud at finite temperature. The total grand potential includes the grand-canonical zero-temperature energy and the finite-temperature energy term resulting from Bogoliubov theory. By minimizing this potential, one obtains the wave function in thermal equilibrium. For more details, see Ref. [180].

The theory mentioned above is valid for a high fraction of condensed atoms and represents properties of the system at thermal equilibrium. Therefore, for describing dynamical processes, such as the supersolid formation, a more appropriate theory is the stochastic GPE (SGPE) formalism [25, 117], whose validity is in a broader temperature range and does not require the major occupation of the lowest energy state, as when applying Bogoliubov theory. In the publication shown in Sec. 4.7, the SGPE with the beyond mean-field quantum fluctuations is used to describe the process developed in our group to experimentally achieve a supersolid state by direct evaporative cooling from a thermal cloud [27].

Chapter 2

Er-Dy experiment

The previous chapter showed how the long-range dipole-dipole interactions can lead to novel quantum phases of matter. Among neutral atoms, long-range and anisotropic DDI can be achieved in several ways. The systems showing the strongest DDI are Rydberg atoms with ϵ_{dd} larger than 10^6. Hetero-nuclear molecules follow with $\epsilon_{\mathrm{dd}} \sim 10^2$. Magnetic lanthanides, such as erbium and dysprosium, with their not completely filled submerged f shell, present a permanent magnetic moment which can be 10 times larger than alkali, giving rise to an $\epsilon_{\mathrm{dd}} \sim 1$. Long-range interactions can also be induced through atom-light coupling. To date four elements from the magnetic lanthanides have been Bose condensed: dysprosium [119] ($\mu_{\mathrm{m}} = 10\mu_B$), erbium [3] ($\mu_{\mathrm{m}} = 7\mu_B$), thulium [49] ($\mu_{\mathrm{m}} = 4\mu_B$), and very recently europium [129] ($\mu_{\mathrm{m}} = 7\mu_B$). Although magnetic atoms have an ϵ_{dd} much smaller than the Rydberg atoms and hetero-nuclear molecules, they feature several interesting properties, such as a rich manifold of internal states, many electronic transitions with various linewidths, and the presence of two main competing interactions (contact interaction and DDI), which are independently tunable. This chapter briefly recalls the basic properties of erbium and dysprosium. It then describes the experimental apparatus and the protocol used to create erbium-dysprosium ultracold gases.

2.1 Basic properties

Erbium and dysprosium are part of the magnetic lanthanides with a permanent magnetic moment of $7\mu_B$ and $10\mu_B$, respectively. Dysprosium was the first to be Bose-condensed in 2011 [119], with erbium following one year later [3]. Few years after, degenerate Fermi gases of dysprosium [118] and erbium [2] were realized via universal dipolar scattering. Since then a lot of theoretical and experimental works brought to the

discovery of novel phenomena arising from the long-range and anisotropic dipole-dipole interaction [43, 135]. Just recently the family of Bose-condensed magnetic lanthanides grew with the addition of thulium [49] and europium [129].

The large permanent magnetic moment arises from the electronic configuration, $[\mathrm{Xe}]4f^m6s^2$, where m=10 and 12 for dysprosium and erbium, respectively, which is characterized by an unfilled $4f$ shell surrounded by a completely filled s shell. The unpaired electrons in the f shell leads to a large angular momentum quantum number L, which has a big impact on the scattering properties (see discussion in Sec. 3.2) and on the atomic polarizability (see Sec. 3.3.3). The submerged shell also leads to a rich energy spectrum with various electronic transitions with linewidths ranging from µHz to hundreds of MHz [10, 59].

In our experiment, the broad transitions at 401 nm and 421 nm, with a linewidth of $\Gamma_{401}/2\pi = 29.4\,\mathrm{MHz}$ and $\Gamma_{421}/2\pi = 32.2\,\mathrm{MHz}$, for erbium and dysprosium, respectively, are used for a first stage of laser cooling and for imaging. The intercombination lines at 583 nm and 626 nm with linewidths of $\Gamma_{583}/2\pi = 186\,\mathrm{kHz}$ and $\Gamma_{626}/2\pi = 135\,\mathrm{kHz}$ are used for the Magneto-Optical trap (MOT) for erbium and dysprosium, respectively. The narrow-line transitions at 741 nm and 841 nm with linewidths of $\Gamma_{741}/2\pi = 2\,\mathrm{kHz}$ and $\Gamma_{841}/2\pi = 8\,\mathrm{kHz}$ can be used for an additional stage of laser cooling, as done for example in the group of M. Greiner at Harvard [152]. The Hz transition at 1299 nm, recently measured in erbium [145], and the 1001 nm in dysprosium [147] can be a powerful tool for optical manipulation and control of the atoms. Two additional narrow-line transitions are at 631 nm and 598 nm for erbium and dysprosium, respectively and their calculated linewidths are $\Gamma_{631}/2\pi = 28\,\mathrm{kHz}$ and $\Gamma_{598}/2\pi = 12\,\mathrm{kHz}$. The open-shell nature of magnetic lanthanides makes, on the one hand, the study of scattering properties and atom-light interaction rather complex but, on the other hand, leads to rich energy spectra, which offer many possibilities for manipulating the atoms. The next section describes the experimental apparatus and the electronic transitions used during the experimental sequence to produce ultracold gases of erbium and dysprosium.

2.2 Experimental apparatus

A detailed description of the experimental apparatus can be found in Ref. [88]. In brief, the experimental apparatus is designed to produce degenerate quantum gases of erbium and dysprosium, both in single and double-species operation. Figure 2.1 displays the experimental apparatus. It is composed by three main modules: the atomic beam source, the atomic beam shutter and the main chamber.

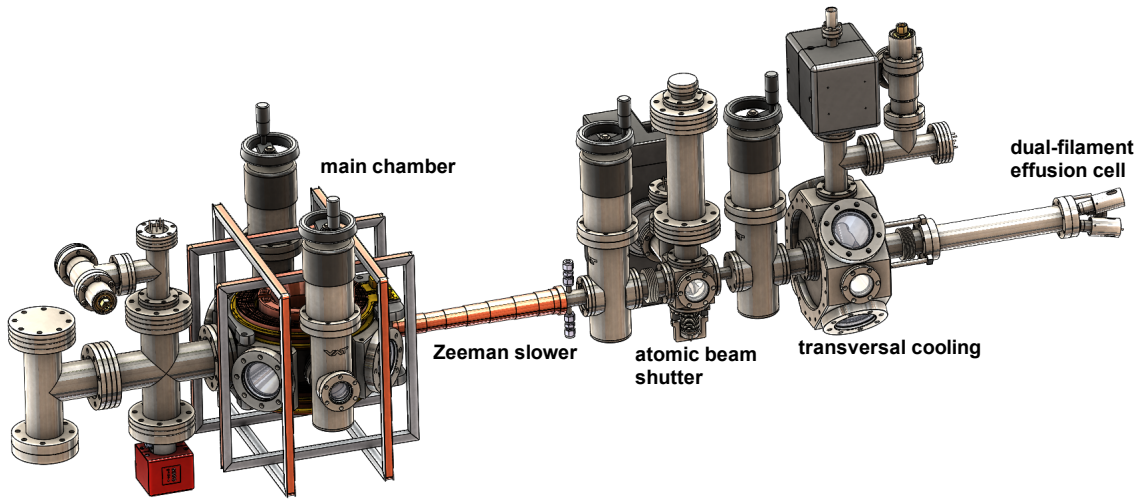

Figure 2.1 Experimental apparatus for the creation of erbium and dysprosium quantum gases. An effusion cell generates the atomic beam, which travels through several steps of collimations (apertures and 2D transversal cooling). After crossing the atomic-beam shutter section, the atoms are slowed down by a Zeeman slower and captured in the main chamber by a two-species five-beam MOT. The atoms are transferred in a crossed optical dipole trap, where quantum degeneracy is reached through evaporative cooling. Credits: Philipp Ilzhöfer

The atomic beam source consists of a dual-filament effusion cell[1] and a transversal cooling (TC) section. An ion pump keeps the whole module at a pressure of 10^{-10}mbar. The effusion cell includes a tantalum crucible with two units. One unit contains the erbium and dysprosium material, cut in small pieces, and its operating temperature is usually set to 1100 °C[2]. The second unit is set to a higher temperature[3] in order to create a temperature gradient and avoid condensation of material inside the crucible. This unit is partially filled with only erbium material in order to compensate for the lower vapor pressure of erbium. In total, the first unit is filled with about 12 g, 9 g of Dy and 3 g of Er[4], whereas the second unit is filled with approximately 2 g of Er. Three apertures inside the effusion-cell section provide a collimated atomic beam source. The atomic beam is further collimated in the TC units, where two orthogonal laser beams cool the atomic beam along the transversal directions.

The second module consists of an atomic beam shutter made of an in-vacuum stainless steel plate that is controlled by a servo and, after the loading of the Magneto-

[1] Createc Fischer & Co. GmbH, DFC-40-10-WK-2B.
[2] A detailed description of the procedure followed to refill the effusion cell can be found in Ref. [65].
[3] The standard operating temperature is 1200 °C.
[4] The larger amount of Dy in the first unit compensates for the lower melting temperature.

Optical-Trap (MOT), prevents the atomic beam from reaching the next module. In addition, two more pumps complete the module: a titanium sublimation pump, which is usually flashed only after a replacement of the effusion cell, and an ion pump, which allows pressure in the whole module down to 10^{-11}mbar.

The final module consists of a spin-flip Zeeman slower (ZS)[5]. The ZS slows down the erbium and dysprosium atoms, which are finally captured by a MOT in the main chamber. Another ion pump keeps the pressure at 10^{-11}mbar.

The MOT operates on the intercombination lines at 583 nm and 626 nm in erbium and dysprosium, respectively. The narrow-line character of the optical transition and the effect of gravity lead to a smile-shaped MOT, which sits below the zero of the magnetic quadrupole field [64, 92]. Therefore, for large enough detunings, the atoms mainly absorb light from the σ^--polarized beam coming from the bottom. As a result, the atoms are spin-polarized in the lowest Zeeman sublevel and the top MOT beam can be removed to leave space for a high resolution objective. Details about the operation of our two-species five-beam MOT can be found in Refs. [87, 88]. The atoms are typically loaded in the MOT for 5 s. A compression phase follows by decreasing the magnetic field gradient, and the laser detuning and power, leading to typical atom numbers and temperatures of $\sim 10^8$ and $\sim 10\,\mu$K. At this step, the atoms are loaded into an optical dipole trap (ODT) made from a laser beam operating at 1064 nm to evaporatively cool the atomic clouds down to quantum degeneracy.

The power of this beam is controlled by an acousto-optic deflector (AOD)[6], whose central frequency is modulated with an *arccos* function. For fast enough modulation frequencies[7], the atoms see a time-averaged potential, whose shape is the one of a Gaussian beam with a horizontal waist that can be actively tuned to maximize the overlap with the MOT volume. Moreover, this tunability allows us to vary the trapping geometry from a cigar-shape to a pancake trap, a fundamental tool for the transition from one to two-dimensional supersolidity (see publications in Sec. 4.5 and Sec. 4.7). The aspect ratio (AR) of the trapping beam can be tuned from 1 to a maximum of 10. We named this optical dipole trap *scanning* ODT. An important element, that influences the performance of the scanning system, is the modulation bandwidth of

[5] In such a configuration, the total magnetic field changes sign over the ZS length. In particular, first it decreases, reaches zero and then increases as a function of the distance from the first coil (see Ref. [88]).

[6] Gooch & Housego AODF, 4075-2, center frequency 75 MHz, bandwidth 32 MHz.

[7] The modulation frequencies need to be much higher than the trap frequencies.

the voltage-controlled oscillator (VCO)[8] used to set the frequency of the AOD. Indeed, the modulation bandwidth affects both the maximum width and the shape of the radio-frequency signal. More details can be found in Refs. [9, 156].

After few seconds, two more ODTs propagating horizontally are switched on in order to reach the optimal density condition for elastic scattering. In contrast to the *scanning* ODT, the waists of these beams are fixed. We named these optical dipole traps *static 1* and *static 2* ODTs. The evaporative cooling last for about 5 s to reach the degenerate quantum gas regime. In 2018, our experiment, produced double BECs of erbium and dysprosium atoms with five different bosonic isotope combinations, as well as a Bose-Fermi mixture[9]. Typical total atom numbers are about 10^5 with a BEC fraction above 50%.

2.2.1 Optical dipole traps

The evaporative cooling of erbium and dysprosium clouds takes place in a crossed optical dipole trap made by three laser beams at $\lambda = 1064\,\text{nm}$. The three beams come from a commercial master oscillator power amplifier (MOPA)[10] with a maximum output power of 55 W.

Figure 2.2 shows the optical setup used to distribute the power from the laser head to the three optical dipole traps. From the laser head the beam goes through a telescope before it is divided into three paths, which are coupled into three Large-Mode-Area (LMA) photonic crystal fibers[11], one for each ODT. The fiber holders[12] consist of two parts: a fiber collimator with a multi-element focusing lens[13] and a water-cooled copper block which cools down the fiber connector. Before splitting the laser beam, an iris masks spurious modes from the main peak, which would not be coupled into the fibers. NTC thermistors and photodiodes interface with an Arduino® microcontroller to monitor the temperature of the fibers and the fiber coupling, respectively. The power is distributed in the following way: about 22 W are sent to the *scanning* ODT path and approximately 10 W are sent to each of the *static* ODTs.

[8] The VCO implemented in the experiment is the model MiniCircuits ZX95-100 with a 3dB modulation bandwidth of 180 kHz. This will be exchanged with the fast VCO DRFA10Y - B – 0 - 50.110 from AAOptoElectronic, with a modulation bandwidth higher than 1 MHz.

[9] At this early stage of the experiment, the crossed ODT was made by one horizontal beam and a vertical beam propagating along gravity. This setting is also the one used for the publication shown in Sec. 3.5.

[10] Coherent Inc., Mephisto MOPA 55 W.

[11] NKT Photonics LMA-PM-15.

[12] Home-built inspired by the Greiner's lab in Harvard.

[13] OptoSigma HFTLSQ-20-30PF1.

[14] Thorlabs AC254-f-C, with f the focal length of the lens.

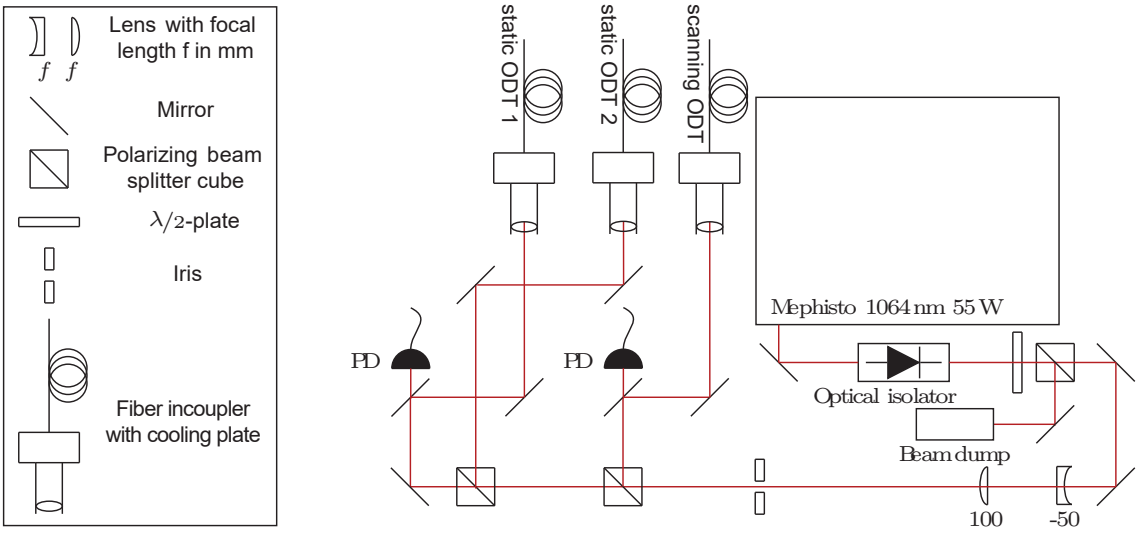

Figure 2.2 Optical setup used to distribute the power from a MOPA, operating at 1064 nm with a maximum output power of 55 W, to the three optical dipole traps used to trap the atomic clouds. A first telescope collimates and shapes the laser beam for an optimal fiber coupling into the LMA photonic crystal fibers. An iris follows to get rid of spurious modes from the main peak. Photodiodes (PDs) and NTC thermistors placed on the fiber connector monitor the incoming power and the temperature, respectively.

Figure 2.3 shows the *scanning*-ODT laser path to the main chamber. From the outcoupler, the laser beam goes through an AOD, which modulates and intensity stabilizes the beam. Four lenses are used to shape the laser beam before being focused onto the atoms. In particular, f_1 converts the diffraction into a parallel displacement of the beam. The distance between f_3 and f_4 is set by the position of two mirrors, which can be tuned by moving a linear stage[15]. This leads to a shift of the focus at the chamber without affecting the waist size (see Fig. 2.4). Finally, the last lens f_5 focuses the light onto the atoms with a final waist of approximately 18 µm. At the position of the f_4 lens, the beam is close to the full aperture of the lens. This makes the alignment quite challenging and leads, in some cases, to an astigmatic beam at the focus position onto the atoms. For this reason, the lenses f_3 and f_4 are mounted on kinematic mirror mounts. Furthermore, the five lenses need to be in a $10f$ imaging system configuration. Deviations from this setting lead to a change in the focus position when varying the modulation amplitude of the AOD, i.e. the AR of the *scanning* ODT beam. Figure 2.4 shows calculations of the beam waist as a function of the propagation distance from the AOD for three different positions of the f_4 lens. By translating the lens by ±5 mm

[15] OWIS GmbH MT 60.

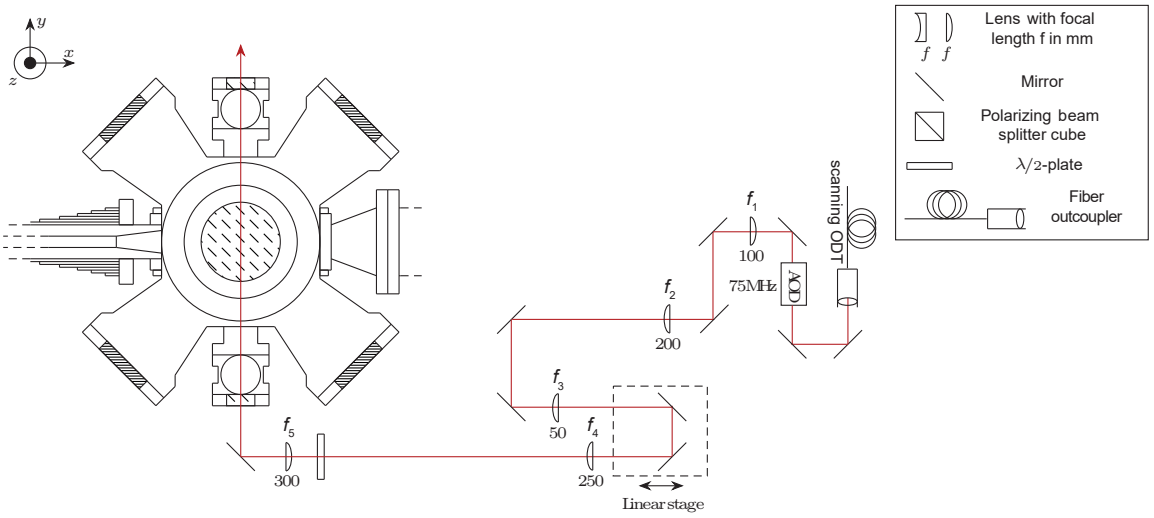

Figure 2.3 Optical setup for the *scanning*-ODT path next to the main chamber. The AOD modulates and intensity stabilizes the beam. The lenses used in this setup are achromatic doublets[14]. A linear stage shifts two mirrors, which translates in changing the distance between f_3 and f_4 and therefore moving the focus at the atoms without affecting the final waist size. Figure adapted from [88].

the focus moves by ±7 mm without variations in its size. Furthermore, modulating the central frequency of the AOD does not affect the focus position and the beam size.

Figure 2.5 shows the *static*-ODTs laser paths to the main chamber. From the outcoupler, the laser beam goes through an acousto-optic modulator (AOM)[16], which intensity stabilizes the beam. Similarly to the *scanning* ODT, two lenses shape the laser beam before focusing the light onto the atoms. In the same way, the beam waist can be translated by changing the distance between f_1 and f_2, which is done by moving two mirrors on a linear stage. For the two *static*-ODTs, the final waist is about 60 µm. Note that the AOD and the AOMs used for the optical dipole traps are mounted on a water-cooled block in order to improve the beam-pointing stability.

2.2.2 Imaging systems

The erbium-dysprosium experiment has two imaging systems. One propagates horizontally at 45° with respect to the y direction, overlapping with the *static*-ODT 1. This imaging system is described in details in Ref [88] and is used to perform absorption imaging of the atomic cloud after Time-of-Flight (TOF) expansion. The pixel size

[16] Gooch & Housego I-M080-2C10G-4-AM3.

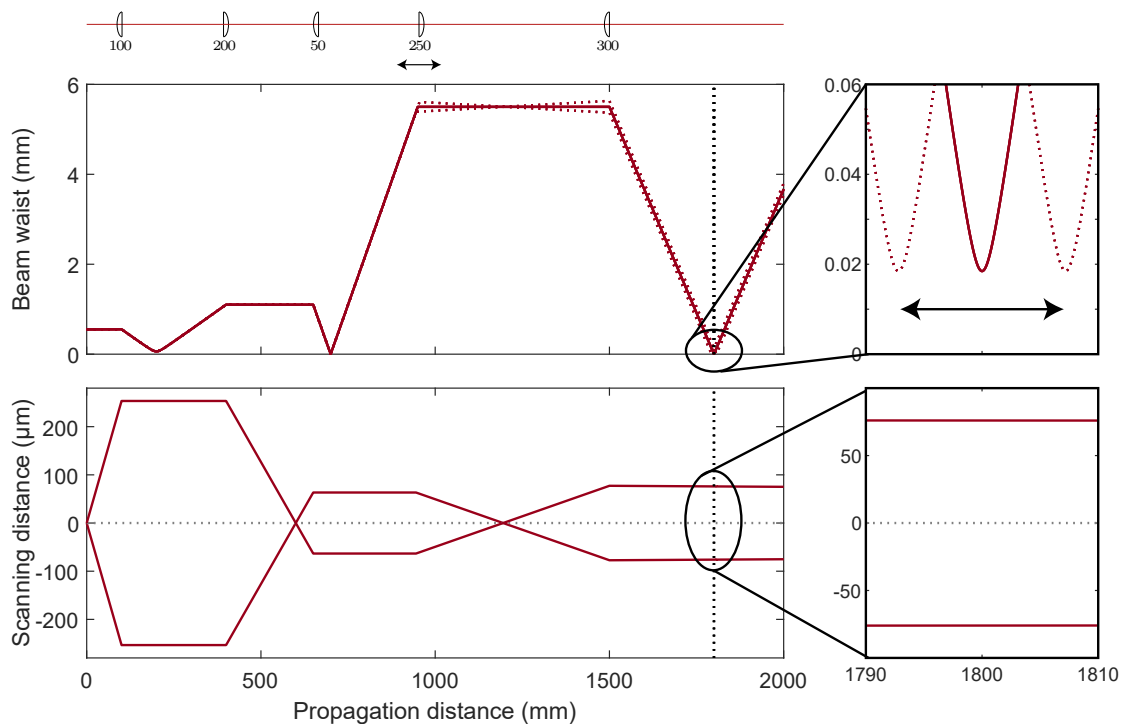

Figure 2.4 Beam waist as a function of the propagation distance from the AOD (upper row) and horizontal displacement of the laser beam for a modulation frequency of 10 MHz (bottom row). When changing the distance between f_3 and f_4 by ± 5 mm the beam waist moves by ± 7 mm without variations in its size. The waist size and position do not change with the scanning amplitude.

of the camera at the position of the atoms is approximately 2.1 µm. This horizontal imaging beam is used in the experiment to get information on the atom number and temperature. In particular, we record the momentum distribution after TOF, which shows, for an unmodulated BEC, the standard profile with a broad contribution given by the thermal component and a narrower peak given by the condensed atoms. We fit a bimodal distribution to the 1D profile and extract atom number and temperature. For a supersolid state, due to the presence of the density modulation resulting in a series of high-density peaks, a different analysis is performed (see e.g. the publications shown in Sec. 4.4 and in Sec. 4.5).

The second imaging system allows both insitu and TOF imaging. The laser beam propagates vertically along the z direction and consists of an objective with a maximum numerical aperture (NA) of 0.45 and a measured resolution of about 700 nm, at 401 nm and 421 nm. The pixel size of the camera at the position of the atoms is approximately 0.4 µm. A detailed description can be found in Ref. [176]. To get information on the insitu density distribution, we perform phase-contrast imaging [34, 193] with

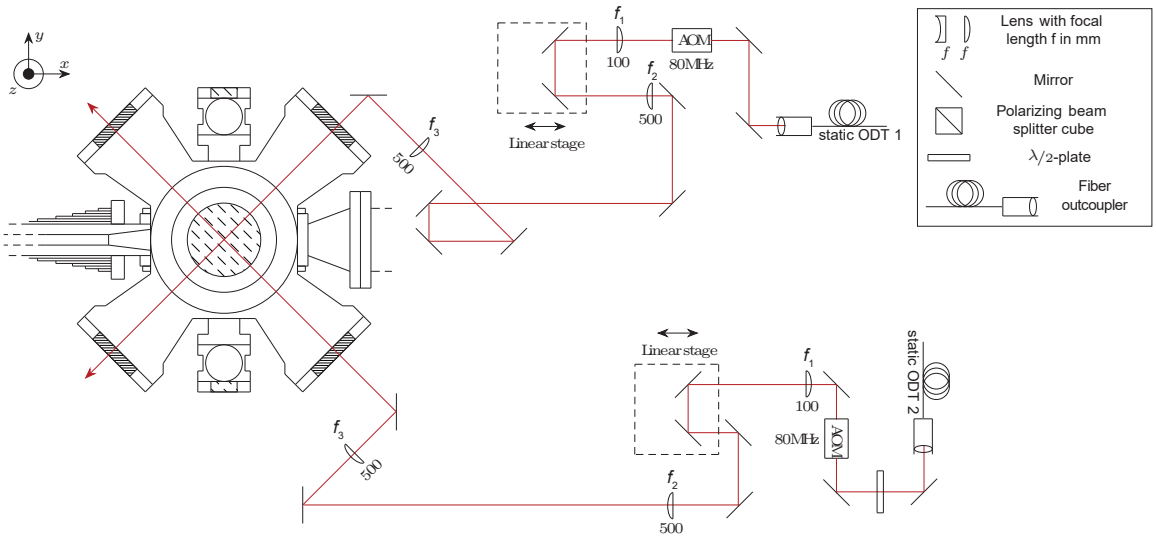

Figure 2.5 Optical setup for the two *static*-ODTs next to the main chamber. The AOMs intensity stabilize the laser beams. The RF frequency that drives the AOM for the *static*ODT 1 is shifted by few MHz from the central frequency to not interfere with the *scanning* ODT when the modulation is on. The lenses used in this setup are achromatic doublets. A linear stage shifts two mirrors, which translates in changing the distance between f_1 and f_2 and therefore moving the focus without affecting the final waist size. Figure adapted from [88].

far-detuned light[17] and linearly polarized light. Whereas, to get information on the momentum distribution, we perform standard absorption imaging after TOF expansion with resonant light and circular polarization. A stepper motor allows to move the objective vertically and switch from insitu and TOF imaging. This imaging system is fundamental to probe density modulation and global phase-coherence of a supersolid state (see Chapter 4).

2.2.3 Quantum gas microscope

In July 2021 a new element was added to the experimental apparatus, namely a glass cell for quantum gas microscopy of erbium and dysprosium atoms. The quantum gas miscroscope consists of an octogonal glass cell[18] and an in-vacuum objective[19] with a maximum NA of approximately 0.89 and a measured resolution of about 300 nm, at 401 nm and 421 nm. The details on the design of the glass cell and the objective, together with its performances can be found in Ref. [176]. The quantum gas microscope

[17] The detuning is set to $\Delta \sim 36\Gamma$.
[18] Manifactured by Precision Glassblowing of Colorado, Inc.
[19] Manifactured by Special Optics, Inc.

is a powerful tool that will open many research directions based on the investigation of new quantum phases in optical lattices arising from the long-range interaction.

Chapter 3

Interspecies interaction in an ultracold dipolar mixture

The previous chapter described the features of our experiment and how erbium-dysprosium ultracold mixtures can be created with different isotope combinations. This chapter focuses on the first study of the interspecies interactions and the determination of the interspecies scattering length a_{12}, done by tracking the in-trap clouds displacement generated by the mean-field interspecies interactions. In particular, the first section gives a general overview of hetero-nuclear mixtures. The second section introduces the methods that are generally used in ultracold experiments to determine a_{12}. The third section introduces the technique developed in our experiment and gives details on the experimental sequence and on the theoretical model based on the Gross-Pitaevskii equation with the energy terms arising from the interspecies interactions. Finally, the last section is dedicated to the numerous possibilities that hetero-nuclear dipolar mixtures offer for studying new quantum phases.

3.1 Hetero-nuclear mixtures: an overview

In the past decades, ultracold homo- and hetero-nuclear mixtures have been realized all around the world driven by multifold reasons. One of the first ultracold mixtures was realized by merging two fermionic spin states of potassium atoms [53] in order to overcome the limitation given by identical fermions in reaching quantum degeneracy. Indeed, reaching quantum degeneracy relies on direct evaporative cooling and therefore on elastic collisions. In the regime of low temperatures, the main contribution to the scattering cross section is given by s-wave states. However, for identical fermions with short-range interactions, the requirement of an antisymmetric wave function

prohibits s-wave scattering. Therefore only distinguishable fermions can interact at these low temperatures. This changes for dipolar fermions interacting via long-range and anisotropic dipole-dipole interactions, where not only s-waves but all partial waves contribute to the scattering cross section [2, 12]. For a similar purpose, Bose-Fermi mixtures have been realized to use the bosonic species as a thermal bath to sympathetically cool fermions [78, 188]. Furthermore, quantum mixtures can be used to study polaron physics, where impurity atoms are immersed in a bosonic or fermionic quantum degenerate bath [86, 90]. Long-range attractive mediated interactions have been studied in Bose-Fermi mixtures, where a trapped BEC is surrounded by a degenerate Fermi gas, leading to an instability of the condensate and, in a quasi 1D trap, to a transition to a Bose-Fermi soliton train [55]. Another important driving motivation for studying hetero-nuclear mixtures is the realization of ultracold molecules, which possess a large electric dipole moment [128]. Finally, by tuning the interspecies interaction to negative values a stable mixture of BECs can perform a phase transition to quantum droplets [37, 54, 149].

All the hetero-nuclear mixtures mentioned so far have been realized by combining alkali-metal atoms, with the advantage to make use of the wide knowledge developed over many years of research on single-species experiments. Ultracold experiments have also combined alkali-metal with alkaline-earth-metal atoms [143, 202] and alkali-metal with alkaline-earth-like atoms [80, 81, 194] motivated by the possibility of realizing molecules having both magnetic and electric dipole moments. In the last few years, the family of hetero-nuclear mixtures has grown including also dipolar atoms. In particular, in our experiment, the first double BECs of magnetic atoms were realized with several isotope combinations of erbium and dysprosium [187]. In the same year, a degenerate Fermi-Fermi mixture with dysprosium and potassium atoms was realized in Innsbruck as well [163].

The presence of long-range and anisotropic interactions is expected to enrich the already fascinating quantum phases predicted with contact-interacting mixtures. Theoretical works addressed the formation of vortex lattices in rotating dipolar mixtures [102, 103], binary quantum droplets [20, 174, 175], pattern formation [197], double supersolid states [169], and domain supersolids [26]. All the phenomena mentioned so far are highly sensitive on the interspecies interaction strength and to be observed require a fine and controlled tuning of a_{12}. In fact, the interaction between the species strongly affects the in-trap density distribution of the clouds, leading in some cases to phase separation [101]. For dipolar mixtures, whether the two species overlap, namely they are miscible, or they are pushed aside, namely they are immiscible, depends on

both the contact and dipolar intra- and interspecies scattering lengths. Whereas for alkali atoms, collisional models can predict the scattering lengths, for dipolar atoms, the complexity of the electronic structure and the anisotropic interactions make a theoretical determination quite challenging [100, 148]. Therefore the determination of the intra- and interspecies scattering lengths relies on experimental measurements. The next section recalls the most common experimental methods for determining the interspecies scattering length, while Sec. 3.3 describes the one developed in our experiment and presented in the publication shown in Sec. 3.5.

3.2 Cross-species thermalization measurements

One of the methods used in ultracold mixtures to infer the interspecies scattering length is the cross-species thermalization technique. This approach consists of driving the system out of thermodynamic equilibrium, e.g. by selectively heating one of the species and then registering the evolution of the temperature towards the equilibrium, through elastic collisions. One can relate the thermalization time τ to the elastic cross section and finally to the interspecies scattering length a_{12}. By following Refs. [4, 76], one can model the cross thermalization through a set of rate equations, as below:

$$\dot{N}_{1,2} = 0, \tag{3.1}$$

$$\dot{T}_{1,2} = \pm \frac{\xi \ \Gamma_{12} \ (T_2 - T_1)}{3N_{1,2}}, \tag{3.2}$$

where N_i, T_i are the atom number and temperature of the i species, respectively. Γ_{12} is the interspecies collisional rate and $\xi = 4 \ m_1 \ m_2/(m_1+m_2)^2$, with $m_1(m_2)$ the mass of the 1(2) species. The factor ξ takes into account the reduced energy transfer caused by different masses. Furthermore, the factor 3 at the denominator, which is usually known as α, considers that about three collisions are needed for thermalization [130]. This factor changes whether the collisions are s-wave or p-wave, where α is about 4 [52]. In the case of dipolar atoms, due to the anisotropic nature of the interactions, the parameter α depends on the direction of the quantization axis, generally given by the magnetic field, with respect to the gravity axis, as well as on the scattering length [30, 191] (see the experimental work done with erbium atoms [144]).

Equations 3.1 and 3.2 neglect the terms coming from evaporative cooling, three-body losses, losses due to collisions with background gas, and heating due to the trapping

laser. From Eq. 3.2 one finds:

$$\dot{T}_2 - \dot{T}_1 = \frac{\xi\Gamma_{12}}{3}\left(\frac{1}{N_1} + \frac{1}{N_2}\right)(T_2 - T_1). \tag{3.3}$$

By assuming that the thermalization time of the temperature difference is the same as the individual temperatures, τ can be defined as:

$$\frac{1}{\tau} = \frac{\xi\Gamma_{12}}{3N_1N_2}(N_1 + N_2). \tag{3.4}$$

The thermalization rate can be linked to the elastic cross section σ_{12} from the relation:

$$\Gamma_{12} = \bar{n}_{12}\sigma_{12}\bar{v}_{12}, \tag{3.5}$$

where $\bar{n}_{12}$ and $\bar{v}_{12}$ are the mean spatial overlap and the mean collisional velocity, respectively. These two quantities have the following form:

$$\bar{n}_{12} = \frac{N_1N_2m_1^{3/2}\bar{\omega}_1^{3/2}}{[(2\pi k_\mathrm{B})(T_1 + \beta^2T_2)]^{3/2}}, \tag{3.6}$$

$$\bar{v}_{12} = \sqrt{\frac{8k_\mathrm{B}}{\pi}\left(\frac{T_1}{m_1} + \frac{T_2}{m_2}\right)}, \tag{3.7}$$

with $\bar{\omega}_{i=1,2}$ the geometric average of the trapping frequencies and $\beta^2 = m_2\bar{\omega}_2^2/m_1\bar{\omega}_1^2$. By combining Eq. 3.4, Eq. 3.6 and Eq. 3.7, one can write:

$$\frac{1}{\tau} = \frac{\xi(N_1 + N_2)}{3N_1N_2}\bar{n}_{12}\sigma_{12}\bar{v}_{12}. \tag{3.8}$$

By measuring τ, $N_{i=1,2}$ and $T_{i=1,2}$ it is possible to estimate σ_{12}. The dependence of α on the polarization angle and on a_{12} makes the determination of the scattering length challenging and dependent on theoretical predictions. However, a rough estimation can be inferred from the relation:

$$\sigma_{12} = 4\pi a_{12}^2 + \frac{64\pi}{45}a_{\mathrm{dd},12}^2, \tag{3.9}$$

where $a_{\mathrm{dd},12}$ is the interspecies dipolar length. This thermalization model was used in the publication presented in A.3 to determine the scattering cross section in the vicinity of an interspecies Feshbach resonance and get insight into the strength and width of the resonance.

3.2.1 Feshbach spectroscopy

Due to the quadratic dependence on a_{12} of the elastic cross-section, the cross-species thermalization method allows determining only the modulus of the interspecies scattering length and not the sign. In order to determine the sign, thermalization measurements can be combined with Feshbach spectroscopy to map out the dependence of a_{12} with the magnetic field B and estimate the background scattering length a_{12}^{bg}. Once an interspecies Feshbach resonance is identified, one can perform cross-species thermalization measurements at different B around the resonance and, by using the model described in Sec. 3.2, determine a_{12}. The magnetic-field dependence of a_{12} can be represented by the following relation [39]:

$$a(B) = a_{\mathrm{bg}}\left(1 - \frac{\Delta}{B - B_0}\right), \tag{3.10}$$

where B_0 is the resonance position and Δ the resonance width[1]. This method is widely used in our community and was adopted to determine the interspecies scattering length in various systems as hetero-nuclear mixtures of alkali atoms [51, 173], in cesium-ytterbium mixtures [77] and lately in dysprosium-potassium mixtures [162, 201].

3.2.2 Other methods

Other methods include the determination of the interspecies scattering length from collective-excitation spectroscopy. The frequencies of excitation modes, e.g. breathing modes, are predicted to be dependent on a_{12} [60, 158]. Theoretical works proposed also the possibility of inferring a_{12} from the insitu density profiles [104]. Finally, a more demanding techinique is lattice-modulation spectroscopy (see Sec. 3.3.3), which was used in ultracold fermionic erbium atoms to determine the interspecies scattering length between the two lowest spin states [8].

3.3 Interspecies scattering length from mean-field shift

The technique developed in our group and presented in Sec. 3.5 consists of a joined theoretical and experimental work to study the effect that dipole-dipole interactions

[1] For dipolar atoms, the presence of a highly dense Feshbach spectrum requires the use of the formula for overlapping resonances: $a(B) = a_{\mathrm{bg}} \prod_i \left(1 - \frac{\Delta_i}{B - B_{0,i}}\right)$ [109].

have on the total mean-field interspecies interactions and to estimate a_{12} from tracing the in-trap cloud displacement as a function of the magnetic field orientation. Let's consider a non-interacting ultracold mixture of Er and Dy atoms trapped in an elongated 1064-nm optical dipole trap. Due to the slight difference in mass and polarizability the two clouds are displaced in the vertical direction by what is known as gravitational sag, $\Delta z_{\mathrm{grav}} = g(1/\omega_{z_1}^2 - 1/\omega_{z_2}^2)$, where g is the gravitational acceleration and ω_{z_i} the trap frequency along the gravity direction for the i species. This effect combines with a repulsive or attractive shift coming from the interspecies interactions; see later discussion. Figure 3.1(a) illustrates the geometry of our system with the two atomic clouds vertically displaced and the magnetic field orientation, which is given by the angles θ and ϕ, can be arbitrarily oriented along any desired direction. Figure 3.1(b) shows the ground state of the system calculated from the binary Gross-Pitaevskii equation (see Sec. 3.3.1) for the non-interacting case, when the magnetic field points along the gravity direction (z-axis). The 2D column density shows that the center-of-masses (COM) are vertically shifted by the gravitational sag, but the atomic clouds merge in the overlapping region.

When switching the interactions on, the clouds displacement is modified by another term, namely the mean-field shift Δz_{MF}. This term includes the mean-field shift due to the contact and dipole-dipole interactions and can push the two clouds closer or further apart, whether the total mean-field interactions are attractive or repulsive, respectively. Figure 3.1(c) shows the ground state of the system for the same parameters as Fig. 3.1(b), but with a repulsive interaction characterized by $a_{12} = 100\ a_0$. Due to the interactions, the two clouds repel each other leading to a larger clouds COM displacement. It becomes clear that the in-trap displacement with respect to the non-interacting position is a measure of the strength of the interactions, namely a_{12}. For repulsive interactions, the stronger a_{12} the larger the in-trap displacement gets.

An effect that plays a big role in dipolar gases and distinguishes them from the short-range interacting ones is magnetostriction [179], which is an elongation of the atomic cloud along the magnetic field direction. Figure 3.1(d) shows the ground state of the system with the same parameters as Fig. 3.1(c), but with the magnetic field pointing along the x-axis. Whereas for a magnetic field pointing along the z-axis, the magnetostriction leads to an increase of the vertical overlap between the clouds, when the magnetic field points along the x-axis, the atomic clouds elongate horizontally, hence reducing the vertical density overlap. This in turn reduces the interspecies repulsion and the two clouds approach the non-interacting clouds displacement, fixed

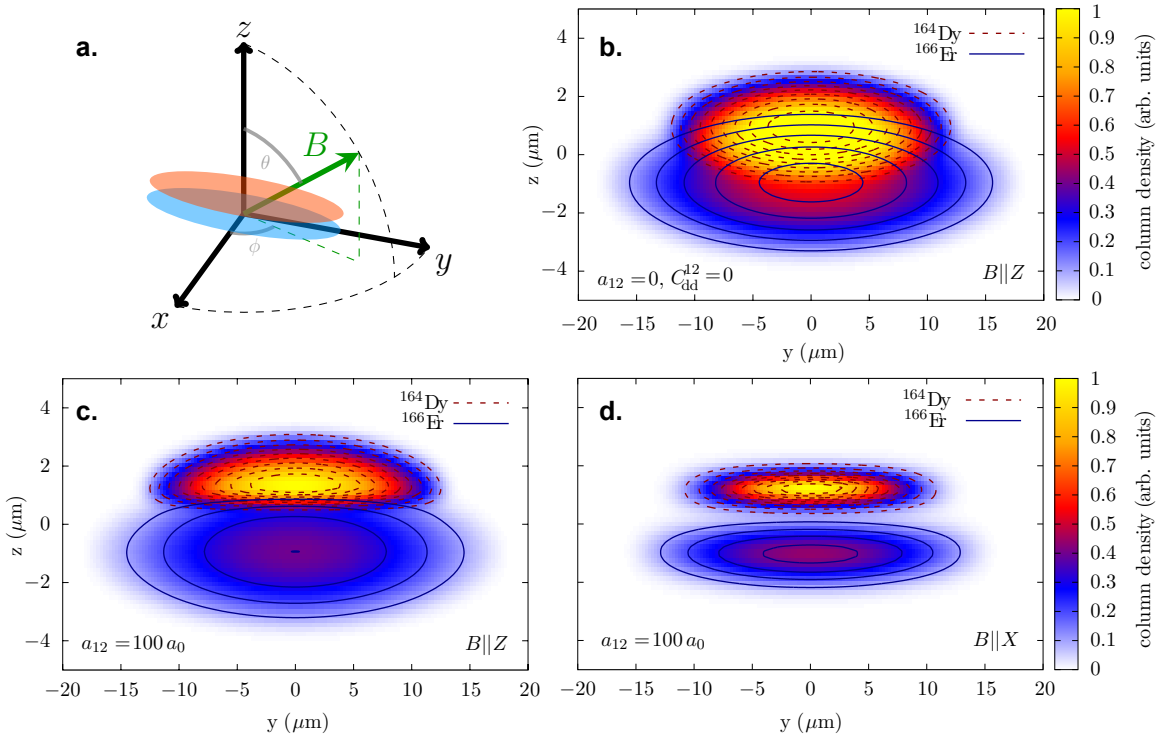

Figure 3.1 (a) Geometry of our dipolar mixture with ^{164}Dy and ^{166}Er shown as red and blue ellipse, respectively. The angles ϕ and θ define the orientation of the magnetic field. (b-d) Ground-state calculation of the column density for a mixture with imbalanced atom numbers: $N_{\rm Dy} = 1.3 \times 10^4$, $N_{\rm Er} = 4.9 \times 10^4$. Iso-density contour levels for Dy (dashed lines) and Er (filled lines). z=0 corresponds to the center of the gravitational sag. The magnetic field points along the z-axis with no interspecies interactions (b) and $a_{12} = 100\ a_0$ (c). The magnetic field is aligned along the x-axis, and $a_{12} = 100\ a_0$ (d). Figure adapted from [155]. (c,d) Credits: Michele Modugno.

by the gravitational sag. Hence, the maximum value of the COM shift occurs when the magnetic field points along the gravity direction, which maximizes the density overlap.

Another knob that can be tuned in dipolar gases is the magnetic field direction. In fact, in an asymmetric trap, for a fixed modulus of the magnetic field, the contribution of the dipolar interaction to the total mean-field interaction can be tuned from attractive to repulsive by varying the magnetic-field orientation. Figure 3.2 shows the dipole potential created by the dysprosium cloud and felt by the erbium atoms for two different magnetic field orientations. On the one hand, when the magnetic field points along the vertical direction, see Fig. 3.2(a), the interspecies interaction is mainly attractive due to the dipoles aligned predominantly head-to-tail. On the other hand, when the magnetic field points along the x-axis, see Fig. 3.2(b), the dipoles mainly sit side-by-side giving rise to a dipole potential felt by erbium atoms which is mainly repulsive (see Eq. 1.1).

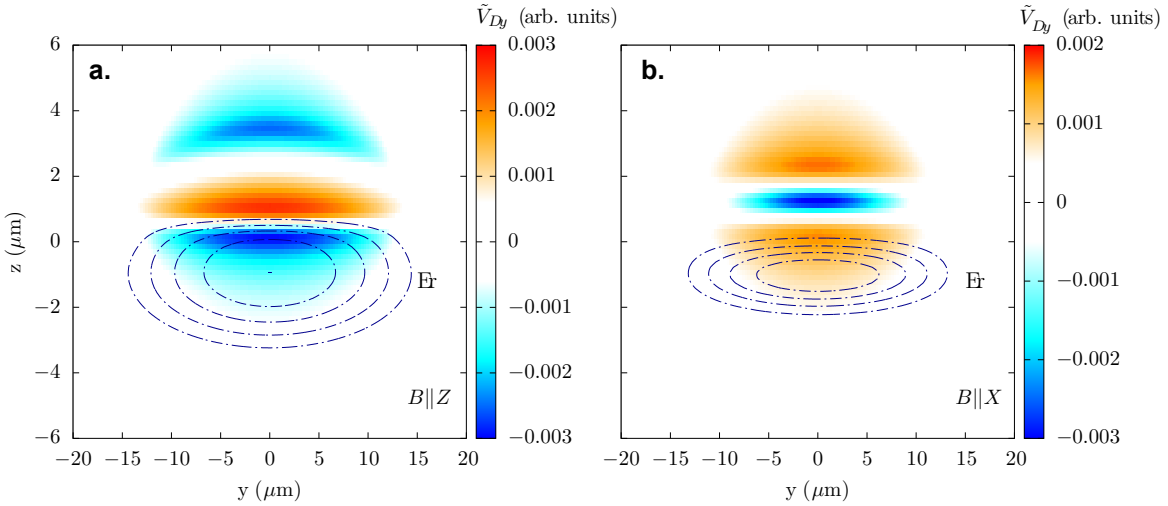

Figure 3.2 Heat map of the dipole potential produced by the Dy condensate $\widetilde{V}_{\mathrm{Dy}}(\mathbf{r}) \equiv \int V_{\mathrm{dd}}(\mathbf{r}-\mathbf{r}')n_{\mathrm{Dy}}(\mathbf{r}')\mathrm{d}\mathbf{r}'$, in the $x = 0$-plane. Iso-density contour levels of the Er component (dotted-dashed lines). The magnetic field is oriented along the z-axis (a) and along the x-axis (b). In the former case, the potential produced by Dy on Er in the overlapping region is negative, indicating that the interspecies dipolar interactions are predominantly attractive. Whereas, for the latter, the potential is positive, indicating that the interspecies dipolar interactions are predominantly repulsive. Figure adapted from [155]. (b) Credits: Michele Modugno.

3.3.1 Extended Gross-Pitaevskii equation

Before giving details on the experimental sequence used to probe the interspecies interactions, the following section briefly recalls the theoretical model developed to represent our system. To describe our mixture of dipolar erbium and dysprosium condensates, the GPE presented in Sec. 1.3 needs to be modified to include the terms arising from the interspecies interactions. These terms include the interspecies contact and dipolar interaction, whose energy functional can be expressed as below:

$$E_{12}^{\mathrm{c}} = g_{12}\int n_1(\mathbf{r})n_2(\mathbf{r})\mathrm{d}\mathbf{r} \tag{3.11}$$

$$E_{12}^{\mathrm{dd}} = \mu_0\mu_1\mu_2\int n_1(\mathbf{r})U_{\mathrm{dd}}(\mathbf{r}-\mathbf{r}')n_2(\mathbf{r}')\mathrm{d}\mathbf{r}\mathrm{d}\mathbf{r}', \tag{3.12}$$

where $n_i(\mathbf{r}) = |\psi_i(\mathbf{r})|^2$ is the density of each condensate, $g_{12} = 2\pi\hbar^2 a_{12}(m_1+m_2)/m_1m_2$ is the interspecies coupling constant, $\mu_1(\mu_2)$ is the magnetic moment of species 1(2), and U_{dd} is the interspecies dipole-dipole interaction. Since the regimes investigated in the experiment and presented in Sec. 3.5 are stable against mean-field collapse, for the results presented in this thesis only the single species beyond-mean field terms, as

in Eq. 1.6, have been taken into account. The interspecies LHY becomes crucial for the stability of the system when, for attractive interspecies dipolar interactions, a_{12} is reduced below a critical value leading to a collapse of both species at the mean-field level. A theoretical description including the interspecies LHY term has been done in Refs [20, 174]. After minimizing the energy functional including all the relevant terms, we determine the ground state of the system, as shown in Fig. 3.1 and Fig. 3.2, and get the calculated in-trap displacement for a fixed value of a_{12}.

3.3.2 Experimental sequence

The experimental sequence used to probe the in-trap cloud displacement is described in details in the publication reported in Sec. 3.5. In brief, the experiment consists of preparing a double BEC of erbium and dysprosium atoms, as described in the previous chapter. The two atomic clouds repel each other due to repulsive interspecies interactions. One of the species is then selectively removed, by shining resonant light. This removal put the remaining species out of equilibrium and induces center-of-mass oscillations around the new equilibrium position, fixed by the minimum of the trap and the gravitational sag. The amplitude of this oscillation can be connected to the strength of the interspecies repulsion (see publication in Sec. 3.5).

After performing this sequence for one magnetic field orientation, we repeat the procedure for various θ and ϕ. As a result, we obtain the mean-field shift as a function of the magnetic field orientation, where the maximum displacement appears for a magnetic field direction oriented along the gravity direction, which maximizes the density overlap of the two clouds due to magnetostriction and therefore the interspecies repulsion. By performing ground-state calculations at different interspecies scattering lengths and for different magnetic field orientations, it is possible to infer the a_{12} that best represents the experimental data, which we estimate to be $a_{12} = 105[-65, +162]\ a_0$. The experimental sequence described above was also used to probe other isotope mixtures (^{162}Dy-^{168}Er, ^{162}Dy-^{170}Er) with all showing a qualitatively similar behaviour with total mean-field repulsive interactions at the operating magnetic field.

3.3.3 Evaluation of the systematic errors

The calculated mean-field shift qualitatively agrees with the experimental one with the largest deviation when the magnetic field points along the horizontal plane. Below, few factors that might be the cause of the disagreement are mentioned. In our theory model, the trap frequencies are assumed to be constant and independent on the magnetic field

orientation. However, unlike alkali atoms, for erbium and dysprosium, the polarizability features a tensorial character [17, 113]. The light shift has a dependence on the angle between the light polarization and the magnetic field orientation (θ_p) and the angle between the light propagation and the magnetic field orientation (θ_k). Following Ref. [113], the total light shift can be expressed as below:

$$\begin{aligned} U_{\text{shift}}(\omega) = -\frac{I(r)}{2\epsilon_0 c}\Bigg[\alpha_s(\omega) + |\mathbf{u}^* \times \mathbf{u}| \cos\theta_k \frac{m_J}{2J}\alpha_v(\omega) \\ + \frac{3m_J^2 - J(J+1)}{J(2J-1)} \frac{3\cos^2\theta_p - 1}{2}\alpha_t(\omega)\Bigg], \end{aligned} \tag{3.13}$$

where I is the light intensity, ϵ_0 is the vacuum permittivity, c is the speed of light, $\mathbf{u}$ is the light polarization vector, $\theta_k(\theta_p)$ is the angle between the magnetic field direction and the light propagation(polarization). α_s, α_v, and α_t are the polarizability coefficients for the scalar, vector, and tensor part, respectively. For our experiments, we trap the atomic cloud in a 1064-nm laser beam, which is linearly polarized. This makes the vectorial term in Eq. 3.13 vanish. Regarding the tensorial term, when tilting the magnetic field from the z-axis into the xy-plane, θ_p can maximally change from $\theta_p = 90°$ to $\theta_p = 0°$. This means that the polarization-dependent factor can change from -1/2 to +1. Taking the values of $\alpha_\text{s} = 184.4(2.4)$ a.u. and $\alpha_\text{t} = 1.7(6)$ a.u. reported in Ref. [161], the contribution of the tensorial term varies from 0.5% up to 1% of the scalar one. The trap frequencies scale as $\propto \sqrt{\alpha_\text{tot}}$, where the polarizability α_tot takes into account all the scalar, vector, and tensor parts. Therefore there would be only a small contribution of the tensorial part to the change in trap frequencies, which we neglect.

The trap frequencies are also affected by the presence of residual magnetic field gradients. To quantify those gradients we performed measurements of the COM position $Z_i(t_\text{TOF})$ for three different orientations of the magnetic field, along the three axes (x, y, z), and as a function of t_TOF. By fitting the function $y = a + b\ t_\text{TOF} + \frac{1}{2}c\ t_\text{TOF}^2$ to $Z_i(t_\text{TOF})$, it is possible to estimate the correction to the gravitational acceleration due to the presence of residual magnetic field gradients. We measure a higher acceleration by 2% and 1% for dysprosium and erbium, respectively, when the magnetic field points along the z-axis. These gradients, which point along the same direction of gravity, slightly decrease the trap frequencies by few % when going from B along the xy-plane to B along z.

Another important input for the theoretical model is the value of the intraspecies scattering length. For erbium, the scattering length was accurately determined using lattice-modulation spectroscopy [144]. This technique is based on the measurement of the on-site interaction between atoms trapped in an optical lattice, from which a_s can be determined. The on-site interaction is measured by modulating the lattice depth and by looking at the induced heating caused by the doubly occupied lattice sites at the specific resonance frequency. Therefore, for the magnetic field value relevant for us, a_s^{Er} was set to $a_s^{Er} = 83(3)\ a_0$ [40]. However, such an accurate determination of the scattering length is still missing for dysprosium and various experiments reported different values [62, 181]. We set $a_s^{Dy} = 95\ a_0$, which gives an unmodulated BEC for our atom numbers and trap geometry.

3.4 Outlook: induced supersolidity in dipolar mixture

In Chapter 1 it was shown that erbium and dysprosium can make a phase transition to a supersolid state and develop density modulation and maintain global phase coherence in a narrow range of scattering lengths, where $\epsilon_{dd} \gtrsim 1.3$. From our ground-state calculations of a double BEC made of erbium and dysprosium atoms, we found that when the scattering length of dysprosium is just above the aforementioned range, whereas erbium is in the contact-dominated regime with $\epsilon_{dd}^{Er} < 1$, by increasing the repulsive interactions a_{12} between the species, it is possible to induce the onset of supersolidity in dysprosium. Furthermore, when pushing the two clouds closer by tightening the trap, the density modulation present in dysprosium can be transferred on erbium.

After this work, several theoretical proposals focused on the different ground-state phases that can be realized by merging two dipolar condensates. In particular, in Ref. [169], the authors study a dipolar mixture with $(\mu_2/\mu_1 \simeq 1)$ in the miscible regime, where $\mu_1(\mu_2)$ is the magnetic moment of species 1(2), and $N_2/N = [0, 0.5]$ with N the total atom number and N_2 the atom number of species 2. The authors show that a binary condensate can be described as a single-component condensate with an effective dipolar strength, which can be tuned by changing the interspecies scattering length and the atom number of the second species. In this work, a peculiar phase with a double supersolid formed by immiscible droplets is predicted. In Ref. [26], the authors investigate the formation of domain supersolids formed after a spin roton instability [195]. Unlike supersolids induced by roton instability, where to sustain

supersolidity a certain density need to be maintained [154], for domain supersolids, such a stringent condition on the density is not present. This leads to extended systems with atom numbers per domain an order of magnitude lower than the case of droplet supersolids, leading to a potentially longer lifetime due to reduced three-body losses.

The aforementioned interesting regimes can be reached by varying the magnetic field value in proximity of an interspecies Feshbach resonance (FR) in order to tune the sign and the strength of a_{12}. In the publication shown in A.3, we experimentally observed interspecies FR in two bosonic isotope mixtures of erbium and dysprosium with a width larger than 1 G, whose interspecies character was probed by looking at the scattering cross-section in proximity of the loss feature, as described in Sec. 3.2. These Feshbach resonances are located in a reasonably low magnetic field region[2] and are promising tools to achieve interesting many-body phases in erbium-dysprosium mixtures.

[2]The isotope mixture ^{164}Dy-^{168}Er presents an interspecies FR at around 13 G, while ^{164}Dy-^{166}Er at around 34 G.

3.5 Publication I:

Interspecies interactions in an ultracold dipolar mixture

The following publication has appeared in

Physical Review A **105**, 023304 (2022)*
submitted 19 Oct 2021; published 3 Feb 2022
DOI: https://doi.org/10.1103/PhysRevA.105.023304
C. Politi,[1,2] A. Trautmann,[1] P. Ilzhöfer,[1,2] G. Durastante,[1,2] M. J. Mark,[1,2] M. Modugno,[3,4] and F. Ferlaino[1,2]

[1] *Institut für Quantenoptik und Quanteninformation, Österreichische Akademie der Wissenschaften, 6020 Innsbruck, Austria*

[2] *Institut für Experimentalphysik, Universität Innsbruck, 6020 Innsbruck, Austria*

[3] *Department of Physics, University of the Basque Country UPV/EHU, 48080 Bilbao, Spain*

[4] *IKERBASQUE, Basque Foundation for Science, 48013 Bilbao, Spain*

*The author of the present thesis performed the measurements together with G. D., analysed the experimental data, wrote the manuscript together with M. M. and F. F. and contributed in interpreting the results together with all the authors.

Editors' Suggestion

Interspecies interactions in an ultracold dipolar mixture

C. Politi,[1,2] A. Trautmann,[1,*] P. Ilzhöfer,[1,2,†] G. Durastante,[1,2] M. J. Mark,[1,2] M. Modugno,[3,4] and F. Ferlaino[1,2,‡]

[1]*Institut für Quantenoptik und Quanteninformation, Österreichische Akademie der Wissenschaften, 6020 Innsbruck, Austria*

[2]*Institut für Experimentalphysik, Universität Innsbruck, 6020 Innsbruck, Austria*

[3]*Department of Physics, University of the Basque Country UPV/EHU, 48080 Bilbao, Spain*

[4]*IKERBASQUE, Basque Foundation for Science, 48013 Bilbao, Spain*

(Received 19 October 2021; accepted 10 January 2022; published 3 February 2022)

We experimentally and theoretically investigate the influence of the dipole-dipole interactions (DDIs) on the total interspecies interaction in an erbium-dysprosium mixture. By rotating the dipole orientation we are able to tune the effect of the long-range and anisotropic DDI, and therefore the in-trap displacements of the erbium and dysprosium clouds. We present a theoretical description for our binary system based on an extended Gross-Pitaevskii theory, including the single-species beyond mean-field terms, and we predict a lower and an upper bound for the interspecies scattering length $a_{12} = 105[-65, +162]a_0$. Our work is a step towards the investigation of the experimentally unexplored dipolar miscibility-immiscibility phase diagram and the realization of quantum droplets and supersolid states with heteronuclear dipolar mixtures.

DOI: 10.1103/PhysRevA.105.023304

I. INTRODUCTION

The ability to tune the interparticle interactions, the geometry and dimensionality of the system, and the possibility of adding complexity in a controlled manner, has made ultracold atomic gases a great platform for studying a plethora of physical phenomena that would be otherwise hard to achieve [1]. Combining two atomic species gives even further opportunities for investigating the effects arising from the interplay between the intra- and interspecies interactions, as polarons [2,3], heteronuclear quantum droplets [4–6], solitons [7], and ultracold molecules [8].

Heteronuclear mixtures are typically realized by combining contact-interacting atomic species (see alkali-alkali mixtures [9–15], alkali-alkaline-earth mixtures [16], and alkali-alkaline-earth-like mixtures [17–19]). Recently, experiments were able to produce novel types of ultracold mixtures where either one or both mixture components are long-range interacting (lanthanide) atomic species [20,21]. In particular, the realization of Er-Dy dipolar quantum mixtures is attracting great interest, driven by the possibility of creating new quantum phases even more exotic than the one achieved in contact-interacting mixtures [1] or in single-species dipolar gases [22]. Several theoretical works reported on the study of miscibility in dipolar condensates [23–26], vortex lattice formation [27,28], and on binary quantum droplets realized with dipolar mixtures [29–31].

In heteronuclear dipolar Bose-Bose mixtures, the phenomena mentioned above rely quite strongly on the miscibility-immiscibility conditions. These conditions define whether the two components mix together with the center of masses overlapping at the trap center or whether they are in a phase-separated state where the two centers of mass are pushed away from each other. The miscibility-immiscibility phase diagram depends on the contact intraspecies scattering lengths a_{11}, a_{22} and dipolar lengths $a_{\mathrm{dd},1}$, $a_{\mathrm{dd},2}$, and the interspecies scattering lengths a_{12} and dipolar lengths $a_{\mathrm{dd},12}$. While $a_{\mathrm{dd},12}$ can be calculated analytically, a_{12} is unknown and its determination relies on experimental measurements.

In this paper, we prepare ultracold degenerate mixtures of erbium and dysprosium, and experimentally investigate the effect of the mean-field dipole-dipole interactions on the total interspecies interaction by tracing the center-of-mass displacement for different dipole orientations. We present a theoretical description for our system, including the single-species beyond mean-field terms, which reproduces qualitatively well the experiment. By matching theory and experiment, we define a lower and upper bound for the interspecies scattering length a_{12}.

II. THEORY

Here, we consider a binary mixture of dipolar condensates of ^{164}Dy and ^{166}Er atoms confined in a harmonic potential, in the presence of a magnetic field $\boldsymbol{B}$ aligned along an arbitrary direction in space. The system can be described in terms of an extended Gross-Pitaevskii energy functional $E = E_{\mathrm{MF}} + E_{\mathrm{dd}} + E_{\mathrm{LHY}}$ with.

$$E_{\mathrm{MF}} = \sum_{i=1}^{2} \int \left[\frac{\hbar^2}{2m_i} |\nabla \psi_i(\boldsymbol{r})|^2 + V_i(\boldsymbol{r}) |\psi_i(\boldsymbol{r})|^2 \right] d\boldsymbol{r} + \sum_{i,j=1}^{2} \frac{g_{ij}}{2} \int n_i(\boldsymbol{r}) n_j(\boldsymbol{r}) d\boldsymbol{r}, \quad (1)$$

$$E_{\mathrm{dd}} = \sum_{i,j=1}^{2} \frac{C_{ij}^{\mathrm{dd}}}{2} \iint n_i(\boldsymbol{r}) V_{\mathrm{dd}}(\boldsymbol{r} - \boldsymbol{r}') n_j(\boldsymbol{r}') d\boldsymbol{r} d\boldsymbol{r}', \quad (2)$$

*Present address: Physikalisches Institut, Auf der Morgenstelle 14 (D-Bau), 72076 Tübingen, Germany.

†Present address: 5. Physikalisches Institut and Center for Integrated Quantum Science and Technology, Universität Stuttgart, Pfaffenwaldring 57, 70569 Stuttgart, Germany.

‡Corresponding author: francesca.ferlaino@uibk.ac.at

and the single-species Lee-Huang-Yang (LHY) correction for the two components

$$E_{\rm LHY} = \frac{256\sqrt{\pi}}{15}\sum_{i=1}^{2}\frac{\hbar^2 a_{ii}^{5/2}}{m_i}\left(1+\frac{3}{2}\epsilon_{{\rm dd},i}^2\right)\int n_i(\boldsymbol{r})^{5/2}d\boldsymbol{r}, \quad (3)$$

where $n_i(\boldsymbol{r}) = |\psi_i(\boldsymbol{r})|^2$ represents the density of each condensate, $V_i(\boldsymbol{r}) = (m_i/2)\sum_{\alpha=x,y,z}\omega_{\alpha,i}^2 r_\alpha^2 + m_i g z$ includes the harmonic trapping and gravity potentials, $g_{ij} = 2\pi\hbar^2 a_{ij}(m_i + m_j)/(m_i m_j)$ is the contact interaction strength, $V_{\rm dd}(\boldsymbol{r}) = (1 - 3\cos^2\bar{\theta})/(4\pi r^3)$ the (bare) dipole-dipole potential, $C_{ij}^{\rm dd} \equiv \mu_0 d_i d_j$ its strength, d_i the modulus of the dipole moment $\boldsymbol{d}_i$ of each species, $\epsilon_{{\rm dd},i} = \mu_0 d_i^2/3g_{ii}$ [32], $\boldsymbol{r}$ the distance between the dipoles, and $\bar{\theta}$ the angle between the vector $\boldsymbol{r}$ and the dipole axis, $\cos\bar{\theta} = \boldsymbol{d}\cdot\boldsymbol{r}/(dr)$ [33]. In the following we identify species 1 with the Er condensate, and species 2 with the Dy condensate (we have also omitted the reference to the mass number, for ease of notations). As described later on, the orientation of the magnetic dipoles is varied along arbitrary directions through an external magnetic field $\boldsymbol{B}$.

Then, for each set of parameters the ground state of the system is obtained by minimizing the energy functional $E[\psi_1, \psi_2]$ by means of a conjugate algorithm (see, e.g., Refs. [33–35]). In the numerical code the double integral appearing in Eq. (2) is mapped into Fourier space where it can be conveniently computed using fast Fourier transform (FFT) algorithms, after regularization (see Appendix B). The LHY correction in Eq. (3) is obtained from the expression for homogeneous three-dimensional (3D) dipolar condensates under the local-density approximation [32,36]. For the sake of simplicity, here we do not include the interspecies LHY correction as it would require a much more complicated treatment [29,30], which is not essential when the system is stable against the mean-field collapse driven by the interspecies interactions, as in the present analysis.

Finally, we remark that the intraspecies scattering lengths are given as the input to the theory and, whereas the value for Er has been measured with high accuracy to be $a_{11} = 83(3)a_0$ at the magnetic field we are working at [37], the scattering length for Dy, a_{22}, still lacks an accurate determination. Several works have reported different values ranging from $60a_0$ to $100a_0$ [38,39]. As in the present work no signs of supersolid or droplet states have been observed [40], we set a_{22} to the minimal value for which Dy is stable against mean-field collapse (without LHY), namely $a_{22} = 95a_0$. This guarantees that the ground state is an unmodulated BEC, for our atom numbers and trap frequencies. Note that, since $a_{11} > a_{{\rm dd},1}$ while $a_{22} \leqslant a_{{\rm dd},2}$, with $a_{{\rm dd},i} = C_{ii}^{\rm dd} m_i/(12\pi\hbar^2)$ the dipolar length, we expect Eq. (3) to be more relevant for Dy than for Er. Indeed, when dropping this term for Er, we observe no changes in the behavior. Instead, for Dy, the system would collapse for $a_{22} < 95a_0$ for $\boldsymbol{B}$ perpendicular to the gravity direction.

III. EXPERIMENT

Our experiment starts with a degenerate mixture of ^{166}Er and ^{164}Dy, similar to Ref. [21]. In brief, after cooling the atomic clouds in a dual-species magneto-optical trap [41], we start the evaporative cooling by loading the mixture into a single-beam optical dipole trap at 1064 nm, which propagates horizontally (y axis); see the reference frame in Fig. 1(a). After about 600 ms, the power of a second trapping beam, propagating vertically along the direction of gravity (z axis), is linearly ramped up to form a crossed optical dipole trap (cODT). Here, the evaporation further proceeds for about 5 s. We perform the evaporation at a magnetic field of $B = 2.028$ G, pointing along the z axis, which allows an efficient cooling of both species.

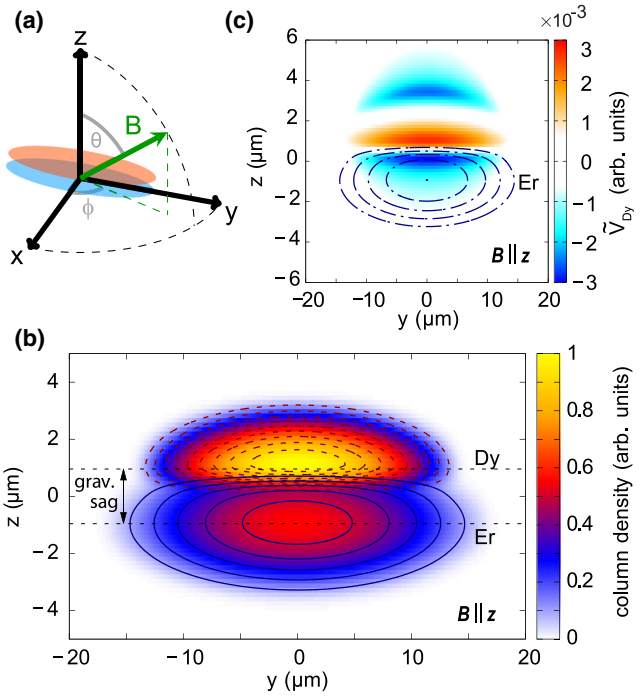

FIG. 1. Trap geometry, ground-state column density, and dipole potential. (a) Illustration of the geometry of our ^{164}Dy (red ellipse) and ^{166}Er (blue ellipse) mixture. The orientation of the magnetic field is defined by the angles ϕ and θ. The imaging beam propagates in the horizontal plane, at an angle of 45° with respect to the y axis (not shown). (b) Ground-state column density for an imbalanced mixture with $N_{\rm Dy} = 1.3\times10^4$, $N_{\rm Er} = 4.9\times10^4$, $a_{12} = 100a_0$. Dashed and solid lines show the isodensity contour levels for Dy and Er, respectively. For comparison, the in-trap displacement due to the gravitational sag for a noninteracting mixture is also shown (black dashed lines). We set $z = 0$ at the center of the gravitational sag. (c) Heat map of the dipole potential produced by the Dy condensate (parameters below), $\tilde{V}_{Dy}(\boldsymbol{r}) \equiv \int V_{\rm dd}(\boldsymbol{r}-\boldsymbol{r}')n_{Dy}(\boldsymbol{r}')d\boldsymbol{r}'$, in the $x = 0$ plane. Here, the magnetic field points along the z axis. The dotted-dashed lines represent the isodensity contour levels of the Er component, indicating that in this regime the interspecies dipolar interaction is predominantly attractive.

The final harmonic trap has a cigarlike shape, axially elongated along the y axis, with frequencies $\omega_{x,y,z} = 2\pi\times[96(1), 18(1), 150(5)]$ s^{-1}, and $\omega_{x,y,z} = 2\pi\times[104(1), 18(1), 165(5)]$ s^{-1} for Er and Dy, respectively. The trapping frequencies of the two species slightly differ. This is due to the small difference in their mass and atomic polarizability [42,43]. In a harmonic trap, each species experiences a shift of its center-of-mass (COM) position along the z axis due to gravity. This effect is known as

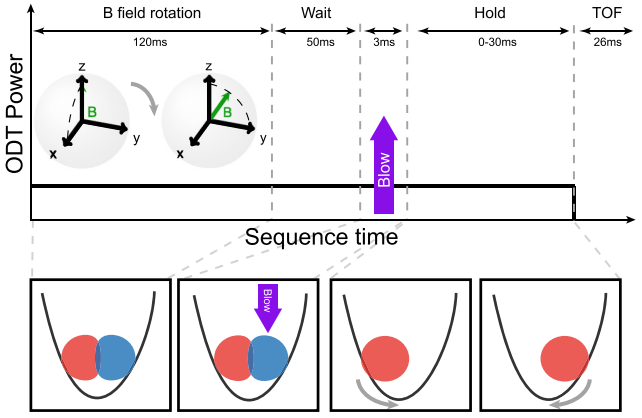

FIG. 2. Experimental protocol. After preparing our Er-Dy mixture with $\boldsymbol{B} \parallel z$, the magnetic field is rotated to an arbitrary direction, defined by θ and ϕ, in 120 ms. The atomic clouds are held in the trap for 50 ms to reach equilibrium, before either of the species is removed with resonant light. The remaining cloud is held for a variable hold time t_h. The cloud is then released from the trap and imaged with standard absorption imaging after a TOF expansion of $t_{\mathrm{TOF}} = 26$ ms. We prepare imbalanced mixtures with condensed atom numbers N_{C} in the range [1–3] $\times 10^4$ and [4–6] $\times 10^4$ for Dy and Er, respectively (see Appendix A).

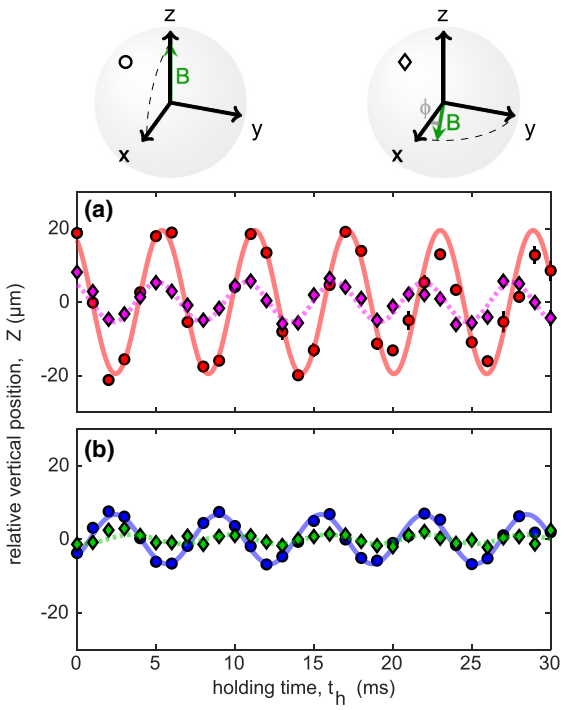

FIG. 3. COM oscillations after removal of either one of the species. (a) Vertical COM position of Dy after removing Er and (b) vice versa. The vertical position Z_i is recorded after a TOF expansion of 26 ms, as a function of the holding time. The offset z_{off} has been subtracted to facilitate comparison. The measurements are repeated for two magnetic-field orientations: $\boldsymbol{B} \parallel z$, $\theta = 0°$, $\phi = 0°$ (circles) and $\boldsymbol{B} \in \boldsymbol{xy}$, $\theta = 90°$, $\phi = 15°$ (diamonds). The atom numbers are $N_{\mathrm{Dy}} = 1.3(2) \times 10^4$, $N_{\mathrm{Er}} = 4.9(7) \times 10^4$ and $N_{\mathrm{Dy}} = 3.1(5) \times 10^4$, $N_{\mathrm{Er}} = 4.7(5) \times 10^4$ for $\boldsymbol{B} \parallel z$ and $\boldsymbol{B} \in \boldsymbol{xy}$, respectively. The error bars reported represent the standard error on the mean over three experimental trials, and are mostly smaller than the markers. We fit Eq. (4) to the data for $\boldsymbol{B} \parallel z$ (solid lines) and $\boldsymbol{B} \in \boldsymbol{xy}$ (dotted lines).

gravitational sag [44–46]. For mixtures, the differential gravitational sag between the components is given by $\Delta z_{\mathrm{grav}} = g(1/\omega_{z1}^2 - 1/\omega_{z2}^2)$, which for our Er-Dy mixture is $\Delta z_{\mathrm{grav}} = 1.9(1)\ \mu$m with Er shifted downwards more than Dy; see Fig. 1(a). Such gravitational sag favors phase separation along the z axis, reducing the interspecies overlap density. In the presence of interspecies interactions, the vertical distance of the clouds' centers is not only determined by the gravitational sag but also by their mutual mean-field attraction or repulsion [13,15,47–49], quantified by the mean-field shift Δz_{MF}. For dipolar mixtures, Δz_{MF} is determined by the interplay between the dipolar and contact interspecies interactions, as we will discuss later. The total vertical in-trap displacement is thus $\Delta z = \Delta z_{\mathrm{grav}} + \Delta z_{\mathrm{MF}}$.

Figure 1(b) shows exemplary calculations of the 2D ground-state column density of an imbalanced mixture for $\boldsymbol{B} \parallel z$ and $a_{12} = 100 a_0$. In this configuration, a COM shift is clearly visible, which exceeds the gravitational sag, indicating a total repulsive mean-field interaction between the components. To understand the role of the DDI, it is interesting to calculate the effective potential generated by one species (e.g., Dy), $\tilde{V}_{Dy}(\boldsymbol{r}) \equiv \int V_{\mathrm{dd}}(\boldsymbol{r} - \boldsymbol{r}') n_{Dy}(\boldsymbol{r}') d\boldsymbol{r}'$, felt by the other species (e.g., Er). Such effective potentials are most relevant in the region where the two species overlap (beside a long-range tail from the DDI). As shown in Fig. 1(c), for our trap geometry and dipole orientation, Er experiences a dominant attractive DDI generated by Dy, which is however weaker than the repulsive interspecies contact interaction for $a_{12} = 100 a_0$.

To experimentally study the interspecies mean-field shift, we selectively remove either one of the two species and follow the COM dynamics of the remaining species towards its new equilibrium position in the trap [21]. Figure 2 illustrates our protocol. After preparing our trapped Bose-Bose Er-Dy mixture with $\boldsymbol{B} \parallel z$, we first adiabatically rotate the magnetic field in 120 ms to the desired orientation (i.e., changing θ and ϕ) and let the mixture equilibrate for 50 ms. We then selectively remove either Er or Dy by shining a resonant light pulse, operating on either of the two strong atomic transitions [401 nm (421 nm) for Er (Dy)]. We have checked that this resonant pulse of 3-ms duration does not affect the remaining species. Finally, we hold the remaining species in trap for a variable time t_h and probe the system with standard absorption imaging after a time-of-flight (TOF) expansion of $t_{\mathrm{TOF}} = 26$ ms.

After the selective removal of either of the two species, the remaining species is out of equilibrium and the cloud COM starts to oscillate around its new equilibrium position, given by the dipole-trap minimum in the presence of gravity. Figure 3(a) [Fig. 3(b)] shows the vertical COM position Z_i (see Appendix A), measured after TOF, for Dy (Er) after removing Er (Dy) and for two different dipole orientations.

The amplitude of the observed oscillation is directly connected to the interspecies mean-field shift experienced by the atoms in the trap. Within the assumption of ballistic expansion, which is justified in the weakly interact-

ing regime, $Z_i(t_h, t_{\rm TOF}) = z_i(t_h) + \dot{z}_i(t_h)t_{\rm TOF} + gt_{\rm TOF}^2/2$, where $z_i(t_h) = \Delta z_{{\rm MF},i}\cos(\omega_i t_h) + \Delta z_{\rm grav}$ is the in-trap COM position. The oscillation frequency ω_i is the trap frequency along the z axis.

By combining the previous equations, one gets the following expression,

$$Z_i(t_h, t_{\rm TOF}) = \Delta z_{{\rm MF},i}\cos(\omega_i t_h) - \Delta z_{{\rm MF},i}\,\omega_i \sin(\omega_i t_h)t_{\rm TOF} + z_{\rm off}, \tag{4}$$

where $z_{\rm off} = \Delta z_{\rm grav} + gt_{\rm TOF}^2/2$. We fit Eq. (4) to the experimental data for the two magnetic-field orientations with the mean-field shift $\Delta z_{{\rm MF},i}$, ω_i, and $z_{\rm off}$ being free fitting parameters.

IV. RESULTS

Figure 3 shows important information on the interspecies interactions. First, by comparing the dynamics of the two species, we observe that the oscillations are counterphase. The Dy cloud starts moving downwards towards the trap center, whereas the Er one moves upwards, confirming a total repulsive interspecies interaction for this geometry. Second, we see a clear difference in the oscillation amplitude between Dy and Er. This is due to the fact that the mixture is imbalanced with Er being the majority species, and therefore the mean-field shift caused by Er on Dy is larger. Finally, for each species, the oscillation amplitude strongly depends on the magnetic-field orientation. This behavior cannot be simply explained by the anisotropy of the DDI. For $\boldsymbol{B} \parallel \boldsymbol{z}$, the DDI is more attractive over the interspecies overlap region than for $\boldsymbol{B}$ in the xy plane, $\boldsymbol{B} \in \boldsymbol{xy}$. Hence, one would expect $\Delta z_{\rm MF,z} < \Delta z_{\rm MF,xy}$, contrasting the observations.

The additional effect to account for is the magnetostriction [50] of each species, i.e., a cloud elongation along the magnetization direction caused by the single-species DDI. For $\boldsymbol{B} \parallel \boldsymbol{z}$, the two clouds elongate along the z axis, thus increasing the interspecies overlap density; see Fig. 1(b). This increased overlap activates a backaction on the strength of the repulsive contact interaction, which acquires a larger weight, leading to an increased repulsion between the clouds. On the contrary, for $\boldsymbol{B} \in \boldsymbol{xy}$, the clouds elongate horizontally, thereby minimizing the overlap density and therefore the interspecies repulsion. The slight difference in frequency observed for the two magnetic-field orientations is due to the presence of small residual magnetic-field gradients (see Appendix C).

To get further insight into the anisotropy of the interspecies interactions, we repeat the above measurement for various dipole orientations, set by the angles θ and ϕ. As before, we perform two sets of measurements: We probe the out-of-equilibrium dynamics of Dy after removing Er and vice versa. To enhance the amplitude of the COM oscillations of one species (Dy), we perform measurements with imbalanced mixtures, where Er is the majority species with condensed atom numbers in the range $[4\text{–}6] \times 10^4$, while the Dy cloud contains about $[1\text{–}3] \times 10^4$ (see Appendix A).

Figure 4 summarizes our results. It shows both the measured and calculated mean-field shift $\Delta z_{{\rm MF},i}$ for each plane of rotation for Dy (red points) and Er (blue points). We observe that $\Delta z_{{\rm MF},i}$ has a maximum for $\boldsymbol{B} \parallel \boldsymbol{z}$ and decreases when approaching the horizontal plane. The gray lines show the theory

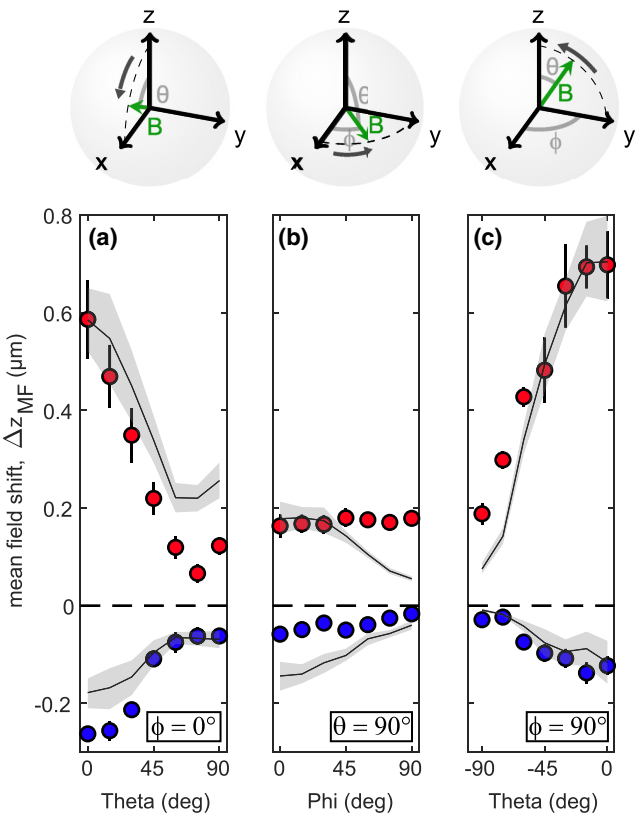

FIG. 4. Mean-field displacement and theory prediction. Experimental estimation of the mean-field displacement $\Delta z_{{\rm MF},i}$ for Dy (red points) and Er (blue points), as a function of the magnetic-field orientation. (a) $\theta = [0°, 90°]$, $\phi = 0°$. (b) $\phi = [0°, 90°]$, $\theta = 90°$. (c) $\theta = [0°, 90°]$, $\phi = 90°$. Theory prediction for an interspecies scattering length $a_{12} = 100a_0$ (gray lines). The gray shaded area takes into account the experimental uncertainty on the estimation of the atom number. The error bars in $\Delta z_{{\rm MF},i}$ correspond to the statistical uncertainty from the fit. The mismatch between the data points at $\theta = 0°$ in (a) and (c) is due to different atom numbers (see Appendix A).

results for an interspecies scattering length $a_{12} = 100a_0$ and for our experimental parameters, i.e., atom numbers and trap frequencies. We chose $a_{12} = 100a_0$ as it describes best the experimental data. The gray shaded area takes into account the experimental uncertainty on the estimation of the atom number.

The theory curves agree qualitatively with the experimental observations. In particular, experiment and theory are in good agreement for $\boldsymbol{B} \parallel \boldsymbol{z}$, while they start to deviate for $\boldsymbol{B} \in \boldsymbol{xy}$. The small mismatch can be due to the presence of residual vertical magnetic-field gradients, which are not taken into account in the theory. These can cause a systematic shift of the trap frequencies to higher values when going from $\boldsymbol{B} \parallel \boldsymbol{z}$ to $\boldsymbol{B} \in \boldsymbol{xy}$, thereby reducing the gravitational sag (see Appendix C). Furthermore, while our Dy ground-state calculations predict the transition to a macrodroplet at $a_{22} = 95a_0$ for $\boldsymbol{B} \parallel \boldsymbol{y}$, and a further reduction of the overlap density, in the experiment we observe a stable Dy BEC. Previous works have also shown a quantitative mismatch between theory and

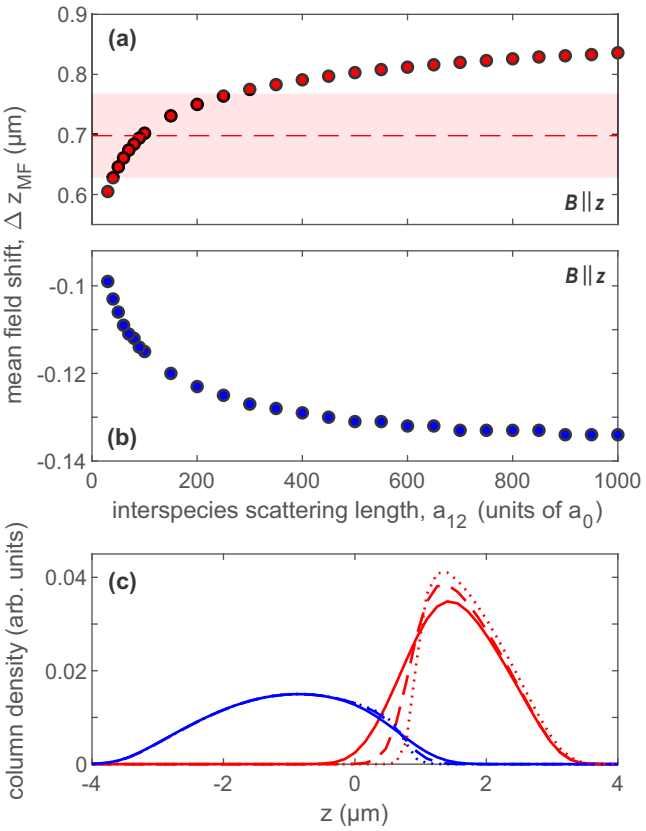

FIG. 5. Calculated mean-field displacement as a function of a_{12}. Calculated mean-field displacement for (a) Dy and (b) Er as a function of the interspecies scattering length a_{12}. The red dashed line and the red shaded area in (a) represent the Dy experimental mean-field displacement and its error, respectively. The magnetic field is oriented along the z axis. (c) In-trap density cut along $y = 0$ for Dy (red) and Er (blue), for $a_{12} = 30a_0$ (solid lines), $a_{12} = 100a_0$ (dashed lines), and $a_{12} = 200a_0$ (dotted lines). Here, $N_{\mathrm{Dy}} = 0.8 \times 10^4$ and $N_{\mathrm{Er}} = 5.9 \times 10^4$.

experiment in predicting the macrodroplet transition, suggesting the need for refined models and an accurate determination of a_{22} [36,37,51].

The overall behavior shown in Fig. 4 can be explained by the effect of the magnetostriction on the interspecies overlap density. In fact, as discussed earlier, for magnetic-field orientations in the horizontal plane, the clouds are elongated horizontally along the direction of $\boldsymbol{B}$, thereby minimizing the density overlap and the interspecies repulsion, whereas when orienting the magnetic field along the vertical direction, the magnetostriction leads to an increase of the density overlap and therefore of the interspecies repulsion, which overcomes the attractive DDI. The system undergoes a transition to a state where the two components are pushed aside, maximizing the in-trap displacement [see Fig. 1(b)].

To study the behavior of the mean-field shift as a function of a_{12}, we consider a specific magnetic-field orientation. In particular, for $\boldsymbol{B} \parallel z$, we perform ground-state calculations varying the interspecies scattering length a_{12} and calculate the Er-Dy mean-field displacement as a function of a_{12}. The results are shown in Fig. 5. The mean-field displacement increases with a_{12} owing to the fact that Dy [Fig. 5(a)] is pushed away from Er [Fig. 5(b)]. Figure 5(c) shows the Dy (red) and Er (blue) density cuts along $y = 0$, for $a_{12} = 30a_0$ (solid lines), $a_{12} = 100a_0$ (dashed lines), and $a_{12} = 200a_0$ (dotted lines). The repulsive interaction between the species leads to a decrease of the density overlap when going to higher a_{12}. We compare the theory results with the experimentally measured mean-field shift at $[\theta = 0°, \phi = 90°]$, and by performing a χ^2 analysis we are able to estimate the interspecies scattering length to be $a_{12} = 105[-65, +162]a_0$ (see Appendix D). From our ground-state calculations, when choosing $a_{12} < 30a_0$ the repulsive contribution of the contact interactions to the mean-field shift is not enough to overcome the attractive contribution from the DDI [see Fig. 1(c)] leading to a collapse of both species. In this regime, it might be necessary to include the interspecies LHY term as done in Refs. [29,30].

V. CONCLUSIONS AND OUTLOOK

In conclusion, we have experimentally investigated the effect of the DDI on the total interspecies interaction by tracing the mean-field in-trap displacement between the species. We have presented a theoretical description for our Er-Dy mixture, including the single-species beyond mean-field corrections, which qualitatively describes well our system and allows us to predict an interspecies scattering length on the order of $a_{12} = 100a_0$. By changing the magnetic-field orientation from the horizontal plane to the vertical direction, we were able to observe a transition to a state in which the two components are pushed apart by the dominant mean-field repulsive interaction. Future studies will focus on the use of interspecies Feshbach resonances, recently reported in our group [52], to reach the conditions in which one or both components exhibit a phase transition to a quantum droplet or supersolid regime. As an example, Fig. 6 shows that the onset of a supersolid phase in the Dy component can be induced by increasing the interspecies contact scattering length a_{12}.

ACKNOWLEDGMENTS

We thank Maximilian Sohmen for experimental support and for valuable discussions. We thank Rick van Bijnen for theoretical support. We also thank Lauriane Chomaz, Matthew Norcia, Lauritz Klaus, and the Innsbruck Erbium team for fruitful discussions. This work is financially supported through an ERC Consolidator Grant (RARE, No. 681432), the QuantERA grant MAQS by the Austrian Science Fund FWF No. I4391-N, the DFG/FWF via FOR 2247/I 4317-N36, and the FWF Grant No. I4426 RSF/Russia 2019. M.M. acknowledges support through Grant No. PGC2018-101355-B-I00 funded by MCIN/AEI/10.13039/501100011033 and by ERDF A way of making Europe, and by the Basque Government through Grant No. IT986-16. We also acknowledge the Innsbruck Laser Core Facility, financed by the Austrian Federal Ministry of Science, Research and Economy.

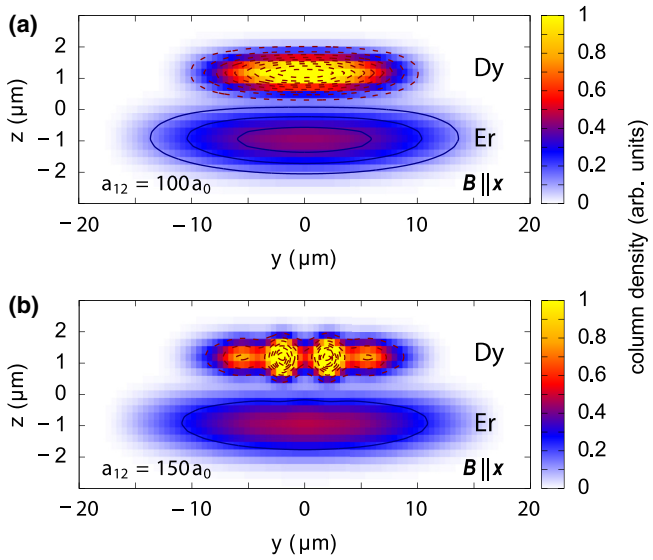

FIG. 6. Calculation of an interaction-induced supersolidity. Ground-state configurations for an imbalanced dipolar mixture with the magnetic field pointing along the x axis, for two different values of the interspecies scattering length: (a) $a_{12} = 100a_0$, (b)$\boldsymbol{a_{12} = 150a_0}$. Dashed and solid lines show the isodensity contour levels for Dy and Er, respectively. Here, $N_{\mathrm{Dy}} = 1.2 \times 10^4$, $N_{\mathrm{Er}} = 6 \times 10^4$, $a_{11} = 83a_0$, and $a_{22} = 95a_0$.

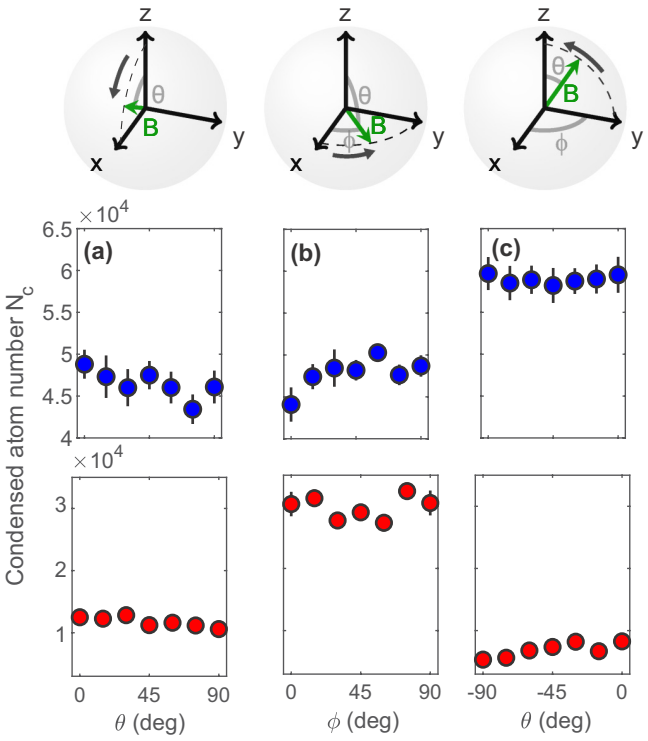

FIG. 7. Condensed atom numbers as a function of the magnetic-field orientation. Measured atom numbers in the BEC for Dy (red points) and Er (blue points) related to the measurement shown in Fig. 4 of the main text. The magnetic field is oriented (a) in the XZ plane, (b) in the XY plane, and (c) in the YZ plane. The error bars reported represent the standard error on the mean over three experimental trials.

APPENDIX A: ATOM NUMBER AND VERTICAL COM POSITION

After each experimental sequence—described in Fig. 2—we release the clouds and perform absorption imaging after a TOF expansion of 26 ms. We measure the condensed atom number for each species after subtracting the thermal part by fitting a symmetric 2D Gaussian to the wings of the density distribution. We then fit an asymmetric Gaussian to the remaining density distribution to extract the vertical COM position Z_i. Figure 7 shows the measured condensed atom numbers N_{C} of Dy (red points) and Er (blue points), related to the results presented in Fig. 4 of the main text. These atom numbers are given as input to the theory for each value of θ and ϕ.

APPENDIX B: FOURIER REPRESENTATION AND REGULARIZATION OF THE DIPOLAR ENERGY

Here, we outline the method used for calculating the double integral in Eq. (2), following the standard approach introduced in Ref. [33]. As anticipated, we start by rewriting the above integral in Fourier space. In particular, we make use of the *Parseval theorem* [34], $\int g(\boldsymbol{x}) h^*(\boldsymbol{x}) d\boldsymbol{x} = \int \tilde{g}(\boldsymbol{k}) \tilde{h}^*(\boldsymbol{k}) d\boldsymbol{k}$, where $\tilde{g}(\boldsymbol{k}) \equiv \mathrm{FT}[g](\boldsymbol{k})$ and $\tilde{h}^*(\boldsymbol{k}) \equiv \{\mathrm{FT}[h](\boldsymbol{k})\}^*$. Then, by defining $f \equiv h^*$ and recalling that $\mathrm{FT}[f^*](\boldsymbol{k}) = \tilde{f}^*(-\boldsymbol{k})$, we have $\tilde{h}^*(\boldsymbol{k}) = \{\mathrm{FT}[f^*](\boldsymbol{k})\}^* = \tilde{f}(-\boldsymbol{k})$, so that

$$E_{\mathrm{dd}} = \frac{1}{2} \int \tilde{n}_i^*(\boldsymbol{k}) \widetilde{V}_{\mathrm{dd}}(\boldsymbol{k}) \tilde{n}_j(\boldsymbol{k}) d\boldsymbol{k}, \tag{B1}$$

where we have used the fact that $n_i(\boldsymbol{r})$ is real, which implies $\tilde{n}_i(-\boldsymbol{k}) = \tilde{n}_i^*(\boldsymbol{k})$ [53]. At this point it is worth recalling that the use of the FT implicitly entails a periodic system, and this brings along an unwanted effect: The long-range dipolar interactions can couple the system to virtual periodic replica. Such a coupling is obviously unphysical, and it can be cured by limiting the range of the dipolar interaction within a sphere of radius R (contained inside the computational box of size L), namely multiplying $V_{\mathrm{dd}}(\boldsymbol{r})$ by the Heaviside step function $\Theta(R - r)$, with $R \leqslant L/2$. The corresponding FT is [33]

$$\widetilde{V}_{\mathrm{dd}}^{\mathrm{cut}}(\boldsymbol{k}) = 4\pi \left(1 + 3\frac{\cos(Rk)}{R^2k^2} - 3\frac{\sin(Rk)}{R^3k^3}\right)\left(\cos^2\alpha - \frac{1}{3}\right). \tag{B2}$$

APPENDIX C: ESTIMATION OF THE RESIDUAL MAGNETIC-FIELD GRADIENT

To evaluate the residual magnetic-field gradient we measure the COM position of Er and Dy as a function of the TOF and for different values of the magnetic field. In this way, we are able to extract the correction to the gravitational acceleration g due to residual magnetic-field gradients. When $\boldsymbol{B}$ is oriented along the z axis we measure an increase in g of about 2% for Dy and 1% for Er. The presence of these residual magnetic-field gradients along the direction of gravity leads to a slight decrease of the trap frequencies (see Fig. 3 in the main text) when orienting $\boldsymbol{B}$ from the XY plane to the z axis. The tensorial polarizability [42,54] could also cause a shift

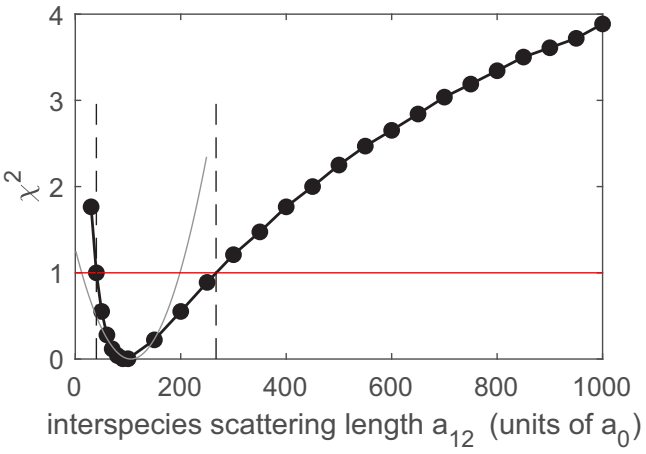

FIG. 8. χ^2 distribution of the mean-field shift. χ^2 distribution for the Dy mean-field shift (black points). We estimate the interspecies scattering length to be $a_{12} = 105[-65, +162]a_0$, by locally doing a Gaussian fit around the minimum of the distribution (gray line) and by defining the lower and upper bounds as the values at which $\chi^2 = 1$ (black dashed lines).

of the trap frequencies when changing the orientation of the magnetic field, but these are negligible in our case.

APPENDIX D: ESTIMATION OF THE INTERSPECIES SCATTERING LENGTH

From the calculated mean-field shift as a function of the interspecies scattering length, shown in Fig. 5 of the main text, we can estimate the value of a_{12} that best represents the experimental results and its confidence interval. Since Er is the majority species, its mean-field displacement is less sensitive to the change in interspecies scattering length [as shown in Fig. 5(b)]. In particular, the change in mean-field shift is within the experimental error. Therefore, we only take Dy into account for our analysis. We perform a χ^2 analysis for the Dy mean-field shift at $[\theta = 0°, \phi = 90°]$, with $\chi^2 = (\Delta z_{\mathrm{MF},2} - \Delta z^{\mathrm{th}}_{\mathrm{MF},2})^2/\sigma^2_{\Delta z_{\mathrm{MF},2}}$, where $\Delta z^{\mathrm{th}}_{\mathrm{MF},2}$ is the theoretically calculated in-trap mean-field displacement, and $\Delta z_{\mathrm{MF},2}$ and $\sigma_{\Delta z_{\mathrm{MF},2}}$ the experimental value and its statistical error. By fitting a Gaussian around the minimum of the distribution and by defining its confidence interval as the range in which $\chi^2 < 1$ [55], we estimate $a_{12} = 105[-65, +162]a_0$, see Fig. 8.

[1] I. Bloch, J. Dalibard, and W. Zwerger, Many-body physics with ultracold gases, Rev. Mod. Phys. **80**, 885 (2008).

[2] M.-G. Hu, M. J. Van de Graaff, D. Kedar, J. P. Corson, E. A. Cornell, and D. S. Jin, Bose Polarons in the Strongly Interacting Regime, Phys. Rev. Lett. **117**, 055301 (2016).

[3] N. B. Jørgensen, L. Wacker, K. T. Skalmstang, M. M. Parish, J. Levinsen, R. S. Christensen, G. M. Bruun, and J. J. Arlt, Observation of Attractive and Repulsive Polarons in a Bose-Einstein Condensate, Phys. Rev. Lett. **117**, 055302 (2016).

[4] D. S. Petrov, Quantum Mechanical Stabilization of a Collapsing Bose-Bose Mixture, Phys. Rev. Lett. **115**, 155302 (2015).

[5] C. R. Cabrera, L. Tanzi, J. Sanz, B. Naylor, P. Thomas, P. Cheiney, and L. Tarruell, Quantum liquid droplets in a mixture of Bose-Einstein condensates, Science **359**, 301 (2018).

[6] C. D'Errico, A. Burchianti, M. Prevedelli, L. Salasnich, F. Ancilotto, M. Modugno, F. Minardi, and C. Fort, Observation of quantum droplets in a heteronuclear bosonic mixture, Phys. Rev. Research **1**, 033155 (2019).

[7] B. J. DeSalvo, K. Patel, G. Cai, and C. Chin, Observation of fermion-mediated interactions between bosonic atoms, Nature (London) **568**, 61 (2019).

[8] K.-K. Ni, S. Ospelkaus, M. H. G. de Miranda, A. Pe'er, B. Neyenhuis, J. J. Zirbel, S. Kotochigova, P. S. Julienne, D. S. Jin, and J. Ye, A high phase-space-density gas of polar molecules, Science **322**, 231 (2008).

[9] G. Modugno, G. Ferrari, G. Roati, R. J. Brecha, A. Simoni, and M. Inguscio, Bose-Einstein condensation of potassium atoms by sympathetic cooling, Science **294**, 1320 (2001).

[10] Z. Hadzibabic, C. A. Stan, K. Dieckmann, S. Gupta, M. W. Zwierlein, A. Görlitz, and W. Ketterle, Two-Species Mixture of Quantum Degenerate Bose and Fermi Gases, Phys. Rev. Lett. **88**, 160401 (2002).

[11] M. Mudrich, S. Kraft, K. Singer, R. Grimm, A. Mosk, and M. Weidemüller, Sympathetic Cooling with Two Atomic Species in an Optical Trap, Phys. Rev. Lett. **88**, 253001 (2002).

[12] C. Silber, S. Günther, C. Marzok, B. Deh, P. W. Courteille, and C. Zimmermann, Quantum-Degenerate Mixture of Fermionic Lithium and Bosonic Rubidium Gases, Phys. Rev. Lett. **95**, 170408 (2005).

[13] D. J. McCarron, H. W. Cho, D. L. Jenkin, M. P. Köppinger, and S. L. Cornish, Dual-species Bose-Einstein condensate of ^{87}Rb and ^{133}Cs, Phys. Rev. A **84**, 011603(R) (2011).

[14] J. W. Park, C.-H. Wu, I. Santiago, T. G. Tiecke, S. Will, P. Ahmadi, and M. W. Zwierlein, Quantum degenerate Bose-Fermi mixture of chemically different atomic species with widely tunable interactions, Phys. Rev. A **85**, 051602(R) (2012).

[15] L. Wacker, N. B. Jørgensen, D. Birkmose, R. Horchani, W. Ertmer, C. Klempt, N. Winter, J. Sherson, and J. J. Arlt, Tunable dual-species Bose-Einstein condensates of ^{39}K and ^{87}Rb, Phys. Rev. A **92**, 053602 (2015).

[16] B. Pasquiou, A. Bayerle, S. M. Tzanova, S. Stellmer, J. Szczepkowski, M. Parigger, R. Grimm, and F. Schreck, Quantum degenerate mixtures of strontium and rubidium atoms, Phys. Rev. A **88**, 023601 (2013).

[17] A. Khramov, A. Hansen, W. Dowd, R. J. Roy, C. Makrides, A. Petrov, S. Kotochigova, and S. Gupta, Ultracold Heteronuclear Mixture of Ground and Excited State Atoms, Phys. Rev. Lett. **112**, 033201 (2014).

[18] V. D. Vaidya, J. Tiamsuphat, S. L. Rolston, and J. V. Porto, Degenerate Bose-Fermi mixtures of rubidium and ytterbium, Phys. Rev. A **92**, 043604 (2015).

[19] K. E. Wilson, A. Guttridge, J. Segal, and S. L. Cornish, Quantum degenerate mixtures of Cs and Yb, Phys. Rev. A **103**, 033306 (2021).

[20] C. Ravensbergen, V. Corre, E. Soave, M. Kreyer, E. Kirilov, and R. Grimm, Production of a degenerate Fermi-Fermi mixture of dysprosium and potassium atoms, Phys. Rev. A **98**, 063624 (2018).

[21] A. Trautmann, P. Ilzhöfer, G. Durastante, C. Politi, M. Sohmen, M. J. Mark, and F. Ferlaino, Dipolar Quantum Mixtures of Erbium and Dysprosium Atoms, Phys. Rev. Lett. **121**, 213601 (2018).

[22] M. A. Norcia and F. Ferlaino, Developments in atomic control using ultracold magnetic lanthanides, Nat. Phys. **17**, 1349 (2021).

[23] R. M. Wilson, C. Ticknor, J. L. Bohn, and E. Timmermans, Roton immiscibility in a two-component dipolar Bose gas, Phys. Rev. A **86**, 033606 (2012).

[24] R. K. Kumar, P. Muruganandam, L. Tomio, and A. Gammal, Miscibility in coupled dipolar and non-dipolar Bose–Einstein condensates, J. Phys. Commun. **1**, 035012 (2017).

[25] K.-T. Xi, T. Byrnes, and H. Saito, Fingering instabilities and pattern formation in a two-component dipolar Bose-Einstein condensate, Phys. Rev. A **97**, 023625 (2018).

[26] R. K. Kumar, L. Tomio, and A. Gammal, Spatial separation of rotating binary Bose-Einstein condensates by tuning the dipolar interactions, Phys. Rev. A **99**, 043606 (2019).

[27] R. K. Kumar, L. Tomio, B. A. Malomed, and A. Gammal, Vortex lattices in binary Bose-Einstein condensates with dipole-dipole interactions, Phys. Rev. A **96**, 063624 (2017).

[28] R. K. Kumar, L. Tomio, and A. Gammal, Vortex patterns in rotating dipolar Bose–Einstein condensate mixtures with squared optical lattices, J. Phys. B: At., Mol. Opt. Phys. **52**, 025302 (2018).

[29] R. N. Bisset, L. A. Pena Ardila, and L. Santos, Quantum Droplets of Dipolar Mixtures, Phys. Rev. Lett. **126**, 025301 (2021).

[30] J. C. Smith, D. Baillie, and P. B. Blakie, Quantum Droplet States of a Binary Magnetic Gas, Phys. Rev. Lett. **126**, 025302 (2021).

[31] J. C. Smith, P. B. Blakie, and D. Baillie, Approximate theories for binary magnetic quantum droplets, Phys. Rev. A **104**, 053316 (2021).

[32] F. Wächtler and L. Santos, Ground-state properties and elementary excitations of quantum droplets in dipolar Bose-Einstein condensates, Phys. Rev. A **94**, 043618 (2016).

[33] S. Ronen, D. C. E. Bortolotti, and J. L. Bohn, Bogoliubov modes of a dipolar condensate in a cylindrical trap, Phys. Rev. A **74**, 013623 (2006).

[34] W. H. Press, S. A. Teukolsky, W. T. Vetterling, and B. P. Flannery, *Numerical Recipes: The Art of Scientific Computing*, 3rd ed. (Cambridge University Press, New York, 2007).

[35] M. Modugno, L. Pricoupenko, and Y. Castin, Bose-Einstein condensates with a bent vortex in rotating traps, Eur. Phys. J. D **22**, 235 (2003).

[36] M. Schmitt, M. Wenzel, F. Böttcher, I. Ferrier-Barbut, and T. Pfau, Self-bound droplets of a dilute magnetic quantum liquid, Nature (London) **539**, 259 (2016).

[37] L. Chomaz, S. Baier, D. Petter, M. J. Mark, F. Wächtler, L. Santos, and F. Ferlaino, Quantum-Fluctuation-Driven Crossover from a Dilute Bose-Einstein Condensate to a Macrodroplet in a Dipolar Quantum Fluid, Phys. Rev. X **6**, 041039 (2016).

[38] Y. Tang, A. Sykes, N. Q. Burdick, J. L. Bohn, and B. L. Lev, *s*-wave scattering lengths of the strongly dipolar bosons ^{162}Dy and ^{164}Dy, Phys. Rev. A **92**, 022703 (2015).

[39] I. Ferrier-Barbut, M. Wenzel, F. Böttcher, T. Langen, M. Isoard, S. Stringari, and T. Pfau, Scissors Mode of Dipolar Quantum Droplets of Dysprosium Atoms, Phys. Rev. Lett. **120**, 160402 (2018).

[40] L. Chomaz, D. Petter, P. Ilzhöfer, G. Natale, A. Trautmann, C. Politi, G. Durastante, R. M. W. van Bijnen, A. Patscheider, M. Sohmen, M. J. Mark, and F. Ferlaino, Long-Lived and Transient Supersolid Behaviors in Dipolar Quantum Gases, Phys. Rev. X **9**, 021012 (2019).

[41] P. Ilzhöfer, G. Durastante, A. Patscheider, A. Trautmann, M. J. Mark, and F. Ferlaino, Two-species five-beam magneto-optical trap for erbium and dysprosium, Phys. Rev. A **97**, 023633 (2018).

[42] J. H. Becher, S. Baier, K. Aikawa, M. Lepers, J.-F. Wyart, O. Dulieu, and F. Ferlaino, Anisotropic polarizability of erbium atoms, Phys. Rev. A **97**, 012509 (2018).

[43] C. Ravensbergen, V. Corre, E. Soave, M. Kreyer, S. Tzanova, E. Kirilov, and R. Grimm, Accurate Determination of the Dynamical Polarizability of Dysprosium, Phys. Rev. Lett. **120**, 223001 (2018).

[44] M. Modugno, F. Ferlaino, F. Riboli, G. Roati, G. Modugno, and M. Inguscio, Mean-field analysis of the stability of a K-Rb Fermi-Bose mixture, Phys. Rev. A **68**, 043626 (2003).

[45] A. H. Hansen, A. Y. Khramov, W. H. Dowd, A. O. Jamison, B. Plotkin-Swing, R. J. Roy, and S. Gupta, Production of quantum-degenerate mixtures of ytterbium and lithium with controllable interspecies overlap, Phys. Rev. A **87**, 013615 (2013).

[46] F. Wang, X. Li, D. Xiong, and D. Wang, A double species ^{23}Na and ^{87}Rb Bose–Einstein condensate with tunable miscibility via an interspecies Feshbach resonance, J. Phys. B: At., Mol. Opt. Phys. **49**, 015302 (2015).

[47] S. B. Papp, J. M. Pino, and C. E. Wieman, Tunable Miscibility in a Dual-Species Bose-Einstein Condensate, Phys. Rev. Lett. **101**, 040402 (2008).

[48] K. L. Lee, N. B. Jørgensen, I.-K. Liu, L. Wacker, J. J. Arlt, and N. P. Proukakis, Phase separation and dynamics of two-component Bose-Einstein condensates, Phys. Rev. A **94**, 013602 (2016).

[49] K. E. Wilson, A. Guttridge, I.-K. Liu, J. Segal, T. P. Billam, N. G. Parker, N. P. Proukakis, and S. L. Cornish, Dynamics of a degenerate Cs-Yb mixture with attractive interspecies interactions, Phys. Rev. Research **3**, 033096 (2021).

[50] J. Stuhler, A. Griesmaier, T. Koch, M. Fattori, T. Pfau, S. Giovanazzi, P. Pedri, and L. Santos, Observation of Dipole-Dipole Interaction in a Degenerate Quantum Gas, Phys. Rev. Lett. **95**, 150406 (2005).

[51] F. Böttcher, M. Wenzel, J.-N. Schmidt, M. Guo, T. Langen, I. Ferrier-Barbut, T. Pfau, R. Bombín, J. Sánchez-Baena, J. Boronat, and F. Mazzanti, Dilute dipolar quantum droplets beyond the extended Gross-Pitaevskii equation, Phys. Rev. Research **1**, 033088 (2019).

[52] G. Durastante, C. Politi, M. Sohmen, P. Ilzhöfer, M. J. Mark, M. A. Norcia, and F. Ferlaino, Feshbach resonances in an erbium-dysprosium dipolar mixture, Phys. Rev. A **102**, 033330 (2020).

[53] We notice that the expression in Eq. (A8) of Ref. [33] can be used only if $n(\boldsymbol{r})$ is even under parity in the three spatial directions, namely when $\tilde{n}(-\boldsymbol{k}) = \tilde{n}(\boldsymbol{k})$.

[54] H. Li, J.-F. Wyart, O. Dulieu, and M. Lepers, Anisotropic optical trapping as a manifestation of the complex electronic structure of ultracold lanthanide atoms: The example of holmium, Phys. Rev. A **95**, 062508 (2017).

[55] P. Young, *Everything You Wanted to Know About Data Analysis and Fitting but Were Afraid to Ask* (Springer, Berlin, 2015).

Chapter 4

Two-dimensional supersolidity in dysprosium

In 2017 the ERBIUM experiment in Innsbruck observed the roton instability in a dipolar quantum gas [45]. Such a find provided first hints of the existence of a novel state of matter, namely a supersolid state, in analogy with the state predicted in helium. Later in 2019, in our experiment and in the ERBIUM experiment, the first dipolar supersolids were realized with ^{164}Dy and ^{166}Er, respectively [42]. Simultaneous results where achieved in the group of Giovanni Modugno [182] in Pisa (Italy), and in the group of Tilman Pfau [32] in Stuttgart (Germany). The realization of a dipolar supersolid triggered many novel theoretical, as well as experimental works, e.g. low-lying excitation modes (Goldstone and Higgs modes) [75, 84, 184], excitation spectrum [132, 151], superfluid fraction [136, 165, 183], out-of-equilibrium dynamics [89], and many more. One method to realize a dipolar supersolid is by first preparing a Bose-Einstein condensate at $a_{\mathrm{s}} > a_{\mathrm{dd}}$, with $\epsilon_{dd} < 1$, and then reach the supersolid regime by ramping the scattering length to lower values, in order to have $\epsilon_{dd} > 1$ (see Chapter 1).

This chapter introduces a different preparation scheme to achieve supersolidity by direct evaporative cooling from a thermal cloud. The first supersolid states were formed by three or four droplets aligned along a single direction. The second section of this chapter points out the fundamental steps necessary to extend the supersolidity from one to two dimensions, first in a zig-zag pattern and finally in a hexagonal pattern. Lastly, the third section describes the possibility offered by two-dimensional states of studying interesting excitation modes, as well as vortices in supersolid states.

4.1 Direct evaporation into the supersolid state

Erbium and dysprosium present many stable isotopes with relatively high abundance, whose interaction properties are different, offering a powerful knob to tune in the experiment. In contrast to ^{166}Er and ^{162}Dy (used in Stuttgart [32] and in Pisa [182]), to prepare a supersolid state we loaded our atomic cloud with the isotope ^{164}Dy. The special property of this isotope is the background scattering length a_{bg}, which is smaller than a_{dd}, where for ^{164}Dy is $a_{\mathrm{dd}} = 131\ a_0$. Figure 4.1 shows an illustration of how the dipolar strength changes with the magnetic field. Figure 4.1(a) shows the ^{164}Dy case, in which the scattering length can be tuned away from the Feshbach resonance to reach the supersolid regime with $\epsilon_{dd} > 1$. Figure 4.1(b) shows instead the ^{166}Er and the ^{162}Dy case where, to reach the dipolar dominated regime, the magnetic field has to be tuned close to the Feshbach resonance. This caused big losses and a short lifetime of the supersolid state due to three-body recombination losses. In fact, while the other groups, using ^{166}Er and ^{162}Dy, observed a lifetime on the order of tens of ms, the ^{164}Dy supersolid survived for several hundreds of ms [42], when prepared via interaction ramp.

The long lifetime motivated us to develop a new preparation scheme, in which we performed direct evaporative cooling into the supersolid state from a thermal cloud [42, 177]. In this way, instead of moving horizontally in the $T = 0$ phase diagram (see Sec. 1.3), we cross the supersolid phase at fixed scattering length from the third dimension, given by the temperature. Although, for linear supersolids, where the droplets are aligned along a single direction, the interaction-ramp protocol can be weakly first order or continuous [18, 23] and therefore causing only small excitations, the direct-evaporative cooling protocol proved to be essential in realizing two-dimensional supersolidity and allowed us to reach lifetime on the order of seconds (see Sec. 4.7).

The formation of a supersolid state requires the breaking of two continuous symmetries: the phase invariance of the superfluid and the translational invariance of the crystal. When accessing the supersolid state from a thermal cloud, the initial state of the system has neither phase coherence nor density modulation. Therefore, it is natural to ask whether the two symmetries are broken simultaneously and, if not, which one occurs first. In our publication in Sec. 4.4, by following the evaporative-cooling process of the atomic cloud, from several hundreds of nK down to tens of nK, we could gain information on the development of the supersolid state. Our first experimental observation pointed at the initial formation of a quasi-condensate crystal, where phase coherence is localized within the droplets, and later, when lowering the temperature, the creation of the supersolid state with the coexistence of density modulation and

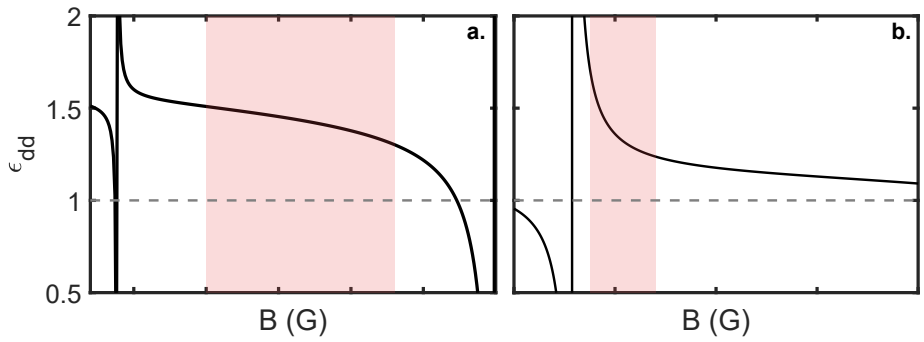

Figure 4.1 Illustration of the dipolar strength ϵ_{dd} as a function of the magnetic field B, for ^{164}Dy (a) and for ^{166}Er and ^{162}Dy (b). In the former case, the condition of $a_{bg} < a_{dd}$ allows us to achieve a supersolid state by moving away from the Feshbach resonance. On the other hand, in the latter case, $a_{bg} > a_{dd}$. Therefore, to reach the dipolar dominated regime, the magnetic field is tuned closer to the Feshbach resonance causing large three-body recombination losses.

global phase coherence [177]. Furthermore, when looking at the modulation contrast for similar atom number but different temperatures, we observed a higher degree of modulation for higher temperatures, underlining the important role that finite temperature plays in the supersolid formation. These findings triggered many theoretical works aimed at improving the understanding of the finite-temperature phase diagram of dipolar gases. Section 4.1.2 and 4.9 show how, not only quantum fluctuations, but also thermal fluctuations have a fundamental role in the formation of a supersolid state. In particular, higher temperatures lower the roton gap in the excitation spectrum and favour the appearance of density modulation.

4.1.1 Probing supersolidity in the experiment

As evidence of supersolidity in the system, both density modulation and global phase coherence need to be proven. In this regard, we use two different imaging techniques: one probing the insitu density distribution, from which we determine the density modulation and therefore the crystalline nature of the state, and a second one probing the momentum distribution after a TOF expansion, from which we determine the global phase coherence and therefore the superfluid nature of the state[1].

[1]The recorded images taken after TOF expansion give also information on the amount of density modulation. More details will be given later in this section.

Insitu imaging. To probe the insitu density distribution, we shine far-detuned light onto the atoms and perform phase-contrast imaging (see Chapter 2). Fig. 4.2a shows the insitu density distribution $n(x, y)$ of a linear supersolid state made of ^{164}Dy atoms. By integrating $n(x, y)$ along the direction orthogonal to the modulation, we obtain the integrated density profile $n_y(x)$ (Fig. 4.2b), which shows a crystalline structure with periodicity l_x. The periodicity depends on the trap geometry and on the scattering length through the relation $1/l_x \propto \kappa\, \epsilon_{dd}^{1/4}/l_z$, where l_z is the harmonic oscillator length along the dipole orientation[2] and κ is a geometrical factor only dependent on f_z/f_y [45]. To gain quantitative information on the amount of modulation present in the system, we perform the Fourier transform of $n_y(x)$. This profile shows peaks in the momentum space at $\pm k^* \simeq 2\pi/l_x$. By taking the ratio of the Fourier component at k^* and the one at zero momentum, we determine the insitu density modulation M (see Fig. 4.2c). Note that, at the moment, the insitu imaging does not allow us to clearly resolve the low-density region between the droplets and extract direct information on the superfluid link. The low-density area is indeed more sensitive to fluctuations of the background, which can lead in some cases to unphysical negative values. Futhermore, for large detunings, the atomic susceptibility can assume a small non-zero value, which makes the dense atomic cloud behave as a lens. This effect is strongly reduced in phase-contrast imaging, but getting rid of it completely remains challenging due to the coupled dependence on detuning and intensity of the light. For this reason, to probe the superfluidity of the system, we look at the matter-wave interference pattern after TOF expansion.

Time-of-Flight imaging. To probe the global phase coherence of the state, we image the cloud after a TOF expansion by shining resonant light and performing standard absorption imaging (see Chapter 2). For an unmodulated dipolar BEC, the recorded picture shows a standard bimodal distribution, with a dense peak given by the condensed atoms and a broad contribution given by the thermal component. For a modulated system, the dense peak develops a pattern arising from the interference between the expanding droplets, with maxima at $\pm k^* \simeq 2\pi/l_x$. Fig. 4.3 displays an example of absorption picture taken after 35ms TOF for a linear modulated state, in the supersolid (a) and in the isolated-droplet (b) regimes. By recording the interference pattern for several runs under the same experimental parameters, it is possible to determine whether the system has global phase coherence. Indeed, on the one hand, if each droplet shared the same phase in trap, the interference pattern is reproducible

[2] $1/l_z = 2\pi\sqrt{m\nu_z/h}$.

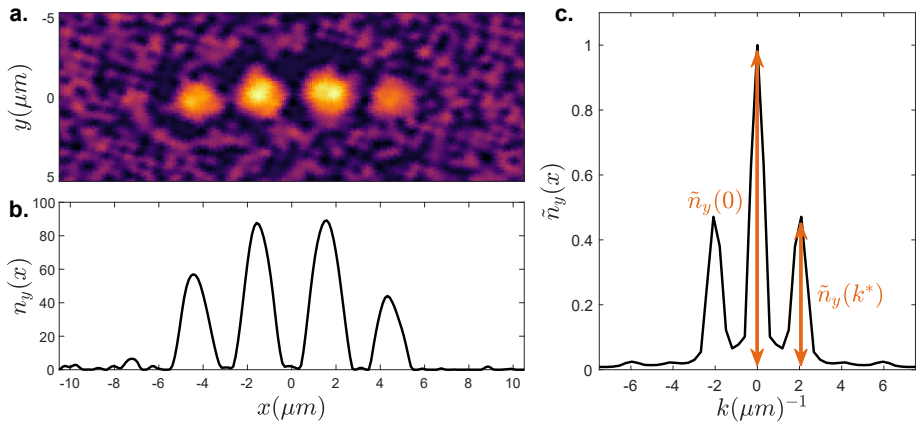

Figure 4.2 (a) In-trap density distribution $n(x, y)$ of a linear supersolid measured from phase-contrast imaging. The low-density link can not be reliably resolved (see discussion in the insitu imaging paragraph). (b) 1D integrated profile $n_y(x)$. (c) Absolute value of the Fourier transform of $n_y(x)$ showing a central peak at $k = 0$ and secondary peaks at $\pm k^*$.

from shot to shot, and survives after averaging the pictures over several experimental runs. On the other hand, if the droplets had all different phases, the interference pattern is not reproducible, exhibiting peaks with random amplitudes from shot to shot, and gets washed out in the average [79] (see Fig. 4.3(a,b)).

To quantify the amount of global phase coherence, as for the insitu pictures, we integrate the momentum distribution $n(k_x, k_y)$ along the direction orthogonal to the modulation and perform the Fourier transform (see Fig. 4.3(c-f)). The Fourier transform $\tilde{n}_y(x)$ holds the information on both the degree of modulation and global phase coherence of the system, through the complex phasors $P_i = \rho_i \exp(-i\Phi_i)$, with ρ_i and Φ_i its magnitude and phase, respectively. We define the phasor amplitudes at k^*, $A_M = \langle |P_i| \rangle$ and $A_\Phi = |\langle P_i \rangle|$, which carry the information on the amount of density modulation and global phase coherence, respectively. For an unmodulated state $A_M = 0$, whereas, for a modulated and fully coherent state $A_M = A_\Phi$. Fig. 4.3(e,f) show $\tilde{n}_y(x)$ in the supersolid and isolated droplets case, respectively. Additionally, by recording the phase Φ_i for each experimental run, it is possible to get a further estimation of the amount of global phase coherence. The insets in Fig. 4.3(e,f) show the polar scatter plots of the phase for two cases: supersolid state and isolated droplet state, respectively. In the former, all the points cluster in a small region of the polar plot whereas, for the latter, the points are spred all over the 2π region.

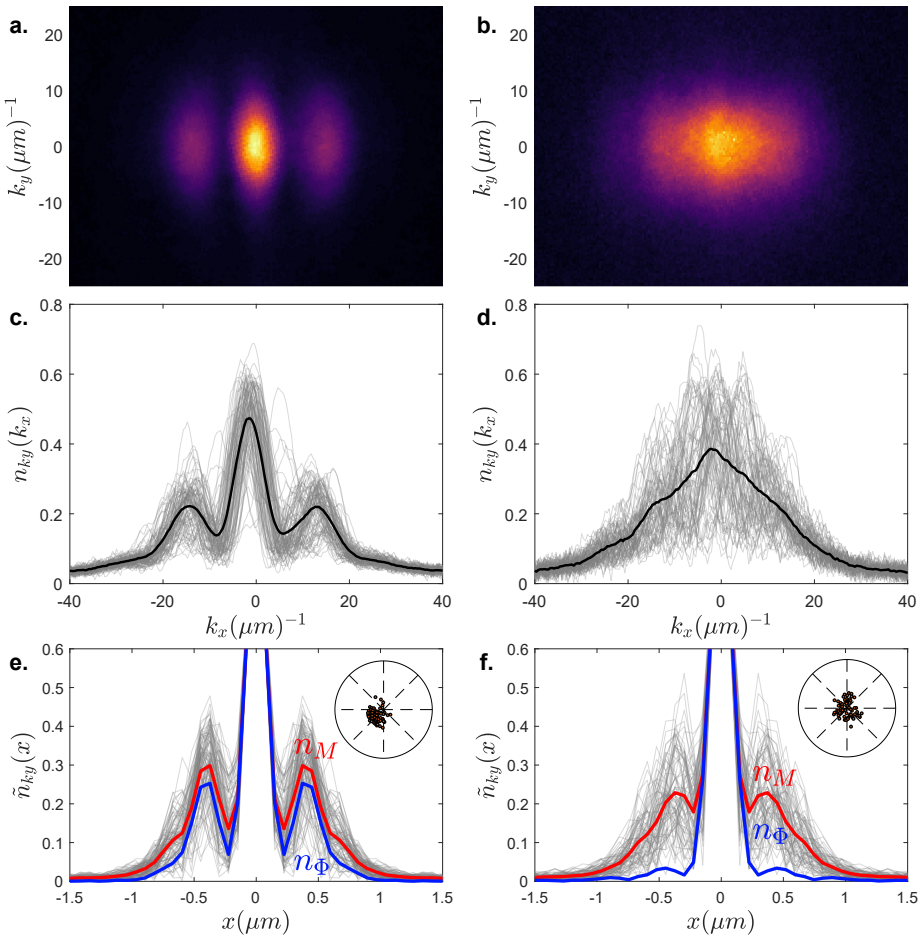

Figure 4.3 (a,b) Absorption images taken after 35ms TOF and averaged over 100 shots, for a modulated state as in Fig. 4.2a, in the supersolid and isolated droplet regime, respectively. (c,d) Integrated density profiles for several runs under the same experimental parameters (gray lines) and the average (black line) for a supersolid state and an isolated droplet array, respectively. (e,f) Fourier transform of the integrated profiles (gray lines) and $n_M = \langle|\tilde{n}_y(x)|\rangle$ (red line) and $n_\Phi = |\langle\tilde{n}_y(x)\rangle|$ (blue line) for a supersolid state and an isolated droplet array, respectively. The insets show the phase Φ_i for each experimental run.

4.1.2 The role of finite temperature

The role played by the temperature in the phase transition to a crystalline phase has drawn particular interest in the community to bridge theory and experiment. Indeed, in the experiment, the temperature of the condensed cloud has a finite value, while theoretical predictions are usually done assuming zero temperature. Recently, we carried out studies in collaboration with the group of Thomas Pohl at Aarhus University on the role of thermal fluctuations in dipolar systems. Our findings reveal

that the interaction between condensed atoms and thermal excitations can have a focusing effect on the density of condensed atoms, facilitating the appearance of density modulation [180]. This behaviour can be understood by looking at how the relevant energy terms scale with the condensate density and interactions. In particular, the energy term describing the quantum fluctuations (Eq. 1.6) is positive, increases with the density of condensed atoms and with the interactions and stabilizes the system against the collapse. The interaction between the condensed atoms and the thermal excitations is also positive and can be described by the following energy term:

$$E_{\mathrm{th}} = \int \frac{\mathrm{d}\mathbf{k}}{(2\pi)^3} \tilde{V}(\mathbf{k}) f_k(\mathbf{r}) \frac{\tau_k}{\epsilon_k(r)}, \tag{4.1}$$

where $\tilde{V}(\mathbf{k})$ is the Fourier transform of the total interaction potential, including contact interaction and long-range DDI, $f_k = 1/(e^{\epsilon_k/k_{\mathrm{B}}T} - 1)$ is the Bose distribution of the thermal excitations, $\tau_k = \hbar^2 k^2/(2m)$ is the kinetic energy of the atoms, and $\epsilon_k = \sqrt{\tau_k(\tau_k + 2|\psi(\mathbf{r})|^2 \tilde{V}(\mathbf{k}))}$ is the dispersion relation of the excitations. A more detailed description of the theoretical formalism can be found in the publication in Sec. 4.9. This energy term decreases when the density of condensed atoms increases, because higher density of condensed atoms means less thermal excitations. Therefore at finite temperatures, in seeking the lowest energy possible, higher densities are preferred [7] leading to a decrease in the roton energy gap Δ_{rot}, supporting density modulation. Another way of understanding this behaviour is by looking at the population of the excitation modes. At finite temperatures, the roton mode has a higher probability to be occupied. A population of this mode is associated with a modulation of the density in real space at the roton wavelength. This modulation locally increases the density, which in turn lowers the roton gap.

These theoretical findings agree well with our experimental observations and shed some light on the role of finite temperatures on the superfluid-supersolid phase transition. Figure 4.4a shows the average integrated profiles $n_y(x)$, for a dysprosium cloud prepared via evaporative cooling at fixed scattering length, with similar condensed atom numbers but different temperatures. The cloud at higher temperature shows a stronger modulation, which is also evident in the Fourier transform (Fig. 4.4b).

A decrease of the roton gap for higher temperatures was also observed in liquid helium [56, 93], where the elementary excitation spectrum is experimentally addressed via inelastic neutron scattering. Furthermore, theoretical predictions on the softening of the roton mode with increasing temperatures were done in BECs with light-induced dipole-dipole interactions, where long-range interactions can be engineered by irradi-

ating a cigar-shaped BEC with far off-resonant laser light [125]. Finally, theoretical works on Bose gases in reduced dimensions underlined the importance of thermal fluctuations and predicted the appearance of a thermally induced roton in contact interacting two-dimensional gases [134], and a decrease and a shift of the roton mode for increasing temperatures [200].

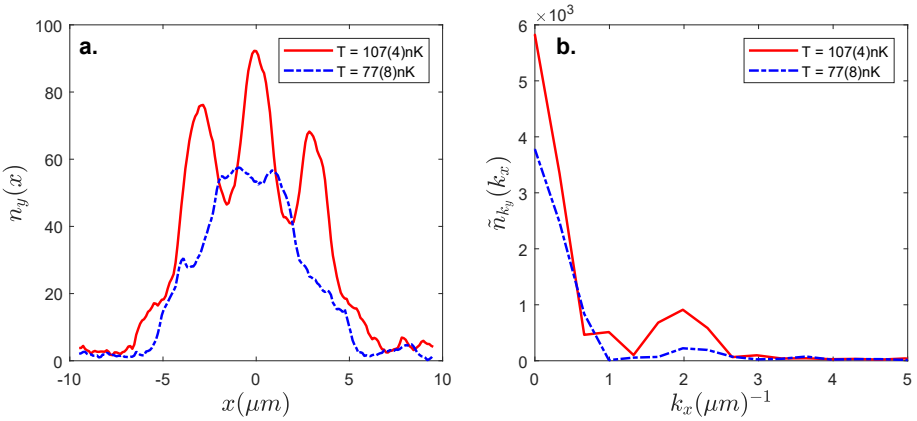

Figure 4.4 (a) Averaged integrated density profile of a ^{164}Dy cloud measured at two different temperatures: $T = 107(4)$ nK (red line) and $T = 77(8)$ nK (blue dash-dotted line). The condensed and the total atom number are $1.42(4) \times 10^4$ and $\sim 7 \times 10^4$, respectively, for the profile at higher temperature, and $1.34(7) \times 10^4$ and $\sim 4 \times 10^4$ for the profile at lower temperature. The trap geometry is cigar shaped with trap frequencies $\omega_{x,y,z} = 2\pi \times (36, 88, 141)\mathrm{s}^{-1}$ (b) Fourier transform of the averaged integrated profiles, showing a peak at the modulation wavevector for the system at higher temperature.

4.2 From one to two-dimensional supersolidity

The previous section described the main tools used in our experiment to create - direct evaporative cooling - and probe - phase-contrast and absorption imaging - supersolidity. As shown in Fig. 4.2a, the early supersolid states consisted of few droplets – three or four – aligned along a single direction, i.e. the elongated axis of a cigar-shaped trap. The clear further step to realize a supersolid state closer to the predicted bulk supersolids [31] was to extend the supersolid properties along a second direction and achieve two-dimensional supersolidity with a larger number of droplets.

The first two-dimensional states showing density modulation were realized in 2016 [91], but the system did not show any global phase coherence. It was not clear, from the beginning, whether it was possible to realize periodic structure and global phase coherence in systems with atom numbers that where realistically achievable in

the actual experiments. Most theoretical works predicted two-dimensional supersolidity for unconfined systems [99], systems confined only along the dipole orientation [204], or for atom numbers larger than the ones reported in the experiments [165]. The first supersolids were indeed realized with $\sim 2 \times 10^4$ atoms [42, 89, 177]. It was clear that to achieve density modulation and global phase coherence along two directions, and a larger system's size, a higher number of atoms was needed to build up the superfluid bath necessary for the particles to flow between droplets, and allow the development of global phase coherence.

In particular, the quantity that plays a key role in the transition from 1D to 2D supersolid states is the averaged 2D density $\rho = N_c f_x f_y$ [154]. In fact, for a fixed atom number, when loosening the trap confinement, e.g. f_y, the supersolidity is lost and the ground state of the system is a standard dipolar BEC. To maintain supersolidity, the 2D density needs to be kept constant, by either increasing the atom number N_c or f_x. Since in the experiment N_c can not be increased indefinitely, to achieve a transition to a 2D supersolid state, N_c can be kept constant while varying f_x and f_y accordingly to keep ρ constant. More details can be found in the publication shown in Sec. 4.6.

In the experiment, after improving the condensed atom number up to $\sim 7 \times 10^4$, we were able to produce states with up to 10 droplets. To reach supersolidity along two dimensions, we employed a similar approach already seen with ion crystals, and performed a structural phase transition from a linear chain of droplets to an arrange of droplets in a zig-zag pattern. In crystals made of singly-charged ions, the location of the ions and therefore the system's structure, arises from the competition between the long-range Coulomb repulsive interaction and the harmonic trapping confinement, usually provided by a Paul or a Penning trap. By tuning the trap frequencies independently, or by fixing the trap and increasing the ion number, the ions can arrange in a linear, zig-zag or helical configuration [19, 160].

In our system, the DDI plays the role of the Coulomb interaction and it is the competition between the contact and the long-range interaction and the trap confinement that induces the transition to a zig-zag supersolid state. In particular, by changing the power of the laser beams that generate our crossed optical dipole trap[3], we were able to prepare the supersolid state at different trap frequencies, while weakening the confinement orthogonal to the droplet direction and increasing the atom number, until the system performed a structural transition from a linear chain to a zig-zag pattern. Figure 4.5 shows the structural phase transition from a linear to a zig-zag pattern for a system made of ion crystals and for our dipolar supersolid made of ^{164}Dy atoms. While

[3]See Chapter 2.2.1 for details on the optical dipole trap.

in the former case releasing the transverse confinement is sufficient to achieve a zig-zag pattern, for a dipolar gas, to maintain supersolidity, while lowering the transverse trap frequency, the atom number needs to be increased.

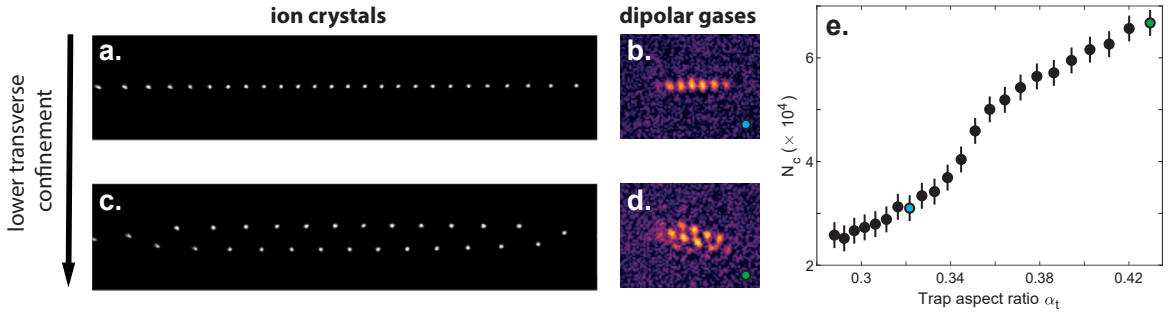

Figure 4.5 Structural phase transition from a linear chain to a zig-zag pattern in ionic crystals (a,c) and in a ultracold dipolar gas of ^{164}Dy atoms (b,d). In the former case, the transition to the zig-zag pattern is obtained by releasing the transverse confinement. In the latter case, to maintain supersolidity, the trap aspect ratio changes from $\alpha_t = 0.32$ (b) to $\alpha_t = 0.43$ (d), while the condensed atom number increases from $3.1(3) \times 10^4$ (b) to $6.7(3) \times 10^4$ (d). The trap frequencies along the other two directions are fixed to $f_x = 33(2)$Hz and $f_z = 167(1)$Hz. (e) Condensed atom number as a function of the trap aspect ratio, $\alpha_t = f_x/f_y$. The blue and green data points correspond to the insitu density distribution shown in (b) and (d), respectively. Figures (a,c) adapted from [159]. Figures (b,d) adapted from [137].

As mentioned in the previous section, to evaluate the global phase coherence of the supersolid state, we switch off the trap and let the droplet fall. While expanding, they interfere with each other and the resulting intereference pattern is reminiscent of the in-trap geometry. Figure 4.6 shows the interference pattern calculated for three different in-trap droplets arrangements: a triangular, a square and a diamond geometry. The interference pattern are obtained by considering free expanding Gaussian droplets with a phase randomly chosen in the narrow range $0.1 \times [0, 2\pi]$ to emulate the supersolid regime, and averaging over 50 trials, as done in the measurement shown in the publication in Sec. 4.5. The peaks distance and the configuration of the interference pattern resemble the in-trap droplets arrangement, with the hexagon pattern reproducing quantitatively well the experimental one. The amount of phase coherence changes the sharpness of the peaks and blurs the average pattern. Figure 4.7 shows the interference pattern for an insitu triangular geometry (as in the experiment) and for three different phase distributions: $0.1 \times [0, 2\pi]$, $0.5 \times [0, 2\pi]$, and $1 \times [0, 2\pi]$, where the first and the last represent the case of supersolid and isolated droplets, respectively.

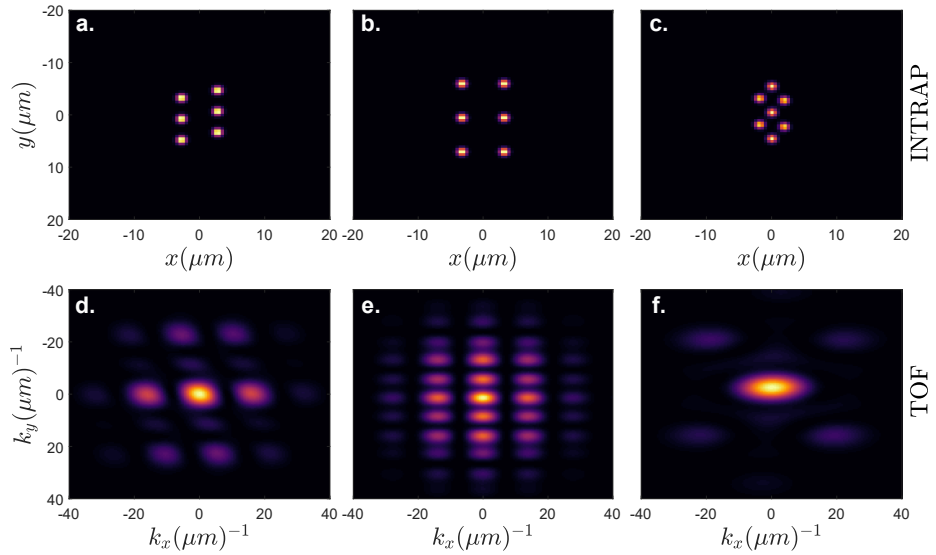

Figure 4.6 Calculated average interference pattern for three different in-trap geometrical droplets configurations: triangular (a,d), square (b,e) and diamond (c,f). (a-c) In-trap droplet configuration. (d-f) Calculated interference pattern for the in-trap configuration of (a-c), respectively. Each droplet is pictured as an expanding Gaussian with a random phase in the narrow range $0.1 \times [0, 2\pi]$. The resulting interference patterns are averaged over 50 trials, as in the experiment.

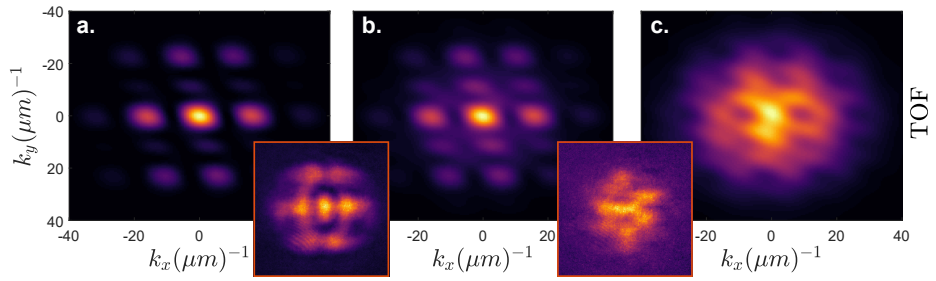

Figure 4.7 Calculated average interference pattern for three different droplets phase distributions: (a) $0.1 \times [0, 2\pi]$, (b) $0.5 \times [0, 2\pi]$, and (c) $1 \times [0, 2\pi]$. Orange boxes: experimental interference pattern obtained after 36ms TOF from absorption imaging for a supersolid (left) and an isolated droplet state (right). Figures in orange boxes adapted from [137].

4.2.1 Supersolidity in a circular trap

After the experimental realization of two-dimensional supersolidity, the natural next step was to go from a zig-zag state towards an isotropic state in a cicular trap. At this stage, in the experiment, the atomic cloud was trapped in a crossed optical dipole trap made of two laser beams crossing at an angle of 45°. One of this laser beam is

modulated to create a time-averaged potential with a Gaussian shape, whose effective waist in one direction can be tuned. The second dipole trap has instead a fixed waist. Due to this geometrical configuration, the maximum trap aspect ratio was limited to $\alpha_t = 0.43$. To be able to increase the aspect ratio to 1 and reach a circular trap, we implemented a third optical dipole trap (see Chapter 2) with similar specifications to the optical dipole trap with fixed waist and that crosses this one at an angle of 90°. In this way, we have an individual control over the trap frequencies by changing the power of the three laser beams independently.

In the publication presented in Sec. 4.7, we could realize a hexagon state made of 7 droplets in a circular trap, as predicted from theory. These two-dimensional states have a lifetime beyond one second. The process of directly evaporating from a thermal cloud has a fundamental role in realizing robust supersolid states in pancake traps. By comparing the dynamic formation of a circular supersolid via an interaction ramp with a temperature ramp, it can be shown that the former leads to a highly excited state, preventing global phase coherence at realistic timescales. Whereas, the latter allows the system to achieve global phase coherence soon after the temperature ramp. Indeed, while for linear systems one roton mode can connect the superfluid state to the supersolid state with a continuous phase transition[4], in 2D systems the transition is predicted to be discontinuous leading to strong excitations, which interfere with the development of global phase coherence across the system [27]. Our theoretical simulations of the interaction ramp from a dipolar superfluid to a supersolid show that this process follows a crystal-growth type of formation, where the central droplets form and are then succeeded by an outer ring of droplets, suggesting that the dipolar BEC cannot be linked to the supersolid by a single roton mode as in the 1D case. More details about the theoretical model are reported in the publication shown in Sec. 4.7.

4.3 Excitations in two-dimensional supersolids

The realization of the hexagon state opens up a whole new experimental research on the excitations of two-dimensional supersolids. In this regard, we investigated the role that angular oscillations can play in determining the superfluid fraction (see publication in Sec. 4.8). Furthermore, supersolids in circular traps pave the way for the study of vortices [165] and persistent currents [185].

[4]Note that, in 1D systems, the phase transition from a superfluid to a supersolid can be continuous or discontinuous depending on the density [18, 23].

4.3.1 Scissors mode and angular oscillations

In the quest for supersolidity, one of the major result was to be able to prove the superfluid nature of the system. In our group, we probe the global phase coherence of the supersolid state by performing matter-wave interference experiments and looking at the resulting pattern (see Sec. 4.1.1). Another way of quantifying the superfluidity of the system can be through the excitation of the scissors mode [74]. The scissors mode is a counter rotation of the atomic cloud with respect to the axes of the trap. It has been widely employed to infer the superfluidity in several systems as trapped BEC [122], Fermi gases [196], 2D Bose gases [167], dipolar quantum droplets [63], and nulcei [29], where protons and neutrons can oscillate out of phase. In the experiment it can be excited by a sudden rotation of the trap.

Given the trap ellipticity $\epsilon = (\omega_x^2 - \omega_y^2)/(\omega_x^2 + \omega_y^2)$, where $\omega_{x,y}$ are the trap frequencies in the plane of rotation, and the atomic cloud ellipticity $\beta = \langle x^2 - y^2\rangle/\langle x^2 + y^2\rangle$, the angular oscillation frequency ω_{sc} can be related to the moment of inertia as below [183]:

$$\Theta = \Theta_{\mathrm{c}}\ \epsilon\beta\frac{\omega_x^2 + \omega_y^2}{\omega_{\mathrm{sc}}^2}, \tag{4.2}$$

where Θ is the moment of inertia and Θ_{c} is its classical value. The angular oscillation frequency strongly depends on whether the system is superfluid or not. Following Leggett's definition for the superfluid fraction f_{s}, $\Theta = (1 - f_{\mathrm{s}})\Theta_{\mathrm{c}}$ [111], which for non isotropic trap can be written as:

$$\Theta = (1 - f_{\mathrm{s}})\Theta_{\mathrm{c}} + f_{\mathrm{s}}\beta^2\Theta_{\mathrm{c}}, \tag{4.3}$$

and using Eq. 4.2, one can derive the angular oscillation frequency for a fully superfluid system ($f_{\mathrm{s}} = 1$) and for a normal fluid performing rigid body rotation ($f_{\mathrm{s}} = 0$). These are given by

$$\begin{aligned} \omega_{\mathrm{sc}}^{\mathrm{SF}} &= \sqrt{(\omega_y^2 - \omega_x^2)/\beta}, \\ \omega_{\mathrm{sc}}^{\mathrm{RBR}} &= \sqrt{(\omega_y^2 - \omega_x^2)\beta}, \end{aligned} \tag{4.4}$$

for superfluid and normal fluid, respectively. Due to the density modulation, a supersolid should respond to a scissors-mode excitation with a frequency ω_{sc} between $\omega_{\mathrm{sc}}^{\mathrm{RBR}}$ and $\omega_{\mathrm{sc}}^{\mathrm{SF}}$.

From the relations above, it is visible that both a change in the superfluid fraction and in the atomic ellipticity lead to a change in the moment of inertia and therefore

in ω_{sc}, with no possibility of distinction between superfluid and normal fluid for very elongated systems where $\beta \simeq 1$ [165]. For that reason, exciting the scissors mode to extract information on the superfluid fraction of a linear supersolid has some limitations. Indeed, the transition from an unmodulated dBEC to a supersolid state is accompanied by a dramatic change in the atomic ellipticity β. In addition, the supersolid state is characterized by interconnected droplets surrounded by a superfluid bath, which we refer to as "halo". This halo feeds the droplets and the low density link between them, which is responsible for the phase coherence of the system. When crossing the transition, there is a change in the density of the halo and of the interdroplet connection. Furthermore, in linear systems, the scissors mode is always orthogonal to the droplet axis, which weakens any conclusion on the exact value of the superfluid link between the droplets.

In this regard, the possibility of realizing two-dimensional supersolids and having control on β allows us to investigate this aspect deeper. Indeed, in two dimensional systems, when crossing the transition from a dBEC to a supersolid state, β stays almost constant. Furthermore, the angular oscillation involves motion that partially happens along the droplet axis. In the publication shown in Sec. 4.8, surprisingly, by exciting the scissors mode with a sudden rotation of the trap, we observe an angular oscillation frequency that is always close to the case of $f_{\mathrm{s}} = 1$, for several scattering lengths corresponding to a standard dBEC, a supersolid and an isolated droplet regime, and for different values of β. These experimental findings are well reproduced by real time simulations based on the eGPE, where a similar protocol for the excitation of the scissors mode and a similar analysis of the oscillation dynamics are performed.

A possible explanation for these observations can be given by the multi-frequency response of the system to the trap excitation. Equation 4.4 is in fact valid under the assumption of shape preserving modes and single-frequency response and, in the case of many frequencies, ω^{SF} and ω^{RBR} are only an upper bound for ω_{sc}. In the experiment the high frequency angular oscillation modes dominate over the low frequency ones. Therefore, to infer the superfluid fraction, a different experimental protocol able to address the scissors mode needs to be implemented [166]. Furthernore, such a low frequency can not easily be probed in the actual experiment, due to e.g. a limited lifetime of the supersolid state. Due to the aforementioned limitations, different techniques might be more reliable to probe the superfluid nature of the supersolid, as the observation of quantized vortices.

4.3.2 Outlook: vortices in dipolar supersolids

Quantized vortices represent a strong evidence of superfluidity and they have been observed in different ultracold systems, as BECs [1, 121, 124] and Fermi gases [205]. In dipolar supersolids, the presence of high density peaks connected by low density regions is predicted to modify the properties of the vortices, e.g. critical angular velocity, angular momentum per particle, and vortex lattice geometry [66]. In particular, the critical angular velocity to nucleate vortices, which follows the relation $\Omega_c = \omega_q/2$, with ω_q the frequency of the quadrupolar mode, decreases in the supersolid regime. This is given by the low density inter-droplet regions that make the nucleation of vortices energetically more favorable. The angular momentum per particle carried by the vortex is predicted to be smaller than $\hbar$, due to the reduction of superfluidity in the supersolid state. Furthermore, for large angular velocities, the presence of high density peaks, arranged in a triangular pattern, modifies the vortex lattice. The vortices are pinned in low density regions between the droplets and form a honeycomb lattice [206].

Recently, in our experiment we demonstrated the first realization of quantized vortices in a dipolar ultracold gas made of dysprosium atoms (see Appendix A.5). So far, vortices have been created by rotating a slightly anisotropic trap [1], by stirring the system with a focused laser beam [121], by rapidly crossing the atomic sample with an obstacle (e.g. blue detuned laser beam) [105, 133], or by Kibble-Zurek mechanisms [192], as topological defects arising from a rapid quench of the system. In dipolar systems, the magnetostriction - dipole alignment along the magnetic field direction - offers an alternative way of deforming the atomic cloud, through the anisotropic nature of the DDI and impart angular momentum into the system. Indeed, by rotating the magnetic field at a constant angular velocity, above the critical one Ω_c, vortices appear in the dysprosium cloud.

By using a similar technique, but preparing the cloud at a lower scattering length during evaporative cooling, it could be possible to nucleate vortices in the circular supersolid state. The major limitation is given by the ability of detecting vortices in the low density region between the high density peaks. A recent theoretical proposal suggested a protocol to nucleate and detect vortices in supersolid states based on a interaction ramp from a superfluid to a supersolid state and then back to the superfluid [206]. The starting condition is a rotating dipolar BEC at an angular velocity below the critical one. By reducing the scattering length, the system enters the supersolid state. Due to the lower value of the critical angular velocity, a vortex can be nucleated in the low density region. For detection, the scattering length can be

increased again, melting the supersolid into an unmodulated dBEC with a vortex at the center, which can now be detected.

4.4 Publication II:

Birth, life, and death of a dipolar supersolid

The following publication has appeared in

Physical Review Letters **126**, 233401 (2021)*
submitted 19 Jan 2021; published 7 Jun 2021
DOI: https://doi.org/10.1103/PhysRevLett.126.233401
M. Sohmen,[1,2] C. Politi,[1,2] L. Klaus,[1] L. Chomaz,[1] M. J. Mark,[1,2] M. A. Norcia,[1] and F. Ferlaino[1,2]

[1] *Institut für Quantenoptik und Quanteninformation, Österreichische Akademie der Wissenschaften, 6020 Innsbruck, Austria*

[2] *Institut für Experimentalphysik, Universität Innsbruck, 6020 Innsbruck, Austria*

*The author of the present thesis performed the measurements together with M. S., M. A. N., and L. K., analysed the data with M. S. and M. A. N., and contributed in writing the manuscript and interpreting the results together with all the authors.

Editors' Suggestion | Featured in Physics

Birth, Life, and Death of a Dipolar Supersolid

Maximilian Sohmen,[1,2] Claudia Politi,[1,2] Lauritz Klaus,[1,2] Lauriane Chomaz,[2,†] Manfred J. Mark,[1,2] Matthew A. Norcia,[1] and Francesca Ferlaino[1,2,*]

[1]*Institut für Quantenoptik und Quanteninformation, Österreichische Akademie der Wissenschaften, 6020 Innsbruck, Austria*
[2]*Institut für Experimentalphysik, Universität Innsbruck, 6020 Innsbruck, Austria*

(Received 19 January 2021; accepted 19 April 2021; published 7 June 2021)

In the short time since the first observation of supersolid states of ultracold dipolar atoms, substantial progress has been made in understanding the zero-temperature phase diagram and low-energy excitations of these systems. Less is known, however, about their finite-temperature properties, particularly relevant for supersolids formed by cooling through direct evaporation. Here, we explore this realm by characterizing the evaporative formation and subsequent decay of a dipolar supersolid by combining high-resolution in-trap imaging with time-of-flight observables. As our atomic system cools toward quantum degeneracy, it first undergoes a transition from thermal gas to a crystalline state with the appearance of periodic density modulation. This is followed by a transition to a supersolid state with the emergence of long-range phase coherence. Further, we explore the role of temperature in the development of the modulated state.

DOI: 10.1103/PhysRevLett.126.233401

Supersolid states, which exhibit both global phase coherence and periodic spatial modulation [1–7], have recently been demonstrated and studied in ultracold gases of dipolar atoms [8–10]. These states are typically accessed by starting with an unmodulated Bose-Einstein condensate (BEC) and then quenching the strength of interatomic interactions to a value that favors a density-modulated state. In this production scheme, the superfluidity (or global phase coherence) of the supersolid is inherited from the preexisting condensate. However, a dipolar supersolid state can also be reached by direct evaporation from a thermal gas with fixed interactions, as demonstrated in Ref. [10].

A thermal gas at temperatures well above condensation has neither phase coherence nor modulation, so both must emerge during the evaporative formation process. This leads one to question whether these two features appear simultaneously, or if not, which comes first. Further, because this transition explicitly takes place at finite temperature T, thermal excitations may play an important role in the formation of the supersolid, presenting a challenging situation for theory. Moreover, in the case of a dipolar supersolid, the nonmonotonic dispersion relation and the spontaneous formation of periodic density modulation lead to important new length and energy scales not present in contact-interacting systems, which dramatically modify the evaporative formation process.

While the ground state and dynamics of a zero-temperature dipolar quantum gas can be computed by solving an extended Gross-Pitaevskii equation [8,11–17] [see also Fig. 1(a)], similar treatments are currently lacking for finite temperatures in the supersolid regime. In principle, effects of finite temperature can be taken into account by perturbatively including the thermal population of excited modes. This can be done either coherently, by adding them in a single classical field that abides the Gross-Pitaevskii equation, as in Refs. [18–20], or incoherently, by iteratively computing mode populations via a set of coupled Hartree-Fock-Bogoliubov equations [9,21,22]. In order to accurately describe dynamical processes occurring at temperatures approaching the critical temperature, both coherent excitations and incoherent interactions with the background thermal gas must be accounted for, requiring either more advanced c-field [18] or quantum Monte Carlo [23–27] techniques. So far, theories with realistic experimental parameters have not been developed to unveil the finite-temperature dipolar phase diagram and to determine the properties of the thermal-to-supersolid phase transition.

In this Letter, we experimentally study the evaporative transition into and out of a supersolid state in a dilute gas of dysprosium atoms. As the atoms cool down to quantum degeneracy, the number of condensed atoms increases, giving birth to the supersolid state. Continued evaporation and collisional loss lead to a reduction of atom number and, eventually, the death of the supersolid. Such an evaporation trajectory, as illustrated in Fig. 1(a), passes through the little-understood finite-temperature portion of the supersolid phase diagram. During the evaporative birth of the supersolid, we discover that the system first establishes strong periodic density modulation of locally coherent atoms and only later acquires long-range phase coherence. When comparing the birth and death of the supersolid, which occur at different temperatures, we observe higher levels of modulation during the birth, suggesting that thermal fluctuations may play an important role in the formation of density modulation.

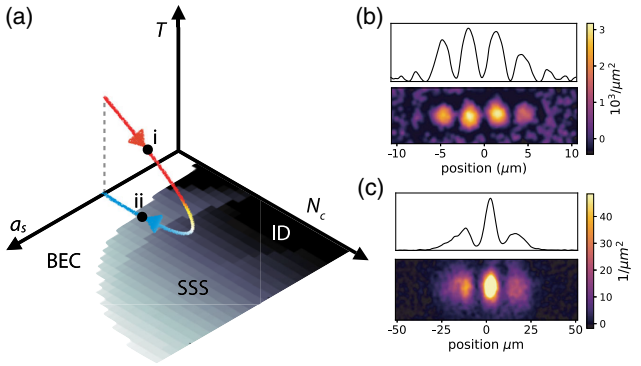

FIG. 1. Evaporation trajectory through the finite-temperature phase diagram. (a) At $T = 0$ (bottom plane), the phase diagram for a gas of dipolar atoms is spanned by the s-wave scattering length a_s and the condensate atom number N_c. In an elongated trap, it features a BEC (white) and independent droplet (ID, black) phases, separated in places by a supersolid state (SSS, gray scale). The plotted lightness in the $T = 0$ phase diagram represents the droplet link strength across the system (cf. Ref. [16]). Away from $T = 0$, the phase diagram is not known. We explore this region through evaporation into [red, near (i)] and out of [blue, near (ii)] the SSS, along a trajectory represented schematically by the colored arrow. (b) Single-shot image of the optical density (OD) of the sample in trap. Here, a system of four "droplets" within the SSS region is shown, together with its projected density profile. (c) Single-shot matter-wave interference pattern after 35 ms TOF expansion (OD) and the corresponding projected profile. The color scale is truncated for visual clarity. The background clouds of thermal atoms present are not visible in the color scales of (b) or (c); for 35 ms TOF and around 50 nK [as in (c)], the thermal atoms show an approximately isotropic 2D Gaussian distribution of mean width $\bar{\sigma} \sim 55$ μm.

For our experiments, we first prepare an optically trapped gas of approximately 10^5 dysprosium atoms (isotope ^{164}Dy), precooled via forced evaporation to temperatures of several hundred nanokelvin, at which point the gas remains thermal. From here, we can apply further evaporation either by a nearly adiabatic ramp-down of the trap depth ("slow ramp") or by a rapid reduction of the trap depth followed by a hold time at fixed depth ("fast ramp") to further lower the temperature and induce condensation into the supersolid state. The slow ramp protocol yields a higher number of condensed atoms ($N_c \sim 2 \times 10^4$; see next paragraph for definition) and lower shot-to-shot atom number fluctuations, whereas the fast ramp protocol ($N_c \sim 10^4$) allows to follow the evolution of the system in a constant trap, disentangling the system dynamics from varying trap parameters. In contrast to protocols based on quenching the interactions in a BEC [8–10], we hold the magnetic field (and hence the contact interaction strength) fixed during the entire evaporation process at 17.92 G, where the system ground state at our N_c is a supersolid [scattering length $\sim 85(5)\, a_0$].

For the present Letter, we have implemented *in-situ* Faraday phase contrast imaging [28,29], which allows us to probe the in-trap density of our quantum gas at micron-scale resolution. During the formation of the density-modulated state, the translation symmetry is broken along the long (axial) direction of our cigar-shaped trap [30], typically giving rise to a chain of 3–6 density peaks, which we call droplets. These droplets have a spacing of roughly 3 μm, clearly visible in our *in-situ* images [Fig. 1(b)]. As in our previous works [10,16], we also image the sample after a time-of-flight (TOF) expansion using standard absorption imaging. These TOF images include a spatially broad contribution that we attribute to thermal atoms, whose number $N_{\rm th}$ and temperature T we estimate by 2D fitting of a Bose-enhanced Gaussian function [31], excluding the cloud center. Surplus atoms at the cloud center (compared to the broad Gaussian) are at least locally coherent, or "(quasi-)condensed" in the sense of Refs. [32–34]. With the total number of atoms N measured by pixel count, we define $N_c = N - N_{\rm th}$ to be the number of these (at least locally) coherent atoms. During TOF, matter-wave interference between the expanding droplets gives rise to a characteristic interference pattern [Fig. 1(c)]. The high contrast of the interference pattern is visible in single TOF images and indicates that each individual droplet is by itself a phase-coherent many-body object. The stability of the interference fringes within the envelope over multiple experimental realizations encodes the degree of phase coherence between droplets (cf. Refs. [10,16] and discussion below). The combination of *in situ* and TOF diagnostics provides complementary information, allowing us to measure both density modulation and its spatial extent (number of droplets), as well as phase coherence.

Figure 2 shows the birth of the supersolid. Starting from a thermal sample, we apply the fast ramp (225 ms) evaporation protocol to the desired final trap depth, too fast for the cloud to follow adiabatically and intermediately resulting in a nonthermalized, noncondensed sample. Simply holding the sample at constant trap depth for a time t_h, collisions and plain evaporation lead to thermalization and cooling. In Fig. 2(a), we plot the average axial *in-situ* density profile [cf. Fig. 1(b)] versus t_h, for about 20 images per time step without any image recentering. At early t_h the atoms are primarily thermal and show up as a broad, low-density background in our images. For $t_h \lesssim 150$ ms, inspection of single-shot images reveals an increasing, though substantially fluctuating, number of droplets appearing out of the thermal cloud. After this time, the droplet number stabilizes to its final value. We observe that the droplet formation happens on the same timescale as the equilibration of N_c and T (see Supplemental Material [35]). This timescale is set by the rate of evaporation, which in turn depends on the thermalization rate and hence on the elastic collision rate $1/\tau_{\rm el}$. For our experimental parameters, we estimate for two thermal atoms $\tau_{\rm el} \approx 3$ ms ($\tau_{\rm el} \approx 10$ ms) before (after) our last evaporation ramp. Once the droplets have formed, other timescales might be relevant in

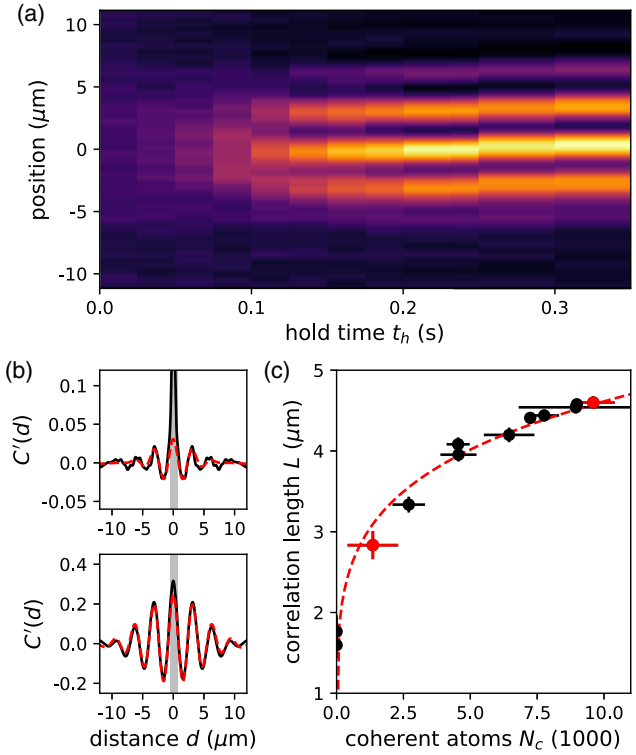

FIG. 2. Growth and spread of density modulation during evaporation. (a) Averaged *in-situ* density profiles (no recentering, approximately 20 shots per time step) along the long trap axis as a function of hold time t_h after the fast ramp reduction of trap depth (see main text). (b) The density correlator $C'(d)$ (solid black line) is fitted by a cosine-modulated Gaussian function (dashed red line) to extract the correlation length L. Gray regions are strongly influenced by imaging noise and excluded from fits. Correlators are displayed for $t_h = 50$ ms (upper) and $t_h = 300$ ms (lower). (c) Density-density correlation length L versus N_c, for the same time steps shown in (a). Horizontal error bars are the standard deviation over repetitive shots, vertical error bars reflect the correlator fit uncertainty, red points correspond to the correlators of (b). The dashed line indicates the simple atom number scaling of the Thomas-Fermi radius of a harmonically trapped BEC, $\propto N_c^{1/5}$.

determining the equilibration rate of their relative positions and phases; the details of this possibility remain an open question [16].

To better quantify the growth of the modulated state, we consider the density-density correlator $C'(d)$ for the *in-situ* density profiles over distances d [35]. We find that $C'(d)$ is well described by a cosine-modulated Gaussian and define the density correlation length L [Fig. 2(b)] as its fitted width. This method provides a way to determine the extent over which density modulation has formed. Figure 2(c) shows L for the dataset of Fig. 2(a) versus the number of coherent atoms N_c, which we extract from TOF absorption images in separate experimental trials with identical parameters. Interestingly, despite the strongly modulated structure of the supersolid state, the density correlation length L closely follows a scaling $\propto N_c^{1/5}$, just as the Thomas-Fermi radius of a harmonically trapped BEC, suggesting a dominant role of interactions over kinetic energy.

While *in-situ* images provide information about density modulation (diagonal long-range order), they do not carry direct information about phase coherence (off-diagonal long-range order), either within or between droplets. For this, we use TOF imaging and address the question of whether the formation of density modulation precedes global (i.e., interdroplet) phase coherence during the evaporative formation of the supersolid, or the other way round.

For this study, we perform a slow (500 ms) final forced evaporation ramp of constant slope that is nearly adiabatic with respect to N_c and T (though not necessarily with respect to excitations of droplet positions and phase) and terminate the ramp at selected crop times t_c [38]. After t_c, we immediately release the atoms and perform TOF imaging. Figure 3(a) shows the observed evolution of the total (N) and (quasi-)condensed (N_c) atom number, as well as the sample temperature (T) versus t_c. We expand on the observed evolution by measuring coherence properties. Following Refs. [10,16], for each measurement i we extract a rescaled complex phasor $P_i = \rho_i \exp(-i\Phi_i)$, i.e., the Fourier component corresponding to the modulation wavelength in the TOF interference profile (see Supplemental Material [35]). For systems with a small number of droplets (but at least 2), the magnitude of the phasor ρ_i encodes the modulation strength and also the (local) degree of coherence within each of the individual droplets. Meanwhile, the phase Φ_i depends primarily on the relative phase between the droplets (cf. [39]).

We plot the phasors for different evaporation times on the polar plane in Fig. 3(b), where two effects become apparent. First, the modulus of the phasors grows during the evaporation, indicating that the degree of modulation increases. Second, the distribution of phases Φ_i is initially uniform and then narrows down over t_c. To determine the time sequence of these two effects, we calculate the incoherent and coherent amplitude means $A_M = \langle |P_i| \rangle_i$, encoding modulation strength and local phase coherence, and $A_\Phi = |\langle P_i \rangle_i|$, encoding the degree of global phase coherence across the system [10,16]. Plotting A_M and A_Φ against t_c [Fig. 3(c)], we notice a time lag of around 40 ms between the increase of A_M and A_Φ, indicating that during evaporation into a supersolid the translational and the phase symmetry are not broken simultaneously [40]. Rather, density modulation and local phase coherence appear before global phase coherence, consistent with predictions from Monte Carlo simulations (cf., e.g., Ref. [27]). A similar effect is observed in the fast ramp protocol [35].

This observation suggests the transient formation of a quasicondensate crystal—a state with local but not

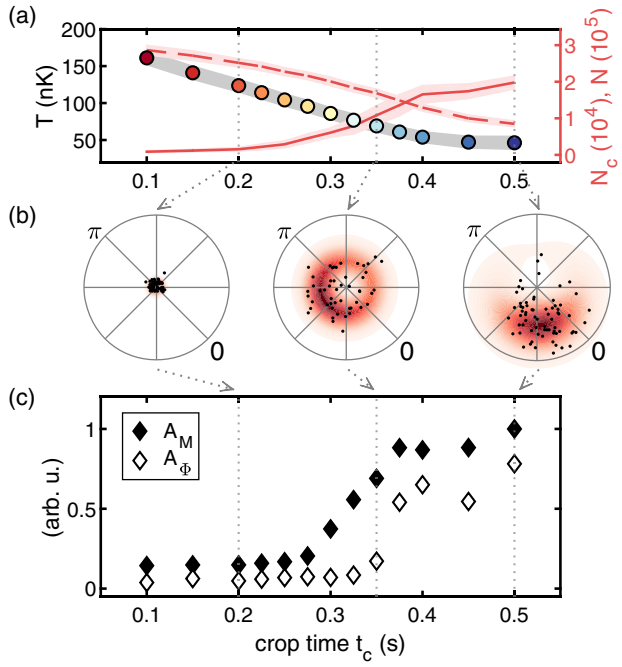

FIG. 3. Development of modulation and coherence while evaporating into the supersolid state. (a) Sample temperature T (left ordinate, bullets), total (N, right ordinate, dashed red line), and coherent atom number (N_c, solid red line) as a function of the ramp crop time t_c. The shadings reflect the respective confidence intervals. (b) The phasors P_i (black dots), representing the magnitude and phase coherence of modulation for selected t_c (dotted lines; same radial scale for all polar plots). The red shading reflects mean and variance of the distribution. (c) Evolution of the Fourier amplitude means A_M (filled markers) and A_Φ (open markers).

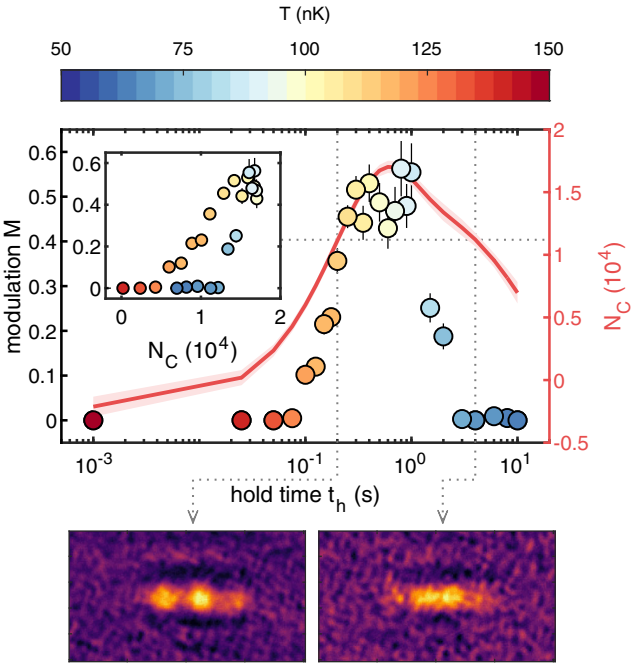

FIG. 4. Life cycle of a supersolid state. Density modulation M (from *in-situ* images) during the evaporation process (left ordinate, bullets; the vertical error bars reflect the propagated uncertainty returned by the fitting routine). The sample temperature decreases during the hold time t_h and is encoded by the color filling. N_c (from TOF images) is the number of coherent atoms over t_h (right ordinate, red line; the light red shading reflects the measurement standard deviation). At two times where $N_c \sim 1.1 \times 10^4$ (vertical dashed lines), but at which the atoms have different temperatures, M differs substantially. The corresponding averaged *in-situ* images below confirm a higher level of modulation at earlier t_h. Inset: the observed modulation M plotted versus N_c.

long-range coherence [32–34], whose increased compressibility relative to a thermal gas allows for the formation of density modulation [41]—prior to the formation of a supersolid with phase coherence between droplets. The lack of global phase coherence could be attributed to a Kibble-Zurek-type mechanism [42], in which different regions of the sample condense independently, to excitation of modes involving the motion or phase of the droplets during the evaporation process, or to the thermal population of collective modes (which reduce long-range coherence) at finite temperature. As the evaporation process does not allow independent control of temperature and condensation rate without also changing density or trap geometry, we cannot reliably determine the relative importance of these effects (or others) from the experiment. Dedicated theoretical studies at finite temperature will thus be needed to elucidate the impact of these types of processes and to understand the exact formation process.

After the birth of the supersolid state, both density modulation and global phase coherence persist for remarkably long times, exceeding 1 s. Figure 4 shows the evolution of the coherent atom number N_c and temperature T at long hold times under conditions similar to Fig. 2—the same fast ramp followed immediately by hold time t_h. Evaporative cooling first increases the coherent atom number until, at long $t_h \geq 1$ s, atom losses become dominant and lead to a continuous decrease of N_c, eventually leading to the disappearance of the modulated state. However, this death of the supersolid is not a mere time reversal of the birth. N_c decreases, i.e., evolves in the opposite direction, but more slowly and at lower temperature than for the birth. Furthermore, phase coherence appears to outlive modulation and to be maintained until the very end [35]. Thus, a comparison between the birth and death process provides us with important clues to the impact of temperature on the supersolid.

We contrast the birth and death of the supersolid in Fig. 4 by also plotting the observed *in-situ* density modulation M, which is calculated by Fourier transforming the *in-situ* density profiles and normalizing the Fourier component corresponding to the modulation wavelength to the zero-frequency Fourier component. By comparing M between

times that have similar N_c during the birth and the death of the supersolid, respectively, we find that the degree of modulation is higher during the birth of the supersolid than during the death. Because the sample is hotter at shorter hold times, this suggests that the observed modulation is increased at higher temperature, perhaps due to thermal population of collective modes or due to finite-temperature modifications to the dispersion relation [43], as predicted in Ref. [22]. Again, further development of finite-temperature theory will be needed to conclusively determine the importance of such effects.

The role of finite temperature in the formation of modulation, as well as the mechanism by which phase variations across the modulated state arise and then ultimately disappear, represent important future directions for theoretical investigations of dipolar supersolids away from the relatively well understood $T = 0$ limit. Experimentally, it would be of great interest to study the evaporative formation process in a larger and more uniform system, where distinct domains may be observed to form and a broader separation of length scales may be explored in correlation measurements. Such measurements, along with improved finite-temperature theory, could enable more precise statements as to the nature of the supersolid phase transition away from zero temperature.

We thank Russell Bisset, Thomas Bland, the Innsbruck Erbium team, Massimo Boninsegni, Philippe Chomaz, Thomas Pohl, Nikolay Prokof'ev, and Boris Svistunov for insightful discussions and Gianmaria Durastante, Philipp Ilzhöfer, and Arno Trautmann for early contributions. This work is financially supported through an ERC Consolidator Grant (RARE, No. 681432), a NFRI Grant (MIRARE, No. ÖAW0600) of the Austrian Academy of Science, the QuantERA Grant MAQS by the Austrian Science Fund FWF No. I4391-N, and the DFG/FWF via FOR 2247/I4317-N36. M. S. acknowledges support by the Austrian Science Fund FWF within the DK-ALM (No. W1259-N27). M. A. N. has received funding from an ESQ Postdoctoral Fellowship from the European Union's Horizon 2020 Research and Innovation Programme under the Marie Skłodowska Curie Grant Agreement No. 801110 and the Austrian Federal Ministry of Education, Science and Research (BMBWF). M. J. M. acknowledges support through an ESQ Discovery Grant by the Austrian Academy of Sciences. L. C. acknowledges support through the FWF Elise Richter Fellowship No. V792. We also acknowledge the Innsbruck Laser Core Facility, financed by the Austrian Federal Ministry of Science, Research, and Economy.

*Corresponding author.
Francesca.Ferlaino@uibk.ac.at
†Present address: Physikalisches Institut der Universität Heidelberg, Germany.

[1] E. P. Gross, Unified theory of interacting bosons, Phys. Rev. **106**, 161 (1957).
[2] E. P. Gross, Classical theory of boson wave fields, Ann. Phys. (N.Y.) **4**, 57 (1958).
[3] A. F. Andreev and I. M. Lifshitz, Quantum theory of defects in crystals, Sov. Phys. JETP **29**, 1107 (1969), http://jetp.ac.ru/cgi-bin/dn/e_029_06_1107.pdf.
[4] G. V. Chester, Speculations on Bose-Einstein condensation and quantum crystals, Phys. Rev. A **2**, 256 (1970).
[5] A. J. Leggett, Can a Solid be "Superfluid"? Phys. Rev. Lett. **25**, 1543 (1970).
[6] J.-R. Li, J. Lee, W. Huang, S. Burchesky, B. Shteynas, F. Ç. Top, A. O. Jamison, and W. Ketterle, A stripe phase with supersolid properties in spin-orbit-coupled Bose-Einstein condensates, Nature (London) **543**, 91 (2017).
[7] J. Léonard, A. Morales, P. Zupancic, T. Esslinger, and T. Donner, Supersolid formation in a quantum gas breaking a continuous translational symmetry, Nature (London) **543**, 87 (2017).
[8] F. Böttcher, J.-N. Schmidt, M. Wenzel, J. Hertkorn, M. Guo, T. Langen, and T. Pfau, Transient Supersolid Properties in an Array of Dipolar Quantum Droplets, Phys. Rev. X **9**, 011051 (2019).
[9] L. Tanzi, E. Lucioni, F. Famà, J. Catani, A. Fioretti, C. Gabbanini, R. N. Bisset, L. Santos, and G. Modugno, Observation of a Dipolar Quantum Gas with Metastable Supersolid Properties, Phys. Rev. Lett. **122**, 130405 (2019).
[10] L. Chomaz, D. Petter, P. Ilzhöfer, G. Natale, A. Trautmann, C. Politi, G. Durastante, R. M. W. van Bijnen, A. Patscheider, M. Sohmen, M. J. Mark, and F. Ferlaino, Long-Lived and Transient Supersolid Behaviors in Dipolar Quantum Gases, Phys. Rev. X **9**, 021012 (2019).
[11] F. Wächtler and L. Santos, Quantum filaments in dipolar Bose-Einstein condensates, Phys. Rev. A **93**, 061603(R) (2016).
[12] L. Chomaz, S. Baier, D. Petter, M. J. Mark, F. Wächtler, L. Santos, and F. Ferlaino, Quantum-Fluctuation-Driven Crossover from a Dilute Bose-Einstein Condensate to a Macrodroplet in a Dipolar Quantum Fluid, Phys. Rev. X **6**, 041039 (2016).
[13] R. N. Bisset, R. M. Wilson, D. Baillie, and P. B. Blakie, Ground-state phase diagram of a dipolar condensate with quantum fluctuations, Phys. Rev. A **94**, 033619 (2016).
[14] F. Wächtler and L. Santos, Ground-state properties and elementary excitations of quantum droplets in dipolar Bose-Einstein condensates, Phys. Rev. A **94**, 043618 (2016).
[15] D. Baillie and P. B. Blakie, Droplet Crystal Ground States of a Dipolar Bose Gas, Phys. Rev. Lett. **121**, 195301 (2018).
[16] P. Ilzhöfer, M. Sohmen, G. Durastante, C. Politi, A. Trautmann, G. Natale, G. Morpurgo, T. Giamarchi, L. Chomaz, M. J. Mark, and F. Ferlaino, Phase coherence in out-of-equilibrium supersolid states of ultracold dipolar atoms, Nat. Phys. **17**, 356 (2021).
[17] S. M. Roccuzzo and F. Ancilotto, Supersolid behavior of a dipolar Bose-Einstein condensate confined in a tube, Phys. Rev. A **99**, 041601(R) (2019).
[18] P. Blakie, A. Bradley, M. Davis, R. Ballagh, and C. Gardiner, Dynamics and statistical mechanics of ultra-cold Bose gases using *c*-field techniques, Adv. Phys. **57**, 363 (2008).

[19] D. Petter, A. Patscheider, G. Natale, M. J. Mark, M. A. Baranov, R. v. Bijnen, S. M. Roccuzzo, A. Recati, B. Blakie, D. Baillie, L. Chomaz, and F. Ferlaino, High-energy Bragg scattering measurements of a dipolar supersolid, arXiv: 2005.02213.

[20] J. Hertkorn, J.-N. Schmidt, F. Böttcher, M. Guo, M. Schmidt, K. S. H. Ng, S. D. Graham, H. P. Büchler, T. Langen, M. Zwierlein, and T. Pfau, Density Fluctuations across the Superfluid-Supersolid Phase Transition in a Dipolar Quantum Gas, Phys. Rev. X **11**, 011037 (2021).

[21] S. Ronen and J. L. Bohn, Dipolar Bose-Einstein condensates at finite temperature, Phys. Rev. A **76**, 043607 (2007).

[22] E. Aybar and M. O. Oktel, Temperature-dependent density profiles of dipolar droplets, Phys. Rev. A **99**, 013620 (2019).

[23] F. Cinti, P. Jain, M. Boninsegni, A. Micheli, P. Zoller, and G. Pupillo, Supersolid Droplet Crystal in a Dipole-Blockaded Gas, Phys. Rev. Lett. **105**, 135301 (2010).

[24] H. Saito, Path-integral Monte Carlo study on a droplet of a dipolar Bose-Einstein condensate stabilized by quantum fluctuation, J. Phys. Soc. Jpn. **85**, 053001 (2016).

[25] A. Macia, J. Sánchez-Baena, J. Boronat, and F. Mazzanti, Droplets of Trapped Quantum Dipolar Bosons, Phys. Rev. Lett. **117**, 205301 (2016).

[26] F. Cinti and M. Boninsegni, Classical and quantum filaments in the ground state of trapped dipolar Bose gases, Phys. Rev. A **96**, 013627 (2017).

[27] Y. Kora and M. Boninsegni, Patterned supersolids in dipolar Bose systems, J. Low Temp. Phys. **197**, 337 (2019).

[28] C. C. Bradley, C. A. Sackett, and R. G. Hulet, Bose-Einstein Condensation of Lithium: Observation of Limited Condensate Number, Phys. Rev. Lett. **78**, 985 (1997).

[29] H. Kadau, M. Schmitt, M. Wenzel, C. Wink, T. Maier, I. Ferrier-Barbut, and T. Pfau, Observing the Rosensweig instability of a quantum ferrofluid, Nature (London) **530**, 194 (2016).

[30] At the end of evaporation, we typically use trap frequencies around $\omega_{x,y,z} = 2\pi \times (36, 88, 141)\ \mathrm{s}^{-1}$, with the tightest trap direction oriented parallel to gravity and to an applied uniform magnetic field, cf. Ref. [10].

[31] W. Ketterle, D. S. Durfee, and D. M. Stamper-Kurn, Making, Probing and Understanding Bose-Einstein Condensates, *Proceedings of the International School of Physics "Enrico Fermi,"* arXiv:cond-mat/9904034.

[32] D. S. Petrov, G. V. Shlyapnikov, and J. T. M. Walraven, Phase-Fluctuating 3D Bose-Einstein Condensates in Elongated Traps, Phys. Rev. Lett. **87**, 050404 (2001).

[33] S. Dettmer, D. Hellweg, P. Ryytty, J. J. Arlt, W. Ertmer, K. Sengstock, D. S. Petrov, G. V. Shlyapnikov, H. Kreutzmann, L. Santos, and M. Lewenstein, Observation of Phase Fluctuations in Elongated Bose-Einstein Condensates, Phys. Rev. Lett. **87**, 160406 (2001).

[34] N. Prokof'ev, O. Ruebenacker, and B. Svistunov, Weakly interacting Bose gas in the vicinity of the normal-fluid–superfluid transition, Phys. Rev. A **69**, 053625 (2004).

[35] See Supplemental Material at http://link.aps.org/supplemental/10.1103/PhysRevLett.126.233401 for formal definitions, supporting datasets, and technical information, which includes Refs. [16,31,36,37].

[36] S. Fölling, F. Gerbier, A. Widera, O. Mandel, T. Gericke, and I. Bloch, Spatial quantum noise interferometry in expanding ultracold atom clouds, Nature (London) **434**, 481 (2005).

[37] L. Chomaz, R. M. W. van Bijnen, D. Petter, G. Faraoni, S. Baier, J.-H. Becher, M. J. Mark, F. Wächtler, L. Santos, and F. Ferlaino, Observation of roton mode population in a dipolar quantum gas, Nat. Phys. **14**, 442 (2018).

[38] While for this protocol the trap parameters do change slightly versus t_c, this protocol proved more robust to shot-to-shot fluctuations in atom number than the fast ramp of Fig. 2, which is important for this measurement.

[39] Z. Hadzibabic, S. Stock, B. Battelier, V. Bretin, and J. Dalibard, Interference of an Array of Independent Bose-Einstein Condensates, Phys. Rev. Lett. **93**, 180403 (2004).

[40] We find that observing this time lag does not require a particular fine-tuning of the experimental parameters (starting atom number, B field, trap frequencies, ramp speed) to a higher degree than other experiments with supersolids. This indicates that this time lag between A_M and A_Φ is a rather general feature of the evaporation into the supersolid.

[41] N. Prokof'ev and B. Svistunov, University of Massachusetts, Amherst (private communication).

[42] B. Damski and W. H. Zurek, Soliton Creation during a Bose-Einstein Condensation, Phys. Rev. Lett. **104**, 160404 (2010).

[43] Th. Pohl, University of Aarhus (private communication).

Supplementary Material: Birth, life, and death of a dipolar supersolid

Maximilian Sohmen,[1,2] Claudia Politi,[1,2] Lauritz Klaus,[1,2] Lauriane Chomaz,[2] Manfred J. Mark,[1,2] Matthew A. Norcia,[1] and Francesca Ferlaino[1,2,*]

[1] *Institut für Quantenoptik und Quanteninformation, Österreichische Akademie der Wissenschaften, Innsbruck, Austria*
[2] *Institut für Experimentalphysik, Universität Innsbruck, Austria*

(Dated: March 12, 2021)

CALCULATION OF DENSITY-DENSITY CORRELATOR

We define our correlator as

$$C(d) = \langle \int n(x)\, n(x+d)\, \mathrm{d}x \rangle\,, \tag{1}$$

where $n(x)$ is the projected density at position x along our cigar-shaped trap, and the expectation value $\langle \ldots \rangle$ is calculated over different runs of the experiment. In practice, we follow a standard procedure (e. g., Ref. [1]) and calculate the correlator by computing the square of the Fourier transform of each image to obtain its power spectral density, then Fourier transform again to obtain its autocorrelation function. The autocorrelation functions for the different images in the sample are then averaged to obtain $C(d)$. Note that we do not normalize this as is typical for a noise correlator, as we are interested in the structure of the density profile and not specifically in its fluctuations. To extract the correlation length, we first subtract off a slowly varying background that represents the envelope of our density profile from $C(d)$ to obtain $C'(d)$, shown in Fig. 2b of the main text. We then fit the product of a Gaussian and a cosine with spatial frequency $k_m = 2\pi/x_m$ corresponding to the in-trap modulation wavelength x_m, i. e. $\cos(k_m x)\, \exp(-x^2/2L^2)$, and define the correlation length as L.

CALCULATION OF COHERENCE QUANTITIES

As described in the main text, we evaluate the coherence of our droplet array by imaging the sample after TOF expansion and Fourier transformation ($\mathcal{F}$) of the projected density profile $n(x')$ (cf. Fig. 1c in main text), where in-situ distances x and the corresponding transforms are denoted as $x \xrightarrow{\text{TOF}} x' \xrightarrow{\mathcal{F}} x''$ [2]. For each experimental repetition i this yields a phasor

$$\tilde{P}_i(x'') = \mathcal{F}\{n(x')\}_{x''}. \tag{2}$$

We can calculate the incoherent and coherent means of the Fourier amplitudes over the experimental repetitions i, writing

$$\tilde{A}_M(x'') = \langle |\tilde{P}_i(x'')| \rangle_i \quad \text{and} \quad \tilde{A}_\Phi(x'') = |\langle \tilde{P}_i(x'') \rangle_i|, \tag{3}$$

respectively.

The quantities A_M and A_Φ from the main text are closely connected to $\tilde{A}_M(x'')$ and $\tilde{A}_\Phi(x'')$. To disentangle the spectral amplitude from the coherent atom number (i. e., the area under the density profile), we calculate the rescaled phasors

$$P_i(x'') = \frac{\tilde{P}_i(x'')}{\int |\tilde{P}_i(x'')| \mathrm{d}x''} \tag{4}$$

mentioned in the main text. The amplitude means corresponding to the in-trap modulation at wavelength x_m are then given by

$$A_M = \langle |P_i(x''_m)| \rangle_i \quad \text{and} \quad A_\Phi = |\langle P_i(x''_m) \rangle_i|. \tag{5}$$

SUPPLEMENTARY DATA FOR FIG. 2

The data of Fig. 2 of the main text is obtained from in-situ images of samples created via the 'fast ramp' evaporation procedure. From corresponding TOF images, taken after the data of Fig. 2, we can study the time evolution of $\tilde{A}_M(x'')$ and $\tilde{A}_\Phi(x'')$ over the hold time t_h. After about a hundred milliseconds a sidepeak has developped in $\tilde{A}_M(x'')$, corresponding to the in-trap density modulation at $x_m \sim 3.5\,\mu\mathrm{m}$ wavelength. A corresponding peak develops in $\tilde{A}_\Phi(x'')$, signalling growing coherence between the droplets. In Fig. S1 we plot a direct comparison of the rescaled Fourier amplitude means, A_M and A_Φ, calculated at $x''_m = 3.5\,\mu\mathrm{m}$. We see that both A_M and A_Φ increase with t_h and the increase of modulation strength starts before the development of phase coherence.

For reference, we plot in Fig. S2 the evolution of the total (N) and coherent (N_c) atom number for the data set of Fig. 2 of the main text, obtained using the 'fast ramp' evaporation protocol.

SUPPLEMENTARY DATA FOR FIG. 4

Fig. 4 of the main text shows the death of the supersolid over long hold times t_h. Here we compare in Fig. S3 the evolution of A_M and A_Φ, calculated at the sidepeak

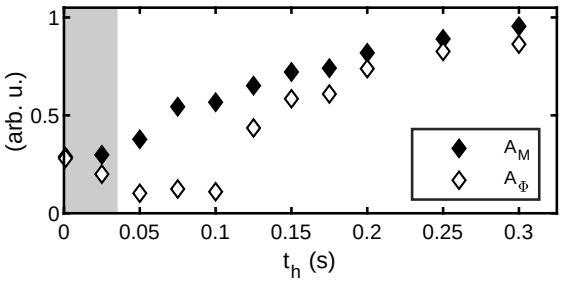

FIG. S1. **Development of coherence after the 'fast ramp' evaporation.** Evolution of the means A_M and A_Φ from the TOF profiles during the hold time t_h. The gray shading marks the region where due to low overall signal the rescaling of the phasors (Eq. 4) is dominated by noise.

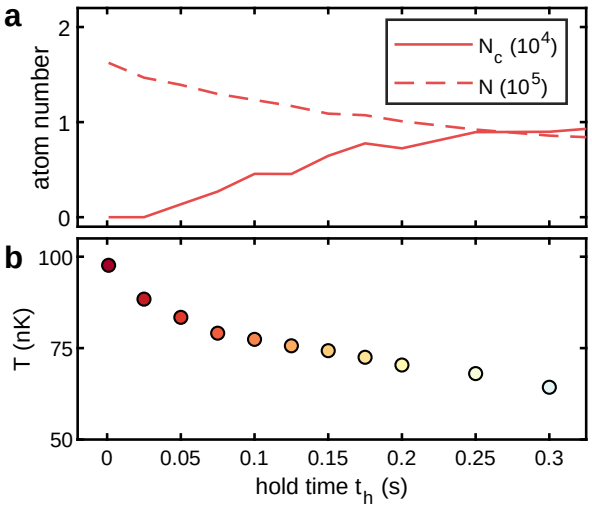

FIG. S2. **Atom number and temperature after the 'fast ramp' evaporation. a.** Evolution of total (N, dashed) and condensed atom number (N_c, solid line). **b.** Evolution of the temperature, as extracted by a Bose-enhanced Gaussian fit to the background cloud of thermal atoms [3].

in $\tilde{A}_M$ at $x'' = 3.5\,\mu$m, during the death of the supersolid. We start our discussion looking at A_M, the measure for in-trap modulation. A_M stays roughly constant for around 600 ms before it starts to decay. At above ~ 1.1 s (gray shading in Fig. S3), the sidepeak in $\tilde{A}_M$ around $x'' = 3.5\,\mu$m has vanished. However, A_M does not go straight to zero, since when the modulation disappears, the fundamental peak (around $x'' = 0$) broadens to $x'' > 3.5\,\mu$m because the condensate size becomes comparable to the (former) droplet spacing. From this point onwards, A_M cannot be used anymore as a measure for modulation. Recall that in the in-situ analysis (Fig. 4 of the main text) a very similar behaviour was observed, with maximal modulation until ~ 600 ms and modulation having disappeared by ~ 1.1 s.

Now turning to A_Φ, we note that over the full duration of this process A_M and A_Φ (which is bounded by A_M) evolve closely together, suggesting that coherence is maintained in the sample throughout the life and death.

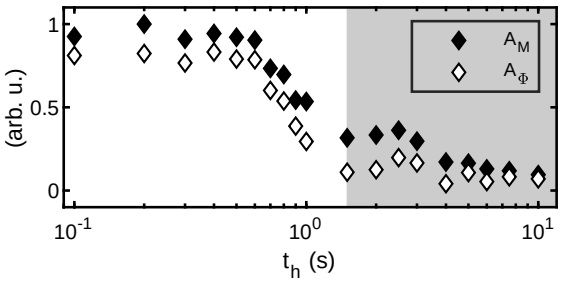

FIG. S3. **Coherence properties during the death of the supersolid.** Evolution of the means A_M and A_Φ from the TOF profiles during t_h after a 'slow ramp' evaporation. The gray shading marks the region from when on the sidepeaks in $\tilde{A}_M$ corresponding to in-trap modulation have disappeared and A_M is not a good measure for modulation anymore.

EVAPORATION RAMPS

In the experiment, once the atoms are loaded into our crossed optical dipole trap (ODT), we perform a near-exponential evaporation ramp of trap power, approximated by piecewise linear ramp sections. The trap frequencies after the penultimate ramp are around $\omega'_{x,y,z} = 2\pi\times(39, 178, 174)\,\mathrm{s}^{-1}$, where we typically have around $N = 3\times10^5$ atoms at around 200 nK. From here, we ramp the power of the ODT linearly down to the final value, giving around $\omega_{x,y,z} = 2\pi\times(36, 88, 141)\,\mathrm{s}^{-1}$. This procedure yields the atom numbers and temperatures presented in Figs. 3–4 of the main text and Fig. S2.

IMAGING SPECIFICATIONS

The images shown in this work have been recorded using a new imaging system recently installed in our experiment. The direction of view of the new system is vertical (counter-directed to gravity).

Images from our imaging along the horizontal direction (as in our earlier works, see, e. g., Refs [4, 5]), in contrast, suffer from the fact that the line of sight is at 45° with respect to the axis connecting the droplets, leading to a small apparent fringe spacing and to the interference peaks partially hiding each other; additionally the interference peaks do not lie in a single focus plane. These drawbacks were eliminated with the vertical imaging setup, which is why the images are much clearer to interpret now.

The fundamental resolution of this imaging system, applicable to in-trap images and characterised by the

Rayleigh criterion, has been measured offline to be approximately 700 nm. We report micron-scale resolution as a conservative claim that accounts for possible alignment imperfections in the finally installed condition, and a reduction of the imaging aperture to increase depth of field. The pixel size of our camera is smaller than the imaging resolution, corresponding to approximately 400 nm at the location of the atoms. Additionally, the images displayed have been supersampled to allow them to be rotated while maintaining resolution.

* Correspondence should be addressed to Francesca.Ferlaino@uibk.ac.at

[1] S. Fölling, F. Gerbier, A. Widera, O. Mandel, T. Gericke, and I. Bloch, Spatial quantum noise interferometry in expanding ultracold atom clouds, Nature **434**, 481 (2005).

[2] We avoid identifying the positions of atoms after TOF with the in-trap momenta (i. e. $k \equiv x'$) because we know from simulation and experiment that in the first few milliseconds of TOF the droplets can still be loosely bound and the expansion is not purely ballistic.

[3] W. Ketterle, D. S. Durfee, and D. M. Stamper-Kurn, Making, probing and understanding Bose–Einstein condensates, Proceedings of the International School of Physics "Enrico Fermi" (1999).

[4] L. Chomaz, R. M. W. van Bijnen, D. Petter, G. Faraoni, S. Baier, J.-H. Becher, M. J. Mark, F. Wächtler, L. Santos, and F. Ferlaino, Observation of roton mode population in a dipolar quantum gas, Nat. Phys. **14**, 442 (2018).

[5] P. Ilzhöfer, M. Sohmen, G. Durastante, C. Politi, A. Trautmann, G. Natale, G. Morpurgo, T. Giamarchi, L. Chomaz, M. J. Mark, and F. Ferlaino, Phase coherence in out-of-equilibrium supersolid states of ultracold dipolar atoms, Nature Physics 10.1038/s41567-020-01100-3 (2021).

4.5 Publication III:

Two-dimensional supersolidity in a dipolar quantum gas

The following publication has appeared in

Nature **596**, 357-361 (2021)[†‡]
submitted 10 Feb 2021; published 18 Aug 2021
DOI: https://doi.org/10.1038/s41586-021-03725-7
M. A. Norcia,[1,4] C. Politi,[1,2,4] L. Klaus,[1] E. Poli,[2] M. Sohmen,[1,2] M. J. Mark,[1,2]
R. N. Bisset,[2] L. Santos,[3] and F. Ferlaino[1,2]

[1] *Institut für Quantenoptik und Quanteninformation, Österreichische Akademie der Wissenschaften, 6020 Innsbruck, Austria*

[2] *Institut für Experimentalphysik, Universität Innsbruck, 6020 Innsbruck, Austria*

[3] *Institut für Theoretische Physik, Universität Hannover, Hannover, Germany*

[4] *These authors contributed equally: M. A. N. and C. P.*

[†]The author of the present thesis performed the measurements together with M. A. N., and L. K., analysed the experimental data with M. A. N., and contributed in writing the manuscript and interpreting the results together with all the authors.

[‡]Here, the preprint version is attached.

Two-dimensional supersolidity in a dipolar quantum gas

Matthew A. Norcia,[1,*] Claudia Politi,[1,2,*] Lauritz Klaus,[1,2] Elena Poli,[2] Maximilian Sohmen,[1,2] Manfred J. Mark,[1,2] Russell Bisset,[2] Luis Santos,[3] and Francesca Ferlaino[1,2,†]

[1] *Institut für Quantenoptik und Quanteninformation, Österreichische Akademie der Wissenschaften, Innsbruck, Austria*

[2] *Institut für Experimentalphysik, Universität Innsbruck, Austria*

[3] *Institut für Theoretische Physik, Leibniz Universität Hannover, Germany*

(Dated: February 11, 2021)

Supersolidity — a quantum-mechanical phenomenon characterized by the presence of both superfluidity and crystalline order — was initially envisioned in the context of bulk solid helium, as a possible answer to the question of whether a solid could have superfluid properties [1–5]. While supersolidity has not been observed in solid helium (despite much effort)[6], ultracold atomic gases have provided a fundamentally new approach, recently enabling the observation and study of supersolids with dipolar atoms [7–16]. However, unlike the proposed phenomena in helium, these gaseous systems have so far only shown supersolidity along a single direction. By crossing a structural phase transition similar to those occurring in ionic chains [17–20], quantum wires [21, 22], and theoretically in chains of individual dipolar particles [23, 24], we demonstrate the extension of supersolid properties into two dimensions, providing an important step closer to the bulk situation envisioned in helium. This opens the possibility of studying rich excitation properties [25–28], including vortex formation [29–31], as well as ground-state phases with varied geometrical structure [7, 32] in a highly flexible and controllable system.

Ultracold atoms have recently offered a fundamentally new direction for the creation of supersolids — rather than looking for superfluid properties in a solid system like ^{4}He, ultracold atoms allow one to induce a crystalline structure in a gaseous superfluid, a system which provides far greater opportunity for control and observation. This new perspective has enabled supersolid properties to be observed in systems with spin-orbit coupling [33] or long-range cavity-mediated interactions [34], though in these cases the crystalline structure is externally imposed, yielding an incompressible state. In contrast, dipolar quantum gases of highly magnetic atoms can spontaneously form crystalline structure due to intrinsic interactions [11–13], allowing for a supersolid with both crystalline and superfluid excitations [14–16]. In these demonstrations, supersolid properties have only been observed along a single dimension, as a linear chain of phase-coherent "droplets", i.e. regions of high density connected by low-density bridges of condensed atoms, confined within an elongated optical trap.

The extension of supersolidity into two dimensions is a key step towards creating an ultracold gas supersolid that is closer to the states envisioned in solid helium. Compared to previous studies of incoherent two-dimensional dipolar droplet crystals [8, 35], we work with both a substantially higher atom number N and relatively strong repulsive contact interactions between atoms. This leads to the formation of large numbers of loosely bound droplets, enabling us to establish phase coherence in two dimensions. In our system, the repulsive dipolar interactions between droplets facilitate a structural transition from a linear to a two-dimensional array, analogous to the Coulomb-interaction-mediated structural phase transitions observed with ions [17–20]. Unlike ions however, our droplets are compressible and result from the spontaneous formation of a density wave, allowing for dynamical variation in both droplet number and size. Further, the exchange of particles between droplets enables the spontaneous synchronization of the internal phase of each droplet across the system, and the associated superfluid excitations [14–16].

Dipolar quantum gases exhibit a rich set of ground- and excited-state phenomena due to the competition between many energetic contributions. These include mean-field interactions of both contact and dipolar nature, quantum fluctuations, and external confinement, parameterized by potentially anisotropic trapping frequencies $f_{x,y,z}$. Such systems can be described with great accuracy by using an extended Gross–Pitaevskii equation (eGPE) [36–39]. Even a fine variation of the

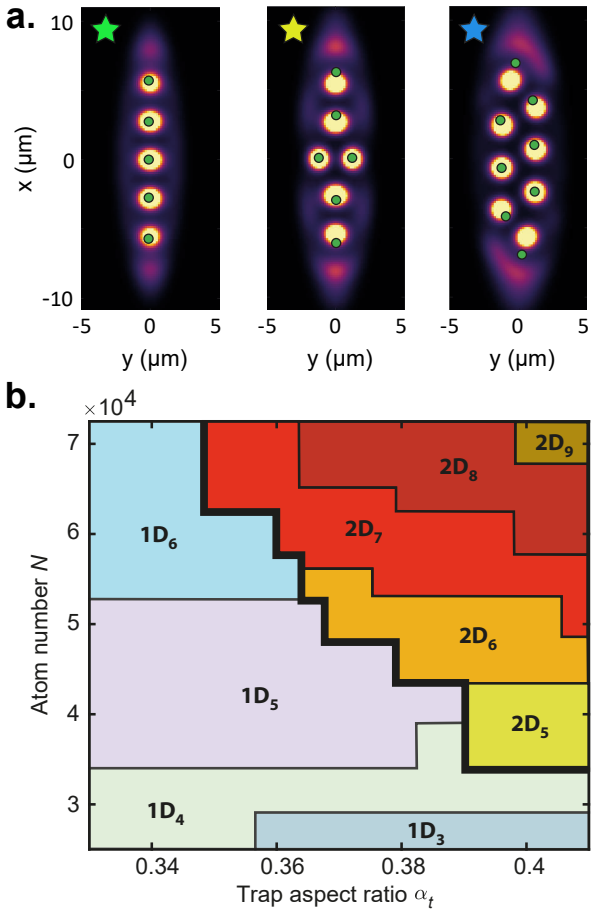

FIG. 1. **Calculated phases of dipolar droplet array. a.** In-trap ground-state density profiles calculated using eGPE for atom numbers $N \in [3.3, 4.4, 5.8] \times 10^4$ in the droplets and trap aspect ratios $\alpha_t = f_x/f_y \in [0.33, 0.35, 0.39]$ (left to right). The scattering length $a = 88\,a_0$, where a_0 is the Bohr radius. Green dots depict the droplet positions obtained from the variational model, assuming the same N and droplet number N_D as the eGPE. Stars connect to experimentally observed density profiles in Fig. 2b. **b.** Phase diagram, obtained from our variational model, as a function of N and α_t for $f_x = 33\,\mathrm{Hz}$, $f_z = 167\,\mathrm{Hz}$. Linear (two-dimensional) phases with N_D droplets are labelled as $1\mathrm{D}_{N_D}$ ($2\mathrm{D}_{N_D}$).

strength of these energetic contributions can lead to dramatic qualitative changes in the state of the system, for example enabling a transition from a uniform condensate to a supersolid, or in our present case, from a linear supersolid to a two-dimensional one.

Fig. 1a shows ground-state density profiles calculated across this transition using the eGPE at zero temperature. These profiles feature arrays of high-density droplets, immersed in a low-density coherent "halo" that establishes phase-coherence across the system. As the trap becomes more round, the initially linear chain of droplets acquires greater transverse structure, eventually forming a zig-zag state consisting of two offset linear arrays.

Although the eGPE has remarkable predictive power, full simulations in three dimensions are numerically intensive, making a global survey of the array properties as a function of our experimental parameters difficult. To overcome this limitation, we employ a variational ansatz that captures the key behavior of the system, and allows us to disentangle the competing energetic contributions. In this approach, we describe an array of N_D droplets by the wavefunction $\psi(\mathbf{r}) = \sum_{j=1}^{N_D} \psi_j(\mathbf{r})$, where the j–th droplet is assumed to be of the form: $\psi_j(\mathbf{r}) \propto \sqrt{N_j} \exp\left(-\frac{1}{2}\left(\frac{|\boldsymbol{\rho}-\boldsymbol{\rho}_j|}{\sigma_{\rho,j}}\right)^{r_{\rho,j}}\right) \exp\left(-\frac{1}{2}\left(\frac{|z-z_j|}{\sigma_{z,j}}\right)^{r_{z,j}}\right)$, interpolating between a Gaussian and a flat-top profile characteristic of quantum droplets [40]. For a given total number of atoms N and droplet number N_D, energy minimization provides the atom number N_j in each droplet, as well as their widths $\sigma_{\rho(z),j}$, exponents $r_{\rho(z),j}$, and positions $\boldsymbol{\rho}_j = (x_j, y_j)$. Repeating this energy minimization as a function of N_D gives the optimal number of droplets. This model provides a good qualitative description of the overall phase diagram (Fig. 1b), revealing that the interplay between intra-droplet physics and inter-droplet interaction results in a rich landscape of structural transitions as a function of the atom number and the trap aspect ratio $\alpha_t = f_x/f_y$.

Several trends are immediately visible from the phase diagram. Larger N and higher α_t generally produce states with larger numbers of droplets. Further, as with ions, a large number of droplets favors a 2D configuration, while tighter transverse confinement (small α_t) favors 1D [17–20]. A transition from 1D to 2D is thus expected when moving towards larger N or to higher α_t. In stark contrast to the case of ions, the number of droplets typically increases across the 1D to 2D transition, implying a first-order nature, while only narrow regions in the phase diagram may allow for a 1D-to-2D transition at constant droplet number.

The variational results are in excellent agreement with our eGPE numerics, in terms of predicting the qualitative structure of droplet array patterns, as shown in Fig. 1a. Slight discrepancies exist between the two theories regarding the predicted droplet positions and the location of the 1D-to-2D transition. This is likely because of the presence of the halo in the eGPE simulation (and presumably in the experiment), visible in Fig. 1a, which is not accounted for in the variational model. This halo appears to accumulate at the ends of the trap, pushing the droplets toward the trap center and likely increasing the effective trap aspect ratio experienced by the droplets.

To explore the 1D to 2D transition experimentally, we

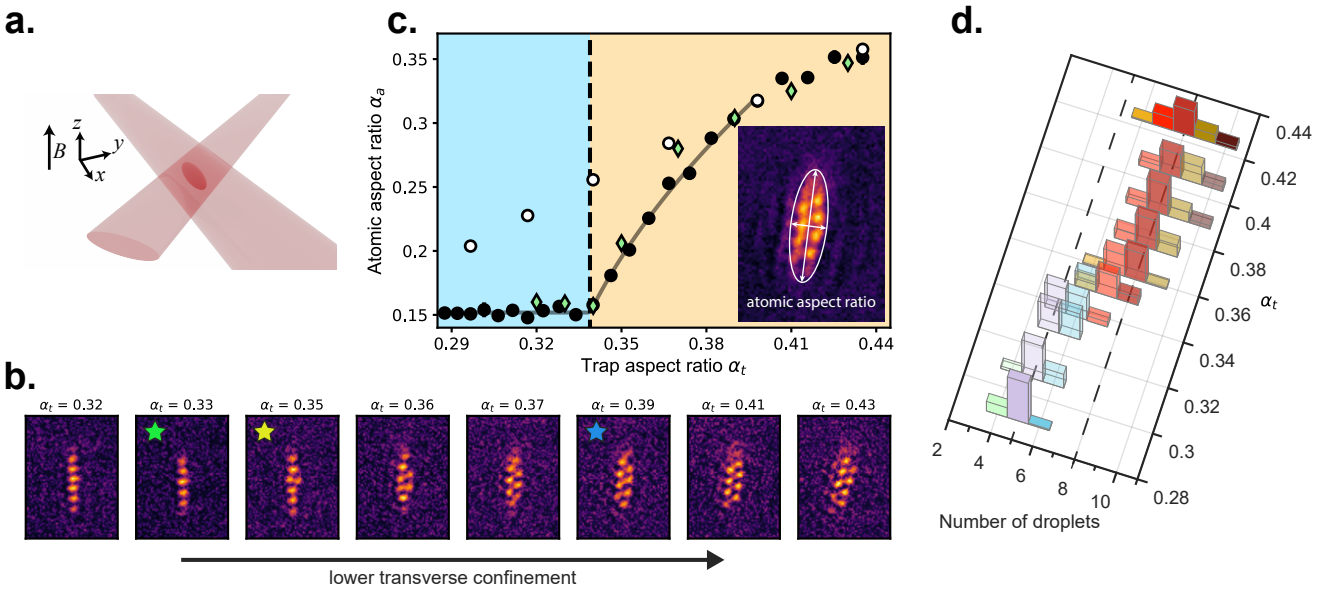

FIG. 2. **Linear to zig-zag transition in an anisotropic trap. a.** We confine and condense dipolar ^{164}Dy atoms within an anisotropic optical dipole trap (ODT) formed by the intersection of two laser beams. By tuning the aspect ratio of the trap in the x-y plane (α_t), perpendicular to an applied magnetic field B, we induce a transition between linear and zig-zag configurations of droplets. **b.** Single-trial images of the in-trap density profile of atoms at different α_t, showing structural transition from linear to zig-zag states, as well as an increase in droplet number for higher α_t. Stars indicate values α_t and N corresponding to the eGPE calculations of Fig. 1a. **c.** Atomic aspect ratio α_a versus trap aspect ratio α_t. α_a is the ratio of minor to major axes of a two-dimensional Gaussian fit to the imaged in-trap density profile (inset). For the supersolid droplet array (black markers) we see an abrupt change in α_a at the critical trap aspect ratio α_t^*, extracted from the fit (gray line, see methods). The shape of the transition agrees well with eGPE prediction (green diamonds, see methods). For an unmodulated condensate (white markers), no abrupt change is evident. **d.** Distribution of droplet number versus α_t, showing a distinct increase in droplet number at the transition of linear to zig-zag configurations.

use a condensate of highly magnetic ^{164}Dy atoms confined within an anisotropic optical dipole trap with independently tunable trap frequencies $f_{x,y,z}$. The trap, shown in Fig. 2a, is shaped like a surf-board with the tight axis along gravity and along a uniform magnetic field that orients the atomic dipoles and allows tuning of the contact interaction strength. Typically, we perform evaporation directly into our state of interest at our desired final interaction strength, as demonstrated in Refs. [13, 41]. A combination of in-trap and time-of-flight (TOF) imaging provides us with complementary probes of the density profile of our atomic states, and the phase coherence across the system.

We begin by studying the transition from one to two dimensions by changing the strength of transverse confinement provided by the trap. Our optical setup allows us to tune f_y from roughly 75 to 120 Hz, while leaving f_x, f_z nearly constant at 33(2), 167(1) Hz, and thus to vary the trap aspect ratio α_t in the plane perpendicular to the applied magnetic field and our imaging axis. For small α_t, the atoms are tightly squeezed transversely, and form a linear-chain supersolid (as seen in in-trap images of Fig. 2b). As we increase α_t above a critical value $\alpha_t^* = 0.34(2)$, we observe a structural phase transition to a two-dimensional (2D) state with two side-by-side droplets in the center of the chain. By further increasing α_t, the 2D structure extends to two offset lines of droplets in a zig-zag configuration. The observed patterns match well with the ground-state predictions from the eGPE calculations when we globally fix the scattering length to $88a_0$.

We obtain higher atom numbers in the more oblate traps (higher α_t), giving $N = 6.5(5) \times 10^4$ at $\alpha_t = 0.44$ and $N = 2.5(4) \times 10^4$ at $\alpha_t = 0.28$. This further facilitates the crossing of the 1D to 2D transition, by favoring states with larger numbers of droplets in the broader traps. In the zig-zag regime, two-dimensional modulation is clearly visible for durations beyond one second. Further, the droplet configuration patterns are fairly repeatable, with clear structure visible in averaged images

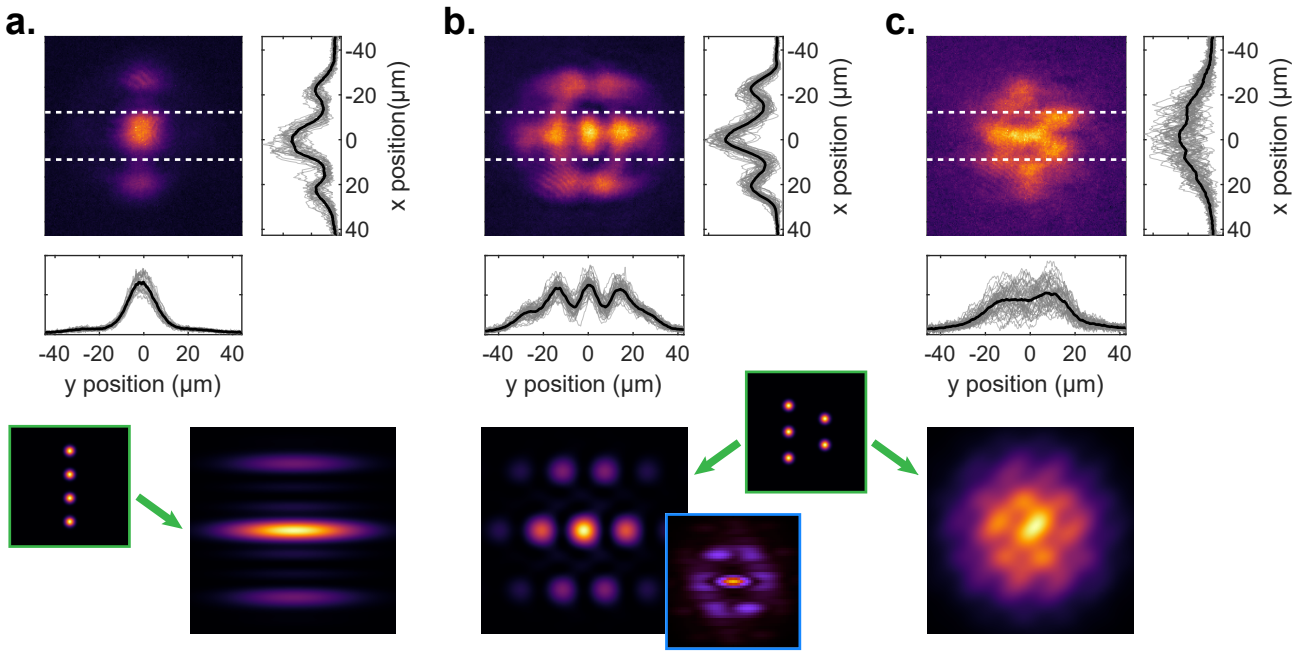

FIG. 3. **Coherence in linear and zig-zag states.** Upper panels show averaged images of experimental TOF interference patterns, along with projections along horizontal and vertical directions of average (solid black lines) and individual images (gray lines). The vertical projection is calculated between the dashed lines. Lower panels show interference patterns calculated for the pictured in-trap droplet configurations (green outlines). **a.** Linear chain of phase-coherent droplets, showing uniaxial modulation persisting in averaged image (26 trials). **b.** Zig-zag configuration of phase-coherent droplets, showing modulation along two directions that persists in averaged image (51 trials), and hexagonal structure. The spacing of rows in the simulation was adjusted to approximate the observed aspect ratio of TOF image. The image outlined in blue shows the average momentum distribution calculated from a series of 20 variational calculations converging to slightly different droplet configurations, showing the tendency of such fluctuations to broaden features in the interference pattern while maintaining the underlying structure. **c.** Zig-zag configuration of phase-incoherent droplets. Modulation remains in single images, as evidenced by the spread of gray traces in projection, but washes out in average (43 trials).

as shown in the inset of Fig. 2c, which is an average of 23 trials taken over roughly two hours.

The transition from 1D to 2D is immediately visible when plotting the atomic aspect ratio α_a versus α_t, as shown in Fig. 2c. We find that α_a undergoes a rapid change at α_t^*, as the single linear chain develops two-dimensional structure. For comparison, we plot α_a measured for an unmodulated BEC, formed at a different magnetic field, which does not feature the sharp kink present for the supersolid state.

In Fig. 2d, we show the number of droplets present for different α_t. In the 1D regime, we typically see between five and six droplets. This number abruptly jumps up by approximately one droplet for 2D states near the transition point, and then increases up to an average value of eight droplets as α_t is further increased. The change in droplet number indicates that the transition that we observe is not of simple structural nature, but is also accompanied by a reconfiguration of atoms within the droplets, as expected from theory (see Fig. 1).

The measurements of in-trap density presented above inform us about the structural nature of the transition, but not about phase coherence, which is the key distinguishing feature between an incoherent droplet crystal and a supersolid. Previous observations of 2D droplet arrays [35] were performed in traps where the ground state is a single droplet [8], and the observed droplet crystal was likely a metastable state lacking inter-droplet phase coherence. In contrast, we expect from our theoretical calculations that the 2D array is the ground state of our surfboard-shaped trap (for $\alpha_t > \alpha_t^*$), facilitating the formation of a phase-coherent, and therefore supersolid state for our experimental parameters.

We experimentally demonstrate the supersolid nature of our 2D modulated state using a matter-wave interference measurement, as previously used in linear supersolid

chains [11–13], (Fig. 3a). In this measurement, an array of uniformly spaced droplets creates an interference pattern with spatial period proportional to the inverse of the in-trap droplet spacing. The relative internal phase of the droplets determines both the contrast and spatial phase of the interference pattern [42]. When averaging over many interference patterns, obtained on separate runs of the experiment, clear periodic modulation persists for phase-coherent droplets, but averages out if the relative droplet phases vary between experimental trials. Thus, the presence of periodic modulation in an average TOF image provides a clear signature of supersolidity in our system, as it indicates both periodic density modulation and phase coherence.

Figure 3a shows an example of such an averaged interference pattern for a linear chain. Uniaxial modulation is clearly present along the direction of the chain, indicating a high degree of phase coherence. For comparison, we also show the expected interference pattern calculated for a linear array of four droplets from free-expansion calculations, showing similar structure.

For conditions where in-trap imaging shows a 2D zig-zag structure, the averaged interference pattern exhibits clear hexagonal symmetry (Fig. 3b). This is consistent with our expectation, and is indicative of the triangular structure of the underlying state. To confirm that the observed modulation is not present without phase coherence, we repeat the measurement of Fig. 3b at a magnetic field corresponding to independent droplets, and also compute averaged interference pattern for a zig-zag state with the phases of the individual droplets randomized between simulated trials (Fig. 3c). In both cases, the averaged image does not show clear periodic modulation.

By exploiting the transition between linear and zig-zag states, we have accessed a regime where the supersolid properties of periodic density modulation and phase coherence exist along two separate dimensions. Future work will focus on further understanding the spectrum of collective excitations in the full two-dimensional system [26–28, 43], where both the crystalline structure and the exchange of particles between droplets will play an important role. Further investigations may elucidate in more detail the nature of the phase transitions and expected configurations in a wider range of trap aspect ratios, as well as the role that defects play in the 2D system, either as phase-slips in the zig-zag patterns [44, 45], or as vortices trapped between droplets of the array [29–31].

We thank the Innsbruck Erbium team and Blair Blakie for discussions. We acknowledge R. M. W. van Bijnen for developing the code for our eGPE ground-state simulations.

Author Contributions: M.A.N, C.P., L.K., M.S., M.J.M and F.F. contributed experimental work. E.P and R.B. performed eGPE calculations. L.S. contributed variational model. All authors contributed to interpretation of results and preparation of manuscript.

Funding: The experimental team is financially supported through an ERC Consolidator Grant (RARE, No. 681432), an NFRI grant (MIRARE, No. ÖAW0600) of the Austrian Academy of Science, the QuantERA grant MAQS by the Austrian Science Fund FWF No I4391-N. L.S and F.F. acknowledge the DFG/FWF via FOR 2247/PI2790. M.S. acknowledges support by the Austrian Science Fund FWF within the DK-ALM (No. W1259-N27). L.S. thanks the funding by the Deutsche Forschungsgemeinschaft (DFG, German Research Foundation) under Germany's Excellence Strategy – EXC-2123 QuantumFrontiers – 390837967. M.A.N. has received funding as an ESQ Postdoctoral Fellow from the European Union's Horizon 2020 research and innovation programme under the Marie Skłodowska-Curie grant agreement No. 801110 and the Austrian Federal Ministry of Education, Science and Research (BMBWF). M.J.M. acknowledges support through an ESQ Discovery Grant by the Austrian Academy of Sciences. We also acknowledge the Innsbruck Laser Core Facility, financed by the Austrian Federal Ministry of Science, Research and Economy. Part of the computational results presented have been achieved using the HPC infrastructure LEO of the University of Innsbruck.

* M. A. N. and C. P. contributed equally to this work.

† Correspondence should be addressed to Francesca.Ferlaino@uibk.ac.at

[1] E. P. Gross, Unified theory of interacting bosons, Phys. Rev. **106**, 161 (1957).

[2] E. P. Gross, Classical theory of boson wave fields, Annals of Physics **4**, 57 (1958).

[3] A. F. Andreev and I. M. Lifshitz, Quantum theory of defects in crystals, Sov. Phys. JETP **29**, 1107 (1969).

[4] G. V. Chester, Speculations on Bose–Einstein condensation and quantum crystals, Phys. Rev. A **2**, 256 (1970).

[5] A. J. Leggett, Can a solid be "Superfluid"?, Phys. Rev. Lett. **25**, 1543 (1970).

[6] M. H.-W. Chan, R. Hallock, and L. Reatto, Overview on solid 4 he and the issue of supersolidity, Journal of Low Temperature Physics **172**, 317 (2013).

[7] Z.-K. Lu, Y. Li, D. S. Petrov, and G. V. Shlyapnikov, Stable dilute supersolid of two-dimensional dipolar bosons, Phys. Rev. Lett. **115**, 075303 (2015).

[8] D. Baillie and P. B. Blakie, Droplet crystal ground states of a dipolar bose gas, Phys. Rev. Lett. **121**, 195301

(2018).

[9] S. M. Roccuzzo and F. Ancilotto, Supersolid behavior of a dipolar bose-einstein condensate confined in a tube, Phys. Rev. A **99**, 041601 (2019).

[10] M. Boninsegni and N. V. Prokof'ev, Colloquium: Supersolids: What and where are they?, Rev. Mod. Phys. **84**, 759 (2012).

[11] L. Tanzi, E. Lucioni, F. Famà, J. Catani, A. Fioretti, C. Gabbanini, R. N. Bisset, L. Santos, and G. Modugno, Observation of a dipolar quantum gas with metastable supersolid properties, Phys. Rev. Lett. **122**, 130405 (2019).

[12] F. Böttcher, J.-N. Schmidt, M. Wenzel, J. Hertkorn, M. Guo, T. Langen, and T. Pfau, Transient supersolid properties in an array of dipolar quantum droplets, Phys. Rev. X **9**, 011051 (2019).

[13] L. Chomaz, D. Petter, P. Ilzhöfer, G. Natale, A. Trautmann, C. Politi, G. Durastante, R. M. W. van Bijnen, A. Patscheider, M. Sohmen, M. J. Mark, and F. Ferlaino, Long-lived and transient supersolid behaviors in dipolar quantum gases, Phys. Rev. X **9**, 021012 (2019).

[14] M. Guo, F. Böttcher, J. Hertkorn, J.-N. Schmidt, M. Wenzel, H. P. Büchler, T. Langen, and T. Pfau, The low-energy goldstone mode in a trapped dipolar supersolid, Nature **574**, 386 (2019).

[15] G. Natale, R. M. W. van Bijnen, A. Patscheider, D. Petter, M. J. Mark, L. Chomaz, and F. Ferlaino, Excitation spectrum of a trapped dipolar supersolid and its experimental evidence, Phys. Rev. Lett. **123**, 050402 (2019).

[16] L. Tanzi, S. Roccuzzo, E. Lucioni, F. Famà, A. Fioretti, C. Gabbanini, G. Modugno, A. Recati, and S. Stringari, Supersolid symmetry breaking from compressional oscillations in a dipolar quantum gas, Nature **574**, 382 (2019).

[17] G. Birkl, S. Kassner, and H. Walther, Multiple-shell structures of laser-cooled 24 mg+ ions in a quadrupole storage ring, Nature **357**, 310 (1992).

[18] M. G. Raizen, J. M. Gilligan, J. C. Bergquist, W. M. Itano, and D. J. Wineland, Ionic crystals in a linear paul trap, Phys. Rev. A **45**, 6493 (1992).

[19] S. Fishman, G. De Chiara, T. Calarco, and G. Morigi, Structural phase transitions in low-dimensional ion crystals, Phys. Rev. B **77**, 064111 (2008).

[20] E. Shimshoni, G. Morigi, and S. Fishman, Quantum zigzag transition in ion chains, Phys. Rev. Lett. **106**, 010401 (2011).

[21] W. K. Hew, K. J. Thomas, M. Pepper, I. Farrer, D. Anderson, G. A. C. Jones, and D. A. Ritchie, Incipient formation of an electron lattice in a weakly confined quantum wire, Phys. Rev. Lett. **102**, 056804 (2009).

[22] A. C. Mehta, C. J. Umrigar, J. S. Meyer, and H. U. Baranger, Zigzag phase transition in quantum wires, Phys. Rev. Lett. **110**, 246802 (2013).

[23] G. E. Astrakharchik, G. Morigi, G. De Chiara, and J. Boronat, Ground state of low-dimensional dipolar gases: Linear and zigzag chains, Phys. Rev. A **78**, 063622 (2008).

[24] J. Ruhman, E. G. Dalla Torre, S. D. Huber, and E. Altman, Nonlocal order in elongated dipolar gases, Phys. Rev. B **85**, 125121 (2012).

[25] L. Santos, G. V. Shlyapnikov, and M. Lewenstein, Roton-maxon spectrum and stability of trapped dipolar bose-einstein condensates, Phys. Rev. Lett. **90**, 250403 (2003).

[26] S. Ronen, D. C. E. Bortolotti, and J. L. Bohn, Radial and angular rotons in trapped dipolar gases, Phys. Rev. Lett. **98**, 030406 (2007).

[27] R. M. Wilson, S. Ronen, J. L. Bohn, and H. Pu, Manifestations of the roton mode in dipolar bose-einstein condensates, Phys. Rev. Lett. **100**, 245302 (2008).

[28] R. N. Bisset, D. Baillie, and P. B. Blakie, Roton excitations in a trapped dipolar bose-einstein condensate, Phys. Rev. A **88**, 043606 (2013).

[29] A. Gallemí, S. M. Roccuzzo, S. Stringari, and A. Recati, Quantized vortices in dipolar supersolid bose-einstein-condensed gases, Phys. Rev. A **102**, 023322 (2020).

[30] S. M. Roccuzzo, A. Gallemí, A. Recati, and S. Stringari, Rotating a supersolid dipolar gas, Phys. Rev. Lett. **124**, 045702 (2020).

[31] F. Ancilotto, M. Barranco, M. Pi, and L. Reatto, Vortex properties in the extended supersolid phase of dipolar bose-einstein condensates, arXiv preprint arXiv:2012.15157 (2020).

[32] Y.-C. Zhang, F. Maucher, and T. Pohl, Supersolidity around a critical point in dipolar bose-einstein condensates, Phys. Rev. Lett. **123**, 015301 (2019).

[33] J.-R. Li, J. Lee, W. Huang, S. Burchesky, B. Shteynas, F. Ç. Top, A. O. Jamison, and W. Ketterle, A stripe

phase with supersolid properties in spin–orbit-coupled Bose-–Einstein condensates, Nature **543**, 91 (2017).

[34] J. Léonard, A. Morales, P. Zupancic, T. Esslinger, and T. Donner, Supersolid formation in a quantum gas breaking a continuous translational symmetry, Nature **543**, 87 (2017).

[35] H. Kadau, M. Schmitt, M. Wenzel, C. Wink, T. Maier, I. Ferrier-Barbut, and T. Pfau, Observing the rosensweig instability of a quantum ferrofluid, Nature **530**, 194 (2016).

[36] I. Ferrier-Barbut, H. Kadau, M. Schmitt, M. Wenzel, and T. Pfau, Observation of quantum droplets in a strongly dipolar bose gas, Phys. Rev. Lett. **116**, 215301 (2016).

[37] L. Chomaz, S. Baier, D. Petter, M. J. Mark, F. Wächtler, L. Santos, and F. Ferlaino, Quantum-fluctuation-driven crossover from a dilute bose-einstein condensate to a macrodroplet in a dipolar quantum fluid, Phys. Rev. X **6**, 041039 (2016).

[38] F. Wächtler and L. Santos, Quantum filaments in dipolar bose-einstein condensates, Phys. Rev. A **93**, 061603 (2016).

[39] R. N. Bisset, R. M. Wilson, D. Baillie, and P. B. Blakie, Ground-state phase diagram of a dipolar condensate with quantum fluctuations, Phys. Rev. A **94**, 033619 (2016).

[40] L. Lavoine and T. Bourdel, 1d to 3d beyond-mean-field dimensional crossover in mixture quantum droplets (2020), arXiv:2011.12394 [cond-mat.quant-gas].

[41] M. Sohmen, C. Politi, L. Klaus, L. Chomaz, M. J. Mark, M. A. Norcia, and F. Ferlaino, Birth, life, and death of a dipolar supersolid, arXiv preprint arXiv:2101.06975 (2021).

[42] Z. Hadzibabic, S. Stock, B. Battelier, V. Bretin, and J. Dalibard, Interference of an array of independent Bose–Einstein condensates, Phys. Rev. Lett. **93**, 180403 (2004).

[43] J.-N. Schmidt, J. Hertkorn, M. Guo, F. Böttcher, M. Schmidt, K. S. Ng, S. D. Graham, T. Langen, M. Zwierlein, and T. Pfau, Roton excitations in an oblate dipolar quantum gas, arXiv preprint arXiv:2102.01461 (2021).

[44] K. Pyka, J. Keller, H. Partner, R. Nigmatullin, T. Burgermeister, D. Meier, K. Kuhlmann, A. Retzker, M. B. Plenio, W. Zurek, *et al.*, Topological defect formation and spontaneous symmetry breaking in ion coulomb crystals, Nature communications **4**, 1 (2013).

[45] S. Ulm, J. Roßnagel, G. Jacob, C. Degünther, S. Dawkins, U. Poschinger, R. Nigmatullin, A. Retzker, M. Plenio, F. Schmidt-Kaler, *et al.*, Observation of the kibble–zurek scaling law for defect formation in ion crystals, Nature communications **4**, 1 (2013).

[46] A. Trautmann, P. Ilzhöfer, G. Durastante, C. Politi, M. Sohmen, M. J. Mark, and F. Ferlaino, Dipolar quantum mixtures of erbium and dysprosium atoms, Phys. Rev. Lett. **121**, 213601 (2018).

Methods

Experimental apparatus and protocols: Our experimental apparatus has been described in detail in Ref. [46]. Here, we evaporatively prepare up to $N = 6.5(5) \times 10^4$ condensed ^{164}Dy atoms in a crossed optical dipole trap formed at the intersection of two beams derived from the same 1064 nm laser, although detuned in frequency to avoid interference. One beam (the static ODT) has an approximately 60 µm waist. The second (the scanning ODT) has an 18 µm waist, whose position can be rapidly scanned horizontally at 250 kHz to create a variably anisotropic time-averaged potential. By tuning the power in each beam, and the scanning range of the scanning ODT, we gain independent control of the trap frequencies in all three directions. The two trapping beams propagate in a plane perpendicular to gravity, and cross at a 45° angle, which leads to the rotation of the zig-zag state at high α_t visible in Fig. 2b.

We apply a uniform magnetic field oriented along gravity and perpendicular to the intersecting dipole traps, with which we can tune the strength of contact interactions between atoms. This allows us to create unmodulated Bose-Einstein condensates, supersolid states, or states consisting of independent droplets at fields of $B = 23.2$ G, 17.92 G, and 17.78 G, respectively.

Details of our imaging setup are provided in Ref. [41]. In-trap and TOF images are performed along the vertical direction (along B and gravity), using standard phase-contrast and absorption techniques, respectively. The resolution of our in-trap images is approximately one micron. We use a 36 ms TOF duration for imaging interference patterns.

Atom number: We extract the condensed atom number N from absorption imaging performed along a horizontal direction in a separate set of experimental trials under otherwise identical experimental conditions. This allows for a larger field of view, and better fitting of thermal atoms. N is determined by subtracting the fitted thermal component from the total absorption signal.

For comparison between experiment and theory, and between the variational and eGPE theory methods, we associate N with the number of atoms in the droplets, and not in the diffuse halo that surrounds the droplets. From simulation of TOF expansion, we find that the halo is repelled at early expansion times, and is likely indistinguishable from the thermal cloud in our TOF measurements. While it is possible that some of the halo is counted in N, we neglect this possibility and assume that N includes only atoms within droplets.

Scattering length: The positions of phase boundaries between different droplet configurations are quite sensitive to the scattering length a, which is not known with high precision in our range of magnetic fields. For all theory, we use a value of $a = 88\,a_0$, where a_0 is the Bohr radius, as this value provides good agreement between experiment and theory for the 1D-to-2D transition point.

Extracting critical aspect ratio: The critical aspect ratio α_t^* is extracted from fit to the function $\alpha_a = \alpha_0$ for $\alpha_t < \alpha_t^*$, $\alpha_a = \sqrt{\alpha_0^2 + b(\alpha_t - \alpha_t^*)^2}$ for $\alpha_t > \alpha_t^*$, where α_t^*, α_0, and b are fit parameters. The error bars reported in Fig. 2c represent the standard error on the mean, and are smaller than the markers on most points.

Interference patterns: The predicted interference patterns of Fig. 3 are calculated by assuming free expansion of Gaussian droplets. In reality, the droplets are probably not Gaussian, and interactions during TOF expansion may modify the interference pattern. However, the droplet shape primarily effects the envelope of the interference pattern, which is not our primary interest here, and from eGPE simulations, we expect the effects of interactions to be minor, provided that the droplets become unbound in a time short compared to the TOF, which we verify by both looking at shorter TOFs and comparing the fringe spacing observed in TOF with that expected from the in-trap droplet spacing. The positions and size of the droplets are tuned to provide illustrative interference patterns.

Droplet number: We extract the droplet number from our in-trap images using a peak-finding algorithm applied to smoothed images. The algorithm finds the local maxima above a threshold, which is chosen to be 40% of the overall peak value. Each in-trap density distribution is classified as linear array or 2D zig-zag based on the atomic aspect ratio. Finally, the counts with a given droplet number are normalized by the total number of trials to get the probability shown in Fig. 2d. Fluctuations in the number of atoms in a given trial can push droplets above or below the threshold value, contributing to the spread in extracted droplet number for a given α_t.

4.6 Publication IV:

Maintaining supersolidity in one and two dimensions

The following publication has appeared in

Physical Review A **104**, 063307 (2021)[§]
submitted 5 Aug 2021; published 9 Dec 2021
DOI: https://doi.org/10.1103/PhysRevA.104.063307
E. Poli,[2] T. Bland,[1] C. Politi,[1,2] L. Klaus,[1] M. A. Norcia,[1] F. Ferlaino,[1,2] R. N. Bisset,[2] and L. Santos[3]

[1] *Institut für Quantenoptik und Quanteninformation, Österreichische Akademie der Wissenschaften, 6020 Innsbruck, Austria*

[2] *Institut für Experimentalphysik, Universität Innsbruck, 6020 Innsbruck, Austria*

[3] *Institut für Theoretische Physik, Universität Hannover, Hannover, Germany*

[§]The author of the present thesis contributed in writing the manuscript and interpreting the results together with all the authors.

Maintaining supersolidity in one and two dimensions

E. Poli,[1] T. Bland,[2,*] C. Politi,[2,1] L. Klaus,[2,1] M. A. Norcia,[2] F. Ferlaino,[2,1] R. N. Bisset,[1] and L. Santos[3]
[1]*Institut für Experimentalphysik, Universität Innsbruck, 6020 Innsbruck, Austria*
[2]*Institut für Quantenoptik und Quanteninformation, Österreichische Akademie der Wissenschaften, 6020 Innsbruck, Austria*
[3]*Institut für Theoretische Physik, Leibniz Universität Hannover, 30167 Hannover, Germany*

(Received 5 August 2021; accepted 19 November 2021; published 9 December 2021)

We theoretically investigate supersolidity in three-dimensional dipolar Bose-Einstein condensates. We focus on the role of trap geometry in determining the dimensionality of the resulting droplet arrays, which range from one-dimensional to zigzag, through to two-dimensional supersolids in circular traps. Supersolidity is well established in one-dimensional arrays, and may be just as favorable in two-dimensional arrays provided that one appropriately scales the atom number to the trap volume. We develop a tractable variational model—which we benchmark against full numerical simulations—and use it to study droplet crystals and their excitations. We also outline how exotic ring and stripe states may be created with experimentally feasible parameters. Our work paves the way for future studies of two-dimensional dipolar supersolids in realistic settings.

DOI: 10.1103/PhysRevA.104.063307

I. INTRODUCTION

A supersolid concurrently exhibits both superfluidity and crystalline order [1–6]. Although predicted over half a century ago, supersolidity was only recently realized in experiments: a feat made possible by the flexibility and high degree of control afforded by quantum gas systems. While supersolid properties were observed in experiments with cavity-mediated interactions [7] and spin-orbit coupling [8,9], those platforms produce rigid lattices that are impervious to the usual excitations expected of crystals. In contrast, supersolids with deformable crystals have now been realized in dipolar Bose-Einstein condensates [10–12], in which genuine crystal and superfluid excitations have been observed [13–15].

Dipolar Bose-Einstein condensates (BECs) can be obtained from highly magnetic atoms such as chromium [16], dysprosium [17], and erbium [18]. It was already predicted in 2003 that dipolar BECs could undergo a roton instability [19]—where the unstable excitations occur at finite momenta—as observed in cigar-shaped Er BECs [13,20] and, more recently, in a pancake-shaped Dy BEC [21]. However, it was also expected from theory that the ensuing periodic density modulations would undergo a runaway collapse, and the regions of high local density would invoke three-body losses that rapidly destroy the underlying BEC. Indeed, a similar process was observed with the implosion of entire chromium BECs, driven by the attractive head-to-tail dipolar interactions [22]. From the perspective of supersolidity, the missing ingredient was a mechanism to stabilize against such implosions, and the answer came from the experimental discovery of dipolar droplets in Dy [23,24] and Er [25] BECs. Intriguingly, the stabilization mechanism is well described by including the leading-order effects of quantum fluctuations, resulting in a theory now known as the extended Gross-Pitaevskii equation (eGPE) [25–28]. These beyond-mean-field effects are especially important for the highly magnetic Er and Dy atoms. With this knowledge in hand, the first dipolar supersolids were created by crossing the roton instability from the BEC regime to the droplet array regime [10–12], or directly by evaporative cooling into the supersolid phase [12]. The supersolid ground-state region exists close to this phase transition, where the droplets overlap enough for the superfluid to globally conduct throughout the crystal.

While almost all dipolar supersolids have been experimentally realized as one-dimensional (1D) droplet arrays (see, for example, Refs. [10–15]), two recent experiments have created two-dimensional (2D) supersolids [29,30], thus opening an exciting frontier. An early theoretical study in 2D predicted a rich phase diagram determined by competing metastable crystal configurations [31]. More recent works in 2D have predicted supersolid edge phases [32], intriguing manifestations of quantum vortices and persistent currents [33–36], honeycomb supersolids [37], as well as ring and stripe phases [38,39].

Associated with this rich physics, dipolar supersolids have a large number of control parameters and their effects on the ground-state phase diagram interplay in a complicated way. Furthermore, the supersolid regime typically lies only within a small range of parameters, located between the ordinary unmodulated BEC and a crystal of isolated droplets. It is therefore paramount to develop strategies for maintaining supersolidity while exploring phase space. From a theoretical perspective, it is also necessary to develop tractable and accurate descriptions to supplement the computationally intensive eGPE.

In this work, we study supersolidity in three-dimensional (3D) dipolar BECs. We systematically explore 1D and 2D droplet arrays, identifying the crucial role that the *average 2D density* plays to maintain supersolidity for various trap geometries and atom numbers. We implement an eGPE formalism—and develop a tractable variational model—to examine the phase diagram from linear supersolids in elongated traps to 2D supersolids in circular traps, passing through

*Corresponding author: thomas.bland@uibk.ac.at

zigzag and multirow elliptical phases along the way. We find that 2D supersolids may be just as favorable as their 1D counterparts, provided that one fixes the average 2D density. Through increasing the average 2D density, we show how to observe the exotic ring and stripe phases [38,39] with realistic experimental parameters. Finally, we extend our variational model to study 2D crystal excitations and benchmark this against full numerical calculations.

The paper is structured as follows. In Sec. II, we outline our system and the eGPE, while Sec. III introduces the concept of the average 2D density and uses it to theoretically build a 1D-2D supersolid phase diagram. We also introduce our droplet crystal variational model. Section IV examines increasing the average 2D density to access the exotic ring and stripe phases. In Sec. V, we present some exemplary 2D crystal excitations, before concluding with Sec. VI.

II. FORMALISM

We consider 3D dipolar BECs under harmonic confinement and we use the eGPE, given by [25–28]

$$i\hbar\frac{\partial\Psi(\mathbf{x},t)}{\partial t}=\Bigg[-\frac{\hbar^2\nabla^2}{2m}+\frac{1}{2}m\left(\omega_x^2x^2+\omega_y^2y^2+\omega_z^2z^2\right)+\int d^3\mathbf{x}'\,U(\mathbf{x}-\mathbf{x}')|\Psi(\mathbf{x}',t)|^2+\gamma_{\mathrm{QF}}|\Psi(\mathbf{x},t)|^3\Bigg]\Psi(\mathbf{x},t), \tag{1}$$

where m is the mass and $\omega_i=2\pi f_i$ are the harmonic trap frequencies. The wave function Ψ is normalized to the total atom number $N=\int d^3\mathbf{x}|\Psi|^2$. For dilute gases, two-body interactions are well described by the pseudopotential,

$$U(\mathbf{r})=\frac{4\pi\hbar^2a_{\mathrm{s}}}{m}\delta(\mathbf{r})+\frac{3\hbar^2a_{\mathrm{dd}}}{m}\frac{1-3\cos^2\theta}{r^3}, \tag{2}$$

with the first term describing the short-range interactions governed by the s-wave scattering length a_s. The second term represents the anisotropic and long-range dipole-dipole interactions, characterized by dipole length $a_{\mathrm{dd}}=\mu_0\mu_m^2m/12\pi\hbar^2$, with magnetic moment μ_m and vacuum permeability μ_0. We take the dipoles to be polarized along z, and θ is the angle between the polarization axis and the vector pointing from one of the interacting particles to the other. We always consider ^{164}Dy, such that $a_{\mathrm{dd}}=130.8a_0$, where a_0 is the Bohr radius. The final term in (1) is the dipolar Lee-Huang-Yang correction arising from quantum fluctuations [40], having the coefficient

$$\gamma_{\mathrm{QF}}=\frac{128\hbar^2}{3m}\sqrt{\pi a_s^5}\,\mathrm{Re}\{\mathcal{Q}_5(\varepsilon_{\mathrm{dd}})\}, \tag{3}$$

where $\mathcal{Q}_5(\varepsilon_{\mathrm{dd}})=\int_0^1 du\,(1-\varepsilon_{\mathrm{dd}}+3u^2\varepsilon_{\mathrm{dd}})^{5/2}$ is the auxiliary function, and the relative dipole strength is given by $\varepsilon_{\mathrm{dd}}=a_{\mathrm{dd}}/a_s$. Note that $\mathcal{Q}_5$ can be calculated analytically (Appendix A), but this is just a monotonically increasing function that is of the order of unity for the regimes that we consider here. Ground-state and metastable solutions of Eq. (1) are calculated by minimizing the energy functional corresponding to the eGPE using a conjugate-gradients technique [41].

III. TWO-DIMENSIONAL SUPERSOLIDITY

A. Average 2D density

In dipolar gases, the strong interplay between the confinement geometry and the long-range and anisotropic dipole-dipole interactions means that the ground-state phase diagram is complex and the relevant parameter space to consider is huge. This may conceal the identification of the most important control parameters. For example, it was demonstrated in Refs. [10–12,31,39,42] that varying a_s and f_z dramatically affects the supersolid ground state, with supersolidity easily being lost. In what follows, we identify an important control parameter for moving between or within the various supersolid regimes, as well as maintaining supersolidity while progressing from 1D to 2D droplet arrays.

Dipolar supersolids require tight confinement along the direction of dipole polarization, and the precise choice of f_z determines the narrow range of a_s over which supersolidity occurs. For this reason, we take both f_z and a_s to be fixed in the following argument. We propose that the *average 2D density* acts as an important control parameter. This can be thought of as an *average* over the droplet and interdroplet regions, and only the *2D density* is considered because f_z is fixed. A simple yet powerful estimate for how the average 2D density scales is furnished by the Thomas-Fermi approximation, where kinetic energy is neglected, and the x and y radii of a BEC scale $\sim 1/f_x$ and $\sim 1/f_y$, respectively, giving a BEC area scaling $\sim 1/f_xf_y$. The key point is then to realize that the average 2D density scales approximately with the parameter $\varrho=Nf_xf_y$. In the next section, we explore the consequences of varying ϱ versus keeping it fixed.

B. From 1D to 2D

In order to illustrate the utility of the average 2D density—characterized by ϱ—the first two columns of Fig. 1 explore the 1D-2D transition for two different phase-space trajectories: first by allowing ϱ to vary and second by fixing ϱ. For both, we consider fixed interactions while moving from a cigar-shaped trap (top row) to a pancake-shaped trap (bottom row). The key difference between the trajectories is that column 1 has a fixed atom number—and hence ϱ decreases as the trap loosens—while column 2 instead fixes ϱ, with N increasing to compensate for the widening of the trap. Crucially, the reduction of ϱ in the first column leads to a loss of the supersolid phase, replaced by an unmodulated BEC, while fixing ϱ allows us to loosen the trap while remaining in the supersolid regime, eventually resulting in a large, 19-droplet supersolid for the circular trap [Fig. 1(j)]. We have theoretically verified in other work that this large 2D supersolid state is robust against thermal fluctuations [30].

C. Droplet variational theory

Although direct simulations of the eGPE have a remarkable predictive power, they are numerically intensive and hinder a thorough overview. We develop a variational model that permits a much simpler determination of the available droplet phases, while presenting an excellent qualitative, and largely quantitative, agreement with our eGPE calculations.

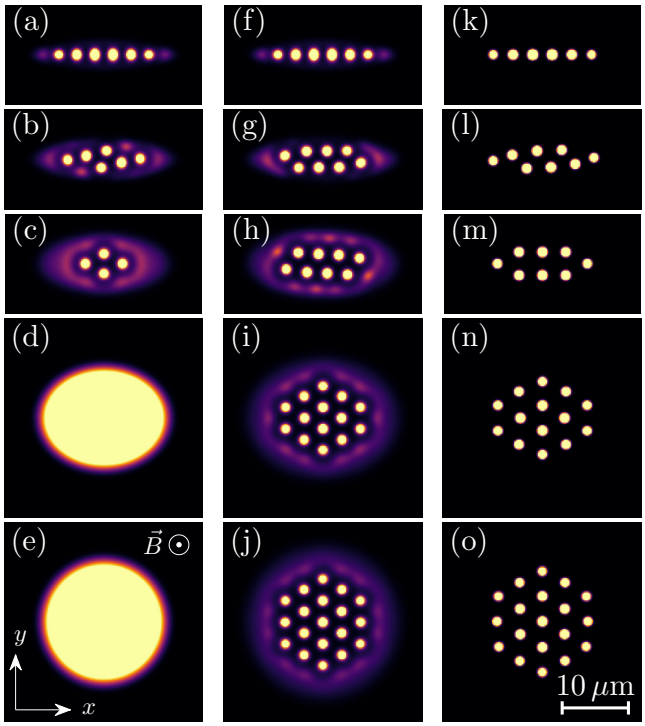

FIG. 1. Opening up the trap from 1D to 2D for ^{164}Dy atoms with $a_s = 88a_0$ and $a_{dd} = 130.8a_0$. In each panel, we fix $(f_x, f_z) = (33, 167)$ Hz and decrease $f_y \in \{110, 84.6, 60, 40, 33\}$ Hz, from top to bottom, showing the integrated column density. Column 1: eGPE result with constant $N = 6.3 \times 10^4$. Column 2: eGPE with constant average 2D density, increasing N to fix $\varrho = N f_x f_y$ with $N \in \{6.3, 8.19, 11.55, 17.325, 21\} \times 10^4$. Column 3: same as column 2, but the variational model. The atom number in the variational model is chosen to match the droplet atom number of the eGPE (see text). We always take the dipoles to be polarized by magnetic field $\vec{B}$ along z.

Inspired by recent work with nondipolar droplets [43], we assume the following *Ansatz* for a dipolar droplet:

$$\Psi(\mathbf{x}) = \sqrt{\mathcal{N}}\phi(\rho)\psi(z), \tag{4}$$

with $\mathcal{N}$ the number of particles and $\rho = \sqrt{x^2 + y^2}$. We again consider dipoles polarized along the z axis, and the droplets are cylindrically symmetric, which we have confirmed as a good approximation by comparing with full eGPE calculations. The radial and axial functions take the form, respectively,

$$\begin{aligned}\phi(\rho) &= \sqrt{\frac{r_\rho}{2\pi\Gamma(2/r_\rho)\sigma_\rho^2}}\, e^{-\frac{1}{2}\left(\frac{\rho}{\sigma_\rho}\right)^{r_\rho}}, \\ \psi(z) &= \sqrt{\frac{r_z}{2\Gamma(1/r_z)\sigma_z}}\, e^{-\frac{1}{2}\left(\frac{|z|}{\sigma_z}\right)^{r_z}},\end{aligned} \tag{5}$$

with $\Gamma(x)$ being the Gamma function. The widths $\sigma_{\rho,z}$ and the exponents $r_{\rho,z}$ are variational parameters. Note that this function permits the interpolation between a Gaussian ($r = 2$) and a flat-top ($r \gg 1$) profile in a natural way. Furthermore, this *Ansatz* allows for a simple evaluation of the various energies in the system using well-known properties of the Gamma function.

Our general strategy is to first numerically minimize the single-droplet problem for a range of possible parameters to build interpolation functions for the variational widths $\sigma_{\rho,z}(\mathcal{N})$ and exponents $r_{\rho,z}(\mathcal{N})$. These functions are then used to solve the many-droplet problem.

For a single droplet, *Ansätze* (4) and (5) can be used to minimize the eGPE energy functional,

$$E_{sd}(\mathcal{N}) = E_{kin} + E_{trap} + E_{sr} + E_{dd} + E_{qf}, \tag{6}$$

where these quantities are the kinetic, trap, short-range interaction, dipole-dipole interaction, and quantum fluctuation contributions, respectively. The evaluation of these terms is detailed in Appendix A.

Now consider a droplet array with N_D droplets, with N_j atoms in the jth droplet. Within the variational model, the energy of the droplet array is then given by

$$E = \sum_{j=1}^{N_D}\left[E_{sd}(N_j) + \frac{m}{2}\left(\omega_x^2 x_j^2 + \omega_y^2 y_j^2\right)N_j\right] + \sum_{j=1}^{N_D}\sum_{j'>j} E_{jj'}, \tag{7}$$

where $E_{jj'}$ is the interdroplet interaction, detailed in Appendix B. By solving the single- then multidroplet problems separately, we effectively reduce the number of variational parameters from $7N_D - 1$ to $3N_D - 1$ ($\{\sigma_{\rho,z}^j, r_{\rho,z}^j, N_j, x_j, y_j\} \to \{N_j, x_j, y_j\}$), where the -1 arises from fixing the total atom number, $N = \sum_j N_j$.

It is worth noting that important early work employed a purely Gaussian variational model (i.e., $r_\rho = r_z = 2$) to explore crystal and supersolid configurations [31]. Our model goes a step further by allowing for the possibility of droplets with flat-top density profiles, which partially acts to shield interdroplet repulsion in the supersolid regime where the droplets are tightly packed together.

Example solutions of our variational *Ansatz* are shown in Fig. 1 (column 3), displaying excellent agreement with the corresponding eGPE results (column 2). It should be noted that for the eGPE solutions, a sizable number of atoms exist outside the droplets in an outer ring, which we term the "halo." To make direct comparisons between the variational and eGPE methods, we estimate the total number of atoms in the droplets alone from the eGPE and use this to set the total atom number for the corresponding variational calculation. For reference, the variational to eGPE atom number ratio varies from $N_{var} = 0.84N_{eGPE}$ for the linear chain [Figs. 1(f) and 1(k)] to $N_{var} = 0.58N_{eGPE}$ for the circular crystal [Figs. 1(j) and 1(o)]. Small deviations in the droplet positions occur between the models due to repulsion between the droplets and the halo in the eGPE, whereas the halo is absent in the variational model. In general, the halo leads to a slight compression of the crystal. Additionally, because the halo density is nonuniform around the perimeter of the droplet array (in some cases forming nearly-droplet-like regions of higher density), its presence can also qualitatively modify the structure and the symmetry of the droplet array in certain situations [cf. Figs. 1(h) and 1(m)].

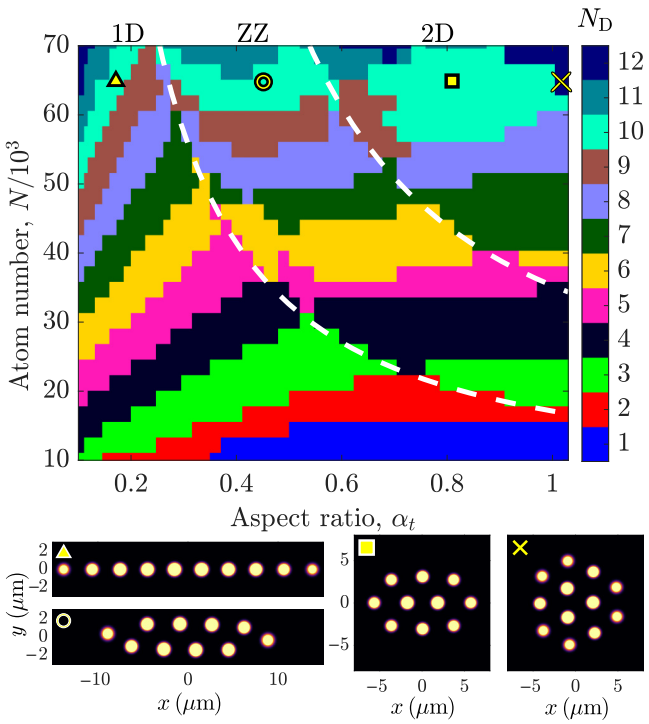

FIG. 2. Crystal phase diagram for ^{164}Dy atoms from 1D (left) to circular trap regime (right) using *Ansätze* (4) and (5). Color indicates ground-state droplet number vs total atom number N and aspect ratio $\alpha_t = f_x/f_y$. A constant average 2D density (controlled by fixing $\varrho = N f_x f_y$) is used throughout, which means the trap tightens from $\sqrt{f_x f_y} = 43$ Hz (top) to $\sqrt{f_x f_y} = 114$ Hz (bottom). White lines separate the 1D, zigzag (ZZ), and 2D regions. Example configurations for fixed $N = 5.4 \times 10^4$ are shown below. Parameters $f_z = 167$ Hz and $a_s = 88a_0$ remain constant.

D. Crystal phase diagram

Here, with the variational model, we seek to explore the full phase diagram of droplet crystal configurations while maintaining a fixed average 2D density, which we control by keeping ϱ constant. Figure 2 shows the droplet configurations of the ground state as a function of the trap aspect ratio $\alpha_t = f_x/f_y$ and atom number. Since ϱ is held fixed throughout, the bottom of the phase diagram corresponds to $N = 10^4$ and $\sqrt{f_x f_y} = 114$ Hz, while the top reaches $N = 7 \times 10^4$ and $\sqrt{f_x f_y} = 43$ Hz. Traversing right on the phase diagram equates to increasing f_x and decreasing f_y, hence moving to more circular configurations.

Several trends are apparent from this phase diagram. Larger N corresponds to ground states with a larger number of droplets. If the configuration is linear (left in Fig. 2), then the droplet number increases incrementally one droplet at a time; however, for large $\alpha_t \sim 1$ (right in Fig. 2), there are occasional jumps of two or more droplets—within the resolution of our phase diagram—corresponding to preferential triangular configurations of the lattice in 2D. For example, we find that for $\alpha_t = 1$, the ground state jumps from $N_D = 8$ to the $N_D = 12$ state shown in Fig. 2 (×), with only a very narrow range of N corresponding to a 10-droplet configuration in between.

Following the solutions from bottom left to top right in Fig. 2, there are two distinct jumps in the average transversal spread ($\Delta y = 1/N_D \sum_j^{N_D} |y_j - \bar{y}|$, for the y position of the jth droplet y_j, and mean y position $\bar{y}$), marked as white dashed lines in Fig. 2. These signify the transition from linear [Fig. 2 (△)] to zigzag [Fig. 2 (◯)] configurations, and then 2D solutions with three [Fig. 2 (□)] or more [Fig. 2 (×)] rows of droplets. The first three of these highlighted solutions contain the same number of droplets for a fixed atom number, until $\alpha_t \approx 1$, where the ground-state configuration consists of 12 droplets. Intriguingly, these jumps in Δy are also usually associated with a change in the ground-state droplet number. It is interesting to note that in the 1D regime, the regions of constant N_D slope downwards to the left. This can be understood by considering a horizontal trajectory, for which both N and ϱ are constant. As we move left along this trajectory, increasing f_y can no longer force the droplets closer together—since the array is already 1D—while the decreasing f_x provides more space for longer droplet arrays, with larger N_D.

IV. INCREASING AVERAGE 2D DENSITY

Previous theoretical works have found exotic two-dimensional supersolid states with either large atom numbers ($\sim 10^6$) or tight trapping (~ 1 kHz) [37–39]. Notably, honeycomb ground states have been predicted [37] with crystal arrays of *holes* rather than droplets. Such states are appealing due to their predicted strong superfluid conductance across the crystal, without relying on low-density connections between droplets. Also predicted are intriguing stripe and ring states [38], as well as labyrinthine instabilities [39] familiar in classical ferrofluids [44].

Using the eGPE, we investigate the feasibility of creating these exotic supersolids by increasing the average 2D density through tightening the radial trap frequencies, without relying on pushing the parameters to unrealistically large values. Figures 3(a)–3(f) show how the solution changes by increasing $f_x = f_y \in \{30, 50, 80, 90, 100, 150\}$ Hz, respectively, while holding fixed $N = 1.4 \times 10^5$, and hence ϱ increases. This trajectory through phase space takes us from an unmodulated BEC [Fig. 3(a)] to a hexagonal supersolid [Fig. 3(b)], a stripe supersolid [Fig. 3(d)], through to a ring state [Fig. 3(e)], and, finally, a macrodroplet [Fig. 3(f)]. Interestingly, while the peak density of the BEC phase is about 1.5×10^{20} m^{-3}, for all droplet and supersolid phases it is roughly constant at $\sim 1.5 \times 10^{21}$ m^{-3}, suggesting that the atom losses from inelastic three-body collisions—and hence also the lifetimes—of these exotic states may be comparable to that for the current generation of supersolid experiments.

V. EXCITATIONS OF A 2D SUPERSOLID

Following the recent experimental observation of a seven-droplet hexagon supersolid [30], we further investigate the excitations of this state in a circular trap using the eGPE [see Fig. 4(a1)] and variational model [see Fig. 4(b1)].

We find excitations in the Bogoliubov–de Gennes (BdG) framework, which consists of a linearization of the eGPE around the stationary solution ψ_0 with perturbations of the form $\delta\psi = u e^{-i\epsilon t/\hbar} + v^* e^{i\epsilon t/\hbar}$ [45]. To visualize the

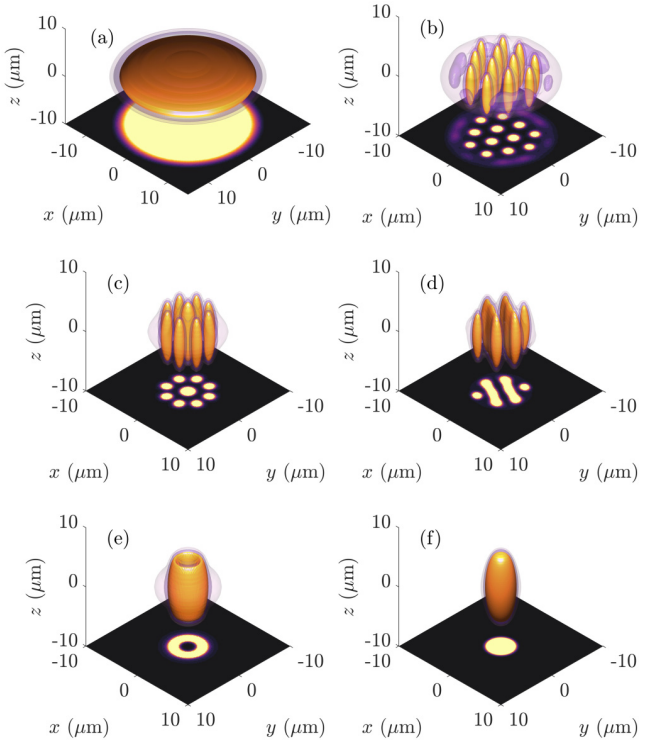

FIG. 3. Increasing the average 2D density. The radial trap frequency is increased from (a)–(f), respectively, as $f_x = f_y \in \{30, 50, 80, 90, 100, 150\}$ Hz, while $N = 1.4 \times 10^5$ is held fixed. Density isosurfaces are shown at the 5%, 0.1%, and 0.01% of the maximum density level. Shadow shows the 2D integrated density. Other parameters: $f_z = 167$ Hz and $a_s = 88\,a_0$.

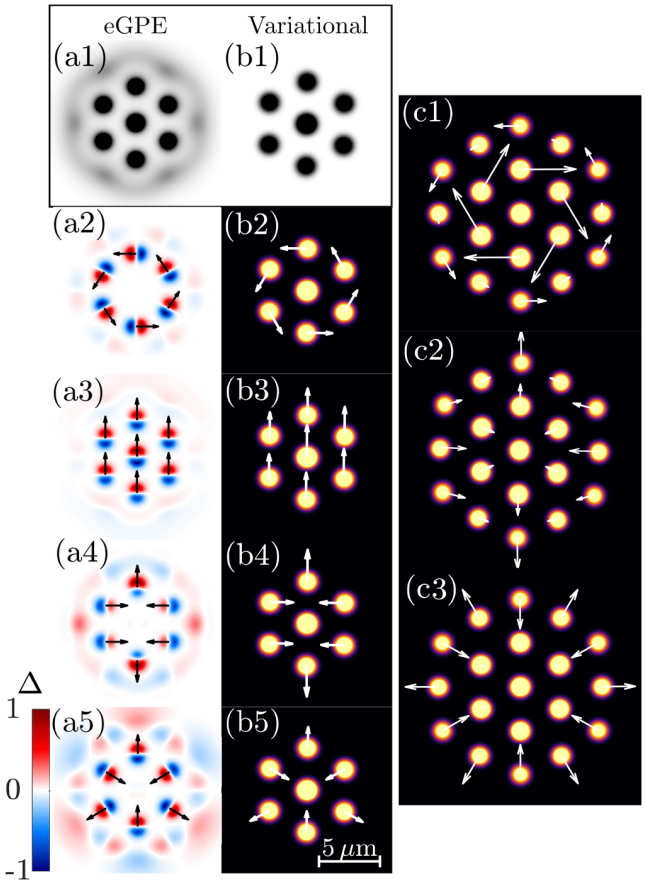

FIG. 4. Crystal excitations. (a1),(b1) Seven-droplet crystal state and corresponding excitations from the (a2)–(a5) eGPE-BdG calculations and (b2)–(b5) variational model. Arrows indicate relative droplet motion (see main text). Parameters: $a_s = 90a_0$, $f_{x,y,z} = (52.83, 52.83, 167)$ Hz, $N = 9.5 \times 10^4$. (c) Exemplary excitations for the 19-droplet state from the variational model shown in Fig. 1(o).

excitations, we plot the density perturbation $\Delta\psi = (u + v^*)|\psi_0|$ for several exemplary excitations in Figs. 4(a2)–4(a5) (arbitrary normalization). The arrows represent the droplet displacement vectors (with arbitrary global scaling), calculated from the shift in density peaks caused by adding a small amount of excitation to the ground-state wave function. These results are compared with the corresponding excitations calculated with the variational model [Figs. 4(b2)–4(b5)], with droplet displacement vectors obtained through linearizing perturbations to the droplet positions (see Appendix C). Since these modes exist in the variational model—which does not account for superfluid flow between droplets—we can classify them as predominantly crystalline in nature.

Due to rotational symmetry, there is a zero-energy rotational mode [Figs. 4(a2) and 4(b2)], which is unique to circular trap supersolids. As expected, there are two degenerate Kohn modes at the radial trap frequency, one of which is shown in Figs. 4(a3) and 4(b3). Also plotted are quadrupole excitations [Figs. 4(a4) and 4(b4)], as well as an example surface crystal mode [Figs. 4(a5) and 4(b5)], which is a unique feature of 2D supersolids highlighting the rich tapestry of excitations. In the last two examples, the mode energy obtained in the BdG framework and the variational models differs. The energies are $E/h = 54$ Hz [Fig. 4(a4)] and $E/h = 72$ Hz [Fig. 4(a5)] from the BdG calculations and $E/h = 65$ Hz [Fig. 4(b4)] and $E/h = 69$ Hz [Fig. 4(b5)] from the variational model. These deviations point to a measurable role played by the superfluid connection between the droplets, and the effect of the surrounding halo, which are not accounted for by the variational model. Such comparisons between models provide an excellent platform to distinguish contributions from the crystal and the superfluid surrounding and connecting the droplets.

The computational cost of obtaining modes from BdG linearization is high, requiring the diagonalization of large dense matrices consisting of the total number of position space grid points squared; in our case, $\sim 10^6 \times 10^6$. We achieve this using an eigensolver based on the implicitly restarted Arnoldi method. We also find that the linearization is slower when there is no appreciable superfluid connection between the droplets, making excitations in the isolated droplet regime difficult to obtain. However, in this regime, the variational model agrees well with the BdG calculations, and the former only requires the diagonalization of a $2N_D \times 2N_D$ matrix [i.e., the total number of (x_j, y_j) pairs]. This allows us to explore excitations of larger crystals.

In Figs. 4(c1)–4(c3), we show excitations of the 19-droplet crystal [Fig. 1(o)] using the variational model, a state that

would require months of computational time to obtain excitations within the eGPE-BdG framework. This configuration consists of two concentric hexagons with a single droplet in the middle, where the inner hexagon consists of six droplets and the outer hexagon has 12. In Fig. 4(c1), we highlight an interesting mode in which the two outer hexagons counterrotate. We also find a quadrupole mode [Fig. 4(c2)] and, in Fig. 4(c3), we show an analog of the surface crystal mode that we saw for the seven-droplet hexagon [Figs. 4(a5) and 4(b5)].

VI. CONCLUSIONS

We have investigated the scope and feasibility of 2D supersolidity in harmonically trapped dipolar Bose gases, identifying the crucial role of the average 2D density in maintaining both the crystal structure and global superfluidity while varying the dimensionality and size of the droplet array. By developing a variational multidroplet model, we explored the phase diagram of crystal configurations for a wide range of atom numbers and aspect ratios for a fixed 2D density, identifying the transition from one- to two-dimensional droplet arrays.

We theoretically explored how increasing the average 2D density may provide a route for creating exotic stripe and ring supersolids under experimentally realistic conditions. We also extended our variational model to explore crystal excitations, verified by direct comparison to the BdG analysis. This method allows for the investigation of crystal modes in large 2D supersolids, where exact diagonalization of the eGPE is demanding.

Future work will further explore the potential of the variational model. Implementing a system of Hamilton equations would allow for dynamics of the droplet arrays, and further open up the study of excitations in two-dimensional supersolid crystals. While we have revealed how to vary an important triplet of coupled parameters, i.e., N, and the two trapping frequencies perpendicular to the direction of dipole polarization, f_x and f_y, enabling the exploration of supersolids of various shapes and sizes, future studies will seek an easy determination for how best to vary other control parameters, such as the coupling between the interaction strengths and the remaining trap frequency, f_z.

ACKNOWLEDGMENTS

We gratefully acknowledge useful discussions with Manfred Mark and the Innsbruck Erbium team. We acknowledge R. M. W. van Bijnen for developing the code for our eGPE and BdG simulations. Part of the computational results presented here have been achieved using the HPC infrastructure LEO of the University of Innsbruck. The experimental team is financially supported through an ERC Consolidator grant (RARE, Grant No. 681432), an NFRI grant (MIRARE, Grant No. OAW0600) of the Austrian Academy of Science, the QuantERA grant MAQS by the Austrian Science Fund FWF (Grant No I4391-N). L.S. and F.F. acknowledge the DFG/FWF (Grant No. FOR 2247/I4317-N36) and a joint-project grant from the FWF (Grant No. I4426, RSF/Russland 2019). L.S. acknowledges the funding by the Deutsche Forschungsgemeinschaft (DFG, German Research Foundation) under Germany's Excellence Strategy–EXC-2123 QuantumFrontiers, Grant No. 390837967. M.A.N. has received funding as an ESQ Postdoctoral Fellow from the European Union's Horizon 2020 research and innovation programme under the Marie Sklodowska-Curie Grant Agreement No. 801110 and the Austrian Federal Ministry of Education, Science and Research (BMBWF). We also acknowledge the Innsbruck Laser Core Facility, financed by the Austrian Federal Ministry of Science, Research and Economy.

APPENDIX A: SINGLE-DROPLET VARIATIONAL MODEL

Here we detail the individual contributions to the single-droplet energy functional for $\mathcal{N}$ atoms,

$$E_{\rm sd}(\mathcal{N}) = E_{\rm kin} + E_{\rm trap} + E_{\rm sr} + E_{\rm dd} + E_{\rm qf}. \tag{A1}$$

These terms are given by

$$\begin{aligned} E_{\rm kin} &= -\frac{\hbar^2}{2m}\int d^3\mathbf{x}\ \Psi^*\nabla^2\Psi, \\ E_{\rm trap} &= \frac{m}{2}\int d^3\mathbf{x}\ \Psi^*\sum_i \omega_i^2 x_i^2\Psi, \\ E_{\rm sr} &= \frac{1}{2}\int d^3\mathbf{x}\ \Psi^* g|\Psi|^2\Psi, \\ E_{\rm dd} &= \frac{g\epsilon_{\rm dd}}{2}\int \frac{d^3\mathbf{k}}{(2\pi)^3}\left(\frac{3k_z^2}{k^2}-1\right)|\tilde{n}(\mathbf{k})|^2, \\ E_{\rm qf} &= \frac{2}{5}\gamma_{\rm QF}\int d^3\mathbf{x}\ |\Psi|^5, \end{aligned} \tag{A2}$$

corresponding to the kinetic, trap, short-range interaction, dipole-dipole interaction, and quantum fluctuation contributions, respectively. Here, the short-range interaction coefficient is $g = 4\pi\hbar^2 a_s/m$, and the quantum fluctuation coefficient is $\gamma_{\rm QF} = \frac{32}{3}g\sqrt{\frac{a_s^3}{\pi}}\mathcal{Q}_5(\varepsilon_{\rm dd})$, where $\mathcal{Q}_5(\varepsilon_{\rm dd}) = {\rm Re}[\int_0^1 du\,(1-\varepsilon_{\rm dd}+3u^2\varepsilon_{\rm dd})^{5/2}]$, and the density in Fourier space is $\tilde{n}(\mathbf{k}) = \int d^3\mathbf{x}\ e^{-i\mathbf{k}\cdot\mathbf{x}}|\Psi(\mathbf{x})|^2$. The integral $\mathcal{Q}_5(\varepsilon_{\rm dd})$ can be evaluated as

$$\begin{aligned} \mathcal{Q}_5(\varepsilon_{\rm dd}) = {\rm Re}\frac{(3\varepsilon_{\rm dd})^{5/2}}{48}\Bigg[&(8+26\epsilon+33\epsilon^2)\sqrt{1+\epsilon} \\ &+ 15\epsilon^3\ln\left(\frac{1+\sqrt{1+\epsilon}}{\sqrt{\epsilon}}\right)\Bigg], \end{aligned} \tag{A3}$$

where $\epsilon = (1-\varepsilon_{\rm dd})/(3\varepsilon_{\rm dd})$. Note that when using this definition, care should be taken for the special cases $\mathcal{Q}_5(0) = 1$ and $\mathcal{Q}_5(1) = 3\sqrt{3}/2$.

These integrals are evaluated upon substitution of the *Ansatz* $\Psi(\mathbf{x}) = \sqrt{\mathcal{N}}\phi(\rho)\psi(z)$ [43] [see main text, Eq. (4)], with $\mathcal{N}$ the number of particles in the droplet. The radial and axial functions, normalized to one, are assumed to be of the form

$$\begin{aligned} \phi(\rho) &= \sqrt{\frac{r_\rho}{2\pi\Gamma(2/r_\rho)\sigma_\rho^2}}e^{-\frac{1}{2}\left(\frac{\rho}{\sigma_\rho}\right)^{r_\rho}}, \\ \psi(z) &= \sqrt{\frac{r_z}{2\Gamma(1/r_z)\sigma_z}}e^{-\frac{1}{2}\left(\frac{|z|}{\sigma_z}\right)^{r_z}}, \end{aligned} \tag{A4}$$

with $\Gamma(x)$ the Gamma function. The widths $\sigma_{\rho,z}$ and the exponents $r_{\rho,z}$ are variational parameters. Substituting the *Ansätze*

given by Eqs. (A4) into the energy contributions given by Eqs. (A2) gives the following results. The kinetic energy of the droplet is of the form

$$\frac{E_{\rm kin}}{\mathcal{N}} = \frac{\hbar^2}{2m\sigma_\rho^2}\frac{r_\rho^2}{4\Gamma(2/r_\rho)} + \frac{\hbar^2}{2m\sigma_z^2}\frac{r_z f_K(r_z)}{2\Gamma(1/r_z)}, \tag{A5}$$

with $f_K(r_z) = (r_z-1)\Gamma(1-1/r_z) - \frac{r_z}{2}\Gamma(2-1/r_z)$. The trap energy is

$$\frac{E_{\rm trap}}{\mathcal{N}} = \frac{m}{2}(\omega_x^2+\omega_y^2)\left[\frac{\sigma_\rho^2\Gamma(4/r_\rho)}{2\Gamma(2/r_\rho)}\right] + \frac{m}{2}\omega_z^2\left[\frac{\sigma_z^2\Gamma(3/r_z)}{\Gamma(1/r_z)}\right]. \tag{A6}$$

Short-range interactions lead to an energy contribution,

$$\frac{E_{\rm sr}}{\mathcal{N}} = \frac{g\mathcal{N}}{8\pi\sigma_\rho^2\sigma_z}\frac{r_\rho r_z}{2^{2/r_\rho+1/r_z}\Gamma(2/r_\rho)\Gamma(1/r_z)}, \tag{A7}$$

whereas quantum fluctuations result in the Lee-Huang-Yang correction:

$$\frac{E_{\rm qf}}{\mathcal{N}} = \frac{64\mathcal{Q}_5(\varepsilon_{\rm dd})}{15\sqrt{\pi}}\left(\frac{2}{5}\right)^{\frac{2}{r_\rho}+\frac{1}{r_z}} g n_0\sqrt{n_0 a^3}, \tag{A8}$$

where $n_0 = \frac{\mathcal{N} r_\rho r_z}{4\pi\Gamma(2/r_\rho)\Gamma(1/r_z)\sigma_\rho^2\sigma_z}$ is the central density.

The dipolar energy is best evaluated in momentum space. The *Ansatz* density in Fourier space can be decomposed as $\tilde{n}(\mathbf{k}) = \tilde{n}_\rho(k_\rho)\tilde{n}_z(k_z)$, with

$$\begin{aligned}\tilde{n}_\rho(k_\rho) &= \frac{r_\rho}{\Gamma(2/r_\rho)}\int_0^\infty d\rho\, \rho e^{-\rho^{r_\rho}} J_0(k_\rho\sigma_\rho\rho),\\ \tilde{n}_z(k_z) &= \frac{r_z}{\Gamma(1/r_z)}\int_0^\infty dz\, e^{-z^{r_z}}\cos(k_z\sigma_z z),\end{aligned} \tag{A9}$$

where J_0 is the first Bessel function of the first kind.

Interestingly, these functions can be very closely approximated by Gaussians: $\tilde{n}_\rho(k_\rho) \simeq e^{-\alpha_\rho(r_\rho)(k_\rho\sigma_\rho)^2}$ and $\tilde{n}_z(k_z) \simeq e^{-\alpha_z(r_z)(k_z\sigma_z)^2}$, where $\alpha_\rho(\rho)$ and $\alpha_z(z)$ are functions found through numerical fitting to Eqs. (A9) prior to variational minimization. The dipole-dipole interaction can then be easily expressed as

$$\frac{E_{\rm dd}}{\mathcal{N}} = \frac{g\varepsilon_{\rm dd}\mathcal{N} f(\ell_\rho/\ell_z)}{2(2\pi)^{3/2}\ell_\rho^2\ell_z}, \tag{A10}$$

where $\ell_{\rho,z}^2 = 4\alpha_{\rho,z}(r_{\rho,z})\sigma_{\rho,z}^2$, and

$$f(\kappa) = \frac{1}{\kappa^2-1}\left[2\kappa^2+1-3\kappa^2\frac{\arctan(\sqrt{\kappa^2-1})}{\sqrt{\kappa^2-1}}\right]. \tag{A11}$$

Our approach is to first minimize the single-droplet energy (A1) for a suitable range of atom numbers. Thus, in preparation for solving the multidroplet problem, we generate interpolating functions $E_{\rm sd}(\mathcal{N})$, $\sigma_{\rho,z}(\mathcal{N})$, and $r_{\rho,z}(\mathcal{N})$, furnishing a library of single-droplet solutions for a given trap and interaction parameters.

Employing this two-step method reduces the number of variational parameters from seven per droplet to three ($\{\sigma_{\rho,z}^j,\ r_{\rho,z}^j, N_j, x_j, y_j\} \to \{N_j, x_j, y_j\}$). Note that the final populations of the droplets are constrained by the total atom number $N = \sum_j N_j$. The effect of interdroplet repulsion is not accounted for in calculating the shape of the droplets. We replace $f_{x,y} \to 110$ Hz to simulate the effect of interdroplet interactions on a given droplet's shape; then, to get the energy, we use the $f_{x,y}$ of the actual trap.

For all minimization procedures related to variational calculations, we use the sequential quadratic programming algorithm implemented in the MATLAB function *fmincon*.

APPENDIX B: INTERDROPLET INTERACTION ENERGY

Let us consider two droplets with N_1 and N_2 atoms, respectively, which are sufficiently separated, such that we can neglect any overlapping. The center of mass of the droplets is placed at $\mathbf{r}_{j=1,2} = (x_j, y_j, 0)$, i.e., we permit displacements on the xy plane, but assume that $z_j = 0$. As for the single-droplet dipolar energy, the interdroplet dipole-dipole interaction is best calculated in momentum space,

$$E_{12} = g\epsilon_{\rm dd}N_1N_2\int\frac{d^3\mathbf{k}}{(2\pi)^3}\left[3\frac{k_z^2}{k^2}-1\right]\tilde{n}_1^*(\mathbf{k})\tilde{n}_2(\mathbf{k}), \tag{B1}$$

where we can approximate the Fourier transform of the density profile of the droplets as

$$\tilde{n}_j(\mathbf{k}) \simeq e^{-k_\rho^2\ell_\rho(N_j)^2/4}e^{-k_z^2\ell_z(N_j)^2/4}e^{ik_\rho(x_j\cos\phi+y_j\sin\phi)}. \tag{B2}$$

The phase ϕ is accumulated due to the central position of the droplets being different from the origin and plays no role in the energy calculation. We can then evaluate the interaction energy E_{12} as a function of the distance $r_{12} = \sqrt{(x_1-x_2)^2+(y_1-y_2)^2}$ between the droplets:

$$E_{12}(r_{12}) = \frac{g\varepsilon_{\rm dd}N_1N_2}{\bar{\ell}_\rho^2\bar{\ell}_z}\frac{\sqrt{2}}{\pi^2} \times\int_0^1 du\,\frac{(\Lambda^2+2)u^2-\Lambda^2}{(1-\Lambda^2)u^2+\Lambda^2}G\left[\frac{2r_{12}^2(1-u^2)}{\bar{\ell}_\rho^2}\right], \tag{B3}$$

where $2\bar{\ell}_{\rho,z}^2 = \ell_{\rho,z}(N_1)^2 + \ell_{\rho,z}(N_2)^2$, $\Lambda = \bar{\ell}_z/\bar{\ell}_\rho$, and

$$G(x) = \frac{\sqrt{\pi}}{4}e^{-x/8}\left\{I_0\left(\frac{x}{8}\right)+\frac{x}{4}\left[I_1\left(\frac{x}{8}\right)-I_0\left(\frac{x}{8}\right)\right]\right\}, \tag{B4}$$

with $I_n(x)$ the modified Bessel function. The interaction energy (B3) is attractive at short distances, a spurious effect up to the radial size of a droplet. In order to prevent the droplets from "piling up"â in this inner region, we instead approximate the interdroplet potential as

$$E_{jj'}(r_{jj'}) \simeq \frac{V_0(N_j,N_{j'})N_jN_{j'}}{[r_{jj'}+r_0(N_j,N_{j'})]^3}, \tag{B5}$$

for any two droplets j and j', where V_0 and r_0 are determined by fitting to Eq. (B3). This term is the last contribution to Eq. (7) and is utilized in the phase diagram given in Fig. 2. By considering a range of particle number pairs between droplets, we determine the interpolating functions $V_0(\mathcal{N},\mathcal{N}')$ and $r_0(\mathcal{N},\mathcal{N}')$ prior to solving the full many-droplet problem. Note that the shift r_0, which results from the z extension of the droplet, is relevant because typical interdroplet distances are comparable to the z size of the droplets.

APPENDIX C: EXCITATIONS OF THE VARIATIONAL MODEL

Expanding around the equilibrium positions $\mathbf{R}_j = (x_j, y_j)$, $\mathbf{r}_j = \mathbf{R}_j + \boldsymbol{\epsilon}_j$, the energy of the array becomes, up to second order in the displacement $\boldsymbol{\epsilon}_j = (\epsilon_{x;j}, \epsilon_{y;j})$, of the form $E = E_0 + E^{(2)}$ (the first-order contribution cancels because we move from an energy minimum), with E_0 the ground-state energy, and

$$E^{(2)} = \sum_{j=1}^{N_D} \boldsymbol{\epsilon}_j^T \cdot \left[\hat{A}_j \cdot \boldsymbol{\epsilon}_j - \sum_{j' \neq j} \hat{B}_{jj'} \cdot \boldsymbol{\epsilon}_{j'} \right], \tag{C1}$$

where

$$\hat{B}_{jj'} = V_0(N_j, N_{j'}) \sqrt{N_j N_{j'}} \begin{pmatrix} \beta_{jj'} + \gamma_{jj'} X_{jj'}^2 & \gamma_{jj'} X_{jj'} Y_{jj'} \\ \gamma_{jj'} X_{jj'} Y_{jj'} & \beta_{jj'} + \gamma_{jj'} Y_{jj'}^2 \end{pmatrix}, \tag{C2}$$

$$\hat{A}_j = \frac{m N_j}{2} \begin{pmatrix} \omega_x^2 & 0 \\ 0 & \omega_y^2 \end{pmatrix} + \sum_{j' \neq j} \hat{B}_{jj'}, \tag{C3}$$

with

$$\beta_{jj'} = \frac{-3}{2R_{jj'}(R_{jj'} + r_{0,jj'})^4}, \tag{C4}$$

$$\gamma_{jj'} = \frac{3}{2R_{jj'}^3(R_{jj'} + r_{0,jj'})^4} + \frac{6}{R_{jj'}^2(R_{jj'} + r_{0,jj'})^5}, \tag{C5}$$

and the separation matrices $X_{jj'} = x_j - x_{j'}$, $Y_{jj'} = y_j - y_{j'}$, and $R_{jj'} = |\mathbf{r}_j - \mathbf{r}_{j'}|$.

We can write $E^{(2)} = \vec{\Phi}^T \cdot \hat{M} \cdot \vec{\Phi}$, with $\vec{\Phi} = (\epsilon_{x,1}, \epsilon_{y,1}, \ldots \epsilon_{x,N_D} \epsilon_{y,N_D})$. Now, we can diagonalize $\vec{M}$ to obtain the eigenvalues λ_ν, which provide the excitation frequencies of the droplet array, $\Omega_\nu = \sqrt{2\lambda_\nu}$. Note that this is an expansion around the equilibrium positions only, and not a perturbation of the individual droplet shape or atom number, so other shape excitations, such as droplet breathing modes, will not be captured by this method. Some example excitations are shown in Figs. 4(b2)–4(b5) and 4(c1)–4(c3), where the arrow indicates the vector between $\mathbf{R}_j$ and $\mathbf{r}_j$ for each droplet j.

[1] E. P. Gross, Unified theory of interacting bosons, Phys. Rev. **106**, 161 (1957).

[2] A. F. Andreev and I. M. Lifshitz, Quantum theory of defects in crystals, Zh. Eksp. Teor. Fiz. **56**, 2057 (1969) [Sov. Phys. JETP **29**, 1107 (1969)].

[3] D. Thouless, The flow of a dense superfluid, Ann. Phys. **52**, 403 (1969).

[4] G. Chester, Speculations on Bose-Einstein condensation and quantum crystals, Phys. Rev. A **2**, 256 (1970).

[5] A. J. Leggett, Can a Solid Be" Superfluid"?, Phys. Rev. Lett. **25**, 1543 (1970).

[6] M. Boninsegni and N. V. Prokofâev, Colloquium: Supersolids: What and where are they?, Rev. Mod. Phys. **84**, 759 (2012).

[7] J. Léonard, A. Morales, P. Zupancic, T. Esslinger, and T. Donner, Supersolid formation in a quantum gas breaking a continuous translational symmetry, Nature (London) **543**, 87 (2017).

[8] J.-R. Li, J. Lee, W. Huang, S. Burchesky, B. Shteynas, F. Ç. Top, A. O. Jamison, and W. Ketterle, A stripe phase with supersolid properties in spin–orbit-coupled Bose-Einstein condensates, Nature (London) **543**, 91 (2017).

[9] T. M. Bersano, J. Hou, S. Mossman, V. Gokhroo, X.-W. Luo, K. Sun, C. Zhang, and P. Engels, Experimental realization of a long-lived striped Bose-Einstein condensate induced by momentum-space hopping, Phys. Rev. A **99**, 051602(R) (2019).

[10] L. Tanzi, E. Lucioni, F. Famà, J. Catani, A. Fioretti, C. Gabbanini, R. N. Bisset, L. Santos, and G. Modugno, Observation of a Dipolar Quantum Gas with Metastable Supersolid Properties, Phys. Rev. Lett. **122**, 130405 (2019).

[11] F. Böttcher, J.-N. Schmidt, M. Wenzel, J. Hertkorn, M. Guo, T. Langen, and T. Pfau, Transient Supersolid Properties in an Array of Dipolar Quantum Droplets, Phys. Rev. X **9**, 011051 (2019).

[12] L. Chomaz, D. Petter, P. Ilzhöfer, G. Natale, A. Trautmann, C. Politi, G. Durastante, R. M. W. van Bijnen, A. Patscheider, M. Sohmen, M. J. Mark, and F. Ferlaino, Long-Lived And Transient Supersolid Behaviors in Dipolar Quantum Gases, Phys. Rev. X **9**, 021012 (2019).

[13] G. Natale, R. M. W. van Bijnen, A. Patscheider, D. Petter, M. J. Mark, L. Chomaz, and F. Ferlaino, Excitation Spectrum of a Trapped Dipolar Supersolid and Its Experimental Evidence, Phys. Rev. Lett. **123**, 050402 (2019).

[14] L. Tanzi, S. Roccuzzo, E. Lucioni, F. Famà, A. Fioretti, C. Gabbanini, G. Modugno, A. Recati, and S. Stringari, Supersolid symmetry breaking from compressional oscillations in a dipolar quantum gas, Nature (London) **574**, 382 (2019).

[15] M. Guo, F. Böttcher, J. Hertkorn, J.-N. Schmidt, M. Wenzel, H. P. Büchler, T. Langen, and T. Pfau, The low-energy goldstone mode in a trapped dipolar supersolid, Nature (London) **574**, 386 (2019).

[16] A. Griesmaier, J. Werner, S. Hensler, J. Stuhler, and T. Pfau, Bose-Einstein Condensation of Chromium, Phys. Rev. Lett. **94**, 160401 (2005).

[17] M. Lu, N. Q. Burdick, S. H. Youn, and B. L. Lev, Strongly Dipolar Bose-Einstein Condensate of Dysprosium, Phys. Rev. Lett. **107**, 190401 (2011).

[18] K. Aikawa, A. Frisch, M. Mark, S. Baier, A. Rietzler, R. Grimm, and F. Ferlaino, Bose-Einstein Condensation of Erbium, Phys. Rev. Lett. **108**, 210401 (2012).

[19] L. Santos, G. V. Shlyapnikov, and M. Lewenstein, Roton-Maxon Spectrum and Stability of Trapped Dipolar Bose-Einstein Condensates, Phys. Rev. Lett. **90**, 250403 (2003).

[20] L. Chomaz, R. M. W. van Bijnen, D. Petter, G. Faraoni, S. Baier, J. H. Becher, M. J. Mark, F. Wächtler, L. Santos, and F. Ferlaino, Observation of roton mode population in a dipolar quantum gas, Nat. Phys. **14**, 442 (2018).

[21] J.-N. Schmidt, J. Hertkorn, M. Guo, F. Böttcher, M. Schmidt, K. S. H. Ng, S. D. Graham, T. Langen, M. Zwierlein, and T. Pfau, Roton Excitations in an Oblate Dipolar Quantum Gas, Phys. Rev. Lett. **126**, 193002 (2021).

[22] T. Lahaye, J. Metz, B. Fröhlich, T. Koch, M. Meister, A. Griesmaier, T. Pfau, H. Saito, Y. Kawaguchi, and M. Ueda, d-Wave Collapse and Explosion of a Dipolar Bose-Einstein Condensate, Phys. Rev. Lett. **101**, 080401 (2008).

[23] H. Kadau, M. Schmitt, M. Wenzel, C. Wink, T. Maier, I. Ferrier-Barbut, and T. Pfau, Observing the Rosensweig instability of a quantum ferrofluid, Nature (London) **530**, 194 (2016).

[24] M. Schmitt, M. Wenzel, F. Böttcher, I. Ferrier-Barbut, and T. Pfau, Self-bound droplets of a dilute magnetic quantum liquid, Nature (London) **539**, 259 (2016).

[25] L. Chomaz, S. Baier, D. Petter, M. J. Mark, F. Wächtler, L. Santos, and F. Ferlaino, Quantum-Fluctuation-Driven Crossover from a Dilute Bose-Einstein Condensate to a Macrodroplet in a Dipolar Quantum Fluid, Phys. Rev. X **6**, 041039 (2016).

[26] I. Ferrier-Barbut, H. Kadau, M. Schmitt, M. Wenzel, and T. Pfau, Observation of Quantum Droplets in a Strongly Dipolar Bose Gas, Phys. Rev. Lett. **116**, 215301 (2016).

[27] F. Wächtler and L. Santos, Quantum filaments in dipolar Bose-Einstein condensates, Phys. Rev. A **93**, 061603(R) (2016).

[28] R. N. Bisset, R. M. Wilson, D. Baillie, and P. B. Blakie, Ground-state phase diagram of a dipolar condensate with quantum fluctuations, Phys. Rev. A **94**, 033619 (2016).

[29] M. A. Norcia, C. Politi, L. Klaus, E. Poli, M. Sohmen, M. J. Mark, R. N. Bisset, L. Santos, and F. Ferlaino, Two-dimensional supersolidity in a dipolar quantum gas, Nature (London) **596**, 357 (2021).

[30] T. Bland, E. Poli, C. Politi, L. Klaus, M. Norcia, F. Ferlaino, L. Santos, and R. Bisset, Two-dimensional supersolidity in a circular trap, arXiv:2107.06680.

[31] D. Baillie and P. B. Blakie, Droplet Crystal Ground States of a Dipolar Bose Gas, Phys. Rev. Lett. **121**, 195301 (2018).

[32] S. Roccuzzo, S. Stringari, and A. Recati, Supersolid edge and bulk phases of a dipolar quantum gas in a box, arXiv:2104.01068.

[33] A. Gallemí, S. M. Roccuzzo, S. Stringari, and A. Recati, Quantized vortices in dipolar supersolid Bose-Einstein-condensed gases, Phys. Rev. A **102**, 023322 (2020).

[34] S. M. Roccuzzo, A. Gallemí, A. Recati, and S. Stringari, Rotating a Supersolid Dipolar Gas, Phys. Rev. Lett. **124**, 045702 (2020).

[35] M. N. Tengstrand, D. Boholm, R. Sachdeva, J. Bengtsson, and S. M. Reimann, Persistent currents in toroidal dipolar supersolids, Phys. Rev. A **103**, 013313 (2021).

[36] F. Ancilotto, M. Barranco, M. Pi, and L. Reatto, Vortex properties in the extended supersolid phase of dipolar Bose-Einstein condensates, Phys. Rev. A **103**, 033314 (2021).

[37] Y.-C. Zhang, F. Maucher, and T. Pohl, Supersolidity Around a Critical Point in Dipolar Bose-Einstein Condensates, Phys. Rev. Lett. **123**, 015301 (2019).

[38] Y.-C. Zhang, T. Pohl, and F. Maucher, Phases of supersolids in confined dipolar Bose-Einstein condensates, Phys. Rev. A **104**, 013310 (2021).

[39] J. Hertkorn, J.-N. Schmidt, M. Guo, F. Böttcher, K. S. H. Ng, S. D. Graham, P. Uerlings, T. Langen, M. Zwierlein, and T. Pfau, Pattern formation in quantum ferrofluids: From supersolids to superglasses, Phys. Rev. Research **3**, 033125 (2021).

[40] A. R. P. Lima and A. Pelster, Quantum fluctuations in dipolar Bose gases, Phys. Rev. A **84**, 041604(R) (2011).

[41] S. Ronen, D. C. E. Bortolotti, and J. L. Bohn, Bogoliubov modes of a dipolar condensate in a cylindrical trap, Phys. Rev. A **74**, 013623 (2006).

[42] S. M. Roccuzzo and F. Ancilotto, Supersolid behavior of a dipolar Bose-Einstein condensate confined in a tube, Phys. Rev. A **99**, 041601(R) (2019).

[43] L. Lavoine and T. Bourdel, Beyond-mean-field crossover from one dimension to three dimensions in quantum droplets of binary mixtures, Phys. Rev. A **103**, 033312 (2021).

[44] A. J. Dickstein, S. Erramilli, R. E. Goldstein, D. P. Jackson, and S. A. Langer, Labyrinthine pattern formation in magnetic fluids, Science **261**, 1012 (1993).

[45] L. Pitaevskii and S. Stringari, *Bose-Einstein Condensation and Superfluidity* (Oxford University Press, Oxford, 2016).

4.7 Publication V:

Two-dimensional supersolid formation in dipolar condensates

The following publication has appeared in

Physical Review Letters **128**, 195302 (2022)[¶]
submitted 14 Jul 2021; published 13 May 2022
DOI: https://doi.org/10.1103/PhysRevLett.128.195302
T. Bland,[1] E. Poli,[2] C. Politi,[1,2] L. Klaus,[1] M. A. Norcia,[1] F. Ferlaino,[1,2] L. Santos,[3] and R. N. Bisset[2]

[1] *Institut für Quantenoptik und Quanteninformation, Österreichische Akademie der Wissenschaften, 6020 Innsbruck, Austria*

[2] *Institut für Experimentalphysik, Universität Innsbruck, 6020 Innsbruck, Austria*

[3] *Institut für Theoretische Physik, Universität Hannover, Hannover, Germany*

[¶]The author of the present thesis performed the measurements together with M. A. N., and L. K., analysed the experimental data with M. A. N., and contributed in writing the manuscript and interpreting the results together with all the authors.

Featured in Physics

Two-Dimensional Supersolid Formation in Dipolar Condensates

T. Bland,[1] E. Poli,[2] C. Politi,[1,2] L. Klaus,[1,2] M. A. Norcia,[1] F. Ferlaino,[1,2] L. Santos,[3] and R. N. Bisset[2,*]
[1]*Institut für Quantenoptik und Quanteninformation, Österreichische Akademie der Wissenschaften, Innsbruck 6020, Austria*
[2]*Institut für Experimentalphysik, Universität Innsbruck, Innsbruck 6020, Austria*
[3]*Institut für Theoretische Physik, Leibniz Universität Hannover, Hannover 30167, Germany*

(Received 14 July 2021; revised 19 January 2022; accepted 11 April 2022; published 13 May 2022)

Dipolar condensates have recently been coaxed to form the long-sought supersolid phase. While one-dimensional supersolids may be prepared by triggering a roton instability, we find that such a procedure in two dimensions (2D) leads to a loss of both global phase coherence and crystalline order. Unlike in 1D, the 2D roton modes have little in common with the supersolid configuration. We develop a finite-temperature stochastic Gross-Pitaevskii theory that includes beyond-mean-field effects to explore the formation process in 2D and find that evaporative cooling directly into the supersolid phase—hence bypassing the first-order roton instability—can produce a robust supersolid in a circular trap. Importantly, the resulting supersolid is stable at the final nonzero temperature. We then experimentally produce a 2D supersolid in a near-circular trap through such an evaporative procedure. Our work provides insight into the process of supersolid formation in 2D and defines a realistic path to the formation of large two-dimensional supersolid arrays.

DOI: 10.1103/PhysRevLett.128.195302

The supersolid phase was predicted to simultaneously exhibit crystalline order and superfluidity [1–6]. While it remains elusive in helium, recent developments in ultracold quantum gases have finally made supersolidity a reality, providing an excellent platform for the control and observation of these states. Important early advances were made in systems with spin-orbit coupling [7,8] and cavity-mediated interactions [9], where supersolid properties were observed in rigid crystal configurations. Bose-Einstein condensates (BECs) with dipole-dipole interactions have now been observed in a supersolid state with deformable crystals [10–13], with their lattices genuinely arising from the atom-atom interactions [14–16].

In the first dipolar supersolid experiments, translational symmetry was broken only along one axis, giving rise to a one-dimensional (1D) density wave, commonly referred to as a 1D droplet array [10–12]. A more recent experiment has created the first states with two-dimensional (2D) supersolidity in elongated traps of variable aspect ratio [13]. This opens the door to study vortices and persistent currents [17–20], as well as exotic ground state phases predicted for large atom numbers [21–24].

It is still an open question whether 2D arrays provide as favorable conditions for supersolidity as 1D arrays do. In 1D, following an interaction quench from an unmodulated to modulated BEC, the density pattern induced by a roton instability [14,25–28] can smoothly connect with the final supersolid array [10–12]. This transition, hence, has a weakly first-order character or is even continuous [29,30], and such quenches through the transition cause only small excitations of the resulting supersolid [10–12]. While it has been predicted that a similar procedure may lead to coherence between three droplets in a triangular configuration [31], earlier work with nondipolar superfluids suggests that such symmetry-breaking quenches may be unfavorable for supersolid formation in 2D and 3D [32,33].

An alternative method exists to experimentally produce dipolar supersolids. Instead of quenching the interactions to trigger a roton instability, it is possible to cool a thermal sample directly into the supersolid state using evaporative cooling techniques [12,34]. Crucially, this is the only known method for producing 2D supersolids to date [13]. While a dynamic interaction quench may be described by the extended Gross-Pitaevskii equation (eGPE) [35–38], we are not aware of any available theory to model the required evaporation process. From a theoretical perspective, much remains unknown about evaporative supersolid formation. Is it a general feature that the droplets form before global phase coherence develops, as reported in Ref. [34]? Under what conditions do defects persist? Such answers will be paramount in the quest for ever-larger 2D supersolids, as well as for the observation of vortices embedded within them.

In this Letter, we explore the formation of large 2D supersolids in circular-shaped traps. We develop a finite-temperature Stochastic eGPE (SeGPE) theory to model the entire evaporative cooling process. Importantly, our theory includes the beyond-mean-field quantum fluctuations responsible for stabilizing the individual droplets.

We compare the evaporative cooling formation dynamics with those resulting from an interaction quench, finding striking differences between the two protocols. Following

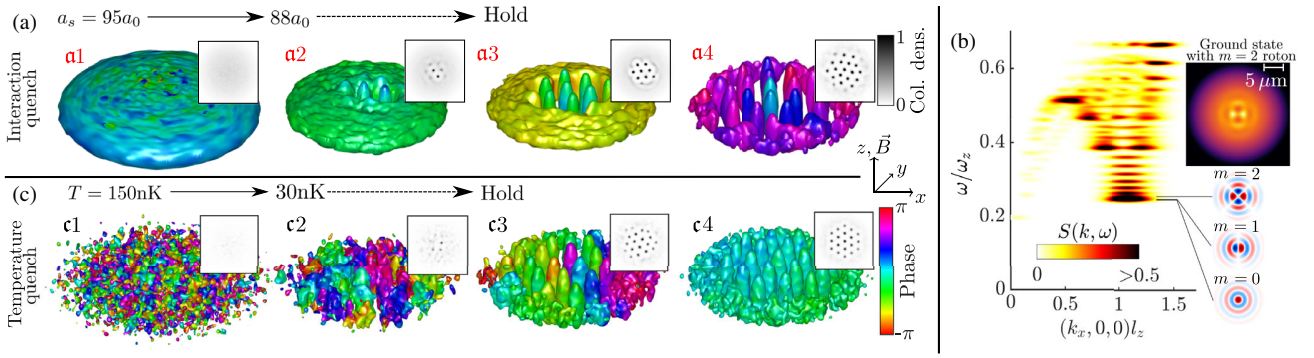

FIG. 1. (a) Crystal preparation from interaction quench, evolved with the eGPE, for $N \approx 2.1 \times 10^5$ Dy atoms [quench (i)]. Isosurfaces are at 5% max density, with color indicating phase. Insets: z column densities normalized to max value from the entire simulation. (b) Dynamic structure factor for an unmodulated BEC ($a_s = 92a_0$) in energy-momentum space, normalized to peak value. The lowest-energy roton modes are indicated, and the ground state with an $m = 2$ roton mode added is shown, revealing the localized nature of the rotons. Parameters are otherwise the same as in (a). (c) Crystal preparation from temperature quench (evaporative cooling) evolved with the SeGPE [quench (ii)]. The temperature decreases as the chemical potential and condensate number rise, with scattering length fixed at $a_s = 88a_0$. For all subplots $f_{x,y,z} = (33, 33, 167)$ Hz, and $l_z = \sqrt{\hbar/m\omega_z}$.

an interaction quench, the 2D crystal grows nonlinearly with the droplets developing sequentially, producing configurations that are unrelated to any roton mode combination of the original unmodulated BEC. The resulting crystal is substantially excited and lacks global phase coherence. Alternatively, by directly cooling into the supersolid regime, our SeGPE theory predicts the formation of large 2D supersolids in circular traps, with global phase coherence that remains robust at finite temperature. To benchmark our theory—as well as to test the direct cooling protocol for pancake-shaped trapping geometries—we perform experiments and observe a 7-droplet hexagonal supersolid in a near-circular trap.

Formalism.—We are interested in ultracold, dipolar Bose gases harmonically confined in 3D with trapping frequencies $\omega_{x,y,z} = 2\pi f_{x,y,z}$. Two-body contact interactions and the long-ranged, anisotropic dipole-dipole interactions are well described by a pseudopotential, $U(\mathbf{r}) = (4\pi\hbar^2 a_s/m)\delta(\mathbf{r}) + (3\hbar^2 a_{\rm dd}/m)[(1 - 3\cos^2\theta)/r^3]$, with a_s being the s-wave scattering length and $a_{\rm dd} = \mu_0\mu_m^2 m/12\pi\hbar^2$ the dipole length, with magnetic moment μ_m, and θ is the angle between the polarization axis (z axis) and the vector joining two particles. The ratio $\epsilon_{\rm dd} = a_{\rm dd}/a_s$ (for $a_s > 0$) is convenient to keep in mind, since for $\epsilon_{\rm dd} \leq 1$ the ground state will be an unmodulated BEC, whereas for the dipole-dominated regime $\epsilon_{\rm dd} > 1$ the unmodulated BEC may become unstable [39]. Here, we always consider ^{164}Dy, with $a_{\rm dd} = 131a_0$. The eGPE has been described elsewhere [35–38], and its details have been deferred to Supplemental Material [40].

We phenomenologically introduce a finite-temperature simple growth SeGPE theory [55]. This describes the "classical" field, $\Psi(\mathbf{r}, t)$, of all highly populated modes up to an energy cutoff. The dynamics are governed by [56]

$$i\hbar\frac{\partial\Psi}{\partial t} = \hat{\mathcal{P}}\{(1 - i\gamma)(\mathcal{L}[\Psi] - \mu)\Psi + \eta\}. \quad (1)$$

Here, $\mathcal{L}$ is the eGPE operator defined in Ref. [40], and γ describes the coupling of the classical field modes to the high-lying modes. We find that $\gamma = 7.5 \times 10^{-3}$ gives good agreement to the condensate number growth rate of a recent experiment under comparable conditions [34] (see also Ref. [40]). The dynamical noise term η, subject to noise correlations given by $\langle\eta^*(\mathbf{r}, t)\eta(\mathbf{r}', t')\rangle = 2\hbar\gamma k_B T\delta(t - t')\delta(\mathbf{r} - \mathbf{r}')$, means that each simulation run is unique. Finally, $\hat{\mathcal{P}}$ is a projector which constrains the dynamics of the system up to energy cutoff $\epsilon_{\rm cut}(\mu) = 2\mu$—consistent with previous treatments [57,58]—where we use the final μ after evaporative cooling.

Supersolid formation simulations.—With these two theories in hand, we perform two kinds of dynamic quench simulations in a pancake-shaped trap, where in both cases the ground state for the final parameters would be a 19-droplet supersolid:

(i) An interaction quench from an unmodulated BEC to the supersolid regime using the eGPE [Fig. 1(a)]. Noise is first added to the BEC ground state [59], and this is evolved for a 20 ms equilibration time before the interaction strength is linearly ramped over the next 30 ms from $a_s = 95a_0$ to $a_s = 88a_0$—crossing the roton phase transition to the supersolid regime—and then held constant again for the remainder of the simulation.

(ii) A temperature quench from a thermal cloud to the supersolid phase using the SeGPE [Fig. 1(c)]. Each simulation begins with a 200 ms equilibration time at fixed high temperature $T = 150$ nK to generate a thermal cloud. To simulate the evaporative cooling process, the chemical potential and temperature are then linearly ramped over 100 ms, from $(\mu, T) = (-12.64\hbar\omega_z, 150\ \text{nK})$ to

$(12.64\hbar\omega_z, 30\ \mathrm{nK})$, mimicking the growing condensate number observed in experiments [60,61], while the scattering length is always held fixed at $a_s = 88a_0$.

Focusing first on the interaction quench, the density isosurfaces in Fig. 1(a) represent snapshots at various times for a single simulation run, revealing intriguing formation dynamics. Initial droplets are seeded through unstable roton modes, but staggered droplet formation reveals a process of *nonlinear crystal growth*, as highlighted by the column densities shown as insets in Fig. 1(a). In Fig. 1(a2), two central droplets have already attained their final peak density, while a secondary ring of droplets is only just beginning to form. Then, in Fig. 1(a3), eight droplets have fully matured, and the process continues radially outward until a 19-droplet crystal is approximately attained. Similar droplet formation dynamics have been predicted in optical media [62].

The colors on the density isosurfaces in Fig. 1(a) represent the wave function phase. The color scale is recentered in each subplot, and an ideal phase coherent solution would have a uniform color everywhere. Importantly, the crystal growth process disrupts the global phase coherence, as evidenced by the various colors in Fig. 1(a4), leaving an excited crystal in which some outer droplets dissolve and reemerge from the halo. Note that the situation does not qualitatively change for reduced initial noise or gentler interaction ramps, suggesting that the strong excitations result from a first-order character of the roton instability in 2D.

We explain the interaction quench dynamics by calculating the elementary excitations of the unmodulated BEC close to the roton instability, i.e., for $a_s = 92a_0$. These results are displayed in Fig. 1(b) as the dynamic structure factor $S(\mathbf{k}, \omega)$, which predicts the system response to perturbations of momentum $\hbar\mathbf{k}$ and energy $\hbar\omega$ [28,63–65] (also see Ref. [40]). A roton minimum can be seen at $k_x l_z \approx 1.1$, and we plot the lowest roton modes corresponding to $m = 0$, 1, 2, with m being the angular quantum number in the z direction [66]. On the top right is the density obtained by adding an $m = 2$ roton mode to the BEC wave function, revealing how rotons are confined to high-density regions [67,68]. This reveals a qualitative difference between the 1D and 2D situations, since, from a simple geometric standpoint, in 2D the high-density region inherently encompasses a smaller proportion of the total atom number. Thus, the roton-induced droplet number is only a small fraction of the final droplet number, meaning the droplets appear sequentially for 2D.

Another qualitative difference between 1D and 2D is a kind of frustration. First, note that our target supersolid ground state for the final quench parameters is a 19-droplet crystal, with a central droplet [see the inset of Fig. 2(b)]. Only an $m = 0$ roton mode [see Fig. 1(b)] could directly trigger the formation of a central droplet, but then only concentric rings could form further out. Thus, unlike for 1D, no single roton mode can smoothly connect the unmodulated BEC to the 2D supersolid ground state.

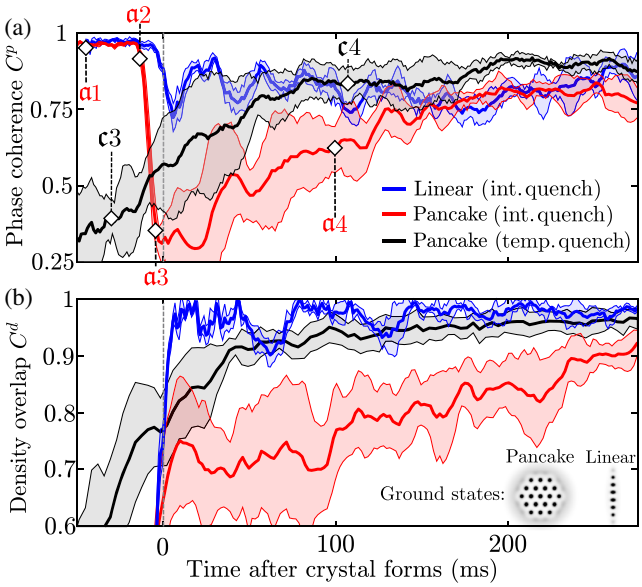

FIG. 2. Supersolid quality. (a) Global phase coherence C^p over time for interaction quenches [quench (i)] into linear chain (blue) and pancake crystal (red) and temperature quenches [quench (ii)] into the pancake crystal (black). Diamonds link to example frames in Figs. 1(a) and 1(c). Each curve is averaged over 3–5 runs with an error band marking one standard deviation. Time $t = 0$ corresponds to when the crystals first fully mature. (b) Density overlap C^d between the time-dependent and ground state densities. Parameters are the same as Fig. 1, but for linear chain $f_{x,y,z} = (33, 110, 167)$ Hz and $N = 82 \times 10^3$.

Next, we analyze the finite-temperature quench results. Figure 1(c) shows snapshots of the condensate growth, demonstrating that both the crystal structure and the global phase coherence—evidenced by the uniform color in Fig. 1(c4)—develop soon after the quench. Note that timescales will be quantified shortly. It is also an important result in itself that we predict such a large 2D supersolid to be stable against thermal fluctuations (recall that $T_{\mathrm{final}} = 30$ nK). As they form, each droplet individually has a uniform phase that may be different from that of its neighbors, sometimes creating vortex pairs between droplets of different phase. In this scenario, the droplets do not form as a result of a roton instability, and the partial phase coherence continues to improve after the crystal has formed, consistent with earlier observations [34]. Occasionally, long-lived isolated vortices remain near the center of the supersolid. Simulation videos are provided in Supplemental Material [40].

Supersolid quality.—We seek to quantify the resulting supersolid quality for both quench protocols. We start by analyzing the phase excitations, taking the phase coherence C^p with a similar measure presented in Ref. [10]. A value of $C^p = 1(0)$ implies global phase

coherence (incoherence) [69]. In Fig. 2(a), we plot this quantity for interaction quenches into the pancake supersolid regime (red) and linear supersolid regime (blue) and temperature quenches into the pancake supersolid (black). The time $t = 0$ indicates when the droplet number has approximately stabilized and the crystal has first matured [70]. For the linear chain, the system remains coherent (high $C^p \approx 0.8$), indicating a stable supersolid. However, quenching into the pancake geometry is qualitatively different, with strong incoherence ($C^p \approx 0.3$) soon after crystal formation, recovering a high value at around 150 ms after the crystal forms. During evaporative cooling, the global phase coherence is predicted by the high value of $C^p \approx 0.8$ around 50 ms after the crystal forms, with qualitatively similar values to the interaction quench simulations for the linear supersolid case.

We quantify the quality of the supersolid crystal by measuring the density overlap C^d between the ground state target solution and the time-dependent wave function [71]. We find the maximal value of C^d after applying translations and rotations to the state, noting that perfect overlap would give $C^d = 1$. In Fig. 2(b), this quantity is presented for the two geometries, with the ground state solutions shown as insets. For the linear chain, once the droplets have formed, the density overlap rapidly attains $C^d > 0.9$ and remains there, consistent with the interaction quenched state being close to the ground state supersolid. However, the pancake case shows weak overlap after the droplets are formed, which only recovers slowly—after around 300 ms—to values comparable with the linear chain. Primarily, this is due to the sensitivity of droplet positions of C^d and indicates that there are many excited supersolid modes present after the droplets form [40]. Direct evaporative cooling for the pancake case, however, shows that after the droplets have formed they rapidly settle into the expected crystal pattern ($C^d \approx 0.95$).

Finally, it is important to note that for the pancake interaction quench, while the phase coherence is restored by around $t = 150$ ms after the droplets are formed, the crystal remains highly excited until around 300 ms. On these timescales, three-body losses become significant, and it is unlikely that a large supersolid would be observed. In contrast, direct evaporative cooling may lead to a robust supersolid within around 50 ms of the crystal first appearing, a timescale that we find to be weakly dependent on the value of γ [40].

Experimental observation.—While experiments have evaporatively cooled directly into the supersolid phase for linear and elongated 2D configurations [12,13,34], this could prove an optimal method in circular traps for avoiding the excitations associated with crossing the roton instability. We confirm this by producing a 7-droplet hexagon supersolid in a near-circular trap, as shown in Fig. 3. The experimental apparatus and procedure is similar to that described previously [13], but new modifications in the optical dipole trap setup have enabled us to tune between anisotropic and round traps. The current optical trap consists of three 1064 nm wavelength trapping beams, each propagating in the plane perpendicular to gravity. Two of the beams, which cross perpendicularly, have approximately 60 μm waists and define the horizontal trapping frequencies. The third, crossing at a roughly 45° angle from the others, has a waist of approximately 18 μm and is rapidly scanned to create a time-averaged light sheet that defines the vertical confinement.

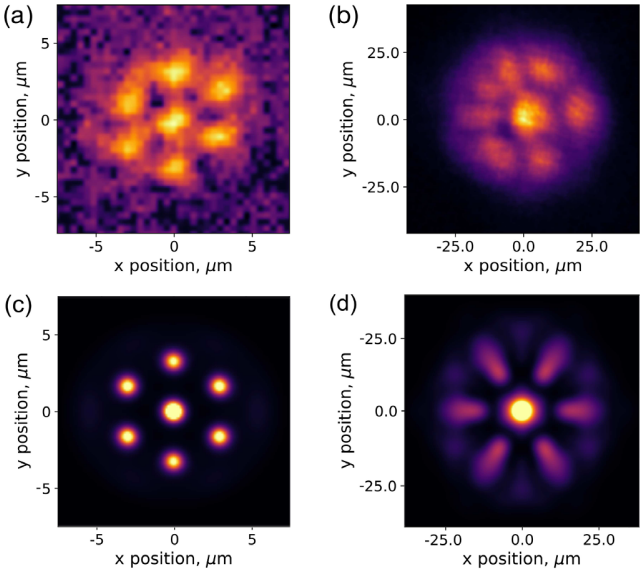

FIG. 3. Experimental realization of a 7-droplet hexagon state. (a) Exemplary *in situ* image of the density profile. (b) Image after 36 ms time-of-flight (TOF) expansion, averaged over 68 trials of the experiment. Hexagonal modulation structure is clearly present in the averaged image. Note the rotation of the hexagon between *in situ* and TOF images. (c),(d) Corresponding simulations for the same trap, and with $a_s = 90a_0$ and $\approx 4.4 \times 10^4$ atoms within the droplets.

In a harmonic trap with frequencies $f_{x,y,z} = [47(1), 43(1), 133(5)]$ Hz, we observe in trap a 7-droplet state consisting of a hexagon with a central droplet, with a condensate atom number of $N \sim 4 \times 10^4$ [Fig. 3(a)]. To confirm that this state is phase coherent, we release the atoms from the trap and image the interference pattern after 36 ms time of flight [Fig. 3(b)]. The presence of clear modulation in the interference pattern averaged over 68 runs of the experiment indicates a well-defined and reproducible relative phase between the droplets and is consistent with our expectations for a phase-coherent state undergoing expansion [Fig. 3(d)], obtained through 3D dynamic simulations starting from the eGPE ground state [Fig. 3(c)]. Even rounder traps are possible, but the slight anisotropy orients the state, helping to observe the reproducible interference pattern.

Summary.—We have theoretically explored the formation of large 2D supersolids using both an interaction

quench from an unmodulated BEC and a temperature quench from a thermal cloud. For the latter, we developed a finite-temperature stochastic Gross-Pitaevskii theory that can simulate evaporative cooling directly into the supersolid regime. Our simulations predict that a temperature quench provides a robust path for creating 2D supersolids in circular traps, and we confirm this experimentally by using this method to create a reproducible hexagonal 7-droplet supersolid.

In contrast, the interaction quench results in highly excited crystals that lack global phase coherence in the period following their formation. Interestingly, droplets appear sequentially rather than simultaneously, with the final crystal structure being unrelated to the roton modes that seeded the instability. This is in contrast to the situation for 1D arrays, where an interaction quench through a roton instability can smoothly connect an unmodulated BEC to the supersolid ground state.

Our finite-temperature theory is broadly applicable for future studies on topics such as formation dynamics, supersolid vortices, improved quench protocols to produce large 2D supersolids, and thermal resilience, as well as dipolar droplets in general.

We thank Manfred Mark and the Innsbruck Erbium team for valuable discussions and thank Péter Juhász for carefully reading the manuscript. We acknowledge R. M. W. van Bijnen for developing the code for our eGPE and BdG simulations. Part of the computational results presented have been achieved using the HPC infrastructure LEO of the University of Innsbruck. The experimental team is financially supported through an ERC Consolidator Grant (RARE, No. 681432), an NFRI grant (MIRARE, No. OAW0600) of the Austrian Academy of Science, and the QuantERA grant MAQS by the Austrian Science Fund FWF No. I4391-N. L. S. and F. F. acknowledge the DFG/FWF (Grant No. FOR 2247/I4317-N36) and a joint-project grant from the FWF (Grant No. I4426, RSF/Russland 2019). L. S. thanks the funding by the Deutsche Forschungsgemeinschaft (DFG, German Research Foundation) under Germany's Excellence Strategy—EXC-2123 QuantumFrontiers—390837967. M. A. N. has received funding as an ESQ postdoctoral fellow from the European Unions Horizon 2020 research and innovation program under the Marie Sklodowska-Curie Grant Agreement No. 801110 and the Austrian Federal Ministry of Education, Science and Research (BMBWF). We also acknowledge the Innsbruck Laser Core Facility, financed by the Austrian Federal Ministry of Science, Research and Economy.

*Corresponding author.
russell.bisset@uibk.ac.at

[1] E. P. Gross, Unified theory of interacting bosons, Phys. Rev. **106**, 161 (1957).
[2] A. Andreev and I. Lifshitz, Quantum theory of defects in crystals, Zh. Eksp. Teor. Fiz. **56**, 2057 (1969) [JETP **29**, 1107 (1969)].
[3] D. Thouless, The flow of a dense superfluid, Ann. Phys. (N.Y.) **52**, 403 (1969).
[4] G. Chester, Speculations on Bose-Einstein condensation and quantum crystals, Phys. Rev. A **2**, 256 (1970).
[5] A. J. Leggett, Can a Solid Be "Superfluid"?, Phys. Rev. Lett. **25**, 1543 (1970).
[6] M. Boninsegni and N. V. Prokof'ev, Colloquium: Supersolids: What and where are they?, Rev. Mod. Phys. **84**, 759 (2012).
[7] J.-R. Li, J. Lee, W. Huang, S. Burchesky, B. Shteynas, F. Ç. Top, A. O. Jamison, and W. Ketterle, A stripe phase with supersolid properties in spin–orbit-coupled Bose–Einstein condensates, Nature (London) **543**, 91 (2017).
[8] T. M. Bersano, J. Hou, S. Mossman, V. Gokhroo, X.-W. Luo, K. Sun, C. Zhang, and P. Engels, Experimental realization of a long-lived striped Bose-Einstein condensate induced by momentum-space hopping, Phys. Rev. A **99**, 051602(R) (2019).
[9] J. Léonard, A. Morales, P. Zupancic, T. Esslinger, and T. Donner, Supersolid formation in a quantum gas breaking a continuous translational symmetry, Nature (London) **543**, 87 (2017).
[10] L. Tanzi, E. Lucioni, F. Famà, J. Catani, A. Fioretti, C. Gabbanini, R. N. Bisset, L. Santos, and G. Modugno, Observation of a Dipolar Quantum Gas with Metastable Supersolid Properties, Phys. Rev. Lett. **122**, 130405 (2019).
[11] F. Böttcher, J.-N. Schmidt, M. Wenzel, J. Hertkorn, M. Guo, T. Langen, and T. Pfau, Transient Supersolid Properties in an Array of Dipolar Quantum Droplets, Phys. Rev. X **9**, 011051 (2019).
[12] L. Chomaz, D. Petter, P. Ilzhöfer, G. Natale, A. Trautmann, C. Politi, G. Durastante, R. M. W. van Bijnen, A. Patscheider, M. Sohmen, M. J. Mark, and F. Ferlaino, Long-Lived and Transient Supersolid Behaviors in Dipolar Quantum Gases, Phys. Rev. X **9**, 021012 (2019).
[13] M. A. Norcia, C. Politi, L. Klaus, E. Poli, M. Sohmen, M. J. Mark, R. N. Bisset, L. Santos, and F. Ferlaino, Two-dimensional supersolidity in a dipolar quantum gas, Nature (London) **596**, 357 (2021).
[14] G. Natale, R. M. W. van Bijnen, A. Patscheider, D. Petter, M. J. Mark, L. Chomaz, and F. Ferlaino, Excitation Spectrum of a Trapped Dipolar Supersolid and Its Experimental Evidence, Phys. Rev. Lett. **123**, 050402 (2019).
[15] L. Tanzi, S. Roccuzzo, E. Lucioni, F. Famà, A. Fioretti, C. Gabbanini, G. Modugno, A. Recati, and S. Stringari, Supersolid symmetry breaking from compressional oscillations in a dipolar quantum gas, Nature (London) **574**, 382 (2019).
[16] M. Guo, F. Böttcher, J. Hertkorn, J.-N. Schmidt, M. Wenzel, H. P. Büchler, T. Langen, and T. Pfau, The low-energy goldstone mode in a trapped dipolar supersolid, Nature (London) **574**, 386 (2019).
[17] A. Gallemí, S. M. Roccuzzo, S. Stringari, and A. Recati, Quantized vortices in dipolar supersolid Bose-Einstein-condensed gases, Phys. Rev. A **102**, 023322 (2020).
[18] S. M. Roccuzzo, A. Gallemí, A. Recati, and S. Stringari, Rotating a Supersolid Dipolar Gas, Phys. Rev. Lett. **124**, 045702 (2020).

[19] M. N. Tengstrand, D. Boholm, R. Sachdeva, J. Bengtsson, and S. M. Reimann, Persistent currents in toroidal dipolar supersolids, Phys. Rev. A **103**, 013313 (2021).

[20] F. Ancilotto, M. Barranco, M. Pi, and L. Reatto, Vortex properties in the extended supersolid phase of dipolar Bose-Einstein condensates, Phys. Rev. A **103**, 033314 (2021).

[21] D. Baillie and P. B. Blakie, Droplet Crystal Ground States of a Dipolar Bose Gas, Phys. Rev. Lett. **121**, 195301 (2018).

[22] Y.-C. Zhang, F. Maucher, and T. Pohl, Supersolidity Around a Critical Point in Dipolar Bose-Einstein Condensates, Phys. Rev. Lett. **123**, 015301 (2019).

[23] Y.-C. Zhang, T. Pohl, and F. Maucher, Phases of supersolids in confined dipolar Bose-Einstein condensates, Phys. Rev. A **104**, 013310 (2021).

[24] J. Hertkorn, J.-N. Schmidt, M. Guo, F. Böttcher, K. S. H. Ng, S. D. Graham, P. Uerlings, T. Langen, M. Zwierlein, and T. Pfau, Pattern formation in quantum ferrofluids: From supersolids to superglasses, Phys. Rev. Research **3**, 033125 (2021).

[25] L. Santos, G. V. Shlyapnikov, and M. Lewenstein, Roton-Maxon Spectrum and Stability of Trapped Dipolar Bose-Einstein Condensates, Phys. Rev. Lett. **90**, 250403 (2003).

[26] S. Giovanazzi and D. H. J. O'Dell, Instabilities and the roton spectrum of a quasi-1d Bose-Einstein condensed gas with dipole-dipole interactions, Eur. Phys. J. D **31**, 439 (2004).

[27] D. Petter, G. Natale, R. M. W. van Bijnen, A. Patscheider, M. J. Mark, L. Chomaz, and F. Ferlaino, Probing the Roton Excitation Spectrum of a Stable Dipolar Bose Gas, Phys. Rev. Lett. **122**, 183401 (2019).

[28] L. Chomaz, R. M. W. van Bijnen, D. Petter, G. Faraoni, S. Baier, J. H. Becher, M. J. Mark, F. Wächtler, L. Santos, and F. Ferlaino, Observation of roton mode population in a dipolar quantum gas, Nat. Phys. **14**, 442 (2018).

[29] P. B. Blakie, D. Baillie, L. Chomaz, and F. Ferlaino, Supersolidity in an elongated dipolar condensate, Phys. Rev. Research **2**, 043318 (2020).

[30] G. Biagioni, N. Antolini, A. Alaa, M. Modugno, A. Fioretti, C. Gabbanini, L. Tanzi, and G. Modugno, Dimensional Crossover in the Superfluid-Supersolid Quantum Phase Transition, Phys. Rev. X **12**, 021019 (2016).

[31] J. Hertkorn, J.-N. Schmidt, M. Guo, F. Böttcher, K. S. H. Ng, S. D. Graham, P. Uerlings, H. P. Büchler, T. Langen, M. Zwierlein, and T. Pfau, Supersolidity in Two-Dimensional Trapped Dipolar Droplet Arrays, Phys. Rev. Lett. **127**, 155301 (2021).

[32] T. Macrì, F. Maucher, F. Cinti, and T. Pohl, Elementary excitations of ultracold soft-core bosons across the superfluid-supersolid phase transition, Phys. Rev. A **87**, 061602 (R) (2013).

[33] N. Henkel, R. Nath, and T. Pohl, Three-Dimensional Roton Excitations and Supersolid Formation in Rydberg-Excited Bose-Einstein Condensates, Phys. Rev. Lett. **104**, 195302 (2010).

[34] M. Sohmen, C. Politi, L. Klaus, L. Chomaz, M. J. Mark, M. A. Norcia, and F. Ferlaino, Birth, Life, and Death of a Dipolar Supersolid, Phys. Rev. Lett. **126**, 233401 (2021).

[35] F. Wächtler and L. Santos, Quantum filaments in dipolar Bose-Einstein condensates, Phys. Rev. A **93**, 061603(R) (2016).

[36] R. N. Bisset, R. M. Wilson, D. Baillie, and P. B. Blakie, Ground-state phase diagram of a dipolar condensate with quantum fluctuations, Phys. Rev. A **94**, 033619 (2016).

[37] I. Ferrier-Barbut, H. Kadau, M. Schmitt, M. Wenzel, and T. Pfau, Observation of Quantum Droplets in a Strongly Dipolar Bose Gas, Phys. Rev. Lett. **116**, 215301 (2016).

[38] L. Chomaz, S. Baier, D. Petter, M. J. Mark, F. Wächtler, L. Santos, and F. Ferlaino, Quantum-Fluctuation-Driven Crossover from a Dilute Bose-Einstein Condensate to a Macrodroplet in a Dipolar Quantum Fluid, Phys. Rev. X **6**, 041039 (2016).

[39] T. Lahaye, C. Menotti, L. Santos, M. Lewenstein, and T. Pfau, The physics of dipolar bosonic quantum gases, Rep. Prog. Phys. **72**, 126401 (2009).

[40] See Supplemental Material http://link.aps.org/supplemental/10.1103/PhysRevLett.128.195302 for a detailed analysis of our finite-temperature theory parameters and discussion of the excitations of a two-dimensional supersolid, which includes additional Refs. [41–54].

[41] S. Ronen, D. C. E. Bortolotti, and J. L. Bohn, Bogoliubov modes of a dipolar condensate in a cylindrical trap, Phys. Rev. A **74**, 013623 (2006).

[42] A. R. P. Lima and A. Pelster, Quantum fluctuations in dipolar bose gases, Phys. Rev. A **84**, 041604(R) (2011).

[43] S. P. Cockburn and N. P. Proukakis, *Ab initio* methods for finite-temperature two-dimensional bose gases, Phys. Rev. A **86**, 033610 (2012).

[44] S. Eckel, A. Kumar, T. Jacobson, I. B. Spielman, and G. K. Campbell, A Rapidly Expanding Bose-Einstein Condensate: An Expanding Universe in the Lab, Phys. Rev. X **8**, 021021 (2018).

[45] M. Ota, F. Larcher, F. Dalfovo, L. Pitaevskii, N. P. Proukakis, and S. Stringari, Collisionless Sound in a Uniform Two-Dimensional Bose Gas, Phys. Rev. Lett. **121**, 145302 (2018).

[46] T. Bland, Q. Marolleau, P. Comaron, B. Malomed, and N. Proukakis, Persistent current formation in double-ring geometries, J. Phys. B **53**, 115301 (2020).

[47] S. De, D. L. Campbell, R. M. Price, A. Putra, B. M. Anderson, and I. B. Spielman, Quenched binary Bose-Einstein condensates: Spin-domain formation and coarsening, Phys. Rev. A **89**, 033631 (2014).

[48] C. W. Gardiner and M. J. Davis, The stochastic Gross-Pitaevskii equation:II, J. Phys. B **36**, 4731 (2003).

[49] S. J. Rooney, P. B. Blakie, and A. S. Bradley, Stochastic projected Gross-Pitaevskii equation, Phys. Rev. A **86**, 053634 (2012).

[50] R. Kubo, The fluctuation-dissipation theorem, Rep. Prog. Phys. **29**, 255 (1966).

[51] E. B. Linscott and P. B. Blakie, Thermally activated local collapse of a flattened dipolar condensate, Phys. Rev. A **90**, 053605 (2014).

[52] D. Petter, A. Patscheider, G. Natale, M. J. Mark, M. A. Baranov, R. van Bijnen, S. M. Roccuzzo, A. Recati, B. Blakie, D. Baillie, L. Chomaz, and F. Ferlaino, Bragg scattering of an ultracold dipolar gas across the phase transition from Bose-Einstein condensate to supersolid in the free-particle regime, Phys. Rev. A **104**, L011302 (2021).

[53] E. Poli, T. Bland, C. Politi, L. Klaus, M. A. Norcia, F. Ferlaino, R. N. Bisset, and L. Santos, Maintaining

supersolidity in one and two dimensions, Phys. Rev. A **104**, 063307 (2021).
[54] J. Goldstone, Field theories with superconductor solutions, Nuovo Cimento (1955–1965) **19**, 154 (1961).
[55] This method has been applied previously in a quasi-two-dimensional setting without quantum fluctuations [51].
[56] P. Blakie, A. Bradley, M. Davis, R. Ballagh, and C. Gardiner, Dynamics and statistical mechanics of ultra-cold Bose gases using c-field techniques, Adv. Phys. **57**, 363 (2008).
[57] S. J. Rooney, T. W. Neely, B. P. Anderson, and A. S. Bradley, Persistent-current formation in a high-temperature Bose-Einstein condensate: An experimental test for classical-field theory, Phys. Rev. A **88**, 063620 (2013).
[58] R. G. McDonald, P. S. Barnett, F. Atayee, and A. S. Bradley, Dynamics of hot Bose-Einstein condensates: Stochastic ehrenfest relations for number and energy damping, SciPost Phys. **8**, 029 (2020).
[59] Our initial state is $\psi(\mathbf{r},0)=\psi_0(\mathbf{r})+\sum_n' \alpha_n\phi_n(\mathbf{r})$, where ϕ_n are the single-particle states, α_n is a complex Gaussian random variable with $\langle|\alpha_n|^2\rangle=(e^{\epsilon_n/k_BT}-1)^{-1}+\frac{1}{2}$, and the sum is restricted to modes with $\epsilon_n\leq 2k_BT$, with $T=30$ nK.
[60] C. N. Weiler, T. W. Neely, D. R. Scherer, A. S. Bradley, M. J. Davis, and B. P. Anderson, Spontaneous vortices in the formation of Bose-Einstein condensates, Nature (London) **455**, 948 (2008).
[61] I.-K. Liu, S. Donadello, G. Lamporesi, G. Ferrari, S.-C. Gou, F. Dalfovo, and N. Proukakis, Dynamical equilibration across a quenched phase transition in a trapped quantum gas, Commun. Phys. **1**, 1 (2018).
[62] F. Maucher, T. Pohl, S. Skupin, and W. Krolikowski, Self-Organization of Light in Optical Media with Competing Nonlinearities, Phys. Rev. Lett. **116**, 163902 (2016).
[63] F. Zambelli, L. Pitaevskii, D. M. Stamper-Kurn, and S. Stringari, Dynamic structure factor and momentum distribution of a trapped bose gas, Phys. Rev. A **61**, 063608 (2000).
[64] P. B. Blakie, R. J. Ballagh, and C. W. Gardiner, Theory of coherent bragg spectroscopy of a trapped Bose-Einstein condensate, Phys. Rev. A **65**, 033602 (2002).
[65] P. B. Blakie, D. Baillie, and R. N. Bisset, Roton spectroscopy in a harmonically trapped dipolar Bose-Einstein condensate, Phys. Rev. A **86**, 021604(R) (2012).
[66] S. Ronen, D. C. E. Bortolotti, and J. L. Bohn, Radial and Angular Rotons in Trapped Dipolar Gases, Phys. Rev. Lett. **98**, 030406 (2007).
[67] M. Jona-Lasinio, K. Łakomy, and L. Santos, Roton confinement in trapped dipolar Bose-Einstein condensates, Phys. Rev. A **88**, 013619 (2013).
[68] R. N. Bisset, D. Baillie, and P. B. Blakie, Roton excitations in a trapped dipolar Bose-Einstein condensate, Phys. Rev. A **88**, 043606 (2013).
[69] We measure phase coherence as $C^p=1-(2/\pi)\int_{\mathcal{C}} dxdy|\psi(x,y)|^2|\theta(x,y)-\beta|/\int_{\mathcal{C}} dxdy|\psi(x,y)|^2$, where $\theta(x,y)$ is the phase of $\psi(x,y)$ in the $z=0$ plane and β is a fitting parameter to maximize C^p at each time. The integration region $\mathcal{C}$ encompasses the droplets.
[70] Relative to the crystal maturation time, each quench ramp ended at 5, −13, and −90 ms for the linear interaction quench, pancake interaction quench, and pancake temperature quench, respectively. Note that evaporative cooling continues after the $\{\mu,T\}$ quench ends, taking approximately a further 100 ms until the classical field modes have equilibrated with the high-energy modes [40].
[71] The density overlap is given by $C^d=\int d^3\mathbf{x}n(\mathbf{x}-\mathbf{x}_0,\phi_0,t)n_{\mathrm{GS}}/\int d^3\mathbf{x}n_{\mathrm{GS}}^2$, with the ground state density and time-dependent density, respectively, normalized as $\int d^3\mathbf{x}n_{\mathrm{GS}}=\int d^3\mathbf{x}n(\mathbf{x}-\mathbf{x}_0,\phi_0,t)=1$. The optimization parameters $\mathbf{x}_0$ and ϕ_0 are translations and a rotation, respectively, applied to the wave function to maximize C^d.

Supplemental material: Two-dimensional supersolid formation in dipolar condensates

T. Bland,[1] E. Poli,[2] C. Politi,[1,2] L. Klaus,[1,2] M. A. Norcia,[1] F. Ferlaino,[1,2] L. Santos,[3] and R. N. Bisset[2]

[1]*Institut für Quantenoptik und Quanteninformation, Österreichische Akademie der Wissenschaften, Innsbruck, Austria*
[2]*Institut für Experimentalphysik, Universität Innsbruck, Austria*
[3]*Institut für Theoretische Physik, Leibniz Universität Hannover, Germany*

(Dated: April 13, 2022)

FORMALISM

We utilize dynamic and ground state calculations of the extended Gross-Pitaevskii equation (eGPE), given by $i\hbar\psi_t = \mathcal{L}[\psi]\psi$, where the eGPE operator is [1–4]

$$\mathcal{L}[\psi] = -\frac{\hbar^2\nabla^2}{2m} + \frac{1}{2}m\left(\omega_x^2x^2 + \omega_y^2y^2 + \omega_z^2z^2\right) + \int \mathrm{d}^3\mathbf{x}'\, U(\mathbf{x}-\mathbf{x}')|\psi(\mathbf{x}',t)|^2 + \gamma_{\mathrm{QF}}|\psi(\mathbf{x},t)|^3\,, \tag{S1}$$

m is the mass and $\omega_{x,y,z} = 2\pi f_{x,y,z}$ are the external trapping frequencies. Two-body contact interactions and the long-ranged, anisotropic dipole-dipole interactions are described by the pseudo-potential

$$U(\mathbf{r}) = \frac{4\pi\hbar^2 a_{\mathrm{s}}}{m}\delta(\mathbf{r}) + \frac{3\hbar^2 a_{\mathrm{dd}}}{m}\frac{1-3\cos^2\theta}{r^3}\,, \tag{S2}$$

respectively, with θ being the angle between the polarization axis (z axis) and the vector joining two particles. This is characterized by s-wave scattering length a_{s} and dipole length $a_{\mathrm{dd}} = \mu_0\mu_m^2 m/12\pi\hbar^2$, with magnetic moment μ_m. To find the ground state we employ a conjugate-gradients technique minimizing the corresponding energy functional [5]. The last term appearing in Eq. (S1) represents quantum fluctuations in the form of a dipolar Lee-Huang-Yang correction [6], $\gamma_{\mathrm{QF}} = \frac{128\hbar^2}{3m}\sqrt{\pi a_s^5}\,\mathrm{Re}\left\{\mathcal{Q}_5(\varepsilon_{\mathrm{dd}})\right\}$, where $\mathcal{Q}_5(\varepsilon_{\mathrm{dd}}) = \int_0^1 \mathrm{d}u\,(1-\varepsilon_{\mathrm{dd}}+3u^2\varepsilon_{\mathrm{dd}})^{5/2}$ is the auxiliary function, which can be solved analytically, and $\varepsilon_{\mathrm{dd}} = a_{\mathrm{dd}}/a_{\mathrm{s}}$.

Primarily, we use the eGPE to simulate the formation dynamics of a supersolid through an interaction quench of the scattering length, constructing an initial state by adding non-interacting noise to an unmodulated BEC ground state (far from the roton instability). Thus, our initial state is $\psi(\mathbf{r},0) = \psi_0(\mathbf{r}) + \sum_n' \alpha_n\phi_n(\mathbf{r})$, where ϕ_n are the single-particle states, α_n is a complex Gaussian random variable with $\langle|\alpha_n|^2\rangle = (e^{\epsilon_n/k_BT}-1)^{-1} + \frac{1}{2}$ with temperature T and the sum is restricted to modes with $\epsilon_n \leq 2k_BT$. On average, this adds about 1000 atoms when $T = 30$nK.

CHOICE OF γ FOR STOCHASTIC EXTENDED GPE THEORY (EQ. 1 OF MAIN TEXT)

Stochastic Gross-Pitaevskii equations have been benchmarked against numerous Bose gas experiments in various geometries [7–13], including Bose-Bose mixtures [14]. These comparisons to experimental data include direct modeling of the evaporative cooling process [7, 8]. In these works, γ is approximated by fitting the condensate atom number growth rate to experimental observations. However, there is also an approximate analytic solution appropriate for near-equilibrium solutions that depends on the chemical potential, energy cut-off, temperature, and interaction strength [15]. One comparison found γ extracted from condensate growth data is an order of magnitude larger than the analytic approximation [8]. The choice of γ does not affect the equilibrium properties of the system [16] (due to the fluctuation-dissipation theorem [17, 18]), however it affects many observables during equilibration.

To the best of our knowledge there does not exist any analytic prediction for γ for the dipolar system [18]. We approximate γ based on direct experiment-theory comparisons with the condensate growth rate in Ref. [19]. For that case we have the relevant experimental data available. There, the supersolid formation was studied in detail for a dysprosium supersolid in a cigar-shaped geometry, and a value of $\gamma = 0.0075$ was found to give quantitatively similar growth behavior as observed experimentally. Here, for a qualitatively similar regime [20] we initially assume the same value.

In Fig. S1 we investigate the γ dependency on the evaporative cooling protocol presented in the main text, namely a ^{164}Dy gas in a pancake trap with $(f_x, f_y, f_z) = (33, 33, 167)$Hz and $a_s = 88a_0$. Further details are given in the main text. We consider both half and double the initial value, i.e. $\gamma = (0.00375, 0.0075, 0.015)$. Interestingly, several observables are sensitive to the choice of γ. This includes: atom number versus time, onset time of global phase coherence versus onset time of crystal structure, and the number of free vortices trapped within the crystal. For our simulations we calculate the phase coherence C^p and density overlap C^d. Despite the c-field atom number increasing faster with larger γ, the growth of phase coherence does not appear as clearly dependent on γ. This is possibly due to the number of vortices gen-

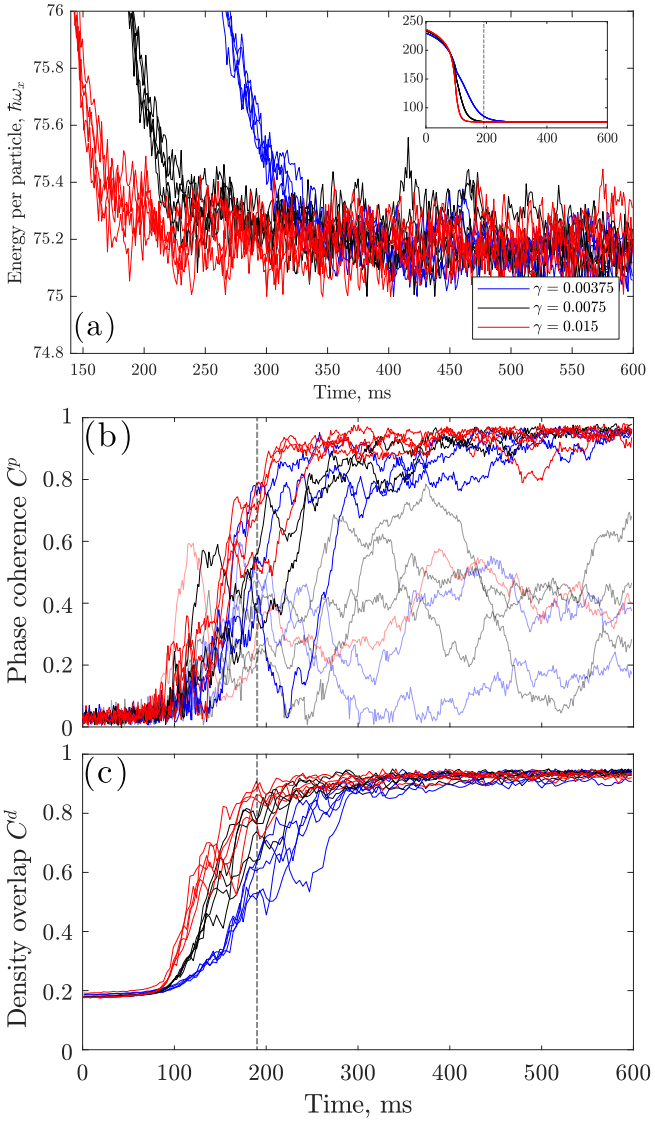

FIG. S1. Effect of varying γ. Five simulations are shown with the same color for each γ. (a) Energy per particle versus time. The average final value is independent of γ, as expected. Inset shows the same data over a longer time range, where $t = 0$ corresponds to the beginning of the 100ms temperature quench. (b) Phase coherence for all data. Curves with a lower opacity correspond to simulations with isolated vortices. (c) Density overlap with the ground state 19 droplet supersolid. In all plots the dashed vertical line indicates $t = 0$ in Fig. 2 of the main text.

erated through the quench, which have been shown to appear more readily with increasing γ, although there is also evidence they are damped quicker too [7]. Curves for simulations with a long-lived single vortex are shown with a lower opacity in Fig. S1(b), as this greatly influences C^p, and these simulations are not included in the averages shown in the main paper. It is also worth noting that we do not see free vortices after the interaction quenches. Even in the presence of a free vortex the final state can still be considered as a coherent supersolid, with $C^d \sim 1$, however $C^p < 1$. Future improvements to this measure could involve finding the vortex centre and multiplying the phase by the opposite circulation. This is not easy however due to the nonlinear azimuthal phase profile of a vortex in a supersolid [21, 22].

The effect of varying γ is most obvious in the overlap between the simulation density and ground state density, C^d [Fig. S1(c)]. Larger γ forces the c-field atom number, and hence density, to rapidly increase, forcing the fast production of droplets. We believe that comparing a spectrum of observables such as these will provide important benchmarks to fine tune the simulations, and that this will also provide an important test in the future for the development of analytic theories that can predict γ. As supersolid production in 2D becomes more routine, direct comparison between the condensate atom number and droplet number growth rates in particular will become crucial in determining the appropriate choice of γ.

It is worth noting that even if the supersolid formation time was a few 100ms longer than the data presented here, the whole process would still be faster than evaporatively cooling into the BEC state, quenching the interactions and then waiting for the phase coherence to reappear. In this latter scenario, significant three-body losses play a negative role. Previous works in 1D have maximized phase coherence by increasing the final a_s, and hence increasing the superfluid connection between droplets [23], and decreasing the droplet peak density. However, the droplet number is strongly dependent on a_s, and we find that such a strategy significantly decreases the number of droplets.

THE ROLE OF ENERGY DURING SUPERSOLID FORMATION

It is instructive to investigate the role of energy during the formation of 2D droplet arrays, via both interaction quenches and the temperature quenches. In Fig. S2 (a), we show the energy versus time for the five interaction quench simulations considered in Fig. 1(a) of the main text. We have also marked the energy of the ground state before the interaction quench ($E_{\rm GS}^{\rm BEC}$), and the energy of the ground state following the interaction quench ($E_{\rm GS}^{\rm SS}$), with the superscript indicating that the ground state is initially in the BEC phase, then later in the supersolid phase. An estimate for the energy added by crossing the phase transition can be evaluated as $[E(t_{\rm final}) - E_{\rm GS}^{\rm SS}] - [E(t_{\rm initial}) - E_{\rm GS}^{\rm BEC}] \approx 0.35\hbar\omega_x$. Note that $E(t_{\rm initial}) - E_{\rm GS}^{\rm BEC}$ does not equal zero due to the random noise added to the initial state.

It is interesting at this point to compare the final energies of the eGPE simulations in Fig. S2 (a) with the final energies of the c-field simulations following the evapo-

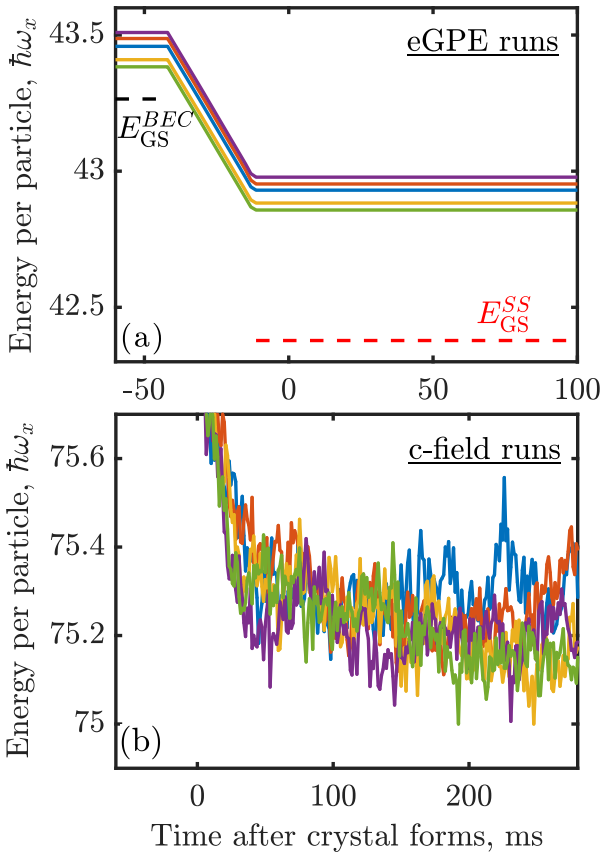

FIG. S2. Energy versus time for the pancake quench simulation runs considered in Fig. 2 of the main text. (a) Interaction quenches simulated using the eGPE with $N \approx 2.1 \times 10^5$. Dashed lines show the ground state energy for the initial parameters, $E_{\rm GS}^{\rm BEC}$, and the final paremeters corresponding to the target supersolid, $E_{\rm GS}^{\rm SS}$. (b) Temperature quenches simulated with the SeGPE. All curves are with fixed $\gamma = 0.0075$. For both subplots $f_{x,y,z} = (33, 33, 167)$ Hz.

rative cooling quench, which are shown in Fig. S2 (b), which differ by more than $30\hbar\omega_x$. From such a comparison we can deduce that the important factor for disrupting supersolid formation following an interacting quench is not so much the total energy injected into the system by crossing the first-order phase transition [in Fig. S2 (a)] but, rather, which modes become excited. This large disparity in energy, however, tells us that at much longer time scales than shown here, the eGPE states may settle down to a better quality supersolid than the SeGPE [see e.g. Fig. 2 of the main text], but this could be on the order of seconds, much larger than the supersolid life time.

From our dynamic structure factor calculations shown in Fig. S3 (which will be discussed shortly), one can see that the out-of-phase Goldstone modes (the low-energy modes at finite momentum that show up as red ovals) are particularly vulnerable to excitation by the interaction quench. Note that although this figure is for the 7-droplet supersolid rather than the 19-droplet one, such low-energy Goldstone modes are a general feature of dipolar supersolids [24, 25]. Since these modes inherently cause both phase and crystal excitations, they directly act to disrupt the supersolid. Furthermore, we also see some vortex pairs after the interaction quench, and these also play a role. Interestingly, even in the interaction-quench simulations, a supersolid is obtained in the long-time limit (although too long to be useful for current experiments due to lifetime limitations), even though the total energy is conserved, thanks to a damping of these phase and crystal excitations.

SUPERSOLID EXCITATIONS

We investigate the 7-droplet hexagon supersolid, the same configuration as shown in Fig. 3 of the main text, using the extended Gross-Pitaevskii equation (eGPE), focusing here on its excitations. We perform a Bogoliubov-de Gennes linearization and present results in the form of the dynamic structure factor,

$$S(\mathbf{k},\omega) = \sum_l \left| \int \mathrm{d}^3\mathbf{x}\, [u_l^*(\mathbf{r}) + v_l^*(\mathbf{x})] e^{i\mathbf{k}\cdot\mathbf{x}} \psi_0(\mathbf{x}) \right|^2 \delta(\omega - \omega_l)\,, \tag{S3}$$

Here, ψ_0 is the ground state wavefunction normalized to unity, i.e. $\int \mathrm{d}^3\mathbf{x}|\psi_0(\mathbf{x})|^2 = 1$, and $\{u_l(\mathbf{x}), v_l(\mathbf{x})\}$ are the quasiparticle excitations with energy ω_l [26, 27]. The dynamic structure factor along two orthogonal directions is displayed in Fig. S3. Note, the asymmetry along k_x and k_y is due to the triangular configuration of the crystal, which can be seen clearly in Fig. S4(b).

To explore the role of dimensionality, Fig. S4 compares the static structure factor, $S(\mathbf{k}) = \int \mathrm{d}\omega\, S(\mathbf{k},\omega)$, for both linear and 7-droplet hexagon supersolids. These results are converged within the dashed ellipses, set by ensuring that the f-sum rule, $\int \mathrm{d}\omega\, \omega S(k,\omega) = \hbar^2 k^2/2m$, is satisfied, and should be ignored outside. Convergence is limited by the number of BdG modes, for which we use 512 modes for both cases. In order to make a fair comparison between a 1D and 2D supersolids we choose to approximately match the average 2D trap density by fixing $\varrho = N f_x f_y$ [28]. As previously reported, the structure factor for the linear case [Fig. S4(a)] has peaks corresponding to the average inter-droplet spacing (2.67μm), $k_x l_z \approx 1.43$, and subsequent peaks at integer multiples of this [24]. We find that the dominant contributing modes to the structure factor peaks are low energy out-of-phase Goldstone modes [24, 25, 29], where the superfluid current and crystal oscillate out-of-phase with one another. Note that for possible comparison with experiments our spectrum in Fig. S4 was energy broadened with a Gaussian of width $\sigma = 0.008\,\hbar\omega_z$, note that Fig. 1(b) of the main text was similarly broadened by $\sigma = 0.004\,\hbar\omega_z$.

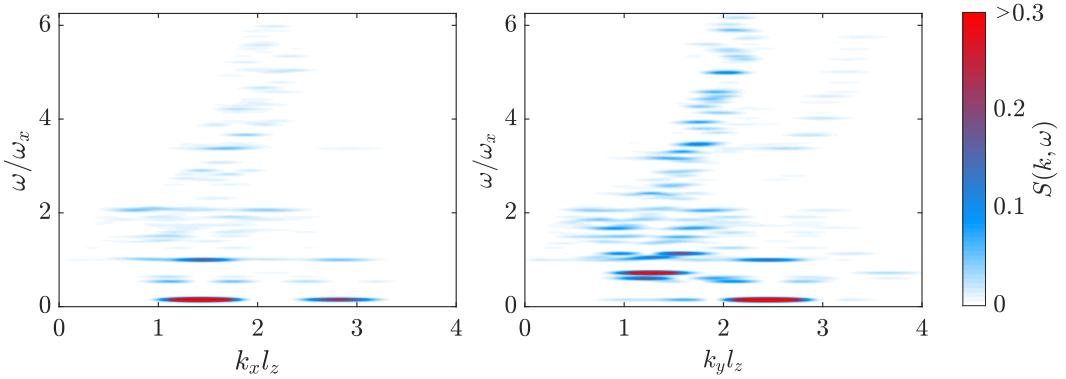

FIG. S3. Dynamic structure factor (DSF), Eq. (S3), normalized to peak value, in energy-momentum space for a ^{164}Dy 7-droplet hexagon supersolid. Left: DSF along k_x with $k_y = k_z = 0$. Right: DSF along k_y with $k_x = k_z = 0$. Parameters: $a_s = 90a_0$, $f_{x,y,z} = (52.83, 52.83, 167)$ Hz, $N = 9.5 \times 10^4$.

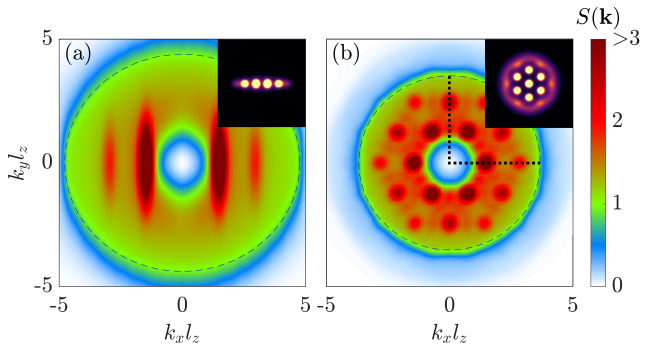

FIG. S4. Static structure factors for (a) linear and (b) 7-droplet hexagon supersolids. Convergence is achieved within the dashed ellipses (see text). Dotted lines in (b) correspond to the trajectories shown in Fig. S3, integrated over energy. Parameters for linear chain: $a_s = 90a_0$, $f_{x,y,z} = (52.83, 130, 167)$ Hz, $N = 4 \times 10^4$. For 2D crystal: $a_s = 90a_0$, $f_{x,y,z} = (52.83, 52.83, 167)$ Hz, $N = 9.5 \times 10^4$.

For the 2D supersolid, Fig. S4(b) displays peaks situated at $k_\rho l_z \approx 1.43$ every 60° azimuthally, where $k_\rho = \sqrt{k_x^2 + k_y^2}$. These peaks reflect the hexagonal structure of the ground state, however this value does *not* directly reflect the inter-droplet spacing (3.05μm, which would correspond to $k_\rho l_z \approx 1.25$), but rather the spacing of lattice planes between droplets. Crucially, the six inner momentum peaks are rotated compared to the droplet crystal, analogous to what we observed experimentally in the TOF images. Similar to the 1D chain, we find that the out-of-phase Goldstone modes–a manifestation of superfluidity–contribute to the majority of the peak signal.

[1] F. Wächtler and L. Santos, Quantum filaments in dipolar bose-einstein condensates, Phys. Rev. A **93**, 061603 (2016).

[2] R. N. Bisset, R. M. Wilson, D. Baillie, and P. B. Blakie, Ground-state phase diagram of a dipolar condensate with quantum fluctuations, Phys. Rev. A **94**, 033619 (2016).

[3] I. Ferrier-Barbut, H. Kadau, M. Schmitt, M. Wenzel, and T. Pfau, Observation of quantum droplets in a strongly dipolar bose gas, Phys. Rev. Lett. **116**, 215301 (2016).

[4] L. Chomaz, S. Baier, D. Petter, M. J. Mark, F. Wächtler, L. Santos, and F. Ferlaino, Quantum-fluctuation-driven crossover from a dilute bose-einstein condensate to a macrodroplet in a dipolar quantum fluid, Phys. Rev. X **6**, 041039 (2016).

[5] S. Ronen, D. C. E. Bortolotti, and J. L. Bohn, Bogoliubov modes of a dipolar condensate in a cylindrical trap, Phys. Rev. A **74**, 013623 (2006).

[6] A. R. P. Lima and A. Pelster, Quantum fluctuations in dipolar bose gases, Phys. Rev. A **84**, 041604 (2011).

[7] C. N. Weiler, T. W. Neely, D. R. Scherer, A. S. Bradley, M. J. Davis, and B. P. Anderson, Spontaneous vortices in the formation of Bose-Einstein condensates, Nature **455**, 948 (2004).

[8] I.-K. Liu, S. Donadello, G. Lamporesi, G. Ferrari, S.-C. Gou, F. Dalfovo, and N. Proukakis, Dynamical equilibration across a quenched phase transition in a trapped quantum gas, Communications Physics **1**, 1 (2018).

[9] S. Cockburn and N. Proukakis, Ab initio methods for finite-temperature two-dimensional bose gases, Physical Review A **86**, 033610 (2012).

[10] S. J. Rooney, T. W. Neely, B. P. Anderson, and A. S. Bradley, Persistent-current formation in a high-temperature bose-einstein condensate: An experimental test for classical-field theory, Phys. Rev. A **88**, 063620 (2013).

[11] S. Eckel, A. Kumar, T. Jacobson, I. B. Spielman, and G. K. Campbell, A rapidly expanding bose-einstein condensate: an expanding universe in the lab, Physical Review X **8**, 021021 (2018).

[12] M. Ota, F. Larcher, F. Dalfovo, L. Pitaevskii, N. P.

Proukakis, and S. Stringari, Collisionless sound in a uniform two-dimensional bose gas, Physical review letters **121**, 145302 (2018).

[13] T. Bland, Q. Marolleau, P. Comaron, B. Malomed, and N. Proukakis, Persistent current formation in double-ring geometries, Journal of Physics B: Atomic, Molecular and Optical Physics **53**, 115301 (2020).

[14] S. De, D. Campbell, R. Price, A. Putra, B. M. Anderson, and I. Spielman, Quenched binary bose-einstein condensates: Spin-domain formation and coarsening, Physical Review A **89**, 033631 (2014).

[15] C. W. Gardiner and M. J. Davis, The stochastic Gross-Pitaevskii equation:II, J Phys. B **36**, 4731 (2003).

[16] S. Rooney, P. Blakie, and A. Bradley, Stochastic projected gross-pitaevskii equation, Physical Review A **86**, 053634 (2012).

[17] R. Kubo, The fluctuation-dissipation theorem, Reports on progress in physics **29**, 255 (1966).

[18] E. B. Linscott and P. B. Blakie, Thermally activated local collapse of a flattened dipolar condensate, Phys. Rev. A **90**, 053605 (2014).

[19] M. Sohmen, C. Politi, L. Klaus, L. Chomaz, M. J. Mark, M. A. Norcia, and F. Ferlaino, Birth, life, and death of a dipolar supersolid, Phys. Rev. Lett. **126**, 233401 (2021).

[20] Despite the different trap geometries, $(f_x, f_y, f_z) = (36, 88, 141)$Hz in Ref. [19] compared to $(f_x, f_y, f_z) = (33, 33, 167)$Hz, the peak densities are similar $n_{\rm peak} = 1.6 \times 10^{21} \mu{\rm m}^{-3}$ compared to $n_{\rm peak} = 1.8 \times 10^{21} \mu{\rm m}^{-3}$ and thus will have similar quality supersolids.

[21] F. Ancilotto, M. Barranco, M. Pi, and L. Reatto, Vortex properties in the extended supersolid phase of dipolar bose-einstein condensates, Physical Review A **103**, 033314 (2021).

[22] S. Roccuzzo, A. Gallemí, A. Recati, and S. Stringari, Rotating a supersolid dipolar gas, Physical review letters **124**, 045702 (2020).

[23] D. Petter, A. Patscheider, G. Natale, M. J. Mark, M. A. Baranov, R. van Bijnen, S. M. Roccuzzo, A. Recati, B. Blakie, D. Baillie, L. Chomaz, and F. Ferlaino, Bragg scattering of an ultracold dipolar gas across the phase transition from bose-einstein condensate to supersolid in the free-particle regime, Phys. Rev. A **104**, L011302 (2021).

[24] G. Natale, R. van Bijnen, A. Patscheider, D. Petter, M. Mark, L. Chomaz, and F. Ferlaino, Excitation spectrum of a trapped dipolar supersolid and its experimental evidence, Physical review letters **123**, 050402 (2019).

[25] M. Guo, F. Böttcher, J. Hertkorn, J.-N. Schmidt, M. Wenzel, H. P. Büchler, T. Langen, and T. Pfau, The low-energy goldstone mode in a trapped dipolar supersolid, Nature **574**, 386 (2019).

[26] F. Zambelli, L. Pitaevskii, D. M. Stamper-Kurn, and S. Stringari, Dynamic structure factor and momentum distribution of a trapped bose gas, Phys. Rev. A **61**, 063608 (2000).

[27] P. Blakie, R. Ballagh, and C. Gardiner, Theory of coherent bragg spectroscopy of a trapped bose-einstein condensate, Physical Review A **65**, 033602 (2002).

[28] E. Poli, T. Bland, C. Politi, L. Klaus, M. A. Norcia, F. Ferlaino, R. N. Bisset, and L. Santos, Maintaining supersolidity in one and two dimensions, Phys. Rev. A **104**, 063307 (2021).

[29] J. Goldstone, Field theories with superconductor solutions, Il Nuovo Cimento (1955-1965) **19**, 154 (1961).

4.8 Publication VI:

Can angular oscillations probe superfluidity in dipolar supersolids?

The following publication has appeared in

Physical Review Letters **129**, 040403 (2022)‖
submitted 17 Nov 2021; published 22 July 2022
DOI: https://doi.org/10.1103/PhysRevLett.128.195302
M. A. Norcia,[1] E. Poli,[2] C. Politi,[1,2] L. Klaus,[1] T. Bland,[1] M. J. Mark,[1,2] L. Santos,[3] R. N. Bisset,[2] and F. Ferlaino[1,2]

[1] *Institut für Quantenoptik und Quanteninformation, Österreichische Akademie der Wissenschaften, 6020 Innsbruck, Austria*

[2] *Institut für Experimentalphysik, Universität Innsbruck, 6020 Innsbruck, Austria*

[3] *Institut für Theoretische Physik, Universität Hannover, Hannover, Germany*

‖The author of the present thesis performed the measurements together with M. A. N., and L. K., analysed the experimental data with M. A. N., and contributed in writing the manuscript and interpreting the results together with all the authors.

Can Angular Oscillations Probe Superfluidity in Dipolar Supersolids?

Matthew A. Norcia,[1] Elena Poli,[2] Claudia Politi,[1,2] Lauritz Klaus,[1,2] Thomas Bland,[1,2] Manfred J. Mark,[1,2] Luis Santos,[3] Russell N. Bisset,[2] and Francesca Ferlaino[1,2,*]

[1]*Institut für Quantenoptik und Quanteninformation, Österreichische Akademie der Wissenschaften, Innsbruck 6020, Austria*
[2]*Institut für Experimentalphysik, Universität Innsbruck, Innsbruck 6020, Austria*
[3]*Institut für Theoretische Physik, Leibniz Universität Hannover, 30167 Hannover, Germany*

(Received 17 November 2021; revised 3 March 2022; accepted 6 June 2022; published 22 July 2022)

Angular oscillations can provide a useful probe of the superfluid properties of a system. Such measurements have recently been applied to dipolar supersolids, which exhibit both density modulation and phase coherence, and for which robust probes of superfluidity are particularly interesting. So far, these investigations have been confined to linear droplet arrays, which feature relatively simple excitation spectra, but limited sensitivity to the effects of superfluidity. Here, we explore angular oscillations in systems with 2D structure which, in principle, have greater sensitivity to superfluidity. In both experiment and simulation, we find that the interplay of superfluid and crystalline excitations leads to a frequency of angular oscillations that remains nearly unchanged even when the superfluidity of the system is altered dramatically. This indicates that angular oscillation measurements do not always provide a robust experimental probe of superfluidity with typical experimental protocols.

DOI: 10.1103/PhysRevLett.129.040403

Some of the most distinctive manifestations of superfluidity in ultracold quantum gases relate to their behavior under rotation. These include the presence of quantized vortices [1–3] and persistent currents in ring traps [4], as well as shape-preserving angular oscillations associated with a "scissors" mode [5]. Measurements of the scissors mode frequency have long been used to illuminate the superfluid properties of a variety of systems [6–11]. With the recent advent of dipolar supersolids [12–18]—states that possess both the global phase coherence of a superfluid and the spatial density modulation of a solid—the scissors mode provides a tempting way to quantify changes in superfluidity across the superfluid-supersolid transition [19,20]. Angular oscillations have also been used to search for superfluid properties in solid helium [21]. In this case, however, a change in oscillation frequency initially attributed to superfluidity was eventually traced, instead, to other reasons [22]. In this Letter, we study more deeply the connection between angular oscillations and superfluidity in dipolar supersolids to determine the extent to which such experiments can inform our understanding of superfluidity in these systems.

The goal of these angular oscillation measurements is to infer the flow patterns allowed for a given fluid. A superfluid is constrained by the single-valued nature of its wave function to irrotational flow (IF), while a nonsuperfluid system faces no such constraint and, in certain situations, may be expected to undergo rigid-body rotation (RBR). Prototypical velocity fields for angular oscillations under IF ($\vec{v} \propto \nabla xy$) and RBR ($\vec{v} \propto r\hat{\theta}$) are depicted in Figs. 1(a) and 1(b), respectively. The velocity field associated with angular rotation is related to the moment of inertia of the system and, thus, the frequency of angular oscillations.

The ability to distinguish between RBR and IF (and, thus, in principle, between a classical and superfluid

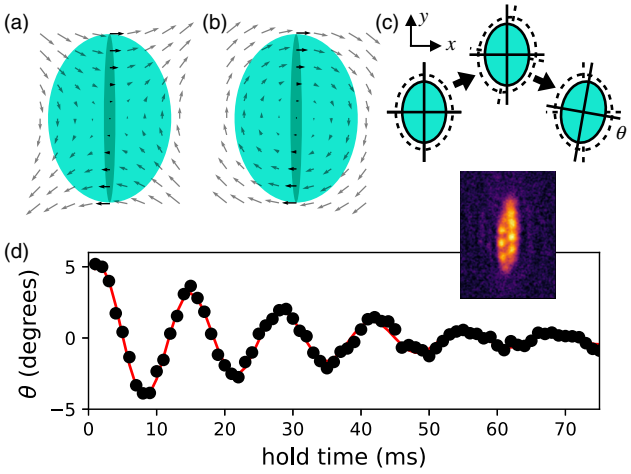

FIG. 1. Characteristic velocity profiles for irrotational flow (a) and rigid-body rotation (b). A wide atomic state (light turquoise oval) samples a region of space where the two differ significantly, while a highly elongated state (dark turquoise oval) samples a region where the two patterns are nearly indistinguishable. (c) We excite oscillations in the angle θ of our atomic gas by rapidly rotating the anisotropic trap (dashed oval), then returning it to its original orientation and observing the subsequent dynamics. (d) Typical example of experimental angular oscillation for the zigzag modulated state shown on the right (image averaged over nine iterations). In this case, the errors from the fit to the state angle are smaller than the markers. The red line is a damped sinusoidal fit used to extract the angular oscillation frequency f_{osc}.

system) depends critically on the geometry of the system, and is sensitive only to the character of the flow pattern where the atomic density is appreciable. As illustrated in Figs. 1(a) and 1(b), highly elongated states sample only the region along the weak axis of the trap (near $x = 0$) where IF and RBR are identical for small rotations (dark turquoise regions), while rounder states (light turquoise regions) sample regions of space where the flow patterns differ significantly and, thus, are far more sensitive to the irrotational constraint. Recent works have focused on systems that form a short linear chain of about two "droplets" [23] in the supersolid regime [19,20].

In this Letter, we study angular oscillations in systems with linear and two-dimensional modulation to disentangle the effect of three important contributions: (i) a narrowing of the aspect ratio of the gas (geometrical change), (ii) a reduction in the population of the low-density superfluid "halo" that occupies the outer regions of the trap, and (iii) a reduction in the density of the interdroplet connection that enables the exchange of atoms between droplets, which is key to the superfluid nature of supersolid systems. We find that, in linear systems, contributions (i) and (ii) dominate the change in oscillation frequency associated with the onset of modulation, while (iii) has a negligible effect.

In dipolar condensates with two-dimensional structure, which have been a focus of recent work [24–28], the effects of geometry and superfluidity may be disentangled, and one may expect to observe a direct link between a change of the superfluid fraction and a modification of the angular oscillation frequency. However, we find that the physics at play is much more complex. Indeed, not only does the oscillation frequency fail to approach its rigid-body value for states with a vanishing superfluid connection, but it remains very close to the value predicted for a superfluid state. We extensively investigate the system behavior as a function of geometry and interaction parameters, revealing a unique multimode response of the dipolar supersolid.

Experimentally, we use a dipolar quantum gas of ^{164}Dy atoms (up to approximately 5×10^4 condensed atoms), confined within an optical dipole trap (ODT) of tunable geometry, formed at the intersection of three laser beams [25,27,29]. The trap geometry and particle number at the end of the evaporative cooling sequence determine the character of the modulated ground state, which can form linear, zigzag, or triangular lattice configurations [28]. By varying the applied magnetic field in the vicinity of Feshbach resonances near 18–23 G, we can access scattering lengths that correspond to either unmodulated BECs or modulated states. In past works, we have demonstrated that modulated states created at the corresponding field have global phase coherence [25,27]. In this Letter, we expect the same to be true, but refer to these experimental states simply as modulated, as we do not repeat the characterization for every trap condition used. We excite angular oscillations by using the well-established protocol of

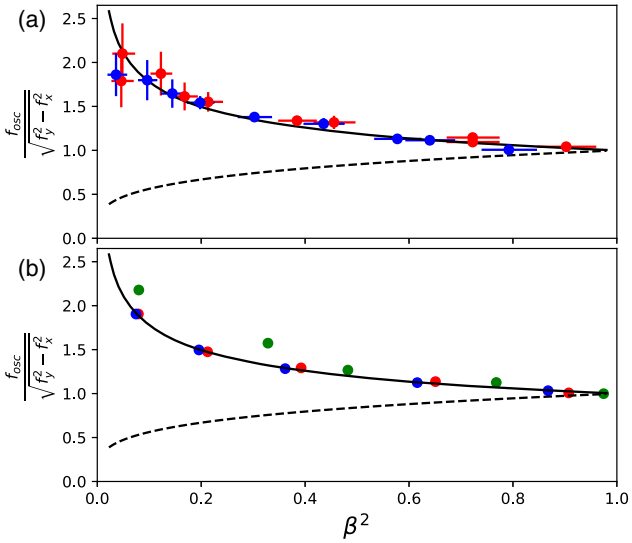

FIG. 2. Normalized oscillation frequencies f_{osc} from experiment (a) and simulation (b). Blue points represent unmodulated BECs, red points represent modulated states (expt.) and supersolid states (sim.), and green points represent independent droplet arrays. Solid lines are predictions for irrotational flow f_{irr}. Dashed lines are predictions for rigid body rotation f_{rig}. The trap frequencies used in the simulation, from left to right, are $(f_x, f_y) = [(43, 53), (40, 57), (37, 62), (32, 70), (26, 87)]$ Hz. $f_z = 122$ Hz for all cases. A similar range is used in the experiment.

applying a sudden small rotation of the trap, by varying the relative powers in the ODT beams for 6 ms before returning them to their original values [Fig. 1(c)]. Using our high-resolution imaging [30], we observe the in-trap density profile at a variable time from the excitation, and extract the angle of the major and minor axes using a two-dimensional Gaussian fit to the state [31].

A typical angular oscillation is shown in Fig. 1(d), for a "zigzag" modulated state [25]. From such oscillation traces, we extract the dominant oscillatory frequency f_{osc} using a fit to an exponentially damped sinusoid. Typically, the statistical error on our measurements of f_{osc} is on the sub-Hertz level, better than our knowledge of the trap frequencies, due to drifts between calibrations. We perform such measurements for trap geometries ranging from an elongated cigar shape to pancake shaped, and for different scattering lengths, as summarized in Fig. 2(a).

Within a single-mode approximation, the angular oscillation frequency f_{osc} can be predicted using either a sum-rule based approach [19,34], or considerations based on hydrodynamic flow [5]. For RBR, the angular oscillation frequency is given by $f_{\mathrm{rig}} = \sqrt{(f_y^2 - f_x^2)\beta}$, whereas for IF, the predicted value is $f_{\mathrm{irr}} = \sqrt{(f_y^2 - f_x^2)/\beta}$ [19,20]. Here, $f_{x,y}$ are the trap frequencies along directions x and y. $\beta = \langle x^2 - y^2 \rangle / \langle x^2 + y^2 \rangle$ is a geometrical factor that quantifies the degree of elongation of the atomic cloud (but carries no

information about the superfluid fraction). As shown in Fig. 2, f_{rig} and f_{rig} are more distinct for smaller values of β. Remarkably, independent of trap geometry or the presence of modulation, we observe f_{osc} close to the IF prediction and far from the RBR prediction when the two predictions differ appreciably.

To gain a deeper understanding of our observations, we theoretically study the oscillation dynamics using a real-time simulation of the extended Gross-Pitaevskii equation (EGPE) [35–37]. To compare to the experimental observations of Fig. 2(a), first, we calculate the ground state for a given trap, scattering length, and atom number. Then, we apply a 0.5° rotation of the trap for 6 ms (we have confirmed that the character and frequency of the response do not change for much larger excitations), and then let the state evolve for 50 ms. Then, we perform the same fitting procedure as used in the experiment to extract f_{osc}. For the simulation, we calculate β directly for the ground state (we confirm that the exact value of β agrees with that extracted from a Gaussian fit at the 5% level). For simulations performed on states ranging from the unmodulated BEC to supersolid (SS) to independent droplet (ID) regimes, with vanishing superfluid connection between droplets, we again find that f_{osc} is always very close to f_{irr}, in very good agreement with the experimental data. For isolated droplet states in particular, f_{osc} can actually be even higher than the expected value for irrotational flow, indicating that the oscillation frequency is not necessarily in between the irrotational and rigid body values.

To further illuminate the dependence f_{osc} on superfluidity, we analyze the results of the simulation as a function of the s-wave scattering length a_s (Fig. 3). Scattering lengths of $85a_0$ yield arrays of (nearly) independent droplets, while $a_s = 97a_0$ produces an unmodulated BEC. In between, we find supersolid states, with low-density connections between droplets. Inspired by the formulation of Leggett [38], we quantify the degree of interdroplet density connection as $\mathcal{C} = [\int dx/\rho(x)]^{-1}$, where $\rho(x)$ is the projected atomic density, evaluated over the interdroplet connection [Fig. 3(a)] [39].

As shown in Fig. 3, despite the rapid reduction of $\mathcal{C}$ with a_s, the simulated f_{osc} exhibits a rather constant behavior with a value always close to the purely irrotational predictions, f_{irr}, for both a linear (1D) and hexagon state (2D). This observation indicates that (i) the degree of interdroplet connection is not actually a major determinant of the angular oscillation frequency and (ii) that the system does not undergo RBR even for vanishingly small interdroplet density connection. The latter conclusion is particularly evident for hexagon states, where the rigid-body prediction substantially departs from the irrotational one. For the linear array, the elongated geometry means that the f_{rig} and f_{irr} differ only slightly; see Supplemental Material for further discussion [31].

At this point, we can clearly see the geometrical limitations of the linear systems. In linear systems, the

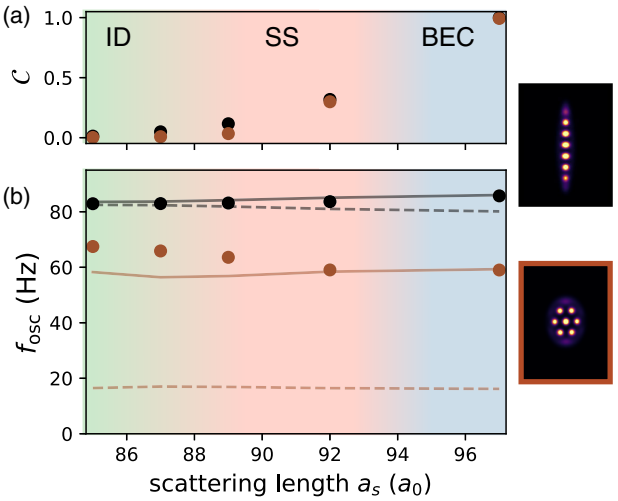

FIG. 3. Impact of scattering length on simulated scissors mode frequencies. (a) Interdroplet connection $\mathcal{C}$ (defined in text) versus scattering length for different trap geometries. The calculated ground state in each trap is shown on the right, with corresponding border colors. (b) Scissors mode frequency versus scattering length. Solid lines are predictions for irrotational flow f_{irr}. Dashed lines are predictions for rigid body rotation f_{rig}. β ranges from 0.93 to 0.99, and 0.27 to 0.31 in the linear and hexagonal cases, respectively.

narrowing of the atomic density distribution that occurs with the onset of modulation causes the dominant contribution to a modification in oscillation frequency as well as a reduction in sensitivity of the oscillation frequency to superfluidity. Simultaneously, the transfer of atoms from the halo to the droplets leads to a reduction of the superfluidity of the composite halo-droplet system, which is accompanied by a small change in the oscillation frequency. However, because the motion induced by rotation in a linear system is perpendicular to the interdroplet axis, these effects should not be interpreted as a result of the weakening superfluid connection along the interdroplet axis. In contrast, systems with two-dimensional structure maintain a relatively round aspect ratio in the modulated regime, and the rotational motion does orient along certain interdroplet axes.

To better understand the nonrigid nature of the angular oscillations, we employ a method to extract the character of the system's response by analyzing our experimental and EGPE simulation dynamics in the frequency domain with respect to time, but in the position domain with respect to the spatial coordinates. A similar technique has been applied along one dimension to understand the mode structure of an elongated condensate [40]. This technique, which for convenience we refer to as "Fourier transform image analysis" (FTIA) [31], allows us to extract a power spectrum of density fluctuations driven by the angular excitation, as well as the spatial form of the density fluctuations at each frequency. For comparison, we also

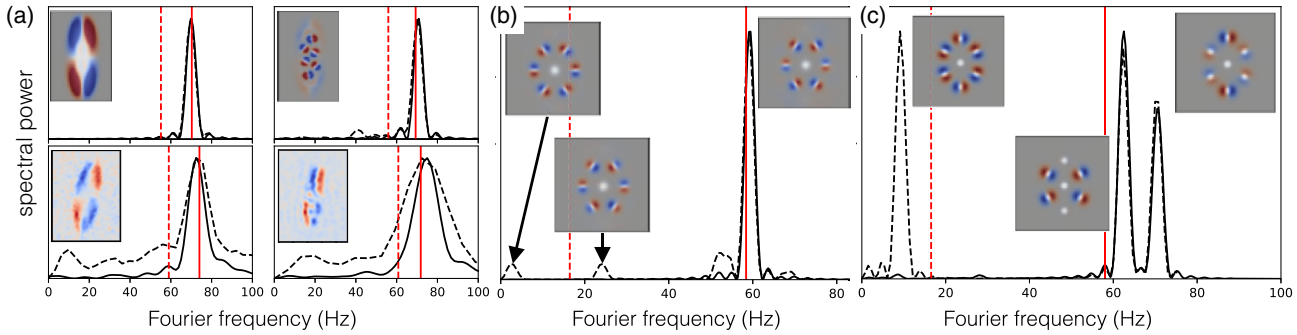

FIG. 4. Analysis of mode shapes and response due to angular excitation. Solid lines are the power spectrum obtained from the rotational signal (θ in the experiment and $\langle xy \rangle$ in the simulation), and dashed lines are obtained from FTIA (see text, Supplemental Material [31] for description). Inset panels show the mode shapes for selected modes. Red and blue indicate out-of-phase changes in density, overlaid onto the average density profile in the panels corresponding to simulation (gray to white). Solid and dashed vertical red lines represent f_{irr} and f_{rig}, respectively. (a) Responses in elongated traps from simulation (top) and experiment (bottom), for an unmodulated BEC (left) and a zigzag droplet state (right). Trap frequencies are $f_{x,y} = [31(1), 73(1), 128(1)]$ Hz, and $f_{x,y,z} = [32, 70, 122]$ Hz for the experiment and theory, respectively. (b) Simulated response of supersolid hexagon state ($a_s = 92a_0$). (c) Simulated response of droplet crystal hexagon state ($a_s = 85a_0$). Note that the ground state has a different orientation for the two scattering lengths in this trap. Trap frequencies are $f_{x,y,z} = [43, 53, 122]$ Hz for (b) and (c).

calculate the spectral power of our rotational signal through a Fourier transform. For computational robustness, we use the fitted angle θ in the experimental case, and $\langle xy \rangle$ for the simulations. To enhance our frequency resolution, we analyze simulations with longer durations than are accessible in the experiment (160 to 290 ms).

We apply the FTIA to both simulation and experimental images in Fig. 4(a). For a BEC, the FTIA gives a dominant peak in both simulation and experiment, whose frequency and shape are consistent with a scissors mode oscillation at the frequency observed from the angular response. For a zigzag modulated state, we again predominantly observe a single peak in the FTIA spectrum at the frequency of the angular oscillation. In the simulation, we can see that the mode corresponds to the motion of the different droplets in a pattern reminiscent of IF in an unmodulated superfluid, and clearly distinct from RBR. In the experiment, the response of individual droplets is not visible due to shot-to-shot fluctuations in the exact number and position of the droplets, but the overall structure is similar to the simulation.

For hexagonal supersolid [Fig. 4(b)] and isolated droplet [Fig. 4(c)] states, the FTIA reveals a clear multifrequency response. For the supersolid, we observe the excitation of modes near 3 and 25 Hz that do not contribute strongly to $\langle xy \rangle$. The droplet motion associated with the 3 Hz mode is approximately (but not exactly) shape preserving, and the frequency is much lower than would be expected for a single-mode RBR response. For the isolated droplet array, we again observe a nearly shape-preserving low-frequency response from FTIA, as well as a dominant angular response that is split into two frequencies, both above the scissors mode frequency f_{irr} expected for a superfluid with the same geometry. In the experiment, the combination of nonangular excitations associated with our method used to rotate the trap and relatively rapid damping of the oscillation prevent us from observing meaningful mode profiles for small β.

Importantly, the FTIA reveals that, even in cases where we observe an apparently single-frequency response in typical rotational observables like θ or $\langle xy \rangle$ [as in Figs. 4(a) and 4(b)], the response of the system may, in fact, be multimode in nature, breaking the single-mode approximation used to analytically extract f_{irr} and f_{rig} [19,34]. In the case of a multifrequency response, f_{irr} and f_{rig}, instead, provide an upper bound for the frequency of the lowest energy excitation—an excitation that is difficult to see with experimentally accessible observables. Features of these subdominant modes, including the lack of a strong rotational signal in the low-frequency oscillations and the apparent similarity between the droplet motion (the motion of the halo is quite different) near 25 Hz to that of the dominant rotational mode, remain interesting topics for future investigation.

As we have noted, not only does the dominant angular response frequency fail to approach the rigid-body value in the isolated droplet regime, but it also stays near to the irrotational prediction. A possible intuitive explanation for this observation is that the flow pattern of Fig. 1(a) resembles that of a quadrupolar surface mode, and it is well known that, for sufficiently strong interactions, the frequency of such modes is predominantly determined by the trap parameters, rather than the details of the interparticle interactions [34].

In conclusion, measurements of angular oscillation frequencies offer a simple way to demonstrate superfluidity in certain conditions. However, care must be taken when making and interpreting such measurements—geometrical

changes can mask the effects of changing superfluidity, and usual predictions to which one might compare rely on the assumption of a single-frequency response of the lowest energy rotational mode. While the moment of inertia of the system is defined as the angular momentum of a system in response to a shape-preserving, steady-state drive, oscillation measurements involve a time-localized change in the rotation rate of the trap, which may excite modes that do not meet this criterion. In small, linear systems, the simple excitation spectra means that approximately shape-preserving oscillations can still be excited [31]. However, we find that a supersolid with 2D structure, which one might expect to be an ideal candidate for such measurements, can exhibit an apparently single-frequency response associated with a mode that is not the lowest in energy. Further, this excitation frequency is typically very close to that of a purely superfluid system, even for systems where the effects of superfluidity are minimal. Therefore, such measurements do not provide a robust indicator of superfluidity for modulated systems. In the future, it may be possible to extract information about superfluidity using a modified excitation scheme to preferentially excite the lower energy modes and a more comprehensive analysis scheme suitable for multifrequency response [41]. However, such techniques would require detailed knowledge of the exact excitation applied and measurement of response amplitudes, both of which are considerably more challenging in an experiment than measuring the frequency of an oscillation.

Finally, we note that, even in the case of single-frequency response, where the frequency of angular oscillations has a direct connection to the moment of inertia of the system, making a clear connection between the moment of inertia and quantities like a superfluid fraction can be problematic. Past works have predicted that a system which is partially superfluid should have a moment of inertia in between the RBR and IF predictions, linearly interpolated according to a superfluid fraction [20,38]. While this interpretation may be valid for systems featuring a rigid crystalline structure and a uniform distribution of crystalline and superfluid components, as in [38], it is not necessarily valid for our small dipolar supersolids, which, in addition to coupled superfluid-crystalline excitations, feature a nonuniform degree of modulation across the system.

We thank Sandro Stringari and Alessio Recati for useful discussions. We acknowledge R. M. W. van Bijnen for developing the code for our EGPE ground-state simulations. The experimental team is financially supported through an ERC Consolidator Grant (RARE, Grant No. 681432), an NFRI grant (MIRARE, Grant No. ÖAW0600) of the Austrian Academy of Science, the QuantERA grant MAQS by the Austrian Science Fund FWF Grant No. I4391-N. L. S. and F. F. acknowledge the DFG/FWF via Grant No. FOR 2247/PI2790. L. S. acknowledges funding by the Deutsche Forschungsgemeinschaft (DFG, German Research Foundation) under Germany's Excellence Strategy—Grant No. EXC-2123 QuantumFrontiers—390837967. M. A. N. has received funding as an ESQ Postdoctoral Fellow from the European Union's Horizon 2020 Research and Innovation Programme under the Marie Skłodowska Curie Grant Agreement No. 801110 and the Austrian Federal Ministry of Education, Science and Research (BMBWF). M. J. M. acknowledges support through an ESQ Discovery Grant by the Austrian Academy of Sciences. We also acknowledge the Innsbruck Laser Core Facility, financed by the Austrian Federal Ministry of Science, Research, and Economy. Part of the computational results presented have been achieved using the HPC infrastructure LEO of the University of Innsbruck.

*Corresponding author.
Francesca.Ferlaino@uibk.ac.at

[1] M. R. Matthews, B. P. Anderson, P. C. Haljan, D. S. Hall, C. E. Wieman, and E. A. Cornell, Vortices in a Bose-Einstein Condensate, Phys. Rev. Lett. **83**, 2498 (1999).
[2] K. W. Madison, F. Chevy, W. Wohlleben, and J. Dalibard, Vortex Formation in a Stirred Bose-Einstein Condensate, Phys. Rev. Lett. **84**, 806 (2000).
[3] M. W. Zwierlein, J. R. Abo-Shaeer, A. Schirotzek, C. H. Schunck, and W. Ketterle, Vortices and superfluidity in a strongly interacting Fermi gas, Nature (London) **435**, 1047 (2005).
[4] A. Ramanathan, K. C. Wright, S. R. Muniz, M. Zelan, W. T. Hill, C. J. Lobb, K. Helmerson, W. D. Phillips, and G. K. Campbell, Superflow in a Toroidal Bose-Einstein Condensate: An Atom Circuit with a Tunable Weak Link, Phys. Rev. Lett. **106**, 130401 (2011).
[5] D. Guéry-Odelin and S. Stringari, Scissors Mode and Superfluidity of a Trapped Bose-Einstein Condensed Gas, Phys. Rev. Lett. **83**, 4452 (1999).
[6] D. Bohle, A. Richter, W. Steffen, A. Dieperink, N. L. Iudice, F. Palumbo, and O. Scholten, New magnetic dipole excitation mode studied in the heavy deformed nucleus ^{156}GD by inelastic electron scattering, Phys. Lett. **137B**, 27 (1984).
[7] O. M. Maragò, S. A. Hopkins, J. Arlt, E. Hodby, G. Hechenblaikner, and C. J. Foot, Observation of the Scissors Mode and Evidence for Superfluidity of a Trapped Bose-Einstein Condensed Gas, Phys. Rev. Lett. **84**, 2056 (2000).
[8] M. J. Wright, S. Riedl, A. Altmeyer, C. Kohstall, E. R. Sanchez Guajardo, J. H. Denschlag, and R. Grimm, Finite-Temperature Collective Dynamics of a Fermi Gas in the BEC-BCS Crossover, Phys. Rev. Lett. **99**, 150403 (2007).
[9] R. M. W. van Bijnen, N. G. Parker, S. J. J. M. F. Kokkelmans, A. M. Martin, and D. H. J. O'Dell, Collective excitation frequencies and stationary states of trapped dipolar Bose-Einstein condensates in the Thomas-Fermi regime, Phys. Rev. A **82**, 033612 (2010).
[10] C. D. Rossi, R. Dubessy, K. Merloti, M. de Goër de Herve, T. Badr, A. Perrin, L. Longchambon, and H. Perrin, The scissors oscillation of a quasi two-dimensional Bose gas as a local signature of superfluidity, J. Phys. Conf. Ser. **793**, 012023 (2017).

[11] I. Ferrier-Barbut, M. Wenzel, F. Böttcher, T. Langen, M. Isoard, S. Stringari, and T. Pfau, Scissors Mode of Dipolar Quantum Droplets of Dysprosium Atoms, Phys. Rev. Lett. **120**, 160402 (2018).

[12] M. Boninsegni and N. V. Prokof'ev, Colloquium: Supersolids: What and where are they?, Rev. Mod. Phys. **84**, 759 (2012).

[13] Z.-K. Lu, Y. Li, D. S. Petrov, and G. V. Shlyapnikov, Stable Dilute Supersolid of Two-Dimensional Dipolar Bosons, Phys. Rev. Lett. **115**, 075303 (2015).

[14] D. Baillie and P. B. Blakie, Droplet Crystal Ground States of a Dipolar Bose Gas, Phys. Rev. Lett. **121**, 195301 (2018).

[15] S. M. Roccuzzo and F. Ancilotto, Supersolid behavior of a dipolar Bose-Einstein condensate confined in a tube, Phys. Rev. A **99**, 041601(R) (2019).

[16] L. Tanzi, E. Lucioni, F. Famà, J. Catani, A. Fioretti, C. Gabbanini, R. N. Bisset, L. Santos, and G. Modugno, Observation of a Dipolar Quantum Gas with Metastable Supersolid Properties, Phys. Rev. Lett. **122**, 130405 (2019).

[17] F. Böttcher, J.-N. Schmidt, M. Wenzel, J. Hertkorn, M. Guo, T. Langen, and T. Pfau, Transient Supersolid Properties in an Array of Dipolar Quantum Droplets, Phys. Rev. X **9**, 011051 (2019).

[18] L. Chomaz, D. Petter, P. Ilzhöfer, G. Natale, A. Trautmann, C. Politi, G. Durastante, R. M. W. van Bijnen, A. Patscheider, M. Sohmen, M. J. Mark, and F. Ferlaino, Long-Lived and Transient Supersolid Behaviors in Dipolar Quantum Gases, Phys. Rev. X **9**, 021012 (2019).

[19] S. M. Roccuzzo, A. Gallemí, A. Recati, and S. Stringari, Rotating a Supersolid Dipolar Gas, Phys. Rev. Lett. **124**, 045702 (2020).

[20] L. Tanzi, J. Maloberti, G. Biagioni, A. Fioretti, C. Gabbanini, and G. Modugno, Evidence of superfluidity in a dipolar supersolid from nonclassical rotational inertia, Science **371**, 1162 (2021).

[21] E. Kim and M. H.-W. Chan, Probable observation of a supersolid helium phase, Nature (London) **427**, 225 (2004).

[22] D. Y. Kim and M. H. W. Chan, Absence of Supersolidity in Solid Helium in Porous Vycor Glass, Phys. Rev. Lett. **109**, 155301 (2012).

[23] Here, the word droplet refers to a high-density region, which is not necessarily self-bound.

[24] J.-N. Schmidt, J. Hertkorn, M. Guo, F. Böttcher, M. Schmidt, K. S. H. Ng, S. D. Graham, T. Langen, M. Zwierlein, and T. Pfau, Roton Excitations in an Oblate Dipolar Quantum Gas, Phys. Rev. Lett. **126**, 193002 (2021).

[25] M. A. Norcia, C. Politi, L. Klaus, E. Poli, M. Sohmen, M. J. Mark, R. Bisset, L. Santos, and F. Ferlaino, Two-dimensional supersolidity in a dipolar quantum gas, Nature (London) **596**, 357 (2021).

[26] J. Hertkorn, J.-N. Schmidt, M. Guo, F. Böttcher, K. S. H. Ng, S. D. Graham, P. Uerlings, H. P. Büchler, T. Langen, M. Zwierlein, and T. Pfau, Supersolidity in Two-Dimensional Trapped Dipolar Droplet Arrays, Phys. Rev. Lett. **127**, 155301 (2021).

[27] T. Bland, E. Poli, C. Politi, L. Klaus, M. A. Norcia, F. Ferlaino, L. Santos, and R. N. Bisset, Two-Dimensional Supersolid Formation in Dipolar Condensates, Phys. Rev. Lett. **128**, 195302 (2022).

[28] E. Poli, T. Bland, C. Politi, L. Klaus, M. A. Norcia, F. Ferlaino, R. N. Bisset, and L. Santos, Maintaining supersolidity in one and two dimensions, Phys. Rev. A **104**, 063307 (2021).

[29] A. Trautmann, P. Ilzhöfer, G. Durastante, C. Politi, M. Sohmen, M. J. Mark, and F. Ferlaino, Dipolar Quantum Mixtures of Erbium and Dysprosium Atoms, Phys. Rev. Lett. **121**, 213601 (2018).

[30] M. Sohmen, C. Politi, L. Klaus, L. Chomaz, M. J. Mark, M. A. Norcia, and F. Ferlaino, Birth, Life, and Death of a Dipolar Supersolid, Phys. Rev. Lett. **126**, 233401 (2021).

[31] See Supplemental Material at http://link.aps.org/supplemental/10.1103/PhysRevLett.129.040403 for more information, which contains refs. [32,33].

[32] I. T. Jolliffe, *Principal Component Analysis*, Springer Series in Statistics (Springer, New York, 2002).

[33] R. Dubessy, C. D. Rossi, T. Badr, L. Longchambon, and H. Perrin, Imaging the collective excitations of an ultracold gas using statistical correlations, New J. Phys. **16**, 122001 (2014).

[34] L. Pitaevskii and S. Stringari, *Bose-Einstein Condensation and Superfluidity* (Oxford University Press, New York, 2016), Vol. 164.

[35] I. Ferrier-Barbut, H. Kadau, M. Schmitt, M. Wenzel, and T. Pfau, Observation of Quantum Droplets in a Strongly Dipolar Bose Gas, Phys. Rev. Lett. **116**, 215301 (2016).

[36] L. Chomaz, S. Baier, D. Petter, M. J. Mark, F. Wächtler, L. Santos, and F. Ferlaino, Quantum-Fluctuation-Driven Crossover from a Dilute Bose-Einstein Condensate to a Macrodroplet in a Dipolar Quantum Fluid, Phys. Rev. X **6**, 041039 (2016).

[37] F. Wächtler and L. Santos, Quantum filaments in dipolar Bose–Einstein condensates, Phys. Rev. A **93**, 061603(R) (2016).

[38] A. J. Leggett, Can a Solid be "Superfluid"?, Phys. Rev. Lett. **25**, 1543 (1970).

[39] We note that the geometry of our system is very different from that considered in Ref. [38], and so, we do not expect this quantity to have a direct connection to the nonclassical moment of inertia of the system. Rather, we simply use it as a convenient way to quantify overlap between droplets.

[40] Edmundo R. Sanchez Guajardo, M. K. Tey, L. A. Sidorenkov, and R. Grimm, Higher-nodal collective modes in a resonantly interacting Fermi gas, Phys. Rev. A **87**, 063601 (2013).

[41] S. M. Roccuzzo, A. Recati, and S. Stringari, Moment of inertia and dynamical rotational response of a supersolid dipolar gas, Phys. Rev. A **105**, 023316 (2022).

Supplemental materials for: Can angular oscillations probe superfluidity in dipolar supersolids?

Matthew A. Norcia,[1] Elena Poli,[2] Claudia Politi,[1,2] Lauritz Klaus,[1,2] Thomas Bland,[1,2] Manfred J. Mark,[1,2] Luis Santos,[3] Russell N. Bisset,[2] and Francesca Ferlaino[1,2,*]

[1] *Institut für Quantenoptik und Quanteninformation, Österreichische Akademie der Wissenschaften, Innsbruck, Austria*
[2] *Institut für Experimentalphysik, Universität Innsbruck, Austria*
[3] *Institut für Theoretische Physik, Leibniz Universität Hannover, Germany*

EXCITATION PROTOCOL

In both experiment and simulation, we excite the atoms by suddenly rotating the trap, holding for 6 ms, then returning it to its initial orientation. This was important in the experiment, as the trap frequencies generally change slightly as the trap is rotated, and we want to observe the evolution of a state that is equilibrated to the trap prior to the rotation. To explore whether the exact excitation protocol influences our results, we performed additional simulations where the trap angle was rotated and held in the new orientation, but not rotated back. We find that the same modes are excited in this case, and the frequency of their responses are the same. For some parameters the relative contributions of the modes to the spectrum of $\langle xy \rangle$ can differ between the two protocols, but for the parameters we explore the frequency of the peak response remains unchanged. In particular, for the droplet crystal hexagon shown in Fig. 4c of the main text, the contribution of the low-frequency mode to the $\langle xy \rangle$ power spectrum becomes appreciable, though is still smaller than the contribution of the modes near 60 Hz. Thus, the multimode response appears to be a generic feature of possible schemes to excite angular oscillations. While the spectral content of the excitation may differ, influencing the relative amplitudes of different modes, the frequency and character of the modes is determined by the system, not the drive.

We have also performed excitation in the simulation by directly imprinting a small phase variation αxy onto the ground-state wavefunction. This protocol produces qualitatively similar results to those described above. Again, the same modes are excited and respond with the same frequencies, though sometimes with different amplitudes. The dominant mode excited is the same as the rotate-and-return protocol for all cases investigated.

EXTRACTING ANGULAR POWER SPECTRUM

Several methods can be used to extract the angular response of our system. For the experiment, we perform a two-dimensional Gaussian fit to the in-trap image, and record the angle of the major and minor axes as a function of time. For the simulation, we report the angular response obtained using one of two observables. For direct comparison to the experiment, we use the state angle extracted from a 2D Gaussian fit, as in the experiment. For more detailed spectral analysis, we use the quantity $\langle xy \rangle$, as this is expected to have a strong response to a rapid rotation of the trap and we find it to be numerically more robust. We have confirmed that these and other similar observables, such as the directions of maximal and minimal variance, provide consistent results (up to overall normalization). In some cases, the Fourier spectrum of $\langle \hat{L}_z \rangle$ (though not experimentally accessible) shows different relative response amplitudes between modes compared to $\langle xy \rangle$, particularly for those modes at low frequencies.

FOURIER TRANSFORM IMAGE ANALYSIS

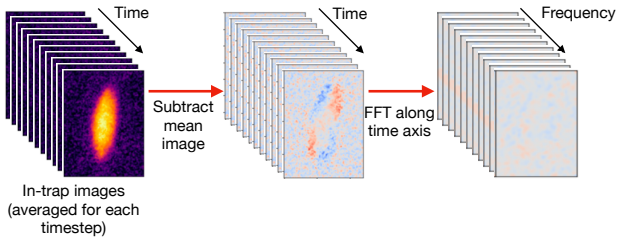

FIG. S1. Procedure for Fourier transform image analysis (FTIA). See text for description.

The goal of our Fourier transform image analysis (FTIA) protocol is to visualize the density response of our atomic system in real-space with respect to position, but in frequency space with respect to time. This provides a simple way to extract the spatial profile of excitation modes. The process is illustrated in Fig. S1. To perform the FTIA, we assemble images of projected density profiles corresponding to single time-steps (directly from the simulation, or averaged over several in-trap images from the experiment), then subtract the average (over all time-steps) image from each. We then Fourier transform the results along the time axis. The output is then a sequence of real-space images, showing the fluctuation pattern at a given frequency. Because each pixel is now represented

by a complex number (encoding the amplitude and phase of the density variations at that location), we plot with respect to the global phase for each frequency that shows maximum variation, thus plotting the in-phase quadrature of the oscillation.

In order to obtain a power spectrum (useful for locating the frequencies of excited modes), we compute the sum of the absolute square of the fluctuations over a region of interest containing the atomic cloud for each frequency. This power spectrum can be used to identify the frequency and spatial character of modes, but is not expressed in physically meaningful units, and so should not necessarily be used to compare the strength of different mode responses.

We note that there are some similarities between the FTIA method and principal component analysis (PCA) [1, 2]. Both provide a model-free way of extracting the form of excitations present in a system. PCA does so by finding correlated patterns of fluctuations within a set of images, with no prior information about the time-sequence of the images. This makes it well-suited to revealing modes that are excited incoherently, for example by thermal or quantum noise. In contrast, our FTIA method explicitly incorporates the time-domain information associated with the images. This makes it well-suited to extracting modes that are coherently excited (FTIA, as we apply it, would not work for incoherently excited modes). In practice, we find that the FTIA is more robust than PCA at extracting fluctuation patterns that each exhibit a single-frequency response. While PCA often returns components whose weights vary with multiple frequencies (indicating that they actually correspond to a linear combination of eigenmodes), FTIA by construction returns a fluctuation pattern associated with a single frequency. We find that this feature makes it more robust for identifying eigenmodes of a system subject to a coherent drive.

SPECTRA/TABLE FOR ALL PARAMS

Excitation power spectra from simulation for a range of traps and scattering lengths used in the main manuscript can be found in Fig. S2.

PREDICTIONS FOR ROTATIONAL MODE FREQUENCIES

The rotational response of a gas can be calculated using hydrodynamic equations [3] or a sum-rule approach [4, 5]. From the sum-rule approach, an expression can be derived for the rotational oscillation frequency, under the assumption that the response is single-frequency:

$$\omega^2 = \frac{m\langle y^2 - x^2\rangle(\omega_x^2 - \omega_y^2)}{\Theta} \tag{1}$$

Here, Θ is the moment of inertia associated with steady-state rotation.

The numerator of Eq. 1 can be interpreted as a rotational spring constant: $k_\tau = -\tau/\theta$, where τ is the torque exerted on a state whose major and minor axes y and x are rotated relative to the their equilibrium position in the trap by an angle θ. To see this, consider a mass element m at position (x, y) in a trapping potential $V = (m\omega_x x^2 + m\omega_y y^2)/2$, which exerts a torque $\tau = xF_y - yF_x = xym(\omega_x^2 - \omega_y^2)$. We can then calculate $k_\tau = -\partial\tau/\partial\theta = -m(y\partial x/\partial\theta + x\partial y/\partial\theta)(\omega_x^2 - \omega_y^2) = m(y^2 - x^2)(\omega_x^2 - \omega_y^2)$. Summing over mass elements provides the numerator of Eq. 1. This highlights that the numerator of this expression is purely geometrical, independent of whether the state is superfluid or classical. In the case of multi-frequency response, Eq. 1 (as defined by the sum rule) becomes an inequality, defining the upper bound for the lowest frequency angular excitation in the system [4].

BETA VERSUS SCATTERING LENGTH FOR 1D AND 2D

In Fig. S3, we show the change in the anisotropy of the atomic state in response to a change in scattering length for a variety of traps, featuring both linear and 2D array modulated configurations. Here, we consider the quantity $\beta^2 = (\langle x^2 - y^2\rangle/\langle x^2 + y^2\rangle)^2$, as this quantity gives the expected change in moment of inertia between irrotational flow (IF) and rigid-body rotation (RBR). As β^2 approached unity, the difference between the two vanishes, so such states can exhibit minimal sensitivity to superfluidity.

States in more elongated traps generally have values of β^2 closer to one than their rounder counterparts. However, even in relatively round traps, such as those of Refs. [5, 6], low atom numbers can lead to the formation of linear arrays, which are highly elongated. In these cases, the sensitivity of the state to superfluidity is dramatically reduced upon entering the modulated regime. In contrast, combinations of trap parameters and atom number that lead to a 2D modulated state typically maintain values of β^2 substantially different from one even in the low scattering length, independent droplet regime.

LINEAR CASE

In Fig. S4, we explore the parameters of refs [5, 6], where a change in scattering length induces a transition from an unmodulated BEC to a linear array of two droplets. This transition is accompanied by a dramatic change in the aspect ratio of the atomic state, as evident in the near convergence of the predictions for rigid body

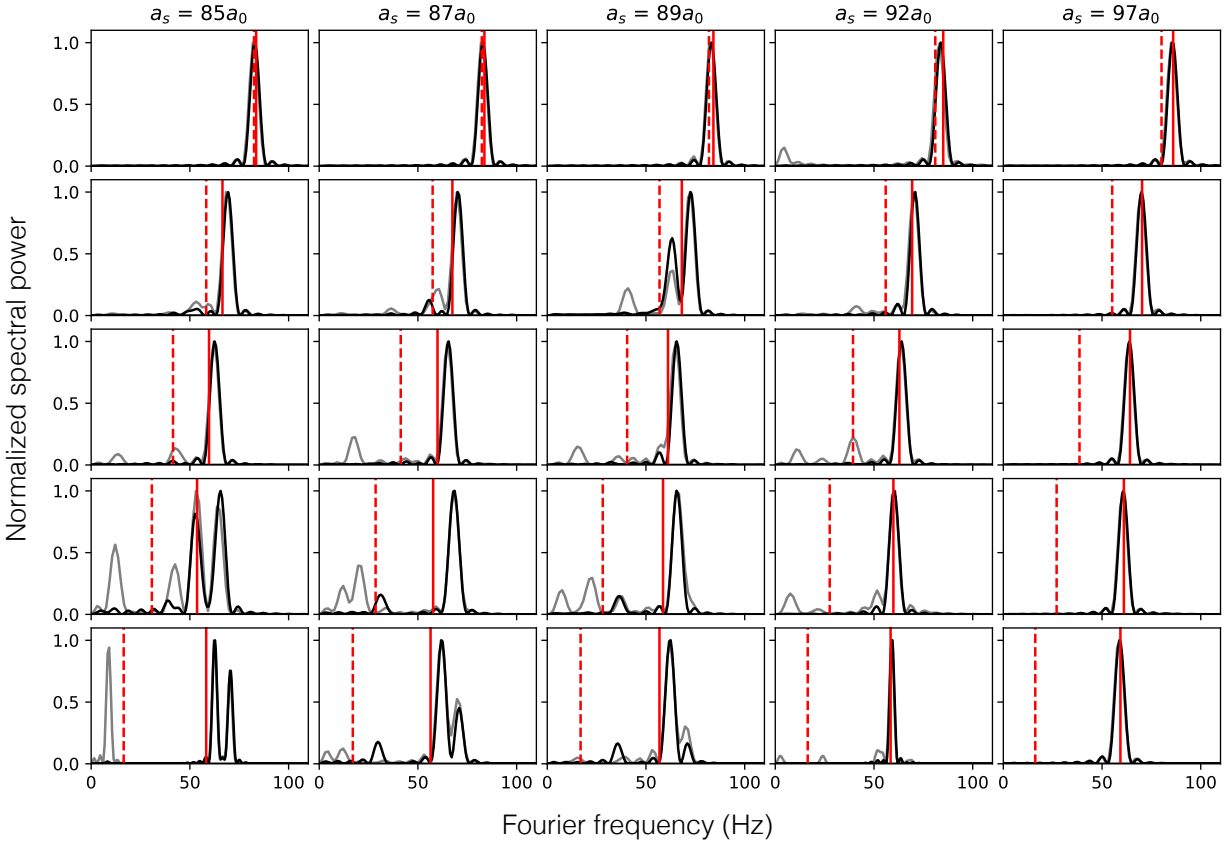

FIG. S2. Response sepctra extracted from simulations for different trap parameters (rows) and scattering lengths (columns). Upper rows correspond to more elongated traps, while lower rows correspond to more round ones. From top to bottom, $(f_x, f_y) = [(26, 87), (32, 70), (37, 62), (40, 57), (43, 53)]$ Hz. $f_z = 122$ Hz for all cases. Red vertical dashed and solid lines correspond to the rigid-body rotation and irrotational flow predictions, respectively. Gray traces are power spectra extracted from FTIA, while black traces are from $\langle xy \rangle$. In all cases, $a_s = 97a_0$ corresponds to an unmodulated BEC, while lower scattering lengths correspond to modulated states, with the overlap between droplets decreasing with scattering length. $(f_x, f_y) = (26, 87)$ is a linear droplet chain for all scattering lengths that produce a modulated state. All other modulated states have transverse structure, increasing in prevalence as the trap becomes more round.

and irrotational flow ($f_{\rm rig}$ and $f_{\rm irr}$) at lower scattering lengths, corresponding to the droplet state.

We see that the dominant frequency of angular response is between $f_{\rm rig}$ and $f_{\rm irr}$, indicating a change in the level of superfluidity in the system. We find that the angular response in the supersolid regime ($a_s = 90$ or 92 a_0) has two clear frequency components, though in this case the dominant frequency observed matches the prediction from the sum rule (with moment of inertia calculated under static rotation). Because of the geometry of the system, rotation does not lead to a significant transfer of mass between the two droplets. Thus, we attribute the change in superfluidity to the low-density halo that surrounds the droplets, rather than the inter-droplet connection itself.

* Correspondence should be addressed to Francesca.Ferlaino@uibk.ac.at

[1] I. T. Jolliffe, *Principal Component Analysis* (Springer Series in Statistics. Springer, New York, NY, 2002).
[2] R. Dubessy, C. D. Rossi, T. Badr, L. Longchambon, and H. Perrin, Imaging the collective excitations of an ultracold gas using statistical correlations, New Journal of Physics **16**, 122001 (2014).
[3] D. Guéry-Odelin and S. Stringari, Scissors mode and superfluidity of a trapped bose-einstein condensed gas, Phys. Rev. Lett. **83**, 4452 (1999).
[4] L. Pitaevskii and S. Stringari, *Bose-Einstein condensation and superfluidity*, Vol. 164 (Oxford University Press, 2016).
[5] S. M. Roccuzzo, A. Gallemí, A. Recati, and S. Stringari, Rotating a supersolid dipolar gas, Phys. Rev. Lett. **124**, 045702 (2020).
[6] L. Tanzi, J. Maloberti, G. Biagioni, A. Fioretti, C. Gab-

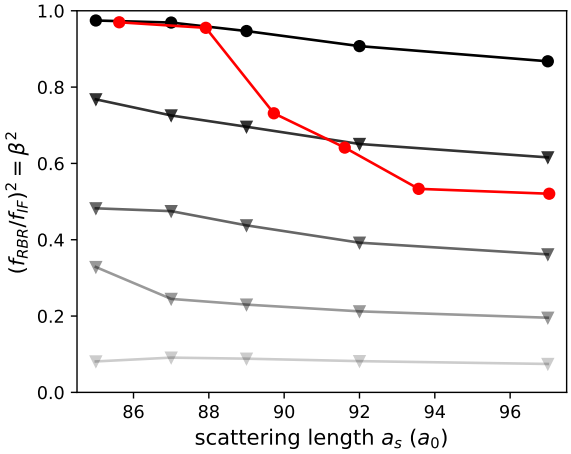

FIG. S3. Difference in moment of inertia between IF and RBR, β^2 for different traps and scattering lengths. Traps and atom numbers that correspond to linear arrays for modulated states are indicated by round markers, while those that correspond to 2D modulated arrays are indicated by triangles. All points except those at $a_s = 97a_0$ are modulated, interdroplet connection decreasing with scattering length. The states explored in Fig. S2 are shown in grey-scale, with lighter saturation corresponding to rounder traps, while the conditions similar to those of Refs. [5, 6] are shown in red.

banini, and G. Modugno, Evidence of superfluidity in a dipolar supersolid from nonclassical rotational inertia, Science **371**, 1162 (2021).

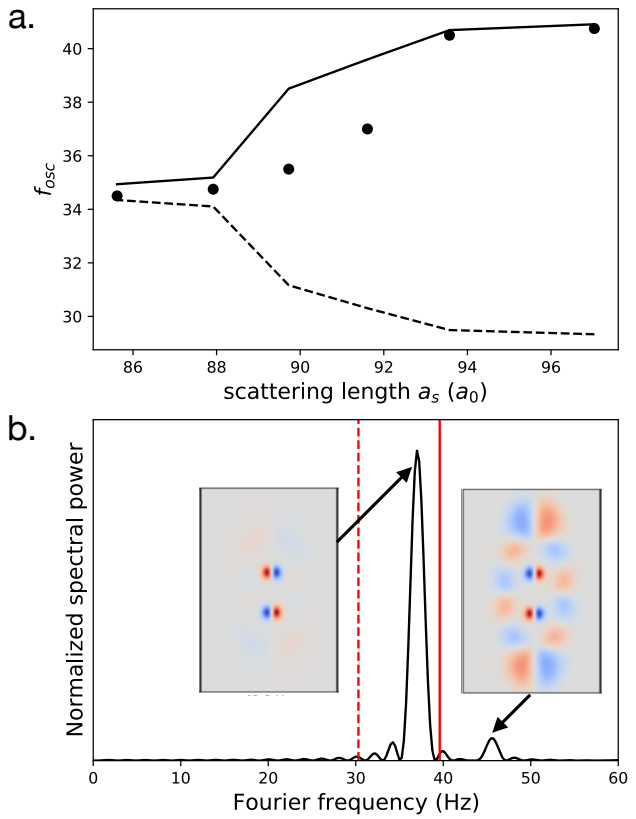

FIG. S4. Analysis of linear two-droplet arrays of [5, 6]. **a.** Dominant angular oscillation frequency (markers) extracted from simulations versus scattering length, through transition from BEC (right) to isolated droplets (left). The irrotational and rigid-body predictions $f_{\rm irr}$ and $f_{\rm rig}$ are shown as solid and dashed lines, respectively. **b.** The Fourier spectrum of $\langle xy \rangle$ for the point near $a_s = 92a_0$ exhibits a response with dominant and sub-dominant mode contributions. The fluctuation profiles associated with these two frequencies are shown in the insets. Solid and dashed vertical red lines represent $f_{\rm irr}$ and $f_{\rm rig}$, respectively.

4.9 Publication VII:

Heating a quantum dipolar fluid into a solid

The following publication has appeared in

arXiv:2209.00335 (2022)**
DOI: https://arxiv.org/abs/2209.00335
J. Sánchez-Baena,[3,4] C. Politi,[1,2] F. Maucher,[3,5] F. Ferlaino,[1,2] and T. Pohl[3]

[1] *Institut für Quantenoptik und Quanteninformation, Österreichische Akademie der Wissenschaften, 6020 Innsbruck, Austria*

[2] *Institut für Experimentalphysik, Universität Innsbruck, 6020 Innsbruck, Austria*

[3] *Center for Complex Quantum Systems, Department of Physics and Astronomy, Aarhus University, DK-8000 Aarhus C, Denmark*

[4] *Departament de Física, Universitat Politècnica de Catalunya, Campus Nord B4-B5, 08034 Barcelona, Spain*

[5] *Departament de Física, Universitat de les Illes Balears & IAC-3, Campus UIB, E-07122 Palma de Mallorca, Spain*

**The author of the present thesis performed the measurements, analysed the data with J. S., and contributed in writing the manuscript and interpreting the results together with all the authors.

Heating a quantum dipolar fluid into a solid

J. Sánchez-Baena,[1,2,*] Claudia Politi,[3,4] F. Maucher,[5,1] Francesca Ferlaino,[3,4] and T. Pohl[1]

[1] *Center for Complex Quantum Systems, Department of Physics and Astronomy, Aarhus University, DK-8000 Aarhus C, Denmark*

[2] *Departament de Física, Universitat Politècnica de Catalunya, Campus Nord B4-B5, 08034 Barcelona, Spain*

[3] *Institut für Quantenoptik und Quanteninformation, Österreichische Akademie der Wissenschaften, Innsbruck, Austria*

[4] *Institut für Experimentalphysik, Universität Innsbruck, Austria*

[5] *Departament de Física, Universitat de les Illes Balears & IAC-3, Campus UIB, E-07122 Palma de Mallorca, Spain*

(Dated: September 2, 2022)

Raising the temperature of a material enhances the thermal motion of particles. Such an increase in thermal energy commonly leads to the melting of a solid into a fluid and eventually vaporises the liquid into a gaseous phase of matter. Here, we study the finite-temperature physics of dipolar quantum fluids and find surprising deviations from this general phenomenology. In particular, we describe how heating a dipolar superfluid from near-zero temperatures can induce a phase transition to a supersolid state with a broken translational symmetry. The predicted effect agrees with experimental measurements on ultracold dysprosium atoms, which opens the door for exploring the unusual thermodynamics of dipolar quantum fluids.

A supersolid is an exotic phase of matter in which particles develop regular spatial order and simultaneously support the frictionless flow of a superfluid. Having evaded experimental verification for several decades [1], supersolidity can now be observed in Bose-Einstein condensates of ultracold atoms with finite-range interactions [2–6]. Spontaneous symmetry breaking in these systems occurs in the form of regular periodic patterns of the condensate density as first predicted by Gross in 1957 [7]. One would thus expect the lowest possible temperatures to provide optimal conditions for supersolidity by ensuring a high degree of phase coherence and maximal population of the Bose-Einstein condensate. On the contrary, we demonstrate here that thermal fluctuations in dipolar condensates do not merely diminish global phase coherence but can instead facilitate the formation of periodic modulations of the condensate density. This finding sheds light on recent experimental observations and reveals an unusual fluid-solid phase transition, whereby a supersolid state of matter emerges upon increasing the temperature.

As we shall see below, this surprising behaviour arises from the anisotropic nature of the dipole-dipole interaction

$$V_{\rm dd}(\mathbf{r}) = \frac{C_3}{4\pi}\frac{1-3\cos^2\theta}{r^3}, \qquad (1)$$

which has repulsive as well as attractive contributions, depending on the angle θ between the atomic dipoles and the distance vector $\mathbf{r}$ of two interacting atoms. The interaction strength C_3 and the atomic mass m define a length scale $a_d = mC_3/(12\pi\hbar^2)$ that competes with the scattering length a of the short-range interaction between the atoms. This competition between a_d and $a > 0$ can cause the condensate to collapse when the stabilizing short-range repulsion is not sufficient to overcome the

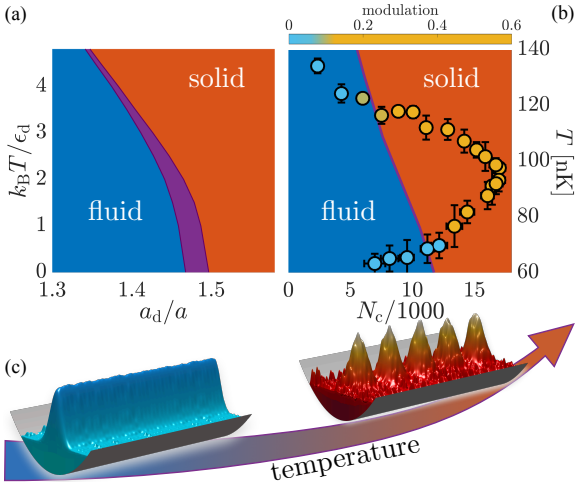

FIG. 1. Heating a dipolar quantum fluid can lead to the emergence of a supersolid phase of matter. (a) This is demonstrated in the thermodynamic phase diagram for an infinitely elongated Bose-Einstein condensate in a radial harmonic trap with no axial confinement, as illustrated in panel (c). In between the superfluid (blue) and supersolid (red) region, both phases coexist (purple region) as characteristic for a first-order phase transition. The calculations were performed for a fixed chemical potential $\mu/\epsilon_d = 1$, where $\epsilon_d = \hbar^2/((12\pi)^2 m a_d^2)$ parametrizes the characteristic energy scale of the dipole-dipole interactions. Our experiments in an ultracold gas of dysprosium atoms demonstrate the temperature-driven emergence of supersolidity. The measured contrast of axial density modulations is shown by the colored dots in panel (b). The observations show that supersolidity at higher temperatures indeed occurs for smaller atom numbers, $N_{\rm c}$ in the condensate, in agreement with the theoretical transition line (purple line).

* jsbaena@phys.au.dk

attractive part of the dipole-dipole interaction between the atoms [8–10]. Subsequent experiments [11–13] have however found a higher level of stability, which arises from quantum fluctuations [14, 15] that prevent the otherwise inevitable collapse of the condensate [16–18]. In fact, the balance of attraction and repulsion effectively enhances the role of quantum fluctuations [17] beyond the semiclassical mean-field physics of weakly interacting quantum gases. This yields a unique setting that has revealed rich physics and a host of new quantum states, from self-bound quantum droplets [12, 13, 19] and supersolid phases [3–5, 20, 21] to complex patterns in two-dimensional fluids [22, 23].

Given this striking role of quantum fluctuations in dipolar Bose-Einstein condensates, one may also anticipate significant effects of thermal fluctuations despite the ultralow temperatures that are required to reach quantum degeneracy. To address this question we start from the grand canonical potential Ω of the system at a finite temperature T. For a weakly interacting gas with a high fraction of atoms in the condensate, one can use Bogoliubov theory to determine Ω. This yields simple expressions for infinitely extended homogeneous systems [24] that can be applied to describe trapped inhomogeneous gases within a local density approximation. Hereby, one determines the Bogoliubov excitation spectrum and all relevant observables for a homogeneous particle density ρ, which is then identified as $\rho \equiv |\psi(\mathbf{r})|^2$ with the local condensate wave function $\psi(\mathbf{r})$ at a given position $\mathbf{r}$. This permits to express the grand canonical potential as

$$\Omega = E_0 + \frac{k_\mathrm{B}T}{(2\pi)^3}\int d\mathbf{r}\int d\mathbf{k}\ \ln\left(1 - e^{-\frac{\varepsilon_\mathbf{k}(\mathbf{r})}{k_\mathrm{B}T}}\right), \qquad (2)$$

where k_B denotes the Boltzmann constant and E_0 is the zero-temperature grand canonical energy that contains the mean-field interaction energy and leading order corrections due to quantum fluctuations [14], i.e. small occupations of excited states above the formed Bose-Einstein condensate. The dispersion $\varepsilon_\mathbf{k} = \sqrt{\tau_\mathbf{k}(\tau_\mathbf{k} + 2|\psi(\mathbf{r})|^2\tilde{V}(\mathbf{k}))}$ of these excitations is determined by the kinetic energy $\tau_\mathbf{k} = \hbar^2k^2/(2m)$ of the atoms and the Fourier transform $\tilde{V}(\mathbf{k}) = \frac{4\pi\hbar^2 a}{m} + \tilde{V}_\mathrm{dd}(\mathbf{k})$ of their total interaction potential.

Minimizing Ω with respect to $\psi(\mathbf{r})$ then yields a nonlinear wave equation that accounts for quantum as well as thermal fluctuations (see Methods Section). At zero temperature, it describes the mean-field physics of the condensate and captures leading-order effects of quantum fluctuations through an effective density-dependent potential H_qu [17] that increases the energy of the system. The second term in Eq.(2) yields an additional potential

$$H_\mathrm{th}(\mathbf{r}) = \int \frac{\mathrm{d}\mathbf{k}}{(2\pi)^3}\tilde{V}(\mathbf{k})f_\mathbf{k}(\mathbf{r})\frac{\tau_\mathbf{k}}{\varepsilon_\mathbf{k}(\mathbf{r})}, \qquad (3)$$

that accounts for finite-temperature effects. It describes the interaction between the condensate and thermally created excitations that populate Bogoliubov modes according to the Bose distribution $f_\mathbf{k} = 1/(e^{\varepsilon_\mathbf{k}/k_\mathrm{B}T} - 1)$. The resulting form of the finite-temperature extended Gross-Pitaevskii equation (TeGPE) agrees with the result of Hartree-Fock Bogoliubov theory [24, 25], and includes relevant fluctuation terms that are commonly neglected within the Popov approximation [26] (see Methods Section).

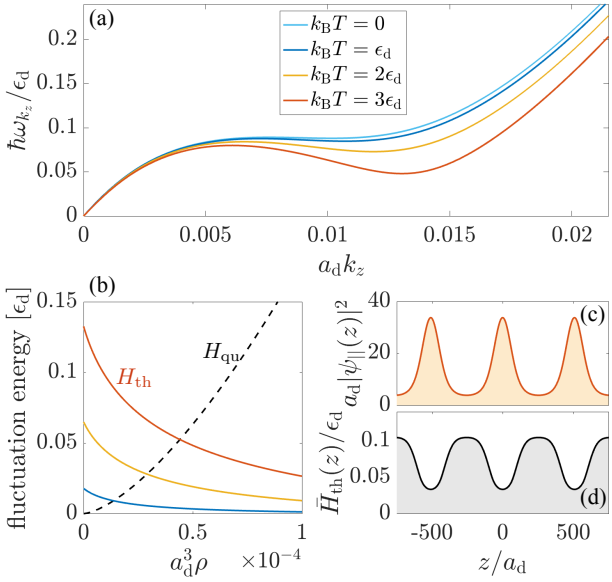

FIG. 2. Raising the temperature of a dipolar quantum fluid can induce a pronounced roton-maxon spectrum of its collective excitations, as shown in panel (a) for an infinitely elongated condensate along the z-axis [see Fig.1(c)]. Heating the fluid tends to lower the energy of the roton minimum and eventually softens the roton excitation as the temperature increases. This effect can be traced back to the density dependence of the energy correction caused by fluctuations, shown in panel (b). While quantum fluctuations yield an energy H_qu (dashed line) that increases with a rising condensate density $\rho = |\psi|^2$, the contribution H_th from thermal fluctuations decreases (solid lines). The thermal energy correction $H_\mathrm{th}(\mathbf{r})$, therefore, acts as a focusing nonlinearity that supports the formation of regular density modulations. This is illustrated in panel (c,d), where we show the axial density $\rho_{||}(z) = \int \mathrm{d}x\mathrm{d}y\rho(\mathbf{r})$ along with the axial potential $\bar{H}_\mathrm{th} = \rho_{||}^{-1}\int \mathrm{d}x\mathrm{d}y\rho(\mathbf{r})\bar{H}_\mathrm{th}(\mathbf{r})$, respectively. The calculations are performed for $a/a_\mathrm{d} = 0.7$ and $\mu = \varepsilon_\mathrm{d}$.

Let us first use this framework to study an elongated atomic gas that is confined harmonically in the $x-y$ plane and extends infinitely in the z-direction without confinement along the z-axis. Figure 1(a) shows the thermodynamic phase diagram obtained by simulating the imaginary time evolution of the TeGPE at a fixed chemical potential μ (see Methods Section). At zero temperature, we find a superfluid-supersolid quantum phase transition, with a co-existence region that is expected for a first-order phase transition [27]. While increasing the temperature may generally be expected to melt the

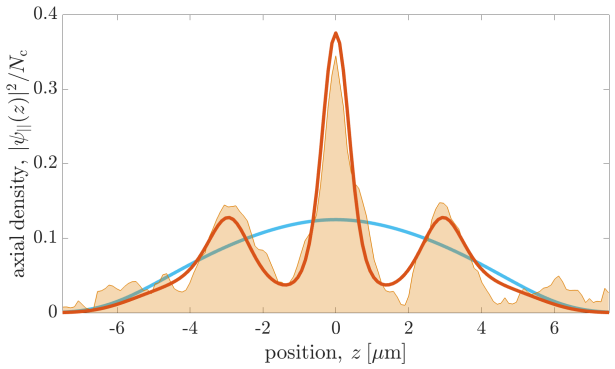

FIG. 3. Our measured axial density $|\psi_{||}(z)|^2$ (filled area), observed for $T = 76.5$ nK and $N_c = 13400$ condensate atoms, demonstrates the formation of a supersolid state and agrees well with the numerical simulation of the TeGPE (red line). On the other hand, equivalent simulations at zero temperature (blue line) disagree qualitatively and instead yield an unmodulated superfluid phase.

supersolid phase [28], we find instead that it shifts the transition towards weaker dipole-dipole interactions. As a result, heating the system effectively drives a phase transition from a fluid into a solid phase.

We can understand this effect from the excitation spectrum of the condensate in the superfluid phase. To this end, we solve the time-dependent TeGPE within linear response theory to find the excitation spectrum ω_{k_z} for periodic plane-wave excitations along the z-direction. As shown in Fig.2, the obtained dispersion exhibits the expected roton-maxon form [29–32], known from low-temperature helium [33] and Bose-Einstein condensates with finite-range interactions [34–37]. The local minimum at finite momenta supports the formation of roton quasiparticles, which were introduced by Landau as elementary vortices to describe superfluidity in ^{4}He [33]. Experiments show that the roton minimum in helium decreases with increasing temperature [38] due to roton-roton scattering [39]. Yet, the roton energy remains sizable at the transition to a normal-fluid phase [38], beyond which it only varies weakly with temperature. The presence of a Bose-Einstein condensate in dilute dipolar superfluids, however, enhances the effect of thermal fluctuations due to the larger energy scale of the interaction between Bogoliubov excitations and the condensate. A similar effect is found for atoms with light-induced interactions and predicted to lower the roton minimum and cause enhanced condensate depletion [40]. In the present case, we find a thermal softening of the roton mode that can drive an instability of the superfluid and thereby cause the formation of a supersolid phase with increasing temperature.

We can gain further intuition about the underlying mechanism by closer inspection of the two fluctuation energies $H_{\rm qu}$ and $H_{\rm th}$ that both contribute a local nonlinearity to the wave equation for $\psi(\mathbf{r})$. $H_{\rm qu} > 0$ is the Lee-Huang-Yang correction to the equation of state [14, 15], and raises the ground state energy due to the small condensate depletion caused by the atomic interactions. It therefore increases for higher particle densities and stronger interactions, as shown in Fig. 2(b). Consequently, $H_{\rm qu}$ generates an effective repulsion that stabilizes the condensate against collapse [17], and shifts the roton instability towards higher densities and stronger dipole-dipole interactions. On the contrary, $H_{\rm th}$ increases as we lower the density of the condensate [see Fig.2(b)]. This behaviour is readily understood as follows. Decreasing the condensate density increases the fraction of thermally excited, non-condensed atoms [25]. In the limit where this fraction remains small, such an increase implies a larger potential energy due to interactions with the thermal atoms. It therefore contributes a positive energy correction that decreases upon increasing the density $\rho = |\psi|^2$ of the condensate. As a result, thermal fluctuations energetically favour higher condensate densities, such that $H_{\rm th}$ acts as a focusing nonlinearity which lowers the roton energy and facilitates the formation of a density-modulated phase, as illustrated in Fig.2c.

We recently observed experimental signatures of this effect by studying the cooling-heating lifecycle of bosonic dysprosium atoms at ultralow temperatures [41]. The experiment starts from a thermal cloud of 10^5 atoms in a cigar-shaped optical dipole trap and traces the time evolution of the gas as it is cooled evaporatively to quantum degeneracy by lowering the depth of the trap. During the continual cooling and thermalization we observed the expected emergence of supersolidity, and studied the equilibrium states of the quantum fluid across the supersolid phase transition. The measured density profiles indicate a higher degree of modulation at higher temperatures. While this has cast mystery on the origin of the observations, they can now be used to corroborate and benchmark our theoretical understanding . Figure 1b shows our measured contrast of the axial density modulations for different temperatures and condensed-atom numbers (see Methods Section). The results confirm the formation of a supersolid phase with increasing temperature in good agreement with the theoretical transition line obtained numerically by the TeGPE. Moreover, Fig. 3 compares our measured axial density, $\rho_{||}(z)$, to the theoretical prediction. The predicted zero-temperature ground state corresponds to an unstructured superfluid and deviates qualitatively from the observed supersolid state. The result of our finite-temperature TeGPE simulation, however, agrees with the experiment and reproduces quantitatively the period and amplitude of the measured density modulations. This remarkable level of agreement offers strong indication that the observed supersolid has indeed been generated by the finite temperature of the atoms.

The possibility to make detailed comparisons between theory and experiments opens up several directions for exploring the surprising thermodynamic behaviour of quantum ferrofluids. Already, the ground state phase diagram exhibits a rich structure, including first-order as

well as second-order quantum phase transitions in one and two-dimensional systems [27, 42, 43]. This offers a promising starting point for investigating how thermal fluctuations influence the nature of the fluid-solid phase transition and may affect the physics of higher dimensional supersolids [44, 45], which can come in a diverse range of complex patterns [22, 23, 42]. Our present findings motivate future experiments and first-principle simulations [46, 47] to expand the phase diagram of Fig.1 into the high-temperature domain and draw a direct connection to the more familiar physics of liquid-solid phase transitions in the absence of superfluidity. Such numerical approaches may also reveal how the present phenomenology extends into the regime of strong interactions, which is becoming accessible in experiments with ultracold polar molecules [48–50]. Equally important, an improved understanding of finite-temperature effects in dipolar quantum fluids could help resolving current questions about quantitative discrepancies between measurements and theory [3, 31].

We thank Yongchang Zhang, Georg Bruun, and Jordi Boronat for valuable discussions and the Er-Dy team in Innsbruck for experimental support. This work was supported by the DNRF through the Center of Excellence "CCQ" (Grant agreement no.: DNRF156) and the Carlsberg Foundation through the 'Semper Ardens' Research Project QCooL. JB acknowledges funding by the European Union, the Spanish Ministry of Universities and the Recovery, Transformation and Resilience Plan through a grant from Universitat Politècnica de Catalunya. FF and CP acknowledge support through an ERC Consolidator Grant (RARE, No. 681432), the QuantERA grant MAQS (No I4391-N) and the FOR grant (2247/PI2790) by the Austrian Science Fund FWF.

Appendix A: The nonlinear wave equation

The grand canonical potential is minimal in equilibrium such that we can minimize Eq.(2) with respect to the condensate wave function $\psi(\mathbf{r})$. This yields the nonlinear wave equation

$$\mu\psi(\mathbf{r}) = \Bigg(-\frac{\hbar^2\nabla^2}{2m} + U(\mathbf{r}) + \frac{4\pi\hbar^2 a}{m}|\psi(\mathbf{r})|^2 + \int \mathrm{d}\mathbf{r}' V_{\mathrm{dd}}(\mathbf{r}-\mathbf{r}')|\psi(\mathbf{r}')|^2 + H_{\mathrm{qu}}(\mathbf{r}) + H_{\mathrm{th}}(\mathbf{r})\Bigg)\psi(\mathbf{r}), \tag{A1}$$

which determines the equilibrium state of the condensate for a given chemical potential μ. We consider a harmonic trapping potential $U(\mathbf{r}) = \frac{m}{2}(\omega_x x^2 + \omega_y y^2 + \omega_z z^2)$, with trapping frequencies $\omega_{x,y,z}$ along the three cartesian axes. The first four terms correspond to the Gross-Pitaevskii equation that describes the mean-field physics of the condensate at zero temperature. The next term is given by $H_{\mathrm{qu}}(\mathbf{r}) = \gamma_{\mathrm{qu}}|\psi(\mathbf{r})|^3$ and accounts for leading order effects of quantum fluctuations with a strength γ_{qu} that increases with a and a_d [14, 15, 17]. Finite-temperature effects are captured by the last term as given in Eq.(3). We note here that the applied local-density approximation can cause an infrared divergence of the momentum integral in Eq.(3). However, the finite system size of trapped systems yields a natural momentum cutoff that ensures converged results. Indeed, we find that our calculated condensate wave functions are not sensitive to the precise choice of the momentum cutoff for relevant trap geometries.

Appendix B: Finite-temperature simulations

We have calculated the condensate wave function at finite temperatures by simulating the imaginary time evolution of the wave equation (A1). More concretely, we replace $\mu\psi$ by $-\partial_t\psi$ in Eq.((A1)) and simulate the time evolution until $\psi(\mathbf{r},t)$ reaches a steady state for a given norm $N_{\mathrm{c}} = \int \mathrm{d}\mathbf{r}|\psi(\mathbf{r},t)|^2$. N_{c} corresponds to the number of condensate atoms under 3D confinement as considered in Figs.1(b) and 3, and yields the axial density $N_{\mathrm{c}}/L = L^{-1}\int \mathrm{d}x\mathrm{d}y \int_0^L \mathrm{d}z|\psi(\mathbf{r},t)|^2$ for a given length L of the periodic simulation box as considered in Figs.1(a) and 2. Finally, we determine the chemical potential from Eq.(A1) in order to construct the thermodynamic phase diagram shown in Fig.1(a). The results shown in Figs.1(b) and 3 are obtained for the experimental trap parameters $\omega_x/2\pi = 88$Hz, $\omega_y/2\pi = 141$Hz, and $\omega_z/2\pi = 36$Hz, and a scattering length of $89a_0$, where a_0 is the Bohr radius. The simulations of Figs.1(a) and 2 have been performed for $w_x = 0.0717\varepsilon_{\mathrm{d}}$, $w_y = 0.142\varepsilon_{\mathrm{d}}$, and $w_z = 0$. In all cases, the dipoles are considered to be polarized along the y-axis .

Appendix C: Experimental determination of the average axial density and the density contrast

We probe the emergence of a supersolid state via time-of-flight measurements and in-situ Faraday phase contrast imaging [41]. The former provides information on the global phase coherence and the latter allows us to extract the modulation contrast from the in-situ atomic density. In particular, to obtain the modulation contrast of the experimental points in Fig. 1c, we proceed as follows. For each $\{N_c,\ T\}$, we record the in-trap density distribution and integrate along the direction orthogonal to the droplet chain to get a 1D density profile $\rho_{||}(z)$. We repeat the measurement under the same experimental conditions for 10-20 times. For each profile, we then calculate its Fourier Transform, $\tilde{\rho}_{||}(k) = \int e^{-ik_z z}\rho_{||}(z)\mathrm{d}z$. Finally, we determine the average of $|\tilde{\rho}_{||}(k)|$ and obtain the modulation contrast as the ratio between the Fourier component at the modulation wavelength and the density $|\tilde{\rho}_{||}(0)|$ at $k_z = 0$.

The experimental profile shown in Fig. 3 is obtained by averaging the density distributions from the repeated measurements. The central maximum in each profile is

shifted to the origin, $z = 0$, to correct for unavoidable center-of-mass fluctuations in the experiment. Moreover, we remove negative density contributions in each density image, which are caused by small but inevitable misalignments of the imaging objective.

[1] M. H. W. Chan, R. B. Hallock, and Reatto L., "Overview on solid ^{4}He and the issue of supersolidity," Journal of Low Temperature Physics **172**, 317 (2013).

[2] J. Léonard, A. Morales, P. Zupancic, T. Esslinger, and T. Donner, "Supersolid formation in a quantum gas breaking a continuous translational symmetry," Nature **543**, 87 (2017).

[3] F. Böttcher, J.-N. Schmidt, M. Wenzel, J. Hertkorn, M. Guo, T. Langen, and T. Pfau, "Transient supersolid properties in an array of dipolar quantum droplets," Phys. Rev. X **9**, 011051 (2019).

[4] L. Chomaz, D. Petter, P. Ilzhöfer, G. Natale, A. Trautmann, C. Politi, G. Durastante, R. M. W. van Bijnen, A. Patscheider, M. Sohmen, M. J. Mark, and F. Ferlaino, "Long-lived and transient supersolid behaviors in dipolar quantum gases," Phys. Rev. X **9**, 021012 (2019).

[5] L. Tanzi, E. Lucioni, F. Famà, J. Catani, A. Fioretti, C. Gabbanini, R. N. Bisset, L. Santos, and G. Modugno, "Observation of a dipolar quantum gas with metastable supersolid properties," Phys. Rev. Lett. **122**, 130405 (2019).

[6] S. C. Schuster, P. Wolf, S. Ostermann, S. Slama, and C. Zimmermann, "Supersolid properties of a Bose-Einstein condensate in a ring resonator," Phys. Rev. Lett. **124**, 143602 (2020).

[7] Eugene P. Gross, "Unified theory of interacting bosons," Phys. Rev. **106**, 161–162 (1957).

[8] L. Santos, G. V. Shlyapnikov, P. Zoller, and M. Lewenstein, "Bose-Einstein condensation in trapped dipolar gases," Phys. Rev. Lett. **85**, 1791 (2000).

[9] D. H. J. O'Dell, S. Giovanazzi, and C. Eberlein, "Exact hydrodynamics of a trapped dipolar Bose-Einstein condensate," Phys. Rev. Lett. **92**, 250401 (2004).

[10] D. C. E. Bortolotti, S. Ronen, J. L. Bohn, and D. Blume, "Scattering length instability in dipolar Bose-Einstein condensates," Phys. Rev. Lett. **97**, 160402 (2006).

[11] H. Kadau, M. Schmitt, M. Wenzel, C. Wink, T. Maier, I. Ferrier-Barbut, and T. Pfau, "Observing the Rosensweig instability of a quantum ferrofluid," Nature **530**, 194 (2016).

[12] M. Schmitt, M. Wenzel, F. Böttcher, I. Ferrier-Barbut, and T. Pfau, "Self-bound droplets of a dilute magnetic quantum liquid," Nature **539**, 259 (2016).

[13] L. Chomaz, S. Baier, D. Petter, M. J. Mark, F. Wächtler, L. Santos, and F. Ferlaino, "Quantum-fluctuation-driven crossover from a dilute Bose-Einstein condensate to a macrodroplet in a dipolar quantum fluid," Phys. Rev. X **6**, 041039 (2016).

[14] Aristeu R. P. Lima and Axel Pelster, "Quantum fluctuations in dipolar bose gases," Phys. Rev. A **84**, 041604 (2011).

[15] A. R. P. Lima and A. Pelster, "Beyond mean-field low-lying excitations of dipolar Bose gases," Phys. Rev. A **86**, 063609 (2012).

[16] D. S. Petrov, "Quantum mechanical stabilization of a collapsing Bose-Bose mixture," Phys. Rev. Lett. **115**, 155302 (2015).

[17] F. Wächtler and L. Santos, "Quantum filaments in dipolar Bose-Einstein condensates," Phys. Rev. A **93**, 061603 (2016).

[18] C. R. Cabrera, L. Tanzi, J. Sanz, B. Naylor, P. Thomas, P. Cheiney, and L. Tarruell, "Quantum liquid droplets in a mixture of Bose-Einstein condensates," Science **359**, 301 (2018).

[19] F. Böttcher, M. Wenzel, J.-N. Schmidt, M. Guo, T. Langen, I. Ferrier-Barbut, T. Pfau, R. Bombín, J. Sánchez-Baena, J. Boronat, and F. Mazzanti, "Dilute dipolar quantum droplets beyond the extended Gross-Pitaevskii equation," Phys. Rev. Research **1**, 033088 (2019).

[20] L. Tanzi, S. M. Roccuzzo, E. Lucioni, F. Famà, A. Fioretti, C. Gabbanini, G. Modugno, A. Recati, and S. Stringari, "Supersolid symmetry breaking from compressional oscillations in a dipolar quantum gas," Nature **574**, 382 (2019).

[21] M. Guo, F. Böttcher, J. Hertkorn, J.-N. Schmidt, M. Wenzel, H. P. Büchler, T. Langen, and T. Pfau, "The low-energy goldstone mode in a trapped dipolar supersolid," Nature **574**, 386 (2019).

[22] Y.-C. Zhang, T. Pohl, and F. Maucher, "Phases of supersolids in confined dipolar Bose-Einstein condensates," Phys. Rev. A **104**, 013310 (2021).

[23] J. Hertkorn, J.-N. Schmidt, M. Guo, F. Böttcher, K. S. H. Ng, S. D. Graham, P. Uerlings, T. Langen, M. Zwierlein, and T. Pfau, "Pattern formation in quantum ferrofluids: From supersolids to superglasses," Phys. Rev. Research **3**, 033125 (2021).

[24] S. Giorgini, L. P. Pitaevskii, and S. Stringari, "Thermodynamics of a trapped Bose-condensed gas," Journal of Low Temperature Physics **109**, 309 (1997).

[25] E. Aybar and M. Ö. Oktel, "Temperature-dependent density profiles of dipolar droplets," Phys. Rev. A **99**, 013620 (2019).

[26] A. Griffin, "Conserving and gapless approximations for an inhomogeneous Bose gas at finite temperatures," Phys. Rev. B **53**, 9341 (1996).

[27] P. B. Blakie, D. Baillie, L. Chomaz, and F. Ferlaino, "Supersolidity in an elongated dipolar condensate," Phys. Rev. Research **2**, 043318 (2020).

[28] F. Cinti, M. Boninsegni, and T. Pohl, "Exchange-induced crystallization of soft-core Bosons," New Journal of Physics **16**, 033038 (2014).

[29] L. Santos, G. V. Shlyapnikov, and M. Lewenstein, "Roton-maxon spectrum and stability of trapped dipolar Bose-Einstein condensates," Phys. Rev. Lett. **90**, 250403 (2003).

[30] R. M. Wilson, S. Ronen, J. L. Bohn, and H. Pu, "Manifestations of the roton mode in dipolar Bose-Einstein condensates," Phys. Rev. Lett. **100**, 245302 (2008).

[31] D. Petter, G. Natale, R. M. W. van Bijnen, A. Patscheider, M. J. Mark, L. Chomaz, and F. Ferlaino, "Probing the roton excitation spectrum of a stable dipolar bose gas," Phys. Rev. Lett. **122**, 183401 (2019).

[32] J.-N. Schmidt, J. Hertkorn, M. Guo, F. Böttcher, M. Schmidt, K. S. H. Ng, S. D. Graham, T. Langen, M. Zwierlein, and T. Pfau, "Roton excitations in an oblate dipolar quantum gas," Phys. Rev. Lett. **126**, 193002 (2021).
[33] L. Landau, "On the theory of superfluidity," Phys. Rev. **75**, 884 (1949).
[34] D. H. J. O'Dell, S. Giovanazzi, and G. Kurizki, "Rotons in gaseous Bose-Einstein condensates irradiated by a laser," Phys. Rev. Lett. **90**, 110402 (2003).
[35] N. Henkel, R. Nath, and T. Pohl, "Three-dimensional roton excitations and supersolid formation in Rydberg-excited Bose-Einstein condensates," Phys. Rev. Lett. **104**, 195302 (2010).
[36] R. Mottl, F. Brennecke, K. Baumann, R. Landig, T. Donner, and T. Esslinger, "Roton-type mode softening in a quantum gas with cavity-mediated long-range interactions," Science **336**, 1570 (2012).
[37] Y.-C. Zhang, V. Walther, and T. Pohl, "Long-range interactions and symmetry breaking in quantum gases through optical feedback," Phys. Rev. Lett. **121**, 073604 (2018).
[38] O. W. Dietrich, E. H. Graf, C. H. Huang, and L. Passell, "Neutron scattering by rotons in liquid helium," Phys. Rev. A **5**, 1377 (1972).
[39] T. Kebukawa, "The Temperature Dependence of Phonon Velocity and Roton Minimum in Liquid He II," Progress of Theoretical Physics **49**, 388. (1973).
[40] I. E. Mazets, D. H. J. O'Dell, G. Kurizki, Davidson N., and W. P. Schleich, "Depletion of a Bose-Einstein condensate by laser-induced dipole-dipole interactions," Journal of Physics B: Atomic, Molecular and Optical Physics **37**, S155 (2004).
[41] M. Sohmen, C. Politi, L. Klaus, L. Chomaz, M. J. Mark, M. A. Norcia, and F. Ferlaino, "Birth, life, and death of a dipolar supersolid," Phys. Rev. Lett. **126**, 233401 (2021).
[42] Y.-C. Zhang, F. Maucher, and T. Pohl, "Supersolidity around a critical point in dipolar bose-einstein condensates," Phys. Rev. Lett. **123**, 015301 (2019).
[43] G. Biagioni, N. Antolini, A. Alaña, M. Modugno, A. Fioretti, C. Gabbanini, L. Tanzi, and G. Modugno, "Dimensional crossover in the superfluid-supersolid quantum phase transition," Phys. Rev. X **12**, 021019 (2022).
[44] M. A. Norcia, C. Politi, L. Klaus, E. Poli, M. Sohmen, M. J. Mark, R. N. Bisset, L. Santos, and . Ferlaino, "Two-dimensional supersolidity in a dipolar quantum gas," Nature **596**, 357 (2021).
[45] L. Tanzi, J. G. Maloberti, G. Biagioni, A. Fioretti, C. Gabbanini, and G. Modugno, "Evidence of superfluidity in a dipolar supersolid from nonclassical rotational inertia," Science **371**, 1162 (2021).
[46] A. Macia, J. Sánchez-Baena, J. Boronat, and F. Mazzanti, "Droplets of trapped quantum dipolar bosons," Phys. Rev. Lett. **117**, 205301 (2016).
[47] F. Cinti, A. Cappellaro, L. Salasnich, and T. Macrì, "Superfluid filaments of dipolar bosons in free space," Phys. Rev. Lett. **119**, 215302 (2017).
[48] L Anderegg, S. Burchesky, Y. Bao, S. S. Yu, T. Karman, E. Chae, K.-K. Ni, W. Ketterle, and J. M. Doyle, "Observation of microwave shielding of ultracold molecules," Science **373**, 779 (2021).
[49] A. Schindewolf, R. Bause, X.-Y. Chen, M. Duda, T. Karman, I. Bloch, and X.-Y. Luo, "Evaporation of microwave-shielded polar molecules to quantum degeneracy," (2022), arXiv:2201.05143 [cond-mat.quant-gas].
[50] M. Schmidt, L. Lassablière, G. Quéméner, and T. Langen, "Self-bound dipolar droplets and supersolids in molecular Bose-Einstein condensates," Phys. Rev. Research **4**, 013235 (2022).

Conclusions

The work discussed in this thesis can be divided into two main topics: the study of the interspecies interactions in an ultracold dipolar mixture of erbium and dysprosium, and the investigation of supersolidity with dysprosium atoms, with the phase transition from one to two-dimensional supersolidity as one of the main results.

Er-Dy interspecies interactions. My journey as a PhD student in the Er-Dy experiment in Innsbruck started in 2018. In the same year, our group merged for the first time the physics of dipolar gases with the one of hetero-nuclear mixtures by combining degenerate quantum gases of erbium and dysprosium with different isotope combinations, among them also a Bose-Fermi mixture [187]. Each of these isotope combinations interact differently due to the different scattering properties. Focusing on one of the mixtures, ^{166}Er-^{164}Dy, already from the first measurements, by looking at the atomic clouds after time-of-flight expansion, a clear deformation of the clouds shape arising from the repulsive interaction between erbium and dysprosium atoms was visible. This observation led to one of the main results of this thesis: the investigation of the interspecies interaction, by measuring the in-trap displacement for different orientations of the magnetic field [155].

In fact, for dipolar mixtures, the in-trap displacement does not only depend on the interspecies contact interactions, but also on the dipole-dipole interactions. At fixed magnetic field, and therefore at fixed interspecies contact interaction, the contribution of the dipole-dipole interaction to the interspecies repulsion and therefore to the in-trap displacement can be tuned by changing the orientation of the magnetic field. In collaboration with M. Modugno from the University of the Basque Country in Bilbao (Spain), we developed a model for our hetero-nuclear mixture. By calculating the in-trap displacement for different interspecies scattering lengths, we could estimate the value that best fitted the experimental results, which we predicted to be about $a_{12} \sim 100\ a_0$. Furthermore, the theoretical calculations revealed interesting regimes in which supersolidity, a state combining density modulation and global phase coherence,

is induced in one of the species by increasing the interspecies repulsive interactions [155]. This regime could be easily achieved in the experiment by tuning the magnetic field in proximity of an interspecies Feshbach resonance.

In 2020, we performed extensive studies of interspecies Feshbach resonances for different isotope combinations [58]. More details can be found in Ref. [57]. This project had as main result the discovery, through atomic-loss spectrocopy, of two Gauss-broad interspecies Feshbach resonances for two isotope mixtures. The interspecies nature of those resonances was probed via cross-species thermalization measurements. These results will allow us in the future to tune the interaction between erbium and dysprosium and reach interesting many-body phases as the one mentioned above.

Dipolar supersolids. The second topic of this thesis regards the study of supersolid states in a system of dysprosium atoms. This project started in 2019, when our group joined the quest for supersolidity and, in collaboration with the ERBIUM experiment in Innsbruck, we demonstrated the existence of a supersolid state in form of quantum droplets linked to each other via a superfluid background [42]. This state, which was found in a regime where dipolar interactions are dominant and the mean-field physics predicts a collapse, is stabilized by quantum fluctuations. Simultaneous results were achieved in the group of G. Modugno in Pisa (Italy) [182], and in the group of T. Pfau in Stuttgart (Germany) [32]. What distinguished the supersolid realized in our experiment from the others was the choice of the isotope. In fact, we created supersolid states with a cloud of ^{164}Dy atoms. ^{164}Dy has the special property that the background scattering length is lower than the dipolar length a_{dd}. For this reason, to reach the dipolar-dominated regime, we could tune our scattering length away from Feshbach resonances and observe supersolidity for times longer than 1s. Furthermore, instead of preparing the supersolid state via the standard interaction ramp from a dBEC adopted by the other groups, we developed a new scheme to create a dipolar supersolid by directly evaporating from a thermal cloud. This technique proved to be a fundamental tool in the realization of two-dimensional supersolid states.

Soon after the realization of the first supersolid, we upgraded the experiment with a vertical imaging characterized by an objective, whose resolution of 700nm at the atoms allows us to probe the supersolid state in trap [176]. This tool, together with the possibility of directly evaporating from a thermal cloud, gave us the opportunity of studying the full life-cycle of the supersolid [177]. We observed that, during the formation of the supersolid via direct evaporative cooling, the system develops first a density modulation with phase coherence only localized within the droplets, and

then acquires global phase coherence. Another important result regards the role of finite temperatures. In particular, our findings show that higher temperatures favour the appearance of density modulation. This underlines that not only quantum fluctuations, but also thermal fluctuations play a significant role in the formation of a supersolid state. In a separate work in collaboration with the group of T. Pohl at Aarhus University (Denmark), we revealed that indeed higher temperatures do not melt the supersolid state but rather help in developing density modulation. This counterintuitive behaviour relates to the excitation spectrum of a dipolar BEC, which softens for higher temperatures [180].

Two-dimensional supersolidity. All the results on supersolidity mentioned above regard a system made of three or four droplets aligned along the elongated axis of a cigar-shaped trap. At the end of the year 2020, improvements in the experimental apparatus allowed us to gain in condensed atoms and therefore also in number of droplets. At the beginning of 2021, we managed for the first time to realize two-dimensional supersolidity, by performing a structural phase transition from a linear chain of droplets to a supersolid in a zig-zag pattern, with up to 10 droplets [137]. This work was done in collaboration with L. Santos (Hannover) and R. Bisset (Innsbruck) and represents one of the main results of this thesis. Soon after, we could extend supersolidity from the zig-zag state to a hexagon state in a circular trap [27]. The realization of this state opened the door towards many research directions, e.g. study the excitation modes [136, 154]. Furthermore, the ability of producing states in an isotropic circular trap allowed recently our group to observe, for the first time, quantized vortices in a dipolar BEC by using the anisotropic nature of the dipole-dipole interaction to impart angular momentum into the system [98].

Outlook. The Er-Dy experiment had so far really productive and exciting years. This was also thanks to the many collaborations we had with external groups as the one of T. Giamarchi (Geneva), L. Santos (Hannover), R. Bisset (Innsbruck), M. Modugno (Bilbao), G. Lamporesi (Trento), and T. Pohl (Aarhus), but also thanks to our theory group with T. Bland and E. Poli, who helped us with daily stimulating discussions and theoretical support. I expect the next years to be as exciting. Next research directions involve the nucleation of vortices in supersolid states, by following a similar approach used in our group to impart angular momentum in a dipolar BEC. Furthermore, the knowledge we gained in the past years on the interspecies interactions and Feshbach resonances opens the door to the realization of binary supersolid states with erbium

and dysprosium. Moreover, in July 2021 we upgraded our experimental apparatus with a second chamber, namely a glass cell for quantum gas microscopy of erbium and dysprosium atoms [176], which will enable us to study interesting many body phases in optical lattices arising from the long-range dipole-dipole interaction.

Bibliography

[1] J. R. Abo-Shaeer, C. Raman, J. M. Vogels, and W. Ketterle. Observation of vortex lattices in Bose-Einstein condensates. *Science*, 292(5516):476–479, 2001.

[2] K. Aikawa, A. Frisch, M. Mark, S. Baier, R. Grimm, and F. Ferlaino. Reaching fermi degeneracy via universal dipolar scattering. *Phys. Rev. Lett.*, 112:010404, Jan 2014.

[3] K. Aikawa, A. Frisch, M. Mark, S. Baier, A. Rietzler, R. Grimm, and F. Ferlaino. Bose-einstein condensation of erbium. *Phys. Rev. Lett.*, 108:210401, May 2012.

[4] M. Anderlini, D. Ciampini, D. Cossart, E. Courtade, M. Cristiani, C. Sias, O. Morsch, and E. Arimondo. Model for collisions in ultracold-atom mixtures. *Phys. Rev. A*, 72:033408, Sep 2005.

[5] M. H. Anderson, J. R. Ensher, M. R. Matthews, C. E. Wieman, and E. A. Cornell. Observation of Bose-Einstein Condensation in a Dilute Atomic Vapor. *Science*, 269:198–201, 1995.

[6] A. F. Andreev and I. M. Lifshitz. Quantum theory of defects in crystals. *Sov. Phys. JETP*, 29:1107, 1969.

[7] E. Aybar and M. Ö. Oktel. Temperature-dependent density profiles of dipolar droplets. *Phys. Rev. A*, 99:013620, Jan 2019.

[8] S. Baier, D. Petter, J. H. Becher, A. Patscheider, G. Natale, L. Chomaz, M. J. Mark, and F. Ferlaino. Realization of a strongly interacting fermi gas of dipolar atoms. *Phys. Rev. Lett.*, 121:093602, Aug 2018.

[9] Simon Baier. *An optical dipole trap for Erbium with tunable geometry.* Master's thesis, Faculty of Mathematics, Computer Science and Physics; University of Innsbruck, 2012.

[10] H Y Ban, M Jacka, J L Hanssen, J Reader, J J McClelland, C Y Chen, Y M Li, K Bailey, W R Anderson, and C C Bradley. Laser cooling transitions in atomic erbium. *J. Phys. D – Appl. Phys*, 36:335–385, 2000.

[11] M. A. Baranov, M. Dalmonte, G. Pupillo, and P. Zoller. Condensed matter theory of dipolar quantum gases. *Chemical Reviews*, 112:5012–5061, 2012.

[12] M.A. Baranov. Theoretical progress in many-body physics with ultracold dipolar gases. *Physics Reports*, 464(3):71–111, 2008.

[13] M. Bartenstein, A. Altmeyer, S. Riedl, S. Jochim, C. Chin, J. Hecker Denschlag, and R. Grimm. Crossover from a molecular bose-einstein condensate to a degenerate fermi gas. *Phys. Rev. Lett.*, 92:120401, Mar 2004.

[14] Kristian Baumann, Christine Guerlin, Ferdinand Brennecke, and Tilman Esslinger. Dicke quantum phase transition with a superfluid gas in an optical cavity. *Nature*, 415:1301–1306, 2010.

[15] J. R. Beamish, A. D. Fefferman, A. Haziot, X. Rojas, and S. Balibar. Elastic effects in torsional oscillators containing solid helium. *Phys. Rev. B*, 85:180501, May 2012.

[16] John Beamish and Sébastien Balibar. Mechanical behavior of solid helium: Elasticity, plasticity, and defects. *Rev. Mod. Phys.*, 92:045002, Oct 2020.

[17] J. H. Becher, S. Baier, K. Aikawa, M. Lepers, J.-F. Wyart, O. Dulieu, and F. Ferlaino. Anisotropic polarizability of erbium atoms. *Phys. Rev. A*, 97:012509, Jan 2018.

[18] Giulio Biagioni, Nicolò Antolini, Aitor Alaña, Michele Modugno, Andrea Fioretti, Carlo Gabbanini, Luca Tanzi, and Giovanni Modugno. Dimensional crossover in the superfluid-supersolid quantum phase transition. *Phys. Rev. X*, 12:021019, Apr 2022.

[19] Gerhard Birkl, Sven Kassner, and Herbert Walther. Multiple-shell structures of laser-cooled 24 mg+ ions in a quadrupole storage ring. *Nature*, 357(6376):310–313, 1992.

[20] R. N. Bisset, L. A. Peña Ardila, and L. Santos. Quantum droplets of dipolar mixtures. *Phys. Rev. Lett.*, 126:025301, Jan 2021.

[21] R. N. Bisset and P. B. Blakie. Crystallization of a dilute atomic dipolar condensate. *Phys. Rev. A*, 92:061603, Dec 2015.

[22] R. N. Bisset, R. M. Wilson, D. Baillie, and P. B. Blakie. Ground-state phase diagram of a dipolar condensate with quantum fluctuations. *Phys. Rev. A*, 94:033619, Sep 2016.

[23] P. B. Blakie, D. Baillie, L. Chomaz, and F. Ferlaino. Supersolidity in an elongated dipolar condensate. *Phys. Rev. Research*, 2:043318, Dec 2020.

[24] P Blair Blakie, D Baillie, and Sukla Pal. Variational theory for the ground state and collective excitations of an elongated dipolar condensate. *Communications in Theoretical Physics*, 72(8):085501, jul 2020.

[25] P.B. Blakie, A.S. Bradley, M.J. Davis, R.J. Ballagh, and C.W. Gardiner. Dynamics and statistical mechanics of ultra-cold bose gases using c-field techniques. *Advances in Physics*, 57(5):363–455, 2008.

[26] T. Bland, E. Poli, L. A. Pe na Ardila, L. Santos, F. Ferlaino, and R. N. Bisset. Domain supersolids in binary dipolar condensates. *arXiv:2203.11119*, Mar 2022.

[27] T. Bland, E. Poli, C. Politi, L. Klaus, M. A. Norcia, F. Ferlaino, L. Santos, and R. N. Bisset. Two-dimensional supersolid formation in dipolar condensates. *Phys. Rev. Lett.*, 128:195302, May 2022.

[28] I. Bloch, T. W. Hänsch, and T. Esslinger. Measurement of the spatial coherence of a trapped Bose gas at the phase transition. *Nature*, 403:166–170, 2000.

[29] D Bohle, A Richter, W Steffen, AEL Dieperink, N Lo Iudice, F Palumbo, and O Scholten. New magnetic dipole excitation mode studied in the heavy deformed nucleus 156gd by inelastic electron scattering. *Physics Letters B*, 137(1-2):27–31, 1984.

[30] John L. Bohn and Deborah S. Jin. Differential scattering and rethermalization in ultracold dipolar gases. *Phys. Rev. A*, 89:022702, Feb 2014.

[31] Massimo Boninsegni and Nikolay V. Prokof'ev. Colloquium: Supersolids: What and where are they? *Rev. Mod. Phys.*, 84:759–776, May 2012.

[32] F. Böttcher, J.-N. Schmidt, M. Wenzel, J. Hertkorn, M. Guo, T. Langen, and T. Pfau. Transient Supersolid Properties in an Array of Dipolar Quantum Droplets. *Phys. Rev. X*, 9:011051, Mar 2019.

[33] T. Bourdel, L. Khaykovich, J. Cubizolles, J. Zhang, F. Chevy, M. Teichmann, L. Tarruell, S. J. J. M. F. Kokkelmans, and C. Salomon. Experimental study of the bec-bcs crossover region in lithium 6. *Phys. Rev. Lett.*, 93:050401, Jul 2004.

[34] C. C. Bradley, C. A. Sackett, and R. G. Hulet. Bose-einstein condensation of lithium: Observation of limited condensate number. *Phys. Rev. Lett.*, 78:985–989, Feb 1997.

[35] C. C. Bradley, C. A. Sackett, J. J. Tollett, and R. G. Hulet. Evidence of bose-einstein condensation in an atomic gas with attractive interactions. *Phys. Rev. Lett.*, 75:1687–1690, Aug 1995.

[36] H. P. Büchler and G. Blatter. Supersolid versus phase separation in atomic bose-fermi mixtures. *Phys. Rev. Lett.*, 91:130404, Sep 2003.

[37] C. R. Cabrera, L. Tanzi, J. Sanz, B. Naylor, P. Thomas, P. Cheiney, and L. Tarruell. Quantum liquid droplets in a mixture of bose-einstein condensates. *Science*, 359(6373):301–304, 2018.

[38] G. V. Chester. Speculations on Bose–Einstein condensation and quantum crystals. *Phys. Rev. A*, 2:256–258, Jul 1970.

[39] Cheng Chin, Rudolf Grimm, Paul Julienne, and Eite Tiesinga. Feshbach resonances in ultracold gases. *Reviews of Modern Physics*, 82:1225–1286, 2010.

[40] L. Chomaz, S. Baier, D. Petter, M. J. Mark, F. Wächtler, L. Santos, and F. Ferlaino. Quantum-Fluctuation-driven crossover from a dilute Bose-Einstein condensate to a macrodroplet in a dipolar quantum fluid. *Physical Review X*, 6, 2016.

[41] L. Chomaz, S. Baier, D. Petter, M. J. Mark, F. Wächtler, L. Santos, and F. Ferlaino. Quantum-fluctuation-driven crossover from a dilute bose-einstein condensate to a macrodroplet in a dipolar quantum fluid. *Phys. Rev. X*, 6:041039, Nov 2016.

[42] L. Chomaz, D. Petter, P. Ilzhöfer, G. Natale, A. Trautmann, C. Politi, G. Durastante, R. M. W. van Bijnen, A. Patscheider, M. Sohmen, M. J. Mark, and F. Ferlaino. Long-Lived and Transient Supersolid Behaviors in Dipolar Quantum Gases. *Phys. Rev. X*, 9:021012, Apr 2019.

[43] Lauriane Chomaz, Igor Ferrier-Barbut, Francesca Ferlaino, Bruno Laburthe-Tolra, Benjamin L. Lev, and Tilman Pfau. Dipolar physics: A review of experiments with magnetic quantum gases. *arXiv:2201.02672*, 2022.

[44] Lauriane Chomaz, Rick M W van Bijnen, Daniel Petter, Giulia Faraoni, Simon Baier, J Hendrik Becher, Manfred J Mark, Falk Wächtler, Luis Santos, and Francesca Ferlaino. Observation of roton mode population in a dipolar quantum gas. *Nat. Phys.*, 14(5):442, 2018.

[45] Lauriane Chomaz, Rick M W van Bijnen, Daniel Petter, Giulia Faraoni, Simon Baier, Jan-Hendrik Becher, Manfred J Mark, Falk Wächtler, Luis Santos, and Francesca Ferlaino. Observation of roton mode population in a dipolar quantum gas. *Nat. Phys.*, 14(5):442–446, 2018.

[46] F. Cinti, P. Jain, M. Boninsegni, A. Micheli, P. Zoller, and G. Pupillo. Supersolid droplet crystal in a dipole-blockaded gas. *Phys. Rev. Lett.*, 105:135301, Sep 2010.

[47] F. Cinti, T. Macrì, W. Lechner, G. Pupillo, and T. Pohl. Defect-induced supersolidity with soft-core bosons. *Nature Communications*, 5(3235), 2014.

[48] K. B. Davis, M. O. Mewes, M. R. Andrews, N. J. Van Druten, D. S. Durfee, D. M. Kurn, and W. Ketterle. Bose-Einstein condensation in a gas of sodium atoms. *Physical Review Letters*, 75:3969–3973, 1995.

[49] E. T. Davletov, V. V. Tsyganok, V. A. Khlebnikov, D. A. Pershin, D. V. Shaykin, and A. V. Akimov. Machine learning for achieving bose-einstein condensation of thulium atoms. *Phys. Rev. A*, 102:011302, Jul 2020.

[50] James Day and John Beamish. Low-temperature shear modulus changes in solid 4He and connection to supersolidity. *Nature*, 450(7171):853–856, 2007.

[51] L. De Sarlo, P. Maioli, G. Barontini, J. Catani, F. Minardi, and M. Inguscio. Collisional properties of sympathetically cooled ^{39}K. *Phys. Rev. A*, 75:022715, Feb 2007.

[52] B. DeMarco, J. L. Bohn, J. P. Burke, M. Holland, and D. S. Jin. Measurement of p-wave threshold law using evaporatively cooled fermionic atoms. *Phys. Rev. Lett.*, 82:4208–4211, May 1999.

[53] B. DeMarco and D. S. Jin. Onset of Fermi Degeneracy in a Trapped Atomic Gas. *Science*, 285:1703–1706, 1999.

[54] C. D'Errico, A. Burchianti, M. Prevedelli, L. Salasnich, F. Ancilotto, M. Modugno, F. Minardi, and C. Fort. Observation of quantum droplets in a heteronuclear bosonic mixture. *Phys. Rev. Research*, 1:033155, Dec 2019.

[55] B. J. DeSalvo, Krutik Patel, Geyue Cai, and Cheng Chin. Observation of fermion-mediated interactions between bosonic atoms. *Nature*, 568:61–64, Apr 2019.

[56] O. W. Dietrich, E. H. Graf, C. H. Huang, and L. Passell. Neutron scattering by rotons in liquid helium. *Phys. Rev. A*, 5:1377–1391, Mar 1972.

[57] Gianmaria Durastante. *Creation of Erbium-Dysprosium Dipolar Quantum Mixtures and Their Interspecies Feshbach Resonances*. PhD thesis, University of Innsbruck, 2020.

[58] Gianmaria Durastante, Claudia Politi, Maximilian Sohmen, Philipp Ilzhöfer, Manfred J. Mark, Matthew A. Norcia, and Francesca Ferlaino. Feshbach resonances in an erbium-dysprosium dipolar mixture. *Phys. Rev. A*, 102:033330, Sep 2020.

[59] V. A. Dzuba and V. V. Flambaum. Theoretical study of some experimentally relevant states of dysprosium. *Phys. Rev. A*, 81:052515, May 2010.

[60] M. Egorov, B. Opanchuk, P. Drummond, B. V. Hall, P. Hannaford, and A. I. Sidorov. Measurement of s-wave scattering lengths in a two-component bose-einstein condensate. *Phys. Rev. A*, 87:053614, May 2013.

[61] Igor Ferrier-Barbut, Holger Kadau, Matthias Schmitt, Matthias Wenzel, and Tilman Pfau. Observation of quantum droplets in a strongly dipolar bose gas. *Phys. Rev. Lett.*, 116:215301, May 2016.

[62] Igor Ferrier-Barbut, Matthias Wenzel, Fabian Böttcher, Tim Langen, Mathieu Isoard, Sandro Stringari, and Tilman Pfau. Scissors mode of dipolar quantum droplets of dysprosium atoms. *Phys. Rev. Lett.*, 120:160402, Apr 2018.

[63] Igor Ferrier-Barbut, Matthias Wenzel, Fabian Böttcher, Tim Langen, Mathieu Isoard, Sandro Stringari, and Tilman Pfau. Scissors mode of dipolar quantum droplets of dysprosium atoms. *Phys. Rev. Lett.*, 120:160402, Apr 2018.

[64] A. Frisch, K. Aikawa, M. Mark, A. Rietzler, J. Schindler, E. Zupanič, R. Grimm, and F. Ferlaino. Narrow-line magneto-optical trap for erbium. *Phys. Rev. A*, 85:051401, May 2012.

[65] Albert Frisch. *Dipolar Quantum Gases of Erbium*. PhD thesis, University of Innsbruck, 2014.

[66] A. Gallemí, S. M. Roccuzzo, S. Stringari, and A. Recati. Quantized vortices in dipolar supersolid bose-einstein-condensed gases. *Phys. Rev. A*, 102:023322, Aug 2020.

[67] Christopher Gaul and Cord A. Müller. A grand-canonical approach to the disordered bose gas. *Applied Physics B*, 117:775–784, Dec 2014.

[68] S. Giovanazzi, D. O'Dell, and G. Kurizki. Self-binding transition in bose condensates with laser-induced "gravitation". *Phys. Rev. A*, 63:031603, Feb 2001.

[69] Goran Gligorić, Aleksandra Maluckov, Milutin Stepić, Ljupč Hadžievski, and Boris A. Malomed. Transition to miscibility in linearly coupled binary dipolar bose-einstein condensates. *Phys. Rev. A*, 82:033624, Sep 2010.

[70] Markus Greiner, Olaf Mandel, Tilman Esslinger, T. W. Hänsch, and Immanuel Bloch. Quantum phase transition from a superfluid to a Mott insulator in a gas of ultracold atoms. *Nature*, 415:39–44, 2002.

[71] Axel Griesmaier, Jörg Werner, Sven Hensler, Jürgen Stuhler, and Tilman Pfau. Bose-Einstein condensation of chromium. *Physical Review Letters*, 94, 2005.

[72] E.P Gross. Classical theory of boson wave fields. *Annals of Physics*, 4(1):57–74, 1958.

[73] Eugene P. Gross. Unified theory of interacting bosons. *Phys. Rev.*, 106(1):161–162, apr 1957.

[74] D. Guéry-Odelin and S. Stringari. Scissors mode and superfluidity of a trapped bose-einstein condensed gas. *Phys. Rev. Lett.*, 83:4452–4455, Nov 1999.

[75] Mingyang Guo, Fabian Böttcher, Jens Hertkorn, Jan-Niklas Schmidt, Matthias Wenzel, Hans Peter Büchler, Tim Langen, and Tilman Pfau. The low-energy Goldstone mode in a trapped dipolar supersolid. *Nature*, 574(7778):386–389, 2019.

[76] A. Guttridge, S. A. Hopkins, S. L. Kemp, Matthew D. Frye, Jeremy M. Hutson, and Simon L. Cornish. Interspecies thermalization in an ultracold mixture of cs and yb in an optical trap. *Phys. Rev. A*, 96:012704, Jul 2017.

[77] A. Guttridge, S. A. Hopkins, S. L. Kemp, Matthew D. Frye, Jeremy M. Hutson, and Simon L. Cornish. Interspecies thermalization in an ultracold mixture of cs and yb in an optical trap. *Phys. Rev. A*, 96:012704, Jul 2017.

[78] Z. Hadzibabic, C. A. Stan, K. Dieckmann, S. Gupta, M. W. Zwierlein, A. Görlitz, and W. Ketterle. Two-species mixture of quantum degenerate bose and fermi gases. *Phys. Rev. Lett.*, 88:160401, Apr 2002.

[79] Zoran Hadzibabic, Sabine Stock, Baptiste Battelier, Vincent Bretin, and Jean Dalibard. Interference of an array of independent bose-einstein condensates. *Phys. Rev. Lett.*, 93:180403, Oct 2004.

[80] Anders H. Hansen, Alexander Khramov, William H. Dowd, Alan O. Jamison, Vladyslav V. Ivanov, and Subhadeep Gupta. Quantum degenerate mixture of ytterbium and lithium atoms. *Phys. Rev. A*, 84:011606, Jul 2011.

[81] Hideaki Hara, Yosuke Takasu, Yoshifumi Yamaoka, John M. Doyle, and Yoshiro Takahashi. Quantum degenerate mixtures of alkali and alkaline-earth-like atoms. *Phys. Rev. Lett.*, 106:205304, May 2011.

[82] Ariel Haziot, Xavier Rojas, Andrew D. Fefferman, John R. Beamish, and Sébastien Balibar. Giant plasticity of a quantum crystal. *Phys. Rev. Lett.*, 110:035301, Jan 2013.

[83] N. Henkel, R. Nath, and T. Pohl. Three-dimensional roton excitations and supersolid formation in rydberg-excited bose-einstein condensates. *Phys. Rev. Lett.*, 104:195302, May 2010.

[84] J. Hertkorn, F. Böttcher, M. Guo, J. N. Schmidt, T. Langen, H. P. Büchler, and T. Pfau. Fate of the Amplitude Mode in a Trapped Dipolar Supersolid. *Phys. Rev. Lett.*, 123:193002, Nov 2019.

[85] J. Hertkorn, J.-N. Schmidt, F. Böttcher, M. Guo, M. Schmidt, K. S. H. Ng, S. D. Graham, H. P. Büchler, T. Langen, M. Zwierlein, and T. Pfau. Density fluctuations across the superfluid-supersolid phase transition in a dipolar quantum gas. *Phys. Rev. X*, 11:011037, Feb 2021.

[86] Ming-Guang Hu, Michael J. Van de Graaff, Dhruv Kedar, John P. Corson, Eric A. Cornell, and Deborah S. Jin. Bose polarons in the strongly interacting regime. *Phys. Rev. Lett.*, 117:055301, Jul 2016.

[87] P. Ilzhöfer, G. Durastante, A. Patscheider, A. Trautmann, M. J. Mark, and F. Ferlaino. Two-species five-beam magneto-optical trap for erbium and dysprosium. *Phys. Rev. A*, 97:023633, Feb 2018.

[88] Philipp Ilzhöfer. *Creation of Dipolar Quantum Mixtures of Erbium and Dysprosium*. PhD thesis, University of Innsbruck, 2020.

[89] Philipp Ilzhöfer, Maximilian Sohmen, Gianmaria Durastante, Claudia Politi, Arno Trautmann, G Natale, G Morpurgo, T Giamarchi, L Chomaz, MJ Mark, et al. Phase coherence in out-of-equilibrium supersolid states of ultracold dipolar atoms. *Nature Physics*, 17(3):356–361, 2021.

[90] Nils B. Jørgensen, Lars Wacker, Kristoffer T. Skalmstang, Meera M. Parish, Jesper Levinsen, Rasmus S. Christensen, Georg M. Bruun, and Jan J. Arlt. Observation of attractive and repulsive polarons in a bose-einstein condensate. *Phys. Rev. Lett.*, 117:055302, Jul 2016.

[91] H. Kadau, M. Schmitt, M. Wenzel, C. Wink, T. Maier, I. Ferrier-Barbut, and T. Pfau. Observing the Rosensweig instability of a quantum ferrofluid. *Nature*, 530(7589):194–197, 02 2016.

[92] Hidetoshi Katori, Tetsuya Ido, Yoshitomo Isoya, and Makoto Kuwata-Gonokami. Magneto-optical trapping and cooling of strontium atoms down to the photon recoil temperature. *Phys. Rev. Lett.*, 82:1116–1119, Feb 1999.

[93] Takeji Kebukawa. The Temperature Dependence of Phonon Velocity and Roton Minimum in Liquid He II. *Progress of Theoretical Physics*, 49(2):388–400, 02 1973.

[94] Duk Y. Kim and Moses H. W. Chan. Absence of supersolidity in solid helium in porous vycor glass. *Phys. Rev. Lett.*, 109:155301, Oct 2012.

[95] E. Kim and M. H. W. Chan. Observation of superflow in solid helium. *Science*, 305(5692):1941–1944, 2004.

[96] E. Kim and M. H. W. Chan. Probable observation of a supersolid helium phase. *Nature*, 427(6971):225–227, 2004.

[97] D. A. Kirzhnits and Y. A. Nepomnyashchii. Coherent crystallization of quantum liquid. *Sov. Phys. JETP*, 32(6), 1971.

[98] Lauritz Klaus, Thomas Bland, Elena Poli, Claudia Politi, Giacomo Lamporesi, Eva Casotti, Russell N. Bisset, Manfred M. Mark, and Francesca Ferlaino. Observation of vortices and vortex stripes in a dipolar Bose-Einstein condensate. *Nature Physics*, 2022.

[99] Youssef Kora and Massimo Boninsegni. Patterned supersolids in dipolar Bose systems. *J. Low Temp. Phys.*, 197(5):337–347, Dec 2019.

[100] Svetlana Kotochigova. Controlling interactions between highly magnetic atoms with Feshbach resonances. *Reports on Progress in Physics*, 77:093901, 2014.

[101] Ramavarmaraja Kishor Kumar, Paulsamy Muruganandam, Lauro Tomio, and Arnaldo Gammal. Miscibility in coupled dipolar and non-dipolar bose–einstein condensates. *Journal of Physics Communications*, 1(3):035012, nov 2017.

[102] Ramavarmaraja Kishor Kumar, Lauro Tomio, and Arnaldo Gammal. Vortex patterns in rotating dipolar bose–einstein condensate mixtures with squared optical lattices. *Journal of Physics B: Atomic, Molecular and Optical Physics*, 52(2):025302, dec 2018.

[103] Ramavarmaraja Kishor Kumar, Lauro Tomio, Boris A. Malomed, and Arnaldo Gammal. Vortex lattices in binary bose-einstein condensates with dipole-dipole interactions. *Phys. Rev. A*, 96:063624, Dec 2017.

[104] P Kuopanportti, Y M Liu, Y Z He, and C G Bao. Effect of the interspecies interaction on the density profiles of miscible two-species bose–einstein condensates. *Journal of Physics B: Atomic, Molecular and Optical Physics*, 52(1):015001, nov 2018.

[105] W. J. Kwon, G. Del Pace, K. Xhani, L. Galantucci, A. Muzi Falconi, M. Inguscio, F. Scazza, and G. Roati. Sound emission and annihilations in a programmable quantum vortex collider. *Nature (London)*, 600(7887):64–69, 2021.

[106] T Lahaye, C Menotti, L Santos, M Lewenstein, and T Pfau. The physics of dipolar bosonic quantum gases. *Reports on Progress in Physics*, 72:126401, 2009.

[107] Thierry Lahaye, Jonas Metz, Bernd Fröhlich, and Tobias Koc. *d*-wave collapse and explosion of a dipolar Bose-Einstein condensate. *Phys. Rev. Lett.*, 101:080401, 2008.

[108] L. Landau. Theory of the superfluidity of helium ii. *Phys. Rev.*, 60:356–358, Aug 1941.

[109] A. D. Lange, K. Pilch, A. Prantner, F. Ferlaino, B. Engeser, H.-C. Nägerl, R. Grimm, and C. Chin. Determination of atomic scattering lengths from measurements of molecular binding energies near feshbach resonances. *Phys. Rev. A*, 79:013622, Jan 2009.

[110] T. D. Lee, K. Huang, and C. N. Yang. Eigenvalues and Eigenfunctions of a Bose System of Hard Spheres and its Low-Temperature Properties. *Phys. Rev.*, 106:1135–1145, 1957.

[111] A. J. Leggett. Can a solid be "Superfluid"? *Phys. Rev. Lett.*, 25:1543–1546, Nov 1970.

[112] J. Léonard, A. Morales, P. Zupancic, T. Esslinger, and T. Donner. Supersolid formation in a quantum gas breaking a continuous translational symmetry. *Nature*, 543(7643):87–90, 2017.

[113] Hui Li, Jean-Fran çois Wyart, Olivier Dulieu, and Maxence Lepers. Anisotropic optical trapping as a manifestation of the complex electronic structure of ultracold lanthanide atoms: The example of holmium. *Phys. Rev. A*, 95:062508, Jun 2017.

[114] J.-R. Li, J. Lee, W. Huang, S. Burchesky, B. Shteynas, F. Çağrı Top, A. O. Jamison, and W. Ketterle. A stripe phase with supersolid properties in spin–orbit-coupled Bose–Einstein condensates. *Nature*, 543(7643):91–94, 2017.

[115] A. R. P. Lima and A. Pelster. Beyond mean-field low-lying excitations of dipolar bose gases. *Phys. Rev. A*, 86:063609, Dec 2012.

[116] Aristeu R. P. Lima and Axel Pelster. Quantum fluctuations in dipolar bose gases. *Phys. Rev. A*, 84:041604, Oct 2011.

[117] E. B. Linscott and P. B. Blakie. Thermally activated local collapse of a flattened dipolar condensate. *Phys. Rev. A*, 90:053605, Nov 2014.

[118] Mingwu Lu, Nathaniel Q. Burdick, and Benjamin L. Lev. Quantum degenerate dipolar fermi gas. *Phys. Rev. Lett.*, 108:215301, May 2012.

[119] Mingwu Lu, Nathaniel Q. Burdick, Seo Ho Youn, and Benjamin L. Lev. Strongly dipolar Bose-Einstein condensate of dysprosium. *Physical Review Letters*, 107, 2011.

[120] Zhen-Kai Lu, Yun Li, D. S. Petrov, and G. V. Shlyapnikov. Stable dilute supersolid of two-dimensional dipolar bosons. *Phys. Rev. Lett.*, 115:075303, Aug 2015.

[121] K. W. Madison, F. Chevy, W. Wohlleben, and J. Dalibard. Vortex formation in a stirred bose-einstein condensate. *Phys. Rev. Lett.*, 84:806–809, Jan 2000.

[122] O. M. Maragò, S. A. Hopkins, J. Arlt, E. Hodby, G. Hechenblaikner, and C. J. Foot. Observation of the scissors mode and evidence for superfluidity of a trapped bose-einstein condensed gas. *Phys. Rev. Lett.*, 84:2056–2059, Mar 2000.

[123] Christoph Maschler and Helmut Ritsch. Cold atom dynamics in a quantum optical lattice potential. *Phys. Rev. Lett.*, 95:260401, Dec 2005.

[124] M. R. Matthews, B. P. Anderson, P. C. Haljan, D. S. Hall, C. E. Wieman, and E. A. Cornell. Vortices in a bose-einstein condensate. *Phys. Rev. Lett.*, 83:2498–2501, Sep 1999.

[125] I E Mazets, D H J O'Dell, G Kurizki, N Davidson, and W P Schleich. Depletion of a bose–einstein condensate by laser-induced dipole–dipole interactions. *Journal of Physics B: Atomic, Molecular and Optical Physics*, 37(7):S155–S164, mar 2004.

[126] D. J. McCarron, H. W. Cho, D. L. Jenkin, M. P. Köppinger, and S. L. Cornish. Dual-species bose-einstein condensate of ^{87}Rb and ^{133}Cs. *Phys. Rev. A*, 84:011603, Jul 2011.

[127] Jonas Metz, Thierry Lahaye, B Fröhlich, Axel Griesmaier, Tilman Pfau, Hiroki Saito, Y Kawaguchi, and Masahito Ueda. Coherent collapses of dipolar Bose–Einstein condensates for different trap geometries. *New J. Phys.*, 11(5):055032, ma 2009.

[128] D. Mitra, K. H. Leung, and T. Zelevinsky. Quantum control of molecules for fundamental physics. *Phys. Rev. A*, 105:040101, Apr 2022.

[129] Yuki Miyazawa, Ryotaro Inoue, Hiroki Matsui, Gyohei Nomura, and Mikio Kozuma. Bose-einstein condensation of europium. arXiv:2207.11692, 2022.

[130] A. Mosk, S. Kraft, M. Mudrich, K. Singer, W. Wohlleben, R. Grimm, and M. Weidemüller. Mixture of ultracold lithium and cesium atoms in an optical dipole trap. *Appl. Phys. B*, 73(8):791, 2001.

[131] P. Münstermann, T. Fischer, P. Maunz, P. W. H. Pinkse, and G. Rempe. Observation of cavity-mediated long-range light forces between strongly coupled atoms. *Phys. Rev. Lett.*, 84:4068–4071, May 2000.

[132] G. Natale, R. M. W. van Bijnen, A. Patscheider, D. Petter, M. J. Mark, L. Chomaz, and F. Ferlaino. Excitation Spectrum of a Trapped Dipolar Supersolid and Its Experimental Evidence. *Phys. Rev. Lett.*, 123:050402, Aug 2019.

[133] T. W. Neely, E. C. Samson, A. S. Bradley, M. J. Davis, and B. P. Anderson. Observation of vortex dipoles in an oblate Bose-Einstein condensate. *Phys. Rev. Lett.*, 104:160401, Apr 2010.

[134] Flavio S. Nogueira and Hagen Kleinert. Thermally induced rotons in two-dimensional dilute bose gases. *Phys. Rev. B*, 73:104515, Mar 2006.

[135] Matthew A. Norcia and Francesca Ferlaino. Developments in atomic control using ultracold magnetic lanthanides. *Nat. Phys.*, 17(12):1349–1357, 2021.

[136] Matthew A. Norcia, Elena Poli, Claudia Politi, Lauritz Klaus, Thomas Bland, Manfred J. Mark, Luis Santos, Russell N. Bisset, and Francesca Ferlaino. Can angular oscillations probe superfluidity in dipolar supersolids? *Phys. Rev. Lett.*, 129:040403, Jul 2022.

[137] Matthew A. Norcia, Claudia Politi, Lauritz Klaus, Elena Poli, Maximilian Sohmen, Manfred J. Mark, Russell N. Bisset, Luis Santos, and Francesca Ferlaino. Two-dimensional supersolidity in a dipolar quantum gas. *Nature*, 596(7872):357–361, Aug 2021.

[138] P. Nozières. Is the roton in superfluid 4he the ghost of a bragg spot? *J. Low Temp. Phys.*, 137(1):45–67, Oct 2004.

[139] D. H. J. O'Dell, S. Giovanazzi, and G. Kurizki. Rotons in gaseous bose-einstein condensates irradiated by a laser. *Phys. Rev. Lett.*, 90:110402, Mar 2003.

[140] S. Ostermann, F. Piazza, and H. Ritsch. Spontaneous crystallization of light and ultracold atoms. *Phys. Rev. X*, 6:021026, May 2016.

[141] Sukla Pal, D. Baillie, and P. B. Blakie. Excitations and number fluctuations in an elongated dipolar bose-einstein condensate. *Phys. Rev. A*, 102:043306, Oct 2020.

[142] S. B. Papp, J. M. Pino, and C. E. Wieman. Tunable miscibility in a dual-species bose-einstein condensate. *Phys. Rev. Lett.*, 101:040402, Jul 2008.

[143] Benjamin Pasquiou, Alex Bayerle, Slava M. Tzanova, Simon Stellmer, Jacek Szczepkowski, Mark Parigger, Rudolf Grimm, and Florian Schreck. Quantum degenerate mixtures of strontium and rubidium atoms. *Phys. Rev. A*, 88:023601, Aug 2013.

[144] A. Patscheider, L. Chomaz, G. Natale, D. Petter, M. J. Mark, S. Baier, B. Yang, R. R. W. Wang, J. L. Bohn, and F. Ferlaino. Determination of the scattering length of erbium atoms. *Phys. Rev. A*, 105:063307, Jun 2022.

[145] A. Patscheider, B. Yang, G. Natale, D. Petter, L. Chomaz, M. J. Mark, G. Hovhannesyan, M. Lepers, and F. Ferlaino. Observation of a narrow inner-shell orbital transition in atomic erbium at 1299 nm. *Phys. Rev. Research*, 3:033256, Sep 2021.

[146] Oliver Penrose and Lars Onsager. Bose-einstein condensation and liquid helium. *Phys. Rev.*, 104:576–584, Nov 1956.

[147] N. Petersen, M. Trümper, and P. Windpassinger. Spectroscopy of the 1001-nm transition in atomic dysprosium. *Phys. Rev. A*, 101:042502, Apr 2020.

[148] Alexander Petrov, Eite Tiesinga, and Svetlana Kotochigova. Anisotropy-induced feshbach resonances in a quantum dipolar gas of highly magnetic atoms. *Phys. Rev. Lett.*, 109:103002, Sep 2012.

[149] D. S. Petrov. Quantum mechanical stabilization of a collapsing bose-bose mixture. *Phys. Rev. Lett.*, 115:155302, Oct 2015.

[150] D. Petter, G. Natale, R. M.W. Van Bijnen, A. Patscheider, M. J. Mark, L. Chomaz, and F. Ferlaino. Probing the Roton Excitation Spectrum of a Stable Dipolar Bose Gas. *Physical Review Letters*, 122(18):183401, 2019.

[151] D. Petter, A. Patscheider, G. Natale, M. J. Mark, M. A. Baranov, R. van Bijnen, S. M. Roccuzzo, A. Recati, B. Blakie, D. Baillie, L. Chomaz, and F. Ferlaino. Bragg scattering of an ultracold dipolar gas across the phase transition from Bose-Einstein condensate to supersolid in the free-particle regime. *Phys. Rev. A*, 104:L011302, Jul 2021.

[152] Gregory A. Phelps, Anne Hébert, Aaron Krahn, Susannah Dickerson, Furkan Öztürk, Sepehr Ebadi, Lin Su, and Markus Greiner. Sub-second production of a quantum degenerate gas. arXiv:2007.10807, 2020.

[153] Lev Pitaevskii and Sandro Stringari. *Bose-Einstein condensation and superfluidity*, volume 164. Oxford University Press, 2016.

[154] E. Poli, T. Bland, C. Politi, L. Klaus, M. A. Norcia, F. Ferlaino, R. N. Bisset, and L. Santos. Maintaining supersolidity in one and two dimensions. *Phys. Rev. A*, 104:063307, Dec 2021.

[155] C. Politi, A. Trautmann, P. Ilzhöfer, G. Durastante, M. J. Mark, M. Modugno, and F. Ferlaino. Interspecies interactions in an ultracold dipolar mixture. *Phys. Rev. A*, 105:023304, Feb 2022.

[156] Claudia Politi. *Optical dipole trap for an erbium and dysprosium mixture*. Master's thesis, Dipartimento di Fisica "E. Fermi", Università di Pisa, 2017.

[157] Yves Pomeau and Sergio Rica. Dynamics of a model of supersolid. *Phys. Rev. Lett.*, 72:2426–2429, Apr 1994.

[158] H. Pu and N. P. Bigelow. Collective excitations, metastability, and nonlinear response of a trapped two-species bose-einstein condensate. *Phys. Rev. Lett.*, 80:1134–1137, Feb 1998.

[159] K Pyka, J Keller, HL Partner, R Nigmatullin, T Burgermeister, DM Meier, K Kuhlmann, A Retzker, Martin B Plenio, WH Zurek, et al. Topological defect formation and spontaneous symmetry breaking in ion coulomb crystals. *Nature communications*, 4(1):1–6, 2013.

[160] M. G. Raizen, J. M. Gilligan, J. C. Bergquist, W. M. Itano, and D. J. Wineland. Ionic crystals in a linear paul trap. *Phys. Rev. A*, 45:6493–6501, May 1992.

[161] C. Ravensbergen, V. Corre, E. Soave, M. Kreyer, S. Tzanova, E. Kirilov, and R. Grimm. Accurate determination of the dynamical polarizability of dysprosium. *Phys. Rev. Lett.*, 120:223001, May 2018.

[162] C. Ravensbergen, E. Soave, V. Corre, M. Kreyer, B. Huang, E. Kirilov, and R. Grimm. Resonantly interacting fermi-fermi mixture of ^{161}Dy and ^{40}K. *Phys. Rev. Lett.*, 124:203402, May 2020.

[163] Cornelis Ravensbergen, Vincent Corre, Elisa Soave, Marian Kreyer, Emil Kirilov, and Rudolf Grimm. Production of a degenerate fermi-fermi mixture of dysprosium and potassium atoms. *Phys. Rev. A*, 98:063624, Dec 2018.

[164] C. A. Regal, M. Greiner, and D. S. Jin. Observation of resonance condensation of fermionic atom pairs. *Phys. Rev. Lett.*, 92:040403, Jan 2004.

[165] S. M. Roccuzzo, A. Gallemí, A. Recati, and S. Stringari. Rotating a supersolid dipolar gas. *Phys. Rev. Lett.*, 124:045702, Jan 2020.

[166] S. M. Roccuzzo, A. Recati, and S. Stringari. Moment of inertia and dynamical rotational response of a supersolid dipolar gas. *Phys. Rev. A*, 105:023316, Feb 2022.

[167] Camilla De Rossi, Romain Dubessy, Karina Merloti, Mathieu de Goër de Herve, Thomas Badr, Aurélien Perrin, Laurent Longchambon, and Hélène Perrin. Probing superfluidity in a quasi two-dimensional bose gas through its local dynamics. *New Journal of Physics*, 18(6):062001, jun 2016.

[168] L. Santos, G. V. Shlyapnikov, and M. Lewenstein. Roton-maxon spectrum and stability of trapped dipolar bose-einstein condensates. *Phys. Rev. Lett.*, 90:250403, Jun 2003.

[169] D. Scheiermann, L. A. Peña Ardila, T. Bland, R. N. Bisset, and L. Santos. Catalyzation of supersolidity in binary dipolar condensates. *arXiv:2202.08259*, 2022.

[170] J.-N. Schmidt, J. Hertkorn, M. Guo, F. Böttcher, M. Schmidt, K. S. H. Ng, S. D. Graham, T. Langen, M. Zwierlein, and T. Pfau. Roton excitations in an oblate dipolar quantum gas. *Phys. Rev. Lett.*, 126:193002, May 2021.

[171] Matthias Schmitt, Matthias Wenzel, Fabian Böttcher, Igor Ferrier-Barbut, and Tilman Pfau. Self-bound droplets of a dilute magnetic quantum liquid. *Nature*, 539(7628):259, 2016.

[172] Jaeho Shin, Jaewon Choi, Keiya Shirahama, and Eunseong Kim. Simultaneous investigation of shear modulus and torsional resonance of solid ^{4}He. *Phys. Rev. B*, 93:214512, Jun 2016.

[173] C. Silber, S. Günther, C. Marzok, B. Deh, Ph. W. Courteille, and C. Zimmermann. Quantum-degenerate mixture of fermionic lithium and bosonic rubidium gases. *Phys. Rev. Lett.*, 95:170408, Oct 2005.

[174] Joseph C. Smith, D. Baillie, and P. B. Blakie. Quantum droplet states of a binary magnetic gas. *Phys. Rev. Lett.*, 126:025302, Jan 2021.

[175] Joseph C. Smith, P. B. Blakie, and D. Baillie. Approximate theories for binary magnetic quantum droplets. *Phys. Rev. A*, 104:053316, Nov 2021.

[176] Maximilian Sohmen. *Supersolidity in dipolar quantum gases in and out of equilibrium*. PhD thesis, University of Innsbruck, 2021.

[177] Maximilian Sohmen, Claudia Politi, Lauritz Klaus, Lauriane Chomaz, Manfred J. Mark, Matthew A. Norcia, and Francesca Ferlaino. Birth, life, and death of a dipolar supersolid. *Phys. Rev. Lett.*, 126:233401, Jun 2021.

[178] J. Stenger, S. Inouye, D. M. Stamper-Kurn, H.-J. Miesner, A. P. Chikkatur, and W. Ketterle. Spin domains in ground-state Bose–Einstein condensates. *Nature*, 396:345–348, 1998.

[179] J. Stuhler, A. Griesmaier, T. Koch, M. Fattori, T. Pfau, S. Giovanazzi, P. Pedri, and L. Santos. Observation of dipole-dipole interaction in a degenerate quantum gas. *Phys. Rev. Lett.*, 95:150406, Oct 2005.

[180] Juan Sánchez-Baena, Claudia Politi, Fabian Maucher, Francesca Ferlaino, and Thomas Pohl. Heating a quantum dipolar fluid into a solid. *arXiv:2209.00335*, 2022.

[181] Yijun Tang, Andrew Sykes, Nathaniel Q. Burdick, John L. Bohn, and Benjamin L. Lev. s-wave scattering lengths of the strongly dipolar bosons ^{162}Dy and ^{164}Dy. *Phys. Rev. A*, 92:022703, Aug 2015.

[182] L. Tanzi, E. Lucioni, F. Famà, J. Catani, A. Fioretti, C. Gabbanini, R. N. Bisset, L. Santos, and G. Modugno. Observation of a Dipolar Quantum Gas with Metastable Supersolid Properties. *Phys. Rev. Lett.*, 122:130405, Apr 2019.

[183] L Tanzi, JG Maloberti, G Biagioni, A Fioretti, C Gabbanini, and G Modugno. Evidence of superfluidity in a dipolar supersolid from nonclassical rotational inertia. *Science*, 371(6534):1162–1165, 2021.

[184] L Tanzi, SM Roccuzzo, E Lucioni, F Famà, A Fioretti, C Gabbanini, G Modugno, A Recati, and S Stringari. Supersolid symmetry breaking from compressional oscillations in a dipolar quantum gas. *Nature*, 574(7778):382–385, 2019.

[185] M. Nilsson Tengstrand, D. Boholm, R. Sachdeva, J. Bengtsson, and S. M. Reimann. Persistent currents in toroidal dipolar supersolids. *Phys. Rev. A*, 103:013313, Jan 2021.

[186] I. Titvinidze, M. Snoek, and W. Hofstetter. Supersolid bose-fermi mixtures in optical lattices. *Phys. Rev. Lett.*, 100:100401, Mar 2008.

[187] A. Trautmann, P. Ilzhöfer, G. Durastante, C. Politi, M. Sohmen, M. J. Mark, and F. Ferlaino. Dipolar Quantum Mixtures of Erbium and Dysprosium Atoms. *Phys. Rev. Lett.*, 121:213601, Nov 2018.

[188] Andrew G. Truscott, Kevin E. Strecker, William I. McAlexander, Guthrie B. Partridge, and Randall G. Hulet. Observation of fermi pressure in a gas of trapped atoms. *Science*, 291(5513):2570–2572, 2001.

[189] F. Wächtler and L. Santos. Ground-state properties and elementary excitations of quantum droplets in dipolar bose-einstein condensates. *Phys. Rev. A*, 94:043618, Oct 2016.

[190] F. Wächtler and L. Santos. Quantum filaments in dipolar bose-einstein condensates. *Phys. Rev. A*, 93:061603, Jun 2016.

[191] Reuben R. W. Wang and John L. Bohn. Anisotropic thermalization of dilute dipolar gases. *Phys. Rev. A*, 103:063320, Jun 2021.

[192] Chad N Weiler, Tyler W Neely, David R Scherer, Ashton S Bradley, Matthew J Davis, and Brian P Anderson. Spontaneous vortices in the formation of bose-einstein condensates. *Nature*, 455(7215):948–951, 2008.

[193] Matthias Wenzel. *A dysprosium quantum gas in highly controllable optical traps.* Master's thesis, Physikalisches Institut; Universität Stuttgart, 2015.

[194] Kali E. Wilson, Alexander Guttridge, Jack Segal, and Simon L. Cornish. Quantum degenerate mixtures of cs and yb. *Phys. Rev. A*, 103:033306, Mar 2021.

[195] Ryan M. Wilson, Christopher Ticknor, John L. Bohn, and Eddy Timmermans. Roton immiscibility in a two-component dipolar bose gas. *Phys. Rev. A*, 86:033606, Sep 2012.

[196] M. J. Wright, S. Riedl, A. Altmeyer, C. Kohstall, E. R. Sánchez Guajardo, J. Hecker Denschlag, and R. Grimm. Finite-temperature collective dynamics of a fermi gas in the bec-bcs crossover. *Phys. Rev. Lett.*, 99:150403, Oct 2007.

[197] Kui-Tian Xi, Tim Byrnes, and Hiroki Saito. Fingering instabilities and pattern formation in a two-component dipolar bose-einstein condensate. *Phys. Rev. A*, 97:023625, Feb 2018.

[198] Kui-Tian Xi and Hiroki Saito. Droplet formation in a bose-einstein condensate with strong dipole-dipole interaction. *Phys. Rev. A*, 93:011604, Jan 2016.

[199] C. N. Yang. Concept of off-diagonal long-range order and the quantum phases of liquid he and of superconductors. *Rev. Mod. Phys.*, 34:694–704, Oct 1962.

[200] Heshmatollah Yavari and Forouzan Forouharmanesh. Effects of thermally induced roton-like excitation on the superfluid density of a quasi-2d dipolar bose condensed gas. *Annalen der Physik*, 532(6):1900412, 2020.

[201] Zhu-Xiong Ye, A. Canali, E. Soave, M. Kreyer, Y. Yudkin, C. Ravensbergen, E. Kirilov, and R. Grimm. Observation of low-field feshbach resonances between ^{161}dy and ^{40}k. *arXiv:2207.03407*, 2022.

[202] Zhu-Xiong Ye, Li-Yang Xie, Zhen Guo, Xiao-Bin Ma, Gao-Ren Wang, Li You, and Meng Khoon Tey. Double-degenerate bose-fermi mixture of strontium and lithium. *Phys. Rev. A*, 102:033307, Sep 2020.

[203] Johannes Zeiher, Rick van Bijnen, Peter Schauß, Sebastian Hild, Jae-yoon Choi, Thomas Pohl, Immanuel Bloch, and Christian Gross. Many-body interferometry of a Rydberg-dressed spin lattice. *Nature Physics*, 12(12):1095–1099, 2016.

[204] Yong-Chang Zhang, Fabian Maucher, and Thomas Pohl. Supersolidity around a critical point in dipolar bose-einstein condensates. *Phys. Rev. Lett.*, 123:015301, Jul 2019.

[205] Martin W Zwierlein, Jamil R Abo-Shaeer, Andre Schirotzek, Christian H Schunck, and Wolfgang Ketterle. Vortices and superfluidity in a strongly interacting fermi gas. *Nature*, 435(7045):1047–1051, 2005.

[206] Marija Šindik, Alessio Recati, Santo Maria Roccuzzo, Luis Santos, and Sandro Stringari. Creation and robustness of quantized vortices in a dipolar supersolid when crossing the superfluid-to-supersolid transition. *arXiv:2206.14100*, 2022.

Appendix A

Additional publications

A.1 Publication:

Dipolar quantum mixtures of erbium and dysprosium atoms

The following publication has appeared in

Physical Review Letters **121**, 213601 (2018)*
submitted 20 July 2018; published 21 Nov 2018
DOI: https://doi.org/10.1103/PhysRevLett.121.213601
A. Trautmann,[1,3] P. Ilzhöfer,[1,2,3] G. Durastante,[1,2] C. Politi,[1,2] M. Sohmen,[1,2] M. J. Mark,[1,2] and F. Ferlaino[1,2]

[1] *Institut für Quantenoptik und Quanteninformation, Österreichische Akademie der Wissenschaften, 6020 Innsbruck, Austria*

[2] *Institut für Experimentalphysik, Universität Innsbruck, 6020 Innsbruck, Austria*

[3] *These authors contributed equally: A. T. and P. I.*

*The author of the present thesis contributed in performing the measurements together with A. T., P. I., G. D., and M. S., analysed the experimental data with A. T., P. I., G. D., and M. S., and contributed in writing the manuscript and interpreting the results together with all the authors.

Editors' Suggestion | Featured in Physics

Dipolar Quantum Mixtures of Erbium and Dysprosium Atoms

A. Trautmann,[1,*] P. Ilzhöfer,[1,2,*] G. Durastante,[1,2] C. Politi,[1] M. Sohmen,[1,2] M. J. Mark,[1,2] and F. Ferlaino[1,2]
[1]*Institut für Quantenoptik und Quanteninformation, Österreichische Akademie der Wissenschaften, 6020 Innsbruck, Austria*
[2]*Institut für Experimentalphysik und Zentrum für Quantenoptik, Universität Innsbruck, Technikerstraße 25, 6020 Innsbruck, Austria*

(Received 20 July 2018; revised manuscript received 8 October 2018; published 21 November 2018)

We report on the first realization of heteronuclear dipolar quantum mixtures of highly magnetic erbium and dysprosium atoms. With a versatile experimental setup, we demonstrate binary Bose-Einstein condensation in five different Er-Dy isotope combinations, as well as one Er-Dy Bose-Fermi mixture. Finally, we present first studies of the interspecies interaction between the two species for one mixture.

DOI: 10.1103/PhysRevLett.121.213601

In recent years, the field of atomic dipolar quantum gases has witnessed an impressive expansion as researchers have made substantial headway in using and controlling a novel class of atoms, the highly magnetic rare-earth species. Since the first experimental successes in creating Bose and Fermi quantum gases of Dy [1,2] or Er [3,4], fascinating many-body phenomena based on the dipole-dipole interaction (DDI) have been observed, including Fermi surface deformation [5], quantum-stabilized droplet states [6–8], and roton quasiparticles [9]. Remarkably, for Dy and Er, the intriguing physics within reach comes with comparatively simple experimental approaches to achieve quantum degeneracy. Several research groups have either recently reported on new experimental realizations of quantum gases with Dy [10,11] or Er [12] or are actively pursuing it [13,14].

An alternative route to access dipolar quantum physics is provided by polar molecules, possessing an electric dipole moment. Up to now, ultracold gases of polar molecules have been created from nondipolar binary quantum mixtures of alkali atoms [15–18] and dipolar spin-exchange interactions have been recently observed with lattice-confined molecules [19]. Besides molecule creation, heteronuclear quantum mixtures have been used as powerful resources to realize a broad class of many-body quantum states (e.g., [20–27]), in which intra- and interspecies short-range contact interactions are at play.

In the experiment described in this Letter, we merge for the first time the physics of heteronuclear mixtures with the one of magnetic dipolar quantum gases. Our motivations to create quantum mixtures by combining two different dipolar species, Er and Dy, are numerous. First, the coupling between the two components acquires an anisotropic and long-range character due to the strong interspecies DDI, in contrast to purely contact-interacting mixtures. The emergent physical richness of the system has only begun to be uncovered by theory. Recent studies include the prediction of anisotropic boundaries in the dipolar immiscibility-miscibility phase diagram [28,29], roton immiscibility [30], vortex lattice formation [31], and impurity physics both in dipolar quantum droplets [32] and dipolar Binary Bose-Einstein condensates (BECs) [33,34]. Moreover, the magnetic moments are large, yet different (7 bohr magneton for Er and 10 for Dy), leading to a DDI twice as strong in Dy as in Er. Such a difference is on one hand advantageous to deeper elucidate the complex scattering and many-body physics by performing comparative single-species studies with Er and Dy in the same experimental environment. On the other hand, we also anticipate

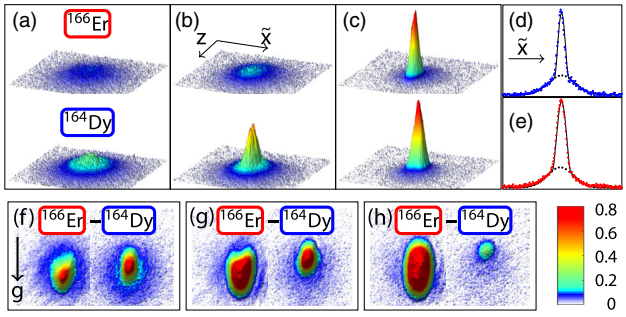

FIG. 1. Binary Bose-Einstein condensation in a ^{166}Er-^{164}Dy mixture. (a)–(c) Pairs of TOF absorption images at different evaporation stages, showing (a) a thermal mixture at about 180 nK, (b) an Er cloud at the onset of condensation coexisting with a thermal Dy gas at about 80 nK, and (c) the binary dipolar BEC with total atom numbers $N = 3.4 \times 10^4 (2.6 \times 10^4)$ for Er(Dy) with condensate fractions of about 45%. $\tilde{x}$ denotes the horizontal axis perpendicular to the imaging axis. (d),(e) Density profiles integrated along z, extracted from (c). Solid lines depict the 1D bimodal fit, the dotted lines show Gaussian fits to the thermal components. (f)–(h) BECs with a controlled number imbalance giving about $N^{\mathrm{Er}} = (3.2, 6.4, 9.2) \times 10^4$ with (35, 70, 85)% condensate fraction and $N^{\mathrm{Dy}} = (3.1, 2.9, 0.9) \times 10^4$ with (30, 55, 30)% condensate fraction for (f)–(h), respectively. The deformations and the relative displacement of the clouds are caused by interspecies interaction (see main text). The color bar indicates the optical density.

that, in mixture experiments, the imbalance in dipolar strength, combined with the interspecies interactions, promises fascinating prospects for creating long-lived quantum-droplet states and for accessing exotic fermionic superfluidity, for which the degree of deformation of the Fermi surface is species-dependent [5].

Second, the rich, but different atomic spectra of Er and Dy open promising prospects for implementing species-dependent optical manipulations schemes, including species-selective optical potentials at magic wavelengths and checkerboard-pattern-like lattice structures. Third, Er and Dy feature many stable bosonic and fermionic isotopes (both elements have four isotopes with natural abundances above 15%). Such an isotope variety allows us to create dipolar Bose-Bose, Bose-Fermi, and Fermi-Fermi heteronuclear mixtures. Last, mixtures composed of two different magnetic species serve as an ideal platform to produce ground-state polar molecules with both an electric and magnetic dipole moment, offering novel degrees of control and competing long-range interactions [35–37].

We here report on the first experimental realization of quantum-degenerate dipolar mixtures of Er and Dy atoms, using an all-optical approach for trapping and cooling. Taking advantage of the isotope richness in Er and Dy, we produce dipolar Bose-Bose mixtures with five different isotope combinations, as well as one Bose-Fermi mixture. We note that, prior to this work, the production of a Dy isotope mixture of a degenerate Fermi gas and a Bose gas near condensation has been reported [2] and, more recently, a doubly degenerate Fermi-Fermi mixture has been created from two Er spin states [39]. Experimental efforts are also devoted to creating Dy-K mixtures [40].

In the following, we detail the production of a double dipolar Bose-Einstein condensate (ddBEC) of ^{166}Er and ^{164}Dy. The same procedure is used for the other isotope mixtures. Our experiment starts with a double magneto-optical trap (MOT) of Er and Dy, as reported in our recent work [41]. For both species, the MOT operates on narrow intercombination lines and yields cold and spin-polarized samples in the absolute lowest Zeeman sublevels [10,13,41,42]. After loading the double MOT, we optically compress the mixture in 400 ms (cMOT phase) by reducing the detuning and power of the MOT beams as well as the magnetic-field gradient.

We then transfer the mixture into an optical dipole trap (ODT) by superposing it with the cMOT for 100 ms. Initially, the ODT consists of a single laser beam at 1064 nm, propagating along the horizontal (y) axis. The beam has a fixed vertical (z) focus of about 22 μm, whereas the horizontal waist can be controlled via a time-averaging-potential technique (see, e.g., [43]). This leads to an elliptic beam with variable aspect ratio (AR). Best transfer efficiency is observed for a beam power of 32 W and an AR of 4, which provides good spatial overlap between the cMOT and the ODT. We then switch off the MOT beams and magnetic-field gradient, and start a 5-sec evaporation sequence, during which we apply a bias magnetic field B_{evap} along the gravity (z) axis to preserve spin polarization.

Our strategy for evaporative cooling can be divided into three main stages. (i) During the initial 600 ms, we reduce the AR to unity while lowering the power of the single-beam ODT. This increases the density of the mixture at a roughly constant trap depth. (ii) We start forced evaporation in the horizontal ODT and add a vertically propagating dipole trap beam. The vertical beam is derived from the same laser source as the horizontal one and has a power of 15 W and a waist of 130 μm. (iii) We proceed with forced evaporation in the crossed ODT by reducing the powers of both beams nearly exponentially until the mixture is close to quantum degeneracy. In the final stage of the evaporation, we increase the AR to 5 to create a pancakelike trapping geometry and further decrease the trap depth until we reach double quantum degeneracy. To probe the atomic mixture, we switch off the ODT and, after a time-of-flight (TOF) expansion of 25 ms, we perform sequential absorption imaging with a resonant light pulse at 401 nm for Er and 500 μs later at 421 nm for Dy [3,44]; both pulses have a duration of 50 μs. The imaging light propagates horizontally with an angle of 45° with respect to the y axis.

Unlike many alkali mixtures [45–48], Er and Dy exhibit very comparable atomic polarizabilities α because of their similar atomic spectra. From single-species experiments [14,49], a ratio $\alpha_{\mathrm{Dy}}/\alpha_{\mathrm{Er}} = 1.06$ at 1064 nm is expected. For our initial ODT parameters, we calculate trap frequencies of about $\nu^{\mathrm{Er}} = (490, 5, 1980)$ Hz and $\nu^{\mathrm{Dy}} = (505, 5, 2050)$ Hz [50], corresponding to trap depths of 380 and 410 μK for Er and Dy, respectively. Although small, the difference in trap depths has an important effect on the evaporation trajectory of the mixture. We observe that the more weakly trapped Er atoms act as a coolant for Dy and are preferentially evaporated from the trap ("sympathetic losses" [47,51]). To sustain Er atom numbers high enough to achieve double quantum degeneracy, we imbalance the initial atom number in the MOT with Er as the majority component. The atom number imbalance can be easily controlled by individually changing the MOT loading time and beam power. This strategy is often employed in multispecies experiments, e.g., [52,53].

Figures 1(a)–1(c) show the phase transition from a thermal Er-Dy mixture (a) to a ddBEC (c). The TOF absorption images reveal the textbooklike fingerprint of condensation, the emergence of a bimodal density distribution, as plotted in Fig. 1(d). The condensation series [Figs. 1(a)–1(c)] is taken for an Er(Dy) MOT loading time of 3 s (1 s), for which we transfer 8×10^6 (7×10^5) Er(Dy) atoms into our ODT and measure a temperature of about 35 μK; this parameter set allows us to create number-balanced ddBECs. In agreement with the expected polarizabilities, we measure ODT trap frequencies of $\nu^{\mathrm{Er}} = (48.6(3), 29.7(9), 144(1))$ Hz and $\nu^{\mathrm{Dy}} = (50.6(3), 30.2(9),$

160(1)) Hz [54]. The resultant gravitational sag between the two species is 2.1(2) μm. By varying the imbalance of the MOT loading, we can produce degenerate mixtures with different atom number ratios and condensate fractions, which is exemplified in Figs. 1(f)–1(h). For large condensates, one directly observes a deformation of the density profiles due to interspecies interaction, as we discuss later in more detail.

To quantify the cooling efficiency, we plot the normalized phase-space density ($\mathrm{PSD}/\mathrm{PSD}_0$) as a function of normalized atom numbers (N/N_0) during the evaporation stages ii and iii [see Fig. 2(a)]. PSD_0 and N_0 are the respective initial values at stage ii. From this plot, we extract $\gamma = -d\ln(\mathrm{PSD}/\mathrm{PSD}_0)/d\ln(N/N_0)$ [55], which captures the evaporation efficiency, via a linear fit to the data. In the single-beam ODT (stage ii), we see similar efficiencies both in mixture and single-species operations, with $\gamma \approx 1.2$. In the crossed ODT (stage iii), we find $\gamma^{\mathrm{Er}} = 2.4(9)$ for Er in the mixture operation. This value is comparable to state-of-the-art single-species Er experiments [56] and, as expected, little affected by a small admixture of Dy atoms. Contrarily, the cooling efficiency of Dy in stage (iii) strongly benefits from the sympathetic cooling by Er: We observe a steep increase of the Dy PSD in the mixture and extract $\gamma^{\mathrm{Dy}}_{\mathrm{sym}} = 7(2)$, whereas for the same N_0^{Dy} but in single-species operation, the evaporation efficiency is considerably lower and would not suffice for condensation. However, with higher N_0^{Dy} we can still produce large Dy BECs in single-species operation.

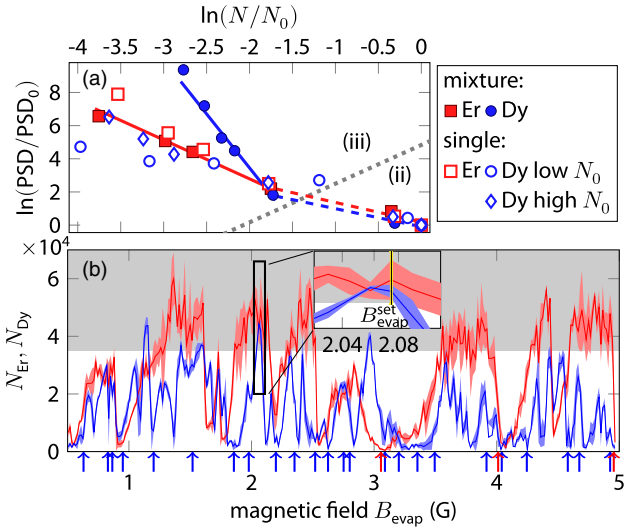

FIG. 2. (a) Evaporation trajectories: $\mathrm{PSD}/\mathrm{PSD}_0$ as a function of N/N_0. Filled squares (circles) indicate the Er(Dy) trajectory in mixture operation. The lines are linear fits to the data for evaporation in the single-beam (ii) and crossed-beam (iii) ODT (see main text). Open symbols show the single-species operation for Er (squares) and for Dy with small (circles) and large (diamonds) initial atom numbers. In the latter case, Dy condenses alone. (b) Atom numbers in the mixture of Er (red) and Dy (blue) at the onset of condensation as a function of the magnetic-field value during evaporation. Condensation is reached for atom numbers above about 3.5×10^4 (gray region). We record the best performance for a ddBEC around 2.075 G. Arrows indicate the position of known single-species Feshbach resonances [57–59].

The proper choice of B_{evap} plays an important role for cooling magnetic rare-earth atoms and becomes even more critical in mixture operation. It has indeed been observed in single-species experiments [57–59] that both Er and Dy exhibit extremely dense and temperature-dependent spectra of homonuclear Feshbach resonances. Figure 2(b) shows the atom numbers of the ^{166}Er-^{164}Dy mixture at the onset of condensation as a function of B_{evap} in a small magnetic-field range from 0.5 to 5 G. As expected, we find a number of broad and narrow loss features. Some of them are connected to known homonuclear Feshbach resonances [57–59], others we attribute to unknown high-temperature resonances or detrimental interspecies scattering conditions. In a few narrow magnetic-field windows, we observe atom numbers large enough for both components to condense. Our magnetic-field stability of about 2 mG is sufficient to reliably operate in most of these small windows. The optimal value of B_{evap}, listed in Table I, depends on the isotope combination.

Combining Er and Dy offers an unprecedented variety of heteronuclear mixtures with 16 possible isotope configurations, including Bose-Bose, Bose-Fermi, and Fermi-Fermi quantum gases (see Table I). Using the cooling and trapping procedure optimized for ^{166}Er-^{164}Dy, we are able to produce five ddBECs and one Bose-Fermi mixture. Concerning the remaining combinations, we know from previous experiments that both ^{167}Er and ^{163}Dy need a different experimental approach since ^{167}Er undergoes light-induced losses in a 1064-nm ODT [4], whereas ^{163}Dy, never brought to quantum degeneracy so far, has an inverted hyperfine structure, requiring most probably additional optical pumping stages. Both isotopes will be investigated for future studies of Fermi-Fermi mixtures.

Figures 3(a)–3(d) show absorption pictures of our doubly degenerate isotope mixtures. We are able to

TABLE I. (Left) List of optimal B_{evap} and $\gamma^{\mathrm{Dy}}_{\mathrm{sym}}$ for the quantum-degenerate Er-Dy mixtures. (Right) Chart of the available isotope mixtures: (✓) realized double-degenerate mixtures, (×) thermal mixtures, where degeneracy is not yet reached. (⋯) Mixtures with ^{167}Er and ^{163}Dy are not investigated here.

mixture	B_{evap}(G)	$\gamma^{\mathrm{Dy}}_{\mathrm{sym}}$
^{166}Er-^{164}Dy	2.075	7(2)
^{168}Er-^{162}Dy	3.300	6(2)
^{168}Er-^{164}Dy	3.300	6(2)
^{170}Er-^{162}Dy	1.540	11(7)
^{170}Er-^{164}Dy	3.210	3(1)
^{168}Er-^{161}Dy	3.455	4(1)

Dy \ Er	166	167	168	170
161	×	⋯	✓	×
162	×	⋯	✓	✓
163	⋯	⋯	⋯	⋯
164	✓	⋯	✓	✓

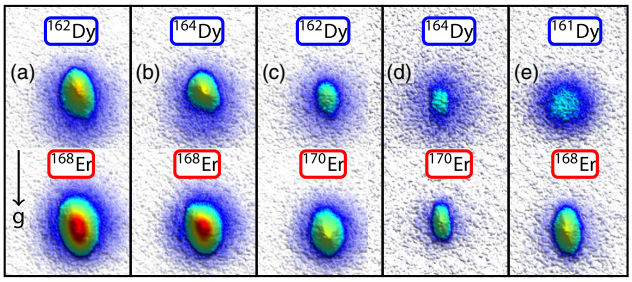

FIG. 3. Absorption pictures of the double-degenerate Bose-Bose mixtures (a)–(d) and the Bose-Fermi mixture (e). The pictures are averaged over 5–10 single shots. For all combinations, degeneracy is reached with the evaporation ramp optimized for the ^{166}Er-^{164}Dy mixture (cf. Fig. 1). B_{evap} is listed in Table I. Typical condensate fractions are around 30%, total atom numbers range between 1×10^4 and 3.5×10^4 atoms. For the imbalanced case, higher condensate fractions can be achieved (see Fig. 1). For the ^{161}Dy Fermi gas, $N = 8 \times 10^3$, $T/T_F \approx 0.5$, and TOF $= 15$ ms.

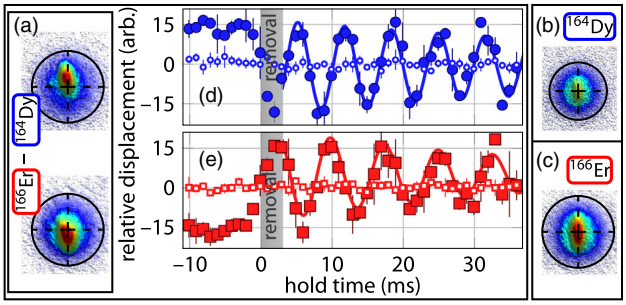

FIG. 4. Evidence of interspecies interactions in the ^{166}Er-^{164}Dy mixture: absorption pictures of Er and Dy in mixture (a) and single-species (b),(c) operation. (d),(e) Filled symbols show the c.m. position along z of the Dy BEC (d) and the Er BEC (e) after removal of the other species with resonant light. The gray region indicates the transient time until full removal. The solid lines are damped sine fits to the oscillations. For comparison, open symbols show the c.m. position in a thermal mixture.

condense all Bose-Bose isotope mixtures with the exception of ^{166}Er-^{162}Dy, for which we record severe losses during the evaporation, potentially due to a very large interspecies scattering length. For all degenerate mixtures, we observe sympathetic cooling of Dy by Er. The atom numbers in the ddBECs differ significantly for the different mixtures, while the initial atom numbers in the MOT are very similar. This points to different intra- and interspecies scattering properties during evaporation. The optimal B_{evap} and the extracted $\gamma_{\mathrm{sym}}^{\mathrm{Dy}}$ are listed in Table I.

We also prepare one Bose-Fermi mixture [see Fig. 3(e)], in which a ^{168}Er BEC coexists with a degenerate Fermi gas of ^{161}Dy. Although the cooling process of spin-polarized fermions can differ substantially from bosons, we are able to reach Bose-Fermi degeneracy with a similar evaporation scheme [60]. We measure a temperature of the Fermi gas of $T/T_F \approx 0.5$, with the Fermi temperature $T_F = 140$ nK. We expect that deeper degeneracy might be reached by using smaller ODT beam waists [4].

Remarkably, in the TOF images in Figs. 1 and 3 hints of interspecies interactions can be spotted: in mixture operation, the center-of-mass (c.m.) position of each BEC is vertically displaced with respect to its thermal-cloud center [see also Fig. 4(a)]. The two BECs are displaced in opposite directions, with the heavier (lighter) Er(Dy) always shifted down (up). Contrarily, in single-species operation the condensates and their thermal clouds are centered [see Figs. 4(b) and 4(c)].

To confirm that the displacement after TOF originates from in-trap interspecies interaction, we prepare a ddBEC, let it equilibrate for 50 ms, and then selectively remove either of the two species from the ODT using a resonant light pulse [61]. After a variable hold time in the ODT, we release the remaining cloud and record its c.m. position after TOF. As shown in Figs. 4(d) and 4(e), we observe a very pronounced c.m. oscillation of the remaining BEC component with a frequency close to its bare trap frequency. The oscillations of Er [removing Dy, Fig. 4(d)] and of Dy [removing Er, Fig. 4(e)] proceed in counterphase, as expected from their initial separation in trap. Repeating the same measurement with a thermal-thermal mixture, or a mixture with just one condensed component (not shown), yields negligible or significantly weaker oscillations, respectively.

The spatial separation between the two condensed components and their oscillating behavior after removal indicate that, for our trap geometry, the overall interspecies interaction—contact plus dipolar—has a repulsive character. We note that the interspecies scattering length, governing the contact interaction, and its Feshbach tuning are presently unknown and beyond reach of state-of-the-art scattering models [57,62]. To isolate the different sources of interaction and determine their signs, future dedicated experiments studying the interplay between trap geometry, dipole orientation, and interspecies scattering length, combined with simulations based on generalized coupled Gross-Pitaeskvii equations are necessary. Indeed, the DDI breaks the angular symmetry of the mean-field interspecies potentials and is expected to render the strength and the sign of the overall interspecies interaction anisotropic and trap dependent.

In conclusion, we have produced heteronuclear dipolar quantum mixtures by combining two strongly magnetic atomic species, Er and Dy. Their isotope variety, the richness of their interactions, the imbalance in the dipolar strength, and simple laser-cooling schemes make Er-Dy mixtures a powerful experimental platform to access many-body quantum phenomena, in which contact and dipolar intra- and interspecies interactions are at play.

This work is supported by the ERC Consolidator Grant (RARE, No. 681432) and a NFRI Grant (MIRARE,

No. ÖAW0600) from the Austrian Academy of Science. G. D. and M. S. acknowledge support by the Austrian Science Fund FWF within the DK-ALM: W1259-N27. We thank the ERBIUM team and the Dy-K team in Innsbruck and the ERBIUM team of Markus Greiner for fruitful discussions.

*These authors contributed equally to this work.

[1] M. Lu, N. Q. Burdick, S. H. Youn, and B. L. Lev, Strongly Dipolar Bose-Einstein Condensate of Dysprosium, Phys. Rev. Lett. **107**, 190401 (2011).
[2] M. Lu, N. Q. Burdick, and B. L. Lev, Quantum Degenerate Dipolar Fermi Gas, Phys. Rev. Lett. **108**, 215301 (2012).
[3] K. Aikawa, A. Frisch, M. Mark, S. Baier, A. Rietzler, R. Grimm, and F. Ferlaino, Bose-Einstein Condensation of Erbium, Phys. Rev. Lett. **108**, 210401 (2012).
[4] K. Aikawa, A. Frisch, M. Mark, S. Baier, R. Grimm, and F. Ferlaino, Reaching Fermi Degeneracy via Universal Dipolar Scattering, Phys. Rev. Lett. **112**, 010404 (2014).
[5] K. Aikawa, S. Baier, A. Frisch, M. Mark, C. Ravensbergen, and F. Ferlaino, Observation of Fermi surface deformation in a dipolar quantum gas, Science **345**, 1484 (2014).
[6] H. Kadau, M. Schmitt, M. Wenzel, C. Wink, T. Maier, I. Ferrier-Barbut, and T. Pfau, Observing the Rosensweig instability of a quantum ferrofluid, Nature (London) **530**, 194 (2016).
[7] L. Chomaz, S. Baier, D. Petter, M. J. Mark, F. Wächtler, L. Santos, and F. Ferlaino, Quantum-Fluctuation-Driven Crossover from a Dilute Bose-Einstein Condensate to a Macrodroplet in a Dipolar Quantum Fluid, Phys. Rev. X **6**, 041039 (2016).
[8] M. Schmitt, M. Wenzel, F. Böttcher, I. Ferrier-Barbut, and T. Pfau, Self-bound droplets of a dilute magnetic quantum liquid, Nature (London) **539**, 259 (2016).
[9] L. Chomaz, R. M. W. van Bijnen, D. Petter, G. Faraoni, S. Baier, J. H. Becher, M. J. Mark, F. Wächtler, L. Santos, and F. Ferlaino, Observation of roton mode population in a dipolar quantum gas, Nat. Phys. **14**, 442 (2018).
[10] T. Maier, H. Kadau, M. Schmitt, A. Griesmaier, and T. Pfau, Narrow-line magneto-optical trap for dysprosium atoms, Opt. Lett. **39**, 3138 (2014).
[11] E. Lucioni, L. Tanzi, A. Fregosi, J. Catani, S. Gozzini, M. Inguscio, A. Fioretti, C. Gabbanini, and G. Modugno, Dysprosium dipolar Bose-Einstein condensate with broad feshbach resonances, Phys. Rev. A **97**, 060701 (2018).
[12] J. Ulitzsch, D. Babik, R. Roell, and M. Weitz, Bose-Einstein condensation of erbium atoms in a quasielectrostatic optical dipole trap, Phys. Rev. A **95**, 043614 (2017).
[13] D. Dreon, L. A. Sidorenkov, C. Bouazza, W. Maineult, J. Dalibard, and S. Nascimbene, Optical cooling and trapping of highly magnetic atoms: The benefits of a spontaneous spin polarization, J. Phys. B **50**, 065005 (2017).
[14] C. Ravensbergen, V. Corre, E. Soave, M. Kreyer, S. Tzanova, E. Kirilov, and R. Grimm, Accurate Determination of the Dynamical Polarizability of Dysprosium, Phys. Rev. Lett. **120**, 223001 (2018).
[15] K.-K. Ni, S. Ospelkaus, M. H. G. de Miranda, A. Pe'er, B. Neyenhuis, J. J. Zirbel, S. Kotochigova, P. S. Julienne, D. S. Jin, and J. Ye, A high phase-space-density gas of polar molecules, Science **322**, 231 (2008).
[16] T. Takekoshi, L. Reichsöllner, A. Schindewolf, J. M. Hutson, C. R. Le Sueur, O. Dulieu, F. Ferlaino, R. Grimm, and H.-C. Nägerl, Ultracold Dense Samples of Dipolar RBCS Molecules in the Rovibrational and Hyperfine Ground State, Phys. Rev. Lett. **113**, 205301 (2014).
[17] P. K. Molony, P. D. Gregory, Z. Ji, B. Lu, M. P. Köppinger, C. R. Le Sueur, C. L. Blackley, J. M. Hutson, and S. L. Cornish, Creation of Ultracold $^{87}Rb^{133}Cs$ Molecules in the Rovibrational Ground State, Phys. Rev. Lett. **113**, 255301 (2014).
[18] S. Moses, J. Covey, M. Miecnikowski, D. Jin, and J. Ye, New frontiers for quantum gases of polar molecules, Nat. Phys. **13**, 13 (2016).
[19] B. Yan, S. A. Moses, B. Gadway, J. P. Covey, K. R. A. Hazzard, A. M. Rey, D. S. Jin, and J. Ye, Observation of dipolar spin-exchange interactions with lattice-confined polar molecules, Nature (London) **501**, 521 (2013).
[20] T.-L. Ho and V. B. Shenoy, Binary Mixtures of Bose Condensates of Alkali Atoms, Phys. Rev. Lett. **77**, 3276 (1996).
[21] S. Ospelkaus, C. Ospelkaus, O. Wille, M. Succo, P. Ernst, K. Sengstock, and K. Bongs, Localization of Bosonic Atoms by Fermionic Impurities in a Three-Dimensional Optical Lattice, Phys. Rev. Lett. **96**, 180403 (2006).
[22] S. Will, T. Best, S. Braun, U. Schneider, and I. Bloch, Coherent Interaction of a Single Fermion with a Small Bosonic Field, Phys. Rev. Lett. **106**, 115305 (2011).
[23] J. Heinze, S. Götze, J. S. Krauser, B. Hundt, N. Fläschner, D.-S. Lühmann, C. Becker, and K. Sengstock, Multiband Spectroscopy of Ultracold Fermions: Observation of Reduced Tunneling in Attractive Bose-Fermi Mixtures, Phys. Rev. Lett. **107**, 135303 (2011).
[24] N. Spethmann, F. Kindermann, S. John, C. Weber, D. Meschede, and A. Widera, Dynamics of Single Neutral Impurity Atoms Immersed in an Ultracold Gas, Phys. Rev. Lett. **109**, 235301 (2012).
[25] N. B. Jørgensen, L. Wacker, K. T. Skalmstang, M. M. Parish, J. Levinsen, R. S. Christensen, G. M. Bruun, and J. J. Arlt, Observation of Attractive and Repulsive Polarons in a Bose-Einstein Condensate, Phys. Rev. Lett. **117**, 055302 (2016).
[26] M.-G. Hu, M. J. Van de Graaff, D. Kedar, J. P. Corson, E. A. Cornell, and D. S. Jin, Bose Polarons in the Strongly Interacting Regime, Phys. Rev. Lett. **117**, 055301 (2016).
[27] T. Rentrop, A. Trautmann, F. A. Olivares, F. Jendrzejewski, A. Komnik, and M. K. Oberthaler, Observation of the Phononic Lamb Shift with a Synthetic Vacuum, Phys. Rev. X **6**, 041041 (2016).
[28] G. Gligorić, A. Maluckov, M. Stepić, L. Hadžievski, and B. A. Malomed, Transition to miscibility in linearly coupled binary dipolar Bose-Einstein condensates, Phys. Rev. A **82**, 033624 (2010).
[29] R. K. Kumar, P. Muruganandam, L. Tomio, and A. Gammal, Miscibility in coupled dipolar and non-dipolar Boseeinstein condensates, J. Phys. Commun. **1**, 035012 (2017).
[30] R. M. Wilson, C. Ticknor, J. L. Bohn, and E. Timmermans, Roton immiscibility in a two-component dipolar Bose gas, Phys. Rev. A **86**, 033606 (2012).

[31] R. K. Kumar, L. Tomio, B. A. Malomed, and A. Gammal, Vortex lattices in binary Bose-Einstein condensates with dipole-dipole interactions, Phys. Rev. A **96**, 063624 (2017).
[32] M. Wenzel, T. Pfau, and I. Ferrier-Barbut, A fermionic impurity in a dipolar quantum droplet, Phys. Scr. **93**, 104004 (2018).
[33] B. Kain and H. Y. Ling, Polarons in a dipolar condensate, Phys. Rev. A **89**, 023612 (2014).
[34] L. A. P. Ardila and T. Pohl, Ground-state properties of dipolar bose polarons, arXiv:1804.06390.
[35] E. Abrahamsson, T. V. Tscherbul, and R. V. Krems, Quantum chaos in ultracold collisions of gas-phase erbium atoms, J. Chem. Phys. **127**, 044302 (2007).
[36] T. M. Rvachov, H. Son, A. T. Sommer, S. Ebadi, J. J. Park, M. W. Zwierlein, W. Ketterle, and A. O. Jamison, Observation of Low-Field Fano-Feshbach Resonances in Ultracold Gases of Dysprosium, Phys. Rev. Lett. **119**, 143001 (2017).
[37] The electric dipole moment of ErDy is currently unknown; Ref. [38] reports the calculation for another rare-earth combination, EuYb, with −0.13 D. Based on electronegativity arguments, a similar value can be expected in ErDy.
[38] M. Tomza, Ab initio properties of the ground-state polar and paramagnetic europium–alkali-metal-atom and 5 europium–alkaline-earth-metal-atom molecules, Phys. Rev. A **90**, 022514 (2014).
[39] S. Baier, D. Petter, J. H. Becher, A. Patscheider, G. Natale, L. Chomaz, M. J. Mark, and F. Ferlaino, Realization of a Strongly Interacting Fermi Gas of Dipolar Atoms, Phys. Rev. Lett. **121**, 093602 (2018).
[40] R. Grimm (private communication).
[41] P. Ilzhöfer, G. Durastante, A. Patscheider, A. Trautmann, M. J. Mark, and F. Ferlaino, Phys. Rev. A **97**, 023633 (2018).
[42] A. Frisch, K. Aikawa, M. Mark, A. Rietzler, J. Schindler, E. Zupanič, R. Grimm, and F. Ferlaino, Narrow-line magneto-optical trap for erbium, Phys. Rev. A **85**, 051401 (2012).
[43] S. Baier, An optical dipole trap for Erbium with tunable geometry, Master's thesis, University of Innsbruck, 2012.
[44] M. Lu, S. H. Youn, and B. L. Lev, Trapping Ultracold Dysprosium: A Highly Magnetic Gas for Dipolar Physics, Phys. Rev. Lett. **104**, 063001 (2010).
[45] G. Modugno, M. Modugno, F. Riboli, G. Roati, and M. Inguscio, Two Atomic Species Superfluid, Phys. Rev. Lett. **89**, 190404 (2002).
[46] Z. Hadzibabic, C. A. Stan, K. Dieckmann, S. Gupta, M. W. Zwierlein, A. Görlitz, and W. Ketterle, Two-Species Mixture of Quantum Degenerate Bose and Fermi Gases, Phys. Rev. Lett. **88**, 160401 (2002).
[47] M. Mudrich, S. Kraft, K. Singer, R. Grimm, A. Mosk, and M. Weidemüller, Sympathetic Cooling with Two Atomic Species in an Optical Trap, Phys. Rev. Lett. **88**, 253001 (2002).
[48] M. Gröbner, P. Weinmann, F. Meinert, K. Lauber, E. Kirilov, and H.-C. Nägerl, A new quantum gas apparatus for ultracold mixtures of K and Cs and KCs ground-state molecules, J. Mod. Opt. **63**, 1829 (2016).
[49] J. H. Becher, S. Baier, K. Aikawa, M. Lepers, J.-F. Wyart, O. Dulieu, and F. Ferlaino, Anisotropic polarizability of erbium atoms, Phys. Rev. A **97**, 012509 (2018).
[50] We use the notation $\nu^{\mathrm{Er,Dy}} = (\nu_x, \nu_y, \nu_z)$.
[51] A. Mosk, S. Kraft, M. Mudrich, K. Singer, W. Wohlleben, R. Grimm, and M. Weidemüller, Mixture of ultracold lithium and cesium atoms in an optical dipole trap, Appl. Phys. B **73**, 791 (2001).
[52] Y. Tang, A. Sykes, N. Q. Burdick, J. L. Bohn, and B. L. Lev, s-wave scattering lengths of the strongly dipolar bosons ^{162}Dy and ^{164}Dy, Phys. Rev. A **92**, 022703 (2015).
[53] C.-H. Wu, I. Santiago, J. W. Park, P. Ahmadi, and M. W. Zwierlein, Strongly interacting isotopic bose-fermi mixture immersed in a fermi sea, Phys. Rev. A **84**, 011601 (2011).
[54] The trap frequencies along the y and z axes are extracted from center-of-mass-oscillation measurement; the frequency along x is calculated based on the beam waist, calibrated via the z frequency, and our knowledge of the polarizability [14,49].
[55] W. Ketterle and N. V. Druten, in *Evaporative Cooling of Trapped Atoms*, edited by B. Bederson and H. Walther, Advances in Atomic, Molecular, and Optical Physics Vol. 37 (Academic Press, New York, 1996), pp. 181–236.
[56] A. Frisch, Dipolar quantum gases of erbium, Ph.D. thesis, University of Innsbruck, 2014.
[57] A. Frisch, M. Mark, K. Aikawa, F. Ferlaino, J. L. Bohn, C. Makrides, A. Petrov, and S. Kotochigova, Nature (London) **507**, 475 (2014).
[58] K. Baumann, N. Q. Burdick, M. Lu, and B. L. Lev, Observation of low-field fano-feshbach resonances in ultracold gases of dysprosium, Phys. Rev. A **89**, 020701 (2014).
[59] T. Maier, H. Kadau, M. Schmitt, M. Wenzel, I. Ferrier-Barbut, T. Pfau, A. Frisch, S. Baier, K. Aikawa, L. Chomaz, M. J. Mark, F. Ferlaino, C. Makrides, E. Tiesinga, A. Petrov, and S. Kotochigova, Emergence of Chaotic Scattering in Ultracold Er and Dy, Phys. Rev. X **5**, 041029 (2015).
[60] For the Bose-Fermi mixture, slightly different final trap parameters are required, with typically $\nu^{\mathrm{Er}} = (95(5), 33(1), 120(1))$, $\nu^{\mathrm{Dy}} = (106(5), 34(1), 142(1))$.
[61] The light pulse at the respective imaging transition has a duration of 1 ms. We have checked that the resonant light of one species does not affect the other.
[62] S. Kotochigova, Controlling interactions between highly magnetic atoms with feshbach resonances, Rep. Prog. Phys. **77**, 093901 (2014).

A.2 Publication:

Long-lived and transient supersolid behaviors in dipolar quantum gases

The following publication has appeared in

Physical Review X **9**, 021012 (2019)[†]
submitted 12 Mar 2019; published 19 April 2019
DOI: https://doi.org/10.1103/PhysRevX.9.021012
L. Chomaz,[2] D. Petter,[2] P. Ilzhöfer,[1,2] G. Natale,[2] A. Trautmann,[1] C. Politi,[1,2] G. Durastante,[1,2] R. M. W. van Bijnen,[1] A. Patscheider,[2] M. Sohmen,[1,2] M. J. Mark,[1,2] and F. Ferlaino[1,2]

[1] *Institut für Quantenoptik und Quanteninformation, Österreichische Akademie der Wissenschaften, 6020 Innsbruck, Austria*

[2] *Institut für Experimentalphysik, Universität Innsbruck, 6020 Innsbruck, Austria*

[†]The author of the present thesis analysed the data relative to the dysprosium experiments with M. S., and M. J. M., and contributed in writing the manuscript and interpreting the results together with all the authors.

Featured in Physics

Long-Lived and Transient Supersolid Behaviors in Dipolar Quantum Gases

L. Chomaz,[1] D. Petter,[1] P. Ilzhöfer,[2] G. Natale,[1] A. Trautmann,[2] C. Politi,[2] G. Durastante,[1,2] R. M. W. van Bijnen,[2] A. Patscheider,[1] M. Sohmen,[1,2] M. J. Mark,[1,2] and F. Ferlaino[1,2,*]

[1]*Institut für Experimentalphysik, Universität Innsbruck, Technikerstraße 25, 6020 Innsbruck, Austria*
[2]*Institut für Quantenoptik und Quanteninformation, Österreichische Akademie der Wissenschaften, Technikerstraße 21a, 6020 Innsbruck, Austria*

(Received 11 March 2019; published 19 April 2019; corrected 25 April 2019)

By combining theory and experiments, we demonstrate that dipolar quantum gases of both ^{166}Er and ^{164}Dy support a state with supersolid properties, where a spontaneous density modulation and a global phase coherence coexist. This paradoxical state occurs in a well-defined parameter range, separating the phases of a regular Bose-Einstein condensate and of an insulating droplet array, and is rooted in the roton mode softening, on the one side, and in the stabilization driven by quantum fluctuations, on the other side. Here, we identify the parameter regime for each of the three phases. In the experiment, we rely on a detailed analysis of the interference patterns resulting from the free expansion of the gas, quantifying both its density modulation and its global phase coherence. Reaching the phases via a slow interaction tuning, starting from a stable condensate, we observe that ^{166}Er and ^{164}Dy exhibit a striking difference in the lifetime of the supersolid properties, due to the different atom loss rates in the two systems. Indeed, while in ^{166}Er the supersolid behavior survives only a few tens of milliseconds, we observe coherent density modulations for more than 150 ms in ^{164}Dy. Building on this long lifetime, we demonstrate an alternative path to reach the supersolid regime, relying solely on evaporative cooling starting from a thermal gas.

DOI: 10.1103/PhysRevX.9.021012

Subject Areas: Atomic and Molecular Physics, Condensed Matter Physics, Quantum Physics

I. INTRODUCTION

Supersolidity is a paradoxical quantum phase of matter where both crystalline and superfluid order coexist [1–3]. Such a counterintuitive phase, featuring rather antithetic properties, has been originally considered for quantum crystals with mobile bosonic vacancies, the latter being responsible for the superfluid order. Solid ^{4}He has long been considered a prime system to observe such a phenomenon [4,5]. However, after decades of theoretical and experimental efforts, an unambiguous proof of supersolidity in solid ^{4}He is still missing [6,7].

In search of more favorable and controllable systems, ultracold atoms emerged as a very promising candidate, thanks to their highly tunable interactions. Theoretical works point to the existence of a supersolid ground state in different cold-atom settings, including dipolar [8] and Rydberg particles [9,10], cold atoms with a soft-core potential [11], or lattice-confined systems [7]. Breakthrough experiments with Bose-Einstein condensates (BECs) coupled to light have recently demonstrated a state with supersolid properties [12,13]. While in these systems indeed two continuous symmetries are broken, the crystal periodicity is set by the laser wavelength, making the supersolid incompressible.

Another key notion concerns the close relation between a possible transition to a supersolid ground state and the existence of a local energy minimum at large momentum in the excitation spectrum of a nonmodulated superfluid, known as the roton mode [14]. Since excitations corresponding to a periodic density modulation at the roton wavelength are energetically favored, the existence of this mode indicates the system's tendency to crystallize [15] and it is predicted to favor a transition to a supersolid ground state [4,5,9].

Remarkably, BECs of highly magnetic atoms, in which the particles interact through the long-range and anisotropic dipole-dipole interaction (DDI), appear to gather several key ingredients for realizing a supersolid phase. First, as predicted more than 15 years ago [16,17] and recently demonstrated in experiments [18,19], the partial attraction in momentum space due to the DDI gives rise to a roton

*Corresponding author.
Francesca.Ferlaino@uibk.ac.at

minimum. The corresponding excitation energy, i.e., the roton gap, can be tuned in the experiments down to vanishing values. Here, the excitation spectrum softens at the roton momentum and the system becomes unstable. Second, there is a nontrivial interplay between the trap geometry and the phase diagram of a dipolar BEC. For instance, our recent observations have pointed out the advantage of axially elongated trap geometries (i.e., cigar shaped) compared to the typically considered cylindrically symmetric ones (i.e., pancake shaped) in enhancing the visibility of the roton excitation in experiments. Last but not least, while the concept of a fully softened mode is typically related to instabilities and disruption of a coherent quantum phase, groundbreaking works in the quantum-gas community have demonstrated that quantum fluctuations can play a crucial role in stabilizing a dipolar BEC [20–26]. Such a stabilization mechanism enables the existence, beyond the mean-field instability, of a variety of stable ground states, from a single macrodroplet [22,24,27] to striped phases [28], and droplet crystals [29]; see also related works [30–33]. For multidroplet ground states, efforts have been devoted to understanding if a phase coherence among ground-state droplets could be established [28,29]. However, previous experiments with ^{164}Dy have shown the absence of phase coherence across the droplets [28], probably due to the limited atom numbers.

Droplet ground states, quantum stabilization, and dipolar rotons have caused a huge amount of excitement with very recent advancements adding key pieces of information to the supersolid scenario. The quench experiments in an ^{166}Er BEC at the roton instability have revealed out-of-equilibrium modulated states with an early-time phase coherence over a timescale shorter than a quarter of the oscillation period along the weak-trap axis [18]. In the same work, it has been suggested that the roton softening combined with the quantum stabilization mechanism may open a promising route towards a supersolid ground state. A first confirmation came from a recent theoretical work [34], considering an Er BEC in an infinite elongated trap with periodic boundary conditions and tight transverse confinement. The supersolid phase appears to exist within a narrow region in interaction strength, separating a roton excitation with a vanishing energy and an incoherent assembly of insulating droplets. Almost simultaneously, experiments with ^{162}Dy BECs in a shallow elongated trap, performing a slow tuning of the contact interaction, reported on the production of stripe states with phase coherence persisting up to half of the weak trapping period [35]. More recently, such observations have been confirmed in another ^{162}Dy experiment [36]. Here, theoretical calculations showed the existence of a phase-coherent droplet ground state, linking the experimental findings to the realization of a state with supersolid properties. The results on ^{162}Dy show, however, transient supersolid properties whose lifetime is limited by fast inelastic losses caused by three-body collisions [35,36]. These realizations raise the crucial question of whether a long-lived or stationary supersolid state can be created despite the usually non-negligble atom losses and the crossing of a discontinuous phase transition, which inherently creates excitations in the system.

In this work, we study both experimentally and theoretically the phase diagram of degenerate gases of highly magnetic atoms beyond the roton softening. Our investigations are carried out using two different experimental setups producing BECs of ^{166}Er [22,37] and of ^{164}Dy [38] and rely on a fine-tuning of the contact-interaction strength in both systems. In the regime of interest, these two atomic species have different contact-interaction scattering lengths a_s, whose precise dependence on the magnetic field is known only for Er [18,22,39], and different three-body-loss rate coefficients. Moreover, Er and Dy possess different magnetic moments μ and masses m, yielding the dipolar lengths, $a_{\mathrm{dd}} = \mu_0\mu^2 m/12\pi\hbar^2$, of $65.5a_0$ and $131a_0$, respectively. Here, μ_0 is the vacuum permeability, $\hbar = h/2\pi$ the reduced Planck constant, and a_0 the Bohr radius. For both systems, we find states showing hallmarks of supersolidity, namely, the coexistence of density modulation and global phase coherence. For such states, we quantify the extent of the a_s parameter range for their existence and study their lifetime. For ^{166}Er, we find results very similar to the one recently reported for ^{162}Dy [35,36], both systems being limited by strong three-body losses, which destroy the supersolid properties in about half of a trap period. However, for ^{164}Dy, we have identified an advantageous magnetic-field region where losses are very low and large BECs can be created. In this condition, we observe that the supersolid properties persist over a remarkably long time, well exceeding the trap period. Based on such a high stability, we finally demonstrate a novel route to reach the supersolid state, based on evaporative cooling from a thermal gas.

II. THEORETICAL DESCRIPTION

As a first step in our study of the supersolid phase in dipolar BECs, we compute the ground-state phase diagram for both ^{166}Er and ^{164}Dy quantum gases. The gases are confined in a cigar-shaped harmonic trap, as illustrated in Fig. 1(a). Our theory is based on numerical calculations of the extended Gross-Pitaevskii equation [40], which includes our anisotropic trapping potential, the short-range contact and long-range dipolar interactions at a mean-field level, as well as the first-order beyond-mean-field correction in the form of a Lee-Huang-Yang (LHY) term [18,22–24,27]. We note that, while both the exact strength of the LHY term and its dependence on the gas characteristics are under debate [18,19,25,31,41], the importance of such a term, scaling with a higher power in density, is essential for stabilizing states beyond the mean-field instability [18,25,41]; see also Refs. [8,42–44].

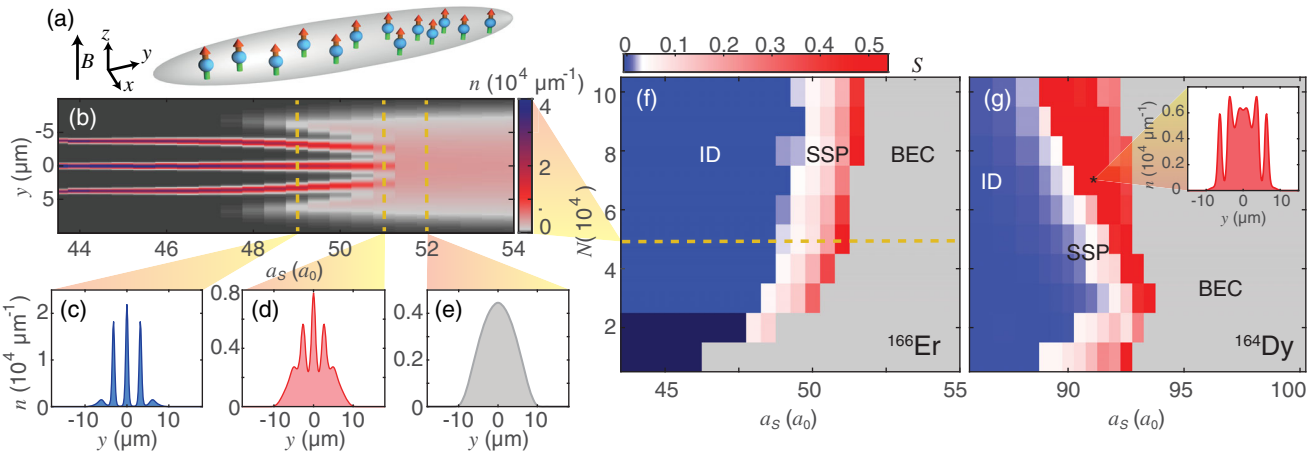

FIG. 1. Phase diagram of an ^{166}Er and a ^{164}Dy dipolar BEC in a cigar-shaped trap. (a) Illustration of the trap geometry with atomic dipoles oriented along z. (b) Integrated density profile as a function of a_s for an ^{166}Er ground state of $N = 5 \times 10^4$. In the color bar, the density scale is upper limited to 4×10^4 μm^{-1} in order to enhance the visibility in the supersolid regime. (c)–(e) Exemplary density profiles for an insulating droplet state (ID) at $a_s = 49a_0$, for a state with supersolid properties (SSP) at $51a_0$, and for a BEC at $52a_0$, respectively. (f),(g) Phase diagrams for ^{166}Er and ^{164}Dy for trap frequencies $\omega_{x,y,z} = 2\pi \times (227, 31.5, 151)$ and $2\pi \times (225, 37, 135)$ Hz, respectively. The gray color identifies ground states with a single peak in $n(y)$ of large Gaussian width, $\sigma_y > 2\ell_y$. The dark blue region in (f) shows the region where $n(y)$ exhibits a single sharp peak, $\sigma_y \leq 2\ell_y$, and no density modulation. The red-to-blue color map shows S in the case of a density-modulated $n(y)$. In (g) the color map is upper limited to use the same color code as in (f) and to enhance visibility in the low-N regime. The inset in (g) shows the calculated density profile for ^{164}Dy at $N = 7 \times 10^4$ and $a_s = 91a_0$.

Our theoretical results are summarized in Fig. 1. By varying the condensed-atom number N and a_s, the phase diagram shows three very distinct phases. To illustrate them, we first describe the evolution of the integrated *in situ* density profile $n(y)$ with fixed N for varying a_s, Fig. 1(b). The first phase, appearing at large a_s, resembles a regular dilute BEC. It corresponds to a nonmodulated density profile of low peak density and large axial size σ_y exceeding several times the corresponding harmonic oscillator length ($\ell_y = \sqrt{\hbar/m\omega_y}$); see Fig. 1(e) and the region denoted BEC in Figs. 1(f) and 1(g). The second phase appears when decreasing a_s down to a certain critical value, a_s^*. Here, the system undergoes an abrupt transition to a periodic density-modulated ground state, consisting of an array of overlapping narrow droplets, each of high peak density. Because the droplets are coupled to each other via a density overlap, later quantified in terms of the link strength S, particles can tunnel from one droplet to a neighboring one, establishing a global phase coherence across the cloud; see Fig. 1(d). Such a phase, in which periodic density modulation and phase coherence coexist, is identified as the supersolid (SSP) one [10,34]; see the SSP region in Figs. 1(f) and 1(g). When further decreasing a_s, we observe a fast reduction of the density overlap, which eventually vanishes; see Fig. 1(c). Here, the droplets become fully separated. Under realistic experimental conditions, it is expected that the phase relation between such droplets cannot be maintained; see later discussion. We identify this third phase as the one of an insulating droplet (ID) array [27,28,45]; see the ID region in Figs. 1(f) and 1(g). For low N, we find a single droplet of high peak density, as in Refs. [24,27]; see dark blue region in Fig. 1(f). Generally speaking, our calculations show that the number of droplets in the array decreases with lowering a_s or N. The existence of these three phases (BEC, SSP, ID) is consistent with recent calculations considering an infinitely elongated Er BEC [34] and a cigar-shaped ^{162}Dy BEC [36], illustrating the generality of this behavior in dipolar gases.

To study the supersolid character of the density-modulated phases, we compute the average of the wave function overlap between neighboring droplets S. As an ansatz to extract S, we use a Gaussian function to describe the wave function of each individual droplet. This is found to be an appropriate description from an analysis of the density profiles of Figs. 1(b)–1(d); see also Ref. [46]. For two droplets at a distance d and of identical Gaussian widths σ_y along the array direction, S is simply $S = \exp(-d^2/4\sigma_y^2)$. Here, we generalize the computation of the wave function overlap to account for the difference in widths and amplitudes among neighboring droplets. This analysis allows us to distinguish between the two types of modulated ground states, SSP and ID in Figs. 1(f) and 1(g). Within the Josephson-junction picture [47–49], the tunneling rate of atoms between neighboring droplets depends on the wave function overlap, and an estimate for the single-particle tunneling rate can be derived within the Gaussian approximation [46]; see also Ref. [40]. The ID phase corresponds to vanishingly small values of S, yielding

tunneling times extremely long compared to any other relevant timescale. In contrast, the supersolid phase is identified by a substantial value of S, with a correspondingly short tunneling time.

As shown in Figs. 1(f) and 1(g), a comparative analysis of the phase diagram for ^{166}Er and ^{164}Dy reveals similarities between the two species (see also Ref. [36]). A supersolid phase is found for sufficiently high N, in a narrow region of a_s, upper bounded by the critical value $a_s{}^*(N)$. For intermediate N, a_s^* increases with increasing N. We note that, for low N, the nonmodulated BEC evolves directly into a single droplet state for decreasing a_s [50]. In this case, no supersolid phase is found in between; see also Refs. [24,27]. Despite the general similarities, we see that the supersolid phase for ^{164}Dy appears for lower atom number than for Er and has a larger extension in a_s. This is mainly due to the different a_{dd} and strength of the LHY term. We note that, at large N and for decreasing a_s, Dy exhibits ground states with a density modulation appearing first in the wings, which then progresses inwards until a substantial modulation over the whole cloud is established [51]; see inset of Fig. 1(g). In this regime, we also observe that a_s^* decreases with increasing N. These types of states have not been previously reported and, although challenging to access in experiments because of the large N, they deserve further theoretical investigations.

III. EXPERIMENTAL SEQUENCE FOR ^{166}Er AND ^{164}Dy

To experimentally access the above-discussed physics, we produce dipolar BECs of either ^{166}Er or ^{164}Dy atoms. These two systems are created in different setups and below we summarize the main experimental steps; see also Ref. [40].

Erbium.—We prepare a stable ^{166}Er BEC following the scheme of Ref. [18]. At the end of the preparation, the Er BEC contains about $N = 8 \times 10^4$ atoms at $a_s = 64.5a_0$. The sample is confined in a cigar-shaped optical dipole trap with harmonic frequencies $\omega_{x,y,z} = 2\pi \times (227, 31.5, 151)$ Hz. A homogeneous magnetic field B polarizes the sample along z and controls the value of a_s via a magnetic Feshbach resonance (FR) [18,22,40]. Our measurements start by linearly ramping down a_s within 20 ms and waiting an additional 15 ms so that a_s reaches its target value [40]. We note that ramping times between 20 and 60 ms have been tested in the experiment and we do not record a significant difference in the system's behavior. After the 15-ms stabilization time, we then hold the sample for a variable time t_h before switching off the trap. Finally, we let the cloud expand for 30 ms and perform absorption imaging along the z (vertical) direction, from which we extract the density distribution of the cloud in momentum space, $n(k_x, k_y)$.

Dysprosium.—The experimental procedure to create a ^{164}Dy BEC follows the one described in Ref. [38]; see also Ref. [40]. Similarly to Er, the Dy BEC is also confined in a cigar-shaped optical dipole trap and a homogeneous magnetic field B sets the quantization axis along z and the value of a_s. For Dy, we will discuss our results in terms of magnetic field B, since the a_s-to-B conversion is not well known in the magnetic-field range considered [25,40,41,52]. In a first set of measurements, we first produce a stable BEC of about $N = 3.5 \times 10^4$ condensed atoms at a magnetic field of $B = 2.5$ G and then probe the phase diagram by tuning a_s. Here, before ramping the magnetic field to access the interesting a_s regions, we slowly increase the power of the trapping beams within 200 ms. The final trap frequencies are $\omega_{x,y,z} = 2\pi \times (300, 16, 222)$ Hz. After preparing a stable BEC, we ramp B to the desired value within 20 ms and hold the sample for t_h [40]. In a second set of measurements, we study a completely different approach to reach the supersolid state. As discussed later, here we first prepare a thermal sample at a B value where supersolid properties are observed and then further cool the sample until a transition to a coherent droplet-array state is reached. In both cases, at the end of the experimental sequence, we perform absorption imaging after typically 27 ms of time-of-flight (TOF) expansion. The imaging beam propagates horizontally under an angle α of $\approx 45°$ with respect to the weak axis of the trap (y). From the TOF images, we thus extract $n(k_Y, k_z)$ with $k_Y = \cos(\alpha)k_y + \sin(\alpha)k_x$.

A special property of ^{164}Dy is that its background scattering length is smaller than a_{dd}. This allows us to enter the supersolid regime without the need of setting B close to a FR, as is done for ^{166}Er and ^{162}Dy, which typically causes severe atom losses due to increased three-body-loss coefficients. In contrast, in the case of ^{164}Dy, the supersolid regime is reached by ramping B away from the FR pole used to produce the stable BEC via evaporative cooling, as the a_s range of Fig. 1(g) lies close to the background a_s reported in Ref. [52]; see also Ref. [40]. At the background level, three-body-loss coefficients below 1.3×10^{-41} m^6 s^{-1} have been reported for ^{164}Dy [25].

IV. DENSITY MODULATION AND PHASE COHERENCE

The coexistence of density modulation and phase coherence is the key feature that characterizes the supersolid phase and allows us to discriminate it from the BEC and ID cases. To experimentally probe this aspect in our dipolar quantum gases, we record their density distribution after a TOF expansion for various values of a_s across the phase diagram. As for a BEC in a weak optical lattice [53] or for an array of BECs [54–56], the appearance of interference patterns in the TOF images is associated with a density modulation of the *in situ* atomic distribution. Moreover, the shot-to-shot reproducibility of the patterns (in amplitude and position) and the persistence of fringes in averaged

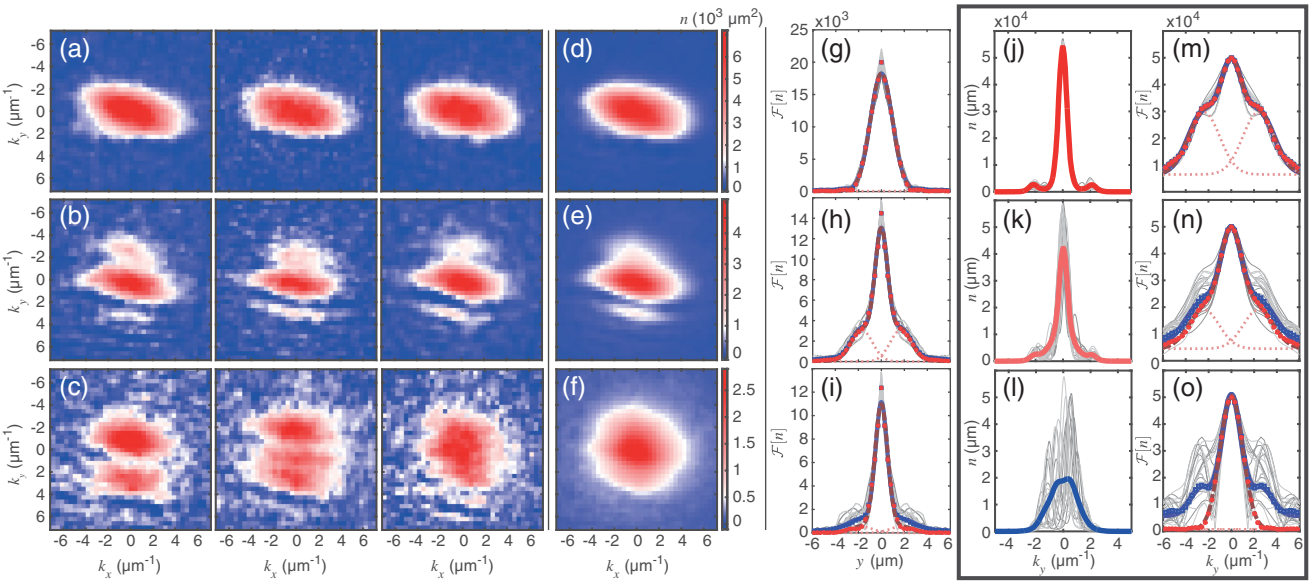

FIG. 2. Coherence in the interference patterns: measurement and toy model. (a)–(c) Examples of single TOF absorption images at $t_h = 5$ ms for ^{166}Er at $a_s = \{54.7(2), 53.8(2), 53.3(2)\}a_0$, respectively. Corresponding average pictures for 100 images obtained under the same experimental conditions (d)–(f) and their Fourier transform (FT) profiles (g)–(i). The gray lines show the FT norm $|\mathcal{F}[n](y)|$ of the individual profiles. The averages, $n_{\mathcal{M}}$ (blue squares) and n_Φ (red dots), are fitted to three-Gaussian functions (blue solid line and brown dashed line, respectively). The dotted lines show the components of the total fitted function corresponding to the two side peaks in n_Φ. (j)–(l) Interference patterns from the toy-model realizations with 100 independent draws using $N_D = 4$, $d = 2.8$ μm, $\sigma_y = 0.56$ μm (see text) and for different ϕ_i distributions: (j) $\phi_i = 0$, (k) ϕ_i normally distributed around 0 with 0.2π standard deviation, (l) ϕ_i uniformly distributed between 0 and 2π. (m)–(o) Corresponding FT profiles for the toy model, same color code as (g)–(i).

pictures, obtained from many repeated images taken under the same experimental conditions, reveals the presence of phase coherence across the sample [56].

Figure 2 exemplifies snapshots of the TOF distributions for Er, measured at three different a_s values; see Figs. 2(a)–2(c). Even if very close in scattering length, the recorded $n(k_x, k_y)$ shows a dramatic change in behavior. For $a_s = 54.7(2)a_0$, we observe a nonmodulated distribution with a density profile characteristic of a dilute BEC. When lowering a_s to $53.8(2)a_0$, we observe the appearance of an interference pattern in the density distribution, consisting of a high central peak and two almost symmetric low-density side peaks [57]. Remarkably, the observed pattern is very reproducible with a high shot-to-shot stability, as shown in the repeated single snapshots and in the average image [Figs. 2(b) and 2(e)]. This behavior indicates a coexistence of density modulation and global phase coherence in the *in situ* state, as expected in the supersolid phase. This observation is consistent with our previous quench experiments [18] and with the recent ^{162}Dy experiments [35,36]. When further lowering a_s to $53.3(2)a_0$, complicated patterns develop with fringes varying from shot to shot in number, position, and amplitude, signaling the persistence of *in situ* density modulation. However, the interference pattern is completely washed out in the averaged density profiles [Fig. 2(f)], pointing to the absence of a global phase coherence. We identify this behavior as the one of ID states.

Toy model—To get an intuitive understanding of the interplay between density modulation and phase coherence and to estimate the role of the different sources of fluctuations in our experiment, we here develop a simple toy model, which is inspired by Ref. [56]; see also Ref. [40]. In our model, the initial state is an array of N_D droplets containing in total N atoms. Each droplet is described by a one-dimensional Gaussian wave function $\psi_i(y)$ of amplitude α_i, phase ϕ_i, width σ_i, and center y_i. To account for fluctuations in the experiments, we allow α_i, $d_i = y_i - y_{i-1}$, and σ_i to vary by 10% around their expectation values. The spread of the phases ϕ_i among the droplets is treated specially as it controls the global phase coherence of the array. By fixing $\phi_i = 0$ for each droplet or by setting a random distribution of ϕ_i, we range from full phase coherence to the incoherent cases. Therefore, the degree of phase incoherence can be varied by changing the standard deviation of the distribution of ϕ_i.

To mimic our experiment, we compute the free evolution of each individual ψ_i over 30 ms, and then compute the axial distribution $n(y,t) = |\sum_i \psi_i(y,t)|^2$, from which we extract the momentum distribution $n(k_y)$, also accounting for the finite imaging resolution [40]. For each computation run, we randomly draw N_D values for ϕ_i, as well as of σ_i, d_i, and α_i, and extract $n(k_y)$. We then collect a set of $n(k_y)$

by drawing these values multiple times using the same statistical parameters and compute the expectation value, $\langle n(k_y)\rangle$; see Figs. 2(j)–2(l). The angled brackets denote the ensemble average.

The results of our toy model show large similarity with the observed behavior in the experiment. In particular, while for each single realization one can clearly distinguish multipeak structures regardless of the degree of phase coherence between the droplets, the visibility of the interference pattern in the averaged $n(k_y)$ survives only if the standard deviation of the phase fluctuations between droplets is small (roughly, below 0.3π). In the incoherent case, we note that the shape of the patterns strongly varies from shot to shot. Interestingly, the toy model also shows that the visibility of the coherent peaks in the average images is robust against the typical shot-to-shot fluctuations in droplet size, amplitude, and distance that occur in the experiments; see Figs. 2(j) and 2(k).

Probing density modulation and phase coherence.—To separate and quantify the information on the *in situ* density modulation and its phase coherence, we analyze the measured interference patterns in Fourier space [36,58–60]. Here, we extract two distinct averaged density profiles, $n_{\mathcal{M}}$ and n_{Φ}. Their structures at finite y spatial frequency (i.e., in Fourier space) quantify the two abovementioned properties.

More precisely, we perform a Fourier transform (FT) of the integrated momentum distributions $n(k_y)$ denoted $\mathcal{F}[n](y)$. Generally speaking, modulations in $n(k_y)$ induce peaks at finite spatial frequency, $y = y^*$, in the FT norm, $|\mathcal{F}[n](y)|$; see Figs. 2(g)–2(i) and 2(m)–2(o). Following the above discussion (see also Refs. [56,61]), such peaks in an individual realization hence reveal a density modulation of the corresponding *in situ* state, with a wavelength roughly equal to y^*. Consequently, we consider the average of the FT norm of the individual images, $n_{\mathcal{M}}(y) = \langle|\mathcal{F}[n](y)|\rangle$, as the first profile of interest. The peaks of $n_{\mathcal{M}}$ at finite y then indicate the mere existence of an *in situ* density modulation of roughly constant spacing within the different realizations. As the second profile of interest, we use the FT norm of the average profile $\langle n(k_y)\rangle$, $n_{\Phi}(y) = |\mathcal{F}[\langle n\rangle](y)|$. Connecting to our previous discussion, the peaks of n_{Φ} at finite y point to the persistence of a modulation in the average $\langle n(k_y)\rangle$, which we identified as a hallmark for a global phase coherence within the density-modulated state. In particular, we point out that a perfect phase coherence, implying identical interference patterns in all the individual realizations, yields $n_{\mathcal{M}} = n_{\Phi}$ and, thus, identical peaks at finite y in both profiles. We note that, by linearity, n_{Φ} also matches the norm of the average of the full FT of the individual images, i.e., $n_{\Phi}(y) = |\langle\mathcal{F}[n](y)\rangle|$; see also Ref. [40].

Figures 2(g)–2(i) and 2(m)–2(o) demonstrate the significance of our FT analysis scheme by applying it to the momentum distributions from the experiment [Figs. 2(d)–2(f)] and the momentum distributions from the toy model [Figs. 2(j)–2(l)], respectively. As expected, for the BEC case, both $n_{\mathcal{M}}$ and n_{Φ} show a single peak at zero spatial frequency, $y = 0$, characterizing the absence of density modulation, Fig. 2(g). In the case of phase-coherent droplets, Fig. 2(e), we observe that $n_{\mathcal{M}}$ and n_{Φ} are superimposed and both show two symmetric side peaks at finite y, in addition to a dominant peak at $y = 0$; see Fig. 2(h). In the incoherent droplet case, we find that, while $n_{\mathcal{M}}$ still shows side peaks at finite y, the ones in n_{Φ} wash out from the averaging, Figs. 2(f), 2(i), 2(l), and 2(o). For both coherent and incoherent droplet arrays, the toy-model results show behaviors matching the above description, providing a further justification of our FT analysis scheme; see Figs. 2(j)–2(o). Our toy model additionally proves two interesting features. First, it shows that the equality $n_{\mathcal{M}} = n_{\Phi}$, revealing the global phase coherence of a density-modulated state, is remarkably robust to noise in the structure of the droplet arrays; see Figs. 2(j) and 2(m). Second, our toy model, however, shows that phase fluctuations across the droplet array on the order of 0.2π standard deviation are already sufficient to make n_{Φ} and $n_{\mathcal{M}}$ deviate from each other; see Figs. 2(k) and 2(n). The incoherent behavior is also associated with strong variations in the side peak amplitude of the individual realizations of $|\mathcal{F}[n]|$, connecting, e.g., to the observations of Ref. [36].

Finally, to quantify the density modulation and the phase coherence, we fit a three-Gaussian function to both $n_{\mathcal{M}}(y)$ and $n_{\Phi}(y)$ and extract the amplitudes of the finite-spatial-frequency peaks, $A_{\mathcal{M}}$ and A_{Φ}, for both distributions, respectively. Note that for a BEC, which is a phase-coherent state, A_{Φ} will be zero since it probes only finite-spatial-frequency peaks; see Figs. 2(g)–2(i) and 2(m)–2(o).

V. CHARACTERIZATION OF THE SUPERSOLID STATE

We are now in the position to study two key aspects, namely, (i) the evolution of the density modulation and phase coherence across the BEC-supersolid-ID phases and (ii) the lifetime of the coherent density-modulated state in the supersolid regime.

Evolution of the supersolid properties across the phase diagram.—The first type of investigation is conducted with ^{166}Er since, contrary to ^{164}Dy, its scattering length and dependence on the magnetic field has been precisely characterized [18,22]. After preparing the sample, we ramp a_s to the desired value and study the density patterns as well as their phase coherence by probing the amplitudes $A_{\mathcal{M}}$ and A_{Φ} as a function of a_s after $t_h = 5$ ms. As shown in Fig. 3(a), in the BEC region (i.e., for large a_s), we observe that both $A_{\mathcal{M}}$ and A_{Φ} are almost zero, evidencing the expected absence of a density modulation in the system. As soon as a_s reaches a critical value a_s^*, the system's behavior dramatically changes with a sharp and simultaneous

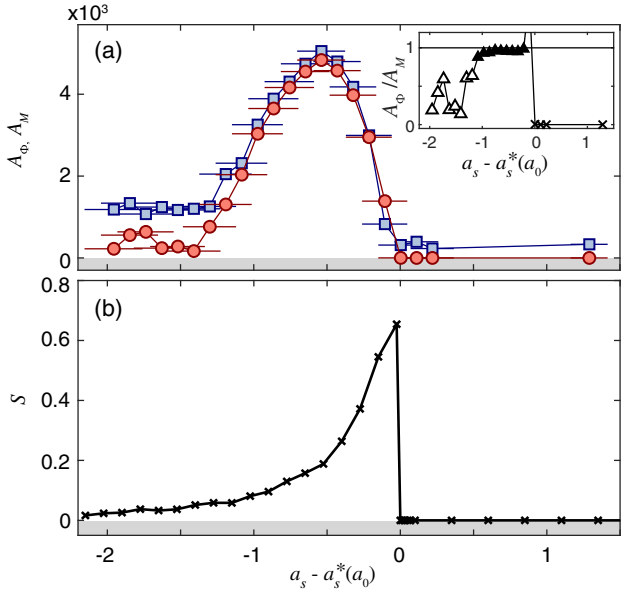

FIG. 3. Supersolid behavior across the phase diagram. Measured side peak amplitudes, A_Φ (circles) and $A_\mathcal{M}$ (squares), with their ratio in inset (a), and calculated link strength S (b) as a function of $a_s - a_s^*$ for ^{166}Er. For nonmodulated states, we set $S = 0$ in theory and $A_\Phi/A_\mathcal{M} = 0$ in experiment (crosses in inset). In the inset, open and closed symbols correspond to $A_\Phi/A_\mathcal{M} > 0.8$ and ≤ 0.8, respectively. In the experiments, we probe the system at a fixed $t_h = 5$ ms. Horizontal error bars are derived from our experimental uncertainty in B, vertical error bars corresponding to the statistical uncertainty from the fit are smaller than the data points. The measured and calculated critical scattering lengths are $a_s^* = 54.9(2)a_0$ and $51.15a_0$, respectively [62]. The numerical results are obtained for the experimental trap frequencies and for a constant $N = 5 \times 10^4$ [63].

increase of both $A_\mathcal{M}$ and A_Φ. While the strength of $A_\mathcal{M}$ and A_Φ varies with decreasing a_s—first increasing then decreasing—we observe that their ratio $A_\Phi/A_\mathcal{M}$ remains constant and close to unity over a narrow a_s range below a_s^* of $\gtrsim 1a_0$ width; see the inset of Fig. 3(a). This behavior pinpoints the coexistence in the system of phase coherence and density modulation, as predicted to occur in the supersolid regime. For $(a_s - a_s^*) < -1a_0$, we observe that the two amplitudes depart from each other. Here, while the density modulation still survives with $A_\mathcal{M}$ saturating to a lower finite value, the global phase coherence is lost with $A_\Phi/A_\mathcal{M} < 1$, as expected in the insulating droplet phase. Note that we also study the evolution of A_Φ and $A_\mathcal{M}$ in ^{164}Dy, but as a function of B, and find a qualitatively similar behavior.

To get a deeper insight on how our observations compare to the phase-diagram predictions (see Fig. 1), we study the link strength S as a function of a_s; see Fig. 3(b). Since S quantifies the density overlap between neighboring droplets and is related to the tunneling rate of atoms across the droplet array, it thus provides information on the ability of the system to establish or maintain a global phase coherence. In this plot, we set $S = 0$ in the case where no modulation is found in the ground state. At the BEC-to-supersolid transition, i.e., at $a_s = a_s^*$, a density modulation abruptly appears in the system's ground state with S taking a finite value. Here, S is maximal, corresponding to a density modulation of minimal amplitude. Below the transition, we observe a progressive decrease of S with lowering a_s, pointing to the gradual reduction of the tunneling rate in the droplet arrays. Close to the transition, we estimate a large tunneling compared to all other relevant timescales. However, we expect this rate to become vanishingly small, on the sub-Hertz level [40], when decreasing a_s 1–$2a_0$ below a_s^*. Our observation also hints at the smooth character of the transition from a supersolid to an ID phase.

The general trend of S, including the extension in a_s where it takes nonvanishing values, is similar to the a_s behavior of $A_\mathcal{M}$ and A_Φ observed in the experiments [62]. We observe in the experiments that the a_s dependence at the BEC-to-supersolid transition appears sharper than at the supersolid-to-ID interface, potentially suggesting a different nature of the two transitions. However, more investigations are needed since atom losses, finite temperature, and finite-size effects can affect, and in particular smoothen, the observed behavior [64–66]. Moreover, dynamical effects, induced by, e.g., excitations created at the crossing of the phase transitions or atom losses during the time evolution, can also play a substantial role in the experimental observations, complicating a direct comparison with the ground-state calculations. The time dynamics as well as a different scheme to achieve a state with supersolid properties is the focus of the remainder of the paper.

Lifetime of the supersolid properties.—Having identified the a_s range in which our dipolar quantum gas exhibits supersolid properties, the next central question concerns the stability and lifetime of such a fascinating state. Recent experiments on ^{162}Dy have shown the transient character of the supersolid properties, whose lifetime is limited by three-body losses [35,36]. In these experiments, the phase coherence is found to survive up to 20 ms after the density modulation has formed. This time corresponds to about half of the weak-trap period. Stability is a key issue in the supersolid regime, especially since the tuning of a_s, used to enter this regime, has a twofold consequence on the inelastic loss rate. First, it gives rise to an increase in the peak density [see Figs. 1(b)–1(d)] and, second, it may lead to an enhancement of the three-body-loss coefficient.

We address this question by conducting comparative studies on ^{166}Er and ^{164}Dy gases. These two species allow us to tackle two substantially different scattering scenarios. Indeed, the background value of a_s for ^{166}Er (as well as for ^{162}Dy) is larger than a_{dd}. Thus, reaching the supersolid regime, which occurs at $a_{dd}/a_s \approx 1.2$–1.4 in our geometry, requires us to tune B close to the pole of a FR. This tuning

also causes an increase of the three-body-loss rate. In contrast, ^{164}Dy realizes the opposite case with the background scattering length smaller than a_{dd}. This feature brings the important advantage of requiring tuning B away from the FR pole to reach the supersolid regime. As we describe below, this important difference in scattering properties leads to a strikingly longer lifetime of the ^{164}Dy supersolid properties with respect to ^{166}Er and to the recently observed behavior in ^{162}Dy [35,36].

The measurements proceed as follows. For both ^{166}Er and ^{164}Dy, we first prepare the quantum gas in the stable BEC regime and then ramp a_s to a fixed value in the supersolid regime for which the system exhibits a state of coherent droplets (i.e., $A_\Phi/A_\mathcal{M} \approx 1$); see previous discussion. Finally, we record the TOF images after a variable t_h and we extract the time evolution of both A_Φ and $A_\mathcal{M}$. The study of these two amplitudes will allow us to answer the question of whether the droplet structure—i.e., the density modulation in space—persists in time whereas the coherence among droplets is lost ($A_\mathcal{M} > A_\Phi \to 0$) or if the density structures themselves vanish in time ($A_\mathcal{M} \approx A_\Phi \to 0$).

As shown in Fig. 4, for both species, we observe that A_Φ and $A_\mathcal{M}$ decay almost synchronously with a remarkably longer lifetime for ^{164}Dy [Fig. 4(b)] than ^{166}Er [Fig. 4(a)].

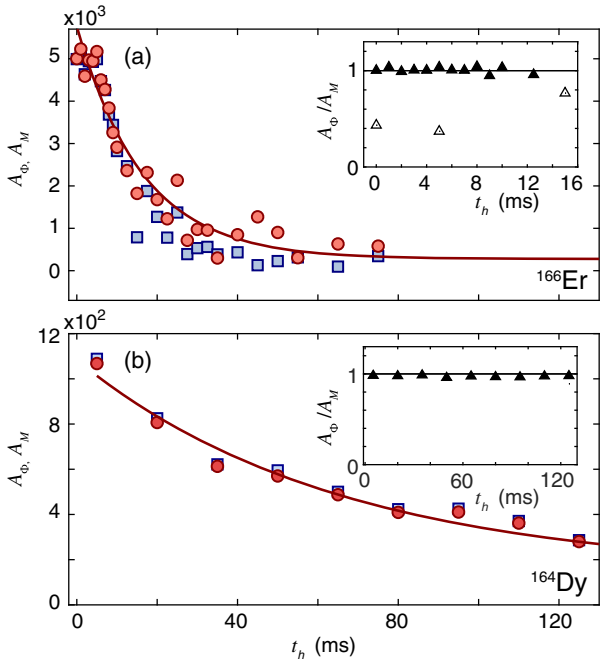

FIG. 4. Time evolution of the supersolid properties. Amplitudes A_Φ (circles) and $A_\mathcal{M}$ (squares) in the supersolid regime as a function of the holding time in trap for (a) ^{166}Er at $54.2(2)a_0$ and for (b) ^{164}Dy at 2.04 G. The solid lines are exponential fits to the data. The insets show the time evolution of $A_\Phi/A_\mathcal{M}$ for the above cases (filled triangles), and, for comparison, in the ID regime (empty triangles) for Er at $a_s = 53.1(2)a_0$ (a).

Interestingly, A_Φ and $A_\mathcal{M}$ remain approximately equal during the whole time dynamics; see insets of Figs. 4(a) and 4(b). This behavior indicates that it is the strength of the density modulation itself and not the phase coherence among droplets that decays over time. Similar results have been found theoretically in Ref. [67]. We connect this decay mainly to three-body losses, especially detrimental for ^{166}Er, and possible excitations created while crossing the BEC-to-supersolid phase transition [40]. For comparison, the inset of Fig. 4(a) shows also the behavior in the ID regime for ^{166}Er, where $A_\Phi/A_\mathcal{M} < 1$ already at short t_h and remains so during the time evolution [40].

To get a quantitative estimate of the survival time of the phase-coherent and density-modulated state, we fit a simple exponential function to A_Φ and extract t_Φ, defined as the 1/10 lifetime; see Fig. 4. For ^{166}Er, we extract $t_\Phi = 38(6)$ ms. For $t_h > t_\Phi$, the interference patterns become undetectable in our experiment and we recover a signal similar to the one of a nonmodulated BEC state [as in Figs. 2(a) and 2(d)]. These results are consistent with recent observations of transient supersolid properties in ^{162}Dy [35]. For ^{164}Dy, we observe that the coherent density-modulated state is remarkably long-lived. Here, we find $t_\Phi = 152(13)$ ms.

The striking difference in the lifetime and robustness of the supersolid properties between ^{166}Er and ^{164}Dy becomes even more visible when studying t_Φ as a function of a_s (B for Dy). As shown in Fig. 5, t_Φ for Er remains comparatively low in the investigated supersolid regime and slightly varies between 20 and 40 ms. Similarly to the recent studies with ^{162}Dy, this finding reveals the transient character of the state and opens the question of whether a stationary supersolid state can be reached with these species. On the contrary, for ^{164}Dy we observe that t_Φ first increases with B in the range from 1.8 G to about 1.98 G. Then, for $B > 1.98$ G, t_Φ acquires a remarkably large and almost constant value of about 150 ms over a wide B range. This shows the long-lived character of the supersolid properties in our ^{164}Dy quantum gas. We note that over the investigated range, a_s is expected to monotonously increase with B [40]. Such a large value of t_Φ exceeds not only the estimated tunneling time across neighboring droplets but also the weak-axis trap period, which together set the typical timescale to achieve global equilibrium and to study collective excitations.

VI. CREATION OF STATES WITH SUPERSOLID PROPERTIES BY EVAPORATIVE COOLING

The long-lived supersolid properties in ^{164}Dy motivate us to explore an alternative route to cross the supersolid phase transition, namely, by evaporative cooling instead of interaction tuning. For this set of experiments, we have modified the waists of our trapping beams in order to achieve quantum degeneracy in tighter traps with respect to

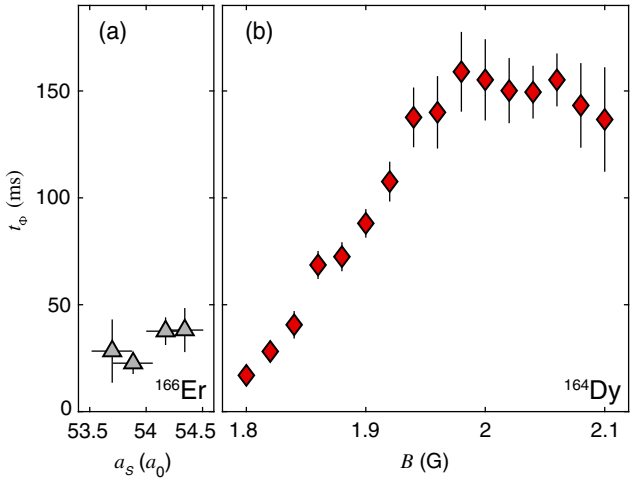

FIG. 5. Survival time of the coherent density-modulated state. t_Φ in ^{166}Er as a function of a_s (a) and ^{164}Dy as a function of B (b). The error bars refer to the statistical uncertainty from the fit. The range of investigation corresponds to the supersolid regime for which phase-coherent density-modulated states are observed. This range is particularly narrow for ^{166}Er.

the one used for condensation in the previous set of measurements. In this way, the interference peaks in the supersolid region are already visible without the need to apply a further compression of the trap since the side-to-central-peak distance in the momentum distribution scales roughly as $1/\ell_z$ [18]. Forced evaporative cooling is performed by reducing the power of the trapping beams piecewise linearly in subsequent evaporation steps until a final trap with frequencies $2\pi \times (225, 37, 134)$ Hz is achieved. During the whole evaporation process, which has an overall duration of about 3 s, the magnetic field is kept either at $B = 2.43$ G, where we observe long-lived interference patterns, or at $B = 2.55$ G, where we produce a stable nonmodulated BEC. We note that these two B values are very close without any FR lying in between [40].

Figure 6 shows the phase transition from a thermal cloud to a final state with supersolid properties by evaporative cooling. In particular, we study the phase transition by varying the duration of the last evaporation ramp, while maintaining the initial and final trap-beam power fixed. This procedure effectively changes the atom number and temperature in the final trap while keeping the trap parameters unchanged, which is important to not alter the final ground-state phase diagram of the system. At the end of the evaporation, we let the system equilibrate and thermalize for $t_h = 100$ ms, after which we switch off the trap, let the atoms expand for 26.5 ms, and finally perform absorption imaging. We record the TOF images for different ramp durations, i.e., for different thermalization times. For a short ramp, too many atoms are lost such that the critical atom number for condensation is not reached, and the atomic distribution remains thermal; see Fig. 6(a).

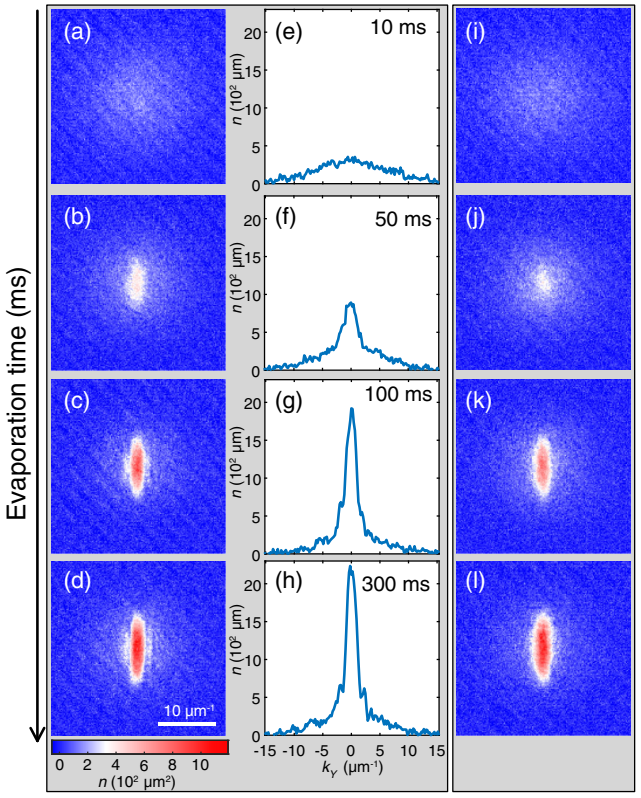

FIG. 6. Evaporative cooling to a state with supersolid properties. ^{164}Dy absorption images showing the transition to a state with supersolid properties at 2.43 G (a)–(d) and to a BEC state at 2.55 G (i)–(l), via different durations of the last evaporation step. These durations are 10 ms (a),(i), 50 ms (b),(j), 100 ms (c),(k), and 300 ms (d),(l). The density profiles (e)–(h) are integrated over the central regions of the corresponding absorption images (a)–(d). The color map indicates the atomic density in momentum space.

By increasing the ramp time, the evaporative cooling becomes more efficient and we observe the appearance of a bimodal density profile with a narrow and dense peak at the center, which we identify as a regular BEC; see Fig. 6(b). By further cooling, the BEC fraction increases and the characteristic pattern of the supersolid state emerges; see Figs. 6(c) and 6(d). The observed evaporation process shows a strikingly different behavior in comparison with the corresponding situation at $B = 2.55$ G, where the usual thermal-to-BEC phase transition is observed; see Figs. 6(i)–6(l).

We finally probe the lifetime of the supersolid properties by extracting the time evolution of both the amplitudes A_Φ and $A_\mathcal{M}$, as previously discussed. We use the same experimental sequence as the one in Fig. 6(d)—i.e., 300-ms duration of the last evaporation ramp and 100 ms of equilibration time—and subsequently hold the sample in the trap for a variable t_h. As shown in Fig. 7(a), we observe a very long lifetime with both amplitudes staying large and almost constant over more than 200 ms. At longer holding

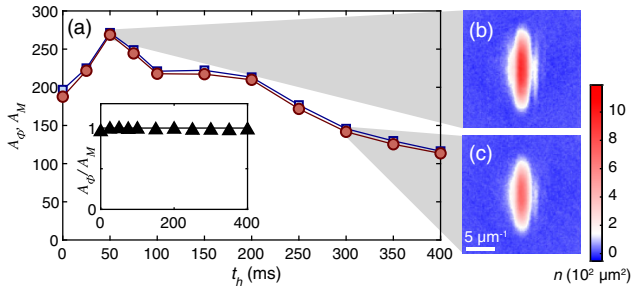

FIG. 7. Lifetime of the supersolid properties achieved via evaporative cooling. Time evolution of the amplitudes A_Φ (red circle) and $A_\mathcal{M}$ (square) after an evaporation time of 300 ms at 2.43 G and an equilibration time of 100 ms. The inset shows the time evolution of $A_\Phi/A_\mathcal{M}$. At $t_h = 0$ ms, the atom number in the phase-coherent density-modulated component is $N = 2.2(2) \times 10^4$. (b),(c) Averaged absorption images of 25 realizations after 50 and 300 ms of holding time, respectively. Note that the thermal background has been subtracted from the images. The color map indicates the atomic density in momentum space.

time, we observe a slow decay of A_Φ and $A_\mathcal{M}$, following the decay of the atom number. Moreover, during the dynamics, the ratio $A_\Phi/A_\mathcal{M}$ stays constant. The long lifetime of the phase-coherent density modulation is also directly visible in the persistence of the interference patterns in the averaged momentum density profiles [similar to Fig. 2(e)], both at intermediate and long times; see Figs. 7(b) and 7(c), respectively. For even longer t_h, we cannot resolve anymore interference patterns in the TOF images. Here, we recover a signal consistent with a regular BEC of low N.

Achieving the coherent droplet phase via evaporative cooling is a very powerful alternative path to supersolidity. We speculate that, for instance, excitations, which might be important when crossing the phase transitions by interaction tuning, may be small or removed by evaporation when reaching this state kinematically. Other interesting questions, open to future investigations, are the nature of the phase transition, the critical atom number, and the role of noncondensed atoms.

VII. CONCLUSIONS

For both ^{166}Er and ^{164}Dy dipolar quantum gases, we have identified and studied states showing hallmarks of supersolidity, namely, global phase coherence and spontaneous density modulations. These states exist in a narrow scattering-length region, lying between a regular BEC phase and a phase of an insulating droplet array. While for ^{166}Er, similarly to the recently reported ^{162}Dy case [35,36], the observed supersolid properties fade out over a comparatively short time because of atom losses, we find that ^{164}Dy exhibits remarkably long-lived supersolid properties. Moreover, we are able to directly create stationary states with supersolid properties by evaporative cooling, demonstrating a powerful alternative approach to interaction tuning on a BEC. This novel technique provides prospects of creating states with supersolid properties while avoiding additional excitations and dynamics. The ability to produce long-lived supersolid states paves the way for future investigations on quantum fluctuations and many-body correlations, as well as of collective excitations in such an intriguing many-body quantum state. A central goal of these future investigations lies in proving the superfluid character of this phase, beyond its global phase coherence [7,34,68–70].

ACKNOWLEDGMENTS

We thank R. Bisset, B. Blakie, M. Boninsegni, G. Modugno, T. Pfau, and, in particular, L. Santos for many stimulating discussions. Part of the computational results presented have been achieved using the HPC infrastructure LEO of the University of Innsbruck. We acknowledge support by the Austrian Science Fund FWF through the DFG/FWF Forschergruppe (FOR 2247/PI2790), by the ERC Consolidator Grant (RARE, No. 681432), and by a NFRI Grant (MIRARE, No. ÖAW0600) from the Austrian Academy of Science. G. D. and M. S. acknowledge support by the Austrian Science Fund FWF within the DK-ALM (No. W1259-N27).

Note added.—Recently, we became aware of related works reporting theoretical studies of the ground-state phase diagram [71,72].

[1] A. F. Andreev and I. M. Lifshitz, *Many-Body Problem in Quantum Mechanics and Quantum Statistical Mechanics*, Sov. Phys. JETP **29**, 1107 (1969).
[2] G. V. Chester, *Speculations on Bose-Einstein Condensation and Quantum Crystals*, Phys. Rev. A **2**, 256 (1970).
[3] A. J. Leggett, *Can a Solid Be "Superfluid"?*, Phys. Rev. Lett. **25**, 1543 (1970).
[4] D. A. Kirzhnits and Y. A. Nepomnyashchii, *Coherent Crystallization of Quantum Liquid*, Sov. Phys. JETP **32**, 1191 (1971).
[5] T. Schneider and C. P. Enz, *Theory of the Superfluid-Solid Transition of* ^{4}He, Phys. Rev. Lett. **27**, 1186 (1971).
[6] S. Balibar, *The Enigma of Supersolidity*, Nature (London) **464**, 176 (2010).
[7] M. Boninsegni and N. V. Prokof'ev, *Colloquium: Supersolids: What and Where Are They?*, Rev. Mod. Phys. **84**, 759 (2012).
[8] Z.-K. Lu, Y. Li, D. S. Petrov, and G. V. Shlyapnikov, *Stable Dilute Supersolid of Two-Dimensional Dipolar Bosons*, Phys. Rev. Lett. **115**, 075303 (2015).
[9] N. Henkel, R. Nath, and T. Pohl, *Three-Dimensional Roton Excitations and Supersolid Formation in Rydberg-Excited Bose-Einstein Condensates*, Phys. Rev. Lett. **104**, 195302 (2010).

[10] F. Cinti, P. Jain, M. Boninsegni, A. Micheli, P. Zoller, and G. Pupillo, *Supersolid Droplet Crystal in a Dipole-Blockaded Gas*, Phys. Rev. Lett. **105**, 135301 (2010).

[11] M. Boninsegni, *Supersolid Phases of Cold Atom Assemblies*, J. Low Temp. Phys. **168**, 137 (2012).

[12] J. Léonard, A. Morales, P. Zupancic, T. Esslinger, and T. Donner, *Supersolid Formation in a Quantum Gas Breaking a Continuous Translational Symmetry*, Nature (London) **543**, 87 (2017).

[13] J.-R. Li, J. Lee, W. Huang, S. Burchesky, B. Shteynas, F. Ç. Top, A. O. Jamison, and W. Ketterle, *A Stripe Phase with Supersolid Properties in Spin–Orbit-Coupled Bose–Einstein Condensates*, Nature (London) **543**, 91 (2017).

[14] L. D. Landau, *The Theory of Superfluidity of Helium II*, J. Phys. (Moscow) **5**, 71 (1941).

[15] P. Nozières, *Is the Roton in Superfluid* ^{4}He *the Ghost of a Bragg Spot?*, J. Low Temp. Phys. **137**, 45 (2004).

[16] D. H. J. O'Dell, S. Giovanazzi, and G. Kurizki, *Rotons in Gaseous Bose-Einstein Condensates Irradiated by a Laser*, Phys. Rev. Lett. **90**, 110402 (2003).

[17] L. Santos, G. V. Shlyapnikov, and M. Lewenstein, *Roton-Maxon Spectrum and Stability of Trapped Dipolar Bose-Einstein Condensates*, Phys. Rev. Lett. **90**, 250403 (2003).

[18] L. Chomaz, R. M. W. van Bijnen, D. Petter, G. Faraoni, S. Baier, J. H. Becher, M. J. Mark, F. Wächtler, L. Santos, and F. Ferlaino, *Observation of Roton Mode Population in a Dipolar Quantum Gas*, Nat. Phys. **14**, 442 (2018).

[19] D. Petter, G. Natale, R. M. W. van Bijnen, A. Patscheider, M. J. Mark, L. Chomaz, and F. Ferlaino, *Probing the Roton Excitation Spectrum of a Stable Dipolar Bose Gas*, arXiv:1811.12115.

[20] H. Kadau, M. Schmitt, M. Wenzel, C. Wink, T. Maier, I. Ferrier-Barbut, and T. Pfau, *Observing the Rosensweig Instability of a Quantum Ferrofluid*, Nature (London) **530**, 194 (2016).

[21] I. Ferrier-Barbut, H. Kadau, M. Schmitt, M. Wenzel, and T. Pfau, *Observation of Quantum Droplets in a Strongly Dipolar Bose Gas*, Phys. Rev. Lett. **116**, 215301 (2016).

[22] L. Chomaz, S. Baier, D. Petter, M. J. Mark, F. Wächtler, L. Santos, and F. Ferlaino, *Quantum-Fluctuation-Driven Crossover from a Dilute Bose-Einstein Condensate to a Macrodroplet in a Dipolar Quantum Fluid*, Phys. Rev. X **6**, 041039 (2016).

[23] F. Wächtler and L. Santos, *Quantum Filaments in Dipolar Bose-Einstein Condensates*, Phys. Rev. A **93**, 061603(R) (2016).

[24] F. Wächtler and L. Santos, *Ground-State Properties and Elementary Excitations of Quantum Droplets in Dipolar Bose-Einstein Condensates*, Phys. Rev. A **94**, 043618 (2016).

[25] M. Schmitt, M. Wenzel, F. Böttcher, I. Ferrier-Barbut, and T. Pfau, *Self-Bound Droplets of a Dilute Magnetic Quantum Liquid*, Nature (London) **539**, 259 (2016).

[26] I. Ferrier-Barbut, M. Wenzel, M. Schmitt, F. Böttcher, and T. Pfau, *Onset of a Modulational Instability in Trapped Dipolar Bose-Einstein Condensates*, Phys. Rev. A **97**, 011604(R) (2018).

[27] R. N. Bisset, R. M. Wilson, D. Baillie, and P. B. Blakie, *Ground-State Phase Diagram of a Dipolar Condensate with Quantum Fluctuations*, Phys. Rev. A **94**, 033619 (2016).

[28] M. Wenzel, F. Böttcher, T. Langen, I. Ferrier-Barbut, and T. Pfau, *Striped States in a Many-Body System of Tilted Dipoles*, Phys. Rev. A **96**, 053630 (2017).

[29] D. Baillie and P. B. Blakie, *Droplet Crystal Ground States of a Dipolar Bose Gas*, Phys. Rev. Lett. **121**, 195301 (2018).

[30] D. S. Petrov, *Quantum Mechanical Stabilization of a Collapsing Bose-Bose Mixture*, Phys. Rev. Lett. **115**, 155302 (2015).

[31] C. R. Cabrera, L. Tanzi, J. Sanz, B. Naylor, P. Thomas, P. Cheiney, and L. Tarruell, *Quantum Liquid Droplets in a Mixture of Bose-Einstein Condensates*, Science **359**, 301 (2018).

[32] G. Semeghini, G. Ferioli, L. Masi, C. Mazzinghi, L. Wolswijk, F. Minardi, M. Modugno, G. Modugno, M. Inguscio, and M. Fattori, *Self-Bound Quantum Droplets of Atomic Mixtures in Free Space*, Phys. Rev. Lett. **120**, 235301 (2018).

[33] P. Cheiney, C. R. Cabrera, J. Sanz, B. Naylor, L. Tanzi, and L. Tarruell, *Bright Soliton to Quantum Droplet Transition in a Mixture of Bose-Einstein Condensates*, Phys. Rev. Lett. **120**, 135301 (2018).

[34] S. M. Roccuzzo and F. Ancilotto, *Supersolid Behaviour of a Dipolar Bose-Einstein Condensate Confined in a Tube*, Phys. Rev. A **99**, 041601(R) (2019).

[35] L. Tanzi, E. Lucioni, F. Fama, J. Catani, A. Fioretti, C. Gabbanini, R. N. Bisset, L. Santos, and G. Modugno, *Observation of a Dipolar Quantum Gas with Metastable Supersolid Properties*, Phys. Rev. Lett. **122**, 130405 (2019).

[36] F. Böttcher, J.-N. Schmidt, M. Wenzel, J. Hertkorn, M. Guo, T. Langen, and T. Pfau, *Transient Supersolid Properties in an Array of Dipolar Quantum Droplets*, Phys. Rev. X **9**, 011051 (2019).

[37] K. Aikawa, A. Frisch, M. Mark, S. Baier, A. Rietzler, R. Grimm, and F. Ferlaino, *Bose-Einstein Condensation of Erbium*, Phys. Rev. Lett. **108**, 210401 (2012).

[38] A. Trautmann, P. Ilzhöfer, G. Durastante, C. Politi, M. Sohmen, M. J. Mark, and F. Ferlaino, *Dipolar Quantum Mixtures of Erbium and Dysprosium Atoms*, Phys. Rev. Lett. **121**, 213601 (2018).

[39] S. Baier, M. J. Mark, D. Petter, K. Aikawa, L. Chomaz, Z. Cai, M. Baranov, P. Zoller, and F. Ferlaino, *Extended Bose-Hubbard Models with Ultracold Magnetic Atoms*, Science **352**, 201 (2016).

[40] See Supplemental Material at http://link.aps.org/supplemental/10.1103/PhysRevX.9.021012 for details on the experimental setup, measurement schemes, analysis, and theory calculations.

[41] I. Ferrier-Barbut, M. Wenzel, F. Böttcher, T. Langen, M. Isoard, S. Stringari, and T. Pfau, *Scissors Mode of Dipolar Quantum Droplets of Dysprosium Atoms*, Phys. Rev. Lett. **120**, 160402 (2018).

[42] A. Gammal, T. Frederico, L. Tomio, and P. Chomaz, *Atomic Bose-Einstein Condensation with Three-Body Interactions and Collective Excitations*, J. Phys. B **33**, 4053 (2000).

[43] A. Bulgac, *Dilute Quantum Droplets*, Phys. Rev. Lett. **89**, 050402 (2002).

[44] D. S. Petrov, *Quantum Mechanical Stabilization of a Collapsing Bose-Bose Mixture*, Phys. Rev. Lett. **115**, 155302 (2015).

[45] F. Wächtler and L. Santos, *Ground-State Properties and Elementary Excitations of Quantum Droplets in Dipolar Bose-Einstein Condensates*, Phys. Rev. A **94**, 043618 (2016).
[46] M. Wenzel, F. Böttcher, J.-N. Schmidt, M. Eisenmann, T. Langen, T. Pfau, and I. Ferrier-Barbut, *Anisotropic Superfluid Behavior of a Dipolar Bose-Einstein Condensate*, Phys. Rev. Lett. **121**, 030401 (2018).
[47] B. D. Josephson, *Possible New Effects in Superconductive Tunnelling*, Phys. Lett. **1**, 251 (1962).
[48] J. Javanainen, *Oscillatory Exchange of Atoms between Traps Containing Bose Condensates*, Phys. Rev. Lett. **57**, 3164 (1986).
[49] S. Raghavan, A. Smerzi, S. Fantoni, and S. R. Shenoy, *Coherent Oscillations between Two Weakly Coupled Bose-Einstein Condensates: Josephson Effects, π Oscillations, and Macroscopic Quantum Self-Trapping*, Phys. Rev. A **59**, 620 (1999).
[50] A similar behavior is also seen for ^{164}Dy for $N < 4000$ [out of the scale of Fig. 1(g)].
[51] We note that a similar behavior is also found in our ^{166}Er phase diagram but for larger N than the one reported here.
[52] Y. Tang, A. Sykes, N. Q. Burdick, J. L. Bohn, and B. L. Lev, *s-Wave Scattering Lengths of the Strongly Dipolar Bosons ^{162}Dy and ^{164}Dy*, Phys. Rev. A **92**, 022703 (2015).
[53] M. Greiner, O. Mandel, T. Esslinger, T. W. Hänsch, and I. Bloch, *Quantum Phase Transition from a Superfluid to a Mott Insulator in a Gas of Ultracold Atoms*, Nature (London) **415**, 39 (2002).
[54] M. Greiner, I. Bloch, O. Mandel, T. W. Hänsch, and T. Esslinger, *Exploring Phase Coherence in a 2D Lattice of Bose-Einstein Condensates*, Phys. Rev. Lett. **87**, 160405 (2001).
[55] B. Paredes, A. Widera, V. Murg, O. Mandel, S. Fölling, I. Cirac, G. V. Shlyapnikov, T. W. Hänsch, and I. Bloch, *Tonks–Girardeau Gas of Ultracold Atoms in an Optical Lattice*, Nature (London) **429**, 277 (2004).
[56] Z. Hadzibabic, S. Stock, B. Battelier, V. Bretin, and J. Dalibard, *Interference of an Array of Independent Bose-Einstein Condensates*, Phys. Rev. Lett. **93**, 180403 (2004).
[57] In our absorption imaging a residual asymmetry can be observed between $\pm k_y$. This asymmetry, providing a sharper peak at $k_y > 0$, stems from optical aberrations in our imperfect optical setup. These imperfections make the quantitative analysis of our data more challenging, yet they do not affect the quantitative interpretation. In particular, we have checked that the peak structures are also observable along a distinct imaging axis, nonorthogonal to y, using an independent imaging setup.
[58] M. Takeda, H. Ina, and S. Kobayashi, *Fourier-Transform Method of Fringe-Pattern Analysis for Computer-Based Topography and Interferometry*, J. Opt. Soc. Am. **72**, 156 (1982).
[59] C. Kohstall, S. Riedl, E. R. S. Guajardo, L. A. Sidorenkov, J. H. Denschlag, and R. Grimm, *Observation of Interference between Two Molecular Bose–Einstein Condensates*, New J. Phys. **13**, 065027 (2011).
[60] L. Chomaz, L. Corman, T. Bienaimé, R. Desbuquois, C. Weitenberg, S. Nascimbène, J. Beugnon, and J. Dalibard, *Emergence of Coherence via Transverse Condensation in a Uniform Quasi-Two-Dimensional Bose Gas*, Nat. Commun. **6**, 6162 (2015).
[61] S. Hofferberth, I. Lesanovsky, B. Fischer, T. Schumm, and J. Schmiedmayer, *Non-Equilibrium Coherence Dynamics in One-Dimensional Bose Gases*, Nature (London) **449**, 324 (2007).
[62] The values of a_s^* extracted from experiments and from theory disagree by $3.8a_0$. Such a mismatch is similar to the one observed in our previous work on the roton instability [18,19]. This behavior might be related to the possibility that beyond-mean-field effects are not properly accounted for by the conventional LHY correction term; see main text. In addition, other effects, such as the dynamics and the atom losses [40], can affect the experimental observations.
[63] This atom number corresponds to the condensed atom number measured within the stabilization time of a_s [40].
[64] M. E. Fisher and A. E. Ferdinand, *Interfacial, Boundary, and Size Effects at Critical Points*, Phys. Rev. Lett. **19**, 169 (1967).
[65] Y. Imry and D. Bergman, *Critical Points and Scaling Laws for Finite Systems*, Phys. Rev. A **3**, 1416 (1971).
[66] Y. Imry, *Finite-Size Rounding of a First-Order Phase Transition*, Phys. Rev. B **21**, 2042 (1980).
[67] See the theoretical analysis in the revised version of Ref. [35].
[68] V. W. Scarola, E. Demler, and S. D. Sarma, *Searching for a Supersolid in Cold-Atom Optical Lattices*, Phys. Rev. A **73**, 051601(R) (2006).
[69] Z.-K. Lu, Y. Li, D. S. Petrov, and G. V. Shlyapnikov, *Stable Dilute Supersolid of Two-Dimensional Dipolar Bosons*, Phys. Rev. Lett. **115**, 075303 (2015).
[70] F. Cinti and M. Boninsegni, *Classical and Quantum Filaments in the Ground State of Trapped Dipolar Bose Gases*, Phys. Rev. A **96**, 013627 (2017).
[71] Y. Kora and M. Boninsegni, *Patterned Supersolids in Dipolar Bose Systems*, arXiv:1902.08256.
[72] Y.-C. Zhang, F. Maucher, and T. Pohl, *Supersolidity around a Critical Point in Dipolar Bose Einstein Condensates*, arXiv:1903.06161.

Correction: The inadvertent omission of a marker indicating "Featured in Physics" has been fixed.

Supplemental Material: Long-lived and transient supersolid behaviors in dipolar quantum gases

L. Chomaz,[1] D. Petter,[1] P. Ilzhöfer,[2] G. Natale,[1] A. Trautmann,[2] C. Politi,[2] G. Durastante,[1,2]
R. M. W. van Bijnen,[2] A. Patscheider,[1] M. Sohmen,[1,2] M. J. Mark,[1,2] and F. Ferlaino[1,2,*]
[1] *Institut für Experimentalphysik, Universität Innsbruck, Technikerstraße 25, 6020 Innsbruck, Austria*
[2] *Institut für Quantenoptik und Quanteninformation, Österreichische Akademie der Wissenschaften, Technikerstraße 21a, 6020 Innsbruck, Austria*

(Dated: March 27, 2019)

GROUND STATE CALCULATIONS

We perform numerical calculations of the ground state following the procedure detailed in the supplementary information of Ref. [1]. The calculations are based on the conjugate-gradients technique to minimize the energy functional of an eGPE [2]. In particular, the eGPE accounts for the effect of quantum fluctuations, by including the LHY term $\Delta\mu[n] = 32g(na_s)^{3/2}(1+3\epsilon_{dd}^2/2)/3\sqrt{\pi}$ in the system's Hamiltonian (here $g = 4\pi\hbar^2 a_s/m$ and $n = |\psi|^2$ is the spatial density of the macroscopic state ψ). $\Delta\mu[n]$ has been obtained under a local density approximation in Refs. [3, 4]. The relevance of the LHY correction has been demonstrated in various studies of dipolar Bose gases close to the mean-field instability [1, 5–9] as it brings an additional repulsive potential, stabilizing the gas against mean-field collapse at large density. We note that the exact functional form of the potential, originating from beyond mean-field effects, has been questioned by several experimental results in finite-size trapped systems [1, 9–11], calling for further theory developments [12].

Our numerical calculations provide us with the three-dimensional ground-state wavefunctions $\psi(\boldsymbol{r})$. From this, we compute the axial in-situ density profile along the trap's weak axis, $n(y) = \int |\psi(\boldsymbol{r})|^2 dxdz$ and find density profiles, corresponding to the BEC, the supersolid or the ID phase, that we plot in Fig. 1. From the density profiles that exhibit a density modulation, we evaluate S by performing Gaussian fits to each droplet, i. e. to $n(y)$ with y ranging between two neighboring local density minima. From these Gaussian fits, we evaluate the sets of centers $\{y_i^{(0)}\}_i$ and widths $\{\sigma_i\}_i$ corresponding to the macroscopic Gaussian wavefunctions $\{\psi_i\}_i$ associated to the individual droplets in the array. We then approximate the droplet wavefunction via $\psi_i(y) \approx \sqrt{n(y \approx y_i^{(0)})} = \alpha_i \exp\left(-(y-y_i^{(0)})^2/2\sigma_i^2\right)$ with α_i a normalization coefficient such that $\int |\psi_i(y)|^2 dy = 1$. We then evaluate the wavefunction overlap S_i between the neighboring droplets $i-1$ and i via:

$$S_i \equiv \int \psi_{i-1}^*(y)\psi_i(y)dy \tag{1}$$

$$= \sqrt{\frac{2\sigma_i\sigma_{i-1}}{\sigma_i^2+\sigma_{i-1}^2}} \exp\left(-\frac{(y_i^{(0)}-y_{i-1}^{(0)})^2}{2(\sigma_i^2+\sigma_{i-1}^2)}\right). \tag{2}$$

The latter equation is obtained via an analytical evaluation of the Gaussian integral. The characteristic link strength defined in the paper is then computed by averaging S_i over all droplet links in the array: $S = \langle S_i \rangle_i$. In our calculation, we only consider as droplets all density peaks of at least 5 % of the global density maximum.

LINK STRENGTH AND ESTIMATE OF TUNNELING RATE

Generally speaking, the wavefunction overlap between neighboring droplets relates to a tunneling term, which sets a particle exchange term between two neighboring droplets [13–16]. Following the work of Ref. [17], we perform a first estimate of the tunneling coefficient by simply considering the single-particle part of the Hamiltonian and evaluate it between two neighboring droplets. We note that, in our particular setting where the density modulation is not externally imposed but arises from the mere interparticle interactions, the inter-droplet interaction may also play a crucial role. To perform a more precise estimation of the tunneling between droplets, one would certainly need to properly account for this effect. Here, we stress that our approach simply gives a rough idea of the magnitude of tunneling while it does not aim to be a quantitative description of it. This consideration calls for further studies making a systematic analysis of the full Hamiltonian and of the full phase diagram within the Josephson junction formalism and beyond.

Generalizing the description of Ref. [17] to neighboring droplets of different sizes and amplitudes, which are described by a three-dimensional wavefunction $\psi_i(\boldsymbol{r})$ approximated to a three-dimensional Gaussian of widths

$(\sigma_{i,x}, \sigma_{i,y}, \sigma_{i,z})$ with $\sigma_{i,y} = \sigma_i$, our estimate writes:

$$J_i = \frac{\hbar^2 S_i}{2m}\left[\sum_{k=x,y,z}\frac{1+\left(\frac{\sigma_{i,k}\sigma_{i-1,k}}{\ell_k^2}\right)^2}{\sigma_{i,k}^2+\sigma_{i-1,k}^2} + \frac{(y_i^{(0)}-y_{i-1}^{(0)})^2}{2\sigma_i\sigma_{i-1}}\frac{(\sigma_i\sigma_{i-1}/\ell_y)^4-1}{\sigma_i^2+\sigma_{i-1}^2}\right], \quad (3)$$

where $\ell_{x,y,z} = \sqrt{\hbar/m\omega_{x,y,z}}$ are the harmonic oscillator lengths.

In general, the tunnelling coefficients set two typical rates relevant for equilibration processes. The first one is the bare single-particle tunneling rate, which is equal to J_i/h, while the second accounts for the bosonic enhancement from the occupation of the droplet modes and writes $\tilde{t}_i = \sqrt{N_i N_{i-1}}|J_i|/h$ where N_i is the number of atoms in droplet i. In our analysis, we then define the average rates over the droplet arrays as characteristic rates $J/h = \langle J_i\rangle_i/h$, and $\tilde{t} = \langle \tilde{t}_i\rangle_i$; see e.g. [18]. While the ground state evolves from a BEC to a supersolid to an ID, the relevant timescale for achieving (global) equilibrium crosses from being set by the trap frequencies to the above-mentioned tunneling rates.

Using our approximate model, we here give a first estimate of the rates J/h and $\tilde{t}$ as a function of a_s, for the parameters of Fig. 1(b-d) of the main text (i.e. Er quantum gas with $N = 5\times10^4$ atoms). Here we find that, for $a_s = a_s^*$, $J/h \sim 400\,\text{Hz}$ and $\tilde{t} \sim 10\,\text{MHz}$ while for $a_s = a_s^* - 2.5\,a_0$, $J/h \sim 10^{-7}\,\text{Hz}$ and $\tilde{t} \sim 10^{-3}\,\text{Hz}$.

TOY MODEL FOR THE INTERFERENCE PATTERN

As described in the main text we use a simple toy model, adapted from Ref. [18], to identify the main features of the TOF interference patterns obtained from an insitu density-modulated state. As a quick reminder, our model considers a one-dimensional array of N_D Gaussian droplets, described by a single classical field, ψ_i, thus neglecting quantum and thermal fluctuations. We compute the TOF density distribution from the free-expansion of the individual ψ_i during a time t via $n(y,t) = |\sum_i \psi_i(y,t)|^2$. In our calculations, we also account for the finite imaging resolution by convolving the resulting $n(y,t)$ with a gaussian function of width σ_{im}. Here we allow the characteristics of the individual ψ_i to fluctuate. In this aim, we introduce noise on the corresponding parameter with a normal distribution around its expectation value and with a variable standard deviation (only ϕ_i can also have a uniform distribution). We then perform a Monte-Carlo study and perform ensemble averages, similar to our experimental analysis procedure. We note that, in this simple implementation, the noise on the different parameters – droplet amplitudes, widths and distances – are uncorrelated.

In the main text, we present results for a single set of parameters, namely $N_D = 4$, $d \equiv \langle d_i\rangle_i = 2.8\,\mu\text{m}$ (mean droplet distance), $\sigma_y \equiv \langle\sigma_i\rangle_i = 0.56\,\mu\text{m}$ (mean droplet size), $t = 30\,\text{ms}$, and $\sigma_{\text{im}} = 3\,\mu\text{m}$, typical for our experimental Er setting and the corresponding theory expectations in the supersolid regime. $\langle\cdot\rangle_i$ denotes the average over the droplets. In this section, we have a deeper look at the impact of the different parameters on both the TOF signal and our FT analysis. We study both the fully phase coherent and fully incoherent case, and the unchanged parameters are set as in Fig. 2(j,m) and (l,o).

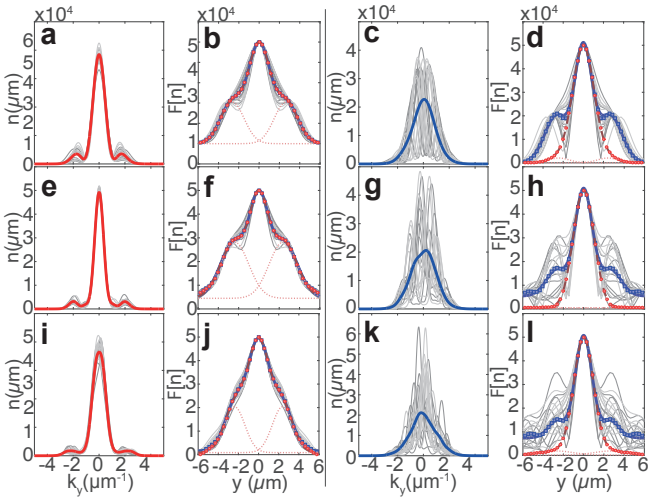

FIG. S1. **Toy model realizations with varying number of droplets** N_D. We use 100 independent draws, and expectation values $d = 2.85\,\mu\text{m}$, $\sigma_y = 0.56\,\mu\text{m}$ (with 10% noise) and either $\phi_i = 0$ (a,b,e,f,i,j), or ϕ_i uniformly distributed between 0 and 2π (c,d,g,h,k,l). (a–d) $N_D = 2$, (e–h) $N_D = 3$ and (i–l) $N_D = 8$. (a,c,e,g,i,k) TOF density profiles and (b,d,f,h,j,l) corresponding FT analysis of the interference patterns, same color code as Fig .2.

In Fig. S1, we first exemplify the TOF and FT profiles for a varying number of droplets, between 2 and 8, which cover the range of relevant N_D over the phase diagram of Fig. 1. The results remain remarkably similar to the realization of Fig. 2 with only slight quantitative changes. The main difference lies in the individual interference patterns obtained in the phase incoherent case. With increasing N_D, those profiles become more complex and made of a larger number of peaks (see (c,g,k)). Yet, in this incoherent case, a similar (non-modulated) profile is recovered in the averaged $n(k_y)$ for all N_D. Additionally, we note that for the coherent case with $N_D = 8$, the side peaks in the FT analysis (see (j)) become less visible. By performing additional tests, we attribute this behavior to the limited TOF duration, t, used in our experiment yielding a typical length scale, $\sqrt{\hbar t/m}$ ($= 3.4\mu\text{m}$), which becomes small compared to the system size ($\approx (N_D-1)d + \sigma_y$) for large N_D. This intermediate regime in the TOF expansion leads to more

complex features, including smaller-sized motifs, in the interference patterns. Finally, when accounting for our imaging resolution, it yields a broadening of the structure observed in the TOF images and less visible peaks in the FT (see (i)). We note that our experiments, because of limited N and additional losses, should rather lie in the regime $2 \leq N_D \leq 5$; see Fig. 1(b).

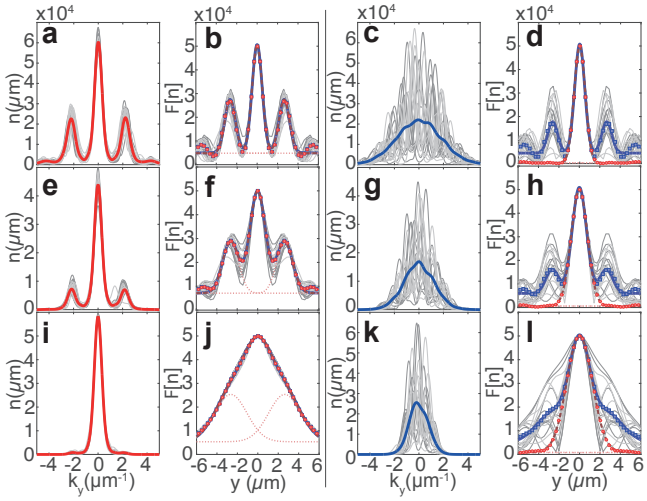

FIG. S2. **Toy model realizations with varying σ_y/d.** We use 100 independent draws, with $N_D = 4$, $d = 2.85\,\mu$m (with 10% noise) and either $\phi_i = 0$ (a,b,e,f,i,j), or ϕ_i uniformly distributed between 0 and 2π (c,d,g,h,k,l). For each realization we also compute the associated mean S. (a–d) $\sigma_y/d = 0.1$, yielding $S = 1.8\times10^{-7}$ (e–h)$\sigma_y/d = 0.15$, matching $S = 1.7\times10^{-4}$ and (i–l) $\sigma_y/d = 0.25$, matching $S = 0.028$. (a,c,e,g,i,k) TOF density profiles and (b,d,f,h,j,l) Corresponding FT analysis of the interference patterns, same color code as Fig. 2.

We then investigate the evolution of the interference patterns and their FT analysis for a varying mean droplet size, σ_y, while keeping their mean distance, d, fixed. This study is particularly relevant recalling that, within the Josephson junction formalism (see main text and corresponding section of this Supplemental Material), the key parameter controlling the tunneling rate between the droplets is set by the ratio σ_y/d, and the link strength parameter that we use to characterize the supersolid regime scales roughly as $\exp(-(d/2\sigma_y)^2)$. Thus, in our experiment, σ_y/d is intrinsically expected to decrease with the scattering length (see Fig. 3). Performing a direct estimate of the average droplet link from the initial state of our toy model, we find $S = 0.004$ for the calculations of Fig. 2(j-o), lying in an expected supersolid regime yet rather close to the supersolid-to-ID transition. Figure S2 investigates the effect of smaller and larger values of σ_y/d (and consequently of S) on the TOF and FT profiles while independently assuming phase coherence or incoherence. Qualitatively, the features remain similar as in Fig. 2(j-o). In the coherent case, side peaks are visible in the individual as well as in the mean $n(k_y)$ (see (a,e,i)) and yield side peaks in the FT profiles, with $n_{\mathcal{M}} \approx n$ (see (b,f,j)). Increasing (decreasing) σ/d mainly results in a stronger (weaker) signal both in the interference pattern and their FT analysis. Within our toy model, we find that, already for $\sigma/d = 0.25$, the signal nearly vanishes; see (i,j). Even if, given the approximations used in our toy model, this exact value may not fully hold for our experimental conditions, we expect a similar trend. It is interesting to keep in mind that this effect may limit our capacity of detecting an underlying supersolid state via matter-wave interference in experiments. In the incoherent case, the effect of decreasing σ_y/d mainly results in a broader shape of the mean density profile, while it remains non-modulated; see (c,g,k). In the FT analysis n_Φ remains structure-less independently of σ_y/d while the structures in $n_{\mathcal{M}}$ becomes sharper with decreasing σ_y/d, as in the coherent case; see (d,h,l).

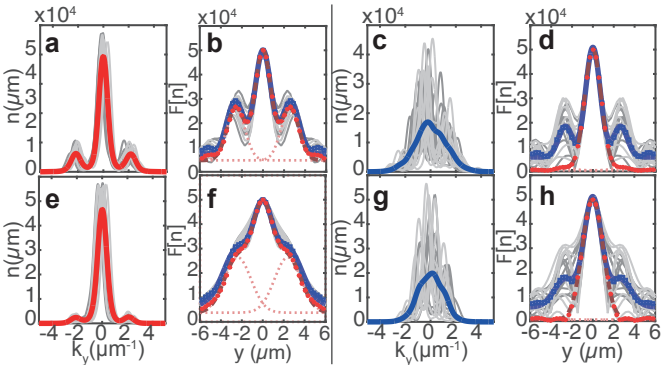

FIG. S3. **Toy model realizations allowing noise in the center position.** We use 100 independent draws, with $N_D = 4$, $d = 2.85\,\mu$m (with 10% noise), $\sigma_y/d = 0.15$ (a–d) or $\sigma_y/d = 0.2$ (e–h), and either $\phi_i = 0$ (a,b,e,f,i,j), or ϕ_i uniformly distributed between 0 and 2π (c,d,g,h,k,l). Center fluctuation are introduced as normal noise around 0 with standard deviation of $2\,\mu\text{m}^{-1}$ in situ (a,c,e,g,i,k) TOF density profiles and (b,d,f,h,j,l) corresponding FT analysis of the interference patterns, same color code as Fig. 2.

Finally, we investigate how a possible shot-to-shot noise on the position of the central interference peak could affect our observables of the density modulation and phase coherence. In the experiments, such fluctuations may occur, for instance, because of beam-pointing fluctuations or excitations of the gas. Although we compensate for such effects by recentering the individual images (see Imaging Analysis section), residual effects may remain, in particular due to center misestimation in the mere presence of the interference patterns of interest. To investigate this aspect, we repeat our toy model calculations now including noise in the global droplet array position and using a standard deviation of $2\,\mu$m for two values of σ_y/d; see Fig.S3. Again, qualitatively the observed features remains similar to our prediction in the main text. The main effect lies in the appearance of a

small discrepancy in the coherent case between n_Φ and $n_\mathcal{M}$, while the structure in the incoherent case remains similar. As the center misestimation should be the most severe in the latter case (due to the variability of the interference patterns observed here), our test shows the robustness of our analysis procedure against this issue.

IMAGING ANALYSIS: ^{164}Dy AND ^{166}Er

The density distributions in momentum space are extracted from the TOF images using the free-expansion expectation. In the Dy case, the thermal component is subtracted from the individual distribution by cutting out the central region of the cloud and performing an isotropic Gaussian fit on the outer region. This subtraction is beneficial because of the large thermal fraction. In the ^{166}Er case, such a subtraction is on the contrary complicated because of the weak thermal component and this pre-treatment may lead to improper estimation of $A_\mathcal{M}$ and A_Φ in the later analysis. The obtained momentum density distributions are then recentered and integrated numerically along $k_z(k_x)$ between $[-2.0, +2.0]\,\mu\mathrm{m}^{-1}$ ($[-1.28, +1.28]\,\mu\mathrm{m}^{-1}$) to obtain $n(k_Y)$ ($n(k_y)$) for ^{164}Dy (^{166}Er). The recentering procedure uses the result a single Gauss fit to the TOF images. The fit is performed after convoluting each image with a Gaussian function of width $0.5\,\mu$m whose purpose is to reduce the impact of the interference pattern on the center estimation [19].

In order to characterise the system's state, we use the Fourier transform, $\mathcal{F}[n](y)$ of the single density profile, $n(k_y)$. We then compute two average profiles, $n_\mathcal{M}$ and n_Φ, relying on ensemble average over all measurements under the same experimental conditions; see below for a detailed discussion on $n_\mathcal{M}$ and n_Φ. In all the measurements reported in this work we use averages over typically 15 to 100 realizations.

To quantify both the existence of a density modulation and global phase coherence on top of this modulation, we fit both $n_\mathcal{M}(y)$ and $n_\Phi(y)$ with a triple-Gaussian function, where one Gaussian accounts for the central peak and the other Gaussians are accounting for the symmetric side peaks. The amplitudes of the latter give $A_\mathcal{M}$ and A_Φ, respectively. The distance between the side peaks and the central one is allowed to vary between $[2.5, 2.7]\,\mu$m ($[2.3, 2.5]\,\mu$m) in the case of ^{164}Dy (^{166}Er).

DETAILS ON THE FOURIER ANALYSIS

In our analysis we rely on two averaged profiles, named $n_\mathcal{M}$ or n_Φ, to quantify both the density modulation and its phase coherence. Here we detail the meaning of the average performed.

The Fourier transform (FT) of the integrated momentum distributions, $n(k_y)$, which reads $\mathcal{F}[n](y) = |\mathcal{F}[n](y)|\exp(i\arg(\mathcal{F}[n](y)))$ sets the ground for our analysis. As stated in the main text, an in-situ density modulation of wavelength y^* yields patterns in $n(k_y)$ and consequently induce peaks at $y \approx y^*$, in the FT norm, $|\mathcal{F}[n](y)|$, see Fig. 2(g-i) and (m-o). Spatial variations of the phase relation within the above-mentioned density modulation translate into phase shifts of the interference patterns, which are stored in the FT argument at $y \approx y^*$, $\arg(\mathcal{F}[n](y^*))$; see also Ref. [18, 20].

The first average that we use is $n_\mathcal{M}(y) = \langle|\mathcal{F}[n](y)|\rangle$, i. e. the average of the FT norm of the individual images. As the phase information contained in $\arg(\mathcal{F}[n](y))$ is discarded from $n_\mathcal{M}$ when taking the norm, the peaks in $n_\mathcal{M}$ probe the mere existence of an insitu density modulation of roughly constant spacing within the different realizations. The second average of interest is $n_\Phi(y) = |\langle\mathcal{F}[n](y)\rangle|$, i. e. the average of the full FT of the individual images. In contrast to $n_\mathcal{M}$, n_Φ keeps the phase information of the individual realizations contained in $\arg(\mathcal{F}[n](y^*))$. Consequently, peaks in n_Φ indicate that the phase relation is maintained over the density modulation, in a similar way for all realizations. Their presence thus provides information on the global phase coherence of a density-modulated state.

EXPERIMENTAL SEQUENCE: ^{164}Dy AND ^{166}Er

^{166}Erbium - The BEC of ^{166}Er is prepared similarly to Refs. [1, 8, 21, 22]. We start from a magneto-optical trap with 2.4×10^7 ^{166}Er atoms at a temperature of 10μK, spin-polarized in the lowest Zeeman sub-level. In a next step we load about 3×10^6 atoms into a crossed optical dipole trap (ODT) operated at 1064 nm. We evaporatively cool the atomic cloud by reducing the power and then increasing the ellipticity of one of the ODT beams. During the whole evaporation a constant magnetic field of $B = 1.9\,\mathrm{G}$ ($a_\mathrm{s} = 80\,a_0$) along z is applied. We typically achieve BEC with 1.4×10^5 atoms and a condensed fraction of 70%. In a next step the ODT is reshaped in 300 ms into the final trapping frequencies $\omega_{x,y,z} = 2\pi \times (227, 31.5, 151)\,\mathrm{Hz}$. Consecutively, we ramp B linearly to $0.62\,\mathrm{G}$ ($64.5\,a_0$) in 50 ms and obtain a BEC with 8.5×10^4 atoms, which are surrounded by 3.5×10^4 thermal atoms. This point marks the start of the ramp to the final a_s.

^{164}Dysprosium - For the production of a ^{164}Dy BEC we closely follow the scheme presented in [23]. Starting from a 3 s loading phase of our 5-beam MOT in open-top configuration [24], we overlap a 1064 nm single-beam dipole trap with a $1/e^2$-waist of about $22\,\mu$m, for 120 ms. Eventually, we transfer typically 8×10^6 atoms utilizing a time averaging potential technique to increase the spatial overlap with the MOT. After an initial 1.1 s evaporative

cooling phase by lowering the power of the beam, we add a vertically propagating beam, derived from the same laser, with a $1/e^2$-waist of about 130 μm to form a crossed optical dipole trap for additional confinement. Subsequently, we proceed forced evaporative cooling to reach quantum degeneracy by nearly exponentially decreasing the laser powers in the two dipole-trap beams over 3.6 s. We achieve BECs of ^{164}Dy with typically 10^5 atoms and condensate fractions of about 40%. During the entire evaporation sequence the magnetic field is kept constant at 2.5 G pointing along the vertical (z-) axis.

To be able to condense directly into the supersolid, we modify the dipole trap to condense at a stronger confinement of $\omega_{x,y,z} = 2\pi \times (225, 37, 134)$ Hz. After a total evaporative cooling duration of 3.1 s, we achieve Bose-Einstein condensation at 2.55 G and reach a state with supersolid properties at 2.43 G, keeping the magnetic field constant throughout the entire evaporation sequence for both cases.

Time of flight and imaging for ^{166}Er *and* ^{164}Dy - In order to probe the momentum distribution of the Dy (Er) gases, we switch off the confining laser beams and let the atoms expand freely for 18 ms (15 ms), while keeping the magnetic field constant. Consecutively the amplitude of B is increased to a fixed amplitude of 5.4 G (0.6 G). In the case of ^{164}Dy, the magnetic field orientation is rotated in order to point along the imaging axis. This ensures constant imaging conditions for different a_s. After an additional 9 ms (15 ms) we perform a standard absorption imaging.

TUNING THE SCATTERING LENGTH IN ^{166}Er AND ^{164}Dy

^{166}*Erbium* - All measurements start with a BEC at 64.5 a_0. In order to probe the BEC-supersolid-ID region, we linearly ramp a_s to its target value in $t_r = 20$ ms by performing a corresponding ramp in B. Due to a finite time delay of the magnetic field in our experimental setup and the highly precise values of a_s needed for the experiment, we let the magnetic field stabilize for another 15 ms before $t_h = 0$ starts. By this, we ensure that the residual lowering of a_s during the entire hold time is $\lesssim 0.3\, a_0$. In the main text, we always give the a_s at $t_h = 0$. Furthermore, we estimate our magnetic field uncertainty to be ± 2.5 mG, leading to a $\pm 0.2\, a_0$ uncertainty of a_s in our experiments.

To choose the best ramping scheme, we have performed experiments varying t_r from 0.5 ms to 60 ms, ramping to a fixed a_s lying in the supersolid regime, and holding for $t_h = 5$ ms after a fixed 15 ms waiting time. We record the evolution of A_Φ as a function of t_r; see Fig. S4. When increasing t_r, we first observe that A_Φ increases, up to $t_r = 20$ ms, and then A_Φ gradually decreases. The initial increase can be due to diabatic effects and larger excitation when fast-crossing the phase transition. On the other hand, the slow decrease at longer t_r can be explained by larger atom loss during the ramp. We then choose $t_r = 20$ ms as an optimum value where a supersolid behavior develops and maintains itself over a significant time while the losses are minimal.

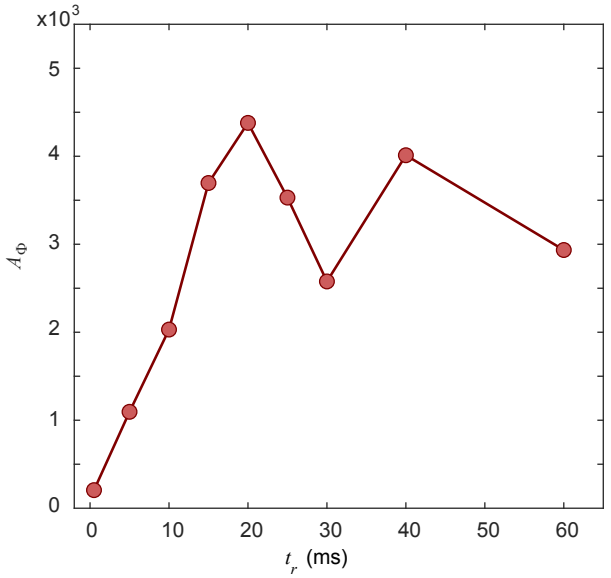

FIG. S4. **Ramp time effect on the supersolid behavior** Measured A_Φ for various durations of the scattering-length ramp with ^{166}Er and a final $a_s = 54.1(2)\, a_0$. All measurements include a 15 ms stabilization time after t_r and are performed with an additional hold of $t_h = 5$ ms.

^{164}*Dysprosium* - As the value of the background scattering, a_{bg} length for ^{164}Dy is still under debate [9, 10, 25], we discuss the experimental settings in terms of magnetic field. Yet, to gain a better understanding of the tunability of a_s in our experiment, we first perform a Feshbach spectroscopy scan on a BEC at $T = 60$ nK. After evaporative cooling at $B = 2.5$ G, we jump to B varying from 1 G to 7.5 G and we hold the sample for 100 ms. Finally, we switch off the trap, let the cloud expand for 26 ms and record the total atom number as a function of B. We then fit the observed loss features with a gaussian fit to obtain the position $B_{0,i}$ and width ΔB_i of the FRs, numbered i. We finally use the standard Feshbach resonance formula to estimate the a_s-to-B dependence via $a_s(B) = a_{bg} \prod_i (1 - \Delta B_i/(B - B_{0,i}))$. Here we account for 8 FRs located between 1.2 G and 7.2 G. Depending on the background scattering length a_{bg}, the overall magnitude of $a_s(B)$ changes. We can get an estimate of a_{bg} from literature. In Fig. S5, we use the value of a_s from Ref. [25] obtained at 1.58 G close to the B-region investigated in our experiment, $a_s = 92(8)\, a_0$. By reverting

the $a_s(B)$ formula, we set $a_{bg} = 87(8)\,a_0$. For the measurements of Figs. 4-5, we ramp B linearly from 2.5 G in 20 ms to a final value ranging from 1.8 to 2.1 G, for which we estimate a_s ranging from $97(9)\,a_0$ to $105(10)\,a_0$. We calibrate our magnetic field using RF spectroscopy, with a stability of about 2 mG. In the Dy case, we do not apply an additional stabilization time. This is justified because of the more mellow a_s-to-B dependence in the B-range of interest as well as of the wider a_s-range of the supersolid regime (see Fig. 1) compared to the Er case. For the measurements of Figs. 6–7, we use two B-values, namely 2.43 G and 2.55 G, at which we perform the evaporative cooling scheme. Here we estimate $a_s = 109(10)\,a_0$ and $a_s = 134(12)\,a_0$, respectively.

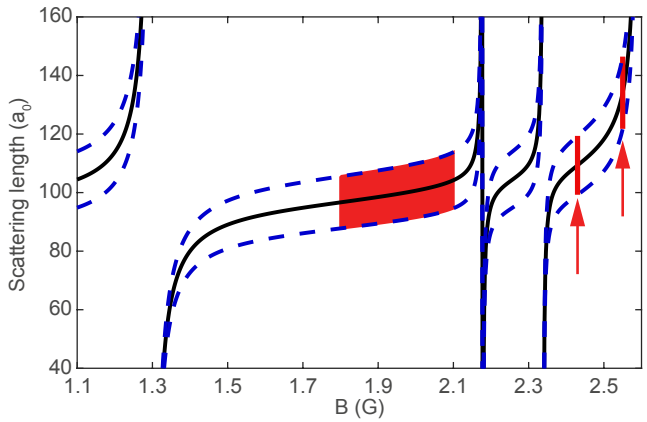

FIG. S5. **Estimated scattering length tuning in** ^{164}Dy Estimated dependence of a_s on B for ^{164}Dy. The FR positions and widths have been extracted from trap-loss spectroscopy measurements, the background scattering length is estimated to $a_{bg} = 87(8)\,a_0$, see text. The blue dashed line gives an error-estimate considering only the errorbar on a_{bg} from the mere a_s measurement of Ref. [25] and not accounting for uncertainty of the Feshhach scan. For Figs. 4-5, we use B between 1.8 G and 2.1 G (red area); for Figs. 6–7, we keep at two constant B-values, namely 2.43 G and 2.55 G (red arrows).

ATOM LOSSES IN ^{166}Er AND ^{164}Dy

As pointed out in the main text, in the time evolution of the quantum gases in both the supersolid and the ID regime, inelastic atom losses play a crucial role. The atom losses are increased in the above mentioned regime as (i) higher densities are required so that a stabilization under quantum fluctuation effects becomes relevant and (ii) the magnetic field may need to be tune close to a FR pole to access the relevant regime of interaction parameters. (i) is at play for all magnetic species but more significant for ^{166}Er due to the smaller value of a_{dd}. (ii) is relevant for both ^{166}Er and ^{162}Dy but conveniently avoided for ^{164}Dy thanks to the special short-range properties of this isotope.

To quantify the role of these losses, we report here the evolution of the number of condensed atoms, N, as a function of the hold time in parallel to the phase coherent character of the density modulation observed. We count N by fitting the thermal fraction of each individual image with a two-dimensional Gaussian function. To ensure that only the thermal atoms are fitted, we mask out the central region of the cloud associated with the quantum gas. Afterwards we subtract this fit from the image and perform a numerical integration of the resulting image (so called pixel count) to obtain N.

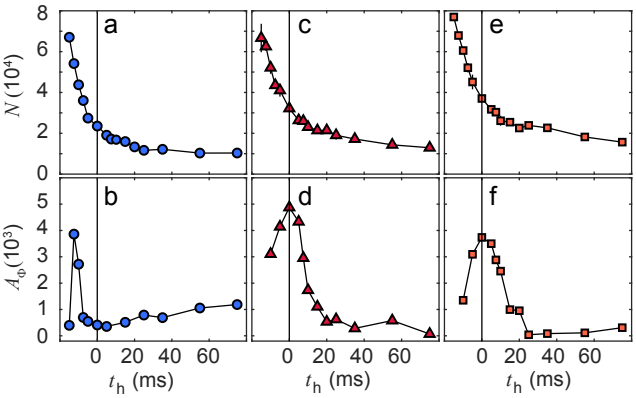

FIG. S6. **atom number and coherence decays in** ^{166}Er Time evolution of N and A_Φ for ^{166}Er at different a_s, including points before $t_h = 0$ ms in the experiment. The corresponding scattering lengths are $53.3(2)\,a_0$ (a,b), $54.0(2)\,a_0$ (c,d), $54.2(2)\,a_0$ (e,f).

^{166}*Erbium* - In the Er case, a 15 ms stabilization time is added to ensure that a_s is reached up to $0.3\,a_0$. During this time, i. e. for $t_h < 0$, we suspect that the time-evolution of the cloud properties is mainly dictated by the mere evolution of the scattering length. Therefore, in the main text, we report on the time evolution for $t_h \geq 0$. We note that because of the narrow a_s-range for the supersolid regime, the long stabilization time for a_s is crucial. However, because of the significant role of the atom losses in our system, in particular for ^{166}Er, the early evolution of N and the cloud's properties are intimately connected. Therefore, the early time evolution at $t_h < 0$ is certainly of high importance for our observations at $t_h \geq 0$.

To fully report on this behavior, we show the evolution of N and A_Φ during both the stabilization and the holding time in Fig. S6 for three different a_s values – either in the ID (a, b) or supersolid regime (c-f). The time evolution shows significant atom loss, prominent already during the stabilization time, and levels off towards a remaining atom number at longer holding times in which we recover small BECs. Simultaneously, in each case reported here, we observe that during the stabilization time A_Φ increases and a coherent density modulated state grows.

TABLE I. Extracted 1/10-lifetime of ^{166}Er atom number decay for $t_h \geq 0$ and remaining atom number at long holding time for data in Fig. S6.

$a_s(a_0)$	t_N (ms)	$N_r(10^4)$	t_Φ (ms)
53.3(2)	32(5)	1.03(5)	-
54.0(2)	51(9)	1.29(11)	25(6)
54.2(2)	46(12)	1.7(2)	32(9)

This density modulation starts to appear at a typical atom number of $N \gtrsim 6 \times 10^4$ and consecutively decays. For the lower $a_s = 53.3(2)\,a_0$ case, we observe that the coherent state does not survive the a_s stabilization time, and decays faster than the atoms loss; see Fig. S6 (a, b). This behavior corresponds to the ID case discussed in the main text. The central point of the present work is to identify a parameter range where the coherence of the density modulated state survives for $t_h > 0$ and its decay time scale is similar to the one of the atom loss. In order to quantify a timescale for the atom number decay, we fit an exponential decay to $t_h \geq 0$ ms. Here we allow an offset N_r of the fit, accounting for the BEC recovered at long holding times. In Table I, we report on the typical 1/10-decay times of the atom number, which are up to 50 ms. These values are of the order as the extracted t_Φ, see Table I and Fig. 5 of the main text. This reveals that in ^{166}Er the extracted lifetime of the coherent density modulated states are mainly limited by atom loss.

Furthermore we note that the extracted N_r values for the recovered BECs are smaller than 2×10^4, which is consistent with the BEC region found in the phase diagram of Fig. 1(f).

^{164}Dysprosium - Differently from the ^{166}Er case, for ^{164}Dy, we operate in a magnetic-field range in which the three-body collision coefficients are small and only moderate atom losses occur. This enables the observation of an unprecendented long-lived supersolid behavior. To understand the effects limiting the supersolid lifetime, we study the lifetime of the condensed-atom number for different B. We perform this detailed study for the data of Fig. 5 of the main text, which are obtained after preparing a stable BEC and then ramping B to the target value. Fig. S7 shows the parallel evolution of N and A_Φ for three different magnetic field values 1.8 G, 2.04 G and 2.1 G. Here we observe that, for all B values, A_Φ seems to decay faster than the atom number. This suggests that the lifetime of the density-modulated state in our ^{164}Dy experiment is not limited by atom losses. To confirm this observation, we extract the 1/10 lifetimes of both N and A_Φ; see Table II. The values confirm our observation and shows an atom number lifetime larger than t_Φ at least by a factor of ≈ 5. In addition, we find that the ratio t_N/t_Φ varies, indicating that atom losses are not the only mechanism limiting the lifetime of the supersolid properties in Dy.

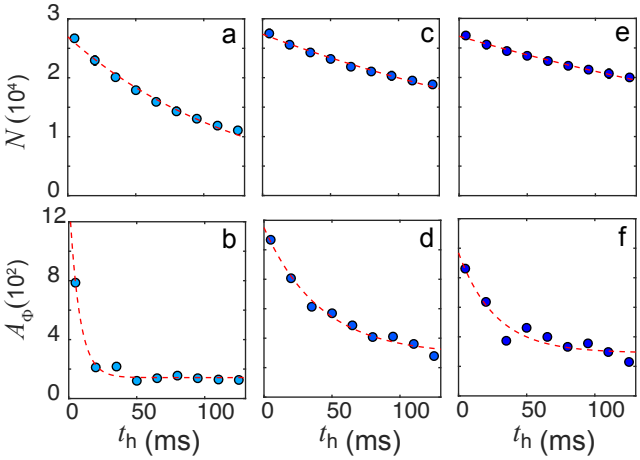

FIG. S7. **atom number and coherence decays in ^{164}Dy** Time evolution of N and A_Φ for ^{164}Dy at different B for the data of Fig. 5. The corresponding magnetic fields are 1.8 G (a,b), 2.04 G (c,d), 2.1 G (e,f).

TABLE II. Extracted 1/10-lifetime of ^{164}Dy atom number decay and A_Φ decay for data in Fig. S7.

B (G)	t_N (ms)	t_Φ (ms)
1.8	300(12)	12(5)
2.04	728(34)	152(13)
2.1	926(36)	133(25)

[1] L. Chomaz, R. M. W. van Bijnen, D. Petter, G. Faraoni, S. Baier, J. H. Becher, M. J. Mark, F. Wächtler, L. Santos, and F. Ferlaino, "Observation of roton mode population in a dipolar quantum gas," Nat. Phys. **14**, 442 (2018).

[2] S. Ronen, D. C. E. Bortolotti, and J. L. Bohn, "Bogoliubov modes of a dipolar condensate in a cylindrical trap," Phys. Rev. A **74**, 013623 (2006).

[3] A. R. P. Lima and A. Pelster, "Quantum fluctuations in dipolar Bose gases," Phys. Rev. A **84**, 041604 (2011).

[4] A. R. P. Lima and A. Pelster, "Beyond mean-field low-lying excitations of dipolar Bose gases," Phys. Rev. A **86**, 063609 (2012).

[5] F. Wächtler and L. Santos, "Quantum filaments in dipolar Bose-Einstein condensates," Phys. Rev. A **93**, 061603(R) (2016).

[6] F. Wächtler and L. Santos, "Ground-state properties and elementary excitations of quantum droplets in dipolar Bose-Einstein condensates," Phys. Rev. A **94**, 043618 (2016).

[7] R. N. Bisset, R. M. Wilson, D. Baillie, and P. B. Blakie, "Ground-state phase diagram of a dipolar condensate

with quantum fluctuations," Phys. Rev. A **94**, 033619 (2016).
[8] L. Chomaz, S. Baier, D. Petter, M. J. Mark, F. Wächtler, L. Santos, and F. Ferlaino, "Quantum-fluctuation-driven crossover from a dilute Bose-Einstein condensate to a macrodroplet in a dipolar quantum fluid," Phys. Rev. X **6**, 041039 (2016).
[9] M. Schmitt, M. Wenzel, F. Böttcher, I. Ferrier-Barbut, and T. Pfau, "Self-bound droplets of a dilute magnetic quantum liquid," Nature (London) **539**, 259–262 (2016).
[10] I. Ferrier-Barbut, M. Wenzel, F. Böttcher, T. Langen, M. Isoard, S. Stringari, and T. Pfau, "Scissors Mode of Dipolar Quantum Droplets of Dysprosium Atoms," Phys. Rev. Lett. **120**, 160402 (2018).
[11] C. R. Cabrera, L. Tanzi, J. Sanz, B. Naylor, P. Thomas, P. Cheiney, and L. Tarruell, "Quantum liquid droplets in a mixture of Bose-Einstein condensates," Science **359**, 301–304 (2018).
[12] V. Cikojevi, L. Vranje Marki, G. E. Astrakharchik, and J. Boronat, "Universality in ultradilute liquid Bose-Bose mixtures," arXiv:1811.04436 (2018).
[13] B. D. Josephson, "Possible new effects in superconductive tunnelling," Phys. Lett. **1**, 251 – 253 (1962).
[14] A. Barone and G. Patern, *Physics and applications of the Josephson effect* (Wiley, New York, NY, 1982).
[15] J. Javanainen, "Oscillatory exchange of atoms between traps containing Bose condensates," Phys. Rev. Lett. **57**, 3164–3166 (1986).
[16] S. Raghavan, A. Smerzi, S. Fantoni, and S. R. Shenoy, "Coherent oscillations between two weakly coupled bose-einstein condensates: Josephson effects, π oscillations, and macroscopic quantum self-trapping," Phys. Rev. A **59**, 620–633 (1999).
[17] M. Wenzel, F. Böttcher, J.-N. Schmidt, M. Eisenmann, T. Langen, T. Pfau, and I. Ferrier-Barbut, "Anisotropic Superfluid Behavior of a Dipolar Bose-Einstein Condensate," Phys. Rev. Lett. **121**, 030401 (2018).
[18] Z. Hadzibabic, S. Stock, B. Battelier, V. Bretin, and J. Dalibard, "Interference of an Array of Independent Bose-Einstein Condensates," Phys. Rev. Lett. **93**, 180403 (2004).
[19] We note that we have also checked our analysis without performing the recentering step and the same features remain. For instance, for our test data of Fig. 2, the effect being mainly that the side peaks in (e) are more washed out and a slight difference occurs between $n_{\mathcal{M}}$ and n_{Φ}, both showing still side peaks.
[20] S. Hofferberth, I. Lesanovsky, B. Fischer, T. Schumm, and J. Schmiedmayer, "Non-equilibrium coherence dynamics in one-dimensional Bose gases," Nature (London) **449**, 324 (2007).
[21] K. Aikawa, A. Frisch, M. Mark, S. Baier, A. Rietzler, R. Grimm, and F. Ferlaino, "Bose-Einstein condensation of Erbium," Phys. Rev. Lett. **108**, 210401 (2012).
[22] D. Petter, G. Natale, R. M. W. van Bijnen, A. Patscheider, M. J. Mark, L. Chomaz, and F. Ferlaino, "Probing the roton excitation spectrum of a stable dipolar Bose gas," arXiv:1811.12115 (2018).
[23] A. Trautmann, P. Ilzhöfer, G. Durastante, C. Politi, M. Sohmen, M. J. Mark, and F. Ferlaino, "Dipolar Quantum Mixtures of Erbium and Dysprosium Atoms," Phys. Rev. Lett. **121**, 213601 (2018).
[24] P. Ilzhöfer, G. Durastante, A. Patscheider, A. Trautmann, M. J. Mark, and F. Ferlaino, "Two-species five-beam magneto-optical trap for erbium and dysprosium," Phys. Rev. A **97**, 023633 (2018).
[25] Y. Tang, A. Sykes, N. Q. Burdick, J. L. Bohn, and B. L. Lev, "s-wave scattering lengths of the strongly dipolar bosons ^{162}Dy and ^{164}Dy," Phys. Rev. A **92**, 022703 (2015).

A.3 Publication:

Feshbach resonances in an erbium-dysprosium dipolar mixture

The following publication has appeared in

Physical Review A **102**, 033330 (2020)[‡]
submitted 12 June 2020; published 21 Sept 2020
DOI: https://doi.org/10.1103/PhysRevA.102.033330
G. Durastante,[1,2] C. Politi,[1,2] M. Sohmen,[1,2] P. Ilzhöfer,[1,2] M. J. Mark,[1,2] M. A. Norcia,[1] and F. Ferlaino[1,2]

[1] *Institut für Quantenoptik und Quanteninformation, Österreichische Akademie der Wissenschaften, 6020 Innsbruck, Austria*

[2] *Institut für Experimentalphysik, Universität Innsbruck, 6020 Innsbruck, Austria*

[‡]The author of the present thesis performed the measurements together with G. D., M. A. N., and M. S., analysed the experimental data with G. D., and M. A. N., and contributed in writing the manuscript and interpreting the results together with all the authors.

Feshbach resonances in an erbium-dysprosium dipolar mixture

Gianmaria Durastante,[1,2] Claudia Politi,[1,2] Maximilian Sohmen,[1,2] Philipp Ilzhöfer,[1,2] Manfred J. Mark,[1,2] Matthew A. Norcia,[1] and Francesca Ferlaino[1,2,*]

[1]*Institut für Quantenoptik und Quanteninformation, Österreichische Akademie der Wissenschaften, 6020 Innsbruck, Austria*

[2]*Institut für Experimentalphysik und Zentrum für Quantenoptik, Universität Innsbruck, Technikerstraße 25, 6020 Innsbruck, Austria*

(Received 12 June 2020; accepted 25 August 2020; published 21 September 2020)

We report on the observation of heteronuclear magnetic Feshbach resonances in several isotope mixtures of the highly magnetic elements erbium and dysprosium. Among many narrow features, we identify two resonances with a width greater than one Gauss. We characterize one of these resonances, in a mixture of ^{168}Er and ^{164}Dy, in terms of loss rates and elastic cross section, and observe a temperature dependence of the on-resonance loss rate suggestive of a universal scaling associated with broad resonances. Our observations hold promise for the use of such a resonance for tuning the interspecies scattering properties in a dipolar mixture. We further compare the prevalence of narrow resonances in an ^{166}Er - ^{164}Dy mixture to the single-species case, and observe an increased density of resonances in the mixture.

DOI: 10.1103/PhysRevA.102.033330

I. INTRODUCTION

Ultracold quantum gases are a highly successful platform for physics research largely because it is possible to create simplified and controllable versions of condensed matter systems [1]. As the field has advanced, great progress has been made by reintroducing complexity in a carefully controlled manner. This complexity can manifest in the form of interparticle interactions [2–4], the species and statistics of the particle under study [5–7], or in the form of the potential landscape, control protocols, and imaging techniques applied to the system [8,9]. In this work, we explore interspecies Feshbach resonances as a means of generating tunable interactions between two different species of complex dipolar atoms.

Atoms with large magnetic dipole moments, such as the lanthanide series elements erbium and dysprosium, interact in a manner that is both long-range and anisotropic. This is in contrast to more commonly used atomic species, such as alkali and alkaline earth metals, which primarily interact in a short-range and isotropic way. The recent creation of degenerate Bose and Fermi gases of such atoms [10–13] has enabled the observation of a wealth of phenomena including quantum-stabilized droplet states [14–16], roton quasiparticles [17], supersolid states [18–20], and a nonisotropic Fermi surface [21].

In a separate direction, degenerate mixtures of multiple atomic species have also provided diverse opportunities for the study of physical phenomena. Examples include studies of polarons that arise when an impurity species interacts with a background gas [22–27], and the formation of heteronuclear molecules with large electric dipole moments [28–31].

We expect that combining dipolar interactions with heteronuclear mixtures will lead to a rich set of physical phenomena, the exploration of which has only recently begun. In particular, dipolar interactions are expected to have dramatic consequences for the miscibility of binary condensates [32–34], and in turn on vortex lattices that arise in such systems [35]. Further, certain properties of polarons are predicted to emerge when either the background [36] or both background and impurity [37] particles experience dipolar interactions [38].

Dipolar heteronuclear mixtures have recently been demonstrated [39], but so far the interspecies scattering properties have not been explored, either experimentally or theoretically. In these complex dipolar species, scattering properties are dictated by both anisotropic long-range dipolar interactions, which can be tuned through a combination of system geometry and magnetic field angle, and by contact interactions, which can be tuned through the use of interspecies Feshbach resonances. While scattering models and experimental demonstrations exist for mixtures of single- and two-valence electron atoms (which lack strong dipolar interactions) [40,41], the scenario of two multivalence electron atoms has yet to be considered, and represents a frontier for our understanding of ultracold scattering. In many commonly used atomic systems, the strength, character, and location of magnetic Feshbach resonances can be predicted with high precision through coupled-channel calculations [3]. However, the complexity of the internal level structure and coupling mechanisms present in lanthanide atoms lead to significant challenges for the development of a microscopic theory with predictive power, and so necessitate an experimental survey to find resonances with favorable properties [42–46].

To this end, we searched for heteronuclear Feshbach resonances broad enough to provide a practical means for tuning the interspecies interaction in Bose-Bose and Bose-Fermi dipolar quantum mixtures. Using atomic-loss spectroscopy to identify resonances, we perform surveys of fermionic ^{161}Dy and bosonic ^{164}Dy together with ^{166}Er, ^{168}Er, and ^{170}Er over

*Corresponding author: Francesca.Ferlaino@uibk.ac.at

TABLE I. Comparatively broad resonances found in specific isotope mixtures together with estimated center positions and widths (FWHM) from Gaussian fits to atom loss spectra. Each value is an average between the fit values of Er and Dy.

Combination	Resonance magnetic field (G)	Width (G)
^{168}Er - ^{164}Dy	13.32(4)	1.7(1)
^{166}Er - ^{164}Dy	34.09(3)	1.5(1)
^{166}Er - ^{161}Dy	161.31(3)	0.84(9)
^{168}Er - ^{161}Dy	161.30(2)	0.93(5)
^{170}Er - ^{161}Dy	161.26(3)	0.91(8)

a magnetic-field range from zero to several hundred gauss (the exact range varies by isotope combination due to availability of favorable evaporation conditions). We also explored a Fermi-Fermi mixture of ^{167}Er and ^{161}Dy, but observed no broad resonances there. In Table I we summarize positions and widths of these features observed in our surveys. As an exemplary case, we present a more detailed characterization of the resonance near 13.5 G in the ^{168}Er - ^{164}Dy Bose-Bose mixture, through measurements of interspecies thermalization and the dependence of atomic loss on temperature.

In addition, our dipolar mixtures host a large number of narrow interspecies resonances. In previous experiments with single species, the density and spacing of these narrow resonances has been studied to reveal a pseudorandom distribution that can be modeled well using random matrices [43,45,46]. By performing high resolution scans over specific magnetic-field ranges, we find that the average density of interspecies resonances exceeds the combined density of intraspecies resonances, perhaps indicating the contribution of odd partial waves or molecular states with antisymmetric electron configurations for the interspecies case, which are not present in the scattering of identical bosons.

Finally, in each Fermi-Bose mixture involving ^{161}Dy we observe a correlated loss feature between fermionic Dy and bosonic Er atoms. Strangely, the loss feature is present at the same magnetic-field value for all three bosonic erbium isotopes studied. Such behavior is inconsistent with a typical interspecies Feshbach resonance, where the magnetic field at which the resonance occurs is strongly dependent on the reduced mass of the atoms involved [47]. The mechanism behind this unusual feature is as of yet unknown and calls for further experimental and theoretical investigations.

II. OBSERVATION OF INTERSPECIES RESONANCES

Our experimental sequence is similar to the one introduced in our previous works [39,48]. After cooling the desired isotope combination of erbium and dysprosium atoms in a dual-species magneto-optical trap (MOT), we load the atoms into a crossed optical dipole trap (ODT) created by 1064-nm laser light. Here we perform evaporative cooling down to the desired sample temperature. During the whole evaporation sequence, we apply a constant and homogeneous magnetic field (B_{ev}), pointing along the z direction opposite to gravity. B_{ev} preserves the spin polarization in the lowest Zeeman sublevel of both species. We use different values of B_{ev} to optimize the evaporation efficiency depending on the isotope combination and on the range of the target magnetic field (B_{FB}) to be investigated. The final ODT has trap frequencies $\omega_{x,y,z} = 2\pi \times (222, 24, 194)\mathrm{s}^{-1}$. We typically obtain mixtures with atom numbers ranging from 3×10^4 to 1×10^5 atoms for each species. The sample is in thermal equilibrium at about 500 nK, which corresponds to about twice the critical temperature for condensation. Typical densities are up to a few $\times 10^{12}\,\mathrm{cm}^{-3}$ for each species. After preparing the mixture, we linearly ramp the magnetic field from B_{ev} to B_{FB} in 5 ms, either in an increasing or decreasing manner. The current flowing in the coils that generate the magnetic fields can be changed on the millisecond time scale, and the field at the position of the atoms settles to the part-per-thousand level in approximately 10 ms. We hold the mixture for a time ranging between 5 ms and 400 ms depending on the experiment. At the end of the hold time, we release the atoms from the ODT in a 15 ms time-of-flight (TOF) expansion after which we record an image of the atoms using a standard low-field absorption imaging technique [12]. Note that we adjust the relative amount of erbium and dysprosium in the final thermal mixture for the specific experiments by independently tuning the MOT loading time for each species between 0.5 and 5 s.

In the isotope combinations and range of magnetic fields that we explore here, we observe two interspecies resonances with widths greater than 1 G (see Table I). We now turn to a more detailed characterization of a feature present in the ^{168}Er - ^{164}Dy combination, for which atom loss is shown in Fig. 1(a). We chose to focus on this feature because it is relatively isolated from the many narrow homonuclear and heteronuclear resonances typical of lanthanides. In this experiment, the starting mixture contains 6.2×10^4 erbium and 9.1×10^4 dysprosium atoms and it is prepared by evaporation at $B_{\mathrm{ev}} = 10.9\,\mathrm{G}$. In order to compensate for loss during magnetic-field ramps and slow drifts of the atom number, we normalize measurements performed with 200-ms hold times at B_{FB} to interleaved measurements at 10-ms hold time at the same field. We further performed independent trap-loss spectra in single-species operation to confirm the interspecies nature of the resonance. Moreover, such scans allow us to identify intraspecies resonances and exclude them from the fit [see empty symbols in Fig. 1(a)]. As shown in the inset for erbium, a high-resolution scan reveals a narrow region with less loss near the center of our broad loss feature, probably due to the influence of a second interspecies resonance—because a resonance contributes a scattering length with a different sign on either side of its pole, the contributions from two nearby resonances may counteract in between them, leading to a reduction in loss. This structure is also visible on the dysprosium loss feature but it is not shown in the inset for ease of reading.

A Gaussian fit to the loss profiles, with known narrow single-species resonance excluded, returns a center value of 13.31(2) and 13.33(4) G and a full width at half maximum (FWHM) value of 1.95(5) and 1.3(1) G for erbium and dysprosium, respectively. The observed difference in the fitted width of the two species can be explained by the imbalance in atom number: because this measurement was performed with fewer erbium atoms than dysprosium, the fractional loss of erbium is higher than that of dysprosium, leading to a

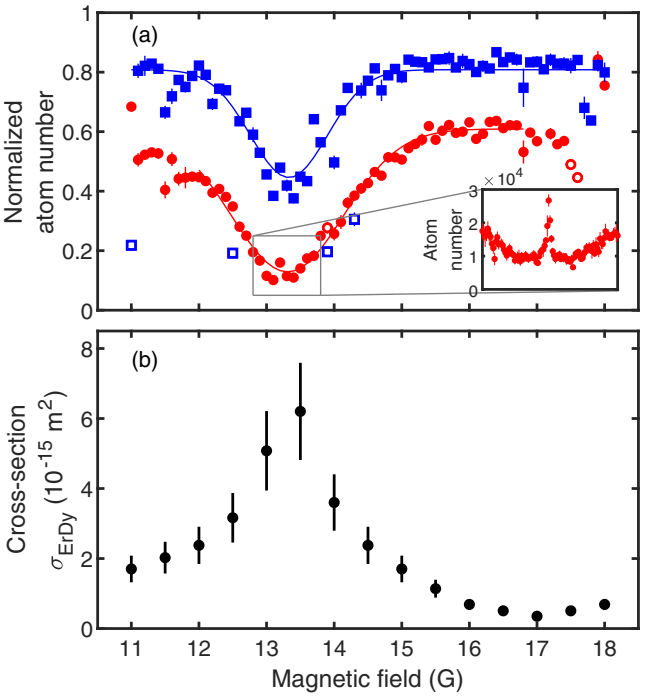

FIG. 1. (a) Trap loss from the 13.5 G resonance in the Bose-Bose mixture ^{168}Er - ^{164}Dy (red circles and blue squares points, respectively). Empty symbols correspond to narrow single-species resonances, which we exclude from fits. Each point is an average over four experimental repetitions. For each magnetic field, the atom number recorded after 200 ms of hold time is normalized to that at a short hold time of 10 ms. The lines are the Gaussian fits to the data. The inset shows erbium loss measured in a different dataset with 5-mG resolution, and highlights the structure present on the center of the feature. The same structure is visible also for the dysprosium atoms in the mixture. (b) Interspecies elastic cross section σ_{ErDy} measured across the Feshbach resonance using cross-species thermalization. Each value of σ_{ErDy} is extracted from thermalization data using a numerical model for thermalization that includes temporal variation in atom number and temperature; see main text and the Appendix.

greater saturation of loss and broadening of the erbium loss feature.

III. INTERSPECIES THERMALIZATION

To get insights on its effective strength and width, we perform cross-species thermalization measurements across the resonance [see Fig. 1(b)]. Interspecies thermalization experiments are well established techniques to extract effective thermalization cross sections, which in turn depend on the scattering length [49–51]. While inferring a precise value of the scattering length would require the development of a detailed and rigorous model that accurately captures the temperature dependence of the interspecies and anisotropic dipolar scattering [52], and would go beyond the scope of this work, we are able to determine a thermally averaged scattering cross-section from which we can estimate the width of the resonance.

In this cross-thermalization experiment, we selectively heat dysprosium by means of a near-resonant 421-nm light pulse along the vertical direction. We confirmed that the light pulse has no direct measurable effect on erbium. The magnetic field is then jumped to the desired value B_{FB} and held for a variable amount of time, during which the temperature of erbium rises to equilibrate with dysprosium due to elastic collisions. We record the temperature of the two species along a direction orthogonal to the heating pulse, as the effects of center of mass motion are less prevalent here [53], and use a numerical model to extract a cross section from the rate of thermalization. This simple model assumes an energy independent cross section, an assumption which may break down near resonance where unitarity limits on scattering may become significant.

From these thermalization measurements, we can see a dramatic increase in the scattering cross section near resonance, as one would expect for an interspecies Feshbach resonance. Further, we observe a significant modification of the cross section associated with the resonance over a Gauss-scale range of magnetic fields, similar to the width we observe in loss measurements. For comparison, the expected contribution to the scattering cross section due to dipolar interactions is 2.4×10^{-16} m^2, over an order of magnitude below what we infer near resonance. While the exact relationship between the measured cross section and scattering length is complicated by the finite temperature of our atoms and anisotropic nature of the interactions, an approximate value can be attained through the simple expression for s-wave scattering $\sigma = 4\pi a_s^2$, where a_s is the s-wave scattering length [3]. Our largest measured cross sections, near resonance at 13.5 G, imply a scattering length of roughly 400 a_0, substantially greater than the dipolar length $a_D = m\mu_0\mu_{\mathrm{Er}}\mu_{\mathrm{Dy}}/4\pi\hbar^2 \simeq 139\ a_0$ associated with interspecies collisions (a_0 is the Bohr radius). In this expression, $m = m_{\mathrm{Er}}m_{\mathrm{Dy}}/(m_{\mathrm{Er}} + m_{\mathrm{Dy}})$ is the reduced mass, and μ_{Er}, μ_{Dy} are the ground-state magnetic dipole moments for erbium and dysprosium, respectively.

For an isolated resonance and pure contact interactions, a common way to characterize the resonance width is the parameter Δ, given by the difference in magnetic field between the pole of the resonance, at which the thermalization rate is maximal, and the nearest zero crossing in the thermalization rate, which would correspond to a lack of scattering [3]. In lanthanides, the presence of anisotropic dipolar interactions leads to a scattering cross section that does not completely vanish. In addition, multiple narrow and overlapping resonances may be present, which may influence the interpretation of such a width measurement. However, to get a rough estimate of the width of the resonance, we can consider the distance between the resonance pole and the apparent minimum in the thermalization rate at 17 G. This suggests a width of $\Delta \simeq 3.5$ G.

IV. DEPENDENCE OF LOSS ON TEMPERATURE

The dependence of the loss feature on the cloud temperature can provide additional information on the nature of the resonance. For broad resonances, a universal regime is expected to emerge near resonance where the scattering cross section and loss are dictated primarily by the atomic momentum, rather than the scattering length [54]. In this regime, the three-body loss parameter L_3 follows a nearly universal form scaling as $1/T^2$, where T is the temperature. Such scaling has

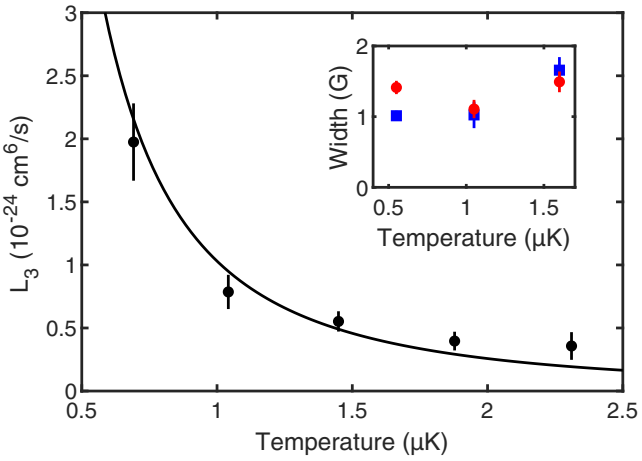

FIG. 2. Three-body loss coefficient L_3 extracted from on-resonance loss measurements at the resonance position for different temperatures (black circles), along with a fit to a $1/T^2$ scaling (black line), as expected for universal three-body loss. The inset shows the resonance width extracted as FWHM from Gaussian fits to the trap-loss spectra versus cloud temperature for a different dataset. Red circles and blue squares refer to erbium and dysprosium, respectively. The reported temperature comes from a TOF estimation.

been observed in broad resonances of several atomic species [54–56].

We observe a temperature dependence of the loss rate near resonance that is suggestive of such universal behavior. By varying the final depth of the ODT reached during evaporation, we tune the temperature of the atomic mixture. For each temperature, we measure atom loss on resonance at 13.4 G as a function of the hold time. We then use a numerical model to extract the rate of interspecies three-body loss, and L_3.

These loss coefficients are plotted as a function of temperature in Fig. 2, along with a fit to a $1/T^2$ dependence, which provides a reasonable description of our data. The universal temperature dependence arises from a maximum value of L_3 possible at a given temperature, given by

$$L_{3,\max} = \frac{\lambda_{3,\max}}{T^2} \simeq \frac{\hbar^5}{m^3} \frac{36\sqrt{3}\pi^2}{(k_B T)^2}. \quad (1)$$

Factors associated with Efimov physics can lead to a lower value for L_3, but not higher [54,57,58]. From our fit to a $1/T^2$ dependence for our data, we extract a value of $\lambda_3 = 1.0(2) \times 10^{-24} \mu\text{K}^2\text{cm}^6\,\text{s}^{-1}$, which is compatible with the predicted bound of $\lambda_{3,\max} = 2.4 \times 10^{-24}\,\mu\text{K}^2\text{cm}^6\text{s}^{-1}$.

A reduction in the peak loss rate with increasing temperature can also result from thermal broadening of the resonance, especially for very narrow resonances [45]. This is unlikely to be the dominant effect here, as for typical differential magnetic moments between entrance and closed channels in our lanthanide system [59], we would expect broadening on the scale of a few times 10 mG for temperatures near 1 μK, much narrower than the Gauss-scale width of our feature. Further, suppression of peak loss is typically accompanied by a commensurate broadening and shift of the loss feature on the scale of its width, which we do not observe (inset in Fig. 2).

V. SURVEY OF NARROW RESONANCES

In addition to the few relatively broad resonances, the lanthanides exhibit many narrow resonances, whose statistical properties have been investigated for single-species gases [43,45,46]. In this section we compare the abundance of interspecies resonances to single-species resonances by performing high-resolution trap-loss spectroscopy on the isotope combination ^{166}Er - ^{164}Dy (see Fig. 3). Here, we investigate four different magnetic-field ranges, each 10 G wide,

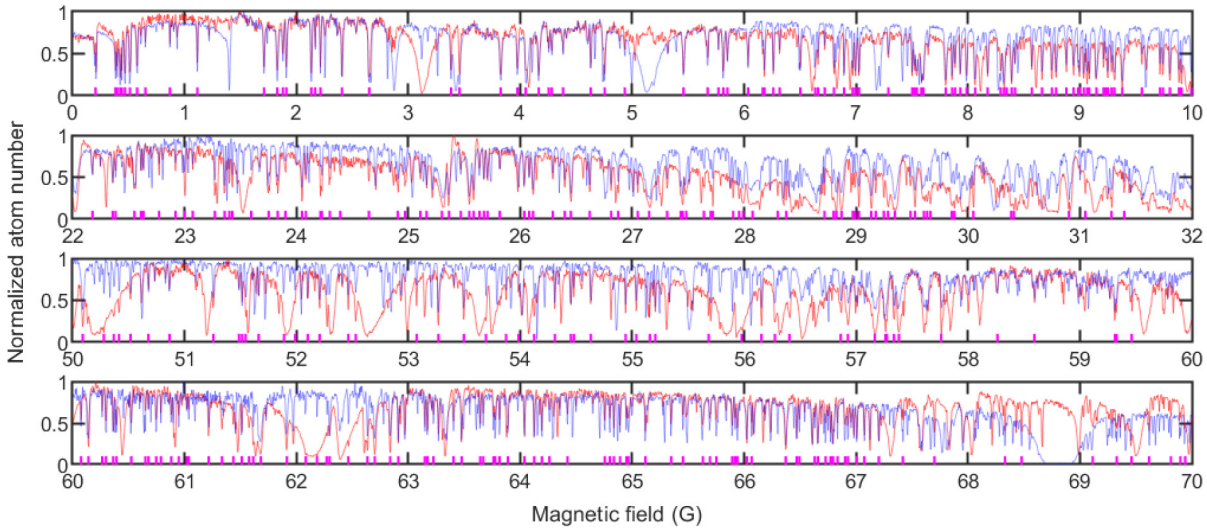

FIG. 3. High-resolution trap-loss spectroscopy for a balanced mixture of ^{166}Er and ^{164}Dy (red and blue curves respectively), with initial atom numbers of roughly 10^5 per species at a temperature of 500 nK after 400 ms of interaction time. The magenta ticks indicate the heteronuclear resonance positions as extracted by our analysis (see main text). The measurement is composed of four datasets [0, 10] G, [22, 32] G, [50, 60] G, and [60, 70] G with a stepsize of 5 mG. Each point is an average over four experimental repetitions. Atom numbers are normalized to the maximum of each dataset for ease of reading. The broad loss feature in Dy near 68.8 G was not observed in previous work [45], and may result from a technical source of loss in our experiment.

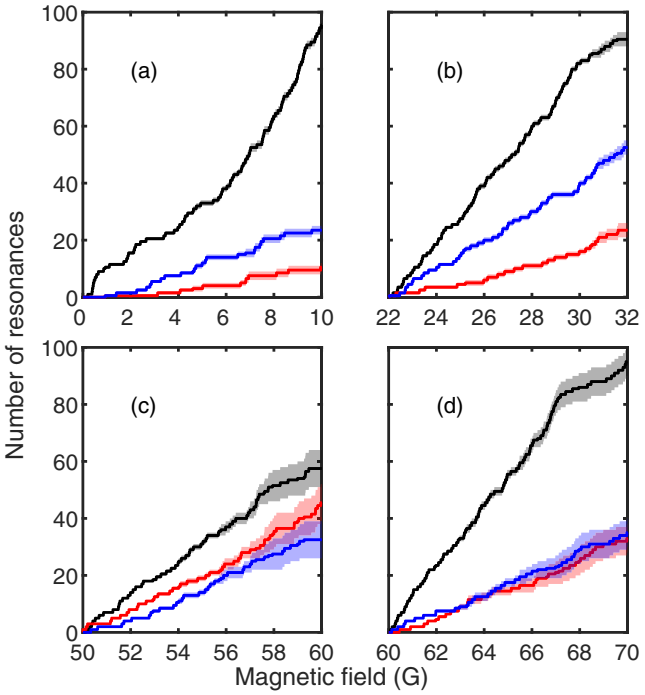

FIG. 4. (a)–(d) Staircase function describing the number of Feshbach resonances as a function of the four investigated magnetic-field ranges: [0, 10] G, [22, 32] G, [50, 60] G, and [60, 70] G respectively. The black line shows the number of heteronuclear resonances. The red and blue lines show the number of homonuclear resonances for ^{166}Er and ^{164}Dy, respectively. The shaded areas represent our confidence intervals (see main text).

with a resolution 40 times higher than the one used for the exploratory surveys. To enable direct comparison with the previous works performed on single species [43,45], we use similar experimental conditions (isotope, atom number, temperature, and hold time).

As expected, we observe many narrow homonuclear resonances [43,45]. In addition, we also identify many narrow heteronuclear resonances. To distinguish these two types of resonance, we first label features with a fractional loss above 30% as resonances. We then categorize these resonances as interspecies if erbium and dysprosium loss features occur simultaneously within a range of ± 10 mG and with a loss amplitude ratio in the range 0.5–2. Features that do not meet both of these criteria, are labeled either as homonuclear or ambiguous, based on comparison with separate scans performed with single species, either within this work or from previously published data [43,45]. The numbers of ambiguous features define our confidence intervals.

In order to visualize the number of resonances, we construct the staircase function $\mathcal{N}(B)$, which describes the cumulative number of resonances from the start of a scan range up to a given magnetic field B_{FB}. Figures 4(a)–4(d) shows $\mathcal{N}(B)$ for the four investigated magnetic-field ranges. The black lines represent heteronuclear Feshbach resonances, while the red and the blue lines represent the homonuclear ^{166}Er and ^{164}Dy resonances, respectively. The shaded regions represent our confidence interval defined by the total number of ambiguous Feshbach resonances.

Our analysis results in a total number of heteronuclear resonances of $\mathcal{N}_{\mathrm{ErDy}}(\mathrm{tot}) = 339(16)$, counting all magnetic-field ranges, and a number of homonuclear resonances of $\mathcal{N}_{\mathrm{Er}}(\mathrm{tot}) = 116(16)$ and $\mathcal{N}_{\mathrm{Dy}}(\mathrm{tot}) = 144(16)$. Within our confidence intervals, we detect a total number of homonuclear resonances comparable with those of previous works [43,45]. The corresponding total density of resonances $\bar{\rho}$, given by the total number of resonances divided by the total range of magnetic fields scanned are $\bar{\rho}_{\mathrm{ErDy}} = 8.5(4)\,\mathrm{G}^{-1}$, $\bar{\rho}_{\mathrm{Er}} = 2.9(4)\,\mathrm{G}^{-1}$, and $\bar{\rho}_{\mathrm{Dy}} = 3.6(4)\,\mathrm{G}^{-1}$.

For our combined dataset, we find that the total number of heteronuclear resonances exceeds the combined number of homonuclear resonances for the two species: $\bar{\rho}_{\mathrm{ErDy}} = \alpha(\bar{\rho}_{\mathrm{Er}} + \bar{\rho}_{\mathrm{Dy}})$, with $\alpha = 1.3(2)$. We would expect that the average density of heteronuclear resonances should be greater than the sum of the two homonuclear resonance densities. This is because each species contributes a set of internal states that can be coupled to, and the heteronuclear resonances are not subject to the same symmetrization requirements as the homonuclear resonances. In resonances involving distinguishable particles, both gerade and ungerade Born-Oppenheimer molecular potentials contribute, as well as both even and odd partial waves for the entrance channel. Our data is consistent with this expectation ($\alpha > 1$). Note that we do observe a lower number of interspecies resonances in the range 50–60 G, perhaps as a result of the nonrandom distribution of resonances as observed in the single-species case [43,45], or to the presence of broad homonuclear erbium resonances that could obscure the observation of interspecies resonances.

VI. COINCIDENT LOSS FEATURE IN DIFFERENT ISOTOPES

Finally, we have also searched for broad (Gauss-range) resonances in Bose-Fermi mixtures consisting of fermionic ^{161}Dy combined with different bosonic isotopes of erbium–^{166}Er, ^{168}Er, and ^{170}Er, as well as Fermi-Fermi mixtures of ^{161}Dy and ^{167}Er. For these combinations, we perform only coarse scans and thus only resolve broad features. In mixtures involving the bosonic isotopes of erbium we observe a correlated loss feature between erbium and dysprosium near 161 G (see Fig. 5). This loss feature is not present at our level of measurement sensitivity with either species alone, or in the mixture with the fermionic ^{167}Er. Surprisingly, the loss feature is centered at the same magnetic field (to within our resolution of 0.1 G) for all bosonic isotopes of erbium. This is quite unexpected as the magnetic-field value of the resonance position is typically highly sensitive to the reduced mass of the atoms involved [47].

To shed more light on this puzzling feature, we conducted further investigations on the exemplary case of ^{168}Er - ^{161}Dy. For such a mixture, we performed loss measurements with erbium numbers ranging from 1.3×10^4 to 3×10^4 (with the number of dysprosium fixed at 2.5×10^4). We found in each case that the number of erbium lost was roughly equal to the number of dysprosium lost, and that the number of total atoms lost was roughly proportional to the number of erbium present. We further varied the temperature of the mixture from

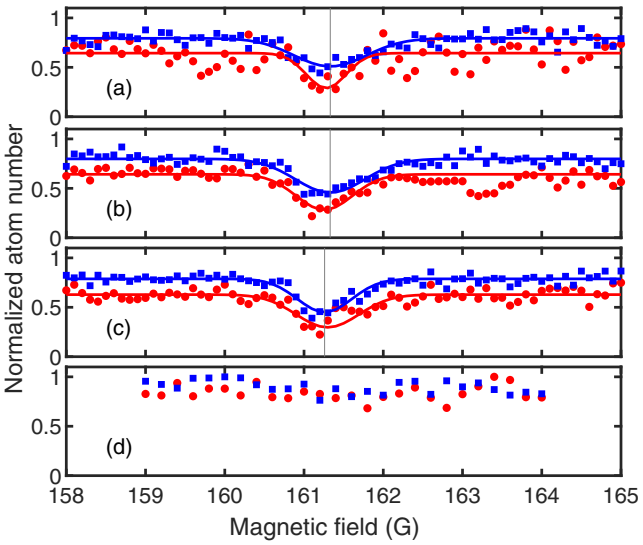

FIG. 5. Trap loss spectra for fermionic ^{161}Dy in combination with bosonic ^{166}Er, ^{168}Er, and ^{170}Er, and fermionic ^{167}Er (a)–(d), respectively. Red circles represent erbium, blues squares represent dysprosium, and lines are Gaussian fits to the losses. The solid vertical gray lines highlight the peak centers from the fit over dysprosium losses. For the plots with bosonic erbium, the atom number after 100 ms of interaction time is normalized to a short hold time of 5 ms. In the plot with ^{167}Er, the normalization is performed using the maximum value in the dataset. For all panels, each point is an average over four experimental repetitions.

600 to 2000 nK, and did not find a dramatic dependence of the loss coefficient on temperature (modeling loss as either two-body Er-Dy loss or three-body loss with equal coefficients for Er-Er-Dy and Er-Dy-Dy).

Several physical mechanisms could be consistent with such a feature. One possibility is that the resonance we observe is associated with a bound state of a shallow molecular potential [60]. Mechanisms to create such potentials have been proposed for species with dipolar interactions [61,62]. However, none are obviously applicable to magnetic atoms in the lowest energy entrance channel. Further, given the level of insensitivity to the mass of erbium, we would expect to see additional resonances of a shallow potential in the magnetic-field range over which we survey, which we do not. A second possibility is that the feature we observe is not a true interspecies resonance, but rather an intraspecies resonance in dysprosium whose loss rate is enhanced by the presence of bosonic erbium atoms. A similar effect was reported in a mixture of fermionic lithium and bosonic rubidium atoms [63]. Finally, it is possible that this feature is not a Feshbach resonance at all, but rather the result of spin-changing processes resulting from unintentional radio-frequency tones in the laboratory, or of an interspecies photoassociation resonance. We have ruled out the most likely culprits for the last effect by varying the relative detuning between our horizontal and vertical dipole traps and observing no change in the resonance position. We hope that our presentation of this mysterious feature may spur theoretical exploration of possible physical mechanisms.

VII. CONCLUSIONS

In conclusion, we have reported experimental observation of heteronuclear magnetic Feshbach resonances in several isotope mixtures of erbium and dysprosium. Among the Gauss-broad features identified in our surveys, we have characterized one in the combination ^{168}Er - ^{164}Dy by means of cross-species thermalization measurement and temperature dependence analysis. We performed high-resolution trap-loss spectroscopy in the combination ^{166}Er - ^{164}Dy to compare the average resonance density of the mixture with respect to the single-species case. In mixtures of fermionic ^{161}Dy and bosonic erbium atoms, we observed a correlated loss feature which appears to be insensitive on the erbium isotope used but absent in dysprosium alone. Our observations pave the way to realize tunable interactions in quantum degenerate mixtures of dipolar atoms. Knowledge of the range of tunability of these interspecies interactions is a key ingredient for varied opportunities including studies of the miscibility of binary condensates, of vortex lattices, and of dipolar polarons [32–37].

ACKNOWLEDGMENTS

We thank J. Hutson, M. Frye, J. Bohn, A. Trautmann, and the Erbium and DyK teams in Innsbruck for insightful discussions. This work is financially supported through an ERC Consolidator Grant (RARE, No. 681432), a NFRI Grant (MIRARE, No. ÖAW0600) from the Austrian Academy of Science, a QuantERA grant MAQS by the Austrian Science Fund FWF No. I4391-N, and a DFG/FWF (FOR No. 2247/PI2790). M.S. and G.D. acknowledge support by the Austrian Science Fund FWF within the DK-ALM (No. W1259-N27). We also acknowledge the Innsbruck Laser Core Facility, financed by the Austrian Federal Ministry of Science, Research and Economy.

APPENDIX: MEASUREMENT AND ANALYSIS DETAILS

1. Cross-species thermalization

As an exemplary case, we study in more detail the resonance found in the ^{168}Er - ^{164}Dy Bose-Bose mixture near 13.5 G. To reliably quantify the value of the interspecies cross section, we developed the following scheme for cross-species thermalization measurements [49–51]. To avoid heating of the sample by crossing Feshbach resonances, we evaporate the mixture at B_{ev} close to resonance. Specifically, when measuring on the low(high)-field side of the feature we evaporate at $B_{\mathrm{evap}} = 10.8\,\mathrm{G}(16.4\,\mathrm{G})$. Once the sample is prepared as previously described (here we use an unbalanced mixture with twice as much Dy as Er), we compress the trap by linearly increasing the horizontal ODT power by a factor of 5 and the vertical ODT power by two in 500 ms to prevent any plain evaporation. The final trap frequencies in the compressed trap are $\omega_{x,y,z} = 2\pi \times (409, 26, 391)\mathrm{s}^{-1}$. Subsequently, we ramp the magnetic field in 5 ms to either 10 or 16 G. Here, a pulse of near-resonant 421-nm light propagating along the magnetic field direction (z) is used to selectively heat dysprosium. We fix the duration of the pulse at 5.5 ms to roughly match the trap

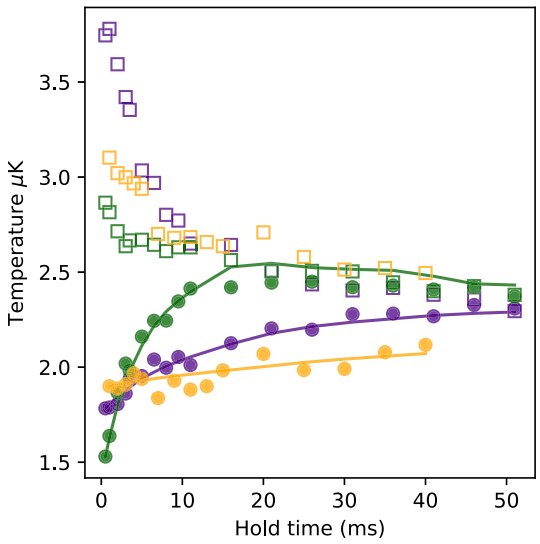

FIG. 6. Sample temperature traces for erbium (filled circles) and dysprosium (hollow squares) after dysprosium is heated. Purple, green, and orange correspond to magnetic fields of 12, 13.5, and 17 G, respectively. Fit lines represent the results of the numerical integration of Eq. (A2), which fits the temperature profile of erbium based on its initial value and the dysprosium temperatures. Different evaporation conditions cause the curves to have slightly different initial and final conditions (see main text).

oscillation period along this direction and set the pulse intensity to give the desired temperature increase of the dysprosium cloud (up to 4 μK). We confirmed that the light pulse has no direct measurable effect on erbium. Finally, with a quench fast compared to the shortest thermalization rate, the magnetic field is set to the desired value B_{FB} and held for a variable amount of time, during which the temperature of erbium rises to equilibrate with dysprosium due to thermalizing collisions (Fig. 6). We note that in the temperature evolution of the clouds, the initial temperatures are slightly different. This behavior is mainly due to different evaporation conditions on the two sides of the resonance, the different strength in the quench to the final B_{FB}, and the heating caused by the resonance itself. By comparing the two species' temperature, we ensure that these different conditions are consistent with general offsets on the single measurement thus not affecting the final estimation of the cross-section.

To extract a scattering cross section from our cross-species thermalization data, we use a fit to a numerical model for the thermalization of two species. In principle, a simple exponential fit to the temperature difference between the two species could also be used, but does not account for changes in the atom number or average temperature of the sample that may arise from residual evaporation during the thermalization time. Our numerical model follows that of Ref. [49]. We treat the scattering cross section as independent of the energy of the colliding particles, an assumption that greatly simplifies the analysis, but inevitably breaks down near enough to resonance where unitarity considerations bound the scattering cross section. This assumption leads to a collision rate for each atom of species 1 with atoms of species 2 given by

$$\gamma_{12} = \frac{N_2 m_1^{3/2} \bar{\omega}_1^3}{\pi^2 k_{\mathrm{B}} (T_1 + \beta^{-2} T_2)^{3/2}} \sqrt{\frac{T_1}{m_1} + \frac{T_2}{m_2}} \sigma_{12}, \tag{A1}$$

where m_1, m_2, T_1, and T_2 are the masses and temperatures of species 1 and 2, $\bar{\omega} = (\omega_x \omega_y \omega_z)^{1/3}$ characterizes the frequency of the trap, $\beta^2 = m_2 \bar{\omega}_2^2 / m_1 \bar{\omega}_1^2$, and σ_{12} is the effective interspecies cross section. We assume that the energy exchanged per collision is given by $\Delta E = \xi k_{\mathrm{B}} (T_2 - T_1)$ where $\xi = 4 m_1 m_2 / (m_1 + m_2)^2$, and that the heat capacity of each atom is $3 k_{\mathrm{B}}$. This leads to a differential equation for the temperature of erbium:

$$\frac{dT_{\mathrm{Er}}}{dt} = \frac{\xi k_{\mathrm{B}} (T_{\mathrm{Dy}} - T_{\mathrm{Er}}) N_{\mathrm{Dy}} m_{\mathrm{Er}}^{3/2} \bar{\omega}_{\mathrm{Er}}^3}{3\pi^2 k_{\mathrm{B}} (T_{\mathrm{Er}} + \beta^{-2} T_{\mathrm{Dy}})^{3/2}} \times \sqrt{\frac{T_{\mathrm{Er}}}{m_{\mathrm{Er}}} + \frac{T_{\mathrm{Dy}}}{m_{\mathrm{Dy}}}} \sigma_{\mathrm{ErDy}}, \tag{A2}$$

which we can numerically integrate using the instantaneous values for T_{Dy} and N_{Dy}, and from this extract the scattering cross section σ_{ErDy} that yields a thermalization profile that best matches our data, as determined through a least-squares difference. Examples of three such fits, for 12, 13.5, and 17 G are shown in Fig. 6, and generally describe our thermalization data well.

2. Temperature dependence of loss

We quantify the temperature dependence of three-body loss in terms of the interspecies three-body loss coefficient. For a single species, the three-body loss coefficient L_3 can be defined by $\dot{N}/N = -L_3 \langle n^2 \rangle$, where N is the total number of atoms, and $\langle n^2 \rangle = \int d^3 r \; n^3(\boldsymbol{r})/N$ represents the average squared density of scattering partners for an atom in the gas. $n(\boldsymbol{r})$ is the local density of the gas.

We define analogous quantities for our two-species mixture, containing particles denoted i and j. In this case,

$$\frac{\dot{N}_i}{N_i} = \frac{-1}{3N_i} \int d^3 r \; (2 L_3^{i,i,j} n_i^2(\boldsymbol{r}) n_j(\boldsymbol{r}) + L_3^{j,j,i} n_i(\boldsymbol{r}) n_j^2(\boldsymbol{r})). \tag{A3}$$

Here, $L_3^{i,i,j}$ represents the loss rate due to collisions involving two atoms of species i and one of j.

To arrive at simple expressions, we make several assumptions and approximations. First, we treat the mass, temperature, and polarizability of the two atomic species as equal, which is a reasonable approximation for erbium and dysprosium isotopes in our 1064-nm wavelength ODT [39]. This assumption implies equivalent spatial distributions for the two species, which we assume to be thermal in our three-dimensional harmonic trap. We next set $L_3^{i,i,j} = L_3^{j,j,i} \equiv L_3^i$ near resonance, essentially assuming that the loss process is primarily determined by the two pairwise interactions between the minority participant and the two majority atoms. We find this assumption leads to a model consistent with our observed relative loss between the two species. With these simplifications in place, we define L_3^i using $\dot{N}_i/N_i =$

$-L_3^i \langle n^2 \rangle_{\text{eff}}^i$, where

$$\langle n^2 \rangle_{\text{eff}}^i = \frac{(2N_iN_j + N_j^2)m^3\bar{\omega}^6}{3^{\frac{5}{2}}8\pi^3(k_BT)^3} \tag{A4}$$

and $\bar{\omega} = (\omega_x\omega_y\omega_z)^{1/3}$ is the geometric mean of the trap oscillation frequencies.

We extract the resonant value of L_3 by measuring remaining atom number versus hold time in mixtures prepared at different temperatures, with the magnetic field set near resonance at 13.4 G. We then fit the resulting data by numerically integrating Eq. (A3). Because we observe significant single-species loss of erbium (the majority species), we treat the erbium atom number measured at each time step as inputs to our fit, and extract the value of L_3 that best predicts the loss of dysprosium. Here, we assume that $L_3^{i,i,j} = L_3^{j,j,i} \equiv L_3$. We bound the effects of single-species loss in dysprosium by repeating the same measurement and analysis protocol off resonance at 11.5 G and 16.5 G. The error bars in Fig. 2 of the main text include a contribution corresponding to the extracted L_3 in the off-resonant condition, which contain both the effects of single-species loss and the small effect of off-resonant interspecies loss. Also included are errors associated with the observed change in temperature during the loss measurement, and relating to the approximations made in estimating the density.

In a regime where the scattering length a exceeds the thermal wavelength $\lambda_{\text{th}} = h/\sqrt{2\pi mk_BT}$, and thermal broadening is small compared to the width of the loss feature, we expect roughly $L_3 \propto 1/T^2$, as has been observed in several experiments involving single atomic species [54–56]. This picture becomes complicated somewhat in the case of a binary mixture due to stronger Efimov effects, which lead to a temperature-dependent modulation of loss relative to the simple $1/T^2$ prediction. In particular, the parameter s_0, which characterizes the strength of the three-body Efimov potential, is equal to approximately 1.006 for identical bosons, but approximately 0.41 for our binary mixture [57,58]. The fractional importance of these temperature-dependent modifications scale as $e^{-\pi s_0}$ [54], making them a minor correction for identical bosons, but a potentially important effect in mixtures. It is possible that such effects contribute to deviations of our data from a $1/T^2$ form, but a true calculation would require knowledge of short-range inelastic processes in our system.

[1] I. Bloch, J. Dalibard, and W. Zwerger, Rev. Mod. Phys. **80**, 885 (2008).

[2] C. Menotti, M. Lewenstein, T. Lahaye, and T. Pfau, in *Dynamics and Thermodynamics of System with Long Range Interactions: Theory and Experiments*, edited by A. Campa, A. Giansanti, G. Morigi, and F. S. Labini, AIP Conf. Proc. No. 970 (AIP, New York, 2008), p. 332.

[3] C. Chin, R. Grimm, P. S. Julienne, and E. Tiesinga, Rev. Mod. Phys. **82**, 1225 (2010).

[4] M. Saffman, T. G. Walker, and K. Mølmer, Rev. Mod. Phys. **82**, 2313 (2010).

[5] B. DeMarco and D. S. Jin, Science **285**, 1703 (1999).

[6] Z. Hadzibabic, C. A. Stan, K. Dieckmann, S. Gupta, M. W. Zwierlein, A. Görlitz, and W. Ketterle, Phys. Rev. Lett. **88**, 160401 (2002).

[7] M. Taglieber, A.-C. Voigt, T. Aoki, T. W. Hänsch, and K. Dieckmann, Phys. Rev. Lett. **100**, 010401 (2008).

[8] W. S. Bakr, J. I. Gillen, A. Peng, S. Fölling, and M. Greiner, Nature (London) **462**, 74 (2009).

[9] C. Gross and I. Bloch, Science **357**, 995 (2017).

[10] M. Lu, N. Q. Burdick, S. H. Youn, and B. L. Lev, Phys. Rev. Lett. **107**, 190401 (2011).

[11] M. Lu, N. Q. Burdick, and B. L. Lev, Phys. Rev. Lett. **108**, 215301 (2012).

[12] K. Aikawa, A. Frisch, M. Mark, S. Baier, A. Rietzler, R. Grimm, and F. Ferlaino, Phys. Rev. Lett. **108**, 210401 (2012).

[13] K. Aikawa, A. Frisch, M. Mark, S. Baier, R. Grimm, and F. Ferlaino, Phys. Rev. Lett. **112**, 010404 (2014).

[14] H. Kadau, M. Schmitt, M. Wenzel, C. Wink, T. Maier, I. Ferrier-Barbut, and T. Pfau, Nature (London) **530**, 194 (2016).

[15] L. Chomaz, S. Baier, D. Petter, M. J. Mark, F. Wächtler, L. Santos, and F. Ferlaino, Phys. Rev. X **6**, 041039 (2016).

[16] M. Schmitt, M. Wenzel, F. Böttcher, I. Ferrier-Barbut, and T. Pfau, Nature (London) **539**, 259 (2016).

[17] L. Chomaz, R. M. W. van Bijnen, D. Petter, G. Faraoni, S. Baier, J.-H. Becher, M. J. Mark, F. Wächtler, L. Santos, and F. Ferlaino, Nat. Phys. **14**, 442 (2018).

[18] F. Böttcher, J.-N. Schmidt, M. Wenzel, J. Hertkorn, M. Guo, T. Langen, and T. Pfau, Phys. Rev. X **9**, 011051 (2019).

[19] L. Chomaz, D. Petter, P. Ilzhöfer, G. Natale, A. Trautmann, C. Politi, G. Durastante, R. M. W. van Bijnen, A. Patscheider, M. Sohmen, M. J. Mark, and F. Ferlaino, Phys. Rev. X **9**, 021012 (2019).

[20] L. Tanzi, E. Lucioni, F. Famà, J. Catani, A. Fioretti, C. Gabbanini, R. N. Bisset, L. Santos, and G. Modugno, Phys. Rev. Lett. **122**, 130405 (2019).

[21] K. Aikawa, S. Baier, A. Frisch, M. Mark, C. Ravensbergen, and F. Ferlaino, Science **345**, 1484 (2014).

[22] S. Ospelkaus, C. Ospelkaus, O. Wille, M. Succo, P. Ernst, K. Sengstock, and K. Bongs, Phys. Rev. Lett. **96**, 180403 (2006).

[23] S. Will, T. Best, S. Braun, U. Schneider, and I. Bloch, Phys. Rev. Lett. **106**, 115305 (2011).

[24] J. Heinze, S. Götze, J. S. Krauser, B. Hundt, N. Fläschner, D.-S. Lühmann, C. Becker, and K. Sengstock, Phys. Rev. Lett. **107**, 135303 (2011).

[25] N. Spethmann, F. Kindermann, S. John, C. Weber, D. Meschede, and A. Widera, Phys. Rev. Lett. **109**, 235301 (2012).

[26] N. B. Jørgensen, L. Wacker, K. T. Skalmstang, M. M. Parish, J. Levinsen, R. S. Christensen, G. M. Bruun, and J. J. Arlt, Phys. Rev. Lett. **117**, 055302 (2016).

[27] M.-G. Hu, M. J. Van de Graaff, D. Kedar, J. P. Corson, E. A. Cornell, and D. S. Jin, Phys. Rev. Lett. **117**, 055301 (2016).

[28] T. Köhler, K. Góral, and P. S. Julienne, Rev. Mod. Phys. **78**, 1311 (2006).

[29] K.-K. Ni, S. Ospelkaus, M. H. G. de Miranda, A. Pe'er, B. Neyenhuis, J. J. Zirbel, S. Kotochigova, P. S. Julienne, D. S. Jin, and J. Ye, Science **322**, 231 (2008).
[30] T. Takekoshi, L. Reichsöllner, A. Schindewolf, J. M. Hutson, C. R. Le Sueur, O. Dulieu, F. Ferlaino, R. Grimm, and H.-C. Nägerl, Phys. Rev. Lett. **113**, 205301 (2014).
[31] P. K. Molony, P. D. Gregory, Z. Ji, B. Lu, M. P. Köppinger, C. R. Le Sueur, C. L. Blackley, J. M. Hutson, and S. L. Cornish, Phys. Rev. Lett. **113**, 255301 (2014).
[32] G. Gligorić, A. Maluckov, M. Stepić, L. Hadžievski, and B. A. Malomed, Phys. Rev. A **82**, 033624 (2010).
[33] R. M. Wilson, C. Ticknor, J. L. Bohn, and E. Timmermans, Phys. Rev. A **86**, 033606 (2012).
[34] R. K. Kumar, P. Muruganandam, L. Tomio, and A. Gammal, J. Phys. Commun. **1**, 035012 (2017).
[35] R. K. Kumar, L. Tomio, B. A. Malomed, and A. Gammal, Phys. Rev. A **96**, 063624 (2017).
[36] B. Kain and H. Y. Ling, Phys. Rev. A **89**, 023612 (2014).
[37] L. A. P. Ardila and T. Pohl, J. Phys. B **52**, 015004 (2018).
[38] M. Wenzel, T. Pfau, and I. Ferrier-Barbut, Phys. Scripta **93**, 104004 (2018).
[39] A. Trautmann, P. Ilzhöfer, G. Durastante, C. Politi, M. Sohmen, M. J. Mark, and F. Ferlaino, Phys. Rev. Lett. **121**, 213601 (2018).
[40] C. A. Stan, M. W. Zwierlein, C. H. Schunck, S. M. F. Raupach, and W. Ketterle, Phys. Rev. Lett. **93**, 143001 (2004).
[41] S. Inouye, J. Goldwin, M. L. Olsen, C. Ticknor, J. L. Bohn, and D. S. Jin, Phys. Rev. Lett. **93**, 183201 (2004).
[42] S. Kotochigova and A. Petrov, Phys. Chem. Chem. Phys. **13**, 19165 (2011).
[43] A. Frisch, M. Mark, K. Aikawa, F. Ferlaino, J. L. Bohn, C. Makrides, A. Petrov, and S. Kotochigova, Nature (London) **507**, 475 (2014).
[44] K. Baumann, N. Q. Burdick, M. Lu, and B. L. Lev, Phys. Rev. A **89**, 020701(R) (2014).
[45] T. Maier, H. Kadau, M. Schmitt, M. Wenzel, I. Ferrier-Barbut, T. Pfau, A. Frisch, S. Baier, K. Aikawa, L. Chomaz, M. J. Mark, F. Ferlaino, C. Makrides, E. Tiesinga, A. Petrov, and S. Kotochigova, Phys. Rev. X **5**, 041029 (2015).
[46] V. A. Khlebnikov, D. A. Pershin, V. V. Tsyganok, E. T. Davletov, I. S. Cojocaru, E. S. Fedorova, A. A. Buchachenko, and A. V. Akimov, Phys. Rev. Lett. **123**, 213402 (2019).
[47] M. D. Frye, S. L. Cornish, and J. M. Hutson, arXiv:1910.09641 (2019).
[48] P. Ilzhöfer, G. Durastante, A. Patscheider, A. Trautmann, M. J. Mark, and F. Ferlaino, Phys. Rev. A **97**, 023633 (2018).
[49] M. Anderlini, D. Ciampini, D. Cossart, E. Courtade, M. Cristiani, C. Sias, O. Morsch, and E. Arimondo, Phys. Rev. A **72**, 033408 (2005).
[50] A. Guttridge, S. A. Hopkins, S. L. Kemp, M. D. Frye, J. M. Hutson, and S. L. Cornish, Phys. Rev. A **96**, 012704 (2017).
[51] C. Ravensbergen, V. Corre, E. Soave, M. Kreyer, E. Kirilov, and R. Grimm, Phys. Rev. A **98**, 063624 (2018).
[52] J. L. Bohn and D. S. Jin, Phys. Rev. A **89**, 022702 (2014).
[53] Along the vertical direction z we observe center-of-mass motion caused by the momentum transfer of the resonant light pulse.
[54] B. S. Rem, A. T. Grier, I. Ferrier-Barbut, U. Eismann, T. Langen, N. Navon, L. Khaykovich, F. Werner, D. S. Petrov, F. Chevy, and C. Salomon, Phys. Rev. Lett. **110**, 163202 (2013).
[55] T. Maier, I. Ferrier-Barbut, H. Kadau, M. Schmitt, M. Wenzel, C. Wink, T. Pfau, K. Jachymski, and P. S. Julienne, Phys. Rev. A **92**, 060702(R) (2015).
[56] U. Eismann, L. Khaykovich, S. Laurent, I. Ferrier-Barbut, B. S. Rem, A. T. Grier, M. Delehaye, F. Chevy, C. Salomon, L.-C. Ha, and C. Chin, Phys. Rev. X **6**, 021025 (2016).
[57] K. Helfrich, H.-W. Hammer, and D. S. Petrov, Phys. Rev. A **81**, 042715 (2010).
[58] J. P. D'Incao, J. Phys. B **51**, 043001 (2018).
[59] A. Frisch, M. Mark, K. Aikawa, S. Baier, R. Grimm, A. Petrov, S. Kotochigova, G. Quéméner, M. Lepers, O. Dulieu, and F. Ferlaino, Phys. Rev. Lett. **115**, 203201 (2015).
[60] J. Hutson and M. Frye (Private communication).
[61] A. V. Avdeenkov, D. C. E. Bortolotti, and J. L. Bohn, Phys. Rev. A **69**, 012710 (2004).
[62] T. Karman, M. D. Frye, J. D. Reddel, and J. M. Hutson, Phys. Rev. A **98**, 062502 (2018).
[63] B. Deh, C. Marzok, C. Zimmermann, and P. W. Courteille, Phys. Rev. A **77**, 010701(R) (2008).

A.4 Publication:

Phase coherence in out-of-equilibrium supersolid states of ultracold dipolar atoms

The following publication has appeared in

Nature Physics **17**, 356–361 (2021)[§]
submitted 21 Dec 2019; published 4 Jan 2021
DOI: https://doi.org/10.1038/s41567-020-01100-3
P. Ilzhöfer,[1,2] M. Sohmen,[1,2] G. Durastante,[1,2] C. Politi,[1,2] A. Trautmann,[1] G. Natale,[2] G. Morpurgo,[3] T. Giamarchi,[3] L. Chomaz,[2] M. J. Mark,[1,2] and F. Ferlaino[1,2]

[1] *Institut für Quantenoptik und Quanteninformation, Österreichische Akademie der Wissenschaften, 6020 Innsbruck, Austria*

[2] *Institut für Experimentalphysik, Universität Innsbruck, 6020 Innsbruck, Austria*

[3] *DQMP, University of Geneva, Geneva, Switzerland*

[4] *These authors contributed equally: P. I. and M. S.*

[§]The author of the present thesis analysed the experimental data with M. S., and M. J. M., and contributed in writing the manuscript and interpreting the results together with all the authors.

ARTICLES
https://doi.org/10.1038/s41567-020-01100-3
nature physics

Phase coherence in out-of-equilibrium supersolid states of ultracold dipolar atoms

P. Ilzhöfer[1,4], M. Sohmen[1,2,4], G. Durastante[1,2], C. Politi[1], A. Trautmann[1], G. Natale[2], G. Morpurgo[3], T. Giamarchi[3], L. Chomaz[2], M. J. Mark[1,2] and F. Ferlaino[1,2]✉

A supersolid is a counterintuitive phase of matter that combines the global phase coherence of a superfluid with a crystal-like self-modulation in space. Recently, such states have been experimentally realized using dipolar quantum gases. Here we investigate the response of a dipolar supersolid to an interaction quench that shatters the global phase coherence. We identify a parameter regime in which this out-of-equilibrium state rephases, indicating superfluid flow across the sample as well as an efficient dissipation mechanism. We find a crossover to a regime where the tendency to rephase gradually decreases until the system relaxes into an incoherent droplet array. Although a dipolar supersolid is, by its nature, 'soft', we capture the essential behaviour of the de- and rephasing process within a rigid Josephson junction array model. Yet, both experiment and simulation indicate that the interaction quench causes substantial collective mode excitations that connect to phonons in solids and affect the phase dynamics.

The notion of phase coherence lies at the foundation of quantum physics. It is considered a key property in understanding many-body quantum phenomena, ranging from superfluidity and the Josephson effect to the more applied examples of matterwave interference, atom lasing processes and quantum transport in meso- and macroscopic systems[1,2]. Although phase-coherent states are well studied at equilibrium, understanding their out-of-equilibrium dynamics remains an open problem at the forefront of statistical and quantum physics, especially when interactions are present[3].

Rephasing dynamics of an initially incoherent many-body quantum system requires, first, the system to be conducting such that different parts can exchange energy and particles, and second, an efficient mechanism to dissipate the phase excitations. As for the first requirement, a famous example illustrating the inhibition of thermalization is many-body localization[4]. The second ingredient—dissipation—is more subtle and multifaceted, relating, for instance, to the growth of thermal correlations in isolated systems[5], complex interaction-mediated dynamics[6,7] or the exponential growth of unstable modes and topological defects in connection with the Kibble–Zurek mechanism[8–10].

The interplay among coherence, self-localization and relaxation dynamics is an intriguing problem. In this respect, the recently discovered[11–13] supersolid states in dipolar quantum gases can potentially provide a new twist in studying non-equilibrium quantum phenomena, about which very little is known so far. A supersolid combines phase coherence and periodic localization in space, properties corresponding to the spontaneous and simultaneous breaking of both gauge and translational symmetry. Intuitively, a supersolid can be viewed as a fully coherent state, which self-establishes compressible density modulation. In this Article, we explore the evolution of a supersolid of ultracold dysprosium (Dy) atoms when brought out of equilibrium after an interaction quench that destroys its global phase coherence. Due to the dynamic formation of the supersolid, an interesting question is whether its phase dynamics are similar to or different from comparable rigid structures, such as a Bose–Einstein condensate (BEC) spliced in an optical lattice[14–16], or if new phenomena can manifest.

In a dipolar supersolid, the particle self-arrangement in space is largely dictated by the many-body interactions[17–22] and can be modified by either tuning the interatomic potentials or changing the atom number (N) in the system. Figure 1a shows the phase diagram of a cigar-shaped quantum gas of bosonic Dy atoms with transverse dipole orientation. It is constructed from the ground-state wavefunctions obtained by numerically solving the extended Gross–Pitaevskii equation (eGPE)[11,13,21] (Methods). Three distinct quantum phases can be accessed by changing N or the s-wave scattering length a_s, which parametrizes the contact interaction. For a given N and large enough a_s, the ground state of the system is a non-modulated dipolar BEC (grey region). By lowering a_s, the influence of the dipolar interaction increases. When reaching a critical value of a_s, the system undergoes a phase transition to a supersolid phase (SSP). Here density modulation at a wavelength close to the roton excitation[23,24] appears in the ground-state density profile (red region). By further lowering a_s, the system evolves into an array of insulating droplets (IDs) with an exponentially vanishing density link between them (blue region).

Our eGPE calculations, following a standard non-stochastic approach, are inherently phase coherent and thus cannot capture uncorrelated local phases. However, recent experiments have shown a connection between the strength of the density modulation and the coherence properties of the system, revealing a clear difference between the SSP and ID phase[11–13,25]. In the SSP, the whole system shares a global phase. In contrast, in the ID case, any fluctuation or excitation can lead to a locally different evolution of the phase. The absence of particle tunnelling between the droplets leads to dephasing of the system.

By performing interaction quenches and moving across the phase diagram, one can create random phase excitations ('phase scrambling') and thus distinguish between the different coherence characters of the ID and SSP, as shown in Fig. 1b. Our experimental

[1]Institut für Quantenoptik und Quanteninformation, Österreichische Akademie der Wissenschaften, Innsbruck, Austria. [2]Institut für Experimentalphysik und Zentrum für Quantenoptik, Universität Innsbruck, Innsbruck, Austria. [3]DQMP, University of Geneva, Geneva, Switzerland. [4]These authors contributed equally: P. Ilzhöfer, M. Sohmen. ✉e-mail: Francesca.Ferlaino@uibk.ac.at

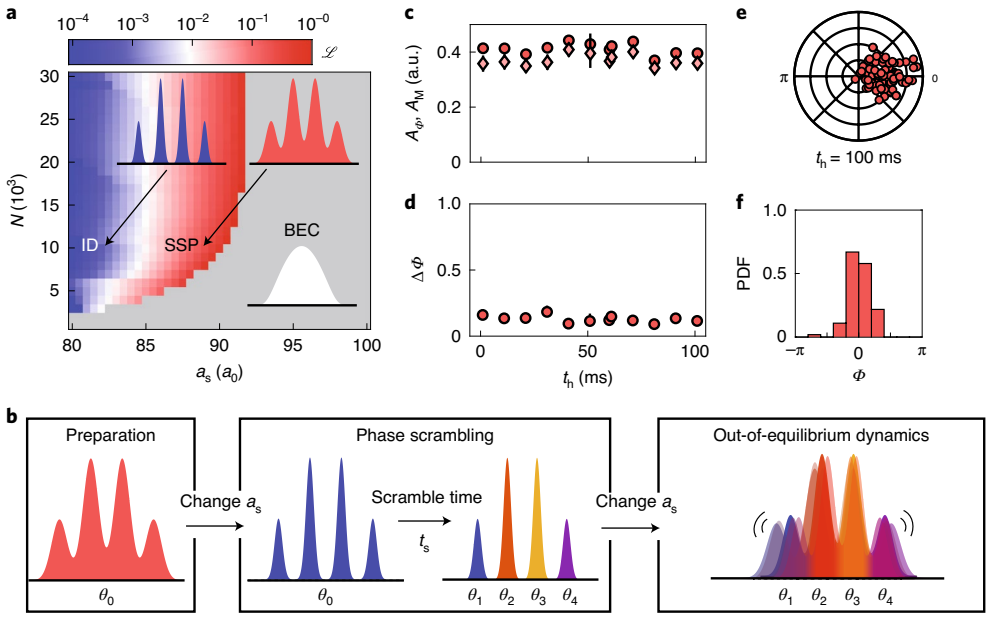

Fig. 1 | Phase diagram, experimental sequence and starting condition. a, Ground-state phase diagram for our cigar-shaped trapped ^{164}Dy gas. The colour map encodes the density modulation via the link strength $\mathscr{L} = 1 - (n_{max} - n_{min})/(n_{max} + n_{min})$, where n_{max} (n_{min}) is the density maximum (minimum) in the central region of the calculated in situ density distribution. $\mathscr{L}$ equals unity for a non-modulated state and zero for a fully modulated state. The grey colour indicates a non-modulated BEC, whereas the red and blue regions correspond to the SSP and ID phase, respectively. The insets show the density profiles along the weak axis for the different phases. **b**, Illustration of the phase-scrambling sequence: starting from an SSP (left) prepared at 2.43 G ($a_s = 87.9a_0$), we reduce a_s to enter the ID regime (middle). During t_S the phases of the droplets evolve independently, leading to phase scrambling between the droplets. Eventually, we jump a_s back into the supersolid regime (right), where the time evolution of the global phase coherence is studied. **c**,**d**, Amplitudes A_M and A_Φ (**c**) and $\Delta\Phi$ (**d**) for our initial SSP (left panel in **b**) when simply held for time t_h. Each data point is derived from $q \in [80, 90]$ individual experimental realizations. The error bars (partly covered by plot symbols) are the 1σ confidence intervals from BCA bootstrapping (Methods)[39]. **e**,**f**, Polar scatter plot for P_i (**e**) and histogram of the probability density function (PDF) (**f**) for Φ_i at $t_h = 100$ ms.

protocol starts by preparing a supersolid state by evaporative cooling from a thermal sample (Fig. 1b, left) (ref. [13]). We then decrease a_s to enter into the ID regime (Fig. 1b, middle). Here the system ground state is an array of IDs, each with a phase that is expected to evolve independently in time. After these phases have become fully uncorrelated, we jump a_s back to its initial value (Fig. 1b, right). We then study the time evolution of the out-of-equilibrium system. We measure phase coherence and density modulation, whose coexistence is a hallmark of supersolidity, using a matterwave interference technique (Methods and refs. [11,13,26–29]). In brief, for each experimental realization i, we take an absorption image after a time-of-flight (TOF) expansion. The recorded image exhibits an interference pattern if in-trap density modulation is present. Via Fourier transform, we extract the phasor $P_i = \rho_i e^{-i\Phi_i}$ with amplitude ρ_i and phase Φ_i at the spatial frequency of the interference pattern (cf. Extended Data Fig. 1a). Averaging over an ensemble of q realizations, the mean of the phasor amplitudes, $A_M = \langle |P_i| \rangle$, characterizes the degree of density modulation, whereas the amplitude of the complex mean, $A_\Phi = |\langle P_i \rangle|$, contains information about the global phase coherence. As an additional measure of coherence, we calculate the circular variance of the phase $\Delta\Phi = 1 - \frac{1}{q}\sqrt{\left(\sum_{i=1}^{q}\cos(\Phi_i)\right)^2 + \left(\sum_{i=1}^{q}\sin(\Phi_i)\right)^2}$ (ref. [30]). For a perfect supersolid (resp. ID) state and in the limit $q \to \infty$, one expects $A_\Phi = A_M > 0$ (respectively $A_\Phi = 0$, $A_M > 0$) and $\Delta\Phi = 0$ (respectively $\Delta\Phi = 1$). In the following, we describe and characterize each step of our phase-scramble-and-rephase protocol (Fig. 1b).

We initially prepare the supersolid state (Fig. 1b, left) of ^{164}Dy atoms[13] ($N = 1.4 \times 10^4$) in an axially elongated optical dipole trap (ODT) with the final harmonic frequencies $\omega_{x,y,z} = 2\pi \times (225, 37, 165)\,s^{-1}$. From our interferometric analysis, we see that this initial state is long lived and has a high degree of phase coherence (Fig. 1c–f). The characteristic quantities of A_Φ and A_M (Fig. 1c) and $\Delta\Phi$ (Fig. 1d) are constant over hold times t_h up to 100 ms. The small mean value $\langle \Delta\Phi \rangle = 0.142(8)$ (the value in parentheses gives the standard error of the last digit) over the entire range of t_h reveals a constantly narrow spread in the phase distribution, as shown for $t_h = 100$ ms in the polar plot (Fig. 1e) of the phasors P_i and the corresponding histogram (Fig. 1f) for Φ_i.

In the next step of our protocol (Fig. 1b, middle), namely, the phase-scrambling excitation, we tune a_s via magnetic Feshbach resonances by varying the external magnetic field B (Methods and Extended Data Fig. 2). From the initial supersolid state (~$87.9a_0$, where a_0 denotes the Bohr radius), we transfer the system into the ID regime (~$76.9a_0$) using a 20 ms linear B-field ramp. Here the atoms are expected to spatially arrange in an array of almost isolated droplets with exponentially small particle tunnelling between them. We then let the system evolve for a variable scrambling time t_S.

Figure 2 shows the evolution of $\Delta\Phi$, A_Φ and A_M with t_S. After completion of the B-field ramp, $\Delta\Phi$ initially keeps rapidly increasing for 20 ms and then slowly saturates to a large $\Delta\Phi$ value. Here the droplets develop uncorrelated phases, as illustrated by the polar plot of P_i at $t_S = 100$ ms (Fig. 2a, inset). We extract a saturation value of $\langle \Delta\Phi \rangle_{sat} = 0.92(1)$ (simple mean for $t_S > 50$ ms). We highlight that $\Delta\Phi$ is not expected to reach unity because of the finite sample size in the experiment ($q \in [90, 100]$ repetitions; slight variations are due to a post-selection by atom number). It is evident that the measured $\langle \Delta\Phi \rangle_{sat}$ agrees with the expectation for a sample with the same q and uniformly random phases (grey shading in Fig. 2a, Extended Data Fig. 1b and Methods). As $\Delta\Phi$ increases and the global phase coherence is lost, A_Φ decreases quickly towards zero (Fig. 2b), whereas the density modulation persists as evidenced by A_M remaining large.

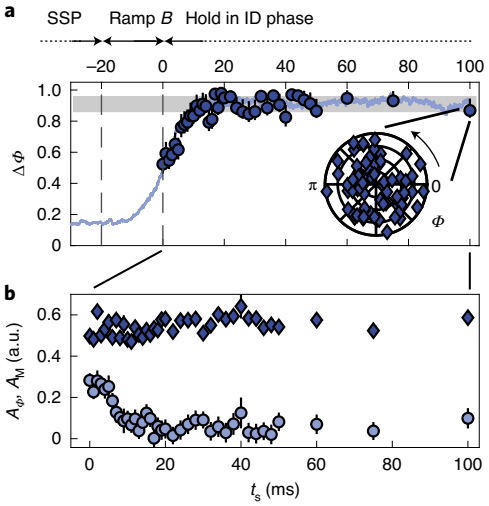

Fig. 2 | Phase scrambling. a, $\Delta\Phi$ as a function of t_S when ramping from the SSP to the ID phase (at 1.65 G; $a_s = 76.9a_0$) within 20 ms (similar results are obtained with a fast quench of ~1 ms). Each point is derived from $q \in [90, 100]$ experimental realizations. The error bars are the 1σ confidence intervals from BCA bootstrapping (Methods)[39]. The grey-shaded area indicates the theoretically expected 1σ confidence interval for $\Delta\Phi$ with same q and uniformly random phases. The inset shows the polar scatter plot of the phasors P_i at $t_S = 100$ ms. The light-blue line shows $\Delta\Phi$ for dephasing in a four-grain JJA model using $q = 100$ and averaging over four simulation runs (main text and Methods). For the simulation, J is ramped from 6,000 to 0.002 Hz in 20 ms and $\eta = 60$. **b**, The corresponding A_Φ (light-blue circles) and A_M (dark-blue diamonds).

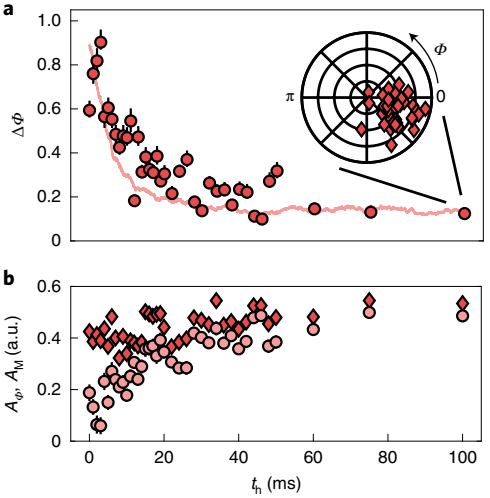

Fig. 3 | Rephasing. a, $\Delta\Phi$ as a function of t_h after $t_S = 20$ ms scrambling in the ID phase and a jump back to the SSP regime at 2.43 G ($a_s = 87.9a_0$). For each point, $q \in [66, 74]$. The error bars are the 1σ confidence intervals from BCA bootstrapping. The inset shows the polar scatter plot of the phasors P_i at $t_h = 100$ ms. The light-red line shows $\Delta\Phi$ for rephasing in a four-grain JJA model using $q = 100$ and averaging over four simulation runs (main text and Methods). For the simulation, we start with a random configuration of grain phases and let the system rephase with $J = 6{,}000$ Hz and $\eta = 60$. **b**, The corresponding A_Φ (light-red circles) and A_M (dark-red diamonds).

The interaction quench into the ID phase is a robust method to create phase-scrambling excitations. It is natural to ask how the relative phases between the individual droplets evolve once the density links between them are restored and whether the system relaxes into an equilibrium supersolid state. To address this question, we perform the last stage of our protocol (Fig. 1b, right). After a scrambling time of $t_S = 20$ ms, we couple the droplets back together by jumping the B field and thus quenching a_s to $87.9a_0$, where the system ground state is a supersolid. However, after the quench, our state is out of equilibrium in terms of both phase and density distribution: since the density-modulated states in dipolar gases are self-assembled, they can deform after a sudden change in the many-body interactions[31–33]. As shown in Fig. 3a, we first observe a rapid reduction in $\Delta\Phi$ and then slower dynamics towards an equilibrium value with $\Delta\Phi$ reaching $\langle\Delta\Phi\rangle_{sat} = 0.13(2)$ (simple mean for $t_h > 50$ ms). Simultaneously, A_Φ approaches A_M on the same timescale, whereas A_M remains nearly constant. These observations show that the system efficiently rephases by dissipating the phase excitation.

Our system of multiple superfluid droplets with individual phases, interconnected via weak links, is reminiscent of a Josephson junction array (JJA)[34]. Motivated by this analogy, we investigate whether a simple JJA model can adequately describe the observed phase dynamics. This is a non-trivial question, since in contrast to a rigid JJA, our droplet array is 'soft' in the sense that the droplet shapes and their distances change with a_s. We construct our model from a one-dimensional (1D) array of four coupled grains. For each grain, the number of particles is N_j and phase is θ_j. The Hamiltonian of this system is

$$H = \sum_{j=1}^{4} \frac{(N_j - \overline{N_j})^2}{2C_j} - \sum_{j=1}^{3} J_j \cos(\theta_{j+1} - \theta_j), \qquad (1)$$

where the overline denotes an ensemble average. The first term is the 'charging' energy of the droplet (corresponding to its mean interaction energy) with the capacitance C_j. The second term describes the tunnelling of particles between the droplets with the Josephson amplitude J_j. The JJA model is appropriate if the droplets are reasonably well separated in space. For simplicity, we assume that C_j and J_j are identical for all the droplets and later denote them as C and J. Note that this Hamiltonian describes a quantum evolution since N_j and θ_j are connected via canonical commutation relations.

We describe the time evolution of the system via a Langevin formalism[35,36]. The phase of the droplet j follows

$$\eta \frac{d\theta_j}{dt} = J[\sin(\theta_{j+1} - \theta_j) - \sin(\theta_j - \theta_{j-1})] + \xi_j(T, \eta, t), \qquad (2)$$

where the friction parameter η is a phenomenological way to account for dissipative mechanisms. The temperature T is introduced via the thermal noise $\xi_j(t)$, which shows Gaussian uncorrelated fluctuations at times t and t' given by $\overline{\xi_j(t)\xi_i(t')} = 2\eta k_B T \delta_{ij} \delta(t - t')$, where δ_{ij} is the Kronecker delta and $\delta(.)$ denotes the Dirac distribution. The thermal energy scale $k_B T$ (for $T = 150$ nK in the experiment and the Boltzmann constant k_B) is much higher than the estimated capacitance effect, allowing to neglect the second-order time derivative term related to C in the evolution of equation (2) (Methods).

This JJA model provides an intuitive understanding of the dephasing and rephasing dynamics shown in Figs. 2 and 3, respectively. It encapsulates the essential physics of a rigid droplet situation at a finite temperature T in terms of the two phenomenological parameters J and η. The timescale of de- and rephasing is dictated by the dissipation η. The dissipation mechanisms include atom losses (cf. Extended Data Fig. 3), energy and particle exchange with the thermal component of the gas or with some internal degrees of freedom of the droplets, as discussed later. In contrast, the phase fluctuations in the equilibrium state, namely, the stationary value of $\Delta\Phi$, are set by the competition between J and T and are independent of η.

We develop a parameter-free theory–experiment comparison for the rephasing dynamics by first fixing the value of J and η from

independent measurements. Taking advantage of the fact that η and J play different roles at different stages of the protocol, we fix J by reproducing the $\Delta\Phi$ measured at the end of evaporation (Fig. 1d). The parameter η is instead extracted from the dephasing dynamics of $\Delta\Phi$ during t_s (Fig. 2 and Methods). We find that $J = 6{,}000$ Hz and $\eta = 60 \pm 10$.

With all the values of the parameters fixed, we now compare the rephasing dynamics from the JJA theory and the experiment. As shown in Fig. 3, we observe that despite its simplicity, the model qualitatively predicts the rephasing curve well. In particular, the plateau value at large t_h as well as the time to reach the plateau are consistent with the experiment. In addition, we note that in the early time evolution ($t_h < 30$ ms), the experimental data is systematically slightly above the JJA curve, namely, the system seems to rephase slower than predicted by the model. This indicates that other phenomena beyond our rigid JJA model are important to fully capture the out-of-equilibrium physics.

To elucidate why the observed experimental rephasing is slower than expected from the JJA model, we simulate the system's real-time evolution (RTE)[24] in the simplified zero-temperature and zero-atom-loss case, with a quench sequence mimicking the experiment. Different from the phenomenological JJA model, the ab initio RTE approach can additionally account for the 'soft' nature of the supersolid, namely, the crystal and phase phonons[31–33]. As shown in Fig. 4a, the RTE simulation shows that the collective modes are initially excited by the interaction quench. The positions and heights of the high-density peaks evolve in time, especially during the initial tens of milliseconds, resulting in time-dependent density links. At longer times, we observe a damping of the collective motion, which can be attributed to an initial redistribution of the population from a few modes to many higher-lying modes over time. This suggests a possible dissipation mechanism of the phase excitations for our experiment. Even though the finite temperature, atom loss and presence of a normal component affect the precise dynamics and damping in the experiment, the RTE calculation strongly indicates that the droplet dynamics play an important role at early times. This is compatible with the observed deviations from the rigid JJA model.

In the experiments, we do not have direct access to the in-trap density evolution. However, by repeating our experiment in a tighter trap, which gives more distinct side peaks in the TOF interference patterns, we observe the indications of collective mode excitations. In Fig. 4b, we plot the time evolution of $\Delta\Phi$ following the rephasing protocol. Here, on top of a global decrease in $\Delta\Phi$, a low-amplitude oscillating behaviour is evident, as highlighted by plotting the residuals of an exponential fit to the data. We extract an oscillation frequency of 50(5) Hz (cf. Extended Data Fig. 4 and Methods).

By comparing the predictions of the JJA and RTE approach to our experimental data, we conclude that the phase dynamics is largely described by a dissipative and 'rigid' JJA picture. We speculate that the phase excitations primarily dissipate via coupling to excited modes[37]. Moreover, the droplet dynamics seems to play an important role, affecting the rephasing efficiency. Note that one could modify the JJA model to take the droplet dynamics into account, at least to a certain degree (Methods). Such coupling between the two types of degree of freedom usually leads to additional dissipation channels[38]. Besides being of intrinsic theoretical interest, this could, for example, open the perspective to using supersolids to study similar dynamics in regular solids between electronic and phononic degrees of freedom. This, however, goes beyond the scope of the present work and will be addressed in future studies.

In a final set of experiments, we investigate the role of the density-link strength between the droplets, namely, the Josephson coupling, in the rephasing dynamics. After phase scrambling (Fig. 1b, middle), we quench a_s to different values and record $\Delta\Phi$ as a function of the hold time t_h (Extended Data Fig. 5a). For each a_s, we quantify the strength of the density link via $\mathscr{L}$, which was

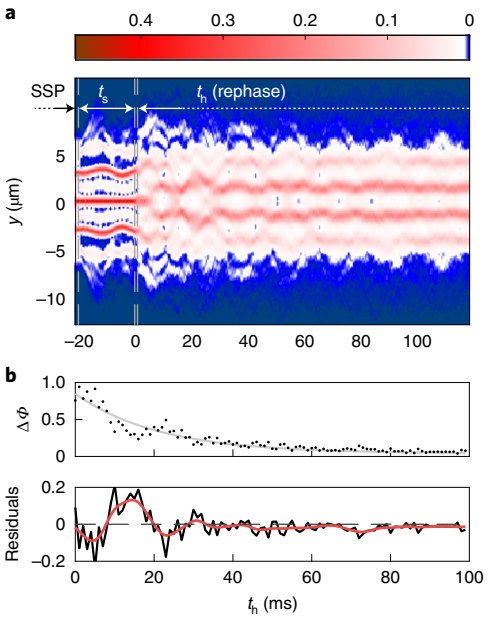

Fig. 4 | Out-of-equilibrium dynamics. a, RTE simulation starting from a zero-temperature cloud of 2×10^4 atoms of ^{164}Dy and performing a scramble-and-rephase sequence. We plot the 1D integrated density profile (colour code) along the weak trap axis as a function of time. Starting from the SSP, the scattering length is linearly ramped at 1 ms to the ID phase (first dashed line), held there for $t_s = 20$ ms (second dashed line), ramped back to the SSP in 1 ms (third dashed line) and then simply held for t_h. The trap frequencies are $\omega_{x,y,z} = 2\pi \times (229, 37, 135)\ \mathrm{s}^{-1}$. **b**, Experimental rephasing data for the same trap. The upper panel shows $\Delta\Phi$ calculated analogously to that shown in Fig. 3 (black dots), as well as an exponential fit (grey line). The lower panel shows the residuals of the fit before (black line) and after (red line) the application of a numerical low-pass filter.

determined from a ground-state calculation (Fig. 1a). We study the short- and long-time evolution of $\Delta\Phi$ by the determination of the initial rephasing rate $|R|$ (the slope of a linear fit to $\Delta\Phi$ for $t_h \leq 20$ ms) and the saturation value $\langle\Delta\Phi\rangle_{sat}$ (simple mean of $\Delta\Phi$ for $t_h > 50$ ms), respectively, as shown in Fig. 5a,b (for A_M and A_Φ see Extended Data Fig. 5b).

We observe different rephasing dynamics depending on $\mathscr{L}$. For extremely weak density links ($\mathscr{L} < 10^{-3}$), which we associate with the ID regime, the system is unable to rephase and it remains incoherent over the whole time evolution as indicated by a low $|R|$ and large $\langle\Delta\Phi\rangle_{sat} \approx 0.9$. As $\mathscr{L}$ slightly increases, the system shows a partial rephasing with $\langle\Delta\Phi\rangle_{sat}$ decreasing to about 0.5. By further increasing the density-link strength, there exists a critical value of $\mathscr{L}$ above which the system recovers its full phase coherence after a long time ($\langle\Delta\Phi\rangle_{sat} = 0.15$). In this regime, $|R| \approx 30\ \mathrm{s}^{-1}$ is large and seems relatively independent of $\mathscr{L}$.

To compare the JJA predictions with our experimental observations, we first extract J for each a_s. For this purpose, we look at the long-time behaviour after scrambling and rephasing when the system has equilibrated, matching the theoretical and experimental $\langle\Delta\Phi\rangle_{sat}$ values. This is justified by the long-time agreement observed in Fig. 3. As expected from the increasing density-link strength $\mathscr{L}$ between the droplets, J globally grows with a_s (Fig. 5a, inset). Using these J values and the single calibrated value of $\eta = 60$ (Fig. 2), we extract the rephasing rate $|R|_{JJA}$ from the short-time evolution of $\Delta\Phi$ within our JJA framework (Fig. 5b, inset). Despite the simplicity of the JJA approach, the $|R|_{JJA}$ values are of the same order of magnitude as our experimental data and show the same qualitative behaviour with respect to a_s. As observed in Fig. 3, $|R|_{JJA}$

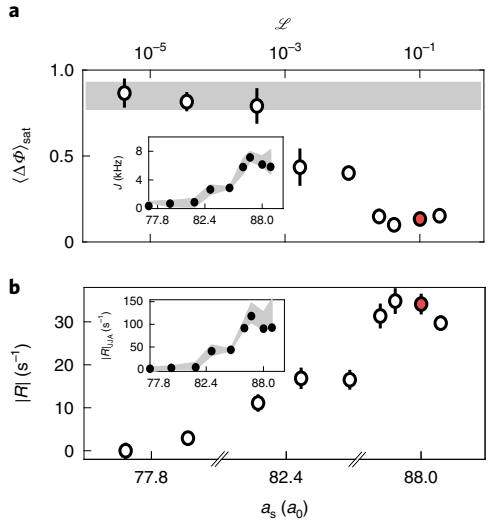

Fig. 5 | Density-link dependence of rephasing dynamics. a, Saturation value of the phase variance $\langle \Delta\Phi \rangle_{sat}$ as a function of the scattering length a_s and the corresponding $\mathscr{L}$. We calculate $\langle \Delta\Phi \rangle_{sat}$ and the error bars as the mean and standard deviation of $\Delta\Phi$ over the three longest hold times (Fig. 3 and Extended Data Fig. 5). The grey-shaded rectangle indicates the theoretical 1σ confidence interval for uniformly random phases. The inset shows the J values for which the JJA simulations yield a $\langle \Delta\Phi \rangle_{sat}$ matching the experimental value at a_s, and the grey shading represents its confidence interval. **b**, Initial rephasing rates $|R|$ for the different a_s values as extracted from the experimental data by using a linear fit. The error bars are the 1σ confidence intervals of the fitted slopes. The inset shows the theoretical $|R|_{JJA}$ (a_s) expected from a linear fit to the initial decrease in the JJA rephasing curves (theory line in Fig. 3); the grey shading represents the confidence interval. The red filled points correspond to the dataset shown in Fig. 3.

generally predicts rephasing faster than that measured in the experiment, suggesting the presence of non-negligible processes beyond the rigid JJA model.

It is interesting that despite the JJA being able to consistently model the phase dynamics in the experiment, the extracted dependence of J on a_s is mild in comparison to the expected ground-state density link $\mathscr{L}$ (Fig. 5a). For instance, J changes only by a factor of two whereas $\mathscr{L}$ changes by two orders of magnitude. Further, J seems to effectively saturate for increasing strength of the ground-state density link $\mathscr{L}$, which is in agreement with the observed plateaus of both $\langle \Delta\Phi \rangle_{sat}$ and $|R|$ for large a_s. Possible explanations include the breakdown of the JJA model for a low-contrast supersolid, the impact of finite temperature on both the equilibrium supersolid state itself and the experimental measurement, or the role of collective dynamics.

In conclusion, we have performed a study of the out-of-equilibrium dynamics of a dipolar supersolid after an interaction-driven phase excitation that fully destroys its phase coherence. We have demonstrated that if the inter-droplet density links are sufficient, this phase-scrambled system relaxes into an equilibrium phase-coherent state. With decreasing link strength, the rephasing substantially slows down and eventually ceases in the ID regime. We find an overall consistency between the phase dynamics observed in the experiment and an intuitive, theoretically easily tractable rigid JJA model. However, both ab initio simulations and experimental observations indicate post-quench collective excitations of the droplet array, which can affect the phase dynamics. Our study shows the evidence of particle flow across a dipolar supersolid, connecting to its superfluidity. It also suggests the efficient dissipation of phase excitations, whose microscopic mechanism is still under question. Future experimental works, combined with advanced out-of-equilibrium theoretical models, will be crucial to understand the relaxation dynamics at play in isolated and open supersolid states of quantum matter.

Online content

Any methods, additional references, Nature Research reporting summaries, source data, extended data, supplementary information, acknowledgements, peer review information; details of author contributions and competing interests; and statements of data and code availability are available at https://doi.org/10.1038/s41567-020-01100-3.

Received: 21 December 2019; Accepted: 22 October 2020;
Published online: 4 January 2021

References

1. Cohen-Tannoudji, C. & Guéry-Odelin, D. *Advances in Atomic Physics: An Overview* (World Scientific, 2011).
2. Svistunov, B. V. et al. *Superfluid States of Matter* (CRC Press, 2015).
3. Eisert, J., Friesdorf, M. & Gogolin, C. Quantum many-body systems out of equilibrium. *Nat. Phys.* **11**, 124–130 (2015).
4. Abanin, D. A., Altman, E., Bloch, I. & Serbyn, M. Colloquium: many-body localization, thermalization, and entanglement. *Rev. Mod. Phys.* **91**, 021001 (2019).
5. Langen, T., Geiger, R., Kuhnert, M., Rauer, B. & Schmiedmayer, J. Local emergence of thermal correlations in an isolated quantum many-body system. *Nat. Phys.* **9**, 640–643 (2013).
6. Wright, E. M., Walls, D. F. & Garrison, J. C. Collapses and revivals of Bose–Einstein condensates formed in small atomic samples. *Phys. Rev. Lett.* **77**, 2158–2161 (1996).
7. Greiner, M., Mandel, O., Hänsch, T. W. & Bloch, I. Collapse and revival of the matter wave field of a Bose–Einstein condensate. *Nature* **419**, 51–54 (2002).
8. Scherer, D. R., Weiler, C. N., Neely, T. W. & Anderson, B. P. Vortex formation by merging of multiple trapped Bose–Einstein condensates. *Phys. Rev. Lett.* **98**, 110402 (2007).
9. del Campo, A. & Zurek, W. H. Universality of phase transition dynamics: topological defects from symmetry breaking. *Int. J. Mod. Phys. A* **29**, 1430018 (2014).
10. Aidelsburger, M. et al. Relaxation dynamics in the merging of N independent condensates. *Phys. Rev. Lett.* **119**, 190403 (2017).
11. Böttcher, F. et al. Transient supersolid properties in an array of dipolar quantum droplets. *Phys. Rev. X* **9**, 011051 (2019).
12. Tanzi, L. et al. Observation of a dipolar quantum gas with metastable supersolid properties. *Phys. Rev. Lett.* **122**, 130405 (2019).
13. Chomaz, L. et al. Long-lived and transient supersolid behaviors in dipolar quantum gases. *Phys. Rev. X* **9**, 021012 (2019).
14. Cataliotti, F. S. et al. Josephson junction arrays with Bose–Einstein condensates. *Science* **293**, 843–846 (2001).
15. Albiez, M. et al. Direct observation of tunneling and nonlinear self-trapping in a single bosonic Josephson junction. *Phys. Rev. Lett.* **95**, 010402 (2005).
16. Levy, S., Lahoud, E., Shomroni, I. & Steinhauer, J. The a.c. and d.c. Josephson effects in a Bose–Einstein condensate. *Nature* **449**, 579–583 (2007).
17. Lu, Z.-K., Li, Y., Petrov, D. S. & Shlyapnikov, G. V. Stable dilute supersolid of two-dimensional dipolar bosons. *Phys. Rev. Lett.* **115**, 075303 (2015).
18. Cinti, F. & Boninsegni, M. Classical and quantum filaments in the ground state of trapped dipolar Bose gases. *Phys. Rev. A* **96**, 013627 (2017).
19. Wenzel, M., Böttcher, F., Langen, T., Ferrier-Barbut, I. & Pfau, T. Striped states in a many-body system of tilted dipoles. *Phys. Rev. A* **96**, 053630 (2017).
20. Baillie, D. & Blakie, P. B. Droplet crystal ground states of a dipolar Bose gas. *Phys. Rev. Lett.* **121**, 195301 (2018).
21. Roccuzzo, S. M. & Ancilotto, F. Supersolid behavior of a dipolar Bose–Einstein condensate confined in a tube. *Phys. Rev. A* **99**, 041601 (2019).
22. Kora, Y. & Boninsegni, M. Patterned supersolids in dipolar Bose systems. *J. Low Temp. Phys.* **197**, 337–347 (2019).
23. Santos, L., Shlyapnikov, G. V. & Lewenstein, M. Roton-maxon spectrum and stability of trapped dipolar Bose–Einstein condensates. *Phys. Rev. Lett.* **90**, 250403 (2003).
24. Chomaz, L. et al. Observation of roton mode population in a dipolar quantum gas. *Nat. Phys.* **14**, 442–446 (2018).
25. Petter, D. et al. High-energy Bragg scattering measurements of a dipolar supersolid. Preprint at https://arxiv.org/abs/2005.02213 (2020).

26. Takeda, M., Ina, H. & Kobayashi, S. Fourier-transform method of fringe-pattern analysis for computer-based topography and interferometry. *J. Opt. Soc. Am.* **72**, 156–160 (1982).
27. Hadzibabic, Z., Stock, S., Battelier, B., Bretin, V. & Dalibard, J. Interference of an array of independent Bose–Einstein condensates. *Phys. Rev. Lett.* **93**, 180403 (2004).
28. Kohstall, C. et al. Observation of interference between two molecular Bose–Einstein condensates. *New J. Phys.* **13**, 065027 (2011).
29. Chomaz, L. et al. Emergence of coherence via transverse condensation in a uniform quasi-two-dimensional Bose gas. *Nat. Commun.* **6**, 6162 (2015).
30. Fisher, N. I. *Statistical Analysis Of Circular Data* (Cambridge Univ. Press, 1993).
31. Natale, G. et al. Excitation spectrum of a trapped dipolar supersolid and its experimental evidence. *Phys. Rev. Lett.* **123**, 050402 (2019).
32. Tanzi, L. et al. Supersolid symmetry breaking from compressional oscillations in a dipolar quantum gas. *Nature* **574**, 382–385 (2019).
33. Hertkorn, J. et al. Fate of the amplitude mode in a trapped dipolar supersolid. *Phys. Rev. Lett.* **123**, 193002 (2019).
34. Fazio, R. & van der Zant, H. Quantum phase transitions and vortex dynamics in superconducting networks. *Phys. Rep.* **355**, 235 (2001).
35. Risken, H. *The Fokker–Planck Equation* (Springer, 1961).
36. Ambegaokar, V. & Halperin, B. I. Voltage due to thermal noise in the dc Josephson effect. *Phys. Rev. Lett.* **22**, 1364–1366 (1969).
37. Dalla Torre, E. G., Demler, E. & Polkovnikov, A. Universal rephasing dynamics after a quantum quench via sudden coupling of two initially independent condensates. *Phys. Rev. Lett.* **110**, 090404 (2013).
38. Leggett, A. J. et al. Dynamics of the dissipative two-state system. *Rev. Mod. Phys.* **59**, 1–85 (1987).
39. Efron, B. Better bootstrap confidence intervals. *J. Am. Stat. Assoc.* **82**, 171–185 (1987).

Methods

Ground-state phase diagram and contrast. Our numerical calculations of the ground-state phase diagram of a cigar-shaped ^{164}Dy dipolar quantum gas follow the procedure described in our earlier works[13,24]. In brief, the calculations are based on minimizing the energy functional of the eGPE using the conjugate gradient technique[40]. The eGPE includes the anisotropic trapping potential, the short-range contact and long-range dipolar interactions at the mean-field level and the first-order beyond-mean-field correction in the form of a Lee–Huang–Yang term[41–43]. From the derived three-dimensional wavefunction $\psi(\mathbf{r})$ at positions $\mathbf{r}$, we calculate the 1D in situ density profile as $n(y) = \int|\psi(\mathbf{r})|^2 \mathrm{d}x\mathrm{d}z$. We evaluate the in situ density contrast as $C = (n_{\max} - n_{\min})/(n_{\max} + n_{\min})$ for profiles that feature density modulations by searching the central extrema of $n(y)$ and determining the maximum ($n_{\max}$) and minimum ($n_{\min}$) values. For profiles without density modulation (ordinary BEC), we set $C = 0$. We use the quantity $\mathscr{L} = 1 - C$ to estimate the density link between the droplets, which is related to the tunnelling strength[13].

RTE. We perform the RTE based on the eGPE and mimicking the experimental parameters and sequence. In particular, in Fig. 4a, we use the parameters of the experimental data shown in Fig. 4b, using a gas of ^{164}Dy atoms ($N = 2\times10^4$) in a trap of frequencies $\omega_{x,y,z} = 2\pi\times(229, 37, 135)\,\mathrm{s}^{-1}$. We start from the eGPE ground state $\psi(\mathbf{r})$ at $a_s = 92a_0$ and calculate the time evolution of the wavefunction $\psi(\mathbf{r},t)$ according to the eGPE using a split-operator technique[24]. For the scramble-and-rephase protocol, the scattering length is linearly ramped from the SSP ($a_s = 92a_0$) to the ID regime ($a_s = 80a_0$) in 1 ms, kept constant for $t_s = 20$ ms, ramped back to $a_s = 92a_0$ in 1 ms and finally held constant for a variable t_h. We compute the 1D integrated density profile $n(y,t) = \int|\psi(\mathbf{r},t)|^2 \mathrm{d}x\mathrm{d}z$, and its time evolution is shown in Fig. 4a. Similar to the work in refs. [12,25], we gain further insights into the rephasing process by extracting the global spatial variation α of the phase of the wavefunction along y defined as

$$\alpha(t) = \frac{\int_{Y^*} n(0,y,0,t)|\theta(0,y,0,t) - \langle\theta(0,y,0,t)\rangle|\mathrm{d}y}{\int_{Y^*} n(0,y,0,t)\mathrm{d}y}, \qquad (3)$$

where $\psi(\mathbf{r},t) = |\psi(\mathbf{r},t)|\exp(i\,\theta(\mathbf{r},t))$ and $\mathbf{r} = (x,y,z)$. Here the average $\langle f(y)\rangle = \int_{Y^*} f(y)\mathrm{d}y$ for any function f and Y^* denotes the inner region $Y^* = [-5, 5]\,\mu$m.

Extended Data Fig. 4a shows the evolution of α with t_h, namely, after ramping a_s back to the SSP. Here, α first quickly decreases, transiently reaching a value close to zero (green filled dot), before increasing again up to an intermediate value (blue filled dot) and finally smoothly decreasing towards zero, setting to a low saturation value ($\alpha^* = 0.027\times2\pi$). After long times, only small variations of α persist (orange filled dot), indicating that an equilibrium distribution is reached. The density and phase profiles corresponding to the coloured filled dots are shown in the inset of Extended Data Fig. 4a. Although α first reaches a low value within a short time, we observe that the corresponding density profile is strongly out of equilibrium (green curve), differing from both the initial ground state (not shown) and the long-time equilibrium state (orange curve). The phase variations are only transiently suppressed here. In contrast, when α reaches the next local maximum, the density profile appears very close to the equilibrium expectation, yet with a remaining phase pattern of large amplitude (blue curves). This opposite behaviour of the phase and density in the early time is reminiscent of the quadrature oscillations of phase and density perturbations associated with a given elementary excitation in the linear regime[31]. The initial oscillatory behaviour of the RTE is also reminiscent of the behaviour of $\Delta\Phi$ from repeated instances of experimental interference patterns observed in Fig. 4b. Here we subject α to a similar analysis as $\Delta\Phi$, performing an exponential fit and calculating the residuals (Extended Data Fig. 4b). The extracted decay time is 6.3(2) ms; from the residuals, we find the main frequency components in the interval of [50, 100] Hz. We note that this frequency is similar to the low-lying mode of the SSP excitation spectrum, as computed from Bogoliubov theory[31]. The observed frequency of oscillation and the time evolution of phase and density profiles in apparent quadrature suggest an important role of the low-lying collective mode of the SSP in the rephasing dynamics.

Experimental sequence. We apply our phase-scrambling protocol to the evaporatively cooled SSP of ^{164}Dy atoms[13]. For this, we initially load our five-beam open-top magneto-optical trap for 3 s and apply a magneto-optical trap compression phase, which lasts for 400 ms (ref. [44]). We then load about 8×10^6 atoms into a single-beam horizontal ODT, propagating along the y axis. The horizontal ODT is derived from a 1,064 nm focused laser beam. After loading, we apply forced evaporative cooling by exponentially reducing the optical power in the horizontal ODT for 0.9 s. Subsequently, we switch on a second ODT beam along the vertical z axis to form a crossed ODT and continue with the last stage of evaporative cooling for 2 s (ref. [45]) until the SSP is reached. During the evaporation sequence, a vertical magnetic field of $B = 2.430(4)$ G sets the dipole orientation. The final trap geometry is axially elongated with harmonic frequencies $\omega_{x,y,z} = 2\pi\times(225, 37, 165)\,\mathrm{s}^{-1}$. After the initial-state preparation (SSP), we apply our phase-scrambling protocol. For that, without any additional waiting time after the evaporative cooling, we change the B field to 1.65 G deep in the ID regime. Here we allow the system's global phase to freely evolve for $t_s = 20$ ms. We have explored two types of protocol: jumping, which results in an effective ~1 ms change in the B field due to the finite time response of the system, and ramping within 20 ms. We observe a similar scrambling behaviour in $\Delta\Phi$ for both jump and ramp protocols. We complete our phase-scrambling sequence by jumping the B field back to its initial value and by letting the system evolve for a variable hold time t_h. Finally, we perform a matter–wave-interference-type experiment during TOF expansion and record the resulting interference pattern by absorption imaging. A TOF duration of 26.5 ms ensures sufficient mapping onto the momentum space. The imaging beam propagates in the horizontal x–y plane at an angle of ~45° with respect to the weak trap axis y.

Tuning the scattering length. To connect the experimental B-field values to the contact scattering length a_s, we use the established formula for overlapping Feshbach resonances: $a_s(B) = a_{bg}\prod_i\left(1 - \Delta B_i/\left(B - B_{0,i}\right)\right)$ (ref. [46]), where $B_{0,i}$ denotes the poles; ΔB_i, the corresponding distance from the pole to the zero crossing; and a_{bg}, the (local) background scattering length. We determine the poles and zero crossings in our B-field region of interest by performing loss spectroscopy and thermalization measurements. Starting from a thermal cloud prepared at 2.55 G, we first ramp the magnetic field to the final value within 5 ms and then lower the trap depth to its final value within 50 ms; we wait an additional hold time of about 400 ms. In the absence of Feshbach resonances, we typically end up with a thermal gas of 5×10^5 atoms at about 500 nK. When scanning the magnetic field in our region of interest, we observe several atom loss features together with peaks in the atom cloud temperature, which we fit by Gaussians to extract the positions of the poles $B_{0,i}$ and widths ΔB_i.

The value of the background scattering length of ^{164}Dy is a more subtle topic, as several measurements have reported different values in the range between $60a_0$ and $100a_0$ (ref. [47]). These measurements were performed using different methods (for example, cross-thermalization and theory–experiment comparisons of oscillation frequencies), for different initial states (thermal gases and quantum droplets) and at different magnetic fields. In particular, the existence of very broad resonances at higher magnetic fields[48] affects the measured local background scattering lengths. Therefore, we set the value of a_{bg} in such a way that the B-to-a_s conversion reproduces the calculated critical scattering length of $a_s = 91a_0$ at the experimentally estimated phase transition point between the BEC and SSP around 2.5 G. This gives a value of $a_{bg} = 73a_0$, which lies within the error bars of the latest published value of $a_{bg} = 69(4)a_0$ (ref. [47]). Extended Data Fig. 2 shows the resulting calculated B-to-a_s conversion from which we estimate $a_{s,SSP} = 88a_0$ at 2.43 G in the SSP and $a_{s,ID} = 76.9a_0$ at 1.65 G in the ID phase, as used in the experiment.

Interference pattern analysis. Our analysis is similar to the one described in ref. [13]. We record $q \in [30, 100]$ experimental repetitions for each parameter set $\mathcal{P}$. Each recorded TOF picture i ($i = 1,\ldots,q$) is processed by first subtracting the thermal background via a symmetric 2D Gaussian fit to the wings of the density distribution. Next we recentre the image of the degenerate cloud and integrate its central region, where the matter–wave interference signal is concentrated, along the z direction within $\pm2\,\mu\mathrm{m}^{-1}$. We obtain a momentum density profile that we normalize by its sum. From such a momentum profile, a fast Fourier transform yields the 1D density profile $n_i(\tilde{y})$. An in situ density modulation in an atomic cloud leads to side peaks in $n_i(\tilde{y})$, symmetrically centred around the peak at zero. To isolate the centre of this specific modulation, we calculate the incoherent and coherent means of $n_i(\tilde{y})$, which are denoted as $n_M(\tilde{y}) = \langle|n_i(\tilde{y})|\rangle_{\mathcal{P}}$ and $n_\Phi(\tilde{y}) = |\langle n_i(\tilde{y})\rangle_{\mathcal{P}}|$, respectively. The incoherent mean (n_M) reflects the mean modulation amplitude of the cloud at the respective wavelength $\tilde{y}$. The coherent mean ($n_\Phi \lesssim n_M$) if the phases of the interference pattern among the q repetitions at the respective $\tilde{y}$ are roughly constant, and $n_\Phi \to 0$ (and hence $n_\Phi \ll n_M$) if the phases are random. Therefore, the most pronounced difference $n_M - n_\Phi$ is observed for the ID regime (Extended Data Fig. 1a). From the maximum of this difference, the modulation wavelength (or 'droplet distance') can be determined as $\tilde{y} \equiv d$. The fast Fourier transform phasors at d can be expressed as $P_i = n_i(d) = \rho_i e^{-i\Phi_i}$, yielding the sets $\{P_1, \ldots, P_q\}_{\mathcal{P}}$. To characterize the distribution of phases Φ_i within our sets, we calculate the circular variance $\Delta\Phi = 1 - \frac{1}{q}\sqrt{\left(\sum_{i=1}^q \cos(\Phi_i)\right)^2 + \left(\sum_{i=1}^q \sin(\Phi_i)\right)^2}$ (ref. [30]). For a phase-coherent sample, and hence interference fringes stable within the envelope, $\Delta\Phi$ is small, whereas for an incoherent sample, it approaches unity. To estimate the confidence intervals of $\Delta\Phi$, we apply a bias-corrected and accelerated (BCA) bootstrapping scheme[39] for each $\mathcal{P}$, resampling 10^6 times from the respective q experimental values. We note that possible non-ballistic (namely, interaction-driven) evolution during the early TOF might have a residual systematic effect on the measured values of n_M, n_Φ and $\Delta\Phi$.

Effect of finite sample size. Even the circular variance $\Delta\Phi$ of a sample of q angles $(\Phi_1,\ldots,\Phi_q)$ drawn from a completely random distribution approaches unity only when $q \to \infty$. To estimate the fully incoherent limit of $\Delta\Phi$ for our finite q, we calculate 10^6 values for $\Delta_q\Phi$, each for q independent draws from a theoretical, uniform distribution in $[0, 2\pi)$. The histograms of $\Delta_q\Phi$ are shown in Extended Data Fig. 1b. The indicated 1σ confidence intervals are [0.77, 0.93] for $q = 35$ draws and [0.86, 0.96] for $q = 100$ draws. We note that the histograms of $\Delta_q\Phi$ seem

to closely follow a beta distribution[49], even if one generalizes the underlying distribution of phases Φ_i to a von Mises distribution, of which the uniform distribution is just a degenerate case.

Interference pattern quantities for a simple model of a droplet array. For simplicity, let us consider here that the state is made of N_D identical droplets. In this case, the full wavefunction of the system would be

$$\psi(x,y,z) = \sum_{j=1}^{N_D} f(x, y - R_j, z)\, e^{i\theta_j}, \tag{4}$$

where R_j is the spatial coordinate of the jth droplet, θ_j is its phase (taken to be uniform over the droplet) and f is the wavefunction of a single droplet localized around $y=0$. With such a wavefunction, the phasor extracted from one realization would be

$$P_i = \int dk_y \sum_{j_1,j_2=1}^{N_D} e^{ik_y(R_{j_1}-R_{j_2}-d)}\, e^{i(\theta_{j_1}-\theta_{j_2})} |\tilde{f}(k_y)|^2, \tag{5}$$

where $\tilde{f}$ is the Fourier transform of the function f and d is the distance between the neighbouring droplets $d = \langle R_{j+1} - R_j \rangle$. It simplifies to

$$P_i = \sum_{j_1,j_2=1}^{N_D} g(R_{j_1} - R_{j_2} - d)\, e^{i(\theta_{j_1}-\theta_{j_2})} \tag{6}$$

$$\approx g(0) \sum_{j=1}^{N_D-1} e^{i(\theta_{j+1}-\theta_j)}, \tag{7}$$

where $g(y)$ is the Fourier transform of $|\tilde{f}(k_y)|^2$, which is thus a peak function with a width of the order of the droplet size.

Equation (7) yields

$$A_M = \langle |P_i| \rangle_{\mathcal{P}} = (N_D - 1) g(0) l_{\Delta\theta} \approx (N_D - 1) g(0), \tag{8}$$

which shows only a weak dependence on the phase relation between the droplets and on the droplets' shape. We note that the residual information on the droplets' phase relation is contained in A_M via the length of the mean phase-difference vector $l_{\Delta\theta} = \langle |\langle \exp(i\Delta\theta_j) \rangle_j| \rangle_{\mathcal{P}}$. In the fully coherent (resp. incoherent) case, $l_{\Delta\theta}=1$ (resp. $l_{\Delta\theta} = 1/\sqrt{N_D - 1}$ on average). The change in $l_{\Delta\theta}$ with the degree of coherence remains limited, especially for the relatively small N_D relevant for our experimental situation (Fig. 1). Here $\langle . \rangle_{\mathcal{P}}$ denotes the average over an ensemble of realizations $\mathcal{P}$ and $\langle . \rangle_j$ denotes the average over the droplet array.

On the contrary, the function $A_\Phi = |\langle P_i \rangle_{\mathcal{P}}|$ contains the average of the phases with

$$\frac{A_\Phi}{A_M} \simeq |\langle \langle e^{i(\theta_{j+1}-\theta_j)} \rangle_j \rangle_{\mathcal{P}}|. \tag{9}$$

Therefore, the ratio A_Φ/A_M essentially measures the mean difference in the phases between two neighbouring droplets in the array.

From equation (7), it is also evident that the phase of the phasor is $\Phi \approx \langle \theta_{j+1} - \theta_j \rangle_j$. The circular variance $\Delta\Phi$ for q realizations can be expressed as

$$\Delta\Phi = 1 - \frac{1}{q} \sqrt{\sum_{i_1=1}^{q} e^{i\Phi_{i_1}} \sum_{i_2=1}^{q} e^{-i\Phi_{i_2}}}. \tag{10}$$

For a totally phase-coherent state, $\Phi=0$ for all the realizations leading to $\Delta\Phi=0$, while for a totally phase-incoherent sample, only the diagonal terms in equation (10) survive, leading to $\Delta\Phi = 1 - \frac{1}{\sqrt{q}}$ for q independent measurements.

Langevin formalism for the JJA model. To model the self-modulated dipolar gas, we use the JJA whose Hamiltonian H is given in equation (1). To describe the dynamics, we use a Langevin formalism (example in ref. [36]), where the time dependence of the phases obeys

$$\eta \frac{d\theta_j}{dt} = -\frac{dH}{d\theta_j} + \xi_j(T, \eta, t), \tag{11}$$

where the two sites are indexed using i and j and the thermal noise is denoted as $\xi_i(t)$, which is uncorrelated from grain to grain and at different times shows the correlations

$$\overline{\xi_j(t)\xi_i(t')} = 2\eta k_B T \delta_{ij}\, \delta(t - t'), \tag{12}$$

where k_B is the Boltzmann constant. This thermal noise ensures that in equilibrium, the configurations are realized with a probability proportional to the Boltzmann weight $e^{-H/(k_B T)}$.

To determine the parameters of the JJA model, we use the procedure described in the main text. With J fixed by the equilibrium value of $\Delta\Phi$, we determine η by comparing to the dephasing timescale.

Discussion on the quantum part of the Hamiltonian. The JJA model contains both quantum evolution and thermal noise. In our case, one can make the additional simplification to neglect the term related to the capacitance leading to quantum fluctuations compared with thermal fluctuations.

To justify this approximation, we estimated the interaction energy cost with a wavefunction given by a variational principle[50]. We obtain an energy to add one particle to the droplet of the order of a few hertz, which is very small compared with the temperature of 150 nK.

This allows to drop the second-order time derivative of the phase in the Langevin equations, leading to equation (2). For a system of four droplets, we have four equations for the phases. For the equations describing the evolution of the droplets at the edge of the array (namely, $j=1$ or $j=4$), we drop the terms of equation (2) containing the phases of non-existent neighbours (namely, θ_0 or θ_5).

Numerical solution of the equations. To solve our system of equations, we discretize the time dependence with a time step adapted to the considered value of J. For J/h up to 6,000 Hz, we used a time step of 10^{-5} s. For larger J, we used a time step of 5×10^{-6} s.

To relate the phases of the four individual droplets to the observables, equation (7) and the phasor definition, we use

$$\Phi = \arg\left(\sum_{j=1}^{3} e^{i(\theta_{j+1}-\theta_j)}\right). \tag{13}$$

To obtain a $\Delta\Phi$ value that can be compared to the experimental one, we compute the evolution over $q=100$ independent realizations, determine Φ for each realization and compute the evolution of $\Delta\Phi$ from these 100 values.

For the scrambling, we initialize each of the 100 runs with random phases and let the system evolve for 80 ms with a finite J to reach the corresponding equilibrium state. We then ramp J down to 0.002 Hz in 20 ms and let the system evolve for 100 ms.

For the rephasing, we initialize 100 configurations with random phases, which corresponds to the equilibrium state for the system with a small J (0.002 Hz). We then let the system evolve with $J=6{,}000$ Hz.

Modified JJA model with droplet dynamics. One can phenomenologically modify the JJA model to take the droplet dynamics into account. Each droplet is characterized by a position u_j. The dynamics of the droplets could be modelled by a phonon-like Hamiltonian:

$$H_D = \sum_j \left[\frac{p_j^2}{2M} + \frac{1}{2} M\omega_0^2 (u_{j+1} - u_j)^2 \right], \tag{14}$$

where M denotes the mass of the droplet, p_j is the momentum conjugate to u_j and ω_0 is the characteristic energy depending on the interactions between the droplets. This motion would be coupled to the degrees of freedom of the phase in the Hamiltonian in equation (1) by introducing a u_j dependence of the Josephson coupling: if two droplets get closer, J should increase. The precise form would need to be determined, but some exponential dependence seems plausible. If the displacements of the droplets are very small, one can expand the Josephson coupling as a function of the displacements of the droplets to obtain the Josephson coupling between the droplets j and $j+1$ via

$$J_{j+1,j} = J_0 - A(u_{j+1} - u_j), \tag{15}$$

where A is a positive quantity. Therefore, the two Hamiltonians in equations (14) and (1) with the coupling in equation (15) would, in principle, allow to incorporate the coupled dynamics of the degrees of freedom of the phase and the vibrations of the droplet 'lattice'.

Time traces of $\Delta\Phi$ and behaviour of A_M and A_Φ. We have studied the rephasing dynamics at different scattering lengths. Extended Data Fig. 5a shows the full time evolution of the experimentally measured $\Delta\Phi$ as a function of the calculated $\mathscr{L}$. From this data, we also extract the initial rephasing rate $|R|$ and the saturation value $\langle \Delta\Phi \rangle_{sat}$, as shown in Fig. 5. For $\mathscr{L}$ within the ID regime, $\Delta\Phi$ remains large (>0.5) for the entire t_h (blue region); therefore, we can conclude that rephasing is absent. As $\mathscr{L}$ increases, $\Delta\Phi$ gradually approaches small final values (~0.15) at longer evolution times (red region), that is, the system rephases.

From the time traces, we also analyse the long-time behaviour of A_Φ and A_M as a function of $\mathscr{L}$. As demonstrated in previous works[13,25], at equilibrium, A_Φ and A_M are powerful parameters to pinpoint the different quantum regimes in the phase diagram. In the SSP, $A_\Phi/A_M \approx 1$, whereas in the ID phase, this ratio tends to zero since A_Φ vanishes. As shown in Extended Data Fig. 5b, the value of A_M at a longer hold time ($t_h = 100$ ms) is substantial in the whole range investigated, indicating the persistence of density modulation in the system, and it varies only weakly with $\mathscr{L}$. Differently, A_Φ has a clear dependence on the density link. Its value at $t_h = 100$ ms nearly vanishes for $\mathscr{L} < 0.001$, evidencing a final phase-incoherent state (ID regime), whereas at large $\mathscr{L} > 0.01$, A_Φ and A_M are nearly equal.

The exact dependence of A_M on $\mathscr{L}$ is not completely obvious and deserves some explanation. From equation (7), we see that A_M, which is expressed as $A_M = \langle |P_i| \rangle = g(0) \langle |\sum_{j=1}^{N_D-1} \exp(i\Delta\theta_j)| \rangle$, contains (1) information on the individual droplet density profile via $g(0)$ and (2) residual information on

the coherence of the system via the averaged length of the vector of the phase difference $\langle|\sum_j \exp(\mathrm{i}\,\Delta\theta_j)|\rangle$. In the fully coherent case, this length is identically equal to $N_D - 1$, whereas in the fully incoherent case, it has an average of only $\sqrt{N_D - 1}$. This change explains the abrupt jump in A_M observed when the droplet array becomes partially incoherent. We note that the observed jump with a value divided by ~1.5 is compatible with the predicted number of droplets in our array, namely, $N_D = 4$. We also note that the smooth increase in A_M for decreasing a_s both in the incoherent ($\mathscr{L} < 0.01$) and in the coherent ($\mathscr{L} > 0.01$) regions are expected from the proportionality to $g(0)$. Here $g(0)$ indicates the individual droplet peak density and typically scales as the inverse of the droplet size. It is thus expected to increase for decreasing a_s. We highlight again, as stated in Methods, that the information on the phase coherence of the array contained in A_M is much less dominant than that in A_Φ, where the length of the phase-difference vector is measured after performing the ensemble average, $|\langle\sum_j \exp(\mathrm{i}\,\Delta\theta_j)\rangle|$. Therefore, A_Φ is expected to cancel in a fully incoherent case rather than simply being reduced by a factor of $\sqrt{N_D - 1}$.

Atom number evolution. When connecting the rephasing behaviour shown in Fig. 4, where $\langle\Delta\Phi\rangle_{sat}$ depends on $\mathscr{L}$, to the phase diagram, the atom numbers of the thermal and coherent part may also show differences after the complete phase-scrambling sequence. To this end, we extract the total atom number, N_{total}, via a pixel count from each unprocessed TOF absorption image. We then subtract the thermal background via a 2D Gaussian fit (Methods) to obtain the atom number in the coherent part, $N_{coherent}$. The width of the thermal background at the given TOF allows to determine the temperature T. Extended Data Fig. 3 shows N_{total}, T, $N_{thermal}$ and $N_{coherent}$ as a function of the hold time t_h for three exemplary rephasing B fields, namely, 1.65 G (blue), 2 G (light blue) and 2.43 G (red). These correspond to $\mathscr{L} \simeq 4\times10^{-6}$, 4×10^{-4} and 1×10^{-1} and thus to the ID, intermediate and SSP regimes, respectively. Regardless of the chosen value of $\mathscr{L}$, the individual N_{total}, $N_{thermal}$ and T essentially coincide and decrease continuously with increasing t_h in a similar manner. This behaviour suggests the remaining plain evaporation from the ODT during t_h.

From the description of an ideal BEC, we can simply approximate

$$N_{coherent} = N_{total}\left(1 - \left(\frac{T}{T_C}\right)^3\right), \tag{16}$$

where the phase transition's critical temperature T_C mainly depends on the trapping frequencies $\omega_{x,y,z}$ and N_{total}. From our measured N_{total} and T, we would expect a decrease in $N_{coherent}$ for all the rephasing B fields. However, similar to A_Φ, A_M, $\langle\Delta\Phi\rangle_{sat}$ and $|R|$ (Fig. 5d), we observe three distinct behaviours for $N_{coherent}$ depending on $\mathscr{L}$. For small $\mathscr{L} < 0.001$ (ID regime) $N_{coherent}$ decreases with t_h, whereas for large $\mathscr{L} > 0.01$ (SSP regime), $N_{coherent}$ increases, with relative changes of up to 30% at $t_h = 100$ ms compared with the respective initial values. In the intermediate-$\mathscr{L}$ regime, $N_{coherent}$ remains almost constant. A possible explanation for the occurrence of these three behaviours might be the differences in their rate of three-body loss. Although in the investigated B-field regime, the three-body loss coefficient is almost constant, the increased peak density expected in the ID regime results in a higher three-body loss rate, which can surpass the plain evaporation rate and thus result in a decreasing $N_{coherent}$. The lower peak density in the SSP, on the contrary, could result in a lower three-body loss rate and thus lead to an increasing $N_{coherent}$ via plain evaporation.

Data availability

Source data are available for this paper[51]. All other data that support the plots within this paper and other findings of this study are available from the corresponding author upon reasonable request.

References

40. Ronen, S., Bortolotti, D. C. E. & Bohn, J. L. Bogoliubov modes of a dipolar condensate in a cylindrical trap. *Phys. Rev. A* **74**, 013623 (2006).
41. Chomaz, L. et al. Quantum-fluctuation-driven crossover from a dilute Bose–Einstein condensate to a macrodroplet in a dipolar quantum fluid. *Phys. Rev. X* **6**, 041039 (2016).
42. Wächtler, F. & Santos, L. Quantum filaments in dipolar Bose–Einstein condensates. *Phys. Rev. A* **93**, 061603 (2016).
43. Wächtler, F. & Santos, L. Ground-state properties and elementary excitations of quantum droplets in dipolar Bose–Einstein condensates. *Phys. Rev. A* **94**, 043618 (2016).
44. Ilzhöfer, P. et al. Two-species five-beam magneto-optical trap for erbium and dysprosium. *Phys. Rev. A* **97**, 023633 (2018).
45. Trautmann, A. et al. Dipolar quantum mixtures of erbium and dysprosium atoms. *Phys. Rev. Lett.* **121**, 213601 (2018).
46. Chin, C., Grimm, R., Julienne, P. S. & Tiesinga, E. Feshbach resonances in ultracold gases. *Rev. Mod. Phys.* **82**, 1225–1286 (2010).
47. Ferrier-Barbut, I. et al. Scissors mode of dipolar quantum droplets of dysprosium atoms. *Phys. Rev. Lett.* **120**, 160402 (2018).
48. Maier, T. et al. Broad universal Feshbach resonances in the chaotic spectrum of dysprosium atoms. *Phys. Rev. A* **92**, 060702 (2015).
49. Forbes, C., Evans, M., Hastings, N. & Peacock, B. *Statistical Distributions* 4th edn, Ch. 8, 55–61 (Wiley, 2010).
50. Blakie, P., Baillie, D., Chomaz, L. & Ferlaino, F. Supersolidity in an elongated dipolar condensate. Preprint at https://arxiv.org/abs/2004.12577 (2020).
51. Sohmen, M. Source Data—Ilzhofer et al.—Phase coherence in out-of-equilibrium supersolid states of ultracold dipolar atoms. *Zenodo* https://doi.org/10.5281/zenodo.4050234 (2020).

Acknowledgements

We are grateful to S. Erne, J. Schmiedmayer and the ERBIUM team for insightful discussions and M. A. Norcia for careful reading the manuscript. We acknowledge R. M. W. van Bijnen for developing the code for our eGPE ground-state simulations. G.M. and T.G. thank N. Caballero for insightful discussions on the numerical solution of the Langevin equation. This work is financially supported through an ERC Consolidator grant (RARE, no. 681432), an NFRI grant (MIRARE, no. ÖAW0600) from the Austrian Academy of Science and DFG/FWF (FOR 2247/PI2790) and by the Swiss National Science Foundation under Division II. M.S. and G.D. acknowledge support by the Austrian Science Fund FWF within the DK-ALM (no. W1259-N27). A.T. acknowledges support by the Austrian Science Fund FWF within the Lise Meitner programme (no. M2683-N36). L.C. acknowledges support through the FWF Elise Richter Fellowship no. V792. We also acknowledge the Innsbruck Laser Core Facility, financed by the Austrian Federal Ministry of Science, Research and Economy. Part of the computational results presented have been achieved using the HPC infrastructure LEO at the University of Innsbruck.

Author contributions

P.I., G.D. and A.T. conducted the experiment and collected the experimental data. M.S. and C.P. analysed the data. G.N., M.J.M., L.C., M.S. and C.P. performed and analysed the eGPE simulations. G.M. and T.G. developed the JJA model and performed the corresponding simulations. All the authors contributed to the writing of the paper. F.F. supervised the project.

Competing interests

The authors declare no competing interests.

Additional information

Extended data is available for this paper at https://doi.org/10.1038/s41567-020-01100-3.

Correspondence and requests for materials should be addressed to F.F.

Peer review information *Nature Physics* thanks the anonymous reviewers for their contribution to the peer review of this work.

Reprints and permissions information is available at www.nature.com/reprints.

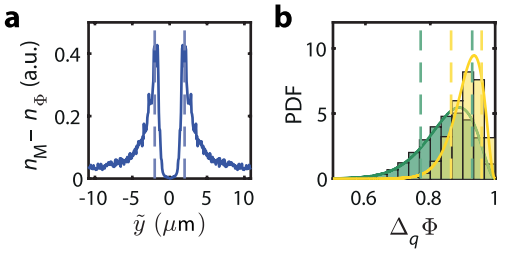

Extended Data Fig. 1 | Wavelength of the modulation and finite-sampling effect. a, Difference between incoherent and coherent mean of the density profiles in the ID regime (1.65 G), peaking at the modulation wavelength $d \simeq \pm 2\,\mu$m (dashed lines). **b**, Histograms of 10^6 realisations (each) for calculations of $\Delta_q \Phi$ from uniformly random phases Φ_i, for $q = 35$ (green) and $q = 100$ (yellow) draws, respectively. The dashed vertical lines reflect the confidence interval enclosing 68.3 % ('one σ') of the calculated values. The solid lines depict a Beta distribution with same mean and variance as the drawn distribution of $\Delta_q \Phi$ (no free fit parameters).

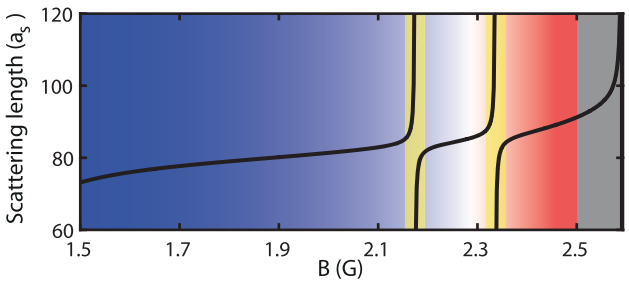

Extended Data Fig. 2 | Estimated scattering length. Calculated B-to-a_s conversion for ^{164}Dy. Red and blue shaded areas indicate the SSP and the ID region, respectively. The grey area indicates the BEC region, while the yellow areas indicate regions around the two narrow Feshbach resonances located at 2.174 G and 2.336 G where we observe increased atom loss. We estimate $a_{s,SSP} = 88\ a_0$ in the SSP at 2.43 G and $a_{s,ID} = 76.9\ a_0$ in the ID at 1.65 G.

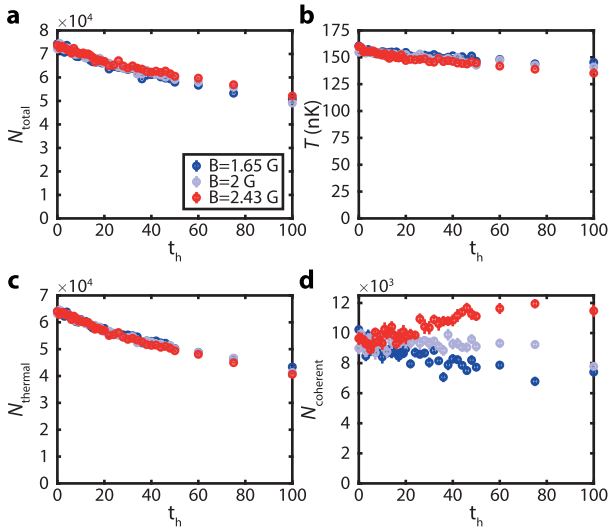

Extended Data Fig. 3 | Temporal evolution of the atom numbers and temperature in the ID regime and SSP. a, Total atom number N_{total}, **b**, temperature T and atom numbers of **c**, the thermal and **d**, the coherent part, $N_{thermal}$ and $N_{coherent}$, as a function of the hold time t_h. The data sets at 1.65 G (blue) and 2.43 G (red) correspond to the ID regime and the SSP, respectively, whereas the one at 2 G (light blue) corresponds to the intermediate regime.

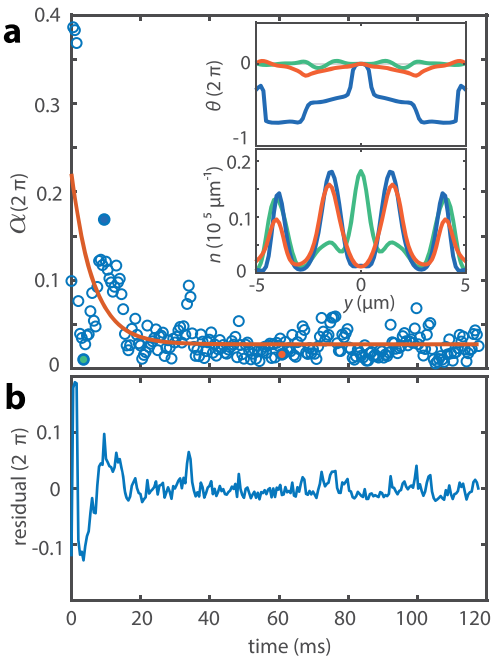

Extended Data Fig. 4 | The global phase variation α from the RTE simulation of a scramble-and-rephase protocol. a, Evolution of α over the hold time t_h. The solid orange line depicts an exponential fit to the data. In the inset, the integrated density n and the phase profile θ are exemplarily shown for $t^* = [3.5, 9.5, 60.5]$ ms (note the corresponding color filling of the plot markers). **b**, Residuals from the exponential fit to α.

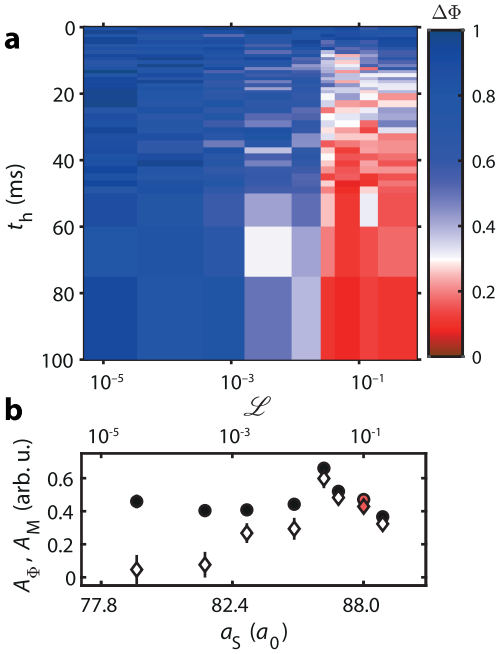

Extended Data Fig. 5 | Dependence of experimental rephasing dynamics on the density link strength $\mathscr{L}$. a, Temporal evolution of $\Delta\Phi$ (color map) at different $\mathscr{L}$ starting from phases scrambled in the ID regime. For each t_h we record $q \geq 35$ individual experimental realizations. For large $\mathscr{L}$ the system recovers its global phase coherence ($\Delta\Phi \simeq 0$), whereas for small $\mathscr{L}$ it does not ($\Delta\Phi \simeq 1$). **b**, A_M (circles) and A_Φ (diamonds) for the same data set at long hold time, $t_h = 100$ ms. The error bars (partly covered by plot markers) are statistical standard errors of A_M and A_Φ. The red filled pair of symbols corresponds to the data set presented in Fig. 3.

A.5 Publication:

Observation of vortices and vortex stripes in a dipolar Bose-Einstein condensate

The following publication has appeared in

Nature Physics (2022)[¶]
submitted 15 Jun 2022; published 31 Oct 2022
DOI: https://arxiv.org/abs/2206.12265
L. Klaus,[1,2,4] T. Bland,[1,4] E. Poli,[2] C. Politi,[1,2] G. Lamporesi,[3] E. Casotti,[1,2] R. N. Bisset,[2] M. J. Mark,[1,2] and F. Ferlaino[1,2]

[1] *Institut für Quantenoptik und Quanteninformation, Österreichische Akademie der Wissenschaften, 6020 Innsbruck, Austria*

[2] *Institut für Experimentalphysik, Universität Innsbruck, 6020 Innsbruck, Austria*

[3] *INO-CNR BEC Center and Dipartimento di Fisica, Università di Trento, 38123, Trento, Italy*

[4] *These authors contributed equally: L. K. and T. B.*

[¶]The author of the present thesis performed the measurements together with L. K., and E. C., analysed the experimental data with L. K., E. C., and M. J. M., and contributed in writing the manuscript and interpreting the results together with all the authors.

nature physics

Article

https://doi.org/10.1038/s41567-022-01793-8

Observation of vortices and vortex stripes in a dipolar condensate

Received: 15 June 2022

Accepted: 8 September 2022

Published online: 31 October 2022

Check for updates

Lauritz Klaus[1,2,4], Thomas Bland[1,2,4], Elena Poli[2], Claudia Politi[1,2], Giacomo Lamporesi[3], Eva Casotti[1,2], Russell N. Bisset[2], Manfred J. Mark[1,2] and Francesca Ferlaino[1,2]

Quantized vortices are a prototypical feature of superfluidity that have been observed in multiple quantum gas experiments. But the occurrence of vortices in dipolar quantum gases—a class of ultracold gases characterized by long-range anisotropic interactions—has not been reported yet. Here we exploit the anisotropic nature of the dipole–dipole interaction of a dysprosium Bose–Einstein condensate to induce angular symmetry breaking in an otherwise cylindrically symmetric pancake-shaped trap. Tilting the magnetic field towards the radial plane deforms the cloud into an ellipsoid, which is then set into rotation. At stirring frequencies approaching the radial trap frequency, we observe the generation of dynamically unstable surface excitations, which cause angular momentum to be pumped into the system through vortices. Under continuous rotation, the vortices arrange into a stripe configuration along the field, in close agreement with numerical simulations.

Since the first experiments on gaseous Bose–Einstein condensates (BECs), the observation of quantized vortices has been considered the most fundamental and defining signature of the superfluid nature of such systems. Their very existence sets a unifying concept encompassing a variety of quantum fluids from liquid helium[1] to the core of neutron stars[2] and from superconductors[3] to quantum fluids of light[4]. Their classical counterparts have as well fascinated scientists from different epochs and fields as vortices are found in many scales of physical systems, from tornadoes in the atmosphere to ferrohydrodynamics.

In the quantum realm, a quantized vortex may emerge as a unique response of a superfluid to rotation. It can be understood as a type of topologically protected singularity with a 2π phase winding that preserves the single-valuedness of the superfluid wave function and the irrotational nature of its velocity field. In contact-interacting BECs, vortical singularities have been observed experimentally in the form of single vortices[5,6], vortex–antivortex pairs[7], solitonic vortices[8,9], vortex rings[10] and vortex lattices[6,11] using a number of different techniques. Moreover, vortices play a fundamental role in the description of the Berezinskii–Kosterlitz–Thouless transition in two-dimensional (2D) systems[12], as well as in the evolution of quantum turbulence[13,14], and have been observed in interacting Fermi gases along the Bose-Einstein condensate to Bardeen-Cooper-Schrieffer crossover[8,15].

Recently, a new class of ultracold quantum gases are being created in various laboratories around the world, using strongly magnetic lanthanide atoms[16,17]. Such a system, providing a quantum analogue of classical ferrofluids, enables access to the physics of dipolar BECs, in which atoms feature a strong long-range anisotropic dipole–dipole interaction (DDI)[18,19] on top of the traditional contact-type isotropic one. This intriguing platform provided the key to observe, for example, extended Bose–Hubbard dynamics[20], roton excitations[21–23], the quantum version of the Rosensweig instability[24] and supersolid states of matter[25–28], and is foreseen to host novel phenomena for quantum simulation and metrology[18,19].

The dipolar interaction is predicted to also intimately change the properties of vortices in quantum gases[29]. For instance, theoretical works predict single vortices to exhibit an elliptic-shaped core for a quasi-2D setting with in-plane dipole orientation[30–33] or the presence of density oscillations around the vortex core induced by the roton

[1]Institut für Quantenoptik und Quanteninformation, Österreichische Akademie der Wissenschaften, Innsbruck, Austria. [2]Institut für Experimentalphysik, Universität Innsbruck, Innsbruck, Austria. [3]INO-CNR BEC Center and Dipartimento di Fisica, Università di Trento, Povo, Italy. [4]These authors contributed equally: Lauritz Klaus, Thomas Bland. e-mail: Francesca.Ferlaino@uibk.ac.at

https://doi.org/10.1038/s41567-022-01793-8

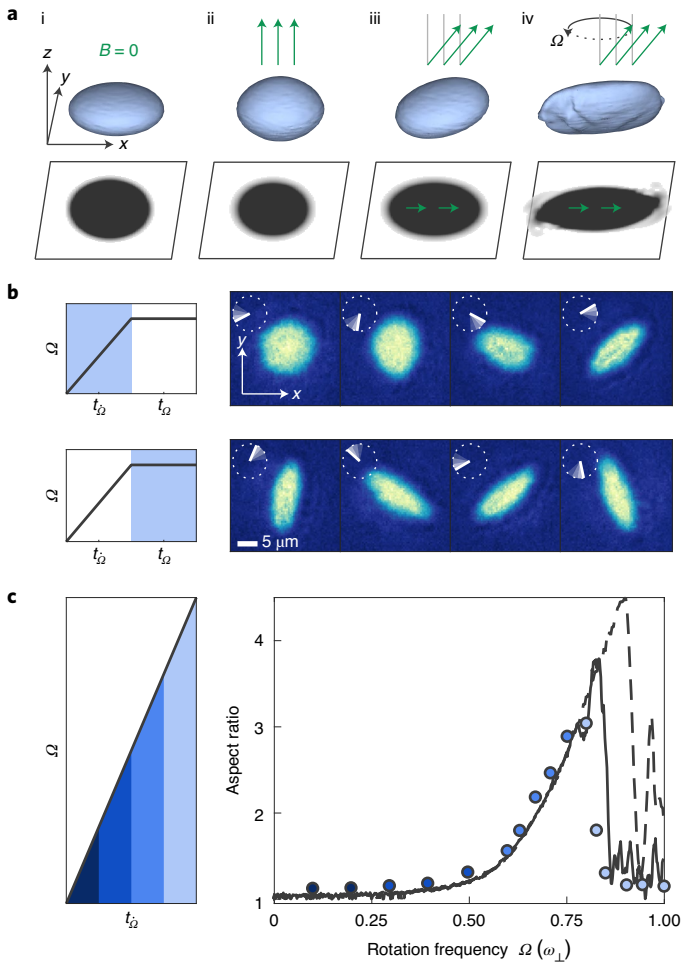

Fig. 1 | Magnetostirring of a Dy dipolar BEC and evolution of the cloud aspect ratio. a, 3D simulations and corresponding shadow on the *x*-*y* plane of a non-dipolar (i) and dipolar BEC with $B \neq 0$ (ii–iv) in a cylindrically symmetric, oblate trap. The magnetic-field (green arrows) angle with respect to the *z* axis varies from $\theta = 0°$ (ii) to $\theta = 35°$ (iii) and rotating at $\theta = 35°$ around *z* (iv). **b**, Left panels show the experimental sequence for the stirring procedure. The grey areas indicate the stage during which the images in the right panels were taken. The right panels are representative axial absorption images showing the dipolar BEC while spinning up the magnetic field for $t_{\dot{\Omega}} = [140, 430, 627, 692]$ ms (top) and subsequent constant rotation at $\Omega = 2\pi \times 36$ Hz for $t_\Omega = [0, 6, 11, 17]$ ms (bottom). The rotation of the magnetic field in the *x*-*y* plane is indicated by the white line. **c**, (left) Time evolution of the magnetic field rotation frequency. Ω is linearly increased to its final value at a speed of $\dot{\Omega} = 2\pi \times 50\ \mathrm{Hz\,s^{-1}}$. (right) Cloud AR for different final rotation frequencies. To mitigate influences of trap anisotropies on the AR, a full period at the final rotation frequency is probed. The error bars, representing the standard error on the mean after 100 trials per point, are smaller than the symbol size. The solid (dashed) black line shows the corresponding eGPE simulations with a 2 s (1 s) ramp and $a_s = 110a_0$, $(\omega_\perp, \omega_z) = 2\pi \times [50, 130]$ Hz, and $N = 15{,}000$. Different colors of the experimental point in the right panel indicate the corresponding time during the ramp in the left panel.

minimum in the dispersion relation[30–34]. For vortex pairs, the anisotropic DDI is expected to alter the lifetime and dynamics[33,35] and can even suppress vortex–antivortex annihilation[33]. These interaction properties are predicted to give rise to a vortex lattice structure that can follow a triangular pattern[30,34], as is typical for non-dipolar BECs[11], or a square lattice for attractive or zero contact interactions[36–38] when the DDI is isotropic (dipoles aligned with the rotation axis). A very striking consequence of the dipoles tilted towards the plane is the formation of vortex stripes[30,39,40]. Moreover, vortices could provide an unambiguous smoking gun of superfluidity in supersolid states[41–43]. However, despite these intriguing predictions, vortices in dipolar quantum gases have not been observed until now.

This Article presents the experimental realization of quantized vortices in a dipolar BEC of highly magnetic dysprosium (Dy) atoms. Following a method proposed in ref. [40], extended to arbitrary magnetic-field angles in ref. [44], we show that the many-body phenomenon of magnetostriction[45], genuinely arising from the anisotropic DDI among atoms, provides a natural route to rotate the systems and nucleate vortices in a dipolar BEC. We carry out studies on the dynamics of the vortex formation, which agree very well with our theoretical predictions. Finally, we observe one of the earliest predictions for vortices in dipolar BECs: the formation of vortex stripes in the system.

In non-dipolar gases, quantized vortices have been produced using several conceptually different techniques, for instance, by rotating non-symmetric optical[6,11] or magnetic[46] potentials, by rapidly shaking the gas[14], by traversing it with obstacles with large enough velocity[7,47], by rapidly cooling the gas across the BEC phase transition[48,49] or by directly imprinting the vortex phase pattern[50]. Dipolar quantum gases, while able to form vortices with these same standard procedures[29], also offer unique opportunities that have no counterpart in contact-interacting gases. Crucially, the DDI gives rise to the phenomenon of magnetostriction in position space[45]. When dipolar BECs are polarized by an external magnetic field **B**—defining the dipole orientation—the DDI causes an elongation of the cloud along the polarization direction. This is a direct consequence of the system tendency to favour head-to-tail dipole configurations, which effectively reduces the interaction energy[19].

Such a magnetostrictive effect provides a simple method to induce an elliptic effective potential and drive rotation with a single control parameter. This modification of the effective potential is shown in Fig. 1a for a BEC in an oblate trap with cylindrical symmetry about the *z* axis. While a non-dipolar BEC takes the same shape as the confining trap (Fig. 1a(i)), introducing dipolar interactions with polarization axis along *z* stretches the cloud along this axis yet maintains cylindrical symmetry (Fig. 1a(ii)). Tilting the magnetic field leads to a breaking of the cylindrical symmetry, resulting in an ellipsoidal deformation of the cloud shape, as seen from the density projection onto the *x*–*y* plane (Fig. 1a(iii)). Finally, under continuous rotation of the magnetic field, which we coin 'magnetostirring', the condensate is predicted to rotate (Fig. 1a(iv)). This unique approach to stir a dipolar condensate can eventually lead to the nucleation of vortices[40,44], realizing genuinely interaction-driven vorticity through many-body phenomena.

We explore this protocol using a dipolar BEC of ^{162}Dy atoms. We create the BEC similar to our previous work[51] with the distinction that here the magnetic-field unit vector, $\hat{\mathbf{B}}$, is kept tilted at an angle of $\theta = 35°$ with respect to the *z* axis both during evaporative cooling and magnetostirring (Fig. 1a(iii) and Methods). After preparation, the sample contains about 2×10^4 condensed atoms confined within a cylindrically symmetric optical dipole trap (ODT) with typical radial and axial trap frequencies $(\omega_\perp, \omega_z) = 2\pi \times [50.8(2), 140(1)]$ Hz. Here, before stirring, the magnetostriction is expected from simulations to increase the cloud aspect ratio (AR) in the horizontal plane from 1 up to 1.03, whereas the trap anisotropy is negligible. We use a vertical (*z*) absorption imaging to probe the radial (*x*,*y*) atomic distribution after a short time-of-flight (TOF) expansion of 3 ms. The atom number is instead measured using horizontal absorption imaging with a TOF of 26 ms.

Similarly to a rotation of a bucket containing superfluid helium or of a smoothly deformed ODT for non-dipolar BECs, magnetostirring is predicted to transfer angular momentum into a dipolar BEC[40,44]. In response to such an imposed rotation, the shape of an irrotational cloud is expected to elongate with an amplitude that increases with the rotation frequency Ω. This phenomenon is clearly visible in our experiments, as shown in Fig. 1b. Here we first revolve the tilted $\hat{\mathbf{B}}$ around the *z* axis with a linearly increasing rotation frequency $(\dot{\Omega} = 2\pi \times 50\ \mathrm{Hz\,s^{-1}})$ and observe that the dipolar BEC starts to rotate

https://doi.org/10.1038/s41567-022-01793-8

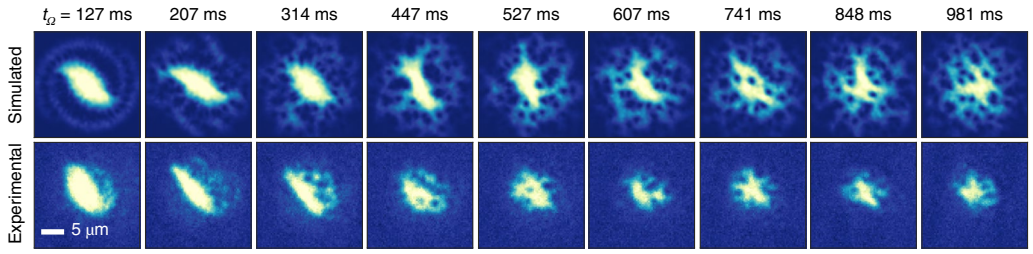

Fig. 2 | Observation of vortices in a dipolar BEC. Each column shows the simulated (top) and experimental (bottom) images for various rotation times t_Ω. For the experiment, the atoms are imaged along the z direction. In each experimental run, we rotate the magnetic field anticlockwise at $\Omega = 0.74\omega_\perp$ for different rotation times t_Ω. The magnetic-field value is kept to $B = 5.333(5)$ G. The initial condensed atom number is $N = 15{,}000$. The decreasing size of the cloud suggests a decrease in atom number. However, for states with vortices or spiral shapes, appearing at large t_Ω, our bimodal fit to extract the atom number breaks down. For the corresponding simulations, the parameters are $a_s = 112a_0$, trap frequencies $(\omega_\perp, \omega_z) = 2\pi \times [50, 150]$ Hz, $N = 8{,}000$ and $\Omega = 0.75\omega_\perp$.

at the same angular speed as the field and deforms with increasing elongation (Fig. 1b, top). We then stop the adiabatic ramp at a given value of Ω and probe the system under continuous rotation. We now find that the cloud continues rotating in the radial plane with an almost constant shape (Fig. 1b, bottom). Note that B is held constant at 5.333(5) G, where we estimate a contact scattering length of about $a_s = 111a_0$, where a_0 is the Bohr radius (Methods).

We further explore the response of our dipolar BEC to magneto-stirring by repeating the measurements in Fig. 1b (top), but stopping the ramp at different final values of Ω. The maximum value used for Ω approaches $\omega_\perp$, corresponding to a ramp duration of 1 s. We quantify the cloud elongation in terms of the aspect ratio AR = $\sigma_{max}/\sigma_{min}$, where the cloud widths σ_{max} and σ_{min} are extracted by fitting a rotated 2D Gaussian function to the density profiles. Figure 1c summarizes our results. We observe that initially the AR slightly deviates from 1 due to magnetostriction. It then slowly grows with increasing Ω, until a rapid increase at around $0.6\omega_\perp$ occurs, as this allows the angular momentum to increase, which decreases the energy in the rotating frame[52]. Suddenly, at a critical rotation frequency $\Omega_c \approx 0.74\omega_\perp$, the AR abruptly collapses back to AR ≈ 1, showing how the superfluid irrotational nature competes with the imposed rotation. This critical frequency is close to the value found in non-dipolar gases with a rotating elliptical harmonic trap, associated with a resonance at the quadrupole frequency[53].

To substantiate our observation, we perform numerical simulations of the zero-temperature extended Gross–Pitaevskii equation (eGPE)[54] (Methods). Quantum and thermal fluctuations are added to the initial states, which are important to seed the dynamic instabilities once they emerge at large enough Ω; see later discussion. The lines in Fig. 1c show our results. The dashed line is obtained through the same procedure as the experiment, whereas for the solid line, we halve the ramp rate, spending more time at each frequency. Both ramp procedures show quantitatively the same behaviour up to $\Omega = 0.8\omega_\perp$ and are in excellent agreement with the experimental results. The stability of the 1 s ramp exceeds the experimentally observed critical frequency. We partly attribute this discrepancy to asymmetries of the rotation in the experiment that are not present in the simulations, which may lead to an effective speed-up of the dynamical instabilities. However, in all cases, the AR rapidly decreases to about 1.

The growing AR and subsequent collapse to 1 is a signature of the dynamical instability of surface modes, known for being an important mechanism for seeding vortices and allowing them to penetrate into the high-density regions of rotated BECs[52,53,55], as also predicted for our dipolar system[40]. To search for quantum vortices in our system, we perform a new investigation where we directly set Ω close to Ω_c, aiming to trigger the instability at an earlier time when more atoms are condensed. We then hold the magnetic-field rotation fixed at this constant frequency for a time t_Ω. As shown in Fig. 2 (bottom), the cloud rapidly elongates, and the density starts to exhibit a spiral pattern, emanating from the tips of the ellipsoid. As early as $t_\Omega = 314$ ms, clear holes are observed in the density profile, forming in the density halo around the centre, the first clear indication of vortices in a dipolar gas. These vortices, initially nucleated at the edge of the sample, persist as we continue to stir and eventually migrate towards the central (high-density) region. Vortices are still visible in the experiment after 1 s of magnetostirring, although our atom number decreases throughout this procedure.

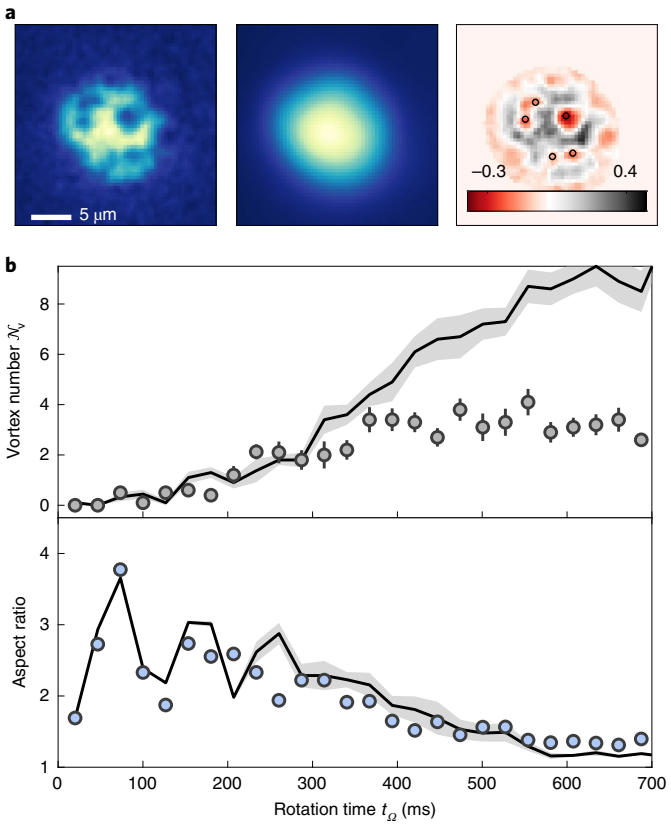

Fig. 3 | Time evolution of the average vortex number, $\mathcal{N}_v$, and cloud AR. a, Left: sample image after rotating for $t_\Omega = 474$ ms. Middle: blurred reference image ($\sigma = 2.1$ μm). Right: residuals with markers (black circles) indicating the identified vortices. **b**, The detected vortex number $\mathcal{N}_v$ (top) and the AR of the cloud (bottom) after the rotation time t_Ω. Data points and error bars show the mean and standard error from about ten experimental runs. Solid lines indicate the averaged results from ten corresponding simulations with different initial noise for parameters $a_s = 110a_0$, $(\omega_\perp, \omega_z) = 2\pi \times [50, 130]$ Hz, $N = 10{,}000$ and $\Omega = 0.75\omega_\perp$; the shaded area gives its standard error.

https://doi.org/10.1038/s41567-022-01793-8

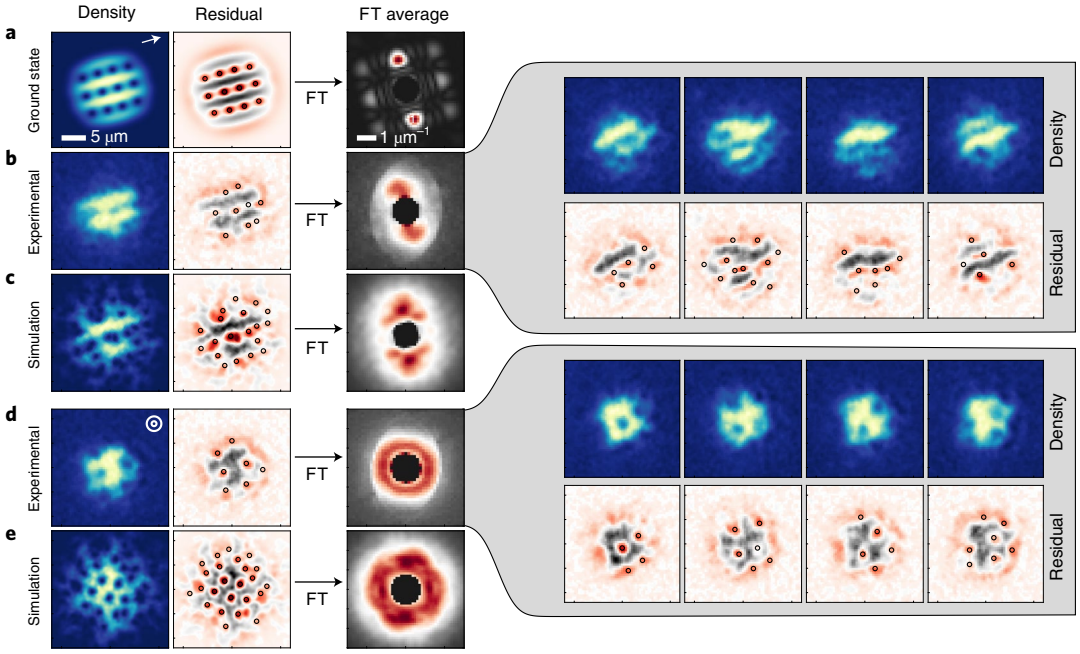

Fig. 4 | Stripe nature of vortices in a dipolar BEC. a, Left: ground-state stripe lattice solution for our experimental parameters $a_s = 109a_0$, trap frequencies $(\omega_\perp, \omega_z) = 2\pi \times [50, 130]$ Hz, $N = 10{,}000$ and $\Omega = 0.75\omega_\perp$. Middle: corresponding residual image, found by subtracting the ground state from the blurred image, with circles showing the detected vortices. Right: Fourier transform of the residual image. **b**, Left: single experimental image after 500 ms of continuous rotation at $\Omega = 0.75\omega_\perp$. Middle: the corresponding residual image. Right: Fourier transform of the residual images, averaged over 49 runs, with example shots shown to the right. **c**, Left: simulation result for the dynamic experimental procedure in **b**. Middle and right: residuals (middle) and FT analysis (right) (115 temporal images) as in **b**. **d**, The same as **b** for 121 runs, but we rotate for an additional 100 ms and then spiral the magnetic field to $\theta = 0°$ over a further 100 ms before imaging. **e**, Simulation result for procedure in **d**. All simulation images are rotated to have the same magnetic-field direction as the experiment, as indicated by the white arrow in **a** and by the circles in **d**.

Our observations bear a remarkable resemblance to the simulations; Fig. 2 (top) shows the in situ column densities. Taking a fixed atom number of $N = 8{,}000$, but otherwise repeating the experimental sequence, we observe many similar features. In the first 100 ms, the system elongates, consistent with Fig. 1, and a spiral density pattern appears before the instability, forming two arms that are filled with vortices close to the central density. Next, turbulent dynamics ensue as the density surface goes unstable and vortices emerge in the central high-density region. For this scattering length and atom number, the relaxation timescale to a stable vortex lattice is longer than the experimentally available (see Extended Data Fig. 3 for more images from this dataset). Note that at angles θ deeper into the plane, more atoms align head-to-tail in the loose radial confinement direction. Thus, when performing the rotation procedure, we find that the BEC is resilient to instability on the timescales of the experiment.

The observed evolution of the system under constant rotation shows some concurrence between the appearance of vortices in the absorption images and the formation of a round density pattern in the radial plane with AR ≈ 1 (Fig. 2). Note that the drop in AR observed in Fig. 1 is concurrent with the creation of vortices, but they reside in the low-density regions at this time, and we do not see them. To study this dynamical evolution in more detail, we adopt an analysis protocol for both the experiment and theory that allows us to quantitatively track the evolution of the average number of vortices, $\mathcal{N}_v$ (Methods). The result is shown in Fig. 3a. In brief, for each single image (Fig. 3a, left), we create a blurred reference image by applying a 2D Gaussian filter[56,57]. We then calculate the difference between each single image (Fig. 3a, left) and the corresponding reference (Fig. 3a, middle) to obtain the residual image (Fig. 3a, right), from which we count $\mathcal{N}_v$ by finding local minima below a certain threshold.

For the experimental density profiles, which are affected by both the limited resolution of the imaging system and the weak contrast in the low-density zones (halo) where the vortices initially nest, we expect $\mathcal{N}_v$ to be underestimated relative to the true value and the number expected by theory. However, to carry out a quantitative comparison with the simulations, we apply a blurring filter and add noise to the latter that mimics the actual resolution in the experiment (Methods).

Figure 3b shows both the evolution of $\mathcal{N}_v$ and cloud AR as a function of rotation time, t_Ω. Solid lines are the results from the eGPE simulations without any adjustable parameters. For $t_\Omega < 200$ ms, $\mathcal{N}_v$ is below 1, where vortices, if present, are at the edge of the cloud. For longer times, $\mathcal{N}_v$ increases and saturates to an average value of about three and a maximum of six vortices (see Fig. 3a for an example of five vortices). The observed saturation might be due to the decreased visibility and to the atom-loss-induced shrinking of the BEC size, which is not accounted for in the theory. We also compare the course of the average vortex number with the AR of the cloud. After initial large oscillations, due to the sudden jump in rotation frequency, the AR declines towards ~1 (ref. [53]). This happens as the vortex number simultaneously increases.

One fascinating prediction with vortices in a strongly dipolar gas under the influence of a rotating magnetic field relates to the structure of the resulting vortex lattice. Due to magnetostriction and the anisotropic vortex cores, the resulting vortex configuration is also anisotropic, producing a stripe phase in the strongly dipolar regime[29,30], instead of the usual triangular lattice in non-dipolar BECs[6]. The ground state stripe lattice solution for our parameters is shown in Fig. 4a, with a cloud AR = 1.08. In the vortex stripe phase, vertical planes of high-density regions, parallel to the magnetic field, alternate with low-density ones, which host rows of vertical vortex filaments. Such a configuration promotes head-to-tail dipolar attraction within the high-density ridges, and this acts to lower the energy. It should be noted that these states are distinct from the oscillating vortex sheets states, which appear after squeezing a triangular vortex lattice[58].

To explore this prediction, we perform two new surveys. First, we slightly reduce the magnetic-field value, reducing the scattering length to $a_s \approx 109a_0$ and hence making the system relatively more dipolar. We magnetostir the BEC at a constant rotation frequency $\Omega = 0.75\omega_\perp$ for 500 ms, but during TOF, we stop the magnetic-field rotation and keep it in place at $\theta = 35°$. The stripe structure is revealed in Fig. 4b (left) for a single experimental run and is clearly visible in the residual image (Fig. 4b, middle) where the vortices align along three stripes. The spatial structure of the residual image can be assessed through the absolute value of 2D Fourier transform (FT). After taking the FT of each residual image, we then average the result (Fig. 4b, right), finding a clear peak at the wave number k of the inter-stripe spacing. This shows that the stripe spatial structure survives the averaging, implying that the majority of images show stripes with the same spacing, and they also have the same orientation as set by the magnetic field, as evidenced by the example images shown in the right of Fig. 4. Note that these observations do not rely on our ability to resolve individual vortices, as the stripes are an ensemble effect of many aligned vortices. In fact, by comparing with the numerical simulations of the dynamical procedure (Fig. 4c), we expect there are more vortices than detected here that fill in the stripes, forging out this structure. In general, our simulations show that the stripes appear faster when the scattering length is lower and when the atom number is larger. In the long time limit of the scenario presented in Fig. 2, we expect the stationary solution to also be the stripe state, but this is not observable on our timescales.

Remarkably, the stripe structure washes out when we subsequently tilt the magnetic-field orientation to $\theta = 0°$ (parallel to the trap symmetry axis), as shown in Fig. 4d (left). Here, after 600 ms of magnetostirring, we add another step in which we spiral up the magnetic field to $\theta = 0°$ (with Ω fixed) over 100 ms, before imaging. Under these conditions, all vortex properties are again isotropic within the plane. The non-equilibrium positioning of the vortices is arbitrary, and if we average the FT of the residuals directly, we observe a homogeneous ring in the average FT (Fig. 4d, right). Also, this behaviour is confirmed by the simulations, as shown in Fig. 4e. The vortices survive long after the magnetostirring has stopped (not shown), due to their topological protection.

By exploiting magnetostirring—a novel, robust method of generating angular momentum—we have observed quantized vortices in a dipolar quantum gas and the appearance of the vortex stripe configuration. Future works will focus on investigations of the individual vortex shape and behaviour, such as the anisotropic nature of the vortex cores for in-plane magnetic fields[30–33], the interplay between the vortex and roton excitations[30–34] and exotic vortex patterns such as square lattices[29], and investigations into anisotropic turbulence[59]. This work also opens the door to studying more complex matter under rotation, such as dipolar droplets[60–62] and supersolid states[41–43,51]. Such proposals will be challenging due to the intricate density patterns[63]; however, such observations would provide conclusive evidence of superfluidity in supersolids. Rotating the magnetic field at frequencies far larger than the radial trap frequencies, but smaller than the Larmor frequency, has been observed to tune the sign and magnitude of the dipole–dipole interaction[64]—a method also employed in nuclear magnetic resonance spectroscopy—but there remain open questions on the stability of this procedure[65,66], which if rectifiable would unlock new research directions[64]. Other vortex generation methods, such as thermally activated pairs in quasi-two dimensions to assess the Berezinskii–Kosterlitz–Thouless transition and stochastically generated vortex tangles through temperature quenches to assess the Kibble–Zurek mechanism, remain unexplored in dipolar gases[29]. The technique introduced here is also applicable to a wide range of systems governed by long-range interactions through the manipulation of magnetic or electric fields.

Online content

Any methods, additional references, Nature Research reporting summaries, source data, extended data, supplementary information, acknowledgements, peer review information; details of author contributions and competing interests; and statements of data and code availability are available at https://doi.org/10.1038/s41567-022-01793-8.

References

1. Donnelly, R. J. *Quantized Vortices in Helium II* (Cambridge Univ. Press, 1991).
2. Pines, D. & Alpar, M. A. Superfluidity in neutron stars. *Nature* **316**, 27–32 (1985).
3. Abrikosov, A. A. Nobel Lecture: Type-II superconductors and the vortex lattice. *Rev. Mod. Phys.* **76**, 975 (2004).
4. Lagoudakis, K. G. et al. Quantized vortices in an exciton–polariton condensate. *Nat. Phys.* **4**, 706–710 (2008).
5. Matthews, M. R. et al. Vortices in a Bose–Einstein condensate. *Phys. Rev. Lett.* **83**, 2498 (1999).
6. Madison, K. W., Chevy, F., Wohlleben, W. & Dalibard, J. Vortex formation in a stirred Bose–Einstein condensate. *Phys. Rev. Lett.* **84**, 806 (2000).
7. Neely, T. W., Samson, E. C., Bradley, A. S., Davis, M. J. & Anderson, B. P. Observation of vortex dipoles in an oblate Bose–Einstein condensate. *Phys. Rev. Lett.* **104**, 160401 (2010).
8. Ku, M. J. H. et al. Motion of a solitonic vortex in the BEC–BCS crossover. *Phys. Rev. Lett.* **113**, 065301 (2014).
9. Donadello, S. et al. Observation of solitonic vortices in Bose–Einstein condensates. *Phys. Rev. Lett.* **113**, 065302 (2014).
10. Anderson, B. P. et al. Watching dark solitons decay into vortex rings in a Bose–Einstein condensate. *Phys. Rev. Lett.* **86**, 2926 (2001).
11. Abo-Shaeer, J. R., Raman, C., Vogels, J. M. & Ketterle, W. Observation of vortex lattices in Bose–Einstein condensates. *Science* **292**, 476–479 (2001).
12. Hadzibabic, Z., Krüger, P., Cheneau, M., Battelier, B. & Dalibard, J. Berezinskii–Kosterlitz–Thouless crossover in a trapped atomic gas. *Nature* **441**, 1118–1121 (2006).
13. Neely, T. W. et al. Characteristics of two-dimensional quantum turbulence in a compressible superfluid. *Phys. Rev. Lett.* **111**, 235301 (2013).
14. Navon, N., Gaunt, A. L., Smith, R. P. & Hadzibabic, Z. Emergence of a turbulent cascade in a quantum gas. *Nature* **539**, 72–75 (2016).
15. Zwierlein, M. W., Abo-Shaeer, J. R., Schirotzek, A., Schunck, C. H. & Ketterle, W. Vortices and superfluidity in a strongly interacting Fermi gas. *Nature* **435**, 1047–1051 (2005).
16. Lu, M., Burdick, N. Q., Youn, S. H. & Lev, B. L. Strongly dipolar Bose–Einstein condensate of dysprosium. *Phys. Rev. Lett.* **107**, 190401 (2011).
17. Aikawa, K. et al. Bose–Einstein condensation of erbium. *Phys. Rev. Lett.* **108**, 210401 (2012).
18. Norcia, M. A. & Ferlaino, F. Developments in atomic control using ultracold magnetic lanthanides. *Nat. Phys.* **17**, 1349–1357 (2021).
19. Chomaz, L. et al. Dipolar physics: a review of experiments with magnetic quantum gases. Preprint at https://arxiv.org/abs/2201.02672 (2022).
20. Baier, S. et al. Extended Bose–Hubbard models with ultracold magnetic atoms. *Science* **352**, 201–205 (2016).
21. Landau, L. Theory of the superfluidity of helium II. *Phys. Rev.* **60**, 356 (1941).
22. Chomaz, L. et al. Observation of roton mode population in a dipolar quantum gas. *Nat. Phys.* **14**, 442–446 (2018).
23. Schmidt, J.-N. et al. Roton excitations in an oblate dipolar quantum gas. *Phys. Rev. Lett.* **126**, 193002 (2021).
24. Kadau, H. et al. Observing the Rosensweig instability of a quantum ferrofluid. *Nature* **530**, 194–197 (2016).

25. Tanzi, L. et al. Observation of a dipolar quantum gas with metastable supersolid properties. *Phys. Rev. Lett.* **122**, 130405 (2019).
26. Böttcher, F. et al. Transient supersolid properties in an array of dipolar quantum droplets. *Phys. Rev. X* **9**, 011051 (2019).
27. Chomaz, L. et al. Long-lived and transient supersolid behaviors in dipolar quantum gases. *Phys. Rev. X* **9**, 021012 (2019).
28. Norcia, M. A. et al. Two-dimensional supersolidity in a dipolar quantum gas. *Nature* **596**, 357–361 (2021).
29. Martin, A. M., Marchant, N. G., O'Dell, D. H. J. & Parker, N. G. Vortices and vortex lattices in quantum ferrofluids. *J. Phys. Condens. Matter* **29**, 103004 (2017).
30. Yi, S. & Pu, H. Vortex structures in dipolar condensates. *Phys. Rev. A* **73**, 061602 (2006).
31. Ticknor, C., Wilson, R. M. & Bohn, J. L. Anisotropic superfluidity in a dipolar Bose gas. *Phys. Rev. Lett.* **106**, 065301 (2011).
32. Mulkerin, B. C., van Bijnen, R. M. W., O'Dell, D. H. J., Martin, A. M. & Parker, N. G. Anisotropic and long-range vortex interactions in two-dimensional dipolar Bose gases. *Phys. Rev. Lett.* **111**, 170402 (2013).
33. Mulkerin, B. C., O'Dell, D. H. J., Martin, A. M. & Parker, N. G. Vortices in the two-dimensional dipolar Bose gas. *J. Phys. Conf. Ser.* **497**, 012025 (2014).
34. Jona-Lasinio, M., Łakomy, K. & Santos, L. Roton confinement in trapped dipolar Bose–Einstein condensates. *Phys. Rev. A* **88**, 013619 (2013).
35. Gautam, S. Dynamics of the corotating vortices in dipolar Bose–Einstein condensates in the presence of dissipation. *J. Phys. B* **47**, 165301 (2014).
36. Cooper, N., Rezayi, E. & Simon, S. Vortex lattices in rotating atomic Bose gases with dipolar interactions. *Phys. Rev. Lett.* **95**, 200402 (2005).
37. Zhang, J. & Zhai, H. Vortex lattices in planar Bose–Einstein condensates with dipolar interactions. *Phys. Rev. Lett.* **95**, 200403 (2005).
38. Kumar, R. K., Sriraman, T., Fabrelli, H., Muruganandam, P. & Gammal, A. Three-dimensional vortex structures in a rotating dipolar Bose–Einstein condensate. *J. Phys. B* **49**, 155301 (2016).
39. Cai, Y., Yuan, Y., Rosenkranz, M., Pu, H. & Bao, W. Vortex patterns and the critical rotational frequency in rotating dipolar Bose–Einstein condensates. *Phys. Rev. A* **98**, 023610 (2018).
40. Prasad, S. B., Bland, T., Mulkerin, B. C., Parker, N. G. & Martin, A. M. Vortex lattice formation in dipolar Bose–Einstein condensates via rotation of the polarization. *Phys. Rev. A* **100**, 023625 (2019).
41. Roccuzzo, S. M., Gallemí, A., Recati, A. & Stringari, S. Rotating a supersolid dipolar gas. *Phys. Rev. Lett.* **124**, 045702 (2020).
42. Gallemí, A., Roccuzzo, S. M., Stringari, S. & Recati, A. Quantized vortices in dipolar supersolid Bose–Einstein-condensed gases. *Phys. Rev. A* **102**, 023322 (2020).
43. Ancilotto, F., Barranco, M., Pi, M. & Reatto, L. Vortex properties in the extended supersolid phase of dipolar Bose–Einstein condensates. *Phys. Rev. A* **103**, 033314 (2021).
44. Prasad, S. B., Mulkerin, B. C. & Martin, A. M. Arbitrary-angle rotation of the polarization of a dipolar Bose–Einstein condensate. *Phys. Rev. A* **103**, 033322 (2021).
45. Stuhler, J. et al. Observation of dipole–dipole interaction in a degenerate quantum gas. *Phys. Rev. Lett.* **95**, 150406 (2005).
46. Haljan, P. C., Coddington, I., Engels, P. & Cornell, E. A. Driving Bose–Einstein condensate vorticity with a rotating normal cloud. *Phys. Rev. Lett.* **87**, 210403 (2001).
47. Kwon, W. J. et al. Sound emission and annihilations in a programmable quantum vortex collider. *Nature* **600**, 64–69 (2021).
48. Corman, L. et al. Quench-induced supercurrents in an annular Bose gas. *Phys. Rev. Lett.* **113**, 135302 (2014).
49. Liu, I. K. et al. Dynamical equilibration across a quenched phase transition in a trapped quantum gas. *Commun. Phys.* **1**, 24 (2018).
50. Del Pace, G. et al. Imprinting persistent currents in tunable fermionic rings. Preprint at https://arxiv.org/abs/2204.06542 (2022).
51. Norcia, M. A. et al. Can angular oscillations probe superfluidity in dipolar supersolids? *Phys. Rev. Lett.* **129**, 040403 (2022).
52. Recati, A., Zambelli, F. & Stringari, S. Overcritical rotation of a trapped Bose–Einstein condensate. *Phys. Rev. Lett.* **86**, 377 (2001).
53. Madison, K. W., Chevy, F., Bretin, V. & Dalibard, J. Stationary states of a rotating Bose–Einstein condensate: routes to vortex nucleation. *Phys. Rev. Lett.* **86**, 4443 (2001).
54. Wächtler, F. & Santos, L. Quantum filaments in dipolar Bose–Einstein condensates. *Phys. Rev. A* **93**, 061603 (2016).
55. Sinha, S. & Castin, Y. Dynamic instability of a rotating Bose–Einstein condensate. *Phys. Rev. Lett.* **87**, 190402 (2001).
56. Abo-Shaeer, J. R., Raman, C. & Ketterle, W. Formation and decay of vortex lattices in Bose–Einstein condensates at finite temperatures. *Phys. Rev. Lett.* **88**, 070409 (2002).
57. Kwon, W. J., Moon, G., Choi, J.-y, Seo, S. W. & Shin, Y.-i Relaxation of superfluid turbulence in highly oblate Bose–Einstein condensates. *Phys. Rev. A* **90**, 063627 (2014).
58. Engels, P., Coddington, I., Haljan, P. C. & Cornell, E. A. Nonequilibrium effects of anisotropic compression applied to vortex lattices in Bose–Einstein condensates. *Phys. Rev. Lett.* **89**, 100403 (2002).
59. Bland, T., Stagg, G. W., Galantucci, L., Baggaley, A. W. & Parker, N. G. Quantum ferrofluid turbulence. *Phys. Rev. Lett.* **121**, 174501 (2018).
60. Cidrim, A., dos Santos, F. E., Henn, E. A. & Macrì, T. Vortices in self-bound dipolar droplets. *Phys. Rev. A* **98**, 023618 (2018).
61. Lee, A.-C., Baillie, D., Bisset, R. N. & Blakie, P. B. Excitations of a vortex line in an elongated dipolar condensate. *Phys. Rev. A* **98**, 063620 (2018).
62. Ferrier-Barbut, I. et al. Scissors mode of dipolar quantum droplets of dysprosium atoms. *Phys. Rev. Lett.* **120**, 160402 (2018).
63. Hertkorn, J. et al. Pattern formation in quantum ferrofluids: from supersolids to superglasses. *Phys. Rev. Res.* **3**, 033125 (2021).
64. Tang, Y., Kao, W., Li, K.-Y. & Lev, B. L. Tuning the dipole–dipole interaction in a quantum gas with a rotating magnetic field. *Phys. Rev. Lett.* **120**, 230401 (2018).
65. Prasad, S. B. et al. Instability of rotationally tuned dipolar Bose–Einstein condensates. *Phys. Rev. Lett.* **122**, 050401 (2019).
66. Baillie, D. & Blakie, P. B. Rotational tuning of the dipole–dipole interaction in a Bose gas of magnetic atoms. *Phys. Rev. A* **101**, 043606 (2020).

Methods

Experimental procedure

We prepare an ultracold gas of ^{162}Dy atoms in an ODT. Three 1,064 nm laser beams, overlapping at their foci, form the ODT. The experimental procedure to BEC is similar to the one followed in our previous work[51], but the magnetic-field unit vector, $\hat{\mathrm{B}}$, is tilted by an angle of $\theta = 35°$ with respect to the z-axis during the whole sequence. After preparation, the sample contains about 2×10^4 condensed atoms. The corresponding trap frequencies are typically $(\omega_\perp, \omega_z) = 2\pi \times [50.8(2), 140(1)]$ Hz. For all our measurements, the deviation of the trap AR in the x–y plane $\mathrm{AR}_{\mathrm{trap}} = \omega_y/\omega_x$ from 1 is always smaller than 0.6%. We evaporate the atoms at $B = 5.423(5)$ G and jump to the final magnetic-field value during the last evaporation ramp. After the preparation of the BEC, the magnetic field is rotated as described in the next section. We use standard absorption imaging to record the atomic distribution. We probe the vortices using the vertical imaging taken along the axis of rotation (z), for which the dark spots within the condensate correspond to the cores of individual vortices. The vertical images are taken with a short TOF of 3 ms and a pulse duration of 3–4 μs. For the data in Figs. 1–3, we let the magnetic-field spinning during TOF, whereas for Fig. 4, we use a static field orientation.

Control of the magnetic field

Calibration. Three pairs of coils—each oriented along a primary axis in the laboratory frame—enable the creation of a homogeneous field with arbitrary orientations. The absolute magnetic-field value B of each pair of coils is independently calibrated using radio frequency (RF) spectroscopy. The RF drives transitions to excited Zeeman states, leading to a resonant dip in the atom number. The long-term stability—measured via the peak position of the RF resonance over the course of several days—is on the order of $\Delta B = \pm 1$ mG, while shot-to-shot fluctuations, measured via the width of the RF resonance for a single calibration set, is $\Delta B = \pm 5$ mG.

Rotation. We drive the rotation of the magnetic field by sinusoidally modulating the magnetic-field value components B_x and B_y with a phase difference of 90° between them. As we want to keep the absolute magnetic-field value B constant during rotation, we measure it for various values of the azimuthal angle ϕ and fixed $\theta = 35°$ by performing Feshbach loss spectroscopy around 5.1 G. We find an average shift of B of about 10 mG from the $\theta = 0°$ case, which we take into account. We also find small deviations as a function of ϕ of $\Delta B < 20$ mG, which might appear due to slightly non-orthogonal alignment of the magnetic fields. We did not correct these deviations for the sake of simplicity.

Scattering length

The scattering length in ^{162}Dy is currently not known with large accuracy[67–70]. To estimate the scattering length in the small magnetic-field range around $B = 5.3$ G, relevant to this work, we use the well-known relation $a_s = a_{bg}\prod_i[1 - \Delta B_i/(B - B_{0,i})]$ (ref. [71]), where $B_{0,i}$ and ΔB_i are the centre position and the width of the i-th feature of the Feshbach loss measurement reported in ref. [70], respectively. The value of the background scattering length, a_{bg}, is empirically fixed by measuring the magnetic-field value at which the supersolid transition occurs and comparing it with the corresponding critical a_s predicted from simulations. Such an approach leads to $a_s = 111(9)a_0$ at $B = 5.333$ G. Extended Data Fig. 1 shows the resulting scattering lengths for the relevant magnetic fields. Although such an approach gives very good agreement between theory and experiments, future works on a precise determination of a_s, similar to the one achieved with erbium[72], would be desirable.

Magnetostirring

Tilting the magnetic-field vector **B** away from the symmetry axis of our cylindrical trap leads to an ellipsoidal deformation of the cloud[45] and therefore to a breaking of the cylindrical symmetry. This allows for the transfer of angular momentum to the sample by rotating the magnetic field (magnetostirring). In all our measurements, we use a **B** tilted with respect to the z axis by 35° and a constant value B. That value is $B = 5.333(5)$ G for the surveys in Figs. 1–3 and $B = 5.323(5)$ G for Fig. 4. For these parameters, the deformed magnetostricted AR of the cloud is AR − 1 = 0.03. For all our measurements, the measured trap $\mathrm{AR}_{\mathrm{trap}} - 1 < 0.006$ is much smaller than the deformation due to magnetostriction. Additionally, we have confirmed with simulations that even with trap asymmetries of up to 10%, for example, $(\omega_x, \omega_y) = (55, 50)$ Hz, this procedure can still generate vortices in a lattice configuration.

At the scattering lengths considered in this work, 35° is an optimal choice to see the vortices within ~500 ms of rotation and anisotropic enough to observe the stripe phase. From the simulations, we find that tilt angles smaller than 35° increase the timescale to vortex nucleation. Similarly, tilting the angle further into the plane increases the number of atoms that are aligned head to tail, making the dipolar interaction dominantly attractive. This attractive force holds the condensate together during the rotation, also increasing the time to vortex nucleation. From the experimental side, increasing the tilt angle reduces the contrast of the absorption imaging, since the magnetic field is not parallel to the imaging axis. As the TOF is only 3 ms, we do not rotate up the magnetic field before imaging to avoid undesired effects, such as losing the anisotropy given by $\theta \neq 0°$.

Adiabatic frequency ramp. We employ different magnetic-field rotation sequences for the different datasets. For the dataset of Fig. 1c, the rotation frequency of the magnetic field is linearly increased to different final values at a speed of $\dot{\Omega} = 2\pi \times 50\,\mathrm{Hz\,s^{-1}}$ and for a duration of $t_{\dot{\Omega}} = 0$–1 s. The ramp time is much longer than the period of the rotation Ω^{-1} for higher rotation frequencies $\Omega \gtrsim \Omega_c$, and, therefore, the ramp is adiabatic for the regimes considered, until the onset of dynamical instabilities. After the ramp, the magnetic-field direction is rotated at the target rotation frequency Ω for one final period (as shown in Fig. 1b). We sample ten different final magnetic-field angles during this last rotation, measuring the corresponding AR and averaging the result to remove any potential biases due to latent trap anisotropies. Each data point is then obtained with eight to ten experimental runs.

Constant rotation frequency. For the dataset of Figs. 2, 3 and 4b, we directly start to rotate at the final rotation frequency Ω without any acceleration phase. The magnetic field is then rotated for a variable time t_Ω, after which the atoms are released from the trap and a vertical image is taken.

Spiral up magnetic field. For the dataset of Fig. 4d, we employ a similar sequence as described above. However, after constantly rotating the magnetic field at $\Omega = 0.75\omega_\perp$, the magnetic field is spiralled up in 100 ms to $\theta = 0°$ by linearly reducing θ while continuing rotating. Afterwards, the atoms are released from the trap and a vertical image is taken.

Theoretical model

We employ an eGP formalism to model our experimental set-up. In this scheme, the inter-particle interactions are described by the two-body pseudo-potential

$$U(\mathbf{r}) = \frac{4\ \hbar^2 a_s}{m}\delta(\mathbf{r}) + \frac{3\hbar^2 a_{dd}}{m}\frac{1 - 3(\hat{\mathbf{e}}(t)\cdot\mathbf{r})^2}{r^3}, \quad (1)$$

with $\delta(\mathbf{r})$ being the Kronecker delta function and $\mathbf{r} = (x, y, z)$. The first term describes the short-range interactions governed by the s-wave scattering length a_s, with Planck's constant $\hbar$ and particle mass m. The second term represents the anisotropic and long-range dipole–dipole interactions, characterized by dipole length $a_{dd} = \mu_0\mu_m^2 m/12\ \hbar^2$, with magnetic moment μ_m and vacuum permeability μ_0. We always consider ^{162}Dy, such that $a_{dd} = 129.2a_0$, where a_0 is the Bohr radius.

The dipoles are polarized uniformly along a time-dependent axis, given by

$$\hat{\mathbf{e}}(t) = (\sin\theta(t)\cos\phi(t), \sin\theta(t)\sin\phi(t), \cos\theta(t)) \quad (2)$$

with time-dependent polarization angle $\theta(t)$ and $\phi(t) = \int_0^t \mathrm{d}t'\Omega(t')$, for rotation frequency protocol $\Omega(t)$.

Beyond-mean-field effects are treated through the inclusion of a Lee–Huang–Yang correction term[73]

$$\gamma_{\mathrm{QF}} = \frac{128\hbar^2}{3m}\sqrt{a_s^5}\,\mathrm{Re}\{Q_5(\epsilon_{\mathrm{dd}})\}, \quad (3)$$

with $Q_5(\epsilon_{\mathrm{dd}}) = \int_0^1 \mathrm{d}u\,(1-\epsilon_{\mathrm{dd}}+3u^2\epsilon_{\mathrm{dd}})^{5/2}$ being the auxiliary function, and the relative dipole strength is given by $\epsilon_{\mathrm{dd}} = a_{\mathrm{dd}}/a_s$. Finally, the full eGPE then reads[54,74–76]

$$i\hbar\frac{\partial\Psi(\mathbf{x},t)}{\partial t} = \Big[-\frac{\hbar^2\nabla^2}{2m} + \frac{1}{2}m\left(\omega_x^2x^2+\omega_y^2y^2+\omega_z^2z^2\right) + \int \mathrm{d}^3\mathbf{x}'\,U(\mathbf{x}-\mathbf{x}')|\Psi(\mathbf{x}',t)|^2 + \gamma_{\mathrm{QF}}|\Psi(\mathbf{x},t)|^3\Big]\Psi(\mathbf{x},t), \quad (4)$$

where $\omega_{x,y,z}$ are the harmonic trap frequencies. The wave function Ψ is normalized to the total atom number $N = \int \mathrm{d}^3\mathbf{x}|\Psi|^2$. The stationary solution for Fig. 4a is found through the imaginary time procedure in the rotating frame, introducing the usual angular momentum operator $\Omega\hat{L}_z$ into equation (4). The initial state $\Psi(\mathbf{x}, 0)$ of the real-time simulations is always obtained by adding non-interacting noise to the ground state $\Psi_0(\mathbf{x})$. Given the single-particle eigenstates ϕ_n and the complex Gaussian random variables α_n sampled with $\langle|\alpha_n|^2\rangle = (e^{\epsilon_n/k_BT}-1)^{-1}+\frac{1}{2}$ for a temperature $T = 20$ nK and Boltzmann's constant k_B, the initial state can be described as $\Psi(\mathbf{x},0) = \Psi_0(\mathbf{x}) + \sum_n{}'\alpha_n\phi_n(\mathbf{x})$, where the sum is restricted only to the modes with $\epsilon_n \le 2k_BT$ (ref. [77]). Throughout, the density images are presented in situ, with a scaling factor to account for the 3 ms TOF for the experimental images.

To obtain the average residual FT images for Fig. 4c,e, we first Fourier transform 115 frames from the simulation between 700 ms and 1.1 s in the rotating frame before averaging the result.

Atom number

Extended Data Fig. 2 shows the condensed atom number N_c for the measurement with an adiabatic ramp of the magnetic-field rotational velocity ($\dot{\Omega} = 2\pi \times 50\,\mathrm{Hz\,s^{-1}}$), corresponding to the data of Fig. 1c. Three-body losses are negligible in the low-density BEC phase, with losses probably coming from imperfections in the rotation procedure and heating. To extract the atom number, we use the horizontal imaging with 26 ms of TOF. About 3 ms before flashing the imaging resonant light to the atoms, we rotate the magnetic field in the imaging plane and perform standard absorption imaging. From the absorption images, we extract N_c from a bimodal fit up to 700 ms. At later times, the system undergoes a dynamic instability (see discussion in the main text), and the density profile deviates from a simple bimodal distribution. During the observation time, we see a slight decrease of N_c, and for our theory simulations, we use a constant atom number of $N_c = 15{,}000$. Note that in all following datasets, in which we abruptly accelerate the magnetic-field rotation to the desired final velocity, we observe a faster decay, and our simulations are performed with either $N_c = 8{,}000$ or $N_c = 10{,}000$.

Vortex detection

Vortex detection algorithm. Since vortices appear as dark holes in the density profile of a BEC, which would otherwise have a smooth profile, our approach to extract the number of vortices is to look at deviations between the image and an unmodulated reference image. To extract the vortex number from the raw images, we proceed as follows.

First, we prepare the image n_{img}, the reference image n_{ref} and the residual image n_{res}. The image is normalized such that the maximum density $\max(n_{\mathrm{img}}) = 1$. We create the reference image by blurring the image via applying a 2D Gaussian filter with $\sigma = 5$ pixel, corresponding to about 2.1 µm. This blurring smoothens any structure on the length-scale of the filter width; therefore, any holes in the density profile wash out. We then normalize the atom number of the reference to be the same as from the image $N_{\mathrm{ref}} = \iint n_{\mathrm{ref}} \doteq N_{\mathrm{img}} = \iint n_{\mathrm{img}}$. The residual image is calculated as the difference between the image and the reference $n_{\mathrm{res}} = n_{\mathrm{img}} - n_{\mathrm{ref}}$. We additionally mask the region where the density of the reference is below a certain threshold ($n_{\mathrm{res}} = 0$, where $n_{\mathrm{ref}} \le 0.1$).

Second, we identify local minima in the residual image and determine whether they are connected to vortices. For this, we create a list of local minima $(x_{\min}, y_{\min})$, defined by the condition that the pixel density $n_{\mathrm{res}}(x_{\min}, y_{\min})$ is lower than of all surrounding pixels. Then we remove minima with density values above zero $n_{\mathrm{res}}(x_{\min}, y_{\min}) \ge 0$ or which are within one pixel distance of the mask border. Now we determine a local contrast for each minimum by calculating the difference between its central density value and the mean of the density values ± 2 pixel values away from it $n_{\mathrm{con}}(x_{\min}, y_{\min}) = n_{\mathrm{res}}(x_{\min}, y_{\min}) - \mathrm{mean}(n_{\mathrm{res}}(x_{\min} \pm 2\,\mathrm{px}, y_{\min} \pm 2\,\mathrm{px}))$, and remove minima above a certain threshold $n_{\mathrm{con}} > -0.11$. As a last step, we check the distance d between all remaining minima to avoid double counting of minima too close to each other. In case d is below the threshold $d < 5$ pixel, the minimum with the higher residual density value n_{res} is discarded.

Preparation of theory density profiles. For the direct comparison of the vortex number shown in Fig. 3b, we apply additional steps to the density profiles obtained from theory. First, we reduce the resolution by a 2 × 2 binning to make the pixel size of the theory density profiles $n_{\mathrm{img}}^{\mathrm{theo}}$ essentially the same as for the experimental images (sizes are within 5%). After normalizing to $\max(n_{\mathrm{img}}^{\mathrm{theo}}) = 1$, we apply Gaussian white noise with zero mean and a variance of 0.01 to each pixel, recreating the noise pattern from empty regions of experimental images. Then we blur the image using a 2D Gaussian filter with $\sigma = 1$ pixel (~0.42 µm); this recreates the same resolution condition as our experimental set-up. The resulting density profile is taken as the input image for the vortex detection algorithm described above.

Benchmarking the vortex detection algorithm. As the vortex positions for the simulation images are known a priori due to the available phase map, we can derive the fidelity of the vortex detection algorithm for simulation data. For the theory data shown in Fig. 3b in the time frame between 600 and 700 ms, the average detected vortex number in the simulated density profiles (applying the preparation scheme described above) is about 9, while the real number of vortices present in the same area of the image is about 33 in average. This mismatch is explained by the conservative choice of the thresholds for vortex detection together with the added noise, which results in only counting clear density dips as vortices, throwing out many vortices in the low-density region. This conservative choice of thresholds on the other hand leads to a very high fidelity of >97%, where we define the fidelity as the percentage of detected vortices that correspond to actual present vortices in the data. For raw simulation data (without resolution reduction, added noise and blurring), the vortex detection algorithm would detect up to 80% of the vortices present with a fidelity of >95%.

Note that for the visualization of the vortex positions for Fig. 4, we slightly increased the local threshold $n_{\mathrm{con}} > -0.08$ and decreased the minimum distance between vortices $d < 3$ pixel, which increases the overall number of vortices detected. For the density distributions obtained from theory, we additionally omit the resolution reduction, addition of noise and blurring steps.

Data availability

Data pertaining to this work can be found at https://doi.org/10.5281/zenodo.7019859.

Code availability

The codes that support the findings of this study are available from the corresponding author upon reasonable request.

References

67. Tang, Y., Sykes, A., Burdick, N. Q., Bohn, J. L. & Lev, B. L. s-wave scattering lengths of the strongly dipolar bosons ^{162}Dy and ^{164}Dy. *Phys. Rev. A* **92**, 022703 (2015).
68. Tang, Y. et al. Anisotropic expansion of a thermal dipolar Bose gas. *Phys. Rev. Lett.* **117**, 155301 (2016).
69. Lucioni, E. et al. Dysprosium dipolar Bose–Einstein condensate with broad Feshbach resonances. *Phys. Rev. A* **97**, 060701 (2018).
70. Böttcher, F. et al. Dilute dipolar quantum droplets beyond the extended Gross–Pitaevskii equation. *Phys. Rev. Res.* **1**, 033088 (2019).
71. Chin, C., Grimm, R., Julienne, P. & Tiesinga, E. Feshbach resonances in ultracold gases. *Rev. Mod. Phys.* **82**, 1225 (2010).
72. Patscheider, A. et al. Determination of the scattering length of erbium atoms. *Phys. Rev. A* **105**, 063307 (2022).
73. Lima, A. R. P. & Pelster, A. Quantum fluctuations in dipolar Bose gases. *Phys. Rev. A* **84**, 041604 (2011).
74. Ferrier-Barbut, I., Kadau, H., Schmitt, M., Wenzel, M. & Pfau, T. Observation of quantum droplets in a strongly dipolar Bose gas. *Phys. Rev. Lett.* **116**, 215301 (2016).
75. Chomaz, L. et al. Quantum-fluctuation-driven crossover from a dilute Bose–Einstein condensate to a macrodroplet in a dipolar quantum fluid. *Phys. Rev. X* **6**, 041039 (2016).
76. Bisset, R. N., Wilson, R. M., Baillie, D. & Blakie, P. B. Ground-state phase diagram of a dipolar condensate with quantum fluctuations. *Phys. Rev. A* **94**, 033619 (2016).
77. Blakie, P., Bradley, A., Davis, M., Ballagh, R. & Gardiner, C. Dynamics and statistical mechanics of ultra-cold Bose gases using c-field techniques. *Adv. Phys.* **57**, 363–455 (2008).

Acknowledgements

We are grateful to S. B. Prasad, M. Norcia, R. M. W. van Bijnen and L. Santos for helpful discussions. We acknowledge M. Norcia and A. Patscheider for experimental contributions. This study received support from the European Research Council through the Consolidator Grant RARE (No. 681432), the QuantERA grant MAQS by the Austrian Science Fund FWF (No. I4391-N), and the DFG/FWF via FOR 2247/PI2790 a joint-project grant from the FWF (No. I4426). M. J. M. acknowledges support through an ESQ Discovery grant by the Austrian Academy of Sciences. We also acknowledge the Innsbruck Laser Core Facility, financed by the Austrian Federal Ministry of Science, Research and Economy. Part of the computational results presented have been achieved using the HPC infrastructure LEO of the University of Innsbruck. G. L. acknowledges financial support from Provincia Autonoma di Trento.

Author contributions

L.K., C.P., G.L., E.C., M.J.M. and F.F. performed the experimental work and data analysis. E.P., T.B. and R.N.B. performed the theoretical work. All authors contributed to the interpretation of the results and the preparation of the manuscript.

Competing interests

The authors declare no competing interests.

Additional information

Extended data is available for this paper at https://doi.org/10.1038/s41567-022-01793-8.

Supplementary information The online version contains supplementary material available at https://doi.org/10.1038/s41567-022-01793-8.

Correspondence and requests for materials should be addressed to Francesca Ferlaino.

Peer review information *Nature Physics* thanks Oliver Gorceix, Han Pu and the other, anonymous, reviewer(s) for their contribution to the peer review of this work.

https://doi.org/10.1038/s41567-022-01793-8

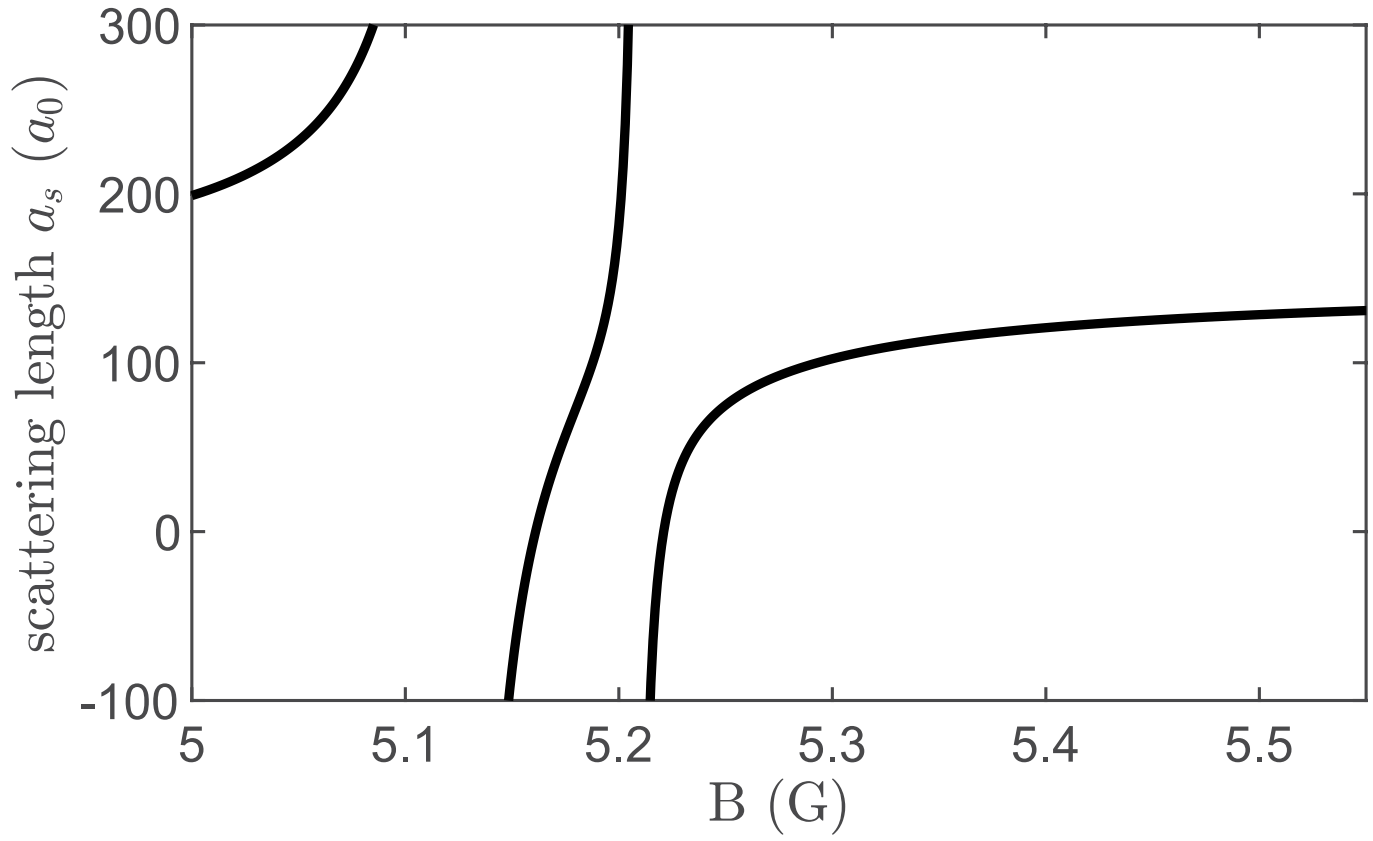

Extended Data Fig. 1 | Calculated B-to-a_s conversion for ^{162}Dy. Scattering length as a function of the magnetic-field value with the background scattering length $a_{bg} = 129(9)\ a_0$. We find $a_s = 111(9)\ a_0$ at $B = 5.333$ G.

https://doi.org/10.1038/s41567-022-01793-8

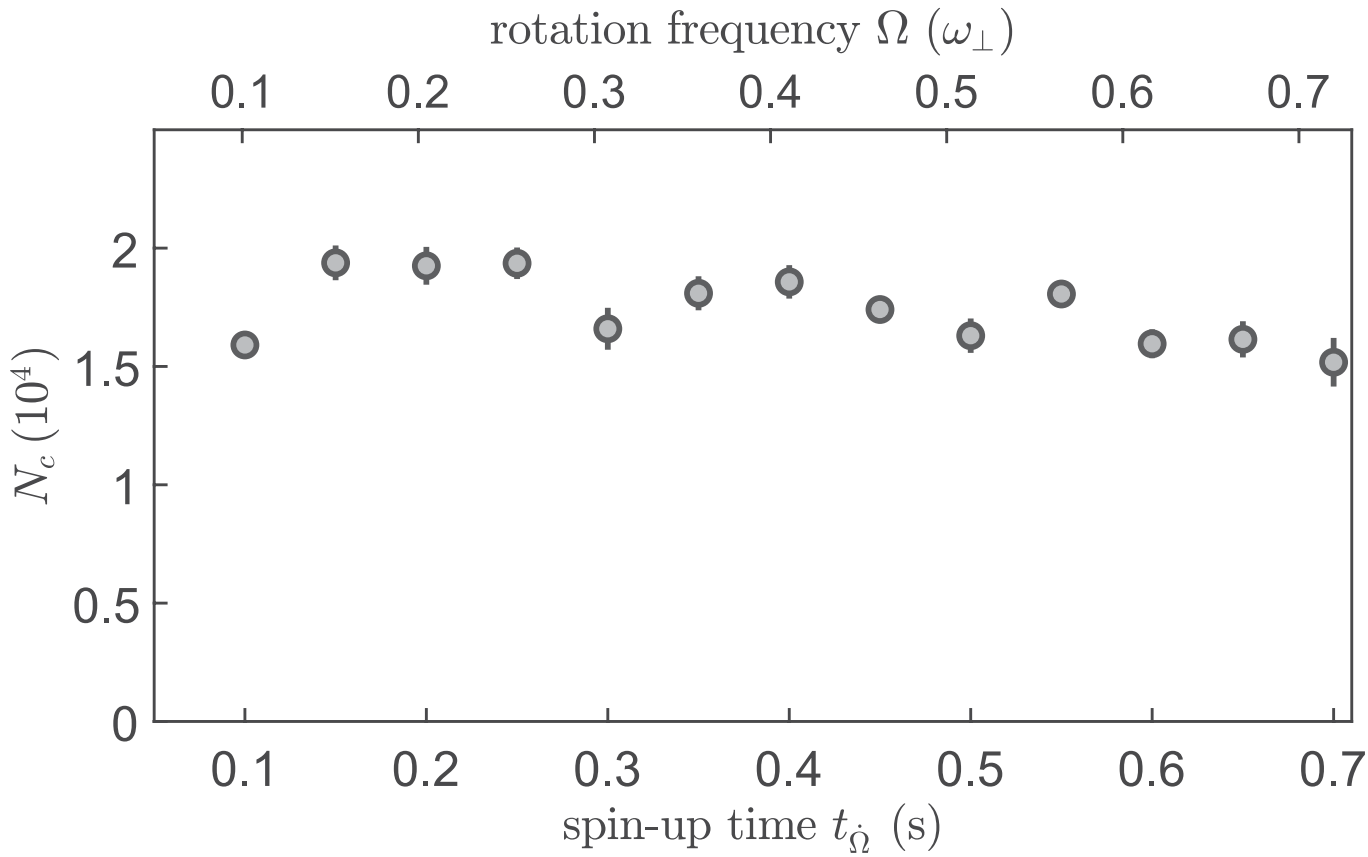

Extended Data Fig. 2 | Condensed atom number N_c during magnetostirring (Fig. 1c). Condensed atom number as a function of spin-up time $t_{\dot{\Omega}}$ for the same sequence as in Fig. 1c. The condensed atom number is extracted by fitting a two-dimensional bimodal distribution of Thomas-Fermi and Gaussian function to the horizontal density distributions.

https://doi.org/10.1038/s41567-022-01793-8

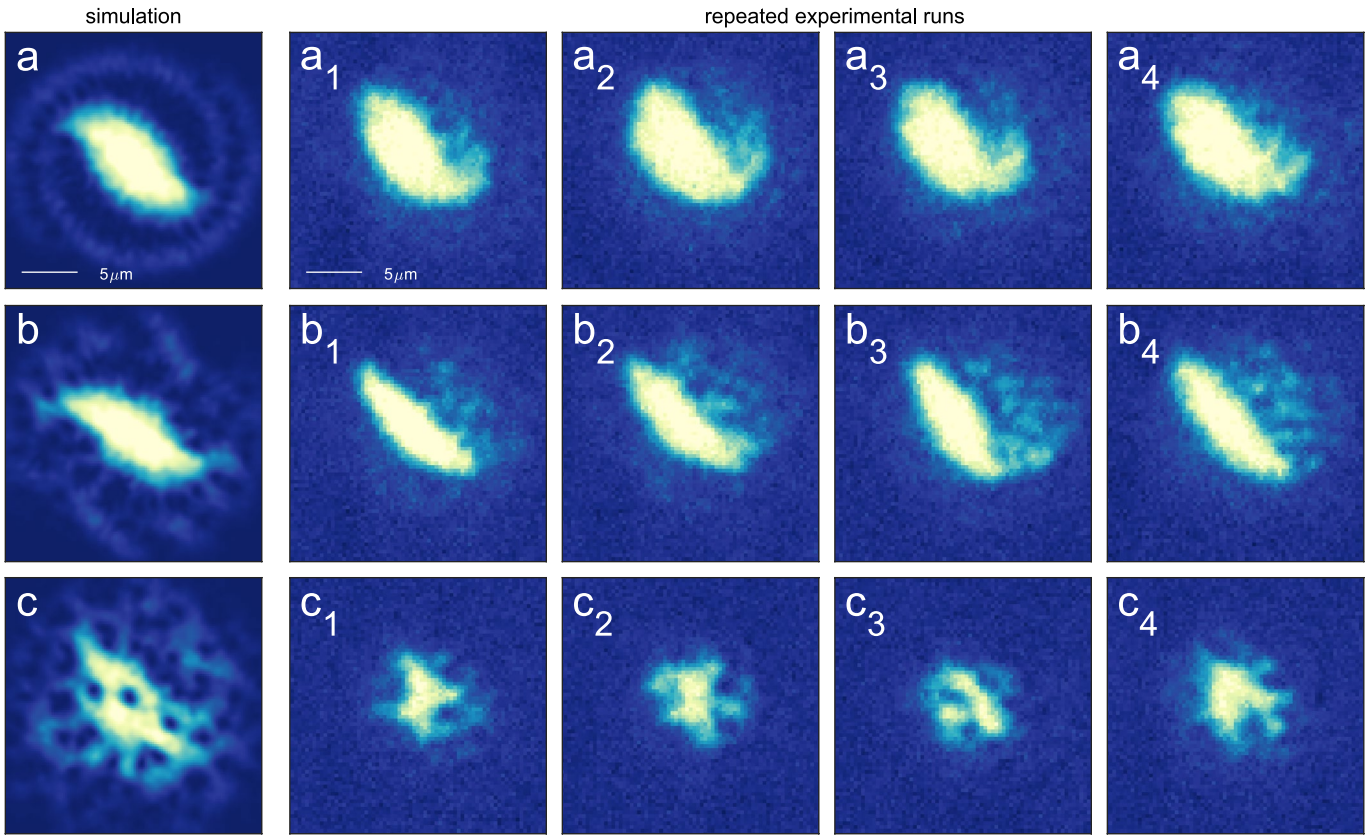

Extended Data Fig. 3 | Repeatability of the vortex generation protocol. Each row shows the simulated image (**a, b, c**) and the corresponding vertical TOF images from independent experimental runs (a_i, b_i, c_i) for a different rotation time: t_a = 127 ms, t_b = 207 ms, and t_c = 741 ms. The rotation frequency is $\Omega = 0.74\omega_\perp$ with the trap frequencies being $\omega_t = 2\pi \times [50.7(1), 50.8(1), 129(1)]$ Hz. The magnetic field value is $B = 5.333(5)$ G. For the simulation the scattering length used is 112 a_0, the trap frequencies are (50, 50, 150) Hz, the condensed atom number is $N = 8000$ and the rotation frequency is $0.75\omega_\perp$.

Acknowledgments

I take now the opportunity to acknowledge all the people that contributed to making this PhD thesis possible.

First, I would like to thank my supervisor *Francesca Ferlaino* for giving me the opportunity to do my PhD in a stimulating and productive environment, such as the Er-Dy lab in Innsbruck. I appreciate her trust in me since I first joined the team for my master's project in 2016. She always tried to get out the best of me, constantly setting the bar higher, and I am really grateful for all the feedback regarding this thesis work and my future research directions.

Such a complex experiment does not run so effectively without the help of everybody and a strong team effort. Therefore, if I got to this point, it is also thanks to my lab colleagues. When I joined the lab for my PhD studies in January 2018, we were at the stage of producing double degenerate mixtures of Er and Dy, and I had the great opportunity to learn from former PhD students and postdocs. In particular, I would like to thank *Philipp Ilzhöfer* (1st PhD student) for transferring part of his great knowledge about optics and laser systems, and the importance of TIGHTLY screwing optics on the experimental table. I thank *Gianmaria Durastante* (2nd PhD student) for teaching me the tricks on water cooling and how to dive into the experimental security system. I thank *Maximilian Sohmen* (3rd PhD student) for his incredible attitude in always finding the time to help people in the lab, and for his natural love for science. I enjoyed the time spent together implementing the phase-contrast imaging. I thank *Arno Trautmann* (1st postdoc) for sharing his knowledge about electronics, including soldering, Arduino®, and LaTeX. I also thank *Matthew Norcia* (2nd postdoc), who joined the experiment in 2020, and with whom I had a really great time in the lab. He joined during the corona pandemic, which was not an easy time. Nevertheless, he did a great job at maintaining a strong team spirit, sometimes leading to outdoor lunch in the snow with freezing temperatures. I appreciate his way of having always an intuitive physical picture and his ability in finding the most efficient path to reach the goal.

I want to thank the current PhD students: *Lauritz Klaus*, *Eva Casotti*, and the newly arrived *Clemens Ulm*. I really enjoyed the cold winter months spent in the lab with Lauritz to get the first two-dimensional supersolid states, and I thank him for always starting the day with a smile. I also thank Eva for always challenging herself and facing the lab's riddles without fear. I am sure the lab is in good hands and will continue to produce fascinating results in the years to come. I thank our senior scientist *Manfred Mark* for all the helpful discussions and for always finding the time to help in the lab if needed. I also thank him for the feedback on part of this thesis. A particular thanks goes to the theory group with *Thomas Bland*, and *Elena Poli*. Your theoretical support and your love and dedication to science were an amazing help for us and the results we had in the experiment would not have been possible without your contribution. I further thank Tom for reading part of this work.

I would also like to thank the master students that worked in the Er-Dy experiment, especially *Sandra Brandstetter* and *Nefeli Sonnberger*, and the other two labs of our dipolar quantum gas group, namely the ERBIUM and the T-REQS, including current and former members. In particular, I would like to thank *Daniel Petter*, *Alexander Patscheider*, *Lauriane Chomaz*, *Gabriele Natale*, *Louis Lafforgue*, *Arfor Houwman*, *Hagai Edri*, *Antonio Ortu*, *Julián Maloberti*, *Samuel White*, *Daniel Grün*, for the interesting discussions and for the time spent outside the lab, including our cooking evenings at Dani's place, bouldering, mountain biking, or a simple beer in the evening.

During the past five years, we had several collaborations with external groups. In particular, I would like to thank *Michele Modugno* from the University of the Basque Country in Bilbao (Spain), with whom I exchanged an uncountable number of emails. I thank *Thomas Pohl* and *Juan Sánchez Baena* from Aarhus University (Denmark), *Luis Santos* from the University of Hannover, and *Russell Bisset* from Innsbruck, for the inspiring discussions. In addition, I would like to acknowledge the support from my co-supervisor *Prof. Helmut Ritsch*.

Our dipolar quantum gas group is part of the big ultracold group in Innsbruck. Therefore, I thank all of them and in particular, I would like to thank *Emil Kirilov*, *Prof. Rudolf Grimm*, and *Prof. Hanns-Christoph Nägerl* for the interesting discussions and questions during our Thursday group seminar.

A special thanks goes to *Elisa Soave*, *Lorenzo Dania*, *Cornee Ravensbergen*, *Cosetta Baroni*, *Deborah Capecchi*, and *Elvia Colella* for the nice time spent inside and outside the university. I will always remember our nice weekend dinners, and the day spent preparing an uncountable amount of cherry jam.

A big thanks goes to the administrative support at the University of Innsbruck and the Institute for Quantum Optics and Quantum Information (IQOQI). In particular, my thanks go to *Silvia Bonazza*, *Leonarda Garcia*, and *Laura Uiberreiter* from the university and *Elisabeth Huck*, and *Nikolaus Falschunger* from IQOQI, who help us to focus our time on the scientific work. I would like to thank *Gerhard Hendl* from the electronic workshop, and the mechanical workshop, particularly *Bernhard Öttl*, who was always available for helping us with the realization and design of mechanical parts for the experiment.

In conclusion, I would like to thank the people outside the physics world that were for me as fresh air and helped to get my mind free and fully re-charged to start a new day in the lab. In particular, I would like to thank my german teacher *Boris* from *inlingua*, who always brought our german lesson to life with interesting discussions and deep questions, and all my colleagues from the course, who helped me improve my german. I would like to thank the 2. Bundesliga basketball team from *TI Innsbruck*, including present and former team members, and coaches. Since I joined the team in 2019, they soon became like a second family for me. I am grateful for their support and for all the time spent together in and outside the basketball court. It has been a great honor to be part of this amazing group.

A special thanks goes to my family: my parents, *Dolores* and *Enzo*, and my sister, *Giulia*. If I reached this goal, it is also thanks to their unconditional love. This made me free from the fear of failing and making mistakes, which was an incredible strength for me. I thank them, for all the support they gave me from the first day of school. At every step of my life, they accepted and respected my choices. They did everything possible and beyond that to satisfy my needs, even if this meant staying away from home. Finally, I thank *Gabriele*, who for more than 10 years is central part of my life and confirms every day to be the best choice I ever made. I am thankful for our late-night physics discussions and how we support and motivate each other to give always our best, from small things, such as a simple cooking recipe, to bigger goals, such as a PhD thesis.